Qubits supraconducteurs protégés basés sur des modes à haute impédance

par

Agustin Di Paolo

Thèse présentée au département de physique
en vue de l'obtention du grade de docteur ès science (Ph.D.)

FACULTÉ des SCIENCES
UNIVERSITÉ de SHERBROOKE

Sherbrooke, Québec, Canada, 10 mars 2020

Le 10 mars 2020

le jury a accepté la thèse de Agustin Di Paolo dans sa version finale.

Membres du jury

Professeur Alexandre Blais
Directeur de recherche
Département de physique

Professeur Yves Bérubé-Lauzière
Membre interne
Département de génie électrique et de génie informatique

Professeur Johannes Fink
Membre externe
Institute of Science and Technology Austria

Professeur Denis Morris
Président rapporteur
Département de physique

Sommaire

Les circuits supraconducteurs quantiques constituent une plateforme de pointe pour le traitement de l'information quantique. L'utilisation de ce type de circuits en tant que qubits est en partie motivée par la grande flexibilité avec laquelle ces dispositifs peuvent être fabriqués. Cette flexibilité fait en sorte que les circuits supraconducteurs sont attractifs comme une architecture pour le design des qubits, des amplificateurs, des détecteurs de photons et d'autres dispositifs quantiques.

Le domaine des qubits supraconducteurs est en rapide évolution depuis quelques années, ce qui a conduit à un certain nombre d'avancées majeures, dont la récente démonstration de la suprématie computationnelle quantique. Cela a été possible en partie grâce à l'introduction de l'architecture de l'électrodynamique quantique des circuits, et du qubit transmon. Le qubit transmon est protégé contre la source de bruit la plus nuisible dans les dispositifs mésoscopiques (bruit de charge), tout en possédant un design simple permettant sa mise en l'échelle.

Cependant, malgré le succès retentissant du qubit transmon, d'autres qubits supraconducteurs, tels que le fluxonium et les circuits $0-\pi$, ont en principe le potentiel d'être plus performants. En particulier, le qubit $0-\pi$ utilise des modes de circuit à haute impédance qui sont réalisés en utilisant de grandes inductances (ou superinductances) afin de rendre le système insensible au bruit de flux. Les superinductances, ainsi que les dispositifs de fluxonium et de $0-\pi$ qubit, sont le principal objet de cette thèse.

Dans cette thèse, je présente un nombre de résultats qui sont liés aux propriétés de cohérence, au contrôle quantique et à la description théorique du fluxonium et des qubits $0-\pi$. Chapter 1 présente les concepts théoriques généraux, nécessaires à la compréhension des mes travaux de recherche. Chapter 2 examine de plus près le qubit $0-\pi$ et pose les bases de chapters 3 to 5, qui décrivent trois articles de recherche concernant les propriétés de cohérence, le contrôle quantique et la première réalisation expérimentale du qubit $0-\pi$. Chapter 6 aborde plusieurs aspects liés à la cohérence quantique, au contrôle et à la struc-

ture multimode du qubit de fluxonium, contenus dans deux articles de recherche. L'un de ces articles fait état de la première réalisation d'un qubit de fluxonium intégrant une superinductance de nanofil. Le second article étudie l'application de techniques de réseaux de tenseurs au qubit de fluxonium. Enfin, appendices A and B sont consacrés à deux articles de recherche qui ne sont pas abordés en profondeur dans cette thèse. Appendix A rapporte la réalisation d'un qubit supraconducteur protégé contre le flux et le bruit inspiré du qubit $0-\pi$, tandis que appendix B présente une approche quantique variationnelle de la simulation du couplage ultra-fort entre la lumière et la matière.

Nous notons que les résultats présentés dans cette thèse ont été obtenus en collaboration avec un nombre de groupes académiques et de l'industrie quantique. Les travaux dans chapter 3 et chapter 4 font partie d'une collaboration avec le groupe de recherche de Jens Koch de l'Université Northwestern. Le travail sur chapter 5 est le résultat d'une collaboration entre les groupes de recherche d'Andrew Houck de l'Université de Princeton, de Jens Koch et de David Schuster (Université de Chicago). Le travail sur le qubit de fluxonium de supraconductivité des nanofils, présenté dans chapter 6, est réalisé en collaboration avec le groupe de recherche d'Andrew Houck. Les travaux sur les techniques de réseaux de tenseurs sont réalisés en collaboration avec le groupe de recherche de David Sénénchal et Thomas E. Baker, tous deux des chercheurs de l'Institut quantique de Sherbrooke. L'article dans appendix A est le résultat d'une collaboration avec les groupes de recherche de Michael Gershenson à l'Université Rutgers et de Mathieu T. Bell de l'Université de Boston. Enfin, le travail dans appendix B est le fruit d'une collaboration avec le groupe de recherche d'Ivano Tavernelli d'IBM Q Zürich.

Summary

Superconducting quantum circuits are a leading platform for quantum-information processing. Part of the motivation behind using superconducting circuits as qubits lies in the fact that these devices can be engineered with great flexibility. This also makes superconducting quantum circuits attractive as an architecture for building devices that go beyond qubits, such as amplifiers, photon detectors, among others, and for the exploration of the rich physics of quantum optics in new parameter regimes.

The field of superconducting qubits has gone through a rapid development in the last few years, leading to a number of major breakthroughs including the recent quantum computational supremacy demonstration. This has been possible thanks in part to the introduction of the circuit quantum electrodynamics architecture and the transmon qubit. This qubit combines insensitivity to the most detrimental source of noise in mesoscopic devices (charge noise), with a simple design and scalable fabrication.

However, despite the overwhelming success of the transmon qubit, other implementations of superconducting qubits, such as the fluxonium and the $0-\pi$ circuits, have the potential to perform better. In particular, the $0-\pi$ qubit makes use of high-impedance circuit modes, which are realized using large inductances (or superinductances), in order to render the system insensitive to flux noise. Superinductances, along with the fluxonium and $0-\pi$ qubit devices are the main focus of this thesis.

In this thesis, I present a number of results that are related to the coherence properties, quantum control and theoretical description of the fluxonium and $0-\pi$ qubits. Chapter 1 introduces the theoretical concepts that are required to understand the research papers and develops the concept of noise protection in the context of superconducting quantum circuits. Chapter 2 takes a closer look at the $0-\pi$ qubit and lays the basis for chapters 3 to 5, which describe three research papers studying the coherence properties, quantum control and the first experimental realization of the $0-\pi$ qubit. Chapter 6 addresses several aspects related to the quantum coherence, control and multimode structure of the fluxonium

qubit, including two research papers. One of these papers reports the first realization of a fluxonium qubit integrating a nanowire superinductance. The second paper in chapter 6 studies the application of tensor network techniques to the fluxonium qubit. Finally, appendices A and B are dedicated to two research papers that are not discussed in depth in this thesis. Appendix A reports the realization of a flux-noise-protected superconducting qubit inspired by the $0 - \pi$ qubit, while appendix B presents a variational quantum approach to the simulation of ultrastrong-light matter coupling.

We note that the results presented in this thesis have been done in collaboration with a number of academic and industrial groups. The work in chapter 3 and chapter 4 is part of a collaboration with Jens Koch's research group at Northwestern University. Work in chapter 5 is the result of a collaboration involving the research groups of Andrew Houck from Princeton University, Jens Koch and David Schuster from University of Chicago. The work on the nanowire-superinductance fluxonium qubit reported in chapter 6 is done again in collaboration with Andrew Houck's research group. The work on tensor network techniques reported in the same chapter is done in collaboration with David Sénéchal's research group and Thomas E. Baker, both from the Institut quantique, Sherbrooke. The paper in appendix A is the result of a collaboration with the research groups of Michael Gershenson's at Rutgers University and Mathieu T. Bell's at Boston University. Finally, the work in appendix B is a collaboration with the research group of Ivano Tavernelli at IBM Q Zürich.

Acknowledgments

First of all, I would like to thank Alexandre. Thank you for giving me the opportunity to work with you, and for guiding and supporting me in many aspects in the last 3+ years. Your openness, focus, serenity and willingness to always give to your students is extraordinary and very helpful. Thank you for teaching me what it means to tackle an important problem in Physics and to produce a valuable result through high-quality work. Thank you for sharing your ideas and your perspective, and for connecting me with brilliant students from other research groups through interesting projects. Thank you also for encouraging me to pursue some of my own research ideas.

Secondly, I would like to thank Alexandre's research group, TheSQuaD: Arne, Baptiste, Jérôme, Lucas, Mathieu, Shruti, Udson, Alex C, Alex P, Camille, Catherine, Élie, Joachim, Jonathan and Ross. I greatly enjoyed working side-by-side with you. Coming to the office has always been interesting, motivating and very fun. Thank you for our countless science discussions.

A special thanks goes to Arne Grimsmo, Peter Groszkowski and András Gyenis, with whom I worked very closely on the $0-\pi$ qubit. Working with you has been inspiring, productive and a great pleasure. In the same spirit, I would like to thank the graduate students and postdocs with whom I have collaborated over the past few years, in particular Catherine Leroux and Thomas Baker for our work together and our friendship.

I would also like to thank Karl T and Alex C for developing with me the Q2 project, and Jean B and Jacques C for coaching us on entrepreneurship. None of this would have been possible without the encouragement and support of Christian S-B. Thank you for being always open my ideas and for providing me with critical feedback.

I would like to thank David Poulin and David Sénéchal for being open to many informal discussions and providing me with guidance. Thank you for your inputs and wonderful insights.

Finally, I would like to thank my family and friends from Argentina and my girlfriend Anca. Attending graduate school far from home entailed some challenges that were softened thanks to your support. Nothing of this would have been possible without your kindness, love and encouragement.

One of the most gratifying feelings that the experience of the PhD leaves me is that of having found something that I deeply care about, love doing, and would like to pursue for as long as possible. I thank all of you who made this possible.

Contents

List of Tables

List of Figures

Chapter 1

Superconducting Quantum Circuits

1.1 Introduction to superconducting circuits

Quantum mechanics is traditionally portrayed as a theory describing physical phenomena at the atomic scales of matter. The hallmark of quantum behavior is the existence of quantized observables such as the energy of a particle. Although macroscopic objects are formed by a collection of atoms, quantization effects are not necessarily guaranteed to emerge at this scale. Superconducting qubits exploit a remarkable fact that applies to certain superconducting electrical circuits: macroscopic degrees of freedom, such as the electric charge stored in a capacitor or the magnetic flux through a superconducting loop, can exhibit a discrete energy-level structure analogous to that of a natural atom [1, 2]. Provided a method for controlling such degrees of freedom, superconducting systems in the quantum regime can be used as a solid-state architecture for quantum information processing.

1.1.1 The benefits of superconductivity

Superconducting circuits are fabricated from standard Bardeen-Cooper-Schrieffer (BCS) superconductors, such as Aluminum or Niobium. At temperatures below a critical value T_c, typically in the range of $1 - 10\,\mathrm{K}$, the superconducting state of these materials emerges from an effective electron-electron attractive interaction due to the exchange of virtual phonons [3]. Because of this, electrons with opposite spin and momentum that are close in energy to the Fermi level are bound to form the so-called Cooper pairs. Since each Copper pair is composed by two fermions, the Cooper-pair ensemble obeys bosonic statistics and can condensate to a unique ground state that is separated from quasiparticle excitations by a

large energy gap [4]. The Cooper pair condensate can then be described by a macroscopic wavefunction $\Psi(\boldsymbol{r}, t)$ known as the order parameter, where $\boldsymbol{r}$ is a position vector and t is the time.

Superconductivity allows for the dynamics of a macroscopic number of electrons to be described by a single collective degree of freedom. Thus, the superconducting state represents a dramatic reduction of complexity in the system. Macroscopic quantum effects come into play when excitations of this collective degree of freedom are considered. This is what makes the engineering of artificial atoms from such systems possible. More importantly, superconductivity allows for a dissipationless flow of electrical current (or supercurrent) which corresponds to the transport of Cooper-pairs. The absence of dissipation is a first requirement for demonstrating coherent quantum behavior.

1.1.2 The Josephson junction

Let us now consider a superconducting electrode insulated from the environment and defining a circuit 'island', i.e. a portion of a superconductor that is not galvanically connected to any other part of the circuit. A state $|N\rangle$ of this system is simply specified by the number of Cooper pairs (N) that are contained on the island [4].

By itself, an island is not a very interesting system because the number of Cooper pairs is fixed by the boundary conditions defined by the superconductor. However, by placing two of such electrodes nearby and separating these by a thin layer of insulator, Cooper pairs can coherently tunnel through the insulating barrier, thus modifying the Cooper-pair-number difference between these islands. This system forms what is known as a Josephson junction.

This coherent dynamics is known as Josephson effect and can be described by the tunneling Hamiltonian [5]

$$H = -\frac{E_J}{2} \sum_n |n\rangle\langle n+1| + |n+1\rangle\langle n|, \tag{1.1}$$

where E_J is the Josephson coupling energy and $|n\rangle$, for $n \in (-\infty, \infty)$, labels the Cooper-pair-number difference between the electrodes. Importantly, Eq. (1.1) couples states of different Cooper-pair number and thus allows for the control of such a degree of freedom. Introducing the phase states $|\theta\rangle = (2\pi)^{-1/2} \sum_n e^{-i\theta n} |n\rangle$, where $\theta \in [-\pi, \pi)$, the Eq. (1.1) takes the form

$$H = -E_J \cos\theta. \tag{1.2}$$

The Josephson junction thus implements a nonlinear inductive potential in terms of the phase difference between the two superconducting electrodes that define the junction. The Josephson junction is, in fact, the only known nonlinear and nondissipative circuit element and sits at the core of all superconducting qubit designs.

1.2 Circuit Quantum Electrodynamics

Circuit quantum electrodynamics (circuit QED) is the combination of superconducting qubits and resonators in a single architecture for quantum control and quantum information. This section introduces the circuit QED theory that is used in the research papers that are part of this thesis. Since our work has been done at a single-qubit level, for both $0-\pi$ and fluxonium devices, we limit the description of the circuit-QED theory to readout and single-qubit manipulation. These concepts are also used in the next section to describe the $0-\pi$ qubit in more details.

1.2.1 The invention of circuit QED

About fifteen years ago, a team led by professors Robert Schoelkopf and Steven Girvin at Yale University introduced the Circuit Quantum Electrodynamics architecture (circuit QED). Loosely speaking, circuit QED emerges from the recognition of a natural mapping between quantum optics, describing the interaction between Nature's atoms and photons, and superconducting quantum circuits. Conceived as a flexible test-bed for quantum optics on a chip, as well as a solid-state quantum-computing architecture, this platform has enabled spectacular progress both in the fundamental understanding of light-matter interaction at the quantum level and in quantum information processing. Through the years, circuit QED has served as a powerful toolbox for quantum engineering, with an impact on the development of novel quantum devices and protocols for the generation, filtering, amplification, routing and readout of microwave quantum signals. Circuit QED is now a very active field of research, and one of the leading quantum-computing hardware architectures developed in universities and companies worldwide.

The emergence of a new technology

Circuit QED is the study of cm-wavelength microwave photons interacting with mesoscopic superconducting quantum circuits at dilution-refrigerator temperatures [6, 7]. With dimensions approximately between 1 μm and 1 cm, and operating at frequencies in the microwave-frequency range of 1-20 GHz, these devices are fabricated by depositing aluminum (or niobium) on a low-loss dielectric substrate such as sapphire or silicon, by a process similar to that in the microelectronics industry. As argued above, superconductivity allows for dissipation-free current flow and enables a simple quantum-mechanical description of such circuits as artificial atoms. The existence of atom-like energy levels was predicted by the Nobel Prize winner Anthony J. Leggett and demonstrated in 1985 by the group of John Clark at UC Berkeley, in an experiment conducted by John Martinis and Michel Devoret [8].

The simplest example of a quantum superconducting circuit is a wire of inductance L shunted by a capacitance C, realizing an LC harmonic oscillator. By choosing L and C such that the resonance frequency $1/\sqrt{LC}$ is in the microwave domain, LC circuits play the role of cavities in which microwave photons can be stored. However, in order to realize an artificial atom, some anharmonicity (equivalently, a nonlinearity) is needed. This, again, is provided by superconductivity and more precisely by Josephson junctions.

In the late '90s, Josephson-junction-based artificial atoms were suggested as candidates to realize a quantum bit [9, 10, 11]. In these proposals, the qubit subspace is composed of the ground and first excited states of the artificial atom. Moreover, the anharmonicity of the atom's energy spectrum prevents leakage of the encoded information out of the qubit subspace and facilitates qubit control. These ideas were soon followed by the experimental demonstration of quantum coherence in a superconducting qubit in 1999 by Y. Nakamura and collaborators, then at NEC in Japan [12]. With this milestone achievement, it did not take much longer for the field of superconducting qubits to gain greater popularity.

Josephson junctions were rapidly incorporated in many other qubit designs, including the flux qubit introduced in 1999 at Delft [13], the phase qubit in 2002 at NIST-Boulder [14], and the quantronium, also in 2002, at CEA-Saclay [15]. However, during this time significant challenges remained to be overcome. In particular, superconducting qubits were being measured using non-optimal readout schemes that introduced noise. The search for better strategies powered the next breakthrough.

Circuit QED emerged at Yale in 2003-2004 as an architecture integrating superconducting microwave resonators (cavities) and Josephson quantum circuits (artificial atoms). This platform provided excellent and single-package control and readout solutions for su-

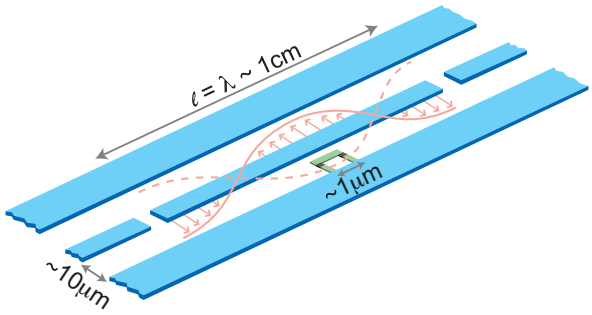

Figure 1.1 The original circuit QED concept showing a superconducting qubit (light green) placed inside a cm-long superconducting coplanar waveguide resonator (light blue), which confines a microwave photon. The electric field associated to this photon is represented by a standing wave (light orange). Qubit control and readout is achieved by voltage driving the resonator through one of its ports. Adapted from [6].

perconducting quantum-information-processing devices [6, 16]. Furthermore, circuit QED realized a mesoscopic analogy to cavity QED (Nobel Prize-winning cavity QED work by Serge Haroche), where optical or microwave photons interact with single atoms in a three-dimensional cavity [17, 18]. Inspired by this correspondence, the work at Yale introduced solid-state analogues to the methods developed in quantum optics. In particular, these techniques included the formalism of master equations (presented below) for the treatment of dissipation and decoherence, this time applied to mesoscopic devices.

A centerpiece of the circuit-QED architecture are the superconducting coplanar waveguide resonators [19] (see Fig. 1.1). Qubits are fabricated in proximity to such resonators, which allow for qubit control and readout. Moreover, the resonators filter the qubits' electromagnetic environment thereby increasing the qubits' coherence times. In 2004, a breakthrough experiment at Yale employed a single qubit in a resonator to demonstrate the coherent exchange of microwave photons between these two systems [7]. This experiment served as a clear evidence of the quantum optical nature of superconducting quantum circuits, opening avenues for new applications bridging the two respective research fields.

As a direct consequence, superconducting quantum devices reemerged as a microwave quantum-optics platform, where the Josephson junction provides the necessary nonlinearity to make microwave photons interact. Furthermore, the two-dimensional confinement of the electromagnetic field in a superconducting chip has allowed circuit-QED setups to display an extraordinarily strong light-matter coupling in flexible geometries. Importantly, these strong, nonlinear engineered interactions have enabled quantum optics to be explored in previously inaccessible regimes by natural atoms.

From a historical point of view, circuit QED was, perhaps, the result of the right combination of an interdisciplinary team and opportune timing. Indeed, while similar ideas were being discussed in a handful of groups, it is worth mentioning that at the time the concept of microwave photons stored in superconducting circuits was not unanimously accepted by the experts [20, 21, 22, 23, 24, 25, 26]. The work at Yale helped to formalize this concept and demonstrate it unambiguously.

Circuit QED strategies for quantum information processing

Circuit QED was recognized early on as a promising platform for quantum information processing. In particular, the work at Yale focused first on implementing the gate-based model for universal quantum computation. The implementation of universal gates in the circuit-QED architecture was originally examined in a setup consisting of two superconducting qubits coupled to a common resonator [6, 16], and is discussed conceptually below.

Single qubits are manipulated by irradiating the resonator with a microwave voltage pulse tuned to the qubit frequency–analogous to shining a laser on an atom. Using this concept, state-of-the-art single-qubit-gate fidelities are now above 99.9% [27]. Regarding two-qubit gates, the resonator plays the role of a communication channel or "quantum bus". As S. Girvin explains, the transmon, which is the simplest of the superconducting qubits (see Sect. 1.5.4), can be thought of as a small antenna with two superconducting halves connected by a Josephson junction [4]. When the qubit is in the excited state, Cooper pairs tunnel back and forth between the two antennae halves. The frequency of this tunneling is in the GHz range and the qubit, which looks like a classical dipole, can radiate (emit) a microwave photon through the resonator. Now in the resonator, the photon can reach a second qubit and be absorbed by it. Thus, this mechanism represents a resonator-mediated two-qubit interaction which forms the basis of quantum two-qubit operations between qubits separated by as much as a centimeter. State-of- the-art two-qubit gate fidelities are now above 99% [27].

Due to a noninvasive scheme known as dispersive readout (described in Sect. 1.2.3) resonator-based qubit measurement is also possible. With state-of-the-art fidelities exceeding 99% [28], this technique is one of the most important achievements of the circuit-QED architecture. Indeed, recall that the low performance of early readout protocols was one of the main motivations that led to the development of circuit QED. As a result, the dispersive readout has offered a fast, high-fidelity and relatively simple alternative, where the qubit state is revealed by detecting a shift of the resonator frequency.

The availability and experimental demonstration of a complete set of high-fidelity universal quantum operations have enabled circuit QED to become one of the leading and most developed quantum-information-processing (QIP) platforms at the moment. Furthermore, the generality of such control and readout protocols has gathered attention from developers of solid-state architectures beyond superconducting qubits. For example, circuit QED is now used with spin qubits in semiconductors [29], and might potentially serve to manipulate and readout Majorana-qubit devices [30]. In the context of superconducting qubits, the circuit QED architecture has recently enabled the demonstration of quantum computational supremacy [31], likely one of the most quantum-computing breakthroughs so far. However, important challenges remain to be solved in order to realize a truly fault-tolerant QIP architecture, some of these being the focus of this thesis.

1.2.2 Circuit QED: Superconducting qubits coupled to LC resonators

As illustrated in Fig. 1.1, a typical circuit QED setup requires a qubit to be fabricated in proximity of a transmission-line [6, 7] (or 3D [32, 33]) superconducting resonator. Close to the its resonance frequency $\omega_r = 1/\sqrt{LC}$, which lies typically in the range $\omega_r/2\pi \in [4, 12]$ GHz, the resonator can be described as a quantum harmonic oscillator with Hamiltonian

$$H_r = \hbar\omega_r a^\dagger a, \tag{1.3}$$

where $a^\dagger$ and a are photon creation and annihilation operators, respectively.

The resonator can be coupled to the qubit capacitively, inductively, or by means of a nonlinear circuit element such as a Josephson junction. Here we focus on the case of capacitive coupling, which is also the most common scenario in circuit-QED setups. In this case, the qubit couples to the resonator voltage operator $V_r = V_{\text{zpf}}(a + a^\dagger)$, where $V_{\text{zpf}} \propto \omega_r\sqrt{Z_r}$ denotes the amplitude of the zero-point fluctuations of the resonator voltage and Z_r is the resonator impedance. An important advantage of the two-dimensional circuit QED setup is that the vacuum energy of the resonator is stored in a small volume, leading to large zero-point fluctuations of the electric field that result in a large qubit-resonator coupling [6].

The qubit-resonator interaction Hamiltonian can generally be written as

$$H_{\text{int}} = 2e\beta\, n\, V_r, \tag{1.4}$$

where $\beta \ll 1$ is a capacitive coupling coefficient and n is the (dimensionless) charge operator of the qubit. As we discuss below, readout, single- and two-qubit gates can be enabled

by the resonator by driving this device appropriately. A microwave tone applied to the resonator can be described by the drive Hamiltonian

$$H_{\text{drive}} = \mathcal{E}^*(t)\, a + \mathcal{E}(t)\, a^\dagger, \tag{1.5}$$

where $\mathcal{E}(t) = \mathcal{A}(t)\exp(-i\omega_d t)$ is a drive pulse of amplitude $\mathcal{A}(t)$ (with units of energy) and frequency ω_d.

1.2.3 Dispersive control and readout of multilevel artificial atoms

The dispersive limit of circuit QED is a regime of operation where the qubit-resonator coupling Hamiltonian of Eq. (1.4) can be perturbatively diagonalized, provided that the effective coupling strength is significantly smaller than the frequency detuning between such systems [6, 34]. For the devices considered in this thesis, the multilevel structure of the artificial atom plays an important role in the parameters that define the dispersive Hamiltonian. For this reason, this section follows closely the formulation of the dispersive theory of Ref. [35].

Since the coupling constant between qubit and resonator is assumed to be small compared to the system frequencies, we start by diagonalizing the qubit in absence of coupling to the resonator. We denote the qubit eigenstates by $|\psi_k\rangle$ with frequencies ω_k. Introducing the notation $\sigma_{kk'} = |\psi_k\rangle\langle\psi_{k'}|$, the qubit-resonator Hamiltonian can be written as

$$H/\hbar = \sum_{k=0}^{M} \omega_k\, \sigma_{kk} + \omega_r\, a^\dagger a + \sum_{k,k'=0}^{M} g_{kk'}\, \sigma_{kk'}\, (a + a^\dagger), \tag{1.6}$$

where $g_{kk'} = 2e\beta\langle\psi_k|n|\psi_{k'}\rangle V_{\text{zpf}}/\hbar$. We moreover assume that the number of levels M considered in Eq. (1.6) is enough to accurately describe the low-frequency physics of the qubit-resonator system. The basic idea behind a dispersive theory is to introduce a canonical transformation, known as Schrieffer-Wolff transformation, that diagonalizes Eq. (1.6) up to a sufficient order in the coupling strength. Equivalently, this is done by transforming the qubit and resonator states and operators to a dressed basis. The Schrieffer-Wolff transformation is defined by an anti-hermitian generator S, such that the transformed Hamiltonian takes the form [36]

$$H'/\hbar = e^{-S} H e^{S} = \sum_{j=0}^{\infty} \frac{1}{j!} [H, S]_j, \tag{1.7}$$

where $[H, S]_j = [[H, S]_{j-1}, S]$ and $[H, S]_0 = H$. S can now be expanded as a power series in $g_{kk'}$, allowing us to diagonalize H up to a desired order in the interaction. Since here we are

interested in the result up to second order in the coupling strength, we now assume that S is linear in $g_{kk'}$. Splitting Eq. (1.6) as $H = H_0 + H_{\text{int}}$, where $H_{\text{int}} = \sum_{k,k'=0}^{M} g_{kk'}\,\sigma_{kk'}\,(a + a^\dagger)$, and retaining terms in Eq. (1.7) that are of order $|g_{kk'}|^2$ at most, we arrive at

$$H'/\hbar \simeq H_0 + H_{\text{int}} + [H_0, S] + \frac{1}{2}[[H_0, S], S]. \tag{1.8}$$

By choosing S such that $H_{\text{int}} + [H_0, S] = 0$ to remove all first-order terms in Eq. (1.8), one finds the generator [35]

$$S = -\sum_{k,k'=0}^{M} \left[\frac{g_{kk'}}{(\omega_k - \omega_{k'}) - \omega_r}\, a - \frac{g_{k'k}}{(\omega_{k'} - \omega_k) - \omega_r}\, a^\dagger\right]\sigma_{kk'}. \tag{1.9}$$

After this, Eq. (1.8) takes the form

$$H'/\hbar \simeq H_0 + \sum_{k,k'=0}^{M} \Big[(v_{kk'} - v_{k'k})a^\dagger a + v_{kk'}\Big]\sigma_{kk}, \tag{1.10}$$

where $v_{kk'} = |g_{kk'}|^2/[(\omega_k - \omega_{k'}) - \omega_r]$. Note that, as desired, this approximate Hamiltonian is now diagonal. It is useful to rewrite Eq. (1.10) as

$$H'/\hbar \simeq \sum_{k=0}^{M} (\omega_k + \Lambda_k)\,\sigma_{kk} + \omega_r\, a^\dagger a + \sum_{k=0}^{M} \chi_k\, a^\dagger a\, \sigma_{kk}, \tag{1.11}$$

where we have defined the constants $\Lambda_k = \sum_{k'=0}^{M} v_{kk'}$ and $\chi_k = \sum_{k'=0}^{M}(v_{kk'} - v_{k'k})$ [35]. The coefficients Λ_k are called Lamb shifts while χ_k are the dispersive shifts. The latter can be seen as a frequency shift of the cavity mode that depends on the state of the qubit, $\omega_r \to \omega_r + \chi_k\,\sigma_{kk}$ for the qubit being in the state $|\psi_k\rangle$, or as a frequency shift of the qubit states that depends on the number of photons in the resonator $\omega_k \to \omega_k + \chi_k\, a^\dagger a$. The former interpretation is the basis for performing the readout of a superconducting qubit coupled to a LC resonator: by detecting a change in the frequency of the LC resonator as a consequence of the qubit-state-dependent dispersive shift, one can thus infer the state of the qubit.

Fig. 1.2 provides an interpretation of Eq. (1.11) in terms of the level structure of the qubit-resonator system, which are labeled according to the resonator's photon number (horizontal axis) and the qubit state (vertical axis). Solid (horizontal) lines correspond to the bare energy levels of the system without interaction. Diagonal dashed lines represent the coupling between the bare energy levels corresponding to states with different photon numbers. A priori, level coupling does not obey any particular selection rule with respect to

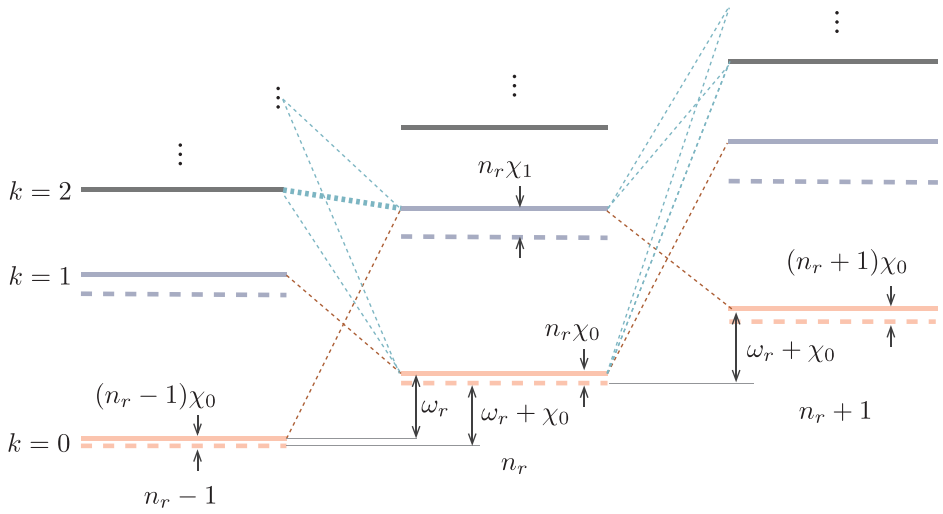

Figure 1.2 Schematic illustration of the dispersive Hamiltonian. Solid (dashed) horizontal lines correspond to the bare (dressed) qubit levels. Diagonal dashed lines represent coupling between bare states with different photon number. Adapted from Ref. [35].

the qubit transitions. Dashed (horizontal) lines are obtained after the qubit-resonator coupling is included to second order, resulting in a dispersive shift of the qubit energy levels that grows linearly with photon number.

1.2.4 Qubit readout

Qubit readout is done by driving the resonator close to its resonance frequency while monitoring the amplitude and phase of the reflected signal [6]. Denoting the complex reflection amplitude of a microwave tone of frequency ω_d by $\Gamma(\omega_d)$, it can be shown that the phase $\varphi(\omega_d) = \text{Arg}\ [\Gamma(\omega_d)]$ of the reflected signal is given by $\varphi(\omega_d) = 2\arctan\left[2Q_{\text{ext}}\frac{\omega_d-\omega_r}{\omega_r}\right]$, where Q_{ext} is the external quality factor of the resonator due to coupling to the measurement circuitry [37]. Assuming that the qubit state at the time of the measurement is $|\psi_k\rangle$, one has $\omega_r \to \omega_r + \chi_k$, resulting in a qubit-state dependence of the phase of the reflected signal as $\varphi(\omega_d) \to \varphi_k(\omega_d)$, where

$$\varphi_k(\omega_d) \simeq 2\arctan\left[2Q_{\text{ext}}\frac{\omega_d - \omega_r - \chi_k}{\omega_r}\right], \tag{1.12}$$

to leading order in χ_k. Setting $\omega_d \simeq \omega_r \gg \chi_k$, and assuming a low Q_{ext} for fast readout, one has $\varphi_k(\omega_r) \propto \chi_k$, implying that the phase of the reflected signal is a direct measurement of the dispersive shift. The total phase difference $\varphi_0(\omega_r) - \varphi_1(\omega_r) \propto (\chi_0 - \chi_1)$ is what allows

us to distinguish between the two qubit states. The optimal choice of Q_{ext} for maximal discrimination (best signal-to-noise ratio) is found to be $\omega_r/2|\chi_0 - \chi_1|$ [38, 28].

1.2.5 Two-tone spectroscopy

A qubit dispersively coupled to a resonator can be probed by a technique called two-tone spectroscopy [39, 40]. In this case, the reflection (or transmission) of the readout resonator, which is driven at the frequency $\omega_d \simeq \omega_r$ is monitored while a second microwave tone of frequency ω_s is swept. Importantly, ω_s is largely detuned from the resonator frequency. In such conditions, this additional drive can simply be seen as a voltage-drive applied on the qubit, which takes the form [41]

$$H'_{\text{drive}} = \mathcal{E}(t) \sum_{kk'} \frac{2\omega_r g_{kk'}}{(\omega_k - \omega_{k'})^2 - \omega_r^2} \sigma_{kk'}. \tag{1.13}$$

This expression follows from the action of the dispersive transformation on the drive Hamiltonian $\mathcal{E}(t)(a + a^\dagger)$.

The purpose of the additional pump tone is to drive a transition between two qubit levels k and k' as ω_s approaches the transition frequency $\omega_{kk'}$. In that case, the phase of the reflected microwave tone of frequency ω_r oscillates between $\varphi_k(\omega_r)$ and $\varphi_l(\omega_r)$, corresponding to an average value of $[\varphi_k(\omega_r) + \varphi_l(\omega_r)]/2$, which is (in principle) different for each qubit transition. The phase shift of the reflected probe tone with respect to a reference indicates when the pump tone has hit a qubit transition. This allows us to map the qubit energy spectrum [35].

1.3 Superconducting circuit quantization

Superconducting quantum circuits integrate circuit elements such as capacitors and inductors, and Josephson junctions. This section provides a systematic formalism to treat the unitary dynamics of such devices.

The theoretical tools developed to describe superconducting quantum circuits have been perfected over many years, up to the point where the underlying superconductivity does not need to be taken into account explicitly. The result is a field theory describing interacting bosonic degrees of freedom associated with the phase of the superconducting order parameter in different (independent) portions of a circuit.

Although there exist a number of methods to derive the Hamiltonian of a superconducting circuit [5, 42, 43, 44], here we follow the most widespread approach due to Michel Devoret [5]. In particular, we describe what is known as the 'method of nodes'. To this end, let us consider an arbitrary superconducting circuit. One first needs to define a spanning tree $\mathcal{ST}$ for the circuit, which consist of a reference node (or ground) and a set of circuit branches that connect the ground to every other circuit node. Moreover, a node flux variable of the form

$$\Phi_i = \int_{-\infty}^{t} V_i(t')dt', \tag{1.14}$$

is defined for the ith circuit node, where $V_i(t)$ is the node voltage with respect to ground at the time t. Note that $\mathcal{ST}$ is not unique, and different choices for the spanning tree are related by gauge transformations.

The energy of a circuit element with two terminals can be expressed in terms of the voltage-difference across its terminals or the current flowing through this circuit component. For this reason, it is convenient to introduce the branch fluxes

$$\begin{aligned} \Phi_{\mathrm{b}\in\mathcal{ST}} &= \Phi_i - \Phi_j \\ \Phi_{\mathrm{b}\in\overline{\mathcal{ST}}} &= \Phi_i - \Phi_j + \Phi^{\mathrm{b}}_{\mathrm{ext}}, \end{aligned} \tag{1.15}$$

where the subindex b denotes a particular circuit branch defined by the node fluxes Φ_i and Φ_j, $\overline{\mathcal{ST}}$ is the complement of $\mathcal{ST}$, and $\Phi^{\mathrm{b}}_{\mathrm{ext}}$ is an external magnetic flux that is added if the flux branch b does not belong to the spanning tree.

Let $T(\dot{\mathbf{\Phi}}, \dot{\mathbf{\Phi}}_{\mathrm{ext}})$ and $U(\mathbf{\Phi}, \mathbf{\Phi}_{\mathrm{ext}})$ denote, respectively, the kinetic- and potential-energy terms, where $\mathbf{\Phi}$ and $\mathbf{\Phi}_{\mathrm{ext}}$ is a vector notation for the node flux operators and external magnetic-flux biases. Then, the Lagrangian of the circuit can be written as

$$L(\dot{\mathbf{\Phi}}, \mathbf{\Phi}) = T(\dot{\mathbf{\Phi}}, \dot{\mathbf{\Phi}}_{\mathrm{ext}}) - U(\mathbf{\Phi}, \mathbf{\Phi}_{\mathrm{ext}}), \tag{1.16}$$

where $T(\dot{\mathbf{\Phi}}, \dot{\mathbf{\Phi}}_{\mathrm{ext}})$ and $U(\mathbf{\Phi}, \mathbf{\Phi}_{\mathrm{ext}})$ follow straightforwardly from the addition of the contributions from all circuit elements: if Φ_{b} is a branch operator, the contribution to the kinetic or potential energies in Eq. (1.16) is given by $C_{\mathrm{b}}\dot{\Phi}^2_{\mathrm{b}}/2$, $\Phi^2_{\mathrm{b}}/2L_{\mathrm{b}}$ or $-E_{J_{\mathrm{b}}}\cos(2\pi\Phi_{\mathrm{b}}/\Phi_0)$, depending on whether the circuit element on this branch is a capacitor (of capacitance C_{b}), an inductor (of inductance L_{b}) or a Josephson junction (of Josephson energy $E_{J_{\mathrm{b}}}$), respectively. In practice, it is also useful to consider the effect of external voltage sources coupled capacitively to the circuit. A voltage source of strength V_i connected to the ith node of the circuit by a gate capacitance C_g is modeled by the kinetic-energy term $C_g(\dot{\Phi}_i - V_i)^2/2$ that needs to be added to Eq. (1.16).

The Hamiltonian of the circuit is then obtained by performing a Legendre transformation on Eq. (1.16). Defining the conjugate charge operators $q_i = \partial L(\dot{\mathbf{\Phi}}, \mathbf{\Phi})/\dot{\Phi}_i$, the circuit Hamiltonian takes the form

$$H(\boldsymbol{q}, \mathbf{\Phi}) = \boldsymbol{q} \cdot \dot{\mathbf{\Phi}} - L(\mathbf{\Phi}, \mathbf{\Phi}_{\text{ext}}), \tag{1.17}$$

where $\boldsymbol{q} \cdot \dot{\mathbf{\Phi}}$ is understood as a scalar product between two vector variables. A quantum theory for the circuit is then defined by promoting flux and charge variables to quantum operators satisfying the commutation relations $[\Phi_i, q_j] = i\hbar\delta_{ij}$.

1.4 Accounting for dissipation

The previous section provided a method to derive the Hamiltonian of a circuit, describing the unitary dynamics of this system. However, a superconducting circuit is always surrounded by an environment. From the point of view of the system, the interaction with this environment leads to incoherent dynamics. The Hamiltonian formulation of the previous section is not enough to describe this situation, and needs to be complemented by the techniques described in this section.

Notably, most of the experiments performed with superconducting quantum devices admit a relatively simple description of dissipation, specified by a Lindblad-form master equation [6, 7]. For this reason, here we provide a derivation of a general Lindblad master equation. The procedure reveals the assumptions which are implicit in this formulation and allows us to introduce the concepts related to the various decoherence mechanisms that are present in superconducting devices. These concepts are analyzed in more detail in the papers presented in this thesis.

We are particularly interested in describing decoherence effects which are not related to the quality factors of the circuit components of a given superconducting circuit. In other words, we do not consider effects such as dielectric losses which can be modeled phenomenologically with a similar formalism (see, for instance, Ref. [45]). We thus consider that the environment couples to the system via a parameter λ that enters in the circuit Hamiltonian, such as an externally applied magnetic flux. More precisely, the environment can be thought as contributing to the external bias with a noise operator $\delta\lambda$, i.e. $\lambda = \lambda_0 + \delta\lambda$, where λ_0 is a controlled parameter defining the circuit's operating point.

Under the assumption of weak system-bath coupling, the circuit Hamiltonian can be approximated by [46]

$$H(\lambda) \simeq H(\lambda_0) + \partial_\lambda H|_{\lambda_0} \times \delta\lambda, \tag{1.18}$$

to first order in the noise operator.

While the first term in the r.h.s of Eq. (1.18) corresponds to the (noiseless) circuit Hamiltonian, the second term is a perturbation that represents the system-bath coupling. The term $\partial_\lambda H|_{\lambda_0}$ in Eq. (1.18) can be seen as a measure of the sensitivity of the system to fluctuations of λ.

1.4.1 Quantum noise

We now proceed with the derivation of the Lindblad master equation in the interaction frame, which follows from the trace of the bath degrees of freedom in the integro-differential equation [47]

$$\partial_t \rho(t) = -\frac{1}{\hbar^2} \int_0^t d\tau \, \mathrm{tr}_B[H_{\mathrm{int}}(t), [H_{\mathrm{int}}(t-\tau), \rho(t-\tau) \otimes \rho_B]], \tag{1.19}$$

where $\rho(t)$ and ρ_B are, respectively, the (reduced) system and bath density matrices, $H_{\mathrm{int}}(t) = \partial_\lambda H|_{\lambda_0}(t) \times \delta\lambda(t)$ is the system-bath interaction and tr_B is a trace operation over the bath degrees of freedom. Note that Eq. (1.19) assumes that the system-bath density matrix is separable at all times, preventing any entanglement between these systems.

Assuming that the bath correlation function $\mathrm{tr}_B[\rho_B \delta\lambda(t)\delta\lambda(t')]$ is peaked at $t - t' = 0$ and decays very rapidly with $\tau = |t - t'|$, then $\rho(t-\tau)$ in Eq. (1.19) can be approximated by $\rho(t)$ with negligible error. This step is known as the Markov approximation, and it is highly convenient because it leads to a first-order differential equation for $\rho(t)$. Because of this, knowing the initial condition $\rho(0) = \rho_0$ is enough to calculate the state of the system at $t > 0$. Moreover, the assumption of short bath correlation times allows us to extend the time integral in Eq. (1.19) to infinitely negative times with also small error. Taking this into consideration, Eq. (1.19) becomes

$$\partial_t \rho(t) = -\frac{1}{\hbar^2} \int_0^t d\tau \, \mathrm{tr}_B[H_{\mathrm{int}}(t), [H_{\mathrm{int}}(t-\tau), \rho(t) \otimes \rho_B]], \tag{1.20}$$

where the upper limit of the integral may be extended as $t \to \infty$ (see below).

Implicit in this treatment is the assumption of weak system-bath coupling. This also means that dissipation occurs in the eigenbasis of the system. This is a valid assump-

tion in most cases although it can break down if the system is strongly driven [48, 49] or strongly coupled to other systems [50]. For weak system-bath coupling, it is useful to project Eq. (1.20) in the eigenbasis $\{|\psi_k\rangle\}$ of the system, leading to

$$\begin{aligned}\partial_t\rho(t) = -\frac{1}{\hbar^2}\int_0^t d\tau \sum_{k,k'}\sum_{l,l'}\partial_\lambda H|^{kk'}_{\lambda_0}\,\partial_\lambda H|^{ll'}_{\lambda_0}\, e^{-i(\omega_{ll'}+\omega_{kk'})t}e^{i\omega_{kk'}\tau} \\ \times \mathrm{tr}_B[|\psi_l\rangle\langle\psi_{l'}|\delta\lambda(t), [|\psi_k\rangle\langle\psi_{k'}|\delta\lambda(t-\tau), \rho(t)\otimes\rho_B]],\end{aligned} \tag{1.21}$$

where we have defined the matrix elements $\partial_\lambda H|^{kk'}_{\lambda_0} = \langle\psi_k|\partial_\lambda H|_{\lambda_0}|\psi_{k'}\rangle$ and the transition frequencies $\omega_{kk'} = \omega_{k'} - \omega_k$ with $H(\lambda_0)|\psi_k\rangle = \hbar\omega_k|\psi_k\rangle$.

Tracing out the bath degrees of freedom leads to the so-called Bloch-Redfield master equation [51]. This formulation has, however, a number of disadvantages that can potentially result in unphysical dissipation channels. Thus, for practical purposes, here we perform a secular (or rotating-wave) approximation that discards terms for which $\omega_{ll'} + \omega_{kk'} \neq 0$. As shown below, this approximation reduces Eq. (1.21) to a Lindblad-form master equation that is accurate enough to describe most superconducting-qubit systems.

Assuming that the qubit has a set of nondegenerate energy transitions, this approximation is equivalent to the conditions $l = k'$ and $l' = k$ for $\omega_{kk'} \neq 0$, and $l = l'$ for $\omega_{kk'} = 0$, after which Eq. (1.21) becomes

$$\begin{aligned}\partial_t\rho = &-\frac{1}{\hbar^2}\sum_{k'>k}\int_0^t d\tau\,\partial_\lambda H|^{kk'}_{\lambda_0}\,\partial_\lambda H|^{k'k}_{\lambda_0}\, e^{i\omega_{kk'}\tau}\mathrm{tr}_B[|\psi_{k'}\rangle\langle\psi_k|\delta\lambda(t), [|\psi_k\rangle\langle\psi_{k'}|\delta\lambda(t-\tau), \rho\otimes\rho_B]] \\ &-\frac{1}{\hbar^2}\sum_{k'>k}\int_0^t d\tau\,\partial_\lambda H|^{k'k}_{\lambda_0}\,\partial_\lambda H|^{kk'}_{\lambda_0}\, e^{-i\omega_{kk'}\tau}\mathrm{tr}_B[|\psi_k\rangle\langle\psi_{k'}|\delta\lambda(t), [|\psi_{k'}\rangle\langle\psi_k|\delta\lambda(t-\tau), \rho\otimes\rho_B]] \\ &-\frac{1}{\hbar^2}\sum_{k,l}\int_0^t d\tau\,\partial_\lambda H|^{kk}_{\lambda_0}\,\partial_\lambda H|^{ll}_{\lambda_0}\,\mathrm{tr}_B[|\psi_l\rangle\langle\psi_l|\delta\lambda(t), [|\psi_k\rangle\langle\psi_k|\delta\lambda(t-\tau), \rho\otimes\rho_B]],\end{aligned} \tag{1.22}$$

where we have rearranged terms such that $\omega_{kk'} > 0$ and defined $\rho \equiv \rho(t)$.

Introducing the noise spectral density $S_\lambda[\omega]$ for the quantum noise $\delta\lambda$, the bath correlation function can be written as [5]

$$\mathrm{tr}_B[\rho_B\,\delta\lambda(t)\delta\lambda(t')] = \frac{1}{2\pi}\int_{-\infty}^{\infty} d\omega\, S_\lambda[\omega]\, e^{-i\omega(t-t')}. \tag{1.23}$$

It then follows that $\int_0^\infty d\tau e^{\pm i\omega_{kk'}\tau}\mathrm{tr}_B[\rho_B\,\delta\lambda(t)\delta\lambda(t-\tau)] = S_\lambda[\pm\omega_{kk'}]/2$ and, analogously, $\int_0^\infty d\tau e^{\pm i\omega_{kk'}\tau}\mathrm{tr}_B[\rho_B\,\delta\lambda(t-\tau)\delta\lambda(t)] = S_\lambda[\mp\omega_{kk'}]/2$, where we have taken the limit $t\to\infty$ in the integral. Here, we have used the relation $\int_0^\infty d\tau e^{i\omega\tau} = \pi\delta(\omega) - \mathcal{P}(1/i\omega)$ and omitted

the principal value that does not contribute to the decoherence rates. We have moreover assumed that $S_\lambda[\omega]$ is bounded. This hypothesis will be revised below in the context of $1/f$ classical noise.

Making use of the above integrals and the projector operators $\sigma_{kk'} = |\psi_k\rangle\langle\psi_{k'}|$, we arrive at a master equation of the form

$$\begin{aligned}\partial_t\rho = &\sum_{k'>k}\Big\{\Gamma_\downarrow^{kk'}\,\mathcal{D}[\sigma_{kk'}]\,\rho + \Gamma_\uparrow^{kk'}\,\mathcal{D}[\sigma_{k'k}]\,\rho\Big\}\\ &+\sum_k \Gamma_\varphi^{kk}\,\mathcal{D}[\sigma_{kk}]\,\rho + \sum_{k>l}\Gamma_\varphi^{kl}\Big\{\tilde{\mathcal{D}}[\sigma_{kk},\sigma_{ll}]\,\rho + \tilde{\mathcal{D}}[\sigma_{ll},\sigma_{kk}]\,\rho\Big\},\end{aligned} \tag{1.24}$$

where we have defined the rates

$$\begin{aligned}\Gamma_\downarrow^{kk'} &= |\partial_\lambda H|_{\lambda_0}^{kk'}|^2\, S_\lambda[\omega_{kk'}]/\hbar^2\\ \Gamma_\uparrow^{kk'} &= |\partial_\lambda H|_{\lambda_0}^{kk'}|^2\, S_\lambda[-\omega_{kk'}]/\hbar^2\\ \Gamma_\varphi^{kl} &= \partial_\lambda H|_{\lambda_0}^{kk}\,\partial_\lambda H|_{\lambda_0}^{ll}\, S_\lambda[0]/\hbar^2,\end{aligned} \tag{1.25}$$

along with the standard ($\mathcal{D}[x]\rho = x\rho x^\dagger - \{x^\dagger x,\rho\}$) and generalized ($\tilde{\mathcal{D}}[x,y]\rho = x\rho y^\dagger - \{y^\dagger x,\rho\}$) dissipator superoperators. Note that the latter can be put in terms of the former by noticing that $\tilde{\mathcal{D}}[\sigma_{kk},\sigma_{ll}] + \tilde{\mathcal{D}}[\sigma_{ll},\sigma_{kk}] = \mathcal{D}[\sigma_{kk}+\sigma_{ll}] - \mathcal{D}[\sigma_{kk}] - \mathcal{D}[\sigma_{ll}]$. As shown in Sect. 1.4.3, $\Gamma_\downarrow^{kk'}$ and $\Gamma_\uparrow^{kk'}$ are, respectively, the rates for incoherent relaxation ($k' \to k$) and excitation ($k \to k'$) processes, while Γ_φ^{kk}, Γ_φ^{ll} and Γ_φ^{kl} contribute to decay of the density matrix coherence ρ_{kl}.

Having derived Eq. (1.24), we now present a qualitative analysis of the decoherence rates in Eq. (1.25). In particular, we consider dissipation due to coupling to an electromagnetic environment modeled as a resistive load connected to the circuit of interest. Notably, a dissipative load admits a conservative representation as an infinite collection of harmonic oscillators [5]. In this representation, known as the Caldeira-Leggett model, dissipation is a consequence of an energy exchange from the system to the load, which cannot be reversed due to the infinite extension of the load that can be modeled as a semi-infinite transmission line.

From an electrical point of view, the load is represented by a circuit component with impedance $Z[\omega]$ or admittance $Y[\omega] = (Z[\omega])^{-1}$, where $\mathrm{Re}[Z[\omega]] > 0$. The system can be connected to the load by a coupling capacitor or a coupling (or mutual) inductance. In the first case, $\delta\lambda \propto V$ where V is an environment voltage operator with noise spectral density $S_V[\omega]$ and thus $S_\lambda[\omega] \propto S_V[\omega]$. For instance, this situation arises when analyzing the effect of charge noise. In the second case, $\delta\lambda \propto I$ where I is a current operator for

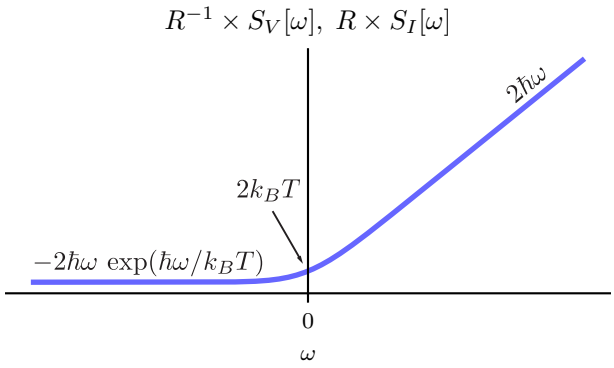

Figure 1.3 Asymptotic behavior of the (quantum) voltage and current noise spectral densities for a frequency-independent resistive load $R = \mathrm{Re}[Z[\omega]]$.

the environment with noise spectral density $S_I[\omega]$ and thus $S_\lambda[\omega] \propto S_I[\omega]$. Flux noise is modeled by the latter. Assuming that the load is at thermal equilibrium at temperature T, one finds [5]

$$\begin{aligned} S_V[\omega] &= \hbar\omega \left[\coth\left(\frac{\hbar\omega}{2k_BT}\right) + 1 \right] \mathrm{Re}\Big[Z[\omega]\Big] \\ S_I[\omega] &= \hbar\omega \left[\coth\left(\frac{\hbar\omega}{2k_BT}\right) + 1 \right] \mathrm{Re}\Big[Y[\omega]\Big]. \end{aligned} \tag{1.26}$$

In these expressions, the structure of the environment is contained in the impedance function. For this reason, Eq. (1.26) can be used to describe several sources of dissipation in the system, including, for instance, quasiparticle losses [45].

Fig. 1.3 shows the noise spectral densities of Eq. (1.26) assuming a frequency-independent load resistance $R = \mathrm{Re}[Z[\omega]]$. According to Eq. (1.25), we observe that the rate of relaxation processes of the form $k' \to k < k'$ ($\propto S_\lambda[\omega_{kk'}]$) scales linearly with the frequency of the $k \to k'$ qubit transition, while excitation processes $k \to k' > k$ ($\propto S_\lambda[-\omega_{kk'}]$) are exponentially reduced with $\omega_{kk'}$. Moreover, the rate of dephasing processes is purely determined by the temperature of the bath. This information will be used below to justify the intrinsic noise protection of certain superconducting qubits.

1.4.2 $1/f$ noise

It follows from the previous section that electromagnetic noise can have a significant contribution to the rate of incoherent relaxation processes of a circuit. In comparison, excitation

and pure dephasing rates are small at milliKelvin temperatures due to the negligible amplitude of $S_\lambda[-\omega_{kk'}]$ for $\omega_{kk'} \geq 0$. Indeed, pure-dephasing rates of superconducting qubits are usually dominated by other sources of noise. The dominant example of a noise source with large spectral weight at low frequencies is known as $1/f$ noise [52, 53, 54]. While it is typically regarded as a pure-dephasing mechanism, there exist some experimental evidence of the impact of $1/f$ on the relaxation rates of low-frequency devices [55].

The treatment of $1/f$ noise differs from the one of the previous section because the noise spectral density, which has the form

$$S_\lambda^{1/f}[\omega] = \frac{A_\lambda^2}{|\omega|/2\pi}, \tag{1.27}$$

is not bounded for $\omega \to 0$. Here, A_λ is the $1/f$ noise amplitude, which depends on the noise source (charge or flux) [56]. In contrast to Eq. (1.26), the even symmetry of Eq. (1.27) reveals that $1/f$ is a classical source of noise, and thus $\delta\lambda$ in Eq. (1.18) should be treated as a classical random process. It must be stressed that Eq. (1.27) is an approximation to the spectral densities measured in the laboratory, which can scale as $|\omega|^{-\mu}$ with $\mu \in [0.6, 1.3]$ [55, 56, 57].

We note that the rates $\Gamma_\downarrow^{kk'}$ and $\Gamma_\uparrow^{kk'}$ in Eq. (1.25) are still well defined for $1/f$ noise because the divergent behavior of Eq. (1.27) occurs only at zero frequency. For this reason, here we present a new theory for estimating the pure-dephasing rates due to $1/f$ noise.

Because pure dephasing probes the noise spectrum at low frequencies, we present here an approach to estimate the rate of this process in the presence of $1/f$ noise. This original derivation exploits a simple, yet interesting mathematical fact. Using Eq. (1.23) and Eq. (1.27), we find that

$$\int_0^t d\tau \, \mathrm{tr}_B[\rho_B \, \delta\lambda(t)\delta\lambda(t-\tau)] \overset{1/f \text{ noise}}{=} \lim_{\omega_{\mathrm{ir}} \to 0} -2A_\lambda^2 \int_0^t d\tau \, \mathrm{Ci}(\omega_{\mathrm{ir}}\tau), \tag{1.28}$$

where $\mathrm{Ci}(y) = -\int_y^\infty dx \, x^{-1} \cos x$ is the so-called cosine integral. Here, ω_{ir} is an infrared frequency cutoff typically in the order of $2\pi \times 1$ Hz that is introduced to regularize the cosine integral and is also motivated by physical reasons. Note that the upper integration limit in the l.h.s of Eq. (1.28) has not been extended to infinity. This is done in order to capture the nonexponential decay of the density matrix coherences that is typical for $1/f$ noise.

We now assume that the time t in which one is interested in computing the time-evolution of the density matrix is small compared to the timescale set by $\omega_{\mathrm{ir}}^{-1}$. This is a

reasonable assumption based on the pure-dephasing coherence times measured for superconducting devices. Under these conditions, we can make use of a series expansion for the cosine integral

$$\mathrm{Ci}(y) = \gamma + \log(y) + \sum_{k=1}^{\infty} \frac{(-y^2)^k}{2k(2k)!}, \tag{1.29}$$

where $y = \omega_{\mathrm{ir}}\tau$ and $\gamma \simeq 0.58$ is the Euler constant. Assuming that $y \ll 1$, we arrive at the approximate expression

$$\int_0^t d\tau\, \mathrm{tr}_B[\rho_B\, \delta\lambda(t)\delta\lambda(t-\tau)] \overset{1/f\ \mathrm{noise}}{\simeq} 2A_\lambda^2 \times t \times [(1-\gamma) - \log(\omega_{\mathrm{ir}} t)]. \tag{1.30}$$

Taking Eq. (1.30) into consideration, Eq. (1.22) results in a master equation formally identical to Eq. (1.24), with a set of decoherence rates given by

$$\begin{aligned} \Gamma_{\downarrow}^{kk'} &= |\partial_\lambda H|_{\lambda_0}^{kk'}|^2\, S_\lambda^{1/f}[\omega_{kk'}]/\hbar^2 \\ \Gamma_{\uparrow}^{kk'} &= |\partial_\lambda H|_{\lambda_0}^{kk'}|^2\, S_\lambda^{1/f}[-\omega_{kk'}]/\hbar^2 \\ \Gamma_{\varphi}^{kl} &= \partial_\lambda H|_{\lambda_0}^{kk}\, \partial_\lambda H|_{\lambda_0}^{ll} \times 4A_\lambda^2 \times t \times [(1-\gamma) - \log(\omega_{\mathrm{ir}} t)]/\hbar^2. \end{aligned} \tag{1.31}$$

Note that, due to the even symmetry of Eq. (1.27), one has $\Gamma_{\downarrow}^{kk'} = \Gamma_{\uparrow}^{kk'}$. Moreover, the pure-dephasing rates Γ_{φ}^{kl} are now time-dependent and lead to a Gaussian decay up to a logarithmic correction (see Sect. 1.4.3). Despite Eq. (1.31) being a relatively simple result and a direct consequence of the relation in Eq. (1.28), to the best of our knowledge the expression for Γ_{φ}^{kl} has not been reported in the literature.

1.4.3 Coherence times

We now use the results of the previous sections to obtain expressions for the relaxation (T_1) and pure-dephasing (T_2) coherence times of a qubit wavefunction. Restricting the master equation of Eq. (1.24) to only two qubit levels $\{|\psi_0\rangle, |\psi_1\rangle\}$, one can show that the populations of the qubit density matrix evolve in time as $\rho_{ii} \propto \exp(-\Gamma_1 t)$, where

$$\Gamma_1 = \Gamma_{\downarrow}^{01} + \Gamma_{\uparrow}^{01}. \tag{1.32}$$

This rate gives the characteristic coherence time $T_1 = 1/\Gamma_1$. Note that Eq. (1.32) implies that T_1 is maximized by minimizing the transition matrix element $\partial_\lambda H|_{\lambda_0}^{01}$. This observation will be useful below.

On the other hand, the pure-dephasing coherence time follows from the terms in the

master equation which are of the form

$$\partial_t \rho = \sum_k \Gamma_\varphi^{kk}\, \mathcal{D}[\sigma_{kk}]\,\rho + \sum_{k>l} \Gamma_\varphi^{kl} \Big\{ \tilde{\mathcal{D}}[\sigma_{kk}, \sigma_{ll}]\,\rho + \tilde{\mathcal{D}}[\sigma_{ll}, \sigma_{kk}]\,\rho \Big\}. \tag{1.33}$$

By projecting Eq. (1.33) in the system eigenbasis, we have

$$\langle \psi_k | \partial_t \rho | \psi_l \rangle = -\frac{1}{2} \Big[\Gamma_\varphi^{kk} + \Gamma_\varphi^{ll} - 2\Gamma_\varphi^{kl} \Big] \langle \psi_k | \rho | \psi_l \rangle. \tag{1.34}$$

We observe that

$$[\Gamma_\varphi^{kk} + \Gamma_\varphi^{ll} - 2\Gamma_\varphi^{kl}] \propto \Big[(\partial_\lambda H|_{\lambda_0}^{kk})^2 + (\partial_\lambda H|_{\lambda_0}^{ll})^2 - 2\partial_\lambda H|_{\lambda_0}^{kk} \partial_\lambda H|_{\lambda_0}^{ll} \Big] = [\partial_\lambda (\hbar\omega_{kl})|_{\lambda_0}]^2, \tag{1.35}$$

implying that the pure-dephasing rate of the density matrix coherence ρ_{kl} is proportional to the dispersion of the $k \leftrightarrow l$ device transition with respect to λ, as expected for first-order dephasing processes. To estimate the pure-dephasing coherence time, we now integrate Eq. (1.34) using the relations of Eq. (1.31), arriving at

$$\rho_{kl}(t) = \rho_{kl}(0) \exp \Big\{ -A_\lambda^2 (\partial_\lambda \omega_{kl}|_{\lambda_0})^2 t^2 \times \Big[\Big(\frac{3}{2} - \gamma \Big) - \log(\omega_{\mathrm{ir}} t) \Big] \Big\}, \tag{1.36}$$

for $1/f$ noise. We then define the coherence time T_φ for the qubit $0-1$ transition as the solution of the implicit equation $\rho_{01}(T_\varphi)/\rho_{01}(0) = 1/e$. Note that T_φ is maximized by reducing the λ-dispersion $\partial_\lambda \omega_{01}|_{\lambda_0}$ of the qubit transition. For this reason, operating points for which $\partial_\lambda \omega_{01}|_{\lambda_0} = 0$ are called 'sweet spots'.

Since incoherent qubit transitions unavoidably destroy phase information, the total coherence time can be limited by relaxation and excitation processes (or T_1-limited). In order to account for this contribution, the total coherence time is given by [42]

$$\frac{1}{T_2} = \frac{1}{2T_1} + \frac{1}{T_\varphi}. \tag{1.37}$$

Note that, as second-order corrections to the pure-dephasing rate at sweet spots are of order A_λ^4, the coherence time T_2 is simply T_1-limited at such operating points for most devices. Finally, a device is said to be protected against noise, or noise-protected, if both T_1 and T_2 can be made exponentially large as a function of a parameter that defines the device's operation regime. If the device operates at a sweet spot, instead, then it is said to be noise-protected to first order or quasiprotected.

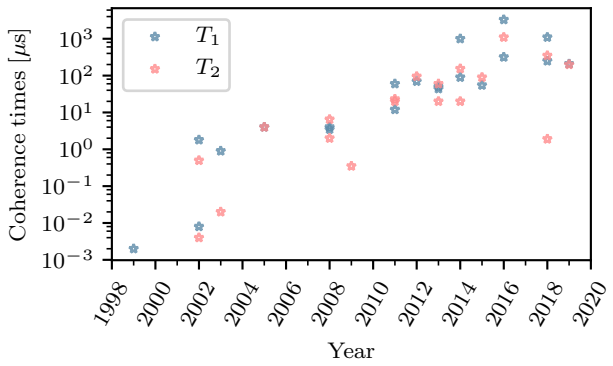

Figure 1.4 Coherence times of superconducting circuits including (2D and 3D) transmon, fluxonium, flux-qubit and cat-qubit devices. Note that the data are displayed for more than one qubit for some of the years, and that only T_1 (or T_2) is reported for some of the devices. The data shows an approximate exponential improvement of both T_1 and T_2 over two decades. Adapted from Ref. [27].

1.5 High-coherence state-of-the-art superconducting qubits

Having introduced metrics for quantifying the quantum coherence of superconducting qubits, this section aims at defining optimal operating points for these devices. In the last two decades, the coherence times of superconducting qubits have been improved by as much as five orders of magnitude [58, 59, 27]. Fig. 1.4 shows the evolution of T_1 and T_2 of selected devices as a function of year of fabrication, displaying a roughly exponential behavior. This extraordinary progress has been made possible thanks in part to advances in areas such as materials and fabrication [60], microwave engineering [61], shielding [62, 63], and the introduction of three-dimensional architectures [32, 33, 64]. In addition to this, qubit design has played an important role by proposing new and more robust ways of encoding quantum information in protected (or quasiprotected) subspaces.

This section is dedicated to the qubit designs that are closely related to the system analyzed in this thesis. First, we describe the two superconducting-qubit architectures with the highest demonstrated (uncorrected) coherence times: the transmon [56] and fluxonium [65] qubits. We show how these two qubits have similar characteristics and we establish a finite theoretical limit for the coherence times of these qubits. As we show below, the reason for this fundamental limit can be traced back to the lack of symmetries in the transmon and the fluxonium qubit Hamiltonians. This leads to a compromise between T_1 and T_2 when optimizing coherence.

Second, we discuss how a new superconducting qubit design, known as the $0-\pi$ qubit

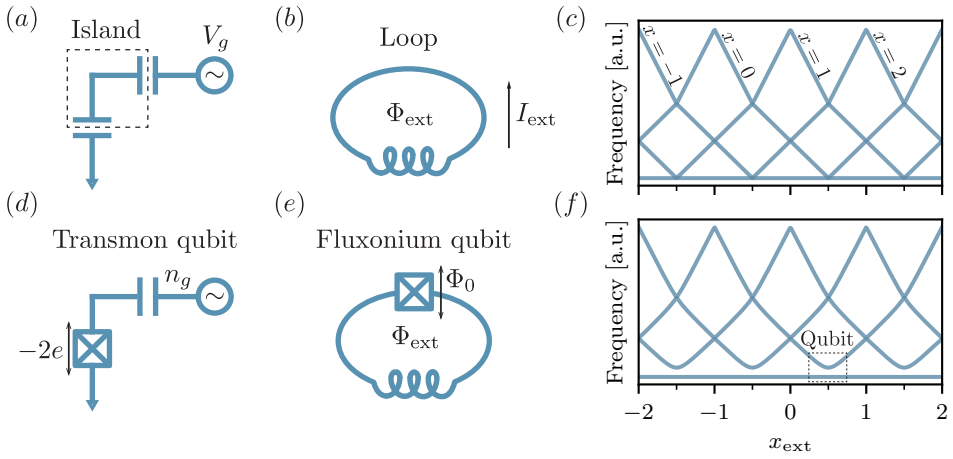

Figure 1.5 Geometries of a superconducting circuit defining charge and flux quantum degrees of freedom. (a) Circuit island. (b) Superconducting loop. (c) Spectrum of a 'quantum box'. (d) Transmon (charge) qubit. (e) Fluxonium (flux) qubit. (f) Spectrum of devices in (d) and (e).

[66], combines the noise insensitivity of both the transmon and fluxonium devices while introducing an additional symmetry that makes the $0-\pi$ circuit fully noise-protected. Unlike the transmon and fluxonium qubits, the $0-\pi$ qubit allows for the optimization of T_1 and T_2 times independently, enabling exponentially large coherence and relaxation times.

1.5.1 Quantum control of charge and flux degrees of freedom in a circuit

An interesting aspect of about superconducting qubits is that, from an elementary perspective, these devices are defined by the geometrical properties of an underlying superconducting circuit. More precisely, there exist two geometries at play in superconducting circuits: islands [Fig. 1.5 (a)] and loops [Fig. 1.5 (b)].

While the quantization of the electrical charge is a familiar concept, flux quantization in a closed loop is a strict consequence of superconductivity. According to the Ginzburg-Landau theory, the Cooper-pair supercurrent density of a superconductor is given by $\boldsymbol{J}_s(\boldsymbol{r},t) = \Lambda^{-1}[\varphi_0\nabla\theta(\boldsymbol{r},t) - \boldsymbol{A}(\boldsymbol{r},t)]$, where Λ is the London parameter, $\varphi_0 = \hbar/2e$, $\nabla\theta(\boldsymbol{r},t)$ is the superconducting phase gradient and $\boldsymbol{A}(\boldsymbol{r},t)$ is the vector potential corresponding to the magnetic field $\boldsymbol{B}(\boldsymbol{r},t)$. By integrating this expression along a contour $\mathcal{C}$ around an opening of the superconductor defining a surface $\mathcal{S}$, one arrives at the condition [67]

$$\oint_{\mathcal{C}} \Lambda \boldsymbol{J}_s(\boldsymbol{r},t)\cdot d\boldsymbol{l} + \int_{\mathcal{S}} \boldsymbol{B}(\boldsymbol{r},t)\cdot d\boldsymbol{s} = m\times\Phi_0, \tag{1.38}$$

where $d\boldsymbol{l}$ and $d\boldsymbol{s}$ are differential elements that correspond to the contour and to the surface, respectively, m is an integer and $\Phi_0 = h/2e$ is the quantum of magnetic flux. Eq. (1.38) is known as the fluxoid quantization condition. Now, by performing the contour integral in the bulk of the superconductor, where $\boldsymbol{J}_s(\boldsymbol{r}, t) = 0$, we arrive at the flux quantization condition $\int_{\mathcal{S}} \boldsymbol{B}(\boldsymbol{r}, t) \cdot d\boldsymbol{s} = m \times \Phi_0$. This shows that the magnetic flux through an opening of a superconductor can only amount to an integer number of quanta of magnetic flux.

Therefore, in the same way that a superconducting island intuitively plays the role of a box where electrical charges (Cooper pairs) can be stored, a superconducting loop acts as a box for fictitious particles of magnetic flux (flux quanta). This fact is the basis for a direct analogy between such systems, which are described by a Hamiltonian with the general form

$$H_{\text{storage}} = E_{\text{storage}} \, (x - x_{\text{ext}})^2. \tag{1.39}$$

Here, E_{storage} is the energy cost of adding a particle to the box, $x = \sum_{x'} x' |x'\rangle\langle x'|$ is a particle number operator (where $x' \in \mathbb{Z}$ and $|x'\rangle$ corresponds to a state with x' particles) and x_{ext} is an external bias parameter equivalent to an offset charge for the island and to an external magnetic flux for the loop. On the one hand, for a superconducting island of capacitance C, Eq. (1.39) takes the form $H_{\text{island}} = 4E_C(n - n_g)^2$, where $E_C = e^2/2C$ is the island's capacitive energy. On the other hand, for a superconducting loop of inductance L, Eq. (1.39) becomes $H_{\text{loop}} = E_L(2\pi m - \varphi_{\text{ext}})^2/2$, where $E_L = \varphi_0^2/L$ is the loop's inductive energy and $\varphi_{\text{ext}} = \Phi_{\text{ext}}/\varphi_0$ is the external flux in units of the reduced flux quantum [68, 69].

Figure 1.5 (c) shows the energy spectrum of the Hamiltonian given in Eq. (1.39) as a function of the external bias parameter x_{ext}. Note that the energy of the ground state has been shifted to zero for all bias conditions for clarity. This also makes the spectrum appear as composed by a set of V-shaped energy transitions that intersect each other, instead of the more typical intersecting parabolas. Each of these V-shaped transitions corresponds to the system having a fixed number x of Cooper pairs in the island or flux quanta in the loop. The level crossings are a consequence of the fact that the transitions $x \to x \pm 1$ cannot occur in this system. In other words, the box is closed and particles cannot be added or removed.

Superconducting qubits use the charge and flux quantum degrees of freedom of a circuit to encode quantum information. Manipulating the quantum information requires to be able to modify the state of the system. Because of this, it is clear that a box Hamiltonian of the form Eq. (1.39) is not enough and needs to be complemented by an additional term enabling the coherent transition $x \to x \pm 1$. The Josephson Hamiltonian Eq. (1.1) provides a possible solution. By adding a Josephson junction to the island [Fig. 1.5 (d)], Cooper pairs can tunnel in and out of the box, thus making it possible to control the charge

degree of freedom. Analogously, interrupting the superconducting loop with a Josephson junction [Fig. 1.5 (e)], allows a flux quantum to tunnel through the opening defined by the insulator of the junction, enabling quantum control of the flux degree of freedom.

In both cases, the Josephson junction acts as a weak link that couples charge and flux states differing by one quantum of charge or flux, respectively. This can be qualitatively described by the tunneling Hamiltonian

$$H_{\text{tunneling}} = -E_{\text{tunneling}}\,(x^- + x^+), \tag{1.40}$$

where $E_{\text{tunneling}}$ is a tunneling amplitude assumed to be real, for simplicity, and $x^- = \sum_x |x-1\rangle\langle x|$ $(x^+ = \sum_x |x+1\rangle\langle x|)$ is an operator that removes (adds) a particle to the box. We stress that, while Eq. (1.40) is exact for the case of the superconducting island, this model is only an approximation for the Hamiltonian loop in Fig. 1.5 (e). In Sect. 1.5.5, we present a complete theoretical model for the later device which is known as the fluxonium qubit.

Fig. 1.5 (f) shows the energy spectrum of the full Hamiltonian

$$H_{\text{qubit}} = H_{\text{storage}} + H_{\text{tunneling}}, \tag{1.41}$$

for the case $E_{\text{tunneling}}/E_{\text{storage}} = 0.25$. The parameter regime of Eq. (1.41) is, however, not relevant for the present discussion and will be addressed in Sects. 1.5.2, 1.5.4 and 1.5.5. In contrast to the case of the box Hamiltonian alone [Fig. 1.5 (c)], the spectrum of Eq. (1.41) displays anticrossings, indicating that a pairs of states characterized by different quantum numbers (charge or flux) are now coherently coupled. Note that anticrossings between the excited states of Eq. (1.41) cannot be seen only because of the scale of Fig. 1.5 (f).

As it follows from the symmetry $x \to x - 1$ of the qubit Hamiltonian in Eq. (1.41), the energy spectrum is periodic in the external bias parameter x_{ext} with period 1. Moreover, H_{qubit} has the inversion symmetry $x_{\text{ext}} \to -x_{\text{ext}}$. These symmetries allow restricting the analysis to half a period, $x_{\text{ext}} \in [0, 0.5]$ for instance. A superconducting charge (flux) qubit is obtained by considering the subspace of the two lowest-energy coherently coupled charge (flux) states of the circuit [see dashed box in Fig. 1.5 (f)].

For typical circuit-element parameters, the $0 \to 1$ transition frequency ω_{01} of such a two-level system lies in the GHz range. Importantly, the transition frequency $1 \to 2$ is chosen to be fairly different form ω_{01} (anharmonic spectrum), allowing for fast quantum control of the qubit wavefunction while minimizing leakage outside of the logical manifold. Regardless of the inherent simplicity of the devices in Fig. 1.5 $(d-e)$, these circuits form

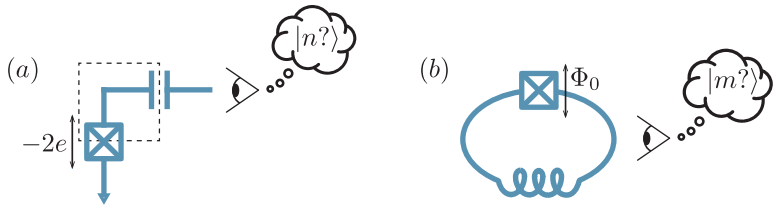

Figure 1.6 Illustration of the system-bath coupling. The environment couples to the particle number operator and is able to distinguish between states of different number of Cooper pairs (a) or flux quanta (b).

the basis for the design of the transmon and fluxonium qubits, which are nowadays the two superconducting architectures with the highest demonstrated coherence times.

1.5.2 Optimal parameter regimes for charge and flux qubits

We are now interested in finding the optimal parameter regime to operate the qubits presented in the previous section. To this end, we need to define how these devices couple to their environment. The system-bath coupling Hamiltonian is defined by the character of the device (charge or flux). While the superconducting island is coupled to the environment via a capacitance, the superconducting loop couples to the environment via a mutual inductance. In both cases, the system-bath coupling can be modeled by letting $x_{\text{ext}} \rightarrow x^0_{\text{ext}} + \delta x_{\text{ext}}$, where x^0_{ext} is a controlled bias [analogous λ_0 in Eq. (1.18)] and δx_{ext} represents fluctuations of the external parameter due to the environment [playing the role of $\delta\lambda$ in Eq. (1.18)].

Following Eq. (1.18), the system-bath Hamiltonian takes the form

$$H_{\text{int}} = -2E_{\text{storage}}\, x\, \delta x_{\text{ext}}, \tag{1.42}$$

which implies that the bath couples to the system through the number operator x. In other words, the environment can 'count' the number of particles that exist in the box, and thus distinguish between states that have a different number of Cooper pairs or flux quanta [see Fig. 1.6]. As shown below, this interaction Hamiltonian is responsible for both pure-dephasing and incoherent transition processes.

The problem of optimizing coherence in these devices is simple, due to the fact that the qubit Hamiltonian of Eq. (1.41) is characterized by a single parameter: the ratio $E_{\text{tunneling}}/E_{\text{storage}}$. Let us first consider the situation of Fig. 1.7 (a), where the qubit energy is dominated by E_{storage}. In this case, the qubit spectrum is highly sensitive to variations of x_{ext}, except at the

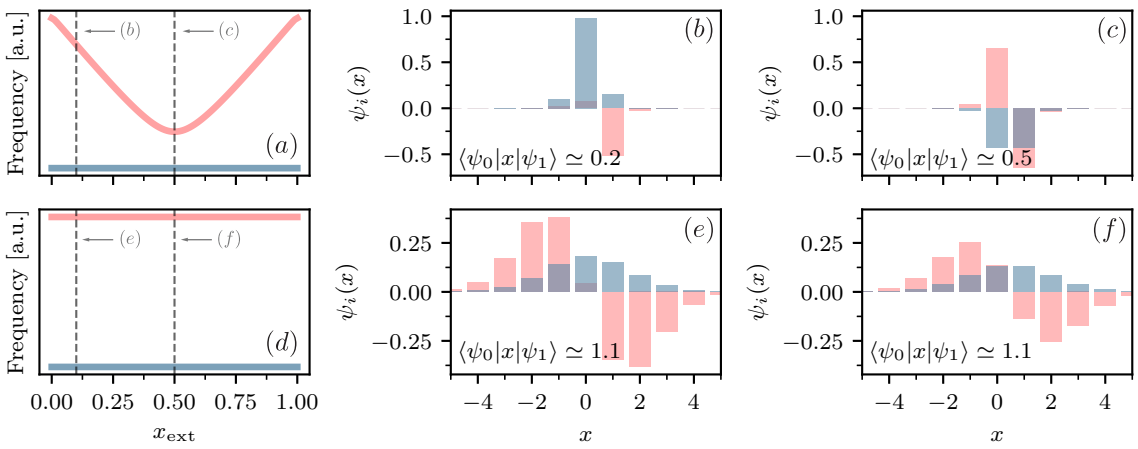

Figure 1.7 Optimizing the pure-dephasing coherence time of a superconducting (charge or flux) qubit. (a) Spectrum for $E_{\text{tunneling}}/E_{\text{storage}} = 0.25$. (b) Qubit wavefunctions for parameters in (a) away from the sweet spot. (c) Qubit wavefunctions for parameters in (a) at the sweet spot. (d) Spectrum for $E_{\text{tunneling}}/E_{\text{storage}} = 12.5$ (sweet-spot everywhere regime). (e) Qubit wavefunctions for parameters in (d) for the bias condition $x_{\text{ext}} = 0.1$. (f) Qubit wavefunctions for parameters in (d) for the bias condition $x_{\text{ext}} = 0.5$.

sweet spots where $\partial\omega_{01}/\partial x_{\text{ext}} = 0$ such that the system becomes noise-insensitive to first order [15]. The variation of the qubit transition frequency with respect to x_{ext} is known as (charge or flux) dispersion. Away from the sweet spot, the qubit wavefunctions are close to the original charge or flux states $|x\rangle$, and now overlap slightly with each other [see Fig. 1.7 (b)]. This leads to a relatively small transition matrix element $\langle\psi_0|x|\psi_1\rangle$ and, therefore, to a larger T_1 as we show below. However, at the sweet spot $x_{\text{ext}} = 0.5$, the logical wavefunctions are close to $|\psi_{0,1}\rangle \simeq (|x\rangle \pm |x+1\rangle)/\sqrt{2}$ [Fig. 1.7 (c)], resulting in an increase of the matrix element $\langle\psi_0|x|\psi_1\rangle \simeq 0.5$.

Next, we consider the case of Fig. 1.7 (d), where the qubit energy is largely dominated by the tunneling Hamiltonian. Here, the dispersion of the qubit transition frequency with x_{ext} has been reduced. This operation regime is often referred to as 'transmon' or 'sweet-spot everywhere' regime [56]. Since the tunneling Hamiltonian is not diagonal in the number basis $\{|x\rangle\}$, the qubit eigenstates are now extended over many charge or flux states. As a consequence of the large overlap between these eigenstates, the transition matrix element [see Fig. 1.7 (e) and Fig. 1.7 (f)] increases and, as expected, is approximately independent of x_{ext}.

Although operating the qubit at the sweet spot in a regime close to that of Fig. 1.7 (a) might appear to be enough to reach high coherence, years of experience with charge

qubits have demonstrated the opposite [54, 70]. Indeed, for charge-like qubits, it is known that the offset charge can drift and experience jumps of the order of e in the timescale of an experiment (see Ref. [71] for a recent experiment). It follows that the sweet-spot bias condition cannot be guaranteed over the timescales relevant for quantum computation, and thus the sweet-spot everywhere regime is a much better option. Section 1.5.3 considers in more details the important differences between charge and flux noise.

In the sweet-spot everywhere regime, the logical eigenstates are maximally delocalized over many charge or flux states. This is a general characteristic of systems that are robust against dephasing, where the tunneling Hamiltonian contributes to the enhancement of the zero-point fluctuations $x_{\text{zpf}} = \sqrt{\langle x^2 \rangle - \langle x \rangle^2}$ of the qubit degree of freedom. For a charge-like qubit, x_{zpf} corresponds to the zero-point fluctuations of the charge operator, while for a flux-like qubit, x_{zpf} is related to the zero-point fluctuations of the superconducting phase (or flux) operator. Since the charge (flux) degrees of freedom is allowed to fluctuate strongly, the system is also rendered insensitive to charge (flux) fluctuations due to the environment. Since the environment 'counts' the number of particles in the box, working on a delocalized logical basis makes it harder for the environment to access to which-state information about the system, reducing the impact of dephasing.

From a point of view of the electrical circuits that define these qubits, it is interesting to reinterpret the parameter regime $E_{\text{tunneling}}/E_{\text{storage}} \gg 1$ that corresponds to the sweet-spot everywhere condition. To make this ratio as large as possible we both need to maximize the tunneling rate and minimize the energy cost of adding an extra (charge of flux) particle to the box. Maximizing the tunneling rate can be done by maximizing the zero-point fluctuations of the respective charge or flux operators. The zero-point fluctuations of the charge operator scale as $q_{\text{zpf}} \propto 1/\sqrt{Z_J}$, while those of the flux operator scale as $\Phi_{\text{zpf}} \propto \sqrt{Z_J}$. Therefore, low-impedance junctions favor charge-noise insensitivity while high-impedance junctions can lead to flux-noise insensitivity. Furthermore, in order to reduce the energy cost of adding a particle to the box, a charge-like qubit needs to include a large capacitance ($E_{\text{storage}} \propto 1/C$) and a flux-like qubit a large inductance ($E_{\text{storage}} \propto 1/L$). Note that, while reaching the charge-insensitive limit for a charge qubit is relatively easy and has led to the transmon qubit becoming one of the most robust and adopted platforms for superconducting quantum-information processing, achieving flux-noise insensitivity with a flux-like qubit represents a daunting challenge. We discuss this fundamental difference in more detail below.

This takes us to the main point of this section. We have found that, in order to maximize pure-dephasing coherence in a charge- or flux-like qubit we need to build a device in a regime where it becomes charge- or flux-insensitive, respectively. In that regime, however,

the transition matrix element $\langle\psi_0|x|\psi_1\rangle$ is large. As $1/T_1 \propto |\langle\psi_0|x|\psi_1\rangle|^2$, it becomes clear that, there exists a trade-off between the pure-dephasing and relaxation/excitation rates. Moreover, since $T_2 \leq 2T_1$, this trade-off leads to a fundamental limit for the coherence of these simple devices.

This compromise is a consequence of the limited number of symmetries of the qubit Hamiltonian of Eq. (1.41). In other words, the simplicity of this system limits how coherent it can be. One possible solution to this problem is to engineer the environment of the qubit, such that $S_x[\omega_{01}]$ is as small as possible, thus increasing T_1, see Eq. (1.25). An example of this strategy is the work on 3D transmon qubits [32, 33], where electromagnetic losses are minimized by reducing the amount of electric field inside lossy dielectrics. This strategy has a limit, however, given by the fact it is not possible to completely get rid of the qubit environment.

A complementary approach to overcome limitations on quantum coherence is to engineer devices with additional symmetries in the qubit Hamiltonian, allowing to encode quantum information in noise-protected subspaces. As it will be shown below, this is strategy is exploited by the $0-\pi$ qubit. Importantly, this qubit makes use of two dispersionless charge- and flux-like circuit modes. The fact that charge- and flux-like modes are required to have very different effective impedances to be noise insensitive makes the task of combining such modes in a single circuit a major challenge. As it will become clear below, this is the main difficulty behind the experimental realization of the $0-\pi$ qubit.

1.5.3 Comparing flux and charge noise in electrical circuits

A fundamental asymmetry

Previous sections have focused on the similarities between the simplest charge and flux qubits that can be fabricated. We now comment on a fundamental asymmetry between flux and charge noise in superconducting quantum circuits, which might make one of these two superconducting-qubit architectures the best suited for applications in quantum information processing. Our discussion follows closely that by V. E. Manucharyan in Ref. [69].

Let us consider an LC harmonic oscillator of frequency $\omega_{\rm LC}$ and reduced impedance

$$z_{\rm LC} = \sqrt{L/C}/R_Q, \tag{1.43}$$

$R_Q = h/(2e)^2 \simeq 6.5\,\mathrm{k}\Omega$ being the superconducting quantum of resistance. Let Φ denote the flux degree of freedom of this oscillator and q the conjugate charge operator. In terms

of the usual harmonic-oscillator ladder operators a and $a^\dagger$, the flux and charge operators can be written as $\Phi/\Phi_0 = \sqrt{z_{\mathrm{LC}}/4\pi}(a + a^\dagger)$ and $q/2e = -i\sqrt{1/4\pi z_{\mathrm{LC}}}(a - a^\dagger)$ [see also Eq. (1.55)].

Qualitatively, this indicates that the strength of the quantum fluctuations of flux and charge, relative to Φ_0 and $2e$, respectively, are controlled by the value of z_{LC}

$$\frac{\Phi_{\mathrm{zpf}}/\Phi_0}{q_{\mathrm{zpf}}/2e} = z_{\mathrm{LC}}. \tag{1.44}$$

Thus, a symmetric situation for which flux and charge fluctuations are of the same relative strength corresponds to $z_{\mathrm{LC}} = 1$. If, instead, $z_{\mathrm{LC}} < 1$, then the relative amplitude of charge fluctuations surpasses that of flux fluctuations. The opposite is true for $z_{\mathrm{LC}} > 1$.

Which of these situations corresponds to the LC circuits that can be built with realistic circuit parameters? The electromagnetic environment of an electrical circuit has a low impedance value, typically in the order of $\mathrm{Re}[Z[\omega]] \simeq 50\,\Omega$. Therefore, considering the electromagnetic environment as a source of noise, Eq. (1.44) indicates that the resulting flux-noise amplitude is expected to be weaker than the charge-noise amplitude by almost two orders of magnitude. Interestingly, this is also the case for other sources of noise, such as $1/f$ noise, which do not have an electromagnetic origin. Indeed, the $1/f$ flux-noise amplitude is reported in the range $A_\Phi \in [10^{-6}, 10^{-5}]\,\Phi_0$, which is about two orders of magnitude smaller than that for $1/f$ charge-noise $A_e \in [10^{-4}, 10^{-3}]\,e$ [56].

The fundamental asymmetry between flux and charge noise suggests that flux-like superconducting qubits can behave more coherently than charge-like qubits. Indeed, since decoherence rates scale quadratically with the noise amplitude, this asymmetry can result in a significant difference between the flux and charge decoherence rates for a given ratio of $E_{\mathrm{tunneling}}/E_{\mathrm{storage}}$ in Eq. (1.41). Does this imply that flux-like devices are better qubits than charge-like devices?

The flip side of this question resides in the fact that the small value of z_{LC} also prevent us from realizing large inductors and, thus, from building a flux-like qubit that operates in the flux-insensitive regime ($E_{\mathrm{storage}} \propto 1/L$). In contrast, realizing a large capacitor is easier due to the fact that charge fluctuations are much larger in comparison. This evident trade-off can eventually equalize the performance of realistic charge- and flux-like devices and makes it hard to tell whether or not there exists an actual performance winner between these two architectures. Moreover, as it will become clear in Sect. 1.5.5, the frequency of a flux-like qubit depends exponentially on the junction energy. As the latter can vary in a few percent from device to device, targeting specific qubit frequencies can be difficult. This

leads to additional challenges regarding scaling up the flux-qubit technology to multi-qubit devices.

Leveraging the kinetic inductance of Cooper pairs to build superinductances

Fortunately, superconductivity provide us with an additional ingredient that is useful to realize large inductances: the kinetic inductance of Cooper pairs. In both conducting and superconducting wires, the kinetic inductance arises from the inertia of the charge carriers and is inversely proportional to the carrier density [72, 73]. In conductors, however, the contribution of the kinetic inductance to the wire inductance is unfortunately greatly surpassed by the wire's resistance [69]. In a superconducting wire the absence of dissipation makes the kinetic inductance the largest contribution to the wire's impedance.

In order to increase the kinetic inductance of a wire, the carrier density needs to be reduced. For instance, in a Josephson junction, the Cooper-pair density can be greatly reduced within the insulator layer. Thus, the junction responds inductively with an effective inductance $L_J = \varphi_0^2/E_J$. An array of N_J Josephson junctions connected in series forms a wire of inductance $L = N_J L_J$, which can be much greater than its geometrical inductance [65, 74].

In order to understand how to properly design such a device, let us first consider a periodic chain of N_J Josephson junctions connected in series. Importantly, these junctions are assumed to be of low impedance, such that at low-frequencies, the junctions behave as linear inductances. In absence of an externally applied magnetic field and circuit-element disorder, the Lagrangian of this system, up to second order in the Josephson potential, is

$$L = \sum_{i=0}^{N_J-1} \frac{C_J}{2}(\dot{\phi}_i - \dot{\phi}_{i+1})^2 + \frac{C_0}{2}\dot{\phi}_i^2 - \frac{1}{2L_J}(\phi_i - \phi_{i+1})^2, \tag{1.45}$$

where C_J (L_J) is the junction capacitance (inductance), C_0 represents a spurious ground capacitance associated with each of the circuit islands, and we take periodic boundary conditions $\phi_0 = \phi_{N_J}$ (or $\phi_i = \phi_{N_J+i}$). In order to diagonalize Eq. (1.45) we introduce the Fourier modes $\{f_k\}$ by the inverse relation

$$\phi_i = \sum_k f_k u_i^k, \tag{1.46}$$

where $\{u_j^k = e^{i2\pi kj/N_J}/\sqrt{N_J}\}$ is a set of N_J independent basis functions for which the values

of k are chosen in the domain [75]

$$k \in \begin{cases} [-n_J+1,\ldots,n_J] & \text{if } N_J = 2n_J \\ [-n_J,\ldots,n_J] & \text{if } N_J = 2n_J+1, \end{cases} \tag{1.47}$$

with n_J an integer. These basis functions satisfy the orthonormality condition $\sum_i u_i^{k'*} u_i^k = \delta_{kk'}$ and the completeness relation $\sum_k u_{i'}^{k*} u_i^k = \delta_{ii'}$. Moreover, since $\phi_i^* = \phi_i$ and $u_i^{k*} = u_i^{-k}$, one has $f_k^* = f_{-k}$. In the Fourier basis, and using the fact that $u_{i+1}^k = e^{i2\pi k/N_J} u_i^k$, Eq. (1.45) takes the form

$$L = \sum_k \frac{C_k}{2} \dot{f}_k \dot{f}_{-k} - \frac{1}{2L_k} f_k f_{-k}, \tag{1.48}$$

where $C_k = 4C_J \sin^2(\pi k/N_J) + C_0$ and $L_k = L_J/[4\sin^2(\pi k/N_J)]$ are effective capacitances and inductances that depend on the mode number k. In order to decouple the Fourier modes, we define real and imaginary components as

$$\begin{aligned} f_k^R &= \frac{f_k + f_k^*}{2} = \frac{f_k + f_{-k}}{2} \\ f_k^I &= \frac{f_k - f_k^*}{2i} = \frac{f_k - f_{-k}}{2i}, \end{aligned} \tag{1.49}$$

in terms of which Eq. (1.48) reduces to

$$L = \begin{cases} \frac{C_0}{2}\dot{f}_0^2 - \frac{1}{2L_0} f_0^2 + \frac{C_{n_J}}{2}\dot{f}_{n_J}^2 - \frac{1}{2L_{n_J}} f_{n_J}^2 + \sum_{\mu=R,I}\sum_{k=1}^{n_J-1} \frac{2C_k}{2}(\dot{f}_k^\mu)^2 - \frac{1}{2\frac{L_k}{2}}(f_k^\mu)^2 & \text{if } N_J = 2n_J \\ \frac{C_0}{2}\dot{f}_0^2 - \frac{1}{2L_0} f_0^2 + \sum_{\mu=R,I}\sum_{k=1}^{n_J} \frac{2C_k}{2}(\dot{f}_k^\mu)^2 - \frac{1}{2\frac{L_k}{2}}(f_k^\mu)^2 & \text{if } N_J = 2n_J+1, \end{cases} \tag{1.50}$$

which is now diagonal. Note that we have removed the superindex $\{R, I\}$ for the modes that satisfy $f_n^I = 0$. As a consequence of Eq. (1.50), a periodic chain with an even (odd) number of junctions $N_J = 2n_J$ ($N_J = 2n_J + 1$) has $n_J - 1$ (n_J) degenerate modes.

In practice, such Josephson-junction arrays are part of a larger circuit and thus not necessarily subject to periodic boundary conditions. In particular, the case of an array with N_J junctions subject to open boundary conditions can be treated in the same way, by performing a periodic extension to an array twice as large ($N_J \to 2N_J$). The effective mode frequencies $\omega_k = 1/\sqrt{L_k C_k}$ for such a device follow as

$$\omega_k = \frac{1}{\sqrt{L_J C_J}} \sqrt{\frac{\sin^2(\pi k/2N_J)}{\sin^2(\pi k/2N_J) + C_0/(4C_J)}}, \tag{1.51}$$

where $\omega_p = 1/\sqrt{L_J C_J}$ is the plasma frequency of the array junctions and $k \in [0, N_J]$ [74].

We note that, in the limit of large N_J, the frequency of the first mode ($k = 1$) is $\omega_1 \simeq \omega_p \times \pi\sqrt{C_J/C_0} \times N_J^{-1}$. Since one desires the device to feature an ideal inductive response for frequencies $\omega \ll \omega_1$, it is important to ensure the condition $\omega_1/2\pi > 10\,\mathrm{GHz}$, as $\omega/2\pi \in [0, 10]\,\mathrm{GHz}$ defines the frequency range of operation for most superconducting-qubit devices. Thus, the quantity $\pi\sqrt{C_J/C_0}$ provides a length scale for the array: if $N_J \gg \pi\sqrt{C_J/C_0}$, then the array modes can dangerously lie at low frequencies [74]. Thus, maximizing the array inductance by increasing N_J is a viable option only if the sources of stray capacitances are mitigated simultaneously. So far, inductances in the range $L \simeq 2.5 - 3.0\,\mu\mathrm{H}$ are among the largest values reported [76, 77].

An alternative implementation of large inductances is based on thin-film superconducting nanowires made of materials such as NbN, TiN, NbTiN and granular Aluminum (grAl), which are generally known as 'disordered' superconductors [72, 73, 78, 79, 80, 81]. In these materials, the Cooper pair density is reduced by introducing impurities, leading to an increased sheet kinetic inductance with respect to a conventional superconductor. In a nanowire, the kinetic inductance is given by [73]

$$L = \frac{m}{2e^2 n_s}\left(\frac{l}{wd}\right), \tag{1.52}$$

where m is the free electron mass, n_s is the density of Cooper pairs, and l/wd is a geometrical factor that includes the length l, width w and thickness d of the nanowire. The latter is assumed to be small compared to the coherence length of the superconductor, such that the sample is effectively two-dimensional [72]. Nanowire inductances can easily surpass $L \simeq 0.1\,\mu\mathrm{H}$ and behave more linearly than junction arrays. We return to nanowire inductances in chapter 6.

We conclude this section by introducing the term 'superinductance' which is used in the literature to refer to a circuit element with effective impedance greater than the quantum of resistance $R_Q = h/(2e)^2 \simeq 6.5\,\mathrm{k}\Omega$ and self-resonance frequencies above 10 GHz [82, 66, 74]. As it will become clear below, superinductances are crucial to many noise-protected qubit designs, including the $0 - \pi$ qubit.

1.5.4 The transmon qubit

We have so far discussed the intuition behind noise-insensitive regimes of single-mode superconducting circuits and qualitative differences between such devices and their sensitivity to noise. We now present some of the technical details that are required to put the results of this thesis in context.

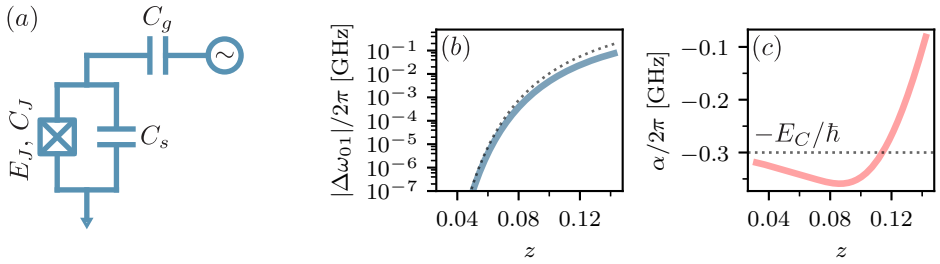

Figure 1.8 The transmon qubit [56]. (a) Schematic of the circuit. (b) Charge dispersion as a function of the reduced impedance z. (c) Spectrum anharmonicity as a function of z. Full lines correspond to numerics whereas dotted lines are based on the asymptotic expressions of Eq. (1.54) and Eq. (1.57) for (b) and (c), respectively.

We first consider the case of the transmon qubit [56]. This qubit is formed by a single Josephson junction of energy E_J and capacitance C_J, shunted by a large capacitance C_s as shown in Fig. 1.8 (a). A small gate capacitance C_g is used to couple the circuit to a voltage source that sets the offset charge n_g and can drive the qubit with an AC microwave tone.

The Hamiltonian of the transmon qubit is simply given by [56]

$$H = 4E_C(n - n_g)^2 - E_J \cos\theta, \tag{1.53}$$

where $E_C = e^2/2C$ is the capacitive energy associated with the total capacitance $C = C_J + C_s + C_g$, and θ is the superconducting phase difference across the junction. In the transmon regime, defined as $E_J/E_C \gg 1$ (typically in the order of $30 - 80$ [56, 54]), the low-frequency spectrum of Eq. (1.53) becomes exponentially insensitive to charge noise. Introducing the effective impedance parameter $z = \sqrt{L_J/C}/R_Q$, the transmon regime corresponds to $z \ll 1$. Note that this agrees with the reasoning presented in Sect. 1.5.2, as the charge-insensitive regime for a charge qubit is reached when both the junction impedance and the energy cost of adding a Cooper pair to the island ($\propto 1/C$) are small.

Interestingly, Eq. (1.53) admits an exact solution in terms of Mathieu functions [83]. This makes it possible to find asymptotic expressions for the charge dispersion $\epsilon_l = \omega_l(n_g = 0.5) - \omega_l(n_g = 0)$ of the lth energy eigenvalue

$$\epsilon_l = (-1)^l \omega_p \frac{2^{4l+3}}{l!}\sqrt{\frac{2}{\pi}}\left(\frac{1}{\pi z}\right)^{l+\frac{1}{2}} \exp\left(-\frac{4}{\pi z}\right), \tag{1.54}$$

where $\omega_p = \sqrt{8E_C E_J}/\hbar$ is referred to as the plasma frequency [56]. Fig. 1.8 (b) shows the charge dispersion of the qubit transition as a function of z compared to an estimation based on Eq. (1.54). This confirms the exponential reduction of the offset-charge sensitivity with

$1/z$.

In the limit $z \ll 1$, Eq. (1.53) is dominated by the potential energy term $-E_J \cos\theta$. As a result, quantum fluctuations of the phase around $\theta = 0$ are expected to be small, allowing us to describe the dynamics by means of a harmonic approximation. To do this, we introduce the harmonic-oscillator creation ($b^\dagger$) and annihilation (b) operators, in terms of which the superconducting phase and (dimensionless) charge operators read

$$\begin{aligned} \theta &= \sqrt{\pi z}\,(b + b^\dagger) \\ n &= \frac{-i}{\sqrt{4\pi z}}\,(b - b^\dagger). \end{aligned} \tag{1.55}$$

satisfying $[\theta, n] = i$. Eq. (1.53) can then be put in the form

$$H = \hbar\omega_p\, b^\dagger b - E_J \sum_{k=2}^{\infty} (-1)^k \frac{(\pi z)^k}{(2k)!} (b + b^\dagger)^{2k}. \tag{1.56}$$

Here, the quadratic part of the Josephson potential has been used to define the harmonic-oscillator Hamiltonian $4E_C n^2 + E_J\theta^2/2 = \hbar\omega_p b^\dagger b$, while terms of higher order correspond to the remaining of the series expansion. For $z \ll 1$, the strength of the higher order terms decays rapidly with k and the first nonlinear correction ($k = 2$) is enough to describe the system accurately. In this condition, Eq. (1.56) can be simplified to $H \simeq \hbar\omega_p\, b^\dagger b - E_C(b + b^\dagger)^4/12$, where we have used the relation $E_C = \pi^2 z^2 E_J/2$. By performing a rotating wave approximation, we arrive at the Hamiltonian of a weakly anharmonic oscillator [56]

$$H = \hbar\omega_q\, b^\dagger b + \frac{\alpha}{2} b^{\dagger 2} b^2, \tag{1.57}$$

where $\omega_q = \omega_p - E_C/\hbar$ is the qubit frequency and $\alpha = -E_C/\hbar$ is the transmon anharmonicity.

The price to pay for an exponential reduction of the offset-charge sensitivity of the transmon qubit is a polynomial decrease of the qubit anharmonicity that reaches the asymptotic value $-E_C$ for $z \to 0$. Decreasing the qubit anharmonicity can in principle result in slower gate operations given that, ideally, the spectral components of a drive pulse at the qubit frequency ω_{01} should not overlap with $\omega_{12} = \alpha + \omega_{01}$ to avoid leakage. In practice, however, leakage can be avoided using optimal control techniques such as Derivative Removal by Adiabatic Gate (DRAG) [84, 85, 86] or GRAPE [87], reaching gate fidelities as large as $\gtrsim 99.9\%$ [27].

Due to the simplicity of fabrication of transmon qubits, reliability and relatively easy

readout and control, this device is the workhorse of superconducting qubits. Moreover, all efforts devoted to scaling up the superconducting-qubit architecture, rely on different variants of the transmon qubit [31].

1.5.5 The fluxonium qubit

From heavy- to light-fluxonium regimes

Charge noise is ubiquitous in mesoscopic devices and can rapidly deteriorate quantum coherence. The transmon regime, presented in Sect. 1.5.4, is a possible solution to this problem, enabling an exponential reduction of the charge-noise sensitivity of a charge-like qubit by design.

An alternative approach to realize a device that is insensitive to charge noise is to shunt a charge-like qubit with an inductor. From an electrical-engineering point of view, an inductor with impedance $Z_L = -i\omega L$ acts as a short-circuit ($Z_L \to 0$) to ground for the low-frequency $1/f$ noise, thus making this noise irrelevant to the system. From a different point of view, an inductively shunted charge-like qubit is nothing else than the device in Fig. 1.5 (e), and can thus be regarded as a flux-like qubit.

Indeed, mitigating the effects of charge noise was the original motivation behind the pioneering work that introduced the fluxonium qubit about 10 years ago [65]. More recently, this system has been of interest due to its demonstrated long coherence times [88, 89, 90] and potential for quantum information processing [91]. In this section, we explore the structure of the fluxonium device, focusing on aspects that are relevant to the $0-\pi$ qubit.

As shown in Fig. 1.9 (left panel), the fluxonium circuit consists of a small Josephson junction, referred to as 'black-sheep' junction, shunted by a superinductance and, possibly, a capacitance. The black-sheep junction receives that name because this junction is different from those that form the superinductance. While a superinductance is in principle a multimode device, it can behave as a single-mode linear inductance under appropriate design conditions [74, 92, 93]. The multimode structure of such a device has, however, important consequences [74, 73], some of which are investigated below. Under a single-mode approximation, this device can be described by the effective circuit in Fig. 1.9 (right panel). There, the junction array has been replaced by a large inductance $L = \sum_{i=1}^{N_J} L_{J_i}$, where L_{J_i} is the Josephson inductance of the ith array junction and N_J is the number of junctions. The relevant degree of freedom to describe this effective circuit is the phase variable $\phi = \sum_{i=1}^{N_J} \theta_i$ which accounts for the total phase drop across the black-sheep junction, and where θ_i is the

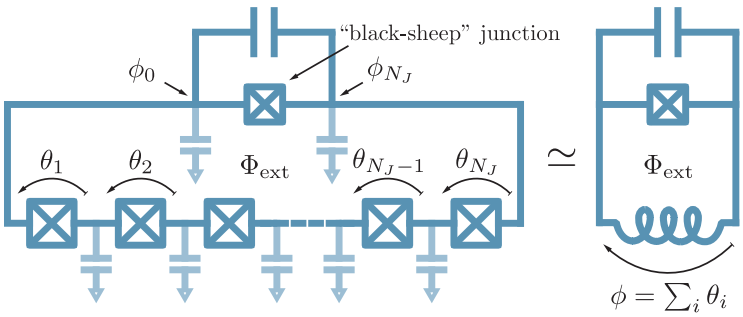

Figure 1.9 Schematic of the fluxonium circuit. (Left panel) Full circuit model of the fluxonium device including a Josephson-junction-array superinductance. (Right panel) Effective single-mode model of the fluxonium circuit.

phase difference across the ith Josephson junction of the array. The variable ϕ is known as the fluxonium or superinductance mode.

Following the usual circuit quantization approach, the effective Hamiltonian of the fluxonium qubit can be written as

$$H = 4E_C n^2 + \frac{E_L}{2}\phi^2 - E_J \cos(\phi + \varphi_{\text{ext}}), \tag{1.58}$$

where $E_C = e^2/2C$ is the capacitive energy associated with the total capacitance C (including shunt and stray capacitances) of the fluxonium mode, $E_L = \varphi_0^2/L$ is the total inductive energy, E_J is the Josephson energy of the black-sheep junction and $\varphi_{\text{ext}} = \Phi_{\text{ext}}/\varphi_0$ the external flux in units of the reduced flux quantum [65]. Note that Eq. (1.58) does not include a DC offset-charge parameter (n_g) since it can be gauged away [68].

Despite the apparent simplicity of the fluxonium Hamiltonian Eq. (1.58), its eigenstates can display a rich structure that depends on the parameter regime. For a systematic analysis, it is useful to redefine the parameters in Eq. (1.58) in terms of the effective black-sheep junction plasma frequency $\omega_p = \sqrt{8E_J E_C}/\hbar$ and the effective (reduced) impedance $z = \pi^{-1}\sqrt{2E_C/E_J}$. The potential energy of Eq. (1.58) is composed of a quadratic potential $E_L\phi^2/2$ with a modulation given by the cosine potential of the black-sheep junction and the external flux. Qualitatively, $\hbar\omega_p$ defines the characteristic energy of intra-well excitations, while z is a measure of the tunneling amplitude between such wells. This statement will appear clearer below.

Figure 1.10 shows the eigenfunctions of the fluxonium qubit for different values of z, taking $\omega_p/2\pi = 10\,\text{GHz}$ and $E_L/h = 0.2\,\text{GHz}$. Panel (a) corresponds to the case of small z, i.e. large E_J compared to E_C, for which tunneling between states localized in different po-

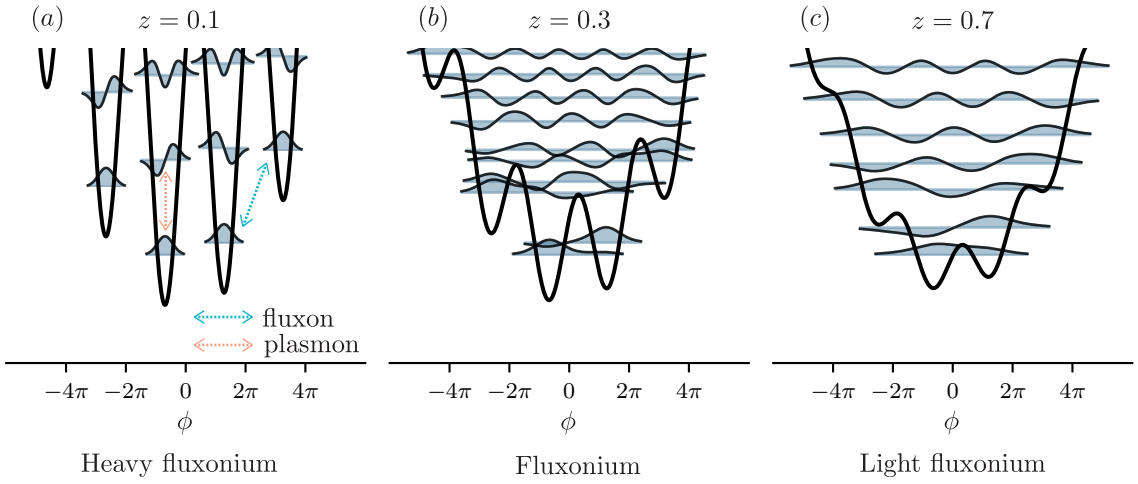

Figure 1.10 Wavefunctions of the fluxonium qubit for a varying black-sheep junction impedance $z \in [0.1, 0.3, 0.7]$, $E_L/h = 0.2\,\mathrm{GHz}$ and $\Phi_{\mathrm{ext}}/\Phi_0 = 0.35$. In the low-impedance regime (a), one can distinguish two type of qubit transitions, including fluxon (or inter-well) and plasmon (or intra-well) transitions. These transitions hybridize slightly for moderate black-sheep junction impedances (b) and strongly for larger z (c).

tential wells is exponentially suppressed in z^{-1}. Excitations within a single well are approximately separated by the energy difference $\hbar\omega_p$ and, for this reason, transitions between two of such states are called plasmon (or intra-well) transitions. Transitions between states that are localized in two different potential wells are called fluxon (or inter-well) transitions. Since the relative position between the potential wells shifts significantly with Φ_{ext}, fluxon transitions are highly sensitive to the external flux. In contrast, plasmon transitions display a very weak flux sensitivity. Since the low-impedance limit requires the fluxonium mode ϕ to have a large effective capacitance (or 'mass'), this regime is called 'heavy-fluxonium' [89, 88, 73].

Fig. 1.10 (b) corresponds to an intermediate value of z where the energy barrier ($\propto E_J$) between potential wells has been lowered with respect to the case in (a). Moreover, the capacitive energy E_C is now larger, such that tunneling between states localized in neighboring potential wells is non-negligible, favoring states that are delocalized over multiple wells. Thus, the low-frequency spectrum of the device has well defined plasmon and fluxon transitions, while such excitations undergo strong hybridization at higher frequencies. Since this intermediate-z regime corresponds to that of the original fluxonium-qubit paper [65], we simply refer to it as the fluxonium regime.

If the impedance of the black-sheep junction is increased further [see Fig. 1.10 (c)], the fluxonium wavefunctions can spread over many potential wells thanks to a lower E_J and to

a larger E_C. In this case, plasmon and fluxon transitions hybridize strongly, such that the distinction between these is no longer useful. The spectrum may instead be regarded as excitations of the harmonic Hamiltonian Eq. (1.58) for which the cosine potential acts as a perturbation leading to a very weak flux sensitivity. This behavior is expected, as a larger z leads to an increase of the ratio $E_{\text{tunneling}}/E_{\text{storage}}$ for this qubit, taking it closer to the sweet-spot everywhere regime. Since this also means that the capacitance associated with the black-sheep junction is relatively small, we refer to this regime as the 'light-fluxonium' regime.

Energy spectrum: from heavy- to light-fluxonium regimes

We now analyze the energy spectrum of the fluxonium qubit from the heavy- to the light-fluxonium regimes. This discussion builds on the intuition developed in the previous section. Fig. 1.11 shows the result of the diagonalization of Eq. (1.58) (solid light-blue lines) for $z \in [0.05, 0.3]$, $E_L/h \in [0.1, 0.4]$ GHz as a function of Φ_{ext} and assuming $\omega_p/2\pi = 10\,\text{GHz}$.

Let us first consider the case of $z = 0.05$ and $E_L/h = 0.1\,\text{GHz}$ in Fig. 1.11. In this case, the low-frequency spectrum is highly sensitive to the external flux, corresponding to a set of inter-well or fluxon transitions [see also Fig. 1.10 (a)]. For a small value of z, tunneling between the wells of the fluxonium potential is suppressed exponentially in $1/z$. The low-frequency spectrum around $\Phi_{\text{ext}}/\Phi_0 = 0.5$ can thus be modeled by the weak coupling of two (fluxon) states $\{|m\rangle, |m+1\rangle\}$ of the form $\langle\phi|m\rangle \propto z^{-1/4}\exp[-(\phi-\phi_m)^2/4\pi z]$ and localized around the flux-dependent positions $\{\phi_m\}$ of two nearly degenerate potential wells. Assuming $E_L \ll E_J$, the fluxonium Hamiltonian once restricted to the subspace $\{|m\rangle, |m+1\rangle\}$ subspace, can be approximated by the spin Hamiltonian [94]

$$H = -\frac{\bar{\epsilon}}{2}\Big(|m\rangle\langle m+1| + |m+1\rangle\langle m|\Big) + \sum_{m'=\{m,m+1\}} \frac{\bar{E}_L}{2}\Big(2\pi m' - 2\pi\frac{\Phi_{\text{ext}}}{\Phi_0}\Big)^2 |m'\rangle\langle m'|. \quad (1.59)$$

Here, the effective inductive energy $\bar{E}_L = E_L(1-b^{-1})$ incorporates a first-order correction in $b^{-1} = E_L/E_J \ll 1$, while $\bar{\epsilon} = 8\sqrt{2}\,\hbar\bar{\omega}_p\,\exp(-4/\pi\bar{z})/\pi\sqrt{z}$ is the tunneling matrix element between the two fluxon states where the effective parameters $\bar{\omega}_p = (8\bar{E}_J\bar{E}_C)^{1/2}$ and $\bar{z} = \pi^{-1}(2\bar{E}_C/\bar{E}_J)^{1/2}$ are defined in terms of $\bar{E}_J = E_J[1-\pi^2(1-b^{-1})/4b]$ and $\bar{E}_C = E_C/(1-b^{-1})^2$ [94].

The two-level model in Eq. (1.59) predicts a linear dispersion $\propto 1/L$ of the first fluxon transition with the external flux and an exponentially small gap opening at $\Phi_{\text{ext}}/\Phi_0 = 0.5$ due to fluxon tunneling. Black dashed lines in the panels of Fig. 1.11 for which $z \lesssim 0.1$ are obtained from the diagonalization of Eq. (1.59) for all E_L and external flux parame-

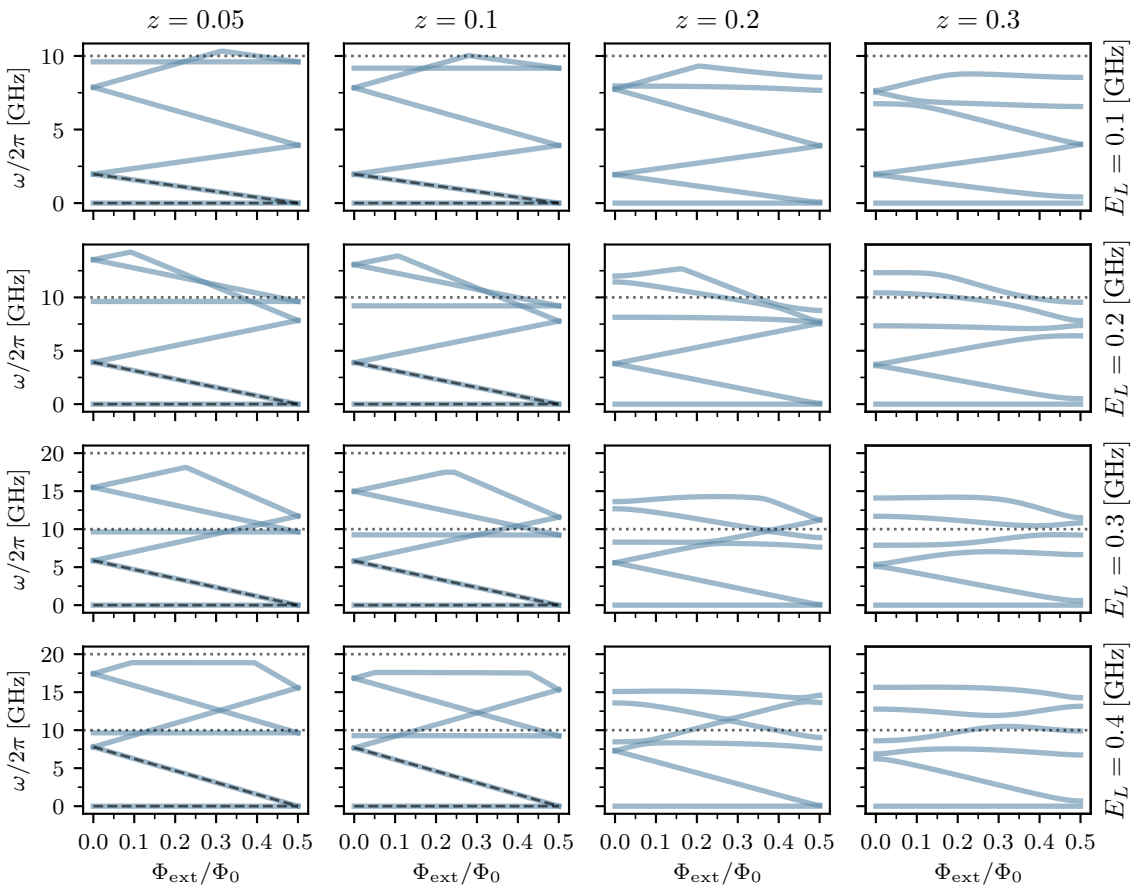

Figure 1.11 Low-lying excitations of the fluxonium qubit with a low-impedance black-sheep junction. Rows correspond to different values of $E_L/h \in [0.1, 0.4]$ GHz, while columns are obtained for different values of the black-sheep junction impedance z. Black dashed lines correspond to a two-level approximation valid for $z \ll 1$. Black dotted lines correspond to multiples of the bare plasma frequency $\omega_p/2\pi = 10$ GHz.

ters. Moreover, for z constant, the flux dispersion of the fluxon transition increases as E_L is made larger (see Fig. 1.11). For E_L constant, the gap opening at $\Phi_{\mathrm{ext}}/\Phi_0 \simeq 0.5$ becomes more noticiable as z increases. This simple model shows the fluxon-tunneling physics that takes place in the fluxonium architecture. The extension of this model to a multilevel theory, that is needed when considering a broader parameter regime, involves a number of technical details that are addressed in Refs. [44, 68]. These details make the fluxonium qubit much more complex than the phase-slip picture discussed in Sect. 1.5.1. Nevertheless, the simplified model in Eq. (1.59) conveys the right intuition and is useful to interpret the results.

Plasmon transitions are not captured by Eq. (1.59) because these involve excitations within a given potential well. For relatively small z, the first plasmon transition appears as a flux-insensitive transition close to the bare plasma frequency $\omega_p/2\pi$. Multiples of $\omega_p/2\pi$ are shown as black dotted lines in all panels of Fig. 1.11. Note that for $z \lesssim 0.1$, the first plasmon transition is slightly shifted below $\omega_p/2\pi$ due to the nonlinearity of the black-sheep junction. Depending on Φ_{ext}, a plasmon transition can be degenerate with a fluxon transition, leading to hybridization between these excitations. This appears as an anticrossing between plasmon and fluxon transitions in the energy spectrum. While this is barely noticeable for the cases $z \lesssim 0.1$ in Fig. 1.11, the anticrossing becomes more appreciable when the black-sheep junction impedance is increased. Note that for $z \gtrsim 0.1$ the frequency of the plasmon transition is pushed further below $\omega_p/2\pi$ as the nonlinearity of the black-sheep junction increases.

The previous paragraphs lay the basis for understanding the structure of the spectrum of the fluxonium qubit. However, as the impedance of the black-sheep junction reaches high values (light-fluxonium regime), the distinction between plasmon and fluxon excitations becomes meaningless. This can be appreciated in Fig. 1.12 [see also Fig. 1.10 (c)], where strong hybridization between plasmon and fluxon excitations characterizes the energy spectrum. In this limit, the system approaches the flux-insensitive regime, as can be anticipated from the reduced flux dispersion of the low-frequency transitions for $z \gtrsim 0.6$ with respect to the case for smaller z values. The light-fluxonium spectrum thus resembles that of a transmon qubit, where the external flux plays the role of the offset-charge parameter for the transmon [76].

Finally, we note that the qualitative behavior described in this section generalizes to other parameter regimes for ω_p and E_L. In practice, the value of these parameters may be found typically in the range $\omega_p/2\pi \in [5, 40]\,\text{GHz}$ and $E_L/h \in [0.05, 1.0]\,\text{GHz}$. This completes the qualitative description of possible solutions of the fluxonium-qubit Hamiltonian. While fluxonium devices are developed in a handful of research groups around the world, this technology is not as mature as the transmon qubit. Moreover, the field has not yet demonstrated coherent operation two coupled fluxonia, despite the existence of theoretical proposals for two-qubit gates [91, 95]. Quite recently, however, the coherence times of fluxonium devices has been shown to surpass $300\,\mu\text{s}$ [90], making this architecture promising for further development.

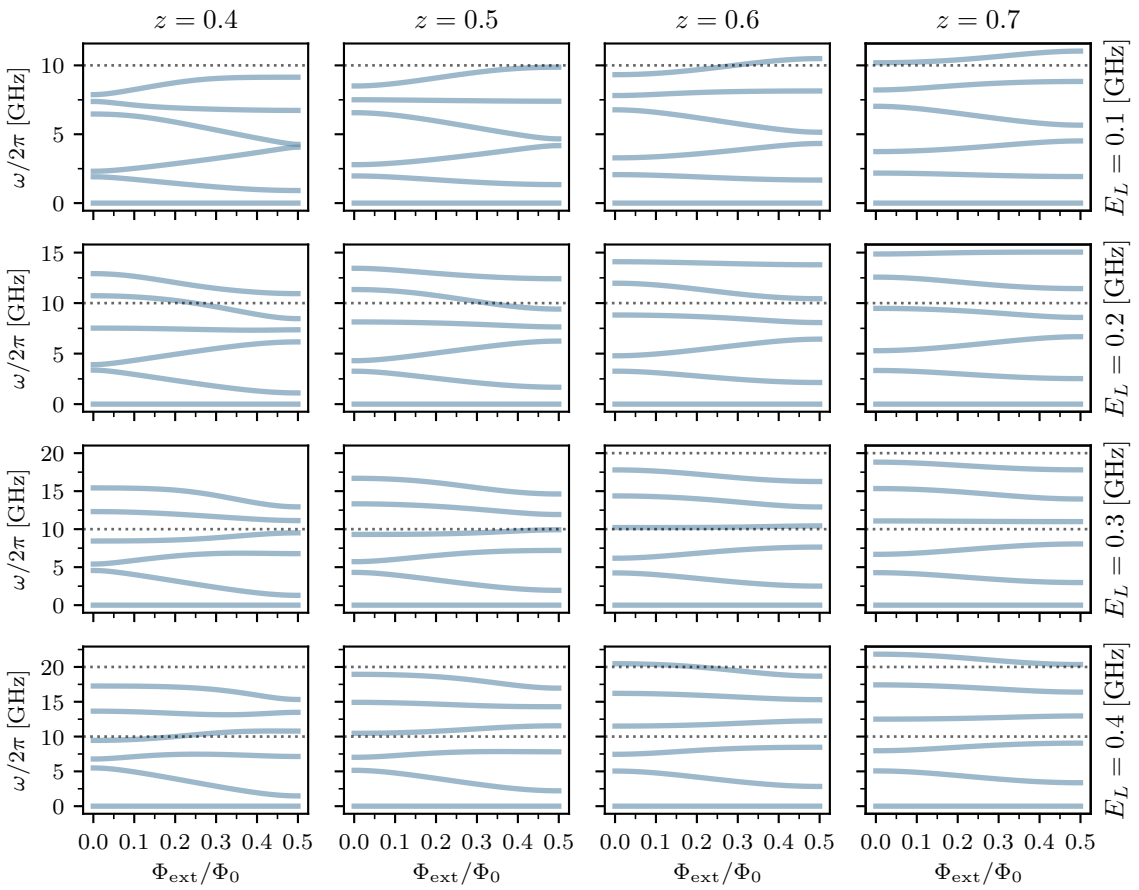

Figure 1.12 Low-lying excitations of the fluxonium qubit with a high-impedance black-sheep junction. Rows correspond to different values of $E_L/h \in [0.1, 0.4]$ GHz, while columns are obtained for different values of the black-sheep junction impedance z. Black dashed lines correspond to a two-level approximation valid for $z \ll 1$. Black dotted lines correspond to multiples of the bare plasma frequency $\omega_p/2\pi = 10$ GHz.

1.5.6 Two different generations of superconducting-qubit technology

We have so far presented the transmon and fluxonium architectures in detail. The purpose of this section is to make explicit, from a practical perspective, the comparison between these two superconducting qubits. As argued above, these devices share a number of similarities although exploiting two fundamentally different degrees of freedom of a circuit. From a technological point of view, this makes device fabrication largely different for these two cases.

The transmon qubit was proposed in 2007 [56] and demonstrated in the same year [96,

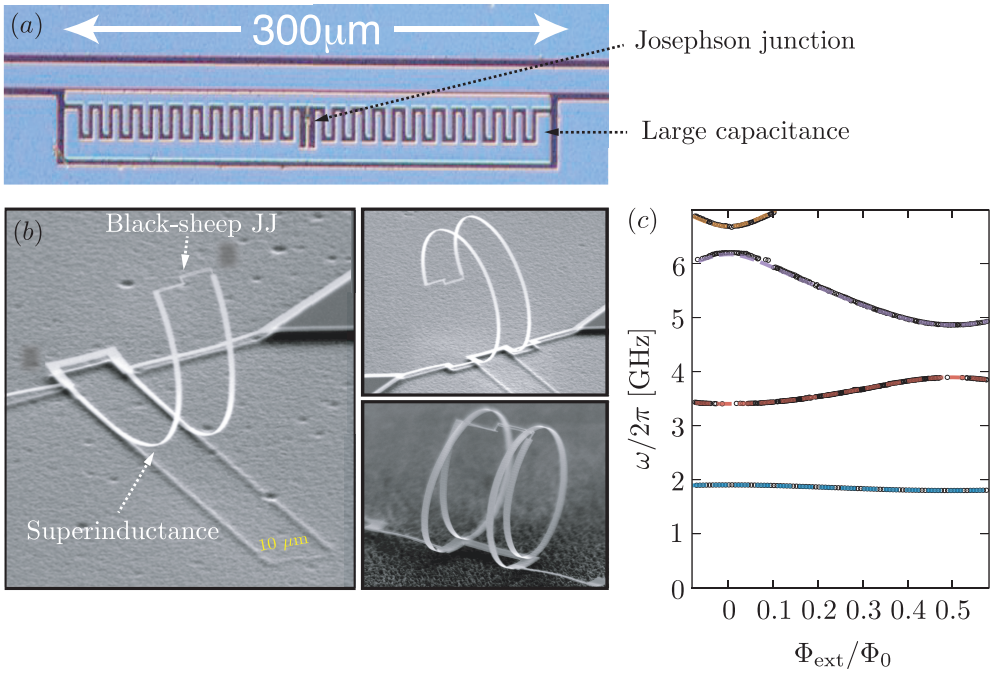

Figure 1.13 Two different generations of superconducting-qubit technology. (a) One of the first reported implementations of a transmon qubit, made of a low-impedance Josephson junction shunted by a large interdigitated capacitor. Adapted from Ref. [97]. (b) First reported implementation of a light-fluxonium qubit, made of a loop where a high-impedance Josephson junction is shunted by a high-impedance superinductance with 400 Josephson junctions. (c) Low-frequency spectrum of the device in (b) as a function of the external flux through the superconducting loop. Black circles correspond to experimental data while color dashed lines are obtained from a theory fit. $(b-c)$ are adapted from Ref. [76].

97]. The transmon qubit used in the experiment of Ref. [97], shown in Fig. 1.13 (a), consist of a low-impedance Josephson junction shunted by a large capacitance and is one of the first reported realizations of a transmon qubit. In this implementation, the required shunt capacitance is realized using an interdigitated capacitor. This geometry has the purpose of maximizing the area between the two capacitor plates, and thus the effective capacitance.

On the other hand, the realization of a light-fluxonium device was reported for the first time this year [76]. The device, shown in Fig. 1.13 (b), uses a Josephson-junction array superinductance made of 400 junctions, shunting a high-impedance black-sheep junction. Importantly, the junction chain is lifted off from the substrate such that stray capacitances, which can dress the capacitance of the black-sheep junction, are minimized. Note that this complex technique is not scalable. Fig. 1.13 (c) shows the low-frequency spectrum of the device in (b). Black circles correspond to the experimental data, which is very well explained by the model of Eq. (1.58). The effective energy parameters extracted from the fit

are $E_L/h = 0.0665\,\text{GHz}$, $E_C/h = 7.07\,\text{GHz}$ and $E_J/h = 4.7\,\text{GHz}$ for Eq. (1.58) [76], or equivalently, $z \simeq 0.55$ and $\omega_p/2\pi \simeq 16.30\,\text{GHz}$ (see also Fig. 1.12 for comparison).

Figure 1.13 $(a-b)$ show how two devices, which are described by a similar effective model, are realized very differently in practice. This difference also highlights the independent challenges that need to be overcome to make these architectures scalable. In the case of the transmon qubit, it is known that dielectric losses due to the large capacitors can limit T_1. In the case of the light-fluxonium qubit, minimizing stray capacitances in a two-dimensional circuit is one of the main difficulties. Additional challenges are discussed in chapter 5 which describes the first experimental realization of the $0-\pi$ qubit.

1.5.7 The $0-\pi$ qubit in a nutshell

We are now in a position to introduce the $0-\pi$ circuit, starting in this section with a conceptual discussion.

Conceptual description of the $0-\pi$ circuit

We begin the discussion with a simple fact: at a basic level, the $0-\pi$ circuit is made of a charge-like and a flux-like circuit modes, which are both operated in their sweet-spot-everywhere regime. Almost by definition, this makes the device insensitive to low-frequency charge and flux noise. The nontrivial $0-\pi$ circuit design, shown in Fig. 1.14 (right) allows these two modes to be integrated in the same circuit and operated at their respective noise-insensitive regimes simultaneously.

More precisely, the $0-\pi$ circuit includes two Josephson junctions and two superinductances forming a superconducting loop. Moreover, the device has two cross-capacitances that connect the top (bottom) terminal of the leftmost (rightmost) junction to the bottom (top) terminal of the rightmost (leftmost) junction. Therefore, the circuit contains two superconducting regions that are galvanically disconnected from one another (top and bottom), defining two circuit islands. Thus, the $0-\pi$ circuit is in part described by a charge degree of freedom that represents the charge difference between such islands.

As originally introduced by Brooks, Kitaev and Preskill [66], the $0-\pi$ circuit requires very large superinductances and cross-capacitances in order to achieve noise protection. As argued above, increasing both L and C can be interpreted as reducing the energy cost of adding a flux quantum or a Cooper pair to the loop and the circuit islands, respectively. Fig. 1.15 shows a schematic decomposition of the $0-\pi$ device into two modes, θ and ϕ. The

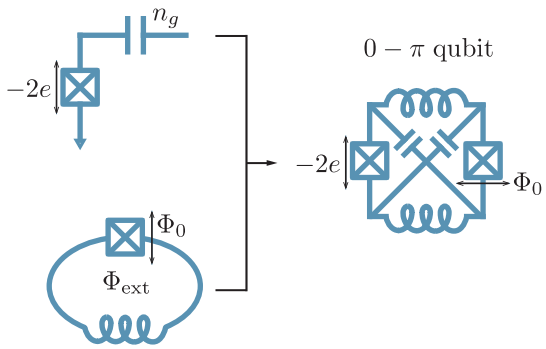

Figure 1.14 Conceptual illustration of the $0-\pi$ qubit. The $0-\pi$ device (right) is made of a transmon- and fluxonium-like modes (left) operating in the charge- and flux-insensitive regimes, respectively.

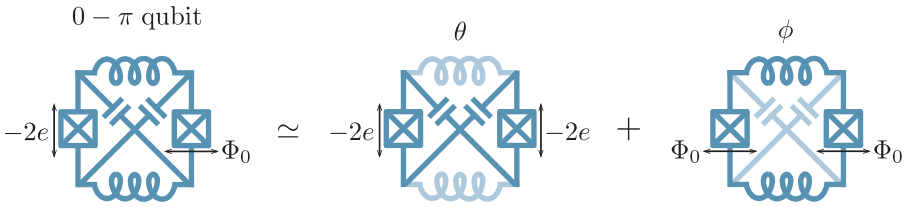

Figure 1.15 The two modes of the $0-\pi$ qubit. θ (ϕ) is a transmon-like (light-fluxonium-like) circuit mode that does not couple to the large superinductances (cross-capacitances) of the $0-\pi$ circuit. The large cross-capacitances of the circuit make the effective impedance of the Josephson junction appear different for the θ and ϕ modes, allowing a large tunneling amplitude for both Cooper pairs and flux quanta through the Josephson junctions. This picture omits two other circuit modes that are analyzed below.

θ mode is a transmon-like degree of freedom that does not couple to the superinductances of the circuit, while the ϕ mode is a light-fluxonium-like variable that does not couple to the cross-capacitances. The impedance of the Josephson junctions is assumed to be large enough such that the tunneling amplitude for flux quanta in and out of the loop is large. This makes the circuit insensitive to flux noise (light-fluxonium response). As regards the θ mode, the large capacitances of the circuit 'renormalizes' the impedance of the Josephson junctions to an effective lower value, making the Cooper pair tunneling amplitude between the circuit islands also large. Charge- and a flux-insensitive modes are thus combined in the same device thanks to the special design of the $0-\pi$ circuit.

It follows that the $0-\pi$ device is protected against dephasing due to charge and flux noise simply by the regime of parameters in which it operates. For this reason, it remains to show how the $0-\pi$ overcomes the T_1 limitations discussed in Sect. 1.5.2 for the simplest charge- and flux-like qubits. In order words, how does the $0-\pi$ qubit implements logical wavefunctions that are both delocalized over charge and flux states (exponentially small

dephasing) and at the same time disjoint (exponentially small relaxation or excitation)? The answer to this question is the existence of an extra symmetry in the $0-\pi$ qubit Hamiltonian, which splits the Hilbert space of the qubit into two disjoint Cooper-pair-number parity subspaces.

To see this, Fig. 1.16 shows an approximate equivalence between the $0-\pi$ circuit (left) and a charge-like qubit where a nonlinear element allows the transfer of pairs of Cooper pairs to a circuit island (right). The co-tunneling of Cooper pairs is a consequence of the particular circuit layout of the $0-\pi$ qubit, which combines high- and low-impedance links, corresponding to the superinductors and cross-capacitances, respectively. Fig. 1.16 (left) shows how a Cooper-pair tunneling event across one of the Josephson junctions is 'mirrored' by a simultaneous Cooper-pair tunneling event across the other Josephson junction. More precisely, a Cooper-pair tunneling event across the leftmost Josephson junction leads to the build up of a charge $-2e$ on one side of the leftmost cross-capacitance, but then this leaves an excess of $+2e$ charges on the lower plate of the rightmost capacitor, hence the appearance also of a $-2e$ charge on the upper plate of the rightmost capacitor (this come from the cross-capacitor coupling). In the $Z_L \to \infty$ limit (open circuit), this is compensated by a second tunneling event across the rightmost junction. This results in the exchange of a pair of Cooper pairs between the circuit islands, or exciton [82].

This exciton-tunneling picture suggests that the $0-\pi$ qubit Hamiltonian may be conceptually written as

$$H = \sum_n 4E_C(n-n_g)^2|n\rangle\langle n| - \frac{E_2}{2}\Big(|n+2\rangle\langle n| + \text{H.c.}\Big) - \frac{E_1}{2}\Big(|n+1\rangle\langle n| + \text{H.c.}\Big), \quad (1.60)$$

where $|n\rangle$ are charge states corresponding to the relative charge difference between the circuit islands, n_g is an offset-charge parameter, and E_2 is the tunneling amplitude for the exchange of a pair of Cooper pairs between these islands. We have moreover included a single-Cooper-pair tunneling Hamiltonian with amplitude E_1 that arises as a perturbation for any finite Z_L. Note that E_2 and E_1 will, in general, be functions of the external flux [98]. This detail is however not relevant to the present discussion.

Let us first consider the case $E_1 = 0$. Defining the Cooper-pair-parity operator $P = \exp(i\pi n)$, where n is the (dimensionless) charge operator, one can see that $[H, P] = 0$. This implies that the eigenstates of the Hamiltonian H have a definite Cooper-pair-number parity. Moreover, one can see that the energy spectrum in Eq. (1.60) is periodic in n_g with period 1, and doubly degenerate at $n_g = 0.5 \mod 1$. Similarly to the case of the transmon qubit, we expect the low-energy wavefunctions to spread over multiple charge states for

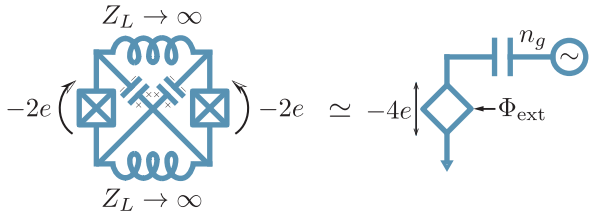

Figure 1.16 Exciton tunneling picture for the $0-\pi$ qubit. Left panel: exciton tunneling event. Right panel: equivalent circuit. The $0-\pi$ circuit can be seen as a charge qubit (right panel) where a weak link transfers pairs of Cooper pairs (charge $-4e$) with a tunneling amplitude that is controlled by the external flux.

$E_2 \gg E_C$, making the system insensitive to charge noise. In addition to this, the presence of flat energy bands and an exact degeneracy at $n_g = 0.5$ indicates that, in such a limit, the system has a ground state doublet.

The observations of the previous paragraph become clearer if the tunneling Hamiltonian is written in terms of the superconducting phase θ, which coincides with the θ mode of the $0-\pi$ circuit. For the case $E_1 = 0$, one has

$$H = 4E_C(n - n_g)^2 - E_2 \cos 2\theta, \tag{1.61}$$

where we have used the definition of the charge states in terms of the superconducting phase θ provided in Sect. 1.1.2. Importantly, while the potential energy $-E_2 \cos 2\theta$ is π-periodic from a mathematical point of view, it is inscribed in the 2π-periodicity of the superconducting phase, leading to two physically distinct energy minima located at $\theta = 0 \mod 2\pi$ and $\theta = \pi \mod 2\pi$.

Let us consider now the case of $n_g = 0 \mod 1$ for this model. Classically ($E_C = 0$), there exist two degenerate ground states, each of them located in one of the two minima of the potential. Any finite E_C leads to hybridization between these ground states, forming a pair of bonding $|\psi_e\rangle$ and antibonding $|\psi_o\rangle$ states. Since the bonding state is invariant under $\theta \to \theta + \pi$, while the antibonding state changes sign, one has $P|\psi_e\rangle = |\psi_e\rangle$ and $P|\psi_o\rangle = -|\psi_o\rangle$, where the parity operator $P = \exp(i\pi n)$ causes a displacement of the θ coordinate by π. Thus, $|\psi_e\rangle$ ($|\psi_o\rangle$) belongs to the even (odd) charge subspace, where e (o) indicates even (odd) Cooper-pair-number parity. In the limit $E_2 \gg E_C$, the energy splitting between these two states can be very well approximated by

$$\epsilon = 4\sqrt{\frac{\sqrt{3}}{\pi}}\sqrt{32E_CE_2}\,(2E_2/E_C)^{1/4}\exp\Big(-\sqrt{2E_2/E_C}\Big), \tag{1.62}$$

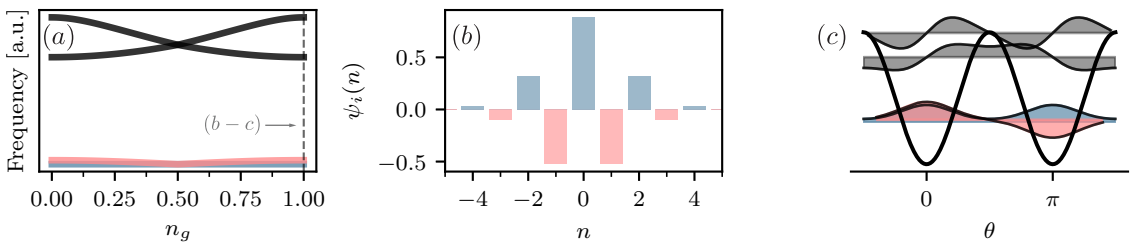

Figure 1.17 Concept for a noise-protected superconducting qubit. (a) Energy spectrum of the Hamiltonian in Eq. (1.61) as a function of n_g, displaying the ground state manifold (color) separated from the excited states (black) by a large energy gap. (b) Logical wavefunctions at $n_g = 0 \mod 1$ in charge space. The ground states have a well defined Cooper-pair-number parity. (c) Eigenstates of the Hamiltonian of Eq. (1.61) for $n_g = 0 \mod 1$ inscribed in the potential energy. The ground state with even (odd) charge components corresponds to the bonding (antibonding) wavefunction in phase space.

where $\sqrt{32E_CE_2}$ and $\sqrt{2E_C/E_J}$ play the role of an effective plasma frequency and impedance, respectively. Note that the asymptotic expression of Eq. (1.62) is found numerically. For $n_g \neq 0$, the energy splitting acquires an offset-charge dependence of the form $\epsilon \to \epsilon(n_g) = \epsilon \cos \pi n_g$, showing that charge dispersion of the ground state doublet is exponentially small for large $2E_2/E_C$. Furthermore, by considering a single potential well and following the treatment of Sect. 1.5.4 for the transmon qubit, we find that the energy gap between the two lowest energy intra-well states is given by $\sqrt{32E_CE_2} - 4E_C$. Therefore, the gap between the ground state manifold and higher excited levels of Eq. (1.61) scales as $\sqrt{32E_CE_2}$ [see Fig. 1.17].

According to the discussion of Sect. 1.5.2, a qubit described by Eq. (1.61) couples to the environment via the charge operator n. Since $|\psi_e\rangle$ and $|\psi_o\rangle$ have disjoint support in charge space, it follows that $\langle\psi_e|n|\psi_o\rangle = 0$, implying that the ground state manifold is composed of two equally metastable states with infinite T_1 and exponentially large T_2. In practice, however, T_1 would be dominated by upwards transition processes, which are exponentially attenuated with the size of the energy gap $\sim \sqrt{32E_CE_2}$, since the spectral density $S_n[\omega] \propto -\omega \exp(\hbar\omega/k_BT)$ for charge noise is exponentially small for excitation processes for which $\omega < 0$ [see Fig. 1.3].

The model in Eq. (1.61) is an idealization since, in the $0-\pi$ qubit, E_1 cannot be made exactly 0 for finite Z_L. This is also true for any other superconducting-qubit implementations of Eq. (1.60). However, it is important to note that this does not represent a major drawback if the single-Cooper-pair tunneling energy remains bounded such that $E_1 \ll E_2$. As we show below, the exponentially small charge dispersion is preserved (or improved)

and T_1 can be made exponentially large (instead of infinite) in this limit.

Indeed, thanks to the large E_2, the subspace spanned by $\{|\psi_e\rangle, |\psi_o\rangle\}$ contains all possible logical qubit states $|\psi_0\rangle$ and $|\psi_1\rangle$ that result from the coupling of the charge-parity subspaces due to $E_1 \ll E_2$. For any finite E_1, the uniform superpositions $|\psi_0\rangle = (|\psi_e\rangle + |\psi_o\rangle)/\sqrt{2}$ and $|\psi_1\rangle = (|\psi_e\rangle - |\psi_o\rangle)/\sqrt{2}$ occur at the degeneracy point $n_g = 0.5$. Away from the charge-degeneracy points, the degree of mixing between the parity subspaces is determined by the interplay between the tunneling energy in Eq. (1.62) and E_1. While the the tunneling energy favors bonding and antibonding states, E_1 favors states that are localized in a given potential well by lifting the degeneracy between the two classical ground states at $\theta = 0$ and $\theta = \pi$.

Let us assume that, for a finite (although small) E_1, the logical states are of the form $|\psi_0\rangle = r_0^e|\psi_e\rangle + r_0^o|\psi_o\rangle$ and $|\psi_1\rangle = r_1^e|\psi_e\rangle + r_1^o|\psi_o\rangle$, where $r_0^e r_1^e = -r_0^o r_1^o$ such that $\langle\psi_0|\psi_1\rangle = 0$. Then, one has

$$|\langle\psi_0|n|\psi_1\rangle|^2 = |r_0^e r_1^e|^2 |\langle\psi_e|n|\psi_e\rangle - \langle\psi_o|n|\psi_o\rangle|^2. \tag{1.63}$$

This condition reveals a connection between the transition matrix element of the qubit with $E_1 \neq 0$ and the charge dispersion $\partial_{n_g} H \propto n$ of the unperturbed qubit ($E_1 = 0$) with eigenstates $|\psi_e\rangle$ and $|\psi_o\rangle$ (see also Sect. 1.4.3). Since we have shown that the charge dispersion for the unperturbed qubit is exponentially attenuated in the large tunneling regime $E_2 \gg E_C$, it follows that the T_1 times of the new qubit ($E_1 \neq 0$) can also be made arbitrarily large. Therefore, Eq. (1.60) for $E_2 \gg E_C$ and $E_1 \ll E_2$ realizes a ground state doublet with exponentially large T_1 and T_2.

There is, however, an additional aspect that needs to be discussed. In the implementation of Eq. (1.61) by the $0-\pi$ qubit, flux noise leads to perturbations of the form $\cos\theta$ and which do not preserve the symmetry of the qubit Hamiltonian. This motivates the search for a regime of operation that is also robust to these perturbations. In particular, any finite E_1 leads to a maximal transition matrix element $\langle\psi_0|\cos\theta|\psi_1\rangle$ at the charge degeneracy points, thus compromising the qubit's T_1.

We can think of the imperfections of the qubit Hamiltonian as a feature rather than as a bug. Indeed, as illustrated in Fig. 1.18, biasing the qubit with a finite $E_1 \ll E_2$ has two important advantages. Panel (a) shows that by increasing the ratio E_1/ϵ the charge dispersion of the ground state doublet is reduced. Importantly, panel (b) shows that the bias also leads to a dramatic reduction of the transition matrix element $\langle\psi_0|\cos\theta|\psi_1\rangle$, while $\langle\psi_0|n|\psi_1\rangle$ remains bounded by an exponentially small value. The value of $\langle\psi_0|\cos\theta|\psi_1\rangle$ is highly dependent on n_g. Close to the degeneracy points $n_g = 0.5 \mod 1$, any finite E_1 leads to states that are localized in each of the two wells of the $\cos 2\theta$ potential thereby

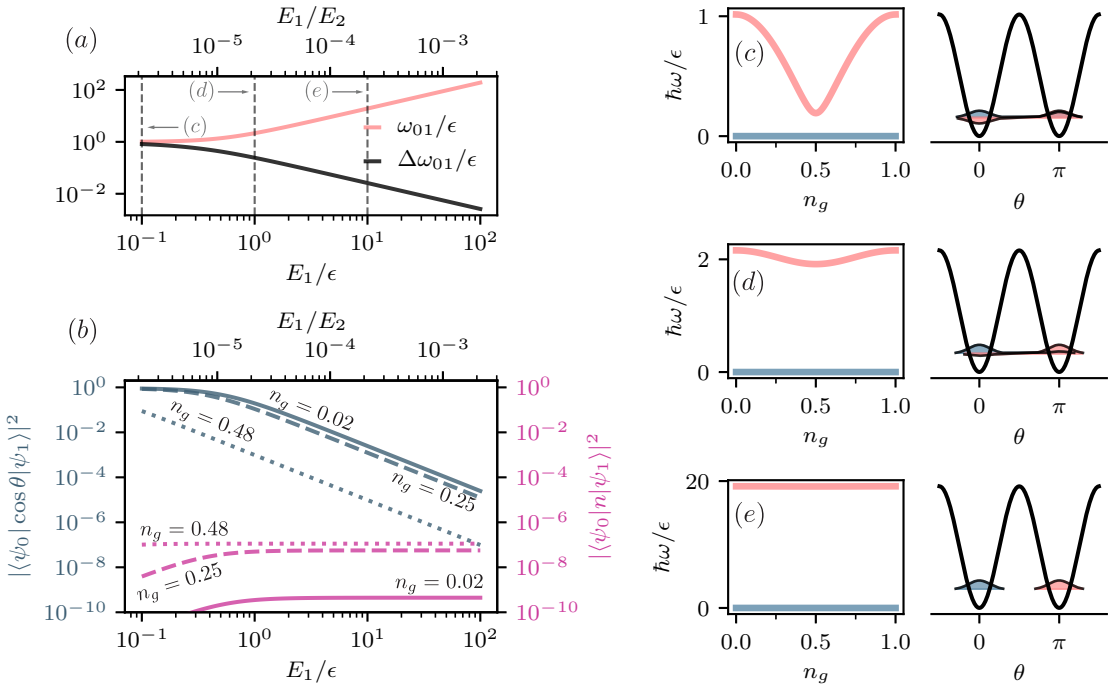

Figure 1.18 From the $\cos 2\theta$ potential to the $0-\pi$ qubit. (a) Qubit frequency ω_{01} and total charge dispersion $\Delta\omega_{01}$ in units of the tunneling amplitude ϵ as a function of E_1/ϵ (and E_1/E_2). (b) Transition matrix element of the $\cos\theta$ and n operators for different values of the offset charge n_g as a function of E_1/ϵ (and E_1/E_2). $(c-e)$ Energy spectrum as a function of n_g (left panels) and logical wavefunctions (right panel) for the configurations indicated as $(c-e)$ in (a), with respective values of $E_1/\epsilon \in [0.1, 1.0, 10.0]$. All plots correspond to the ratio $E_2/E_C = 80$ in Eq. (1.60).

reducing $\langle\psi_0|\cos\theta|\psi_1\rangle$ thanks to the disjoint support of the qubit wavefunctions. Away form the charge degeneracy points, the competition between E_1 and ϵ is stronger, leading to logical states that have spectral weight in both wells. Thus, for a given E_1/ϵ, $\langle\psi_0|\cos\theta|\psi_1\rangle$ is larger away from $n_g = 0.5 \mod 1$. Note, however, that the maximum value of this matrix element, which occurs for $n_g = 0 \mod 1$, can be made small by increasing the bias (E_1).

According to panel (b), the maximum of $\langle\psi_0|n|\psi_1\rangle$ is reached at the charge degeneracy point. This is a consequence of the symmetric combination of $|\psi_e\rangle$ and $|\psi_o\rangle$ in the logical state wavefunctions for any finite E_1 at such operating points, which maximizes the value of $|r_0^e r_1^e|$ in Eq. (1.63). Away from the charge degeneracy points, the Cooper-pair-number parity of the qubit eigenstates is better preserved, leading to a reduced $\langle\psi_0|n|\psi_1\rangle$.

Figure 1.18 $(c-e)$, shows the qubit spectrum as a function of n_g and the logical wavefunctions in phase space. As anticipated, the spectrum becomes flatter with n_g as E_1/ϵ increases, while the qubit wavefunctions become more localized in the $\theta = 0$ and $\theta = \pi$

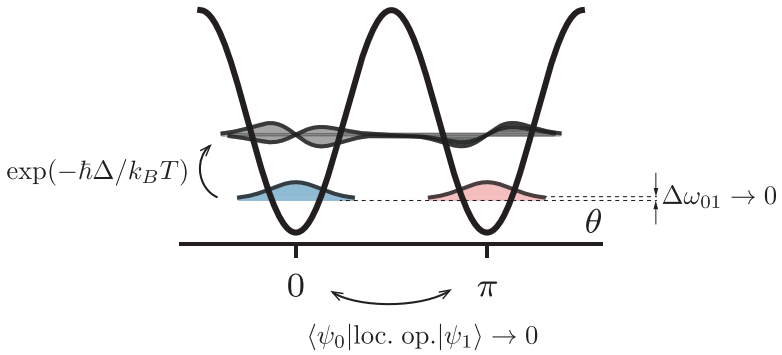

Figure 1.19 Summary of the strategies exploited to reach full noise protection in the $0-\pi$ qubit.

wells of the potential. This is the regime of operation of the $0-\pi$ qubit [66]. In this regime, the qubit features exponentially small charge and flux dispersion and exponentially large T_1 times for all noise processes.

The price to pay for a reduced charge sensitivity and negligible transition matrix elements is a linear dispersion of the qubit transition energy with E_1/ϵ for $E_1/\epsilon \gg 1$, which can enhance the pure-dephasing rates. Moreover, an increase of the qubit frequency ω_{01} can in principle lead to larger relaxation rates, as $S_n[\omega] \propto \omega$ for $\omega > 0$. However, these effects are very small in practice, as E_1 is an exponentially small quantity in the $0-\pi$ qubit regime [98] (although sufficiently larger than ϵ). Furthermore, since E_1 depends on the external flux, it is possible to find flux-bias points for which $E_1/\epsilon \gg 1$ but $\partial E_1/\partial\Phi_{\text{ext}} = 0$, i.e. a sweet spot, removing any first-order dephasing processes due to flux noise.

Figure 1.19 summarizes the strategies exploited in the $0-\pi$ qubit for achieving full noise protection. Transitions to the excited manifold are prevented by a large energy gap $\hbar\Delta$, with $\Delta/2\pi \sim$ GHz. T_1 is made arbitrarily large by engineering two metastable states with disjoint support, such that the matrix element of any local operator (loc. op.) is exponentially small. T_2 is made arbitrarily large by working simultaneously at the charge- and flux- insensitive regimes of the device, and operating at a flux sweet spot.

Chapter 2

A closer look at the $0-\pi$ qubit

Having discussed the basic elements regarding the transmon, fluxonium and circuit QED architectures, we are now in a position to describe the $0-\pi$ qubit in more details. The information provided here is in principle enough to understand the research papers following chapters of this thesis.

2.0.1 Introduction

As mentioned previously, the basic idea behind the $0-\pi$ qubit [66] is to encode quantum information in a noise-protected subspace of a superconducting circuit. Noise protection arises in this system because the circuit includes two degrees of freedom that have large zero-point fluctuations (preventing pure-dephasing) while the logical states have disjoint support (preventing relaxation). We now focus on the Hamiltonian description of the device, robustness to noise (see also chapter 3), control strategies and challenges that need to be overcome in order to make this system scalable (see also chapter 4). We furthermore motivate the first experimental realization that is presented in more details in chapter 5.

2.0.2 The $0-\pi$ circuit Hamiltonian

Modeling the $0-\pi$ circuit requires us to introduce the flux (phase) node operators Φ_i ($\varphi_i = \Phi_i/\varphi_0$) for $i \in [1,4]$, which are shown in Fig. 2.1 (leftmost panel). These node operators can be rearranged to define the normal modes: θ, ϕ, ζ and Σ [see Fig. 2.1]. The θ and ϕ modes are crucial to the $0-\pi$ qubit Hamiltonian, and have been discussed before. The ζ and Σ modes are spurious modes. In particular, ζ is a harmonic mode that couples to

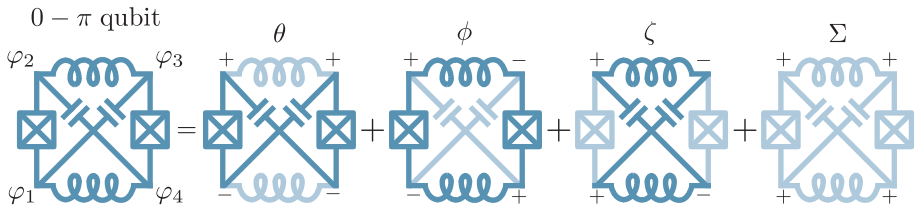

Figure 2.1 The full $0-\pi$ circuit including 4 circuit modes θ, ϕ, ζ and Σ. The $+/-$ symbol on the ith circuit node corresponds to the phase of φ_i in the definition of the θ, ϕ, ζ or Σ, according to the panel.

the large cross-capacitances and superinductances of the circuit, while Σ is a cyclic mode that couples to the ground and gate capacitances of the circuit (if any).

In order to address control and readout of the $0-\pi$ qubit, we also assume the circuit being coupled to external voltage sources V_i via gate capacitances C_{g_i}, one for every circuit node $i \in [1,4]$. These voltage operators can be rearranged in a vector of the form $\boldsymbol{V}_\Phi = (V_1,\ldots,V_4)^T$, where the subindex Φ denotes the flux node basis $\{\Phi_i\}$. The circuit Lagrangian then takes the form

$$L_\Phi = \dot{\boldsymbol{\Phi}}^T \cdot \frac{\boldsymbol{C}_\Phi}{2} \cdot \dot{\boldsymbol{\Phi}} - \dot{\boldsymbol{\Phi}}^T \cdot \boldsymbol{C}_g \cdot \boldsymbol{V}_\Phi - U(\boldsymbol{\Phi}, \Phi_{\text{ext}}), \tag{2.1}$$

where $\boldsymbol{\Phi} = (\Phi_1,\ldots,\Phi_4)^T$, $\boldsymbol{C}_\Phi$ is the capacitance matrix of the circuit with components $[\boldsymbol{C}_\Phi]_{ij} = \partial L_\Phi / \partial\dot{\Phi}_i \partial\dot{\Phi}_j$, $\boldsymbol{C}_g = \text{diag}(C_{g_1},\ldots,C_{g_4})$ is the capacitance matrix corresponding to the gate capacitances that connect the $0-\pi$ circuit to the voltage sources, and $U(\boldsymbol{\Phi}, \Phi_{\text{ext}})$ is the potential energy due to the Josephson junctions and superinductances. More precisely, the circuit capacitance matrix is given by

$$\boldsymbol{C}_\Phi = \begin{pmatrix} C_1 & -C_J' & -C' & 0 \\ -C_J' & C_2 & 0 & -C'' \\ -C' & 0 & C_3 & -C_J'' \\ 0 & -C'' & -C_J'' & C_4 \end{pmatrix}, \tag{2.2}$$

where $C_1 = C_J' + C' + C_{g_1} + C_{0_1}$, $C_2 = C_J' + C'' + C_{g_2} + C_{0_2}$, $C_3 = C_J'' + C' + C_{g_3} + C_{0_3}$ and $C_4 = C_J'' + C'' + C_{g_4} + C_{0_4}$. Here we also assume a ground capacitance C_{0_i} for every circuit node, and possible disorder in the junction ($C_J' \neq C_J''$) and cross-capacitances ($C' \neq C''$) of the circuit. Note that Eq. (2.1) also describes the $0-\pi$ qubit coupled to a resonator if V_i is replaced by the resonator's voltage operator.

We now move to the $0-\pi$ mode basis defined by $\boldsymbol{\Theta} = (\phi, \theta, \zeta, \Sigma)^T$, by the change of basis $\boldsymbol{\Theta} = \boldsymbol{R} \cdot \boldsymbol{\Phi}$, where

$$\boldsymbol{R} = \frac{1}{2} \begin{pmatrix} -1 & 1 & -1 & 1 \\ -1 & 1 & 1 & -1 \\ 1 & 1 & -1 & -1 \\ 1 & 1 & 1 & 1 \end{pmatrix}. \tag{2.3}$$

Under this transformation, Eq. (2.1) reads

$$L_\Theta = \dot{\boldsymbol{\Theta}}^T \cdot \frac{\boldsymbol{C}_\Theta}{2} \cdot \dot{\boldsymbol{\Theta}} - \dot{\boldsymbol{\Theta}}^T \cdot \tilde{\boldsymbol{C}}_g \cdot \boldsymbol{V}_\Theta - U(\boldsymbol{\Theta}, \Phi_{\text{ext}}), \tag{2.4}$$

where $\boldsymbol{C}_\Theta = (\boldsymbol{R}^{-1})^T \cdot \boldsymbol{C}_\Phi \cdot \boldsymbol{R}^{-1}$ and $\tilde{\boldsymbol{C}}_g = (\boldsymbol{R}^{-1})^T \cdot \boldsymbol{C}_g \cdot \boldsymbol{R}^{-1}$ are the transformed capacitance matrices, and $\boldsymbol{V}_\Theta = \boldsymbol{R} \cdot \boldsymbol{V}_\Phi$ is the original voltage-drive vector expressed in the $0-\pi$ mode basis. Performing a Legendre transformation, we obtain the circuit Hamiltonian as

$$H = (\boldsymbol{q}_\Theta + \tilde{\boldsymbol{C}}_g \cdot \boldsymbol{V}_\Theta)^T \cdot \frac{\boldsymbol{C}_\Theta^{-1}}{2} \cdot (\boldsymbol{q}_\Theta + \tilde{\boldsymbol{C}}_g \cdot \boldsymbol{V}_\Theta) + U(\boldsymbol{\Theta}, \Phi_{\text{ext}}), \tag{2.5}$$

where $\boldsymbol{q}_\Theta = \partial L_\Theta / \partial \dot{\boldsymbol{\Theta}}$ is a vector notation for the conjugate charge operators. Note that Eq. (2.5) can be split as

$$H = H_{0-\pi} + H_{\text{drive}}, \tag{2.6}$$

where

$$H_{0-\pi} = \boldsymbol{q}_\Theta^T \cdot \frac{\boldsymbol{C}_\Theta^{-1}}{2} \cdot \boldsymbol{q}_\Theta + U(\boldsymbol{\Theta}, \Phi_{\text{ext}}), \tag{2.7}$$

is the undriven $0-\pi$ qubit Hamiltonian and

$$H_{\text{drive}} = \boldsymbol{q}_\Theta^T \cdot (\boldsymbol{C}_\Theta^{-1} \cdot \tilde{\boldsymbol{C}}_g) \cdot \boldsymbol{V}_\Theta, \tag{2.8}$$

is a voltage-drive term.

We now simplify the description provided by Eq. (2.6). Omitting the cyclic variable Σ, Equation (2.7) can then be written as

$$H_{0-\pi} \simeq 4E_{C_\theta}(n_\theta - n_g)^2 + 4E_{C_\phi} n_\phi^2 + \hbar g_{\phi\theta} n_\phi n_\theta + 4E_{C_\zeta} n_\zeta^2 + \hbar g_{\theta\zeta} n_\theta n_\zeta + U(\boldsymbol{\Theta}, \Phi_{\text{ext}}), \tag{2.9}$$

where we have introduced the capacitive energies $E_{C_\theta} = e^2/2C_\theta$, $E_{C_\phi} = e^2/2C_\phi$ and $E_{C_\eta} = e^2/2C_\eta$, defined in terms of the mode capacitances $C_\theta \propto 2(C_J + C)$, $C_\phi \propto 2C_J$ and $C_\zeta \propto 2C$, with $C_J = (C_J' + C_J'')/2$ and $C = (C' + C'')/2$ being the mean values for the junction

and cross capacitances of the circuit [98]. We have moreover introduced an offset-charge parameter n_g for the θ mode, given that this degree of freedom is compact. Additionally, the spurious capacitive coupling coefficients $g_{\phi\theta} \propto dC_J = (C_J' - C_J'')/C_J$ and $g_{\theta\zeta} \propto dC = (C' - C'')/C$ are only nonzero in the presence of circuit-element disorder.

In absence of circuit-element disorder, the drive Hamiltonian Eq. (2.8) can also be recast into a simpler form

$$H_{\text{drive}} \simeq 2e\beta_\theta n_\theta V_\theta + 2e\beta_\phi n_\phi V_\phi + 2e\beta_\eta n_\eta V_\eta, \tag{2.10}$$

where $\beta_\theta \propto C_g/C_\theta$, $\beta_\phi \propto C_g/C_\phi$ and $\beta_\zeta \propto C_g/C_\zeta$ are capacitive coupling ratios for the θ, ϕ and ζ modes, respectively, V_μ is the corresponding voltage-drive for $\mu \in \{\theta, \phi, \zeta\}$, and C_g is a mean value for the coupling capacitances. Circuit-element disorder can unfortunately introduce spurious drive terms by which a voltage-drive intended to drive the ϕ coordinate, for instance, can also drive the θ degree of freedom. These spurious drive terms are not relevant for the present discussion and are provided in Ref. [98].

It remains to specify the potential energy as

$$U(\mathbf{\Theta}, \Phi_{\text{ext}}) = -2E_J \cos\theta \cos\left(\phi - \frac{\varphi_{\text{ext}}}{2}\right) + E_L(\phi^2 + \zeta^2) + dU(\mathbf{\Theta}, \Phi_{\text{ext}}), \tag{2.11}$$

where $E_J = (E_J' + E_J'')/2$ and $E_L = (E_L' + E_L'')/2$ are the mean values for the junction and inductive energies. Moreover,

$$dU(\mathbf{\Theta}, \Phi_{\text{ext}}) = E_J dE_J \sin\theta \sin\left(\phi - \frac{\varphi_{\text{ext}}}{2}\right) + dE_L E_L \phi\zeta, \tag{2.12}$$

where $dE_J = (E_J' - E_J'')/E_J$ and $dE_L = (E_L' - E_L'')/E_L$ is a spurious potential energy that arises in the presence of circuit element disorder. This completes the derivation of the most general $0 - \pi$ circuit Hamiltonian.

2.0.3 The $0 - \pi$ qubit parameter regime

In order to specify the device's parameter regime for which a ground state doublet is realized, we now consider the $0 - \pi$ circuit in absence of all circuit-element disorder. In this limit, the θ and ϕ modes decouple from the ζ mode, and the (undriven) circuit Hamiltonian takes the form

$$H_{0-\pi} = 4E_{C_\theta}(n_\theta - n_g)^2 + 4E_{C_\phi} n_\phi^2 - 2E_J \cos\theta \cos\left(\phi - \frac{\varphi_{\text{ext}}}{2}\right) + E_L\phi^2. \tag{2.13}$$

Here, we recover the intuition developed in the previous sections. The $0-\pi$ qubit is made of a transmon-like mode θ and a fluxonium-like mode ϕ. Both of these modes should operate in the charge- and flux-noise sweet-spot everywhere regimes, respectively, for which the eigenvalues of the Hamiltonian of Eq. (2.13) behave robustly against external perturbations. In this regime, the energy cost of adding a Cooper pair $E_{C_\theta} \propto 1/C_\theta$ or a quantum of flux $E_L \propto 1/L$ is small. Furthermore, the Josephson junctions of the circuit should behave as small (large) impedance circuit elements when regarding the θ (ϕ) mode. Combined, these conditions require E_L to be reduced as much as possible, while ensuring the condition that $E_J/E_{C_\theta} \gg E_J/E_{C_\phi}$. Since the mode impedance is a measurement of the tunneling amplitude between two degenerate potential wells, the latter condition implies that tunneling in the θ direction is strongly suppressed in comparison to tunneling in the ϕ direction. Thus, this regime favors logical wavefunctions that are strongly localized in θ while being delocalized over ϕ.

The parameter regime of the $0-\pi$ qubit can be better understood by analyzing the potential energy landscape corresponding to Eq. (2.11) for no circuit-element disorder. Fig. 2.2 (a) shows a density plot of the potential energy, where ϕ corresponds to the x axis, and θ to the y axis. Let us first consider the cases where θ is fixed to 0 or π, which we call the 0 and π valleys. The potential energy associated with these two valleys is $U(\phi, \theta = \{0, \pi\}) = \mp 2E_J \cos(\phi - \varphi_{\text{ext}}/2) + E_L\phi^2$. These two potentials are similar to two fluxonium-qubit potentials that are displaced with respect to each other by an effective flux bias such that, at $\Phi_{\text{ext}} = 0$, the $\theta = 0$ valley has its minima at $\phi \simeq 2k\pi$, whereas the $\theta = \pi$ valley has its minima at $\phi \simeq (2k+1)\pi$ for $k \in \mathbb{Z}$ [99]. These values are only approximate and are valid for relatively small k, as the effect of the quadratic potential $E_L\phi^2$ becomes more important as ϕ increases. A relatively large value of E_{C_ϕ}/E_J (and junction plasma frequency) results in a large tunneling amplitude between these potential wells and thus in wavefunctions that spread over several minima along the ϕ direction. This is illustrated in Fig. 2.2 (b) and (c), which show the first two eigenstates of the $0-\pi$ qubit being strongly delocalized over ϕ, for a particular parameter set. Furthermore, due to a very low ratio E_{C_θ}/E_J, tunneling in the θ direction is exponentially suppressed compared to E_L, leading to a very weak coupling of states belonging to different wells. Therefore, these conditions naturally lead to a doublet structure of the low-frequency eigenstates of the $0-\pi$ qubit. This is illustrated in Fig. 2.2 (d), but given the small size of the doublet splittings, some of the doublets look like single energy levels (including the ground-state doublet). The transmon- and light-fluxonium-like regimes of operation of θ and ϕ, respectively, make these low-frequency excitations exponentially insensitive to both charge and flux noise.

As originally suggested in Ref. [99], the parameter regime of the $0-\pi$ qubit can be

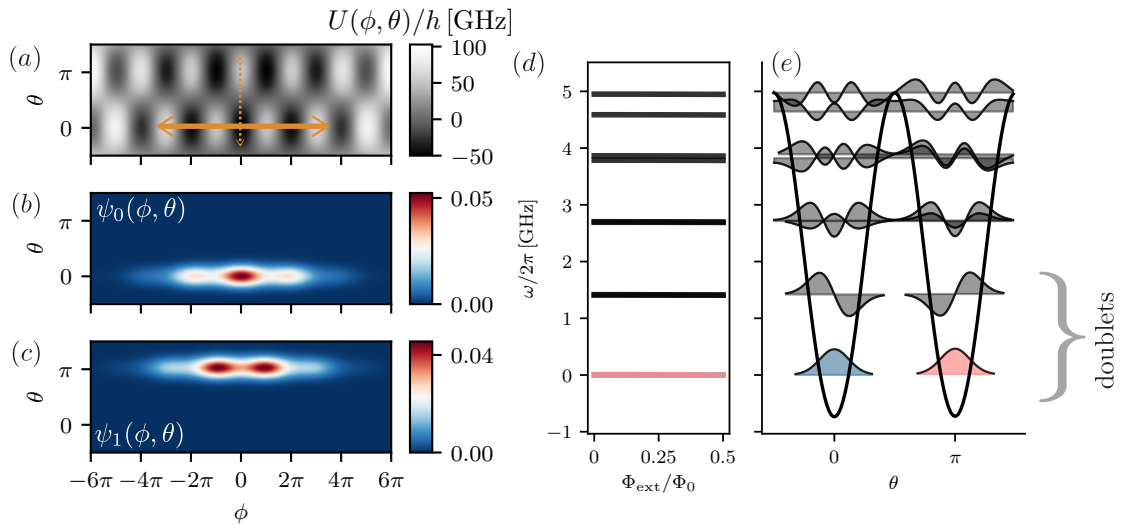

Figure 2.2 The structure of the $0-\pi$ qubit spectrum and eigenstates. (a) Potential energy landscape for $\Phi_{\rm ext}=0$. A thick orange arrow indicates a large tunneling probability along the ϕ direction, while a dashed orange arrow indicates a strongly suppressed tunneling probability along the θ direction. (b) ground state wavefunction. (c) First-excited state wavefunction. (d) Energy spectrum as a function of the external flux. (e) Effective one-dimensional model at zero applied flux, featuring the $\cos 2\theta$ structure of the $0-\pi$ Hamiltonian. Parameters: $E_{C_\theta}/h = 0.026\,$GHz, $E_{C_\phi}/h = 56.7\,$GHz, $E_J/h = 24.75\,$GHz, $E_L/h = 0.15\,$GHz, corresponding to a very deep $0-\pi$ regime [99].

summarized by the condition

$$E_L, E_{C_\theta} \ll E_J, E_{C_\phi}. \tag{2.14}$$

Although useful, this condition only serves as a starting point for engineering such a device. Indeed, the multilevel structure of the qubit can display qualitatively different regimes depending on the exact ratio between the energy parameters in Eq. (2.14), while still satisfying this condition. We say that a device is in the 'soft', 'moderate,' or 'deep/hard' $0-\pi$ regime, depending on the degree to which Eq. (2.14) is satisfied.

To complement our analysis, Fig. 2.2 (e) shows an effective one-dimensional model for the device, which is derived by eliminating the light degree of freedom (ϕ) by means of the Born-Oppenheimer approximation [98]. While we defer the details of such model to chapter 4, the purpose of panel (e) is to show that there exists a formal procedure to derive the $\cos 2\theta$ potential of the $0-\pi$ qubit, as explained in previous sections. In this effective picture, the external flux introduces a finite bias between the two nearly degenerate potential minima, leading to the localization of the logical wavefunctions in the $\theta=0$ or $\theta=\pi$ potential wells away from $\Phi_{\rm ext}=\Phi_0/2$. A zero applied external flux corresponds to

a sweet spot of the system for which the bias between the potential wells is maximal.

2.0.4 Challenges associated with the $0-\pi$ circuit

As defined in the previous section, the $0-\pi$ qubit involves a number of conceptual and fabrication challenges. We now outline some of these challenges and motivate some of the results that are presented in this thesis.

Stray capacitances

One of the main difficulties in realizing the $0-\pi$ qubit is the large anisotropy between the capacitive energies E_{C_θ} and E_{C_ϕ} that is required. Conceptually, this anisotropy can simply be realized by increasing the cross-capacitances of the circuit as much as possible. However, in practice these large cross-capacitances also result in large stray capacitances between nodes 1 and 2, and nodes 3 and 4 [see Fig. 2.3 (a)]. These stray capacitances can substantially dress C_ϕ, making the ϕ mode much more massive and lowering E_{C_ϕ}. Furthermore, any other stray capacitances arising, for instance, from the ground capacitance of the superinductors, would also contribute to the dressing of C_ϕ.

Michel Devoret has pointed out to this unfortunate situation in a very succinct way: The $0-\pi$ circuit is a device that can be drawn on a blackboard but that cannot be built in real life [100]. As shown by the first experimental realization of the $0-\pi$ (in a soft regime where the device is protected only to first order against flux-noise) the dressing of C_ϕ can be overcome to some extent by careful electromagnetic engineering of the circuit. However, complementary solutions are still needed to reach the fully noise-protected regime of this device.

Circuit-element disorder and coupling to the ζ mode

As specified in Sect. 2.0.2, circuit-element disorder can lead to spurious coupling between the qubit modes, θ and ϕ, and the ζ mode. Assuming that the latter mode is off-resonant with the qubit transitions, we can model this spurious coupling by means of a dispersive theory (see Sect. 1.2.3). Restricting the analysis to the qubit manifold, the coupling Hamiltonian takes the form [101]

$$H_{\{\theta,\phi\}-\zeta} = \frac{\chi_{01}}{2}\,\sigma_z\, a_\zeta^\dagger a_\zeta, \tag{2.15}$$

where $\chi_{01} = \chi_1 - \chi_0$ is the dispersive shift corresponding to the qubit $0-1$ transition, $\sigma_z = |\psi_1\rangle\langle\psi_1| - |\psi_0\rangle\langle\psi_0|$ is the qubit logical Z operator, and $a_\zeta^\dagger$ (a_ζ) is the photon creation

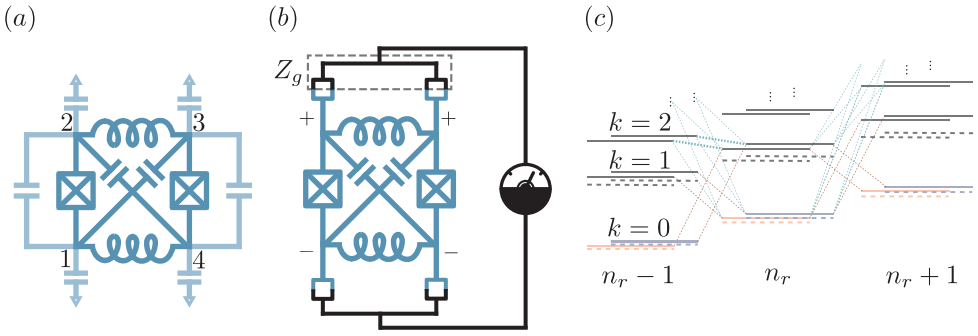

Figure 2.3 Practical challenges associated to the $0 - \pi$ circuit. (a) Effect of spurious capacitances (lighter shade of blue) arising from the large cross-capacitances of the circuit and ground capacitances. (b) Coupling the $0 - \pi$ qubit to a measurement apparatus. The small circuit components (half black, half blue) represent arbitrary coupling elements. (c) Conceptual level structure and dispersive shifts of the $0 - \pi$ qubit.

(annihilation) operator for the ζ mode. Since the frequency ω_ζ of the ζ mode is $\propto 1/\sqrt{LC}$, the mean photon-number population of this mode can be large for typical $0 - \pi$ parameters. According to Eq. (2.15), large thermal fluctuations of the photon number lead to dephasing of the qubit wavefunction, known as photon shot-noise dephasing [102, 32].

The effect of photon shot-noise dephasing on the $0 - \pi$ qubit has been studied in Ref. [101] that is presented in chapter 3. Importantly, this noise channel is found to be the main limitation to the coherence times of $0 - \pi$ devices in a realistic regime of parameters. There exists, however, ways of alleviating this effect. In particular, in chapter 4, we propose to engineer a cooling mechanism for the ζ mode, by coupling the $0 - \pi$ qubit to a low-Q resonator. We show that this scheme has the potential to enhance the coherence times by several orders of magnitude.

Coupling to a measurement apparatus

A more fundamental challenge arises if we now consider coupling the $0 - \pi$ qubit to a measurement apparatus, as shown in Fig. 2.3 (b). There, the black-blue circuit components represent arbitrary coupling elements, such as capacitors, inductors or Josephson junctions. The coupling layout is chosen to address the θ mode, which can potentially differentiate between the states of the ground state manifold corresponding to $\theta = \{0, \pi\}$.

Importantly, the coupling geometry imposes an effective shunt of the superinductances of the $0 - \pi$ circuit, leading to a combined impedance Z_g between the terminals of each superinductors. Since, according to the discussion in Sect. 1.5.7, the large impedance of the

superinductors is crucial to realize an effective $\cos 2\theta$ potential, the effective shunt due to the coupling circuitry can severely compromise the device operation.

In order to overcome this issue, the impedance of the coupling elements needs to be made as large as the impedance of the superinductors. However, the coupling elements cannot be superinductors themselves, as this would lead to an inductive shunt of the circuit islands through the measurement apparatus. As we have pointed out in [98], this rules out several possibilities for effective coupling elements. We address these issues in further details in chapter 4.

Vanishing small dispersive shifts

As argued above, the spectrum of the $0-\pi$ qubit is composed by doublets. In other words, the spectrum looks like two superimposed copies of the spectrum corresponding to a single potential well. Since tunneling between wells is exponentially suppressed, these two copies are only weakly coupled, and one can in principle neglect such a coupling. As a consequence, the dispersive shift of states in a given doublet is expected to be nearly identical [see Eq. (1.11)], as illustrated in Fig. 2.3 (c). Evidently, this situation poses a challenge to the dispersive readout techniques described in Sect. 1.2.4. We consider this problem in more details in chapter 4.

On the flip side, according to Eq. (2.15), a vanishing dispersive shift of the qubit transition can potentially reduce the impact photon-shot noise arising from coupling to the ζ mode. Note that this is not guaranteed as the frequency of the ζ mode tends to zero as the circuit enters in the deep regime, leading to a diverging photon population of ζ. We expand on this in chapter 3.

Chapter 3

Coherence properties of the $0-\pi$ qubit

3.1 Motivation

In this section, we present the paper titled "Coherence properties of the $0-\pi$ qubit". This work demonstrates the noise protection of the $0-\pi$ qubit by means of a rigorous theory and full numerics.

The $0-\pi$ qubit is a device that exploits a great deal of intuition about noise protection. However, the pioneering work by Brooks et al. [66] did not provide a detailed treatment of decoherence. Because of this, the extent to which the device is protected against noise, and the optimal parameter regime for operation, which is also compatible with fabrication, remained unclear. Here we go beyond the treatment of Ref. [66] conducting an in-depth analysis of decoherence using rigorous theoretical techniques that complement intuition.

The objective of the paper is to quantify the device sensitivity to various noise channels, including charge, flux and critical-current noise. Moreover, we evaluate the coherence times in the presence of circuit-element disorder. As anticipated, disorder leads to coupling of the qubit degrees of freedom to the low-frequency ζ mode. This opens up new channels for relaxation (Purcell) and dephasing (photon shot noise). An objective of this work is to quantify the impact of these additional decoherence processes and in particular, decide whether or not the device preserves its noise protection.

The study is done in three regimes of parameters that each have different dominant decoherence processes. Our results suggest favorable design configurations dependent on the available experimental capabilities.

3.2 Main results of the paper

We analyze of decoherence processes with and without circuit-element disorder for 3 parameter sets labeled PS1, PS2 and PS3. The value of E_L/h in these parameter sets increases from 8 MHz in PS1, to 40 MHz in PS2 and 130 MHz in PS3. We note that, in general, these are small values for the inductive energy, although $E_L/h \simeq 66.5$ MHz has been recently realized in a light-fluxonium device [76]. Other parameters in the $0-\pi$ qubit Hamiltonian also vary between these parameter sets, but these differences are not relevant for the purpose of this introductory discussion.

In absence of circuit-element disorder, we first demonstrate that it is highly advantageous to operate the system at the flux sweet spot $\Phi_{\text{ext}} = 0$ (instead of $\Phi_{\text{ext}} = \Phi_0/2$) for all parameter sets. As justified in the previous sections, operating at $\Phi_{\text{ext}} = 0$ introduces a finite energy difference between the two valleys of the effective $\cos 2\theta$ potential, favoring logical wavefunctions that are localized in $\theta = 0$ or $\theta = \pi$. The disjoint support of these wavefunctions in phase space significantly reduces the rate of incoherent transitions between the qubit states which contributes to T_1. Indeed, we observe that the T_1 times for $\Phi_{\text{ext}} = 0$ or $\Phi_{\text{ext}} = \Phi_0/2$ can differ by several orders of magnitude for the 3 parameter sets. Moreover, this difference remains unaffected if the rate of upwards transitions (out of the qubit manifold) is taken into account in the definition of T_1.

We also verify that operating a symmetric $0-\pi$ qubit at the $\Phi_{\text{ext}} = 0$ sweet spot leads, as expected, to very large coherence times. More precisely, we find that critical-current noise can eventually limit the pure-dephasing coherence times, as this operating point does not necessarily corresponds to a sweet spot with respect to the junction energy E_J. However, the estimated pure-dephasing coherence times still remain large, ranging from hundreds of seconds for PS1, to tens and a few milliseconds for PS2 and PS3, respectively. We note that, as E_L is increased, the flux sensitivity also increases. Thus, operating away from the sweet spot makes flux noise the dominant contribution to dephasing, instead of critical-current noise. Furthermore, considering upwards transitions, we find that T_1 can go from thousands of seconds for PS1, to hundreds and tens of seconds in PS2 and PS3. These numbers demonstrate that, even in the less favorable situation of PS3, a symmetric $0-\pi$ is

expected to have very long T_1 times in comparison to other devices such as the transmon or fluxonium qubits.

The situation is different if circuit-element disorder is taken into account. In particular, we consider disorder that couples the qubit modes, θ and ϕ, to the ζ mode. This coupling contributes to T_1 (Purcell) and T_φ (photon shot noise). While the absolute value of this contribution depends strongly on the quality factor of the ζ mode, which is difficult to estimate, we find that these decoherence channels dominate the coherence times for a conservative value of the ζ-mode linewidth, taken as $\kappa_\zeta = 1/100\,\mu$s. While the Purcell contribution to the T_1 times is significant, T_1 remains above 10 s for the less favorable case of PS3. However, the photon shot noise contribution to the pure-dephasing rates is quite severe as compared to other sources of noise, as we discuss below.

In our paper, we use a result that is derived for a qubit dispersively coupled to a cavity whose role here is played by the ζ mode. In these conditions, the effective pure-dephasing rate of the qubit wavefunction takes the form [32, 103]

$$\Gamma_\varphi^{\mathrm{SN}} = \frac{\kappa_\zeta}{2}\mathrm{Re}\left[\sqrt{\left(1+\frac{2i\chi_{01}^\zeta}{\kappa_\zeta}\right)^2+\frac{8i\chi_{01}^\zeta n_{\mathrm{th}}(\omega_\zeta)}{\kappa_\zeta}}-1\right], \tag{3.1}$$

where $\chi_{01}^\zeta = (\chi_1^\zeta - \chi_0^\zeta)/2$ is the dispersive shift of the qubit transition due to coupling to the ζ mode, and $n_{\mathrm{th}}(\omega_\zeta) = 1/[\exp(\hbar\omega_\zeta/k_BT)-1]$ is the thermal photon population of this mode. Importantly, if $\chi_{01}^\zeta \gg \kappa_\zeta$, then $\Gamma_\varphi^{\mathrm{SN}} \simeq \kappa_\zeta n_{\mathrm{th}}(\omega_\zeta)$ decreases by increasing the quality factor of the ζ mode. In the opposite limit where $\chi_{01}^\zeta \ll \kappa_\zeta$, one has $\Gamma_\varphi^{\mathrm{SN}} \simeq 4(\chi_{01}^\zeta)^2 n_{\mathrm{th}}(\omega_\zeta)[n_{\mathrm{th}}(\omega_\zeta)+1]/\kappa_\zeta$, which decreases as κ_ζ increases.

Figure 3.1 shows the main result of the paper. There, we consider the parameter set PS2 of intermediate fabrication difficulty for all circuit parameters with the exception of E_L, which is varied between the values of PS1 (hardest regime) and PS3 (accessible regime). Disorder in the cross-capacitances of the circuit and E_L is assumed to be at the 5% level. The solid line shows the coherence time estimated using Eq. (3.1), while the dashed and dotted lines show the result of the asymptotic expressions for the coherence time in the limits $\chi_{01}^\zeta \gg \kappa_\zeta$ and $\chi_{01}^\zeta \ll \kappa_\zeta$, respectively. Note that we have changed the definition of the x-axis of Fig. 3.1 with respect to Figure 10 in our paper (Ref. [101]), in order to employ the parameter definitions adopted in this thesis.

The results of Fig. 3.1 are not completely intuitive. Indeed, let us consider first the case of small E_L (deep $0-\pi$ regime). In this limit, the frequency of the ζ mode is also small and $n_{\mathrm{th}}(\omega_\zeta)$ grows very rapidly as E_L decreases. Thus, one might naively expect

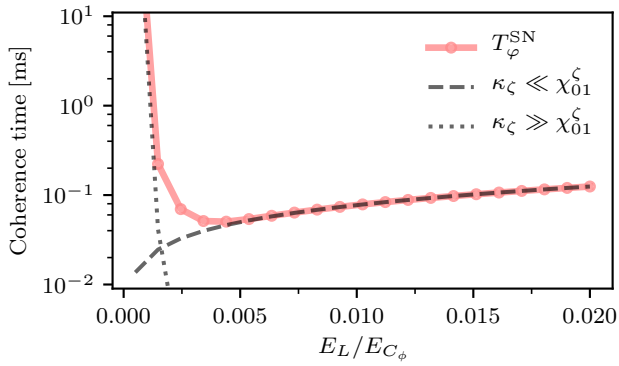

Figure 3.1 Photon shot noise induced dephasing due to coupling to the ζ mode. Adapted from [101].

Eq. (3.1) to diverge such that $T_\varphi^{\mathrm{SN}} \to 0$ in this limit. However, the opposite occurs, and the explanation for this behavior is subtle. As E_L is decreased, the $0-\pi$ qubit enters in the deep regime, for which the dispersive shift of the qubit manifold is expected to vanish [see Sect. 2.0.4]. Thus, according to the asymptotic expression $\Gamma_\varphi^{\mathrm{SN}} \sim 4(\chi_{01}^\zeta)^2 n_{\mathrm{th}}^2(\omega_\zeta)/\kappa_\zeta$, the dispersive shift χ_{01}^ζ should decrease exponentially fast with $E_L \to 0$, in order to compensate for the exponential divergence of n_{th}. This remarkable fact demonstrates that the $0-\pi$ qubit is protected against any possible noise mechanism, including those that arise in the presence of circuit-element disorder. This was an unanticipated result.

On the other hand, as E_L is increased, χ_{01}^ζ increases and the qubit becomes more sensitive to photon fluctuations in the ζ mode. This is reflected by the rapid drop of T_φ^{SN} for $E_L/E_{C_\phi} \lesssim 0.003$. However, as χ_{01}^ζ increases to a value comparable to κ_ζ the tendency of Eq. (3.1) changes, eventually leading to a saturation value that is independent of χ_{01}^ζ for $\chi_{01}^\zeta \gg \kappa_\zeta$. Moreover, this is complemented by a favorable increase of ω_ζ which leads to a smaller $n_{\mathrm{th}}(\omega_\zeta)$ as E_L is made larger. Therefore, decreasing the size of the superinductance can to some extent be beneficial. This comes at a cost of increasing the sensitivity to flux noise, which can be compromised up to the point where photon-shot-noise and flux-noise dephasing are of the same order.

As a result of the competition between different effects, Fig. 3.1 is not monotonic and features a clear absolute minimum. To the left of this minimum, χ_{01}^ζ is already small and mitigating disorder can help to reduce $\Gamma_\varphi^{\mathrm{SN}}$ and therefore increase the coherence time even further. To the right of this minimum, smaller values of $\Gamma_\varphi^{\mathrm{SN}}$ can be achieved by increasing the quality factor of the ζ mode or decreasing $n_{\mathrm{th}}(\omega_\zeta)$ by means of cooling. This last observation motivated part of the research work that is presented in chapter 4.

3.3 Conclusion and outlook

In this work, we studied the coherence of $0-\pi$ devices from experimentally hard to achieve regimes. We demonstrated that the $0-\pi$ qubit is indeed a noise-protected device, even in the presence of circuit-element disorder. However, we noticed that full noise protection might be out of reach of current- and near-future-term generations of superconducting-qubit technology.

This study revealed two counterintuitive results in the presence of circuit-element disorder, that would not have been obtained without a rigorous treatment of decoherence. First, the qubit can effectively decouple from the ζ mode in the deep $0-\pi$ regime. Second, devices working in a softer regime of parameters might benefit from superinductance values smaller than those originally required.

Overall, we demonstrated that the $0-\pi$ qubit has potential for high-coherence in a realistic regime of parameters, thus motivating the experimental realization of this circuit that is presented in chapter 5.

New Journal of Physics
The open access journal at the forefront of physics

Deutsche Physikalische Gesellschaft DPG
IOP Institute of Physics

Published in partnership with: Deutsche Physikalische Gesellschaft and the Institute of Physics

OPEN ACCESS

RECEIVED
4 December 2017

ACCEPTED FOR PUBLICATION
19 March 2018

PUBLISHED
25 April 2018

PAPER

Coherence properties of the 0-π qubit

Peter Groszkowski[1], **A Di Paolo**[2], **A L Grimsmo**[2], **A Blais**[2,5], **D I Schuster**[3], **A A Houck**[4] **and Jens Koch**[1]

[1] Department of Physics and Astronomy, Northwestern University, Evanston, IL 60208, United States of America
[2] Institut Quantique and Département de Physique, Université de Sherbrooke, Sherbrooke J1K 2R1 QC, Canada
[3] Department of Physics and James Franck Institute, University of Chicago, Chicago, IL 60637, United States of America
[4] Department of Electrical Engineering, Princeton University, Princeton, NJ 08540, United States of America
[5] Canadian Institute for Advanced Research, Toronto, ON, Canada

E-mail: piotrekg@northwestern.edu

Keywords: quantum computing, superconducting circuits, decoherence

Abstract

Superconducting circuits rank among some of the most interesting architectures for the implementation of quantum information processing devices. The recently proposed 0-π qubit (Brooks *et al* 2013 *Phys. Rev.* A **87** 52306) promises increased protection from spontaneous relaxation and dephasing. In this paper we present a detailed theoretical study of the coherence properties of the 0-π device, investigate relevant decoherence channels, and show estimates for achievable coherence times in multiple parameter regimes. In our analysis, we include disorder in circuit parameters, which results in the coupling of the qubit to a low-energy, spurious harmonic mode. We analyze the effects of such coupling on decoherence, in particular dephasing due to photon shot noise, and outline how such a noise channel can be mitigated by appropriate parameter choices. In the end we find that the 0-π qubit performs well and may become an attractive candidate for the implementation of the next-generation superconducting devices for uses in quantum computing and information.

1. Introduction

Research towards realizing a quantum computer poses a formidable challenge due to the need for a subtle compromise between two conflicting requirements: maximizing coherence by isolating qubits from environmental noise on one hand, and coupling qubits strongly for fast qubit control and readout, on the other hand. Over the last two decades substantial progress has been made in the field of superconducting circuits, where coherence times have increased by nearly 6 orders of magnitude to milliseconds [1], while gate times stayed in the range of tens of nanoseconds. This impressive improvement is largely due to more advanced qubit designs which minimize the qubit's coupling to unwanted environmental noise sources, such as flux noise [2] or charge noise [3], all while keeping the qubit susceptible to control pulses essential for performing gate operations as well as readout.

Recently, there have been several proposals for a new generation of *protected* qubits [4–7], projected to be especially well isolated from relevant sources of noise responsible for decoherence. This protection is typically a result of an exponential suppression in the unwanted interactions between the qubit and its environment. The expected long coherence times often result from a combination of factors: near-degeneracy of the qubit's ground and first excited states, a large energy gap between the two lowest energy levels and the higher energy landscape, and finally, strongly localized noise effects, which can only weakly affect the qubit's eigenstates. In the field of superconducting circuits, existing proposals for implementations typically involve arrays of Josephson junctions arranged in specific geometries to achieve some, or all of the characteristics outlined above. For a detailed review of the possible realizations that have been studied, a summary of recent progress, as well as a discussion of the connection between the protected qubits and topological error correcting codes [8–11], we point the reader to [12] and the references therein.

In this work, we concentrate on a particular, recently proposed superconducting circuit referred to as the 0-π qubit. It was first discussed by Brooks, Kitaev and Preskill (BKP) in [13], and is based on work in [5].

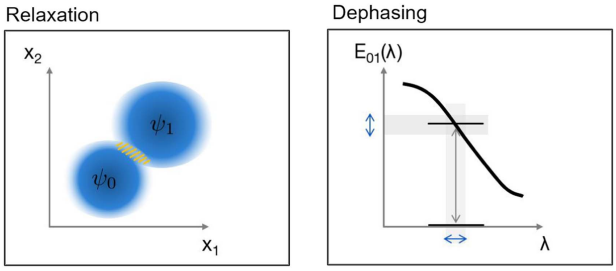

Figure 1. Protection offered by the 0-π qubit. T_1 processes are exponentially suppressed due to nearly disjoint support of the qubit wave functions, i.e., wave functions 'live' in nearly separate regions of the generalized-variable space; pure-dephasing rates, proportional to the qubit-energy susceptibility $\partial E_{10}/\partial\lambda$ with respect to the noise variable λ, are exponentially suppressed when nearly degenerate eigenstates of the 0-π device are used as qubit states.

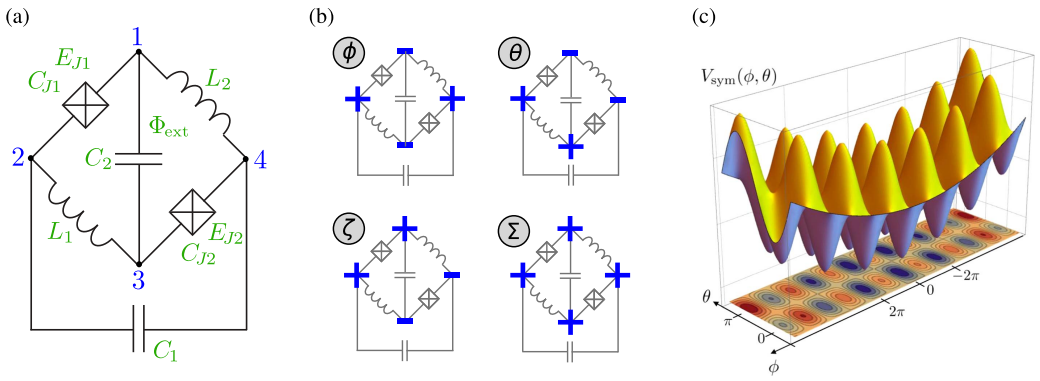

Figure 2. (a) 0-π circuit diagram, consisting of two Josephson junctions, two large inductors and two large capacitors. (b) Schematic representation of the normal modes of the linearized circuit (no parameter disorder), which define the new circuit variables ϕ, θ, ζ and Σ. (c) Potential energy of the disorderless 0-π qubit.

Conceptually, the 0-π circuit exhibits a rudimentary form of topological protection that combines exponential suppression of noise-induced transitions (dissipation) with exponential suppression of dephasing, see figure 1. The former is achieved by engineering qubit states with disjoint support, the latter by rendering qubit states (nearly) degenerate and exponentially suppressing the sensitivity of the corresponding energies to low-frequency environmental noise.

The circuit underlying the 0-π qubit consists of four nodes connected by a pair of linear inductors, a pair of capacitors, and a pair of Josephson junctions as shown in figure 2. Two issues pose challenges to the implementation of the 0-π design: first, to achieve the desired regime it is necessary to simultaneously realize large superinductances, large shunting capacitors, and high junction charging energies (very low stray capacitances); second, circuit elements should ideally be pairwise identical (no disorder in circuit element parameters) in order to prevent coupling of the qubit to a spurious circuit mode [14], which we will refer to as the ζ-mode[6].

While notable increases in accessible inductance values by means of junction-array based superinductances may partially address the first issue [15–19], some amount of circuit parameter disorder and hence residual coupling to the ζ-mode is unavoidable. In the present work, we theoretically assess the coherence properties of 0-π devices, ones that are possible to realize with today's state-of-the art fabrication techniques, as well as those that will require technological advances. Specifically, we present calculations of relevant decoherence rates resulting from the qubit's coupling to known noise sources, including both intrinsic sources, such as flux, charge and critical current noise, which couple directly to the qubit's degree of freedom, as well as noise mediated by the coupling to the spurious ζ-mode. We concentrate our study on three representative parameter sets, which primarily differ in the magnitude of the inductance and are motivated by both current, as well as future experimental capabilities.

[6] This low-energy mode was originally called χ-mode [14], but is here renamed to avoid confusion with dispersive shifts commonly denoted by 'χ'.

This paper is organized as follows. In the subsequent section, we briefly review the quantization of the 0-π circuit, properly accounting for parameter disorder, and the coupling of the qubit degree of freedom to the ζ-mode [14]. In section 3 we then present 0-π eigenspectra for the parameter sets considered, and discuss the dependence of spectral properties on the different energy scales. In section 4 we describe relevant noise processes affecting the 0-π qubit, and discuss the calculation of decoherence rates. In section 5, we present the resulting decoherence rates and identify the processes likely to limit coherence. Finally, we summarize and conclude in section 6.

2. Hamiltonian of the 0-π qubit

We begin by briefly reviewing the circuit of the 0-π qubit as well as the corresponding Hamiltonian. As shown in figure 2(a), the 0-π circuit consists of two Josephson junctions (Josephson energies $E_{J1,2}$, junction capacitances $C_{J1,2}$) and two large (super-)inductors (inductances $L_{1,2}$), linked to form a loop. The opposing nodes $j = 1, 3$ and $j = 2, 4$ are connected by two large capacitors $C_{1,2}$. As usual [20, 21], we initially employ generalized flux variables φ_j for each circuit node $j = 1, \ldots, 4$. We then switch to physically more meaningful variables ϕ, θ, ζ, and Σ [14] associated with the normal modes of the linearized, non-disordered circuit (see figure 2(b)):

$$\begin{aligned} 2\phi &= (\varphi_2 - \varphi_3) + (\varphi_4 - \varphi_1), \quad & 2\zeta &= (\varphi_2 - \varphi_3) - (\varphi_4 - \varphi_1), \\ 2\theta &= (\varphi_2 - \varphi_1) - (\varphi_4 - \varphi_3), \quad & 2\Sigma &= \sum_j \varphi_j. \end{aligned} \tag{1}$$

Both the ϕ-mode and θ-mode involve phase differences across the Josephson junctions and are coupled by the junction nonlinearity, as we will see momentarily. The ζ-mode does not bias the junctions and is therefore, a fully harmonic mode. Finally, the variable Σ is cyclic, remains decoupled from the other variables, and can thus be omitted. (Alternatively, one can reach this conclusion by invoking gauge freedom and setting one of the nodes to ground.)

In the absence of disorder among circuit elements, we have $E_{J1} = E_{J2} \equiv E_J$ etc, and we can write the symmetric 0-π Hamiltonian as

$$H_{\rm sym} = -2E_{\rm CJ}\,\partial_\phi^2 - 2E_{\rm Cs}\,\partial_\theta^2 - 2E_{\rm J}\cos\theta\,\cos\left(\phi - \frac{\varphi_{\rm ext}}{2}\right) + E_{\rm L}\phi^2 + H_\zeta, \tag{2}$$

where

$$H_\zeta = -2E_{\rm C}\,\partial_\zeta^2 + E_{\rm L}\,\zeta^2, \tag{3}$$

is the Hamiltonian for the harmonic ζ-mode. The various parameters are defined as follows: $E_{\rm L} = (\Phi_0/2\pi)^2/2{\rm L}$ is the inductive energy scale, and $E_{\rm C} = e^2/2C$, $E_{\rm CJ} = e^2/2C_{\rm J}$, $E_{\rm Cs} = (1/E_{\rm C} + 1/E_{\rm CJ})^{-1} = e^2/2C_s$, are the relevant charging energies, where in the last expression we have taken[7] $C_{\rm s} = C + C_{\rm J}$. Finally, $\varphi_{\rm ext} = 2\pi\Phi_{\rm ext}/\Phi_0$ is the external magnetic flux through the loop written in terms of the magnetic flux quantum $\Phi_0 = h/2e$. Evidently, the mode decouples in the disorderless case, leaving only the ϕ and θ degrees of freedom to form the effective qubit Hilbert space. (For a detailed discussion of the resulting qubit wave functions and the origin of protection from noise, we refer the reader to [14].) figure 2(c) shows the potential energy of the Hamiltonian from equation (2).

Once imperfections in fabrication are taken into account, nominally identical circuit elements will acquire slight parameter deviations. It is therefore convenient to introduce the parameter averages $X = \frac{1}{2}(X_1 + X_2)$ and relative deviations ${\rm d}X = (X_1 - X_2)/X$, where $X \in \{E_{\rm L}, E_{\rm J}, C, C_{\rm J}\}$. Using this notation and employing a leading-order expansion in the capacitive disorder, one can cast the Hamiltonian into the form $H = H_{0-\pi} + H_\zeta + H_{\rm int}$, where

$$H_{0-\pi} = H_{\rm sym} + 2E_{\rm Cs}{\rm d}C_{\rm J}\partial_\phi\,\partial_\theta + E_{\rm J}\,{\rm d}E_{\rm J}\sin\theta\,\sin\left(\phi - \frac{\varphi_{\rm ext}}{2}\right) + \mathcal{O}({\rm d}C^2, {\rm d}C_{\rm J}^2), \tag{4}$$

captures the primary 0-π qubit degrees of freedom, including effects of disorder in junction parameters, and

$$H_{\rm int} = 2E_{\rm Cs}{\rm d}C\partial_\theta\,\partial_\zeta + E_{\rm L}{\rm d}E_{\rm L}\phi\,\zeta + \mathcal{O}({\rm d}C^2, {\rm d}C_{\rm J}^2), \tag{5}$$

describes the coupling between 0-π and the ζ-mode. As discussed in detail in [14], disorder in junction parameters gives rise to minor corrections to the 0-π qubit spectrum, but leave the ζ-mode decoupled. Such coupling does arise from disorder in C and $E_{\rm L}$, and can have important consequences on the coherence of the 0-π qubit, as we will see in the following sections. For this analysis, it will be helpful to write the Hamiltonian in the product basis comprised of the eigenstates of $H_{0-\pi}$ and the ζ-mode:

[7] We have changed the subscript label in the definition of $C_{\rm s}$ from the one used in [14].

Table 1. Table of circuit parameters for parameter sets 1, 2 and 3 (PS1, PS2, PS3). Josephson, inductive and capacitive energies are given in units of $h \times$ GHz as well as in units of the plasma energy of the Josephson junctions, $\hbar\omega_p = \sqrt{8E_{CJ}E_J}$, with $\omega_p/2\pi =$ 40 GHz for PS1 and PS2, and $\omega_p/2\pi = 20$ GHz for PS3. Disorder in energies and capacitances is assumed to be at the 5% level, i.e., $\mathrm{d}X = 2(X_1 - X_2)/(X_1 + X_2) = 5\%$ for $X \in \{E_L, E_J, C, C_J\}$.

	Parameter set 1		Parameter set 2		Parameter set 3	
	[h·GHz]	[$\hbar\omega_p$]	[h·GHz]	[$\hbar\omega_p$]	[h·GHz]	[$\hbar\omega_p$]
E_C	0.02	0.0005	0.04	0.001	0.15	0.008
E_{CJ}	20.0	0.5	20.0	0.5	10.0	0.5
E_J	10.0	0.25	10.0	0.25	5.0	0.25
E_L	0.008	0.0002	0.04	0.001	0.13	0.007

$$H = \sum_l E_l^q \, |l\rangle\langle l| + \hbar\Omega_\zeta \, a^\dagger a + \sum_{l,l'} (g_{ll'}|l\rangle\langle l'| \, a + \text{h.c.}), \tag{6}$$

where $a^\dagger$ (a) are the creation (annihilation) operators for the ζ-mode, $\Omega_\zeta = \sqrt{8E_L E_C}/\hbar$ is its angular frequency, E_l^q the energy of the lth primary 0-π eigenstate, and

$$g_{ll'} = g_{ll'}^\phi + \mathrm{i}g_{ll'}^\theta = \frac{1}{2}E_L \mathrm{d}E_L \left(\frac{8E_C}{E_L}\right)^{1/4} \langle l|\phi|l'\rangle + \mathrm{i}\frac{1}{2}\mathrm{d}CE_{Cs}\left(\frac{32E_L}{E_C}\right)^{1/4} \langle l|\mathrm{i}\,\partial_\theta|l'\rangle \tag{7}$$

the strength of the coupling that mediates transitions among $H_{0-\pi}$ eigenstates $|l\rangle$, $|l'\rangle$ via emission/absorption of ζ-mode excitations.

In the dispersive limit, where the detunings $\Delta_{ll'} = E_l^q - E_{l'}^q - \hbar\Omega_\zeta$ are large compared to the coupling, $|g_{ll'}/\Delta_{ll'}| \ll 1$, a Schrieffer–Wolff transformation yields the effective Hamiltonian [14, 22]

$$H' = \sum_{l=0}^{\infty}(E_l^q + \Lambda_l)|l\rangle\langle l| + \hbar\Omega_\zeta \, a^\dagger a + \sum_l \chi_l \, |l\rangle\langle l| \, a^\dagger a, \tag{8}$$

where the ac Stark shifts and Lamb shifts are given by

$$\chi_l = \sum_{l'} |g_{ll'}|^2 \left(\frac{1}{\Delta_{ll'}} - \frac{1}{\Delta_{l'l}}\right), \qquad \Lambda_l = \sum_{l'} \frac{|g_{ll'}|^2}{\Delta_{ll'}}, \tag{9}$$

respectively.

So far, we have neglected capacitances between each node and ground. The effect of such ground capacitances depends on their uniformity. If all ground capacitances are identical and the circuit is symmetric, then the effect is minimal: Σ remains decoupled and the charging energies E_C, E_{Cs} and E_{CJ} are merely renormalized. Node-to-node variations in ground capacitances complicate the situation slightly by inducing coupling between the primary degrees of freedom to the charge operator of Σ. In the present work, we will focus on the case of small ground capacitances where corrections of this type are negligible.

3. Eigenspectrum of the 0-π qubit

Our goal is to understand the key coherence properties of the 0-π qubit. Since these properties have significant dependence on various circuit parameters, we choose three specific parameter sets that explore the balance between coherence times and current fabrication capabilities. Table 1 details our choices for inductive, Josephson, and charging energies for parameter sets 1, 2 and 3 (PS1, PS2, PS3). In all cases, we take the relative parameter deviations of nominally identical circuit elements to be at the 5% level (which can be considered pessimistic). While we introduce some variations in all energies, the central scheme behind the parameter choices, is the increasing size of the inductive energy E_L as we go from PS1, through PS2, to PS3.

Figure 3 shows the PS1 energy spectra plotted as a function of flux, as well as a few selected wave functions. Since in this parameter set both E_L, and E_C are smallest of all we consider, the spectrum is densely populated with levels that mainly correspond to ζ-mode excitations, and hence, only a few of those are explicitly drawn. The plots of wave functions assume a special case where only nonzero disorder in E_J and C_J is included, (with ζ-mode decoupled), and hence their dependence only in terms of θ and ϕ is presented. Similarity, figure 4 shows the energy spectra and eigenfunctions for both PS2 and PS3, again with a subset of eigenfunctions. The panels (a) and (c) in figure 4 present the pure 0-π spectra obtained when the ζ-mode remains decoupled from the θ and ϕ degrees of freedom, as realized when setting $\mathrm{d}E_L = \mathrm{d}C = 0$, such that $g_{ll'}$ in equation (6) vanishes. In the (b) and (d) panels, disorder in E_L and C is taken into account, and the spectra show dressed-state excitations of both the 0-π and the ζ-mode.

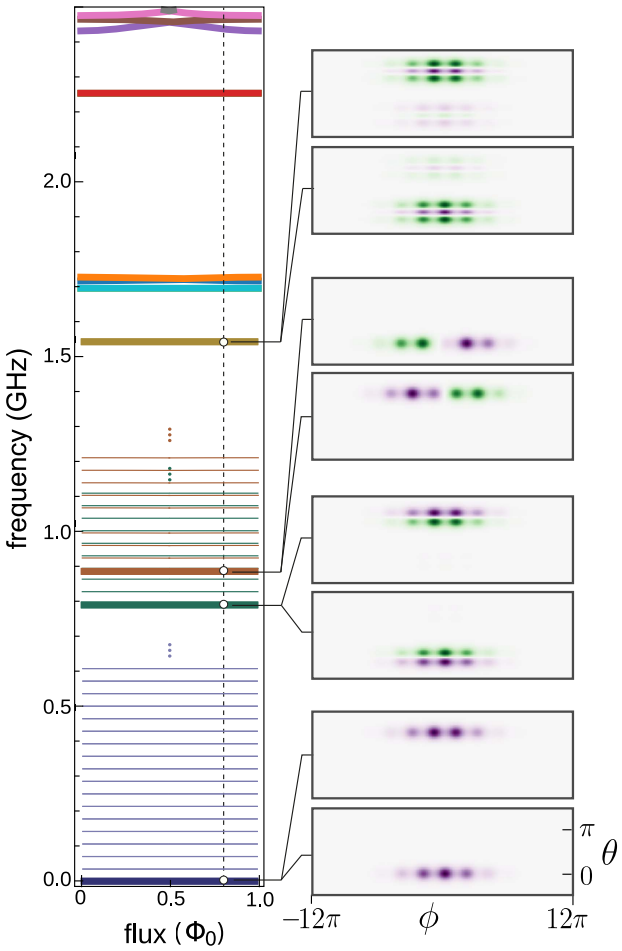

Figure 3. Energy spectrum of parameter set 1 (see table 1), plotted as a function of flux, along with a few selected 0-π wave functions calculated at $\Phi_{\text{ext}} = 0.8\ \Phi_0$. (Only a limited number of ζ-mode excitations is shown.)

To discuss the generic aspects of parameter choices and 0-π qubit spectra, we first consider the specific case of PS2 (figures 4(a) and (b)), and comment on the impact of parameter changes leading to PS1 and PS3 subsequently. Figure 4(a) shows that the low-lying eigenstates of $H_{0-\pi}$ are localized close to $\theta = 0$ or $\theta = \pi$ (hence the name '0-π qubit'), while spreading over multiple wells in ϕ direction. As intended, qubit ground and first excited states are close to being degenerate and are well-separated from higher excitation levels over the entire flux range. We note that the distinct insensitivity of the qubit energy with respect to flux is a crucial feature that distinguishes the 0-π-qubit physics from that of the effectively 1D double-well physics prevalent for flux qubits [23].

Choosing favorable parameters for 0-π devices is, in part, driven by three central criteria. First, we wish to maximize the state-localization on the θ axis to realize disjoint-support wave functions, in order to exponentially suppresses all transition matrix elements that enter qubit relaxation/depolarization rates. Such localization can be achieved by rendering the effective mass in θ direction heavy, $C_{\text{J}} \ll C$, and making the local potential wells deep enough to hold localized states, $E_{\text{J}} \gg E_{\text{L}}$ and $E_{\text{Cs}} \ll E_{\text{J}}$. Second, we aim for maximal delocalization along the ϕ axis, which suppresses susceptibility to flux variations by the same mechanism responsible for flux insensitivity of metaplasmon energies in fluxonium [24]. As a result, ground and excited states become near-degenerate, and sensitivity to $1/f$ flux noise is suppressed. This regime requires parameters to obey $E_{\text{L}} \ll E_{\text{CJ}} \ll E_{\text{J}}$. Third, charge-noise sensitivity of the device is minimized by ensuring $E_{\text{Cs}} \ll E_{\text{J}}$, in analogy to the mechanism harnessed for the transmon qubit [3]. Decreasing E_{L} even further, as done in PS1, pushes the system closer towards ground-state degeneracy [13, 14]. However, unless E_{L} decreases past a certain threshold, one can run into a coherence bottleneck arising from coupling to the ζ-mode (see sections 4 and 5).

Still concentrating our discussion on PS2, we note that once parameter deviations in C and E_{L} are taken into account, the ζ-mode weakly couples to the primary qubit degrees of freedom. The resulting energy spectrum shown in figure 4(b), then includes levels that reflect excitations of the ζ degree of freedom. However, since this

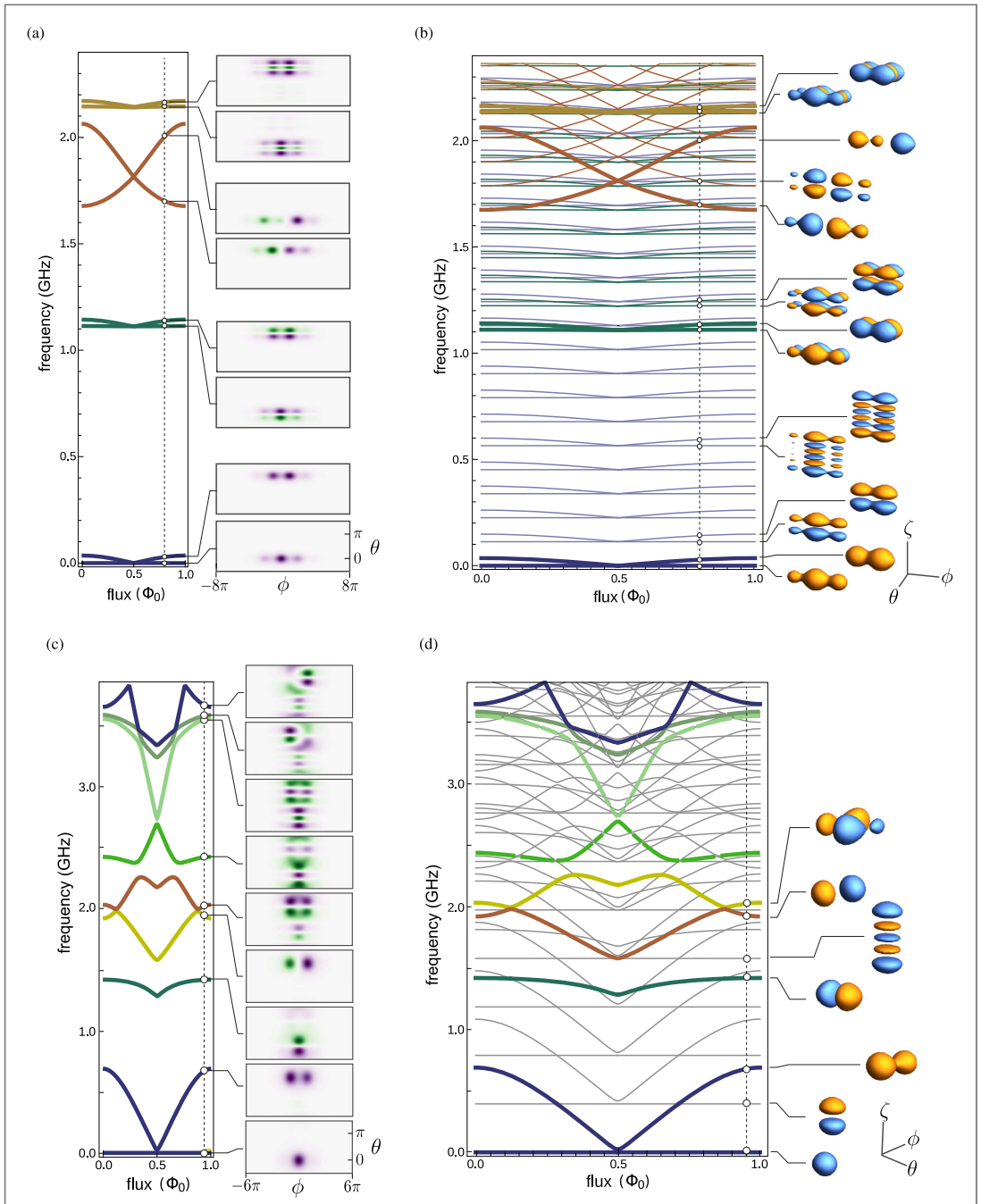

Figure 4. Energy spectrum calculated for parameter sets 2 and 3 (see table 1), and selected wave functions calculated at $\Phi_{\rm ext} = 0.8\ \Phi_0$ (PS2) and $0.9\ \Phi_0$ (PS3). (a) PS2 spectrum of $H_{0-\pi}$ for vanishing coupling to the ζ-mode, calculated by setting $\mathrm{d}E_{\rm L} = \mathrm{d}C = 0$ and retaining θ and ϕ degrees of freedom only. (b) Spectrum for PS2 in the presence of disorder in the parameters $E_{\rm L}$, C where the ϕ, θ and ζ-mode couple. On the far right: select wave function orbitals, obtained as contour surfaces obeying $\Psi(\theta, \phi, \zeta) = \pm$const with orange/blue color indicating positive/negative wave function amplitude. (c) and (d) show the analogous results for parameter set 3.

coupling is weak, and 0-π and ζ-mode excitations are generally off resonance, eigenstates are only weakly dressed and can usually safely be labeled by $|l,\ n\rangle$ with $l,\ n$ denoting the excitation numbers of the 0-π and the ζ-mode, respectively. One consequence easily spotted in the spectrum—especially for frequencies below $\sim$1.1 GHz in parameter set 2—is that each 0-π energy level $E_{l,n=0}$ appears 'copied' at regular intervals set by the ζ-mode frequency, $E_{l,n} \approx E_{l,0} + n\ \hbar\Omega_\zeta$. This physics is also evident in the shapes of the corresponding wave function orbitals presented in figure 4(b), which clearly shows the proliferation of nodes along the ζ axis as the excitation number of the ζ-mode is increased one by one.

Relative to parameter set 2, parameter set 1 contains a lower inductive and charging energies $E_{\rm L}$ and $E_{\rm C}$. This leads to almost flat spectrum as a function of flux, and hence, this choice of energies represents a 'deep' 0-π

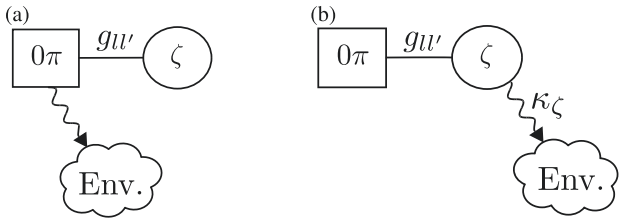

Figure 5. Two noise mechanisms contributing to decoherence of the 0-π qubit. (a) The primary 0-π qubit degrees of freedom, θ and ϕ, can couple directly to a noisy environment. (b) The 0-π qubit may couple to environmental noise indirectly via the ζ-mode which has an intrinsic lifetime κ_ζ.

regime, envisioned in [13]. When $dE_L = dC = 0$, at $\Phi_{ext} = 0$, the energy splitting is $(E_1^q - E_0^q)/h \approx 24$ kHz, while $(E_2^q - E_0^q)/h \approx 792$ MHz. Using such parameters helps in limiting both dephasing due to $1/f$ noise, but also various relaxation mechanisms. Another feature of this low-E_L regime is that the dispersive coupling to the stray ζ-mode is highly suppressed. As we discuss in section 5, this limits the dephasing due to thermal shot noise which is relevant, or even dominant, in the other parameter sets we study. The central difficulty of experimentally realizing a circuit using PS1, however, is the ability to build large enough linear superinductance, hence, its near-future prospects may be limited.

Finally, the parameter choices in PS3 closely match current fabrication capabilities. In particular, the inductive energy scale is increased from PS2 by a factor of more than 3, mitigating the challenge of superinductor fabrication. At the same time, E_C is increased relative to PS2, thus giving rise to an overall upwards shift of the ζ-mode frequency to $\Omega_\zeta/2\pi = \sqrt{8E_C E_L}/h \approx 395$ MHz. The resulting decrease in thermal ζ-mode excitations will play role in our discussion of coherence properties below. As seen in figures 4(c) and (d), the change in parameters comes at the cost of increased flux susceptibility and loss of near-degeneracy. Moreover, eigenstates beyond the lowest four are seen to break localization at $\theta = 0$ and $\theta = \pi$. In figure 4(d), where coupling to the ζ-mode is included, the spectrum again shows 'copies' of energy levels which arise from the addition of ζ-mode excitations.

4. Noise channels affecting the 0-π qubit

To characterize the coherence properties of the 0-π qubit, we need to identify its most damaging noise channels. We thus calculate and compare various depolarization and dephasing rates that originate from coupling to different known noise sources. In our analysis we make the common assumption [2, 3, 25–29] that noise in different channels is uncorrelated and individual rates can, hence, be calculated separately and then added up to give cumulative rates for depolarization and pure dephasing, similar to the treatment in [25, 30]. We further assume that the interaction with the environment to be sufficiently weak, so that the corresponding coupling V_λ to the full 0-π circuit Hamiltonian can be treated perturbatively. In that case, decoherence rates can be calculated either using Fermi's Golden Rule (for relaxation/depolarization), or by studying the effects of V_λ on eigenenergies and, in turn, on the time evolution of the off-diagonal elements of the density matrix (for pure dephasing).

As schematically illustrated in figure 5, we distinguish between two different pathways for decoherence of the 0-π qubit. First, the primary 0-π qubit degrees of freedom, θ and ϕ, can directly interact with a noisy environment. In this case, we generally find that disorder-induced coupling to the ζ-mode only leads to subdominant corrections to decoherence rates. Second, baths coupled to the ζ-mode can also influence the primary 0-π qubit degrees of freedom and lead to indirect decoherence processes. Despite the fact that the interaction H_{int} (equation (5)) is expected to be weak, we will discover that such indirect decoherence processes can play a crucial role in the performance of the 0-π qubit in some parameter regimes.

4.1. Pure dephasing (T_φ)

We first consider pure dephasing, the dissipationless loss of phase information. Pure dephasing is quantified by the time scale T_φ needed for a quantum superposition to turn into a classically mixed state, observed as the decay time for off-diagonal elements of the qubit's density matrix, when expressed in the eigenenergy basis. Within Bloch–Redfield theory, the total dephasing rate due to a noise channel λ, is given by $\Gamma_2^\lambda = \frac{1}{2}\Gamma_1^\lambda + \Gamma_\varphi^\lambda$ [31, 32], where Γ_1^λ is the depolarization rate (combining relaxation and thermal excitation of the qubit, see section 4.2) and Γ_φ^λ the pure dephasing rate. As usual, we define corresponding decoherence time scales via $T_2^\lambda = 1/\Gamma_2^\lambda$, $T_1^\lambda = 1/\Gamma_1^\lambda$ and $T_\varphi^\lambda = 1/\Gamma_\varphi^\lambda$ respectively.

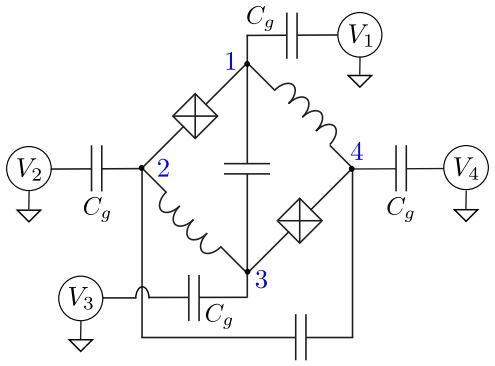

Figure 6. 0-π circuit coupled capacitively to voltage sources $V_j(t)$, as used in the modeling of charge noise.

Following [3, 25, 29], we may consider dephasing due to classical noise entering the circuit Hamiltonian in the form of an external parameter $\lambda(t) = \lambda_0 + \delta\lambda(t)$. Here, $\delta\lambda(t)$ is a noise signal assumed to arise from a stationary, Gaussian process with zero mean, $\langle\delta\lambda(t)\rangle = 0$, and spectral density

$$S_\lambda(\omega) = \int_{-\infty}^{\infty} \mathrm{d}t\ \mathrm{e}^{-\mathrm{i}\omega t}\langle\delta\lambda(0)\ \delta\lambda(t)\rangle. \tag{10}$$

The effects of weak noise, can be captured through an operator V_λ obtained by Taylor-expanding the Hamiltonian,

$$H \approx H_0 + \frac{\partial H}{\partial\lambda}\delta\lambda(t) + \frac{1}{2}\frac{\partial^2 H}{\partial\lambda^2}\delta\lambda^2(t) = H_0 + V_\lambda, \tag{11}$$

where $H_0 = H(\lambda_0)$, and all derivatives are evaluated at $\lambda = \lambda_0$. Empirical evidence shows that superconducting qubits are typically exposed to multiple noise channels with approximate $1/f$ spectrum

$$S_\lambda^{1/f}(\omega) = \frac{2\pi A_\lambda^2}{|\omega|^\gamma} \qquad (\gamma \approx 1), \tag{12}$$

where A_λ is the noise amplitude for channel λ (flux, charge, or critical current) [33–39]. Such noise is most detrimental at low frequencies and thus important for qubit dephasing. The calculation of the corresponding pure-dephasing rates Γ_φ^λ has been developed in [25, 26, 40], and a brief outline is also presented in appendix A. The resulting pure-dephasing time, as measured in a Ramsey experiment, is given by

$$T_\varphi^\lambda = \{2A_\lambda^2(\partial_\lambda\omega_{\mathrm{ge}})^2|\ln\omega_{\mathrm{ir}}t| + 2A_\lambda^4(\partial_\lambda^2\omega_{\mathrm{ge}})^2[\ln^2(\omega_{\mathrm{uv}}/\omega_{\mathrm{ir}}) + 2\ln^2(\omega_{\mathrm{ir}}t)]\}^{-1/2}, \tag{13}$$

where ω_{ge} is the angular frequency difference between the excited and ground states of the qubit, ω_{ir} and ω_{uv} correspond to the low and high-frequency cutoffs of the noise, and t defines the measurement time scale under consideration. The above expression is valid in the generic case where noise affects the qubit energy to linear order, as well as in the vicinity of 'sweet spots' [41] where the linear noise susceptibility vanishes, $\partial_\lambda\omega_{\mathrm{ge}} = 0$. In line with [27, 39, 42], we assume that $\omega_{\mathrm{ir}}/2\pi = 1\,\mathrm{Hz}$, $\omega_{\mathrm{uv}}/2\pi = 3.0\ \mathrm{GHz}$, and use a conservative value of $t = 10\ \mu\mathrm{s}$ in our calculations. Next, we consider specific $1/f$ noise channels known to be important, namely $1/f$ charge [34, 37], flux [33, 36, 38], and critical-current noise [35].

Charge noise—Charge noise can be modeled as a set of noisy voltage sources capacitively coupled to the nodes of the circuit, see figure 6. We assume that the noise signals V_j on different circuit nodes are independent. Repeating the steps of circuit quantization in the presence of these additional capacitive couplings yields a Hamiltonian $H' = T + U$ with the same potential energy as previously in H,

$$U = -2E_{\mathrm{J}}\cos\theta\ \cos\left(\phi - \frac{\varphi_{\mathrm{ext}}}{2}\right) + E_{\mathrm{L}}\ \phi^2 + E_{\mathrm{L}}\zeta^2 + E_{\mathrm{J}}\,\mathrm{d}E_{\mathrm{J}}\sin\theta\ \sin\left(\phi - \frac{\varphi_{\mathrm{ext}}}{2}\right) + E_{\mathrm{L}}\mathrm{d}E_{\mathrm{L}}\phi\ \zeta. \tag{14}$$

and a modified expression for the kinetic energy,

$$\begin{aligned} T = (-2E'_{\mathrm{Cs}}\partial_\theta^2 - 2E'_{\mathrm{CJ}}\partial_\phi^2 - 2E'_{\mathrm{C}}\partial_\zeta^2) + \left(2E'_{\mathrm{Cs}}\frac{E'_{\mathrm{CJ}}}{E_{\mathrm{CJ}}}\,\mathrm{d}C_{\mathrm{J}}\partial_\theta\,\partial_\phi + 2E'_{\mathrm{Cs}}\frac{E'_{\mathrm{C}}}{E_{\mathrm{C}}}\,\mathrm{d}C\partial_\theta\,\partial_\zeta\right) \\ + (-4\mathrm{i}E'_{\mathrm{Cs}}n_g^\theta\,\partial_\theta - 4\mathrm{i}E'_{\mathrm{CJ}}n_g^\phi\,\partial_\phi - 4\mathrm{i}E'_{\mathrm{C}}n_g^\zeta\,\partial_\zeta). \end{aligned} \tag{15}$$

Here, primes denote small corrections to charging energies due to the presence of the coupling capacitances C_g. The effective offset charges n_g^ϕ, n_g^θ, and n_g^ζ are $1/f$ noise signals, obtained from linear superpositions of the fluctuating voltage signals $V_j(t)$ (for details, see appendix B). The first group of terms in T comprises of the

kinetic energies of the symmetric 0-π qubit and of the ζ-mode, the second group collects coupling terms originating from capacitive disorder, and the third group shows new terms describing the coupling to charge noise. Each offset charge may, in principle, consist of an intentional dc bias and $1/f$ fluctuations from the environment: $n_g^x(t) = n_0^x + \delta n_g^x(t)$. Employing the Hamiltonian H', the dephasing due to n_g^θ charge noise can now be calculated directly by extracting the n_g^θ dependence of $\omega_{\rm ge}$, and employing equation (13). We assume a charge-noise amplitude of $A_{n_g^\theta} = 10^{-4}e$ [34]. Furthermore, we absorb any renormalization of charging energies due to gate capacitance into a redefinition of the parameter values given in table 1.

While wave functions of the 0-π qubit are 2π-periodic in θ, they are extended along the ϕ and ζ axis. As a consequence, low-frequency charge fluctuations in ϕ and ζ are not expected to give rise to significant dephasing [24, 43]. To see this explicitly, we write the kinetic energy in the form $T = \hat{\mathbf{n}}^\top \mathsf{E}\hat{\mathbf{n}} + \mathbf{n}_g^\top \mathsf{D}\hat{\mathbf{n}}$, where $\hat{\mathbf{n}}^\top = -\mathrm{i}(\partial_\phi, \partial_\theta, \partial_\zeta)$, $\mathbf{n}_g^\top = (n_g^\phi, n_g^\theta, n_g^\zeta)$, and E (D) is a symmetric (diagonal) 3×3 matrix of energy coefficients to be read off of equation (15). We may complete the square,

$$T = \left(\hat{\mathbf{n}} + \tfrac{1}{2}\mathsf{E}^{-1}\mathsf{D}\mathbf{n}_g\right)^\top \mathsf{E}\left(\hat{\mathbf{n}} + \tfrac{1}{2}\mathsf{E}^{-1}\mathsf{D}\mathbf{n}_g\right) - c\,\mathbb{I} \tag{16}$$

and drop the irrelevant c-number term, and finally perform a unitary transformation using $R = \exp\left[-\mathrm{i}\tfrac{1}{2}(\phi, \theta, \zeta)\mathsf{E}^{-1}\mathsf{D}\mathbf{n}_g\right]$, which produces a momentum shift $\hat{\mathbf{n}} \to \hat{\mathbf{n}} - \tfrac{1}{2}\mathsf{E}^{-1}\mathsf{D}\mathbf{n}_g$. We find the resulting Hamiltonian

$$H'' = R^\dagger H' R + \mathrm{i}\dot{R}^\dagger R = \hat{\mathbf{n}}^\top \mathsf{E}\hat{\mathbf{n}} - \tfrac{1}{2}(\phi, \theta, \zeta)\mathsf{E}^{-1}\mathsf{D}\dot{\mathbf{n}}_g + U \tag{17}$$

and note that the transformation does not affect the boundary conditions for the extended variables ϕ and ζ (L^2-integrability). Hence, the transformation reveals that fluctuations in n_g^ϕ and n_g^ζ only enter in terms of the time derivative of the noise. As discussed previously in [24], the $1/f$ charge-noise spectrum thereby transforms into an Ohmic spectral density, $S_{\dot{n}_g}(\omega) = \omega^2 S_{n_g}^{1/f}(\omega) \sim \omega$. The effect of such fluctuations is insignificant for dephasing, since $T_\varphi \sim S(0)$ for non-singular noise spectral densities.

Critical-current noise—Next, we consider $1/f$ noise in the critical current $I_c = 2\pi E_{\rm J}/\Phi_0$ characterizing the two Josephson junctions in the 0-π circuit. Microscopically, fluctuations in the critical current are suspected to be due to trapping/de-trapping of charges at defect sites in the tunneling barrier of junctions [29, 35, 44]. The trapped, charges block tunneling through a given region of the junction, thus reducing the effective junction area. Under suitable conditions, the ensemble dynamics of many trapping centers can give rise to $1/f$ noise [45, 46]. In this case, the Josephson energy is the Hamiltonian parameter that acquires a fluctuating component, $E_{\rm J,tot} = E_{\rm J} + \delta E_{\rm J}(t)$. Critical-current noise is thus amenable to the same treatment as charge noise. In our calculations, we use a typical noise amplitude for the critical current of $A_{I_c} = 10^{-7} I_c$ [3, 35].

We note that critical-current noise may, in principle, also affect the large inductors, if realized as a Josephson junction array. However, for uncorrelated noise affecting each of the array's $N_{\rm J} \gg 1$ junctions independently, one finds an overall suppression of the noise amplitude by a factor of $1/\sqrt{N_{\rm J}}$ [16]. We will see that critical-current noise is a subdominant noise channel even without this suppression, and hence, neglect the effect of such fluctuations on superinductances.

Flux noise—The third canonical $1/f$ noise source known to affect superconducting qubits is $1/f$ flux noise. We model the fluctuations of the magnetic flux through the loop enclosed by the two junctions and inductors by treating $\Phi_{\rm ext}$ as the noisy parameter λ. Flux noise is ubiquitous in current superconducting circuit devices. There is growing evidence that fluctuating spins on thin-film surfaces [38, 39, 47] may be the microscopic origin of this noise. In our calculations of pure dephasing times due to flux noise, we make again use of equation (13) with a typical noise amplitude of $A_{\Phi_{\rm ext}} = 1\mu\Phi_0$ [39].

Shot-noise dephasing due to thermal excitations of the ζ-mode—The dephasing channels discussed so far are of the direct kind, shown in figure 5(a). We next analyze an indirect source associated with the disorder-induced coupling to the ζ-mode. Since the 0-π qubit is operated in the regime of small $E_{\rm L}$ and $E_{\rm C}$, the ζ-mode with frequency $\Omega_\zeta = \sqrt{8E_{\rm C}E_{\rm L}}/\hbar$ is generally a low-frequency mode, and can be subject to significant thermal excitations. Specifically, for the three parameter sets, the ζ-mode frequencies are given by $\Omega_\zeta/2\pi = 36,\ 113,\ 395$ MHz, leading to average thermal occupation numbers of $n_{\rm th} = 8.25,\ 2.29,\ 0.39$, respectively (with assumed temperature of $T = 15$ mK). Dephasing of the primary 0-π degrees of freedom from thermal fluctuations can be significant when operating in the strong dispersive limit, where the qubit-state dependent shift of the ζ-mode frequency is large compared to the width of the ζ-mode resonance. In that limit, the addition/loss of a single ζ-mode excitation number essentially measures the qubit state, leading to potentially strong dephasing. This noise mechanism, referred to as shot-noise dephasing, can be modeled within the master equation formalism and produces pure dephasing at the rate [48, 49]

$$\Gamma_{\varphi}^{\mathrm{SN}} = \frac{\kappa_\zeta}{2}\,\mathrm{Re}\left[\sqrt{\left(1+\frac{2\mathrm{i}\chi_{01}}{\kappa_\zeta}\right)^2+\frac{8\mathrm{i}\chi_{01}n_{\mathrm{th}}(\Omega_\zeta)}{\kappa_\zeta}}\;-1\right]. \tag{18}$$

Here, κ_ζ is the intrinsic lifetime of the harmonic ζ-mode, $n_{\mathrm{th}}(\omega) = 1/[\exp(\hbar\omega/k_{\mathrm{B}}T) - 1]$ the average number of thermal photons with (angular) frequency ω in thermal equilibrium at temperature T, and $\chi_{01} = (\chi_1 - \chi_0)/2$ the qubit's ac Stark shift due to a single excitation. (See equation (9) for the definition of χ_l.) Equation (18) applies whenever the 0-π qubit and ζ-mode are coupled dispersively. It can be further simplified in the strong dispersive limit where $\kappa_\zeta \gg \chi_{01}$, and written as

$$\Gamma_{\varphi}^{\mathrm{SN}} \approx \frac{1}{\kappa_\zeta}4\chi_{01}^2 n_{\mathrm{th}}(\Omega_\zeta)(n_{\mathrm{th}}(\Omega_\zeta)+1), \tag{19}$$

while in the opposite limit $\chi_{01} \gg \kappa_\zeta$, as

$$\Gamma_{\varphi}^{\mathrm{SN}} \approx \kappa_\zeta n_{\mathrm{th}}(\Omega_\zeta). \tag{20}$$

From the above equations, we see that both χ_{01}, as well as the thermal occupation $n_{\mathrm{th}}(\Omega_\zeta)$ can play a crucial role in determining the strength of the resulting dephasing rate.

4.2. Depolarization (T_1)

Decoherence due to depolarization comprises of processes associated with spontaneous transitions between energy eigenstates. Such transitions may occur within the two-level subspace of the 0-π qubit, or lead to leakage to states outside of this subspace. The characteristic time scale for depolarization is the T_1 time [25]. We define the operator coupling the 0-π circuit degrees of freedom to noise channel labeled λ as $V_\lambda = G_\lambda \delta\lambda$, where G_λ is an operator on the Hilbert space spanned by θ, ϕ and ζ. $\delta\lambda$ refers to the bath degrees of freedom and may be an operator acting on the Hilbert space of the bath, or a classical, stochastic variable with appropriately chosen statistics. Using Fermi's Golden Rule, one obtains the rate for transitions from the initial state $|\psi_i\rangle$ to a final state $|\psi_f\rangle$ [25, 30, 50] as

$$\gamma_{i\to f}^{\lambda,\pm} = \frac{1}{\hbar^2}\,|\langle\psi_f|G_\lambda|\psi_i\rangle|^2 S_\lambda(\mp|\omega_{fi}|). \tag{21}$$

Here, initial and final states are eigenstates of the full 0-π Hamiltonian, equation (6), with eigenenergy difference $\hbar\omega_{fi} = E_f - E_i$, and $S_\lambda(\omega)$ is the noise spectral density, see equation (10). The coupling operator G_λ and spectral density $S_\lambda(\omega)$ depend on the specific noise channel and its statistical properties. Furthermore, the $\pm$ notation describes whether the rate is upwards ($\gamma_{i\to f}^{\lambda,+}$), where $E_f > E_i$, or downwards ($\gamma_{i\to f}^{\lambda,-}$), where $E_f < E_i$.

We expect to operate the 0-π qubit in the dispersive regime with respect to the ζ-mode (see equation (8)). In such case, dressed states can be suitably labeled by excitation numbers n and l referring to ζ-mode and primary 0-π subspace, respectively: $|\psi_j\rangle = |\psi_{l,n}\rangle$. In practice, we base the assignment of labels l, n on the maximum overlap between exact eigenstates of the full Hamiltonian (6) and bare product states $|l\rangle_{0\pi} \otimes |n\rangle_\zeta$. (Alternatively, perturbation theory can be used, see appendix C.) We may thus write the above transition rates in the form $\gamma_{l,n\to l',n'}^{\lambda,\pm} = \gamma_{i\to f}^{\lambda,\pm}$.

Since we aim to evaluate the depolarization of the primary 0-π degrees of freedom, i.e., transitions which change the state index l, we define the composite transition rate

$$\Gamma_{l\to l'}^{\lambda} = \sum_{n,n'} P_\zeta(n)\,\gamma_{l,n\to l',n'}^{\lambda,\pm}, \tag{22}$$

which includes a summation over all the ζ-mode states n and n', where each initial ζ-mode state is weighted by the thermal occupation probability $P_\zeta(n) = [1 - \exp(-\hbar\Omega_\zeta/k_{\mathrm{B}}T)]\exp(-n\hbar\Omega_\zeta/k_{\mathrm{B}}T)$, with k_{B} denoting Boltzmann's constant. Finally, we define an effective depolarization rate Γ_1^λ and corresponding time $T_1^\lambda = 1/\Gamma_1^\lambda$ for noise channel λ as[8]

$$\Gamma_1^\lambda = \Gamma_{1\to 0}^\lambda + \Gamma_{0\to \mathrm{up}}^\lambda + \Gamma_{1\to \mathrm{up}}^\lambda. \tag{23}$$

Here, $\Gamma_{1\to 0}^\lambda$ is the ordinary qubit relaxation rate, and $\Gamma_{0\to \mathrm{up}}^\lambda$, $\Gamma_{1\to \mathrm{up}}^\lambda$ are the excitation rates from ground and first excited state to all higher levels. For the 0-π qubit, we find that upward transitions to states outside the two-level subspace typically dominate over the downward rate $\Gamma_{1\to 0}^\lambda$, even at low temperatures. This is precisely due to the disjoint-support of the eigenstates with $l = 0,\ 1$ and the resulting exponential suppression of the corresponding matrix elements in equation (21). We elaborate on this further in section 5.

Depolarization from critical-current noise—Based on these considerations, we can assess the effects of critical-current noise on qubit depolarization. Similar to section 4.1, we expand the critical current into a static and a

[8] Often, depolarization rates are exclusively based on transitions within the two-level subspace [25]. In the 0-π qubit, transitions to states outside this subspace can be dominant and, hence, are included.

fluctuating part, $I_{c,\mathrm{tot}} = I_c + \delta I_c$. Keeping terms up to leading order, we can write the interaction V_{I_c} as[9]

$$V_{I_c} = \frac{\partial H}{\partial I_c}\delta I_c = G_{I_c}\delta I_c = \left[-\frac{\Phi_0}{\pi}\cos\theta\,\cos\left(\phi - \frac{\varphi_{\mathrm{ext}}}{2}\right) + \frac{\Phi_0}{2\pi}\,\mathrm{d}E_{\mathrm{J}}\sin\theta\,\sin\left(\phi - \frac{\varphi_{\mathrm{ext}}}{2}\right)\right]\delta I_c. \tag{24}$$

Employing equations (12), (22) and (23), this enables us to calculate the depolarization rate $\Gamma_1^{I_c}$ due to $1/f$ critical-current noise.

Depolarization from flux noise—In analogous fashion, we characterize depolarization due to flux noise. Identifying λ as the external flux Φ_{ext}, and assuming $\Phi_{\mathrm{ext,tot}} = \Phi_{\mathrm{ext}} + \delta\Phi_{\mathrm{ext}}$, we obtain the coupling operator[10]

$$V_{\Phi_{\mathrm{ext}}} = \frac{\partial H}{\partial \Phi_{\mathrm{ext}}}\delta\Phi_{\mathrm{ext}} = G_{\Phi_{\mathrm{ext}}}\,\delta\Phi_{\mathrm{ext}} = \left[-\frac{2\pi E_{\mathrm{J}}}{\Phi_0}\cos\theta\,\sin\left(\phi - \frac{\varphi_{\mathrm{ext}}}{2}\right) - \frac{\pi E_{\mathrm{J}}}{\Phi_0}\mathrm{d}E_{\mathrm{J}}\sin\theta\,\cos\left(\phi - \frac{\varphi_{\mathrm{ext}}}{2}\right)\right]\delta\Phi_{\mathrm{ext}}. \tag{25}$$

For flux nose, two different noise channels may be considered: flux noise due to current-fluctuations in the flux-bias line, as well as $1/f$ noise. For the former, we consider fluctuations in magnetic flux due to Ohmic current noise in the flux-bias line which couples to the 0-π circuit via a mutual inductance M [3]. The spectral density for such current noise can be described by

$$S_I^{\mathrm{Ohm}}(\omega) = \frac{2\hbar\omega}{R}\left[1 + \coth\left(\frac{\hbar\omega}{2k_{\mathrm{B}}T}\right)\right], \tag{26}$$

where R is taken as 50 Ω. This leads to the flux noise spectral density of $S_{\Phi_{\mathrm{ext}}}(\omega) = M^2 S_I^{\mathrm{Ohm}}(\omega)$. We will assume a mutual inductance between the qubit loop and the biasing line to be $M = 2500\ \Phi_0\ \mathrm{A}^{-1}$, a value substantially larger than the one used in [3], and motivated by the fact that larger inductors will likely require a bigger effective circuit. Together, this allows us to calculate the flux-noise depolarization rate $\Gamma_1^{\Phi_{\mathrm{ext}},\mathrm{Ohm}}$. The analysis of $1/f$ intrinsic flux noise proceeds in a straightforward way from equations (12) and (25), leading to a depolarization rate $\Gamma_1^{\Phi_{\mathrm{ext}}}$.

Purcell depolarization via ζ-mode—Depolarization of the qubit may also occur due to processes analogous to Purcell decay, since the 0-π qubit's θ and ϕ degrees of freedom are coupled to the harmonic ζ-mode which, itself, is subject to intrinsic decay with rate κ_ζ. The resulting relaxation and excitation rates are enhanced or suppressed depending how dispersive the coupling to the ζ-mode is. We show in appendix C that the resulting rates for upward and downward transitions can be written as

$$\Gamma_{l\to l'}^{\mathrm{Purcell}} = \kappa_\zeta\, n_{\mathrm{th}}(\omega_{l'l}^q)\sum_{n,n'} P_\zeta(n)\,|\langle\psi_{l',n'}|a^\dagger|\psi_{l,n}\rangle|^2 \approx \kappa_\zeta\, n_{\mathrm{th}}(\omega_{l'l}^q)\frac{|g_{ll'}|^2}{|E_l^q - E_{l'}^q + \hbar\Omega_\zeta|^2} \tag{27}$$

in the case of $E_{l'}^q > E_l^q$, and

$$\Gamma_{l\to l'}^{\mathrm{Purcell}} = \kappa_\zeta[n_{\mathrm{th}}(\omega_{ll'}^q) + 1]\sum_{n,n'} P_\zeta(n)\,|\langle\psi_{l',n'}|a|\psi_{l,n}\rangle|^2 \approx \kappa_\zeta[1 + n_{\mathrm{th}}(\omega_{ll'}^q)]\frac{|g_{ll'}|^2}{|E_l^q - E_{l'}^q - \hbar\Omega_\zeta|^2} \tag{28}$$

in the case of $E_{l'}^q < E_l^q$. In the above expressions, we use $\omega_{ll'}^q = (E_l^q - E_{l'}^q)/\hbar$, and sum over ζ-mode occupation numbers with the appropriate thermal weights, analogous to our previous treatment in equation (22). The approximations given in equations (27) and (28) can be obtained with perturbation theory (see appendix C). Summation as indicated in equation (23) then allows us to obtain the effective depolarization rate due to the ζ-mode mediated Purcell effect, $\Gamma_1^{\mathrm{Purcell}}$.

5. Calculated coherence times

The coherence times calculated using expressions from section 4, for parameter sets 1, 2 and 3 (see section 3) are shown in figures 7–9 respectively. Panels (a) present pure dephasing times versus flux, namely: $T_\varphi^{\Phi_{\mathrm{ext}}}$ due to $1/f$ flux noise (orange curve), $T_\varphi^{I_c}$ due to $1/f$ critical-current noise (green curve), as well as T_φ^{SN} due to shot noise from the ζ-mode coupling (blue curve). The approximate expressions for T_φ^{SN}, from equation (19) in the case of PS1, and from equation (20) in the case of PS2 and PS3 (dashed red line) are also presented for comparison. Panels (b) show the pure dephasing time $T_\varphi^{n_g^\theta}$ due to $1/f$ charge noise as a function of offset charge n_g^θ. The three curves correspond to three different values of external flux: $\Phi_{\mathrm{ext}} = 0.0$ (blue curve), $\Phi_{\mathrm{ext}} = 0.25\ \Phi_0$ (orange curve), and $\Phi_{\mathrm{ext}} = 0.50\ \Phi_0$ (green curve). Panels in (c)–(f) outline the relevant T_1 depolarization times: (c) depolarization from $1/f$ critical current noise; (d) depolarization due to $1/f$ flux noise; (e) depolarization

[9] In the regime of weak parameter disorder considered here, we may neglect the fact that the 0-π circuit has two independent junctions, and instead associate a single random noise process with the mean critical current.

[10] We stress that there is an ambiguity in expression (25) that arises from the choice of flux grouping with different terms of the Hamiltonian. The details related to such flux grouping may be covered in a future publication.

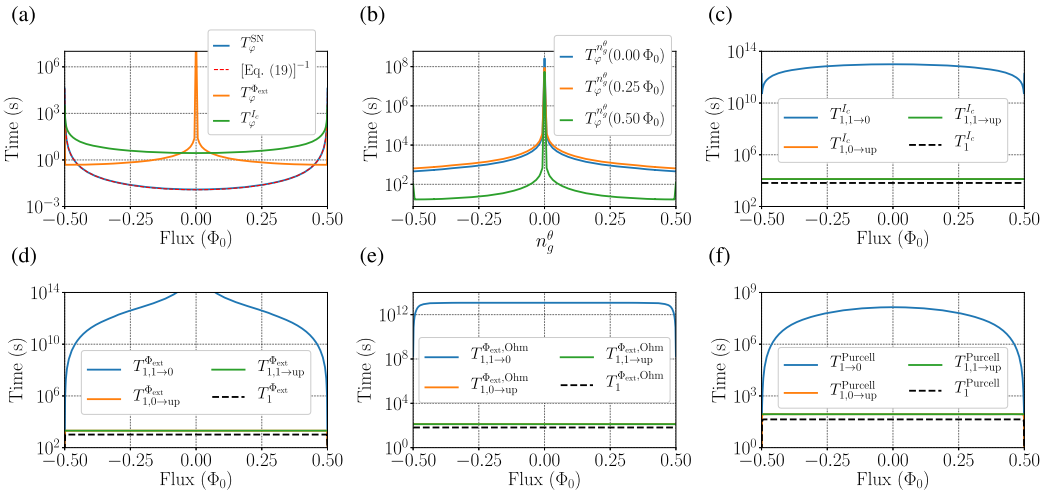

Figure 7. Calculated coherence times for parameter set 1. (a) Pure dephasing times due to $1/f$ flux noise $T_\varphi^{\Phi_{\rm ext}}$ (orange curve), $1/f$ critical current noise $T_\varphi^{I_c}$ (green curve) as well as shot noise $T_\varphi^{\rm SN}$ (blue curve), with its approximation $\kappa_\zeta[4\chi_{01}^2 n_{\rm th}(\Omega_\zeta)(n_{\rm th}(\Omega_\zeta)+1)]^{-1}$ from equation (19) (dashed red line), valid when $\chi_{01} \ll \kappa_\zeta$. (b) Pure dephasing time due to $1/f$, charge noise $T_\varphi^{n_g^\theta}$ along the θ direction, plotted as a function of n_g^θ and calculated at $\Phi_{\rm ext} = 0.0\ \Phi_0$ (blue curve), $\Phi_{\rm ext} = 0.25\ \Phi_0$ (orange curve), and $\Phi_{\rm ext} = 0.50\ \Phi_0$ (green curve). (c) T_1 due to $1/f$ critical current noise. (d) T_1 due to $1/f$ flux noise. (e) T_1 due to biasing flux line noise. (f) Purcell depolarization time. Plots in (c)–(f), show transition times of states 1 to 0 (blue curves), $0 \to$ upwards (orange curves), $1 \to$ upwards (green curves), and finally effective (combined) times (dashed black curves). See main text for analysis.

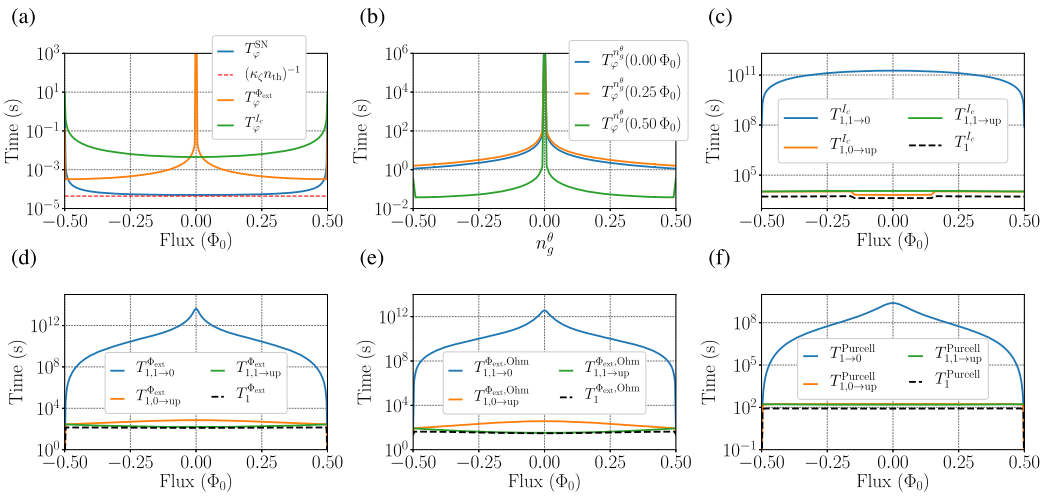

Figure 8. Calculated coherence times for parameter set 2. (a) Pure dephasing times due to $1/f$ flux noise $T_\varphi^{\Phi_{\rm ext}}$ (orange curve), $1/f$ critical current noise $T_\varphi^{I_c}$ (green curve) as well as shot noise $T_\varphi^{\rm SN}$ (blue curve), with its approximation $1/\kappa_\zeta n_{\rm th}(\Omega_\zeta)$ (dashed red line), valid when $\chi_{01} \gg \kappa_\zeta$. (b) Pure dephasing time due to $1/f$, charge noise $T_\varphi^{n_g^\theta}$ along the θ direction, plotted as a function of n_g^θ and calculated at $\Phi_{\rm ext} = 0.0\ \Phi_0$ (blue curve), $\Phi_{\rm ext} = 0.25\ \Phi_0$ (orange curve), and $\Phi_{\rm ext} = 0.50\ \Phi_0$ (green curve). (c) T_1 due to $1/f$ critical current noise. (d) T_1 due to $1/f$ flux noise. (e) T_1 due to biasing flux line noise. (f) Purcell depolarization time. Plots in (c)–(f), show transition times of states 1 to 0 (blue curves), $0 \to$ upwards (orange curves), $1 \to$ upwards (green curves), and finally effective (combined) times (dashed black curves). See main text for analysis.

due to Ohmic noise in the flux-bias line; (f) depolarization due to ζ-mode mediated Purcell processes. All plots in (c)–(f) show inverse rates for transitions between states 1 to 0 (blue curves), $0 \to$ upwards (orange curves), $1 \to$ upwards (green curves), and finally effective (combined) times (dashed black curves).

Figure 7 shows that the PS1, which corresponds to the 'deep 0-π limit' is the best performing of the parameter sets that we study. However, as was discussed in section 3, it may not be easily experimentally realizable, mainly due to difficulties in building large linear inductors. Hence, below, besides discussing the numerical results in detail for all three parameter sets, we outline how under some circumstances actually

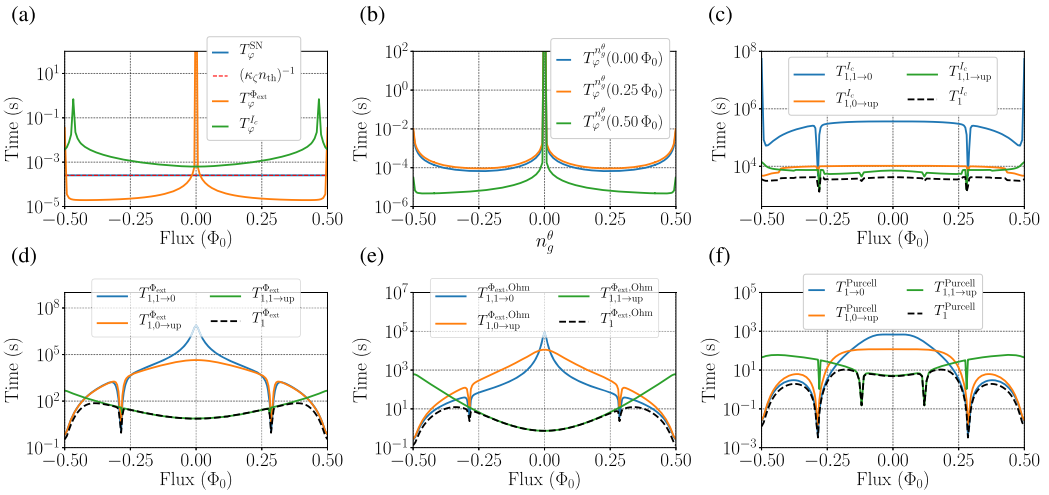

Figure 9. Calculated coherence times for parameter set 3. (a) Pure dephasing times due to $1/f$ flux noise $T_\varphi^{\Phi_{\rm ext}}$ (orange curve), $1/f$ critical current noise $T_\varphi^{I_c}$ (green curve) as well as shot noise $T_\varphi^{\rm SN}$ (blue curve), with its approximation $1/\kappa_\zeta n_{\rm th}(\Omega_\zeta)$ (dashed red line), valid when $\chi_{01} \gg \kappa_\zeta$. (b) Pure dephasing time due to $1/f$, charge noise $T_\varphi^{n_g^\theta}$ along the θ direction, plotted as a function of n_g^θ and calculated at $\Phi_{\rm ext} = 0.0\ \Phi_0$ (blue curve), $\Phi_{\rm ext} = 0.25\ \Phi_0$ (orange curve), and $\Phi_{\rm ext} = 0.50\ \Phi_0$ (green curve). (c) T_1 due to $1/f$ critical current noise. (d) T_1 due to $1/f$ flux noise. (e) T_1 due to biasing flux line noise. (f) Purcell depolarization time. Plots in (c)–(f), show transition times of states 1 to 0 (blue curves), $0 \rightarrow$ upwards (orange curves), $1 \rightarrow$ upwards (green curves), and finally effective (combined) times (dashed black curves). See main text for analysis.

decreasing the circuit inductance (increasing $E_{\rm L}$), and therefore going away from the 'deep 0-π limit', may be also beneficial to the overall coherence properties of the 0-π qubit.

In both PS1 and PS2, the pure dephasing is dominated by ζ-mode shot noise. Even the relatively small amount of disorder (5% in $E_{\rm L}$ and/or $E_{\rm C}$) causes the primary qubit degrees of freedom to couple to the ζ-mode, which for PS1 and PS2 has a low frequency of $\Omega_\zeta/2\pi \approx 36$ MHz and $\Omega_\zeta/2\pi \approx 113$ MHz respectively. At a temperature of $T = 15$ mK, this corresponds to a thermal occupations of $n_{\rm th}(\Omega_\zeta) \approx 8.25$ and $n_{\rm th}(\Omega_\zeta) \approx 2.29$ photons. In PS1, the dispersive shift χ_{01} is, however, much smaller than κ_ζ, and a small χ_{01} dominates $T_\varphi^{\rm SN}$ (see equation (19)), which is not particularly damaging, as even in worst case, at $\Phi_{\rm ext} = 0$, $T_\varphi^{\rm SN} \approx 20$ ms. In PS2, on the other hand, over most of the flux range, the χ_{01} is larger than the ζ-mode decay rate—taken here as $\kappa_\zeta = 1/100\ \mu$s. There, we observe that $T_\varphi^{\rm SN}$ is well approximated by the asymptotic expression $1/\kappa_\zeta n_{\rm th}(\Omega_\zeta) \approx 43\ \mu$s over most of the flux range, in which case the shot noise rate is dominated by the thermal photon count occupying the ζ-mode (we discuss the interplay between χ_{01} and $n_{\rm th}(\Omega_\zeta)$ in more detail below).

For PS3, as shown in figure 9(a), $T_\varphi^{\rm SN}$ is no longer the bottleneck across the full flux range. Here $T_\varphi^{\rm SN}$, as in PS2 away from $\Phi_{\rm ext} = 0.50\ \Phi_0$, is still well approximated using equation (20), but both $E_{\rm L}$ and $E_{\rm C}$ are over 3 times larger than in PS2, leading to an increased ζ-mode frequency $\Omega_\zeta/2\pi \approx 395$ MHz and therefore decreased corresponding thermal occupation of $n_{\rm th}(\Omega_\zeta) \approx 0.39$ photons. This results in an approximate $T_\varphi^{\rm SN} \approx 254\ \mu$s, but comes at the cost of increased flux-noise sensitivity (as well as charge-noise sensitivity, see below). Away from the flux sweet spot, this can produce a $T_\varphi^{\Phi_{\rm ext}}$ as low as 20 μs. This unfavorable behavior is a consequence of the large energy-flux dispersion, easily observed in figures 4(c) and (d). Near the sweet spot, however, the flux noise is subdominant and shot-noise dephasing quantified by $T_\varphi^{\rm SN}$ remains the limiting factor. Therefore, perhaps somewhat surprisingly, as long as qubit operation is performed in the vicinity of zero flux, actually increasing $E_{\rm L}$ and $E_{\rm C}$ (from that of PS2 to PS3) can be beneficial to the qubit's effective pure dephasing time. While decreasing disorder ultimately also mitigates shot-noise sensitivity, we find that disorder levels as small as $\sim$2% and $1/\kappa_\zeta = 100\ \mu$s still lead to significant dispersive shifts $\chi_{01} \gg \kappa_\zeta$ (for $E_{\rm L}$ and $E_{\rm C}$ of PS2 and PS3) away from $\Phi_{\rm ext} = 0.5\ \Phi_0$. If $E_{\rm L}$ cannot be decreased as done in PS1, the resolution to this challenge is to either further decrease the thermal population of the ζ-mode, or to decrease κ_ζ itself.

Indeed, one key result of our calculations is the non-trivial dependence of shot-noise sensitivity on $E_{\rm L}$. In PS1, both $E_{\rm L}$ and $E_{\rm C}$ are decreased relative to their values in PS2, by factors of 5 and 2 respectively, which leads to a substantial mitigation of shot noise. The origin of the observed improvement is subtle, as decreasing $E_{\rm C}$ and $E_{\rm L}$ also decreases Ω_ζ, which actually increases the thermal population of the ζ-mode and could make shot noise even more damaging. However, while $n_{\rm th}(\Omega_\zeta)$ gets larger, beyond a certain threshold, the dispersive shift χ_{01} decreases very rapidly. Specifically, the dispersive shifts χ_0 and χ_1 for the two qubit states become essentially identical, thus rendering ζ-mode shot noise ineffective for dephasing.

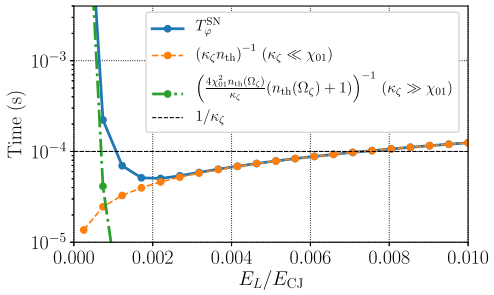

Figure 10. Plot of dephasing time $T_\varphi^{\rm SN}$ due to ζ-mode shot noise as a function of $E_{\rm L}/E_{\rm CJ}$ (blue curve) for PS2. $E_{\rm L}$ is varied while keeping all other energies fixed. At $E_{\rm L}/E_{\rm CJ} \approx 0.0021$ (i.e. $E_{\rm L} = 0.042$ GHz), the dephasing time $T_\varphi^{\rm SN}$ reaches a minimum. For $E_{\rm L}/E_{\rm CJ} \gg 0.0021$, $T_\varphi^{\rm SN}$ can be approximated by $1/\kappa_\zeta n_{\rm th}(\Omega_\zeta)$ (orange curve), and increasing $E_{\rm L}$ is beneficial because it (slowly) decreases the thermal population of the ζ-mode. For $E_{\rm L}/E_{\rm CJ} \ll 0.0021$, $T_\varphi^{\rm SN}$ can be approximated using equation (19) (green curve). In that case, the dispersive shift decreases at a faster rate than $n_{\rm th}(\Omega_\zeta)$ increases, leading to an overall increase in $T_\varphi^{\rm SN}$. The lifetime $1/\kappa_\zeta$ is shown for comparison (black dashed line).

To illustrate this effect in more detail, figure 10 presents $T_\varphi^{\rm SN}$ as a function of $E_{\rm L}$ while keeping all other parameters fixed to the values of PS2. The plot shows that $T_\varphi^{\rm SN}$ goes through a minimum at $E_{\rm L}/E_{\rm CJ} \approx 0.0021$ (or equivalently $E_{\rm L} = 0.042$ GHz). For $E_{\rm L}/E_{\rm CJ}$ well above the minimum at $E_{\rm L}/E_{\rm CJ} = 0.0021$, $T_\varphi^{\rm SN}$ can be approximated by $1/\kappa_\zeta n_{\rm th}(\Omega_\zeta)$, and increasing $E_{\rm L}$ is beneficial because it decreases the thermal population of the ζ-mode. This is consistent with the benefit we observe when increasing $E_{\rm L}$ (and $E_{\rm C}$) from the values of PS2 to PS3. In the opposite limit, $E_{\rm L}/E_{\rm CJ} \ll 0.0021$, $T_\varphi^{\rm SN}$ can be approximated using equation (19). Since the dispersive shift decreases at a faster rate than $n_{\rm th}(\Omega_\zeta)$ increases, the sensitivity to ζ-mode shot noise is actually reduced and $T_\varphi^{\rm SN}$ gets larger, matching the observations made for PS1. Hence, this leads us to believe, that it may be beneficial to keep decreasing $E_{\rm L}$, but only when beyond the threshold corresponding the to the minimum of $T_\varphi^{\rm SN}$.

As can be expected from the energy-flux dependence (see figures 3 and 4(a) and (b)), in both PS1 and PS2, the qubit is well-protected from $1/f$ flux noise near the sweet spots at $\Phi_{\rm ext} = 0$. This is mainly due to the $E_{\rm L}$ being small enough, which contributes to the localization of the 0-π qubit wave functions in the $\theta = 0$ and $\theta = \pi$ potential energy wells, and lead to near-degeneracy as well as suppressed flux dispersion. Pure dephasing due to critical current fluctuations, by contrast, has its flux sweet spot close to half-integer flux, and constitutes the second most dominant pure dephasing mechanism at $\Phi_{\rm ext} = 0$, the natural operating point for the 0-π qubit. Panels (b) of figures 7–9 show the effects of charge noise. For PS1 and PS2, dephasing due to charge noise is weak, and at $\Phi_{\rm ext} = 0$, in worst case, away from charge sweet spots, the dephasing times exceed $T_\varphi^{n_g^\theta} = 500$ s and $T_\varphi^{n_g^\theta} \approx 1$ s respectively. For PS3, charge noise can become a limiting factor away from charge sweet spots, as seen in figure 9(b) if the qubit is biased near $\Phi_{\rm ext} = 0.5\,\Phi_0$. Here, the charge-noise sensitivity is increased by the larger charging energy $E_{\rm C}$ as well as the decreased Josephson energy $E_{\rm J}$ which in total reduce the ratio $E_{\rm J}/E_{\rm Cs} \sim E_{\rm J}/E_{\rm C}$. Altogether, this increases the energy-charge dispersion (not explicitly shown) and leads to the reduction in dephasing time. Since in practice it may be difficult to limit stray charge offsets, in PS3, one might need to operate the qubit as close to $\Phi_{\rm ext} = 0$ as possible, where $T_\varphi^{n_g^\theta} \geqslant 10^{-4}$ s. Alternatively, a more detail optimization of PS3 would be possible where $E_{\rm C}$ could be decreased, while $E_{\rm L}$ further increased. This could potentially limit $T_\varphi^{n_g^\theta}$, while still minimizing the impact of shot noise (over PS2).

Depolarization times T_1 from critical-current and flux noise are shown in panels (c)–(e), while from Purcell effect, in panels (f) of figures 7–9. For all three parameter sets, the effective (combined) results (black, dashed lines) are large, with values exceeding 10 s (PS1), 10 s (PS2), 600 ms (PS3) at $\Phi_{\rm ext} = 0$. We note that the relaxation rates from the first excited to the ground state (blue curves) are typically substantially smaller when compared to excitation rates towards higher states (orange and green curves). This, 'by-design' behavior is a result of the significant suppression of all matrix elements between ground and first excited states of the qubit. Figures 3 and 4 show that for all parameters sets we study, the two lowest eigenfunctions exhibit strong localization along the θ direction—even for PS3 away from $\Phi_{\rm ext} = 0.5\,\Phi_0$, where the near-degeneracy of the states is lost. As a result, upwards transitions leaking out of the two-level qubit subspace are much more likely than ordinary relaxation/excitation processes within it. We also see that the T_1 results for PS1 and PS2 are generally flat, while in the case of PS3, we observe not just more variation as a function of flux, but also abrupt dips, especially near $\Phi_{\rm ext} \approx 0.29\,\Phi_0$. The increased flux variation has to do with a much larger dependence of the wave functions on changes in flux, which is mainly a result of an increased $E_{\rm L}$. The dips correspond to anticrossings between the states of the qubit and the ζ-mode. In the case of $T_1^{\rm Purcell}$, for example, right at, or very

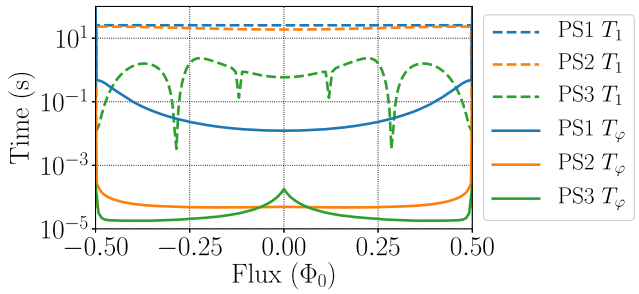

Figure 11. Effective coherence times for PS1 (blue), PS2 (orange), and PS3 (green). The displayed pure-dephasing times T_φ, and depolarization times T_1 are obtained from the cumulative rates combining all processes described in section 4.

near such dips, we expect the dispersive approximation to break down. There, the qubit is no loner protected by its detuning from the ζ-mode, which results in rates that increase the effective depolarization [51].

Figure 11 summarizes our results with a plot of the total coherence times for PS1 (blue), PS2 (orange), and PS3 (green). The displayed pure-dephasing times[11] T_φ, and depolarization times T_1 are obtained from the cumulative rates combinining all noise processes described in section 4. At the zero-flux working point, we find: $T_\varphi \approx 20$ ms and $T_1 \approx 10$ s for PS1, $T_\varphi \approx 50$ μs and $T_1 \approx 10$ s for PS2, and $T_\varphi \approx 200$ μs and $T_1 \approx 600$ ms for PS3. These rates confirm that the 0-π qubit is a promising device benefitting from intrinsic protection. This applies especially to the 'deep 0-π limit' exemplified by PS1 and envisioned by BKP [13]. Future work on superinductors based on Josephson junction arrays and high-inductance materials will have to explore ways to reach the needed high inductance values. In the meantime, PS2 and PS3 show that the effect of intrinsic protection can already be reaped with intermediate parameter choices accessible with current capabilities in superinductor fabrication.

6. Conclusions

We have studied the coherence properties of the 0-π qubit and presented calculations of coherence times for three representative sets of circuit parameters. We find that the inductive energy E_L has a key impact on the coherence properties: despite spurious coupling to the low-frequency ζ-mode, very large inductances currently beyond experimental capabilities could indeed realize the promise of an intrinsically protected superconducting qubit.

In the absence of disorder in circuit parameters, the ζ-mode remains decoupled and the 0-π qubit is expected to be well-protected against noise-induced transitions leading to depolarization, and against fluctuations in qubit energies leading to pure dephasing. Once disorder in the inductive or charging energies (E_L, E_C) is present, the coupling of the primary qubit degree of freedom to the low-energy, harmonic ζ-mode introduces additional decoherence channels that can change the optimal parameter landscape of the qubit. Even with a moderate amount of disorder of a few percent, the thermal population of the ζ-mode can lead to significant shot-noise dephasing of the qubit. In particular, we found that in the case of parameter set 2, T_φ^{SN} has a minimum around $E_L^{\min} \approx 0.042$ GHz. for $E_L > E_L^{\min}$, the shot-noise rate is dominated by the thermal occupation of the ζ-mode, and hence can be minimized by making Ω_ζ larger. This comes at a cost of larger flux dispersion and, hence, enhanced sensitivity to $1/f$ flux noise which can become the limiting factor. In the opposite regime of $E_L < E_L^{\min}$ (large inductance limit), the rise of the ζ-mode thermal occupation $n_{\mathrm{th}}(\omega_\zeta)$ is compensated by a dramatic decrease in the qubit's dispersive shift χ_{10}, leading in fact to an overall reduction in the shot-noise dephasing rate—see equation (19). The 0-π qubit is generally found to behave well with respect to depolarization processes across the parameter sets we considered.

The effective (combined) pure dephasing and depolarization rates at $\Phi_{\mathrm{ext}} = 0$ were found to be $T_\varphi \approx 20$ ms and $T_1 \approx 10$ s for PS1, $T_\varphi \approx 50$ μs and $T_1 \approx 10$ s for PS2, and $T_\varphi \approx 200$ μs and $T_1 \approx 600$ ms for PS3. We believe that further optimization might lead to even more favorable results, motivating future research into experimentally realizing even larger superinductances. In summary, we conclude that the coupling to the spurious ζ-mode does not invalidate the prospects of intrinsic noise protection in 0-π qubits. We predict that noise protection is at work even in the regime of modest, currently accessible superinductances, rendering the 0-π qubit an attractive candidate for next-generation superconducting devices.

[11] In the case of the combined T_φ, the charge noise rate $1/T_\varphi^{n_g^\theta}$ is not includeded in the calculations. Its inclusion, however, would have minimal (i.e. visually indistinghishable) impact on the the result, except in PS3, at $\Phi_0 = 0.5\,\Phi_0$ and the near charge bias of $n_g^\theta = 0.5$.

Acknowledgments

We acknowledge valuable discussions with Andy C Y Li, and the hospitality from the ICTS-TIFR (JK). ADP acknowledges support from the Fundación Williams en Argentina and the Bourse d'excellence de 3e cycle, Faculté des Sciences, Université de Sherbrooke. This work was supported by the Army Research Office under Grant no. W911NF-15-1-0421 and NSERC. This research was undertaken thanks in part to funding from the Canada First Research Excellence Fund.

Appendix A. Pure dephasing due to classical noise

In this appendix, we review the derivation of pure dephasing rates. We retain terms up to second order in the noise coupling, so that the full crossover from linear noise susceptibility to second-order susceptibility at sweet spots [41] can be evaluated. Our treatment here is in part based on previous work published in [25, 40].

We consider an external parameter $\lambda(t) = \lambda_0 + \delta\lambda(t)$ subject to a classical noise signal $\delta\lambda(t)$ arising from a stationary, Gaussian process with a mean $\langle\delta\lambda(t)\rangle = 0$ and given noise power spectrum $S(\omega) = \int_{-\infty}^{\infty} \mathrm{d}t\ \mathrm{e}^{-\mathrm{i}\omega t}\langle\delta\lambda(t)\delta\lambda(0)\rangle$. The system Hamiltonian depends parametrically on the external parameter, $H = H(\lambda(t))$, and we assume that the effect of noise is sufficiently small to allow an expansion in powers of $\delta\lambda$

$$H = H_0 + \frac{\partial H}{\partial\lambda}\delta\lambda(t) + \frac{1}{2}\frac{\partial^2 H}{\partial\lambda^2}\delta\lambda^2(t) + \mathcal{O}(\delta\lambda^3) \approx H(\lambda_0) + V_\lambda(t), \tag{A.1}$$

where $H_0 = H(\lambda_0)$, and the derivatives are evaluated at $\lambda = \lambda_0$. To analyze how the noise terms $V_\lambda(t)$ affect the phase coherence of the system, it is convenient to switch to the interaction picture, in which states and operators take the usual form $|\bar{\psi}(t)\rangle = \mathrm{e}^{\mathrm{i}H_0 t}|\psi(t)\rangle$ and $\bar{X}(t) = \mathrm{e}^{\mathrm{i}H_0 t}X\mathrm{e}^{-\mathrm{i}H_0 t}$. We further employ the eigenbasis $\{|n\rangle\}$ of H_0 to express the state $|\bar{\psi}(t)\rangle$ in terms of the probability amplitudes $c_n(t) = \langle n|\bar{\psi}(t)\rangle$. In the interaction picture, the time-dependent Schrödinger equation thus takes the form $\mathrm{i}\frac{\mathrm{d}}{\mathrm{d}t}c_n(t) = \langle n|\bar{V}_\lambda(t)|\bar{\psi}(t)\rangle = \sum_{n'}\langle n|\bar{V}_\lambda(t)|n'\rangle c_{n'}(t)$. In general, the noise operator $\bar{V}_\lambda(t)$ incorporates both longitudinal and transverse terms

$$\bar{V}_\lambda(t) = \sum_n v_n(t)|n\rangle\langle n| + \sum_{n\neq m} v_{n,m}(t)|n\rangle\langle m|, \tag{A.2}$$

where the former is responsible for pure dephasing, while the latter introduces transitions among different states. In the following discussion we concentrate on pure dephasing, and, hence ignore the transverse portion of the Hamiltonian. In such case, the system of differential equations for $c_n(t)$ decouples, and we find

$$|\bar{\psi}_n(t)\rangle = \exp\left(-\frac{\mathrm{i}}{\hbar}\int_0^t \mathrm{d}t'\ v_n(t')\right)|n\rangle, \tag{A.3}$$

for the time evolution of the initial state $|n\rangle$. As expected, the longitudinal coupling only affects the phase of the state. Next, we make use of the decomposition of the noise into contributions of first and second order,

$$v_n(t) = \langle n|\partial_\lambda H|n\rangle\,\delta\lambda(t) + \frac{1}{2}\langle n|\partial_\lambda^2 H|n\rangle\,\delta\lambda^2(t) = d_n\,\delta\lambda(t) + \frac{1}{2}D_n\,\delta\lambda^2(t). \tag{A.4}$$

(Again, derivatives are evaluated at $\lambda = \lambda_0$.) The first-order coefficient d_n can be written as

$$d_n = \langle n|\left(\partial_\lambda\sum_m E_m(\lambda)|m(\lambda)\rangle\langle m(\lambda)|\right)|n\rangle = \partial_\lambda E_n + E_n(\lambda_0)(\langle n|\partial_\lambda|n(\lambda)\rangle + \text{c.c.}) = \partial_\lambda E_n, \tag{A.5}$$

where all derivatives are evaluated at $\lambda = \lambda_0$, and the term proportional to $E_n(\lambda_0)$ on the right-hand side is zero, since $|n(\lambda)\rangle$ is normalized. The second order coefficient is

$$D_n = \partial_\lambda\langle n|\partial_\lambda H|n\rangle = \partial_\lambda^2 E_n, \tag{A.6}$$

evaluated at $\lambda = \lambda_0$.

To extract the pure dephasing times, we consider a Ramsey-type experiment, starting in an initial superposition $|\bar{\psi}(0)\rangle = (|0\rangle + |1\rangle)/\sqrt{2}$. The pure dephasing time is related to the decay of off-diagonal elements of the density matrix in the relevant 2×2 subspace,

$$\rho(t) = \frac{1}{2}\begin{pmatrix} 1 & \rho_{01}(t) \\ \rho_{01}^*(t) & 1 \end{pmatrix} \qquad \text{with} \qquad \rho_{01}(t) = \exp\left(-\mathrm{i}\,\partial_\lambda\omega_{01}\int_0^t \mathrm{d}t'\,\delta\lambda(t') - \mathrm{i}\,\tfrac{1}{2}\partial_\lambda^2\omega_{01}\int_0^t \mathrm{d}t'\,\delta\lambda^2(t')\right), \tag{A.7}$$

where $\omega_{01} = (E_0 - E_1)/\hbar$, and its derivatives are evaluated at $\lambda = \lambda_0$. Upon averaging over noise realizations $\delta\lambda(t)$, the phase factor ρ_{01} approaches zero at long times, $\lim_{t\to\infty}\langle\rho_{01}\rangle(t) = 0$. We will see that the details of this

decay depend on the noise power spectrum $S_\lambda(\omega)$. However, in common cases the decay occurs on some characteristic time scale T_φ, the pure dephasing time. To proceed, we note that the exponent of ρ_{01} is a Gaussian random variable, such that $\langle e^{iY}\rangle = e^{-\langle Y^2\rangle/2}$, which lets us write the noise average as

$$\langle\rho_{01}\rangle(t) = \exp\Bigg(-\tfrac{1}{2}(\partial_\lambda\omega_{01})^2\int_0^t dt_1\int_0^t dt_2\,\langle\delta\lambda(t_2-t_1)\delta\lambda(0)\rangle - \tfrac{1}{4}(\partial_\lambda^2\omega_{01})^2\int_0^t dt_1\int_0^t dt_2\,\langle\delta\lambda^2(t_2-t_1)\delta\lambda^2(0)\rangle\Bigg). \tag{A.8}$$

Here, we have used $\langle\delta\lambda(t_2-t_1)\delta\lambda^2(0)\rangle = 0$. Next, we treat the integrals from first and second order contributions:

$$I_1(t) = \int_0^t dt_1\int_0^t dt_2\,\langle\delta\lambda(t_2-t_1)\delta\lambda(0)\rangle = \int_0^t dt_1\int_0^t dt_2\int_{-\infty}^{\infty}\frac{d\omega}{2\pi}e^{i\omega(t_2-t_1)}S_\lambda(\omega) = t^2\int_{-\infty}^{\infty}\frac{d\omega}{2\pi}\mathrm{sinc}^2\left(\frac{\omega t}{2}\right)S_\lambda(\omega). \tag{A.9}$$

For the second-order expression, we apply Wick's theorem to obtain $\langle\delta\lambda^2(t_2-t_1)\delta\lambda^2(0)\rangle = \langle\delta\lambda^2(0)\rangle^2 + 2\langle\delta\lambda(t_2-t_1)\delta\lambda(0)\rangle^2$. Also noting that $\langle\delta\lambda^2(t_2-t_1)\rangle^2 = \langle\delta\lambda^2(0)\rangle^2$, we find

$$I_2(t) = \int_0^t dt_1\int_0^t dt_2\,\langle\delta\lambda^2(t_2-t_1)\delta\lambda^2(0)\rangle = t^2\sigma_\lambda^4 + 2t^2\int_{-\infty}^{\infty}\frac{d\Omega}{2\pi}\int_{-\infty}^{\infty}\frac{d\omega}{2\pi}\mathrm{sinc}^2\left(\frac{(\Omega+\omega)t}{2}\right)S_\lambda(\omega)\,S_\lambda(\Omega), \tag{A.10}$$

where $\sigma_\lambda^2 = \langle\delta\lambda^2(0)\rangle = \int_{-\infty}^{\infty}\frac{d\omega}{2\pi}S_\lambda(\omega)$.

A.1. $1/f$ noise

For $1/f$ noise, $S_\lambda(\omega)$ is singular for $\omega\to 0$, and the noise variance diverges logarithmically. As a result, infrared and ultraviolet regularizations are needed, and are commonly introduced by appropriate cutoffs at ω_{ir} and ω_{uv}. (Note that certain quantities may depend on the type of cutoff chosen, i.e., abrupt or 'soft' [25].) Returning to equation (A.8) and evaluating the integral $I_1(t)$ for the noise spectrum $S_\lambda(\omega) = 2\pi A_\lambda^2/|\omega|$, leads to

$$I_1(t) = 8(2\pi A_\lambda^2)\int_{\omega_{ir}}^{\infty}\frac{d\omega}{2\pi}\frac{1}{\omega^3}\sin^2\left(\frac{\omega t}{2}\right) \simeq 2A_\lambda^2|\ln\omega_{ir}t|\,t^2, \tag{A.11}$$

where we have extracted the leading log-divergent term for $\omega_{ir}\to 0$ and assumed $t\ll\omega_{ir}^{-1}$. For the second-order contribution, taking the upper frequency limit as ω_{uv}, the leading log-divergent contribution is

$$I_2(t) = 4A_\lambda^4\ln^2(\omega_{uv}/\omega_{ir})\,t^2 + 8A^4\ln^2(\omega_{ir}t)\,t^2. \tag{A.12}$$

Equations (A.11) and (A.12) imply that the decay of the off-diagonal elements of the density matrix follows a Gaussian (up to logarithmic corrections):

$$\langle\rho_{01}\rangle(t) \sim \exp\{-A_\lambda^2(\partial_\lambda\omega_{01})^2|\ln\omega_{ir}t|\,t^2 - A_\lambda^4(\partial_\lambda^2\omega_{01})^2[\ln^2(\omega_{uv}/\omega_{ir}) + 2\ln^2(\omega_{ir}t)]\,t^2\}. \tag{A.13}$$

Therefore, using the standard variation of the Gaussian as a measure of the dephasing time, we obtain

$$T_\varphi = \{2A_\lambda^2(\partial_\lambda\omega_{01})^2|\ln\omega_{ir}t| + 2A_\lambda^4(\partial_\lambda^2\omega_{01})^2[\ln^2(\omega_{uv}/\omega_{ir}) + 2\ln^2(\omega_{ir}t)]\}^{-1/2}, \tag{A.14}$$

which is equation (13) shown in the main text.

Appendix B. Capacitive coupling to circuit nodes

The analysis of capacitive coupling to the 0-π nodes, shown in figure 6, proceeds by including the gate capacitances C_g and external voltage signals $V_j(t)$ ($j = 1, \ldots, 4$) in the circuit Lagrangian. The transformation of variables $\varphi_j\to\phi$, θ, ζ, Σ, is accompanied by defining analogous superpositions of external voltage signals $V_j\to V_\phi$, V_θ, V_ζ, V_Σ, namely $2V_\phi = (V_2 - V_3) + (V_4 - V_1)$ etc, see equation (1). After Legendre transform of the circuit Lagrangian, one finds that the charging energies are renormalized due to the presence of gate capacitances. Denoting the renormalized capacitances $C_J' = (C_J + C_g/2)$, $C' = (C + C_g/2)$ and $C_s' = (C_s + C_g/2)$, we can write the renormalized charging energies (see equation (15)) as $E_{CJ}' = e^2/2C_J'$, $E_C' = e^2/2C'$, and $E_{Cs}' = e^2/2C_s'$ respectively. In the final expression of the kinetic energy, equation (15), the fluctuating voltages are compactly written in terms of effective offset charges. If we define the offset charges associated with each linearized-mode variable by $\bar{n}_g^x = \frac{C_g V_x}{2e}$, with $x\in\{\theta,\phi,\zeta\}$, then the effective offset charges used in equation (15) are given by

$$n_g^\theta = \bar{n}_g^\theta - \frac{1}{2}\frac{E'_{\rm CJ}}{E_{\rm CJ}}\,{\rm d}C_{\rm J}\bar{n}_g^\phi - \frac{1}{2}\frac{E'_{\rm C}}{E_{\rm C}}\,{\rm d}C\bar{n}_g^\zeta, \qquad n_g^\phi = \bar{n}_g^\phi - \frac{1}{2}\frac{E'_{\rm Cs}}{E_{\rm CJ}}{\rm d}C_{\rm J}\bar{n}_g^\theta, \qquad n_g^\zeta = \bar{n}_g^\zeta - \frac{1}{2}\frac{E'_{\rm Cs}}{E_{\rm C}}{\rm d}C\bar{n}_g^\theta. \quad \text{(B.1)}$$

These expressions show that disorder in the capacitances C and $C_{\rm J}$ leads to non-trivial 'mixing' between the circuit degrees of freedom θ, ϕ and ζ and the corresponding voltages—a fact that may be of importance when performing 0-π qubit gates by driving capacitively coupled resonators[12].

Appendix C. Purcell depolarization via the ζ-mode

In this appendix we review the derivation of relaxation and excitation rates associated with the Purcell effect. In the context of the 0-π qubit, Purcell depolarization may occur due to the coupling of the primary 0-π degrees of freedom (variables ϕ and θ) to the lossy ζ-mode. The Hamiltonian for 0-π circuit interacting with a bath can be written as $H = H_{\rm sys} + H_{\rm int} + H_{\rm bath}$ where the individual contributions are:

$$H_{\rm sys} = \sum_k E_k^{\rm sys}|\psi_k^{\rm sys}\rangle\langle\psi_k^{\rm sys}|, \quad H_{\rm bath} = \sum_k \hbar\omega_k b_k^\dagger b_k, \quad H_{\rm int} = \sum_k \hbar\lambda_k(ab_k^\dagger + a^\dagger b_k). \quad \text{(C.1)}$$

Here, $H_{\rm sys}$ is the full 0-π circuit Hamiltonian, including the ζ-mode. The latter couples linearly to a bath via $H_{\rm int}$, where a and b_k correspond to the lowering operators of the ζ-mode and bath modes, respectively. Using Fermi's Golden Rule, we find that $H_{\rm int}$ induces transitions among the eigenstates of $H_{\rm sys} + H_{\rm bath}$ with a rate

$$\gamma_{i\to f} = \frac{2\pi}{\hbar}\delta(E_i - E_f)\,|\langle\psi_f|H_{\rm int}|\psi_i\rangle|^2. \quad \text{(C.2)}$$

The states

$$|\psi_i\rangle = |\psi_i^{\rm sys}\rangle\bigotimes_k|m_k\rangle \quad \text{and} \quad |\psi_f\rangle = |\psi_f^{\rm sys}\rangle\bigotimes_k|m_k{}'\rangle, \quad \text{(C.3)}$$

are the initial and final eigenstates of $H_{\rm sys} + H_{\rm bath}$, and E_i and E_f are the corresponding eigenenergies. Substituting these expressions into equation (C.2) and simplifying leads to

$$\gamma_{i,\{m_k\}\to f,\{m_k{}'\}} = \frac{2\pi}{\hbar}\delta(E_i - E_f)\sum_k \hbar^2\,|\lambda_k|^2[|\langle\psi_f^{\rm sys}|a^\dagger|\psi_i^{\rm sys}\rangle|^2 m_k\,\delta_{m_k{}',m_k-1} + |\langle\psi_f^{\rm sys}|a|\psi_i^{\rm sys}\rangle|^2(m_k+1)\delta_{m_k{}',m_k+1}]\prod_{k'\neq k}\delta_{m_{k'}{}',m_{k'}}, \quad \text{(C.4)}$$

where $\{m_k\}$ and $\{m_k{}'\}$ denote the initial and final configuration of the bath modes. Next, we note that the bare energies of $|\psi_i\rangle$ and $|\psi_f\rangle$ can be written as

$$E_i = E_i^{\rm sys} + \hbar\sum_{m_k} m_k\omega_k \quad \text{and} \quad E_f = E_f^{\rm sys} + \hbar\sum_{m_k{}'} m_k{}'\omega_k. \quad \text{(C.5)}$$

To obtain the effective rate for the transition $i \to f$, we sum over all initial and final states of the bath, weighting initial states by their probability of occurrence $P(\{m_k\})$, as appopriate for a bath in a thermal state at temperature T. With this, we obtain

$$\Gamma_{i\to f} = \sum_{m_k,m_k{}'} P(\{m_k\})\gamma_{i,\{m_k\}\to f,\{m_k{}'\}} = 2\pi\hbar\sum_k |\lambda_k|^2\delta(E_i^{\rm sys} - E_f^{\rm sys} + \hbar\omega_k)\,|\langle\psi_f^{\rm sys}|a^\dagger|\psi_i^{\rm sys}\rangle|^2 n_{\rm th}(\omega_k) + 2\pi\hbar\sum_k |\lambda_k|^2\delta(E_i^{\rm sys} - E_f^{\rm sys} - \hbar\omega_k)\,|\langle\psi_f^{\rm sys}|a|\psi_i^{\rm sys}\rangle|^2(n_{\rm th}(\omega_k)+1), \quad \text{(C.6)}$$

where $n_{\rm th}(\omega_k)$ represents the mean thermal occupation number for bath mode k (mode energy $\hbar\omega_k$). Finally, we take the continuum limit, define $\kappa = 2\pi\hbar\rho(\omega_k)|\lambda_k|^2$ with $\rho(\omega)$ denoting the bath density of states, and introduce $\omega_{jj'}^{\rm sys} = (E_j^{\rm sys} - E_{j'}^{\rm sys})/\hbar$, to obtain

$$\Gamma_{i\to f}^{\rm Purcell,+} = \kappa_\zeta n_{\rm th}(\omega_{fi}^{\rm sys})|\langle\psi_f^{\rm sys}|a^\dagger|\psi_i^{\rm sys}\rangle|^2, \quad \text{(C.7)}$$

when $E_f^{\rm sys} > E_i^{\rm sys}$, as well as a downward one

$$\Gamma_{i\to f}^{\rm Purcell,-} = \kappa_\zeta(1 + n_{\rm th}(\omega_{fi}^{\rm sys}))\,|\langle\psi_f^{\rm sys}|a|\psi_i^{\rm sys}\rangle|^2, \quad \text{(C.8)}$$

when $E_f^{\rm sys} < E_i^{\rm sys}$. The final step is to note that over most of the relevant parameters discussed here, the qubit is in the dispersive regime with respect to the ζ-mode. One can use this fact to label the eigenstates $|\psi_j^{\rm sys}\rangle$ with quantum numbers l and n corresponding to the number of qubit and ζ-mode excitations respectively. As discussed in section 4.2, one way to do this is to look at a maximum overlap between the exact (numerically calculated) eigenstates and bare states where the coupling between the $\{\theta,\ \phi\}$ and ζ is set to zero. Another way is to approximate the eigenstates by treating the coupling $\sum_{l,l'}(g_{ll'}|l\rangle\langle l'|a + {\rm h.c.})$ from equation (6) as a perturbation. In that case, we can express the dressed states $|\overline{l,\ n}\rangle$ in terms of bare eigenstates $|l,\ n\rangle$ as

[12] To be discussed in a future publication.

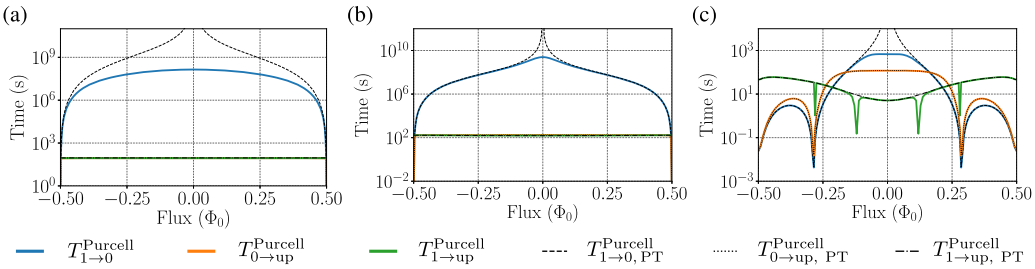

Figure C1. Purcell depolarization times obtained for parameters (a) PS1, (b) PS2 and (c) PS3. Results obtained by numerically are shown in solid, colored lines, while using perturbation theory in black, dashed, dotted and dashed-dotted lines.

$$|\overline{l,\,n}\rangle = |l,\,n\rangle + \sum_k \alpha_k^{l,n}|k,\,n-1\rangle + \sum_k \beta_k^{l,n}|k,\,n+1\rangle + ..., \tag{C.9}$$

where we have taken

$$\alpha_k^{l,n} = \frac{g_{kl}\sqrt{n}}{E_{l,n}^{\mathrm{sys}} - E_{k,n-1}^{\mathrm{sys}}} \quad \text{and} \quad \beta_k^{l,n} = \frac{g_{kl}\sqrt{n+1}}{E_{l,n}^{\mathrm{sys}} - E_{k,n+1}^{\mathrm{sys}}}, \tag{C.10}$$

with bare energies $E_{l,n}^{\mathrm{sys}} = E_l^q + n\hbar\Omega_\zeta$. Defining $|\psi_i^{\mathrm{sys}}\rangle = |\overline{l,\,n}\rangle, |\psi_f^{\mathrm{sys}}\rangle = |\overline{l',\,n'}\rangle$, we thus find for the matrix element the leading-order expression

$$\begin{aligned}|\langle\psi_f^{\mathrm{sys}}|a|\psi_i^{\mathrm{sys}}\rangle|^2 = &|\beta_{l'}^{l,n}\sqrt{n+1}\,\delta_{n,n'} + (\alpha_l^{l',n})^*\sqrt{n}\,\delta_{n-1,n'-1}|^2 \\ &+ |\alpha_{l'}^{l,n}\sqrt{n-1}\,\delta_{n-2,n'} + (\beta_l^{l',n-2})^*\sqrt{n}\,\delta_{n-1,n'+1}|^2,\end{aligned} \tag{C.11}$$

where we neglect terms beyond second order in α and β from equation (C.10). Substituting equation (C.11) and an analogous expression for $|\langle\psi_f^{\mathrm{sys}}|a^\dagger|\psi_i^{\mathrm{sys}}\rangle|^2$ into (C.6), leads to the expressions (27) and (28). In the last two steps we summed over the final ζ-mode states n', which conveniently resulted in the expression that is independent of n. In figure C1 we show a comparison between the depolarization rates due to Purcell effect for PS1 (a), PS2 (b), and PS3 (c), calculated using both methods: the solid colored lines use numerical maximum-state-overlap method, while the black lines are from perturbation theory.

References

[1] Devoret M H and Schoelkopf R J 2013 *Science* **339** 1169–74
[2] Manucharyan V E, Koch J, Glazman L I and Devoret M H 2009 *Science* **326** 113–6
[3] Koch J, Yu T M, Gambetta J M, Houck A A, Schuster D I, Majer J, Blais A, Devoret M H, Girvin S M and Schoelkopf R J 2007 *Phys. Rev.* A **76** 42319
[4] Ioffe L, Feigel'man M, Ioselevich A, Ivanov D, Troyer M and Blatter G 2002 *Nature* **415** 503–6
[5] Kitaev A 2006 arXiv:cond-mat/0609441
[6] Gladchenko S, Olaya D, Dupont-Ferrier E, Douçot B, Ioffe L B and Gershenson M E 2009 *Nat. Phys.* **5** 48–53
[7] Bell M T, Paramanandam J, Ioffe L B and Gershenson M E 2014 *Phys. Rev. Lett.* **112** 167001
[8] Bravyi S B and Kitaev A Y 1998 arXiv:quant-ph/9811052
[9] Raussendorf R and Harrington J 2007 *Phys. Rev. Lett.* **98** 190504
[10] Fowler A G, Stephens A M and Groszkowski P 2009 *Phys. Rev.* A **80** 052312
[11] Fowler A G, Mariantoni M, Martinis J M and Cleland A N 2012 *Phys. Rev.* A **86** 032324
[12] Douçot B and Ioffe L 2012 *Rep. Prog. Phys.* **75** 072001
[13] Brooks P, Kitaev A and Preskill J 2013 *Phys. Rev.* A **87** 52306
[14] Dempster J M, Fu B, Ferguson D G, Schuster D I and Koch J 2014 *Phys. Rev.* B **90** 94518
[15] Manucharyan V E, Koch J, Glazman L I and Devoret M H 2009 *Science* **326** 113–6
[16] Manucharyan V E 2012 Superinductance *PhD Thesis* Yale University
[17] Masluk N A, Pop I M, Kamal A, Minev Z K and Devoret M H 2012 *Phys. Rev. Lett.* **109** 137002
[18] Bell M, Sadovskyy I, Ioffe L, Kitaev A Y and Gershenson M 2012 *Phys. Rev. Lett.* **109** 137003
[19] Pop I M, Geerlings K, Catelani G, Schoelkopf R J, Glazman L I and Devoret M H 2014 *Nature* **508** 369–72
[20] Devoret M 1995 Quantum fluctuations in electrical circuits *Quantum Fluctuations* (*Les Houches Session no LXIII*) (Amsterdam: Elsevier) p 351
[21] Burkard G, Koch R H and DiVincenzo D P 2004 *Phys. Rev.* B **69** 064503
[22] Zhu G, Ferguson D G, Manucharyan V E and Koch J 2013 *Phys. Rev.* B **87** 024510
[23] Mooij J, Orlando T, Levitov L, Tian L, Van der Wal C H and Lloyd S 1999 *Science* **285** 1036–9
[24] Koch J, Manucharyan V, Devoret M and Glazman L 2009 *Phys. Rev. Lett.* **103** 217004
[25] Ithier G *et al* 2005 *Phys. Rev.* B **72** 134519
[26] Shnirman A, Makhlin Y and Schön G 2002 *Phys. Scr.* **T102** 147
[27] Yan F *et al* 2016 *Nat. Commun.* **7** 12964
[28] You J, Hu X, Ashhab S and Nori F 2007 *Phys. Rev.* B **75** 140515
[29] Martinis J, Nam S, Aumentado J, Lang K and Urbina C 2003 *Phys. Rev.* B **67** 094510

[30] Clerk A A, Devoret M H, Girvin S M, Marquardt F and Schoelkopf R J 2010 *Rev. Mod. Phys.* **82** 1155
[31] Wangsness R K and Bloch F 1953 *Phys. Rev.* **89** 728
[32] Geva E, Kosloff R and Skinner J 1995 *J. Chem. Phys.* **102** 8541–61
[33] Wellstood F, Urbina C and Clarke J 1987 *Appl. Phys. Lett.* **50** 772
[34] Zorin A B, Ahlers F J, Niemeyer J, Weimann T, Wolf H, Krupenin V A and Lotkhov S V 1996 *Phys. Rev.* B **53** 13682
[35] Harlingen D J V, Robertson T L, Plourde B L, Reichardt P, Crane T and Clarke J 1988 *Phys. Rev.* B **70** 064517
[36] Yoshihara F, Harrabi K, Niskanen A, Nakamura Y and Tsai J 2006 *Phys. Rev. Lett.* **97** 167001
[37] Pourkabirian A, Gustafsson M V, Johansson G, Clarke J and Delsing P 2014 *Phys. Rev. Lett.* **113** 256801
[38] Kumar P, Sendelbach S, Beck M A, Freeland J W, Wang Z, Wang H, Yu C C, Wu R Q, Pappas D P and McDermott R 2016 *Phys. Rev. Appl.* **6** 041001
[39] Hutchings M, Hertzberg J B, Liu Y, Bronn N T, Keefe G A, Chow J M and Plourde B 2017 *Phys. Rev. Appl.* **8** 044003
[40] Makhlin Y and Shnirman A 2004 *Phys. Rev. Lett.* **92** 178301
[41] Vion D, Aassime A, Cottet A, Joyez P, Pothier H, Urbina C, Esteve D, Devoret M H and Urbina C 2002 *Science* **296** 886
[42] Quintana C *et al* 2017 *Phys. Rev. Lett.* **118** 057702
[43] Vool U and Devoret M 2017 *Int. J. Circuit Theory Appl.* **45** 897
[44] Nugroho C, Orlyanchik V and Van Harlingen D 2013 *Appl. Phys. Lett.* **102** 142602
[45] Dutta P and Horn P 1981 *Rev. Mod. Phys.* **53** 497
[46] Weissman M 1988 *Rev. Mod. Phys.* **60** 537
[47] Sendelbach S, Hover D, Kittel A, Mück M, Martinis J M and McDermott R 2008 *Phys. Rev. Lett.* **100** 227006
[48] Rigetti C *et al* 2012 *Phys. Rev.* B **86** 100506
[49] Clerk A and Utami D W 2007 *Phys. Rev.* A **75** 042302
[50] Schoelkopf R, Clerk A, Girvin S, Lehnert K and Devoret M 2003 *Proc. SPIE* **5115**
[51] Sete E A, Gambetta J M and Korotkov A N 2014 *Phys. Rev.* B **89** 104516

Chapter 4

Control and coherence-time enhancement of the $0-\pi$ qubit

4.1 Motivation

In this section, we present the paper titled "Control and coherence-time enhancement of the $0-\pi$ qubit". Controlling a noise-protected device is a hard task since noise protection results in a decoupling of the qubit degrees of freedom from any external noise or control operator. Very early on, we noticed that the original proposal for the $0-\pi$ qubit [66] lacked some important details in the description of the suggested control and readout techniques. For this reason, in this paper, we address these aspects in greater detail.

More precisely, we introduce control and readout strategies for the $0-\pi$ qubit which are of reduced complexity compared to the original proposal. Moreover, this is done using a rigorous and realistic model of the device. This work is also a continuation of the study presented in chapter 3, as we discuss a method to increase the coherence times of the device by actively cooling the ζ mode.

4.2 Main results of the paper

The paper introduces a intuitive interpretation of the $0-\pi$ device in terms of co-tunneling of Cooper pairs. This intuition was in part used in Sect. 1.5.7 to motivate the $0-\pi$ device. Moreover, we formalize the intuitive picture by deriving an effective one-dimensional Hamiltonian for the $0-\pi$ qubit, where the $\cos 2\theta$ structure of the device is made explicit. This is done employing a semi-analytical formalism based on the Born-Oppenheimer approximation, by means of which we can eliminate the 'light' degree of freedom ϕ from the circuit Hamiltonian.

Moreover, we study coupling strategies to perform control and readout operations on the $0-\pi$ qubit. We find that the only viable coupling strategy that preserves the symmetries of the $0-\pi$ qubit Hamiltonian involves the use of small gate capacitances. Coupling elements including superinductances, Josephson junctions, or even the use of mutual inductances, are excluded because of symmetry arguments or poor performance. This finding renders some of the ideas discussed in Ref. [66] impractical.

We explore dispersive readout by capacitive coupling of the $0-\pi$ qubit to a resonator. As pointed out in Sect. 2.0.4, intuition indicates that the dispersive shift associated with the qubit manifold should be negligible. This is indeed the case when we consider the dispersive shift associated with capacitive coupling to the θ degree of freedom, using the full circuit model of the device. However, we notice something counterintuitive: by coupling the $0-\pi$ circuit to an external resonator using n_ϕ (the conjugate charge operator associated with ϕ) instead, we can find qubit parameters and resonator frequencies for which the dispersive shift associated with the qubit transition is several orders of magnitude larger than that associated with θ. This is similar to what is known as straddling regime in the transmon qubit [56]. Importantly, in the $0-\pi$ qubit, the existence of a large dispersive shift can be useful for readout, control, but also to resolve the groundstate doublet and characterize the device.

We also propose an alternative method to perform a single-qubit gate, which we now discuss. Since the qubit manifold consist of two metastable states with exponentially small overlap, performing a nontrivial operation within the qubit subspace requires to make use of the multilevel structure of the device. The natural way to take advantage of the multilevel structure is to drive the system in such a way as to cause a Raman transition between the logical states through virtual excitations of the higher energy states. However, we encounter the difficulty that the amplitude of Raman processes is exponentially small in a moderate-to-deep parameter regime. While this is not the case for the soft regime, in this

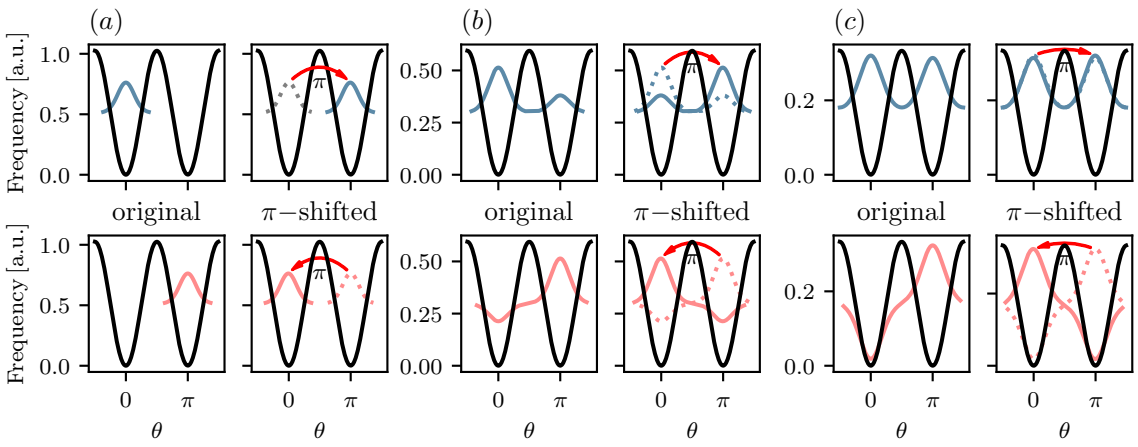

Figure 4.1 Scheme for a single-qubit gate on the $0-\pi$ qubit. Ground (light blue) and first-excited (light red) wavefunctions are displayed on the top- and bottom-left corner of each panel, respectively. To the right of the panels, we show the effect of a π-shift on such wavefunctions, which demonstrates the gate operation. The gate implements a Pauli X operation in (a), a Hadamard in (b), and a Pauli Z in (c). Adapted from [98].

paper we are interested in the applicability of the control strategies in a general context. This forces us to consider strategies where higher energy levels are explicitly rather than only virtually populated during the gate operation.

At first, populating high-energy levels appears to be dangerous, as the noise protection is only guaranteed for the eigenstates in the groundstate manifold. However, if excited states are populated for a very short amount of time, errors arising from the finite coherence time of these states can be largely reduced. We thus propose a way to implement a X, Z or Hadamard gate by exploiting the multilevel structure of the qubit[1]. More precisely, the gate can smoothly interpolate between a logical X and a logical Z as a function of the qubit parameters or the external flux. Our proposal is based on the fact that the states in the groundstate manifold of the $0-\pi$ qubit can be approximately mapped to each other by the displacement transformation $\theta \to \theta + \pi$.

Figure 4.1 shows a schematic of the gate operation within the one-dimensional model for different parameter regimes of the $0-\pi$ qubit. From (a) to (c) the potential bias between the two valleys is reduced, either by applying an external flux or by increasing the tunneling energy in the θ direction with respect to E_L. For the case in (a) corresponding to the standard operation regime of the $0-\pi$ qubit, displacing the logical wavefunctions

[1]We employ the definitions $X = |0\rangle\langle 1| + |1\rangle\langle 0|$, $Z = |1\rangle\langle 1| - |0\rangle\langle 0|$ and $H = (X+Z)/\sqrt{2}$, where H is the Hadamard gate.

leads to a logical X operation. In (b), we show a configuration in which the same displacement leads to a Hadamard operation, while in (c), which corresponds to a vanishing small bias between the wells, $\theta \to \theta + \pi$ leads to a logical Z operation.

As the operation $\theta \to \theta + \pi$ corresponds to the action of the operator $\exp(-i\pi n_\theta)$, we can envision implementing this gate by voltage driving the qubit through the θ degree of freedom. We thus consider a driven $0-\pi$ Hamiltonian of the form

$$H = H_{0-\pi} + 2e\beta\, V_\theta(t)\, n_\theta, \tag{4.1}$$

where $\beta \ll 1$ is a capacitive coupling ratio and V_θ is a microwave voltage drive. We then optimize numerically the parameters that define V_θ, integrating the full master equation of the device that includes all circuit modes and (multilevel) decoherence rates, such that the gate fidelity is maximized. It is remarkable that the intuition presented in Fig. 4.1 still works when all the degrees of freedom of the $0-\pi$ device, including θ, ϕ and the ζ mode are taken into account. For the case of a symmetric $0-\pi$ qubit, we find single-qubit gate fidelities in the order of 99.9% and 99.99% in a broad range of parameters. We moreover consider the effect of circuit element disorder [which also leads to spurious drive terms in Eq. (4.1)] and deviations in $V_\theta(t)$ from its optimal pulse shape. In all cases, we find that the single-qubit gate behaves very robustly against such deviations, leading to minor corrections to the gate fidelity.

Finally, as shown in chapter 3, photon shot noise dephasing due to coupling to the ζ mode is the dominant decoherence mechanism for realistic $0-\pi$ devices. One possible solution to this problem is to reduce the effective temperature of the ζ mode. To this end, we develop a scheme to actively cool the ζ mode, by coupling this mode to a frequency-tunable heavily damped (and high-frequency) resonator. This is inspired by previous work on nanomechanical resonators [104]. By modulating the frequency of the external low-Q mode at the frequency detuning between this mode and the ζ mode, we activate a process that enables ζ-mode photons to be transferred to the external resonator and then lost to the environment at a high rate. The inverse process, where photons are transfered from low-Q mode to the ζ mode is strongly suppressed since the external resonator is lossy and remains close to vacuum at all times.

Figure 4.2 illustrates the improvement on T_φ^{SN} that can be achieved in this way, using realistic parameters for both the $0-\pi$ circuit and the low-Q resonator. Note that we use the same parameters as for Fig. 3.1, but this time we keep the quality factor of the ζ mode constant instead of κ_ζ. This difference does not change the qualitative behavior. The cooling protocol has the most impact as one approaches the deep $0-\pi$ regime (low values of E_L).

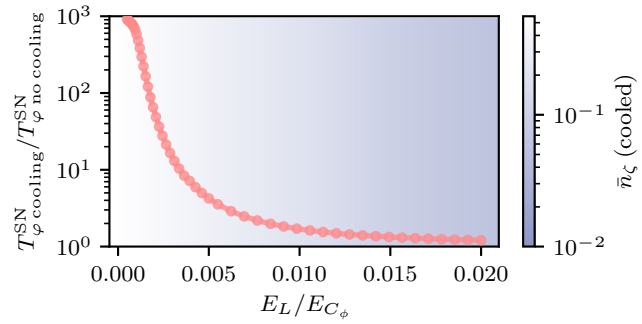

Figure 4.2 Improving the coherence times of the $0-\pi$ qubit by cooling the ζ mode. The device parameters are the same as in Fig. 3.1, although the quality factor of the ζ mode is kept constant, instead of κ_ζ. The density plot (background) corresponds to the steady-state photon number of the ζ mode under the cooling protocol. Light red dots correspond to the ratio between the coherence time due to photon shot noise with and without cooling. Adapted from [98].

Indeed, in this regime, the photon shot noise dephasing rate scales quadratically with the number of thermal photons in the ζ mode [see Eq. (3.1)], and reducing this number can have a large impact. Away from the deep $0-\pi$ regime, the photon shot noise dephasing rate scales only linearly with the number of photons in the ζ mode and, consequently, the improvement is only modest.

4.3 Conclusion and outlook

In this work, we review control and readout strategies for the $0-\pi$ qubit using a complete and rigorous model of the device. We argue that the control ideas introduced in Ref. [66] cannot work in practice. For this reason, we consider alternative approaches to control and readout. We find that dispersive readout by coupling to the ϕ mode is possible in certain parameter regimes. We also propose a single-qubit gate that can attain fidelities as large as 99.99%, and can be implemented simply by a voltage drive through θ. Furthermore, we develop a cooling scheme to enhance the device coherence times, in cases in which the latter is dominated by spurious coupling to the ζ mode. We estimate that the cooling protocol can improve the device coherence times by three orders of magnitude.

Some open questions remain about how to best use the ingredients presented in this paper to realize a universal set of gates for the $0-\pi$ qubit that can work including all circuit details. In particular, we believe that optimal-control techniques are among the best options to achieve universal control on $0-\pi$ devices in the near term [41].

New Journal of Physics
The open access journal at the forefront of physics

Deutsche Physikalische Gesellschaft DPG
IOP Institute of Physics

Published in partnership with: Deutsche Physikalische Gesellschaft and the Institute of Physics

OPEN ACCESS

RECEIVED
3 December 2018

REVISED
11 February 2019

ACCEPTED FOR PUBLICATION
22 February 2019

PUBLISHED
4 April 2019

PAPER

Control and coherence time enhancement of the 0–π qubit

Agustin Di Paolo[1], **Arne L Grimsmo**[1,2], **Peter Groszkowski**[3,5], **Jens Koch**[3] and **Alexandre Blais**[1,4]

[1] Institut quantique and Département de Physique, Université de Sherbrooke, Sherbrooke, QC, Canada
[2] Centre for Engineered Quantum Systems, School of Physics, The University of Sydney, Sydney, NSW, Australia
[3] Department of Physics and Astronomy, Northwestern University, Evanston, IL 60208, United States of America
[4] Canadian Institute for Advanced Research, Toronto, ON, Canada
[5] Present Address: Institute for Molecular Engineering, University of Chicago, Chicago, Illinois 60637, United States of America.

E-mail: Agustin.Di.Paolo@USherbrooke.ca

Keywords: superconducting qubits, quantum information, superinductances

Abstract

Kitaev's 0–π qubit encodes quantum information in two protected, near-degenerate states of a superconducting quantum circuit. In a recent work, we have shown that the coherence times of a realistic 0–π device can surpass that of today's best superconducting qubits (Groszkowski *et al* 2018 *New J. Phys.* **20** 043053). Here we address controllability of the 0–π qubit. Specifically, we investigate the potential for dispersive control and readout, and introduce a new, fast and high-fidelity single-qubit gate that can interpolate smoothly between logical X and Z. We characterize the action of this gate using a multi-level treatment of the device, and analyze the impact of circuit-element disorder and deviations in control and circuit parameters from their optimal values. Furthermore, we propose a cooling scheme to decrease the photon shot-noise dephasing rate, which we previously found to limit the coherence times of 0–π devices within reach of current experiments. Using this approach, we predict coherence time enhancements between one and three orders of magnitude, depending on parameter regime.

1. Introduction

Fault-tolerant quantum computation is likely to require daunting hardware resources [1, 2]. This fact motivates the search for strategies to reduce the qubit overhead needed for quantum error correction, and drives the development of new quantum error correcting codes [3–7]. Furthermore, the reduction of gate errors for physical qubits offers a direct and impactful way of reducing qubit overhead [2, 8]. The latter can be achieved both through longer qubit coherence times and better quantum control for gates.

For superconducting circuits, coherence time improvements by as much as five orders of magnitude have been demonstrated [9, 10]. This has been possible thanks to advances in several areas, including materials [11], microwave engineering [12], shielding [13, 14], and the use of 3D architectures [15–17]. Crucially, order-of-magnitude leaps in coherence have also been the result of new qubit designs, such as the transmon and the fluxonium qubits [18, 19].

In this paper, we consider the superconducting circuit introduced in [20], commonly referred to as the 0–π qubit, and closely related to Kitaev's current mirror proposal [21]. With a set of non-overlapping logical wave functions and very low flux and charge dispersion, the 0–π qubit displays exponential suppression of relaxation and dephasing. It has been shown that the 0–π qubit can be used to encode quantum information in a protected subspace [20–23], but in a regime of parameters that is challenging to realize with current superconducting quantum circuits. In fact, the fully protected regime of this device exploits a degree of freedom with large quantum fluctuations, something which requires an effective impedance surpassing the quantum of resistance by orders of magnitude. Achieving this regime requires the use of superinductors, which are circuit elements with inductance greater than ~100 nH and with very little stray or ground capacitances [19, 24–26]. We have recently shown that for circuit parameters attainable with *current* superconducting technology, the 0–π qubit dephasing time is limited by photon shot noise arising from a parasitic circuit mode (which we referred to as the

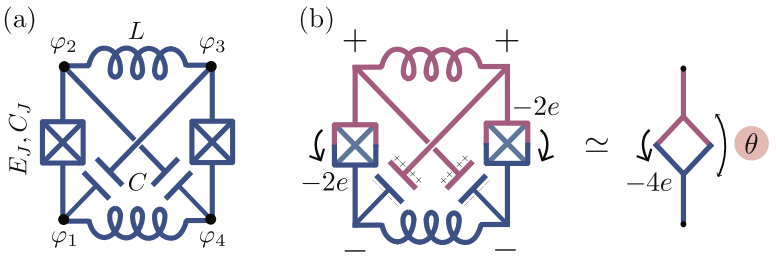

Figure 1. The 0–π qubit in a nutshell. (a) Circuit diagram for the symmetric 0–π qubit, with pairwise identical circuit elements. (b) Pictorial illustration of co-tunneling of pairs of Cooper pairs across the two junctions, explaining the approximate π-periodic potential energy, and an equivalent circuit-element with only a single degree of freedom θ.

ζ-mode) [22]. Nevertheless, we found that the 0–π qubit still has the potential to outperform state-of-the-art superconducting devices. Below, we propose a method to further enhance the coherence time by orders of magnitude by cooling the ζ-mode.

However, as can be expected, the price of intrinsic noise protection in the 0–π qubit is that it is difficult to perform logical operations on this device. In particular, protection from noise comes in part from the exponentially small overlap of its logical wave functions. As a result, matrix elements of local operators between the two logical states will also be small, thus resulting in extremely slow gates. In [20], Brooks *et al* proposed a universal set of protected logical operations based on coupling to an ultra-high impedance LC oscillator. However, these operations were based on an idealized model of the qubit and with parameters that are difficult to realize in practice. Further work is required to determine the potential of this approach in a more realistic setting.

Motivated by the prospect of realizing 0–π qubits in the near term, we investigate alternative approaches to measurement and control with lower experimental complexity. The operations we propose are not protected in the same sense as those proposed in [20], because they rely either on operating the device in a regime where the qubit is not fully isolated from the environment, or they make use of excited states outside the qubit manifold. In particular, we develop a single-qubit gate based on a multi-level excursion through higher energy levels. Nevertheless, we hope that these schemes will be useful for both characterization and control of 0–π qubits in near-to-medium-term experiments.

This work is organized as follows. In section 2, we introduce the 0–π qubit and provide a simplified effective model for the 0–π circuit with only a single degree of freedom. In section 3, we discuss general coupling strategies for qubit control and readout, and derive the 0–π circuit Hamiltonian accounting for stray and parasitic capacitances, disorder in circuit-element parameters, as well as coupling to microwave voltage sources and a readout resonator. In section 4, we analyze dispersive coupling to a resonator, and find that there are regimes of dispersive shift akin to the straddling regime of the transmon qubit [18]. In section 5, we introduce a single-qubit gate that achieves population inversion of the 0–π qubit and can interpolate between logical X and Z by varying the qubit operation point. Furthermore, we characterize the gate operation as a function of circuit design parameters and analyze its robustness. In section 6, we propose a method to fight the main qubit dephasing mechanism, analyze its performance as a function of circuit parameters, and discuss its implementation. We conclude in section 7.

2. The 0–π qubit in a nutshell

In this section we introduce the 0–π qubit in the ideal case of no circuit-element disorder and briefly discuss its properties. In particular, we give an intuitive picture in terms of co-tunneling of Cooper pairs leading to an approximately π-periodic qubit potential, which is further verified by an effective model accurately describing the low-energy physics of the system.

2.1. The circuit Hamiltonian

We first consider the symmetric 0–π circuit, as illustrated in figure 1(a), consisting of two Josephson junctions with energy E_J, capacitance C_J and plasma frequency $\omega_p = \sqrt{8E_J E_{C_J}}/\hbar$, two superinductors with inductance L, and two large capacitors with capacitance C. The normal modes of this circuit are

$$2\phi = (\varphi_2 - \varphi_3) + (\varphi_4 - \varphi_1),\ 2\theta = (\varphi_2 - \varphi_1) - (\varphi_4 - \varphi_3),$$
$$2\zeta = (\varphi_2 - \varphi_3) - (\varphi_4 - \varphi_1),\ 2\Sigma = \varphi_1 + \varphi_2 + \varphi_3 + \varphi_4, \quad (1)$$

where φ_i is the superconducting phase operator at node i of the circuit. Using these definitions, the symmetric 0–π qubit Hamiltonian reads [23]

$$H_{0-\pi}^{\text{ideal}} = \frac{q_\phi^2}{2C_\phi} + \frac{q_\theta^2}{2C_\theta} - 2E_\text{J}\cos\theta\cos(\phi - \varphi_\text{ext}/2) + E_L\phi^2, \quad (2)$$

where $q_\phi = 2en_\phi$ and $q_\theta = 2en_\theta$ are the conjugate charge operators associated with ϕ and θ (i.e. $[\phi, n_\phi] = i$ and $[n_\theta, e^{i\theta}] = e^{i\theta}$) respectively, and $\varphi_\text{ext} = \Phi_\text{ext}/\varphi_0$ is the external magnetic flux in units of the reduced flux quantum $\varphi_0 = \hbar/2e$. Moreover, we have introduced capacitances for the two qubit modes ϕ and θ given by $C_\phi = 2C_\text{J}$ and $C_\theta = 2(C + C_\text{J})$, respectively, and the inductive energy $E_L = \varphi_0^2/L$.

In the 0–π qubit, quantum information is stored in the $\{\phi, \theta\}$ degrees of freedom, while ζ is a spurious low-frequency harmonic mode and Σ is a cyclic coordinate. In absence of circuit-element disorder, the ζ and Σ modes do not couple to ϕ and θ, and are therefore excluded from equation (2).

Introducing the effective impedances $Z_\phi = \sqrt{(L/2)/C_\phi}$ and $Z_\theta = \sqrt{(L_\text{J}/2)/C_\theta}$, where $L_\text{J} = \varphi_0^2/E_\text{J}$, the 0–$\pi$ regime is defined by

$$Z_\theta \ll R_Q \ll Z_\phi, \quad (3)$$

where $R_Q = h/(2e)^2 \simeq 6.5\ \text{k}\Omega$ is the superconducting quantum of resistance. We say that a device is in the 'moderate,' or 'deep' 0–π regime, depending on the degree to which the impedance relations are satisfied. The problem of fabricating a qubit in the deep 0–π regime, includes that of realizing a high-impedance superinductor [27–29].

2.2. Exciton tunneling picture

Figure 1(b) shows an approximate equivalence between the 0–π circuit (to the left) and a circuit-element describing tunneling of pairs of Cooper pairs (to the right). The co-tunneling of Cooper pairs or 'exciton' in the 0–π circuit can be understood as a consequence of a circuit layout combining branches of superinductors (high impedance) and large capacitances (low impedance). Here, we schematically illustrate how tunneling of a Cooper-pair across the left junction of the 0–π circuit is 'mirrored' by the simultaneous tunneling of a Cooper-pair across the right junction: a Cooper-pair tunneling event across the left junction leads to a build up of $-2e$ negative charge on one side of one of the large capacitors, which must be compensated for by a positive charge on the other side. This can happen through a simultaneous $-2e$ Cooper-pair tunneling event across the right junction in the same direction. The co-tunneling of Cooper pairs through the left and right junctions form together an effective exciton tunneling event [21].

Note that no current flows through the superinductors in the limit of $L \to \infty$ ($Z_\phi/R_Q \to \infty$). Superinductors are, however, crucial in defining the non-trivial topology of the circuit, as in their presence we can identify two distinct circuit islands shown as blue (bottom) and pink (top) in figure 1(b). Due to the simultaneous co-tunneling of Cooper pairs across the two junctions, we expect the potential energy to be π-periodic rather than 2π-periodic in the superconducting phase difference across the two islands, in the limit $L \to \infty$. This expectation can be verified by an effective model for the θ degree of freedom alone, derived in appendix B following a Born–Oppenheimer approach and resulting in the effective Hamiltonian

$$H_{0-\pi}^{\text{eff}} = 4E_{C_\theta}(n_\theta - n_g^\theta)^2 - E_2(\varphi_\text{ext})\cos 2\theta - E_1(\varphi_\text{ext})\cos\theta, \quad (4)$$

where $E_{C_\theta} = e^2/2C_\theta$ and n_g^θ are, respectively, the charging energy and the offset charge corresponding to the θ coordinate. The flux-dependence of the potential energy is given by the coefficients $E_2(\varphi_\text{ext}) = E_\alpha - E_\beta\cos(\varphi_\text{ext})$ and $E_1(\varphi_\text{ext}) = E_\gamma\cos(\varphi_\text{ext}/2)$, where E_α, E_β and E_γ are constants dependent on the qubit design parameters and studied below.

In the moderate-to-deep 0–π regime, the relations $E_\alpha \gg E_{C_\theta}$ and $E_\alpha \gg E_\beta$, E_γ are satisfied. The effective one-dimensional potential in equation (4) is shown in figure 2(a) for a set of 0–π circuit parameters. As a function of flux, the two nearly degenerate minima are detuned one with respect to the other, except at $\varphi_\text{ext} = \pi$, where the potential becomes perfectly π-periodic. With $E_2 \gg E_{C_\theta}$, tunneling between the two wells is highly suppressed. In the presence of a small, positive E_1 ($-\pi < \varphi_\text{ext} < \pi$), the lowest-energy state is localized in $\theta = 0$ and a nearly degenerate first excited state is localized in $\theta = \pi$. At $\varphi_\text{ext} = \pi$, the two minima at $\theta = 0$ and $\theta = \pi$ are exactly degenerate and the logical wave functions become hybridized independently of the circuit design parameters. For E_1 smaller than or comparable to the tunneling rate between the potential wells, hybridization can also occur at $\varphi_\text{ext} \neq 0$.

Figure 2(b) shows the values of $\{E_\alpha, E_\beta, E_\gamma\}$ obtained from a numerical calculation of the coefficients in equation (4) as a function of Z_ϕ/R_Q for fixed Z_θ (see appendix B for details). We observe an exponential suppression of the $\cos\theta$ potential term relative to the $\cos 2\theta$ term, justifying the π-periodicity suggested by the

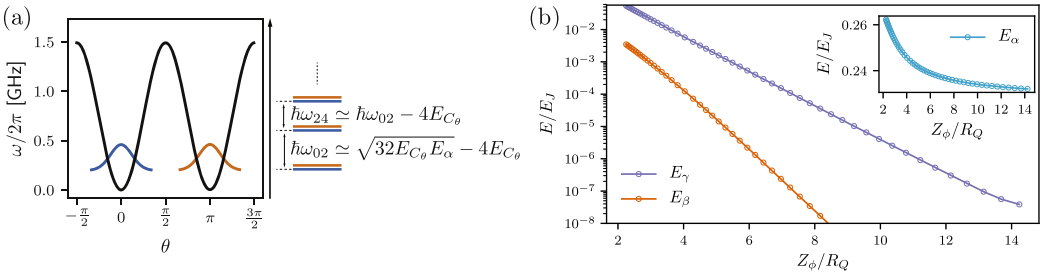

Figure 2. (a) Effective one-dimensional potential (black) and wave functions for the two lowest lying energy states (color), extracted using a Born–Oppenheimer approach (see appendix B). To the right of the effective potential we show a schematic of the energy diagram (not to scale). In the moderate-to-deep 0–π regime, the low-energy spectrum consists of nearly degenerate doublets in a weakly anharmonic ladder, closely resembling a transmon qubit spectrum with each transmon level replaced by a doublet. The two lowest doublets are split by approximately $\sqrt{32E_{C_\theta}E_\alpha}$, corresponding to the plasma frequency of the π-periodic Josephson element. (b) Energy parameters of the one-dimensional Hamiltonian equation (4) as a function of Z_ϕ for fixed Z_θ. We observe an exponential suppression of both E_β and E_γ, indicating that the qubit becomes a flux-insensitive π-periodic Josephson element in the deep 0–π regime. E_α remains almost unchanged in comparison. Circuit parameters: $E_L/\hbar\omega_p \in [1.25 \times 10^{-4}, 5 \times 10^{-3}]$ and $(E_{C_\phi}/\hbar\omega_p, E_{C_\theta}/\hbar\omega_p, E_J/\hbar\omega_p) = (0.25, 0.5 \times 10^{-3}, 0.25)$.

intuitive picture of co-tunneling of Cooper pairs. We note that the effective Hamiltonian equation (4) in the limit $E_1 = 0$ resembles that of a transmon qubit, with the crucial distinction that the two minima at $\theta = 0$ and $\theta = \pi$ are physically distinct. We also note, as shown in the inset in figure 2(b), that $E_2 \simeq E_\alpha \sim E_J$. The condition $E_2 \gg E_{C_\theta}$ thus translates to $E_J \gg E_{C_\theta}$, or equivalently $Z_\theta \ll R_Q$.

Based on this simple picture, the 0–π qubit approximately reduces to a device with one effective degree of freedom, θ, whose conjugate charge operator, n_θ, determines the Cooper-pair number difference between the two circuit islands identified in figure 1(b). Since n_θ changes in units of two, Cooper-pair parity is a conserved quantity and an approximate symmetry of the circuit Hamiltonian. We emphasize that the symmetry is approximate, since for finite Z_ϕ, the $\cos\theta$ term in equation (4) breaks the symmetry.

2.3. Qualitative explanation of robustness to noise

Cooper-pair parity conservation partitions the qubit spectrum into doublets with exponentially small charge sensitivity in the 'transmon limit' $E_J \gg E_{C_\theta}$ [18, 30]. The π-periodicity of the Hamiltonian moreover allows us to draw several qualitative conclusions about the qubit's generic properties. Formally, we define a symmetry operator $U = \exp(-in_\theta\pi)$ which displaces θ by π, and note that

$$UH^{\text{ideal}}_{0-\pi}U^\dagger = H^{\text{ideal}}_{0-\pi} + ..., \tag{5}$$

where the ellipses refer to exponentially small corrections in the deep 0–π regime, as we have verified above. Denoting the ground state of the Hamiltonian by $|0\rangle$ with energy E_0, it follows that a second eigenstate with energy exponentially close to E_0 is given approximately by $U|0\rangle$. This follows from $H^{\text{ideal}}_{0-\pi}(U|0\rangle) = (UH^{\text{ideal}}_{0-\pi}U^\dagger)(U|0\rangle) + ... = E_0(U|0\rangle) + ...$ We can denote this eigenstate by $|1\rangle$. Moreover, the argument continues to hold in the presence of any perturbation to the Hamiltonian that respects the (approximate) symmetry equation (5), i.e.

$$\langle 0|V|0\rangle = \langle 1|V|1\rangle + ..., \tag{6}$$

where V satisfies $UVU^\dagger = V + ...$ It follows that dephasing noise is expected to be exponentially suppressed for *symmetry-preserving* noise processes. In particular, equation (4) shows that external flux noise does not break the π-periodicity [recall that $E_1(\varphi_{\text{ext}})$ is exponentially suppressed in the deep 0–π regime].

The condition $E_J \gg E_{C_\theta}$ (or equivalently $Z_\theta \ll R_Q$) moreover leads to exponential suppression of tunneling between the two potential wells located at $\theta = 0$ and $\theta = \pi$, as already discussed. When the two nearly degenerate ground states are localized in the two different wells, this thus leads to an exponential suppression of bit-flips[6]

$$\langle 0|V|1\rangle = 0 + ..., \tag{7}$$

for V any weak perturbation to the Hamiltonian that is local in phase space, i.e. any low-degree polynomials in $\{\phi, \theta, q_\phi, q_\theta\}$. Equations (6), (7) lead together to the remarkably long coherence times expected for the qubit in the deep 0–π regime, as recently confirmed quantitatively in [22].

[6] Depending on the circuit parameters and external flux, the two ground states can be localized in the two different wells, or in some cases symmetric and anti-symmetric superpositions of such localized states [23]. In the latter case, the Z and X basis are exchanged.

3. Coupling to external circuitry

3.1. General remarks about coupling strategies

With the goal of controlling and measuring the 0–π qubit, we now outline different strategies to couple the qubit to external degrees of freedom. Noise protection in the 0–π qubit is achieved at a high price: the protection from bit-flips implies negligible matrix elements for qubit transitions making many coupling schemes inefficient. Moreover, great care has to be taken to not introduce coupling circuitry explicitly breaking the π-periodicity, opening the qubit to dephasing noise. Some general remarks about coupling strategies can be made based on the qualitative discussion of the 0–π qubit in the previous section.

3.1.1. Direct inductive coupling

Any galvanic linear inductive coupling to the four circuit nodes leads to contributions of the generic form $\sim E_{L,\theta}\theta^2$ to the Hamiltonian, explicitly breaking the 0–π periodicity and lifting the groundspace degeneracy. It might be possible to approximately restore the 0–π periodicity by using superinductors such that $E_{L,\theta} \to 0$. However, this in turn leads to negligible coupling to any external circuitry, rendering such an approach ineffective.

3.1.2. Mutual inductive coupling

As mentioned above, in the limit $L \to \infty$, moderate variations of the external flux through the qubit loop do not break the 0–π symmetry, such that mutual inductive coupling can potentially be a symmetry-preserving coupling mechanism. However, for precisely the same reason that the qubit is highly insensitive to flux noise [22], control and readout strategies based on mutual inductive coupling are ineffective. Large external flux excursions, in contrast, can be used to move between regimes where the logical states are localized in different potential wells, to a regime where they are in a superposition of both wells. We discuss exploiting this in a control strategy in section 5.

3.1.3. Capacitive coupling

Capacitive coupling to the circuit nodes has the advantage that it only couples directly to the charge degrees of freedom, leaving the 0–π periodicity and the two-island topology in figure 1(b) intact. Moreover, as long as the coupling capacitances are kept small, they should not compromise the inequality equation (3). In general, the extremely small matrix elements coupling the logical qubit states make many conventional control and readout strategies inefficient. Nevertheless, we show below that capacitive coupling can be used to perform device spectroscopy in a moderate-to-deep regime of parameters, enable single-qubit control by means of fast voltage drives, and cool the parasitic ζ-mode to improve the qubit coherence times.

3.1.4. Nonlinear symmetry-preserving inductive coupling

Although we have argued that any straightforward coupling strategy based on inductive elements is either ineffective or breaks the qubit's protection from noise, it might still be possible to engineer *nonlinear* inductive couplers that respects the 0–π symmetry. This means that the inductive contribution to the energy has to satisfy $E_{\text{coupler}}(\theta) = E_{\text{coupler}}(\theta + \pi) + ...$, where the ellipses again refer to terms that vanish in the deep 0–π regime. In [20], it was proposed that such a coupling mechanism can be achieved by using a tunable Josephson coupler (SQUID loop) connecting the 0–π qubit to an LC oscillator. For the qubit to remain protected, the LC oscillator with impedance Z_r is required to satisfy $Z_r \gg R_Q$, much like the internal ϕ mode of the 0–π circuit. Moreover, it was shown that such a coupling could be used to enact one- and two-qubit phase gates. We briefly return to this scheme below, and point out some additional challenges which have previously been overlooked.

3.2. Addressing the 0–π qubit degree of freedom

Coupling to the qubit mode θ in the 0–π circuit has an additional challenge, beyond the general points already made above. Because the coordinate θ is a combination of phase operators of all nodes of the circuit [see equation (1)], addressing only this coordinate requires a coupling element acting symmetrically on both ports of each superinductor. As illustrated schematically in figure 3(a), where the boxes represent unspecified coupling elements and could be capacitive or inductive in general, this coupling circuitry necessarily shunts the 0–π qubit superinductors. According to the discussion in section 2.2, if the impedance of the coupler is not greater than or comparable to that of the qubit superinductors, this effect can potentially compromise regime of operation of the device. At first glance, a possible solution to this problem appears to be the use of additional superinductors replacing each of the box-shaped couplers in figure 3(a). However, this would lead to an inductive shunt of the 0–π circuit islands identified in figure 1(b) through the readout or control circuit [represented by a meter in figure 3(a)], breaking the Cooper-pair parity symmetry.

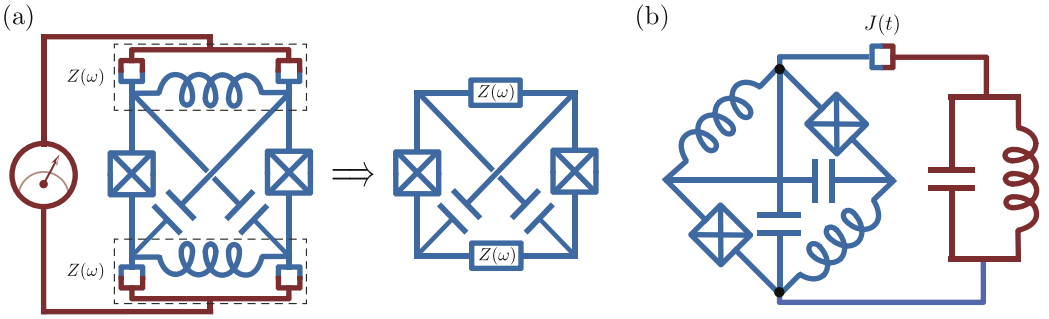

Figure 3. (a) Addressing the qubit main degree of freedom θ. The small box-shaped couplers are used to represent arbitrary coupling circuit elements, and the meter represents a readout or control circuit. As illustrated by a dashed frame, the required coupling circuitry (in red) necessarily shunts the device superinductors, leading to a combined link impedance $Z(\omega)$ that can compromise the qubit operation. (b) Coupling layout originally considered in [20]. The interaction strength $J(t)$ stands for the potential energy of a flux-tunable device.

An alternative coupling scheme considered in [20] is illustrated in figure 3(b). In this scheme, the coupling element (i.e. the box in the figure) is a SQUID loop giving a tunable Josephson element between the 0–π circuit and the LC oscillator. This coupling layout overcomes the difficulty described at the beginning of this section by relaxing the symmetry requirements of the coupling circuitry. However, this leads to an interaction Hamiltonian that involves both θ and the spurious ζ-mode

$$U_J = -J(t)\cos(\theta + \zeta - \phi_r), \tag{8}$$

where $J(t)$ is the tunable Josephson-energy of the coupling element, and ϕ_r the resonator phase operator. We have previously shown that the ζ-mode frequency goes to zero in the deep 0–π regime leading to diverging thermal occupation of this mode [22], something which was not taken into account in [20]. The impact of thermal fluctuations due to the 0–π circuit internal modes thus requires further study and we propose in section 6 a cooling scheme that can help approximate the ideal behavior considered in [20].

Based on this discussion, the most viable option for near-term experiments appears to be the use of capacitive coupling. This means replacing the box-shaped couplers in figure 3(a) by capacitors. Formally, small coupling capacitors operate as high-impedance links while preserving the circuit islands. The coupling capacitances must be kept small to ensure $Z_\phi/R_Q \gg 1$ since these add to C_ϕ [see equation (A.1)]. Therefore, a downside of this approach resides in the fact that the capacitive couplings cannot be very large. Nevertheless, we find that capacitive coupling allows for significant dispersive shifts (section 4), and a fast, single-qubit gate (section 5).

We emphasize that the control strategies we consider in the following are not fault-tolerant in the sense of [20, 21]. They either rely on operating the qubit in a regime that is not fully protected, or involve populating higher and less robust excited states. Nevertheless, these operations can be performed with high-fidelity and are thus suitable for implementation in realistic devices in the near future.

3.3. Capacitive coupling to voltage sources

We now consider the 0–π circuit in the presence of voltage sources V_i connected to the nodes $i = 1, \ldots, 4$ of the circuit, as shown in figure 4(a). Since we have found that circuit-element disorder is a limiting factor for the qubit coherence for parameters within reach of current experiments [22], we include such effects here. In particular, we account for any superinductance and Josephson-energy asymmetries, denoted by $\mathrm{d}E_L$ and $\mathrm{d}E_\mathrm{J}$, respectively, as well as capacitance asymmetries, denoted by $\mathrm{d}C_\mathrm{J}$ and $\mathrm{d}C$. Additionally, there can be disorder in the gate capacitances ($\mathrm{d}C_{g_i}$), as well as in the parasitic capacitances to ground ($\mathrm{d}C_{0_i}$), such that the node gate and ground capacitances for node i are $C_{g_i} = C_g(1 + \mathrm{d}C_{g_i})$ and $C_{0_i} = C_0(1 + \mathrm{d}C_{0_i})$, respectively. We note that, in practice, the stray capacitances may arise from the superinductances and the large capacitors of the 0–π circuit [28]. Following the standard approach to circuit quantization [31, 32] we find the Hamiltonian

$$H = H_{0-\pi} + H_\mathrm{drive}^\mathrm{symm} + H_\mathrm{drive}^\mathrm{asymm}, \tag{9}$$

where $H_{0-\pi} = H_{0-\pi}^\mathrm{symm} + H_{0-\pi}^\mathrm{asymm}$ describes the un-driven qubit. The first contribution

$$H_{0-\pi}^\mathrm{symm} = \sum_\mu \frac{q_\mu^2}{2C_\mu} - 2E_\mathrm{J}\cos\theta\cos(\phi - \varphi_\mathrm{ext}/2) + E_L(\phi^2 + \zeta^2), \tag{10}$$

with $q_\mu/2e = -\mathrm{i}\partial_\mu$ for $\mu = (\phi, \theta, \zeta, \Sigma)$ is the ideal 0–π Hamiltonian, where we now explicitly include the ζ and Σ degrees of freedom and the mode capacitances C_μ defined explicitly in appendix A. On the other hand,

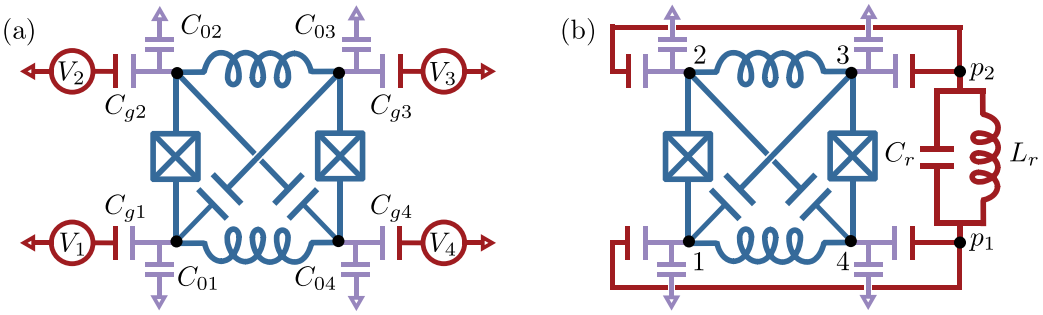

Figure 4. (a) Lumped-element model for the 0–π circuit coupled to microwave voltage sources, including gate and ground capacitances for each circuit node. (b) 0–π circuit connected to a resonator with nodes p_1 and p_2. The shown coupling layout couples the resonator charge operator to q_θ, and corresponds to the second row in table 1.

Table 1. Capacitively coupling the 0–π qubit to an external resonator. The second and third columns specify which 0–π nodes are connected to the resonator nodes p_1 and p_2, respectively, thus determining the replacement rule for V_μ in equation (9), as indicated in the fourth column ($\delta_{\mu,\nu}$ is here the Kronecker delta). The resonator voltage is given by $V_r = q_r/C_r = \mathrm{i}V_{\mathrm{rms}}(a_r^\dagger - a_r)/2$, where V_{rms} is the resonator root-mean-squared voltage fluctuations in the ground state, and a_r the resonator annihilation operator.

0–π mode	0–π nodes connected to p_1	0–π nodes connected to p_2	Replacement rule in equation (9)
ϕ	1, 3	2, 4	$V_\mu \to \delta_{\mu,\phi}\, V_r$
θ	1, 4	2, 3	$V_\mu \to \delta_{\mu,\theta}\, V_r$
ζ	3, 4	1, 2	$V_\mu \to \delta_{\mu,\zeta}\, V_r$

$$H_{0-\pi}^{\mathrm{asymm}} = -\frac{C\,\mathrm{d}C}{C_\zeta C_\theta} q_\theta q_\zeta - \frac{C_\mathrm{J}\,\mathrm{d}C_\mathrm{J}}{C_\phi C_\theta} q_\phi q_\theta + E_\mathrm{J}\,\mathrm{d}E_\mathrm{J} \sin\theta \sin(\phi - \varphi_{\mathrm{ext}}/2) + E_L\,\mathrm{d}E_L\,\phi\zeta + H_{\mathrm{d}C_g,\mathrm{d}C_0}, \tag{11}$$

describe unwanted spurious couplings between the circuit modes to leading order in circuit-element disorder. The last term $H_{\mathrm{d}C_g,\mathrm{d}C_0}$ is a purely capacitive term accounting for disorder of the gate and ground capacitances, and its full expression can be found in appendix A. Since these capacitances are expected to be much smaller than the internal circuit capacitances C, we however neglect $H_{\mathrm{d}C_g,\mathrm{d}C_0}$ in the remainder of this work. Finally, the drive term

$$H_{\mathrm{drive}}^{\mathrm{symm}} = \sum_\mu \frac{C_g}{C_\mu} V_\mu q_\mu, \tag{12}$$

describe voltage drives of the four normal modes where V_μ is defined in terms of the node voltages V_i with $i = 1, \ldots, 4$ according to the transformation rule in equation (1). Circuit-element disorder furthermore introduces additional drive terms. This is accounted for by the Hamiltonian $H_{\mathrm{drive}}^{\mathrm{asymm}}$, given explicitly in appendix A.

As can be seen from equation (11) the coupling between the qubit degrees of freedom $\{\phi, \theta\}$ and the spurious ζ-mode appears when the large circuit capacitors or the superinductors are not symmetrical: $\mathrm{d}C \neq 0$ or $\mathrm{d}E_L \neq 0$, respectively. As we have shown recently [22], this leads to the limiting contribution to the qubit's coherence time for realistic parameters due to photon shot noise for the ζ-mode. We return to how to alleviate this issue in section 6.

3.4. Capacitive coupling the 0–π qubit to a microwave resonator

With the goal of controlling and reading out the 0–π qubit, we consider its capacitive coupling to a microwave resonator as illustrated in figure 4(b). The Hamiltonian of the combined qubit-resonator system can be obtained from equation (9), by adding the free resonator Hamiltonian, $H_r = \hbar\omega_r a_r^\dagger a_r$, and letting V_μ correspond to the resonator voltage[7]. Table 1 specifies the replacement rules for the voltages V_μ in equation (9) that produce the qubit-resonator interaction Hamiltonian. Three possible coupling layouts addressing the 0–

[7] Although applicable in most circuit QED setups, a cautionary remark is that this procedure is only valid in the weak capacitive coupling regime, where the capacitances of coupled qubit and resonator modes are large compared to the coupling capacitance.

π degrees of freedom θ [shown in figure 4(b)], ϕ and ζ are considered. These capacitive coupling schemes are employed in section 4 for dispersive readout strategies, in section 5 to drive qubit transitions via multiple excited levels, and in section 6 to cool the low-frequency ζ-mode as a strategy to enhance the qubit coherence times.

4. Dispersive readout

The transmon-like structure of the 0–π energy spectrum illustrated in figure 1(d) suggests that we might exploit known techniques for dispersive readout and control for transmon qubits [18]. The strong symmetry between the two potential wells at $\theta = 0$ and $\theta = \pi$, however, means that each 'transmon level' is split into a doublet, leading to important differences in dispersive coupling for a 0–π qubit as compared to a conventional transmon.

Dispersive coupling to a resonator relies on having unequal qubit-dependent dispersive shifts of the resonator frequency for the two logical states $|0\rangle$ and $|1\rangle$. We compute the dispersive shifts numerically, assuming capacitive coupling between either of the two 0–π modes $\{\theta, \phi\}$ and a readout resonator of frequency $\omega_r/2\pi$ (see table 1). Denoting by a_r the annihilation operator of the readout resonator and including M qubit levels, the qubit-resonator Hamiltonian can be written as

$$H = \sum_{i=0}^{M} \hbar\omega_i \sigma_{ii} + \hbar\omega_r a_r^\dagger a_r + \sum_{i,j=0}^{M} g_{ij}^\mu \sigma_{ij}(a_r^\dagger + a_r), \tag{13}$$

where $\sigma_{ij} = |i\rangle\langle j|$, $g_{ij}^\mu = \frac{C_g}{C_\mu}(eV_{\mathrm{rms}})\langle i|n_\mu|j\rangle$ and $\mu = \{\theta, \phi\}$. Note that the resonator drive has not been explicitly included in equation (13). In the dispersive regime defined by $|\Delta_{ij}| \gg |g_{ij}|\sqrt{\bar{n}+1}$, where $\Delta_{ij} = (\omega_i - \omega_j) - \omega_r$ and $\bar{n}$ is the mean number of photons in the resonator, the above Hamiltonian takes the form [33]

$$H = \sum_{i}^{M} \hbar(\omega_i + \Lambda_i^\mu)\sigma_{ii} + \hbar\omega_r a_r^\dagger a_r + \sum_{i}^{M} \hbar\chi_i^\mu \sigma_{ii} a_r^\dagger a_r \simeq \frac{\hbar\tilde{\omega}_q}{2}\sigma_z + \hbar\tilde{\omega}_r a_r^\dagger a_r + \hbar\chi^\mu \sigma_z a_r^\dagger a_r, \tag{14}$$

where the dispersive shift of the ith qubit level is given by $\chi_i^\mu = \sum_j^M(\chi_{ij}^\mu - \chi_{ji}^\mu)$, with $\chi_{ij}^\mu = |g_{ij}^\mu|^2/\Delta_{ij}$, and $\Lambda_i^\mu = \sum_j^M \chi_{ij}^\mu$ is the corresponding Lamb-shift. The second line in equation (14) is a two-level truncation where we have defined $\sigma_z = |1\rangle\langle 1| - |0\rangle\langle 0|$, $\tilde{\omega}_q = \omega_1 + \Lambda_1^\mu - \omega_0 - \Lambda_0^\mu$, $\tilde{\omega}_r = \omega_r + \chi_0^\mu/2 + \chi_1^\mu/2$ and $\chi^\mu = (\chi_1^\mu - \chi_0^\mu)/2$.

We investigate the dispersive coupling χ^μ as a function of the 0–π design parameters. We choose the resonator frequency such that χ^μ is maximized while ensuring the validity of the dispersive approximation. For the case of coupling to θ, we observe that χ^θ is heavily attenuated in the parameter space corresponding to a moderate-to-deep 0–π qubit regime. This is due to the fact that, in contrast to a transmon qubit, the strong symmetry between the left and right potential wells of the 0–π qubit leads to vanishing dispersive coupling to the resonator for most parameters. Moreover, since the external flux does not break this symmetry [see equation (4)], χ^θ can only slightly change by flux excursions.

Quite surprisingly, however, we find a significant dispersive shift for the coupling operator n_ϕ, as shown in figure 5. This behavior is qualitatively reminiscent to what is known as the straddling regime for the transmon qubit, in which the dispersive shift can increase by orders of magnitude [18]. Note, however, that the narrow straddling-like regime indicated in figure 5 is related to the splitting of doublets rather than the plasma-frequency separation between two sets of doublets, and the large number of qubit levels involved makes the situation more complex than in a transmon. Interestingly, the value of χ^ϕ adds a significant contribution from qubit levels generated by excitations of the ϕ degree of freedom, which are not captured by the effective model in section 2.2.

In practice, we find that the absolute value of $\chi^\phi/2\pi$ does not increase beyond a few hundred kHz in a moderate-to-deep 0–π parameter regime. This would lead to rather slow readout and resonator-mediated gates as compared to those for the transmon qubit [34, 35]. However, an appreciable χ^ϕ could be useful to resolve the qubit nearly degenerate doublet by means of spectroscopy, and thus play an important role for device characterization. Moreover, we emphasize that the example parameter set in figure 5 is rather deep in the 0–π regime, where qubit lifetimes are predicted to be extremely long [22]. Reduced gate and and readout times might therefore be an acceptable compromise.

5. Single-qubit control through multilevel excursions

5.1. Qualitative picture

In this section, we study a process achieving population inversion between the logical qubit states. Such an operation seems challenging at first, given that, by design, the off-diagonal matrix elements of charge and phase operators in the qubit subspace are exponentially small in the deep 0–π regime [22, 23]. In particular, transition

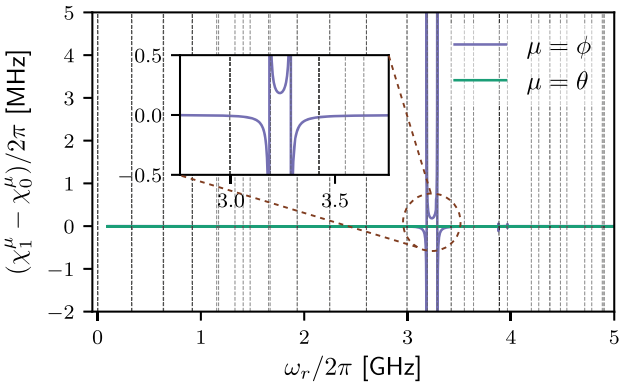

Figure 5. Dispersive shift for the ground state doublet of the 0–π qubit as a function of the readout resonator frequency $\omega_r/2\pi$. The qubit spectrum is shown in black dashed lines. Note that many of such lines are superimposed due to the doublet structure of the qubit spectrum, and in particular for the ground state doublet around 0 GHz. For ϕ coupling, we observe a remarkable increase of the dispersive shift in the highlighted region, reminiscent of the straddling regime of a transmon qubit. Here the qubit design parameters correspond to a moderate-to-deep 0–π regime at $\varphi_{\rm ext} = 0$, with $(E_L/\hbar\omega_p, E_{C_\phi}/\hbar\omega_p, E_{C_\theta}/\hbar\omega_p, E_{\rm J}/\hbar\omega_p) = (1.25 \times 10^{-3}, 0.374, 1.25 \times 10^{-4}, 0.167)$. Furthermore, we assume $C_g/C_\mu = 0.2$.

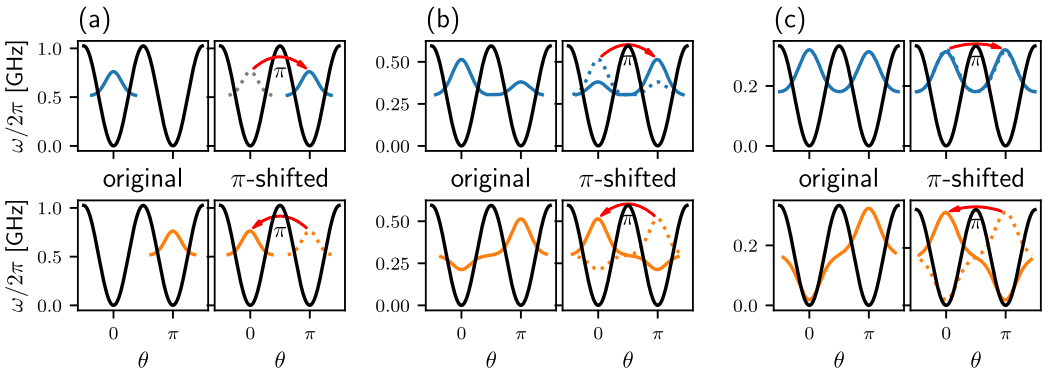

Figure 6. Single-qubit gate operation within the effective 0–π model for three chosen configurations: (a)–(c) correspond (respectively from top to bottom) to the qubit parameters highlighted with light-blue dots in figure 7(b). Ground (in blue) and excited (in orange) wave functions are displayed on the top- and bottom-left corner of each panel, respectively. To the right of the panels, we show the effect of a π-shift on such wave functions, demonstrating the gate operation. Note that because of the 2π-periodicity of the 0–π potential (in black), a π-shift to the left is equivalent to a a π-shift to the right. The gate implements a Pauli X operation for the case (a), a Hadamard for (b), and a Pauli Z for (c).

matrix elements for the charge operator can easily be 10^{-8} times smaller than those for the transmon qubit. We overcome this situation by exploiting the multilevel structure of the device for gate operations.

A first possible approach to circumvent the small overlap between logical states relies on Raman transitions, with the advantage of only virtually populating states outside of the protected subspace. However, in appendix C, we show that due to destructive interference the amplitudes of Raman processes in general vanish as the system approaches the deep 0–π limit. For this reason, we consider instead a gate scheme that temporarily populates excited states during the gate [36]. The gate lifts some of the qubit's protection from noise, as it populates higher energy levels. Nevertheless, the proposed strategy requires leaving the qubit subspace only for very short times, and we consequently find high fidelities for a broad range of parameters.

An intuitive understanding of the proposed gate can be gained by returning to the effective one-dimensional model for the 0–π qubit presented in section 2.2. In this simplified scenario, we have already suggested that logical $|1\rangle$ can approximately be obtained from $|0\rangle$ using a displacement by π along θ. Such an operation corresponds to the unitary $\exp(-in_\theta\pi)$, which can be generated by voltage driving the qubit. The precise logical action of such a displacement, however, depends on circuit and external parameters, as this determines the structure of the logical wave functions in the two wells. Figure 6 shows the logical wave functions corresponding to three different points in parameter space that will be studied in detail below. The figure shows the logical wave functions before and after a shift of $\theta \to \theta + \pi$ that represents the gate operation. When ground and excited states are respectively localized in the $\theta = 0$ and $\theta = \pi$ wells of the 0–π qubit potential (figure 6(a)), a π-shift

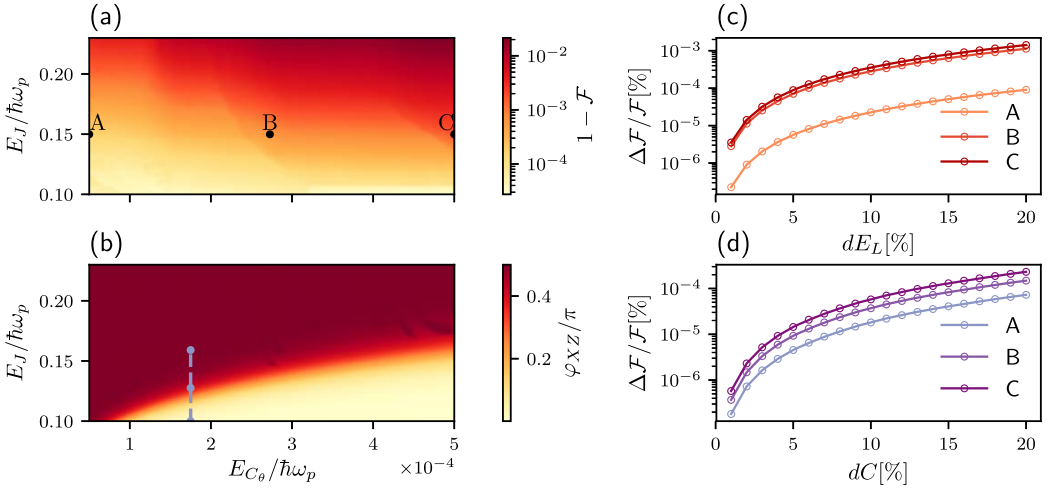

Figure 7. Single-qubit gate infidelity and logical action on the Bloch sphere. (a) Gate infidelity for a device with no disorder, computed from the unitary (non-dissipative) dynamics of the system. As $E_{C_\theta}/\hbar\omega_p$ and $E_J/\hbar\omega_p$ increase, we observe a decrease in gate fidelity. This is qualitatively understood as the effect of increasingly longer multilevel excursions during the gate time. (b) Induced rotation on the Bloch sphere. Here we show the polar angle φ_{XZ} for the XZ plane, while the azimuthal angle φ_{XY} remains bounded below 10^{-5}. We note that as $E_J/\hbar\omega_p$ is reduced, the qubit rotation smoothly interpolates between a Pauli X and Pauli Z. The light-blue dots are used as a reference for figure 6. Panels (c) and (d) show the relative change in the gate fidelity for the configurations A–C in panel (a), when dissipation and disorder in E_L and C are included. The gate fidelity proves to be robust to parasitic coupling to the ζ-mode for moderate amounts of circuit-element disorder, and it is not significantly affected by dissipation. The latter is a consequence of the fast gate time compared to the expected decoherence rates. For numerical reasons, simulations in panel (c) and (d) assume a cooled ζ-mode (see section 6). For the most demanding master equation simulations in (c) and (d) we have included $M = 40$ qubit levels, prudently exceeding the number required for convergence.

corresponds to a Pauli X operation. If E_J/E_{C_θ} is lowered, the hybridization of the qubit logical states increases. In the situation illustrated in figure 6(b), the logical wave functions are no longer perfectly localized and the gate implements a Hadamard operation. If, instead, the logical wave functions are completely hybridized (figure 6(c)), a π-shift corresponds to a Pauli Z gate. We can alternatively achieve the same wave function control by varying the external flux where $\varphi_{\rm ext} = 0$ corresponds to localized wave functions (for large E_J/E_{C_θ}) and $\varphi_{\rm ext} = \pi$ to completely hybridized wave functions. In the following sections we study this qualitative picture in detail.

5.2. Gate fidelity with respect to circuit parameters

When the full 0–π Hamiltonian is considered, the asymmetry of the two-dimensional logical wave functions along the ϕ-direction (see figure B1(c)) make clear that $|1\rangle$ and $|0\rangle$ cannot be simply exchanged by means of a θ-translation alone. Taking this into consideration, this section studies the gate employing the full circuit Hamiltonian equation (9). We characterize the gate fidelity as a function of the 0–π design parameters, and analyze the effect of circuit-element disorder and pulse shaping in the following sections.

We first consider a square microwave voltage pulse applied to the qubit and driving the θ coordinate, in absence of circuit-element disorder. In equation (9), this situation corresponds to setting all V_μ to zero with the exception of V_θ, such that the circuit Hamiltonian reads

$$H = H_{0-\pi}^{\rm symm} + \frac{C_g}{C_\theta} V_\theta(t) q_\theta. \tag{15}$$

In this section, we assume that the microwave drive is turned on at $t = 0$, reaching an amplitude $V_{\rm sq}$ for a period of time t_g. The effect of pulse shaping is analyzed below. To determine the optimal drive strength given the 0–π design parameters, we compute the multilevel evolution operator as a function of the pulse parameters ($V_{\rm sq}$, t_g), and minimize its distance to a unitary acting only on the qubit subspace[8]. This procedure ensures that leakage errors are kept as small as possible at the end of the gate. For the optimal drive configuration, we determine the closest qubit unitary to the multilevel propagator, and compute the average gate fidelity of the latter with respect to the former, including leakage errors [39].

[8] Denoting $u_{\rm red}$ as the reduced propagator, we define its distance to a unitary as $d(u_{\rm red}) = \max_s|1 - s|$, where $\{s\}$ are the singular values obtained from the singular value decomposition $u_{\rm red} = W_{\rm pre} S W_{\rm post}^\dagger$. The closest unitary is defined as $u_{\rm closest} = W_{\rm pre} W_{\rm post}^\dagger$, and identifies the qubit rotation that the voltage drive implements on the logical subspace [37, 38].

Setting $E_L/\hbar\omega_p = 10^{-3}$, we compute the gate infidelity as a function of E_J and $E_{C_\theta} = e^2/2C_\theta$, see figure 7(a). Note that the chosen range of parameters and the value of E_L corresponds to a moderate-to-deep 0–π regime. With these choices, we find gate fidelities between 99.99% and 99.9% for a broad range of system parameters, with decreasing values for increasing E_J and E_{C_θ}. This effect can be understood by contrasting the results of figure 7(a) with the qubit energy level structure. In fact, we find that the gate performs better for circuit design parameters leading to increased ground state degeneracy and moderate effective potential barriers. We give an explanation for this in section 5.4, where we show that these conditions results in multilevel excursions limited to very few excited doublets.

The logical action of the π translation is shown in figure 7(b), where the angle φ_{XZ} characterizes the qubit rotation performed on the Bloch sphere in the XZ plane. Note that the azimuthal angle φ_{XY} is not shown, as it remains approximately zero with deviations smaller than 10^{-5}. We observe that, as a function of the qubit design parameters, the gate interpolates continuously from Pauli X for large E_J/E_{C_θ} to Pauli Z for smaller E_J/E_{C_θ}. This feature is the result of hybridization between the ground state wave functions, as discussed above and illustrated in figure 6.

5.3. Gate fidelity with respect to circuit-element disorder in C and E_L

We next study the gate behavior in presence of realistic circuit-element disorder leading to coupling of the 0–π qubit to the ζ-mode. Circuit disorder also prevents independent control of the circuit degrees of freedom, and implies a parasitic drive acting on ζ when θ is driven for $\mathrm{d}C \neq 0$. Given that the ζ-mode is the main qubit-decoherence channel, in this section we compute the gate fidelity including dissipation. Recall that Purcell relaxation and dephasing by photon shot noise arise as a consequence of the parasitic coupling of $\{\phi, \theta\}$ to ζ [22].

To treat this case, relaxation and dephasing are included into a Lindblad-form master equation

$$\dot{\rho} = -\frac{\mathrm{i}}{\hbar}[H,\ \rho] + \sum_i^M \gamma_i^{\varphi}\mathcal{D}[\sigma_{ii}]\rho + \sum_{i\neq j}^M \gamma_{ij}\mathcal{D}[\sigma_{ij}]\rho + [\kappa_\zeta(n_{\mathrm{th}}(\omega_\zeta)+1)+\Gamma_\downarrow]\mathcal{D}[a]\rho + [\kappa_\zeta n_{\mathrm{th}}(\omega_\zeta)+\Gamma_\uparrow]\mathcal{D}[a^\dagger]\rho, \tag{16}$$

which is integrated in superoperator form for the configurations identified as A–C in figure 7(a). Here, H is the 0–π circuit Hamiltonian in equation (9), a ($a^\dagger$) corresponds to the ζ-mode annihilation (creation) operator, and $\mathcal{D}[x]\rho = x\rho x^\dagger - \frac{1}{2}x^\dagger x\rho - \frac{1}{2}\rho x^\dagger x$ is the usual dissipative superoperator. The results of the master equation integration are shown in figure 7(c) for disorder in E_L and in figure 7(d) for disorder in C. In these simulations, qubit dephasing ($\{\gamma_i^\varphi\}$) and transition ($\{\gamma_{ij}\}$) rates are computed numerically, using the theory developed in [22]. We consider a worst-case scenario by using the maximum of the dephasing, relaxation and excitation rates obtained in full $\varphi_{\mathrm{ext}} \in [0, 2\pi]$ and $n_g^\theta \in [-1/2,\ 1/2]$ excursions. The photon-loss rate, κ_ζ, of the ζ-mode is evaluated as a function of the mode's frequency, assuming a quality factor of $Q_\zeta = 30\,000$ [12]. Moreover, we assume a temperature of 15 mK. We note that taking into account the ζ-mode thermal population $n_{\mathrm{th}}(\omega_\zeta)$ at dilution refrigerator temperatures would lead to photon numbers prohibitively large for numerical simulations. Therefore, we assume this mode being cooled using the strategy proposed in section 6. As discussed below, the cooling mechanism leads to the rates $\Gamma_\downarrow$ and $\Gamma_\uparrow$ in equation (16), reducing the effective temperature of the ζ-mode. The gate fidelity in (c) and (d) is computed with respect to the closest qubit unitary determined in section 5.2 in absence of circuit-element disorder and dissipation. We have verified that the result does not change when the cooling power is continuously varied, and thus with the ζ-mode effective thermal population up to an average of five photons.

We find that, as a consequence of a fast Hamiltonian dynamics, the gate fidelity is almost unaffected by the relatively slow dephasing and relaxation rates and that circuit-element disorder is the limiting factor. We note that, despite a small-to-moderate degradation of the gate fidelity for disorder below 10%, leakage errors are appreciable for higher disorder values. Moreover, the fast unitary dynamics of the gate poses a control challenge. As the gate operates at a frequency which is roughly one order of magnitude smaller than the plasma frequency, the necessary time-resolution must match such a time-scale within the capability of commercially available arbitrary-waveform generators [40, 41]. Optimal control techniques such as GRAPE could be useful to further improve the gate fidelity, but this may require even finer time-resolution and thus be rather challenging [42–44].

The single-qubit gate fidelity is also found to be remarkably robust to the detailed form of the voltage pulse, moderate deviations in the external flux, and disorder in E_J and C_J. A study of these effects is provided in appendix D.

5.4. Multilevel excursion during gate time

As stated above, the proposed gate exploits the multilevel structure of the 0–π qubit. In this section, we qualitatively discuss how this multilevel excursion takes place and the effect of leakage errors on the gate fidelity.

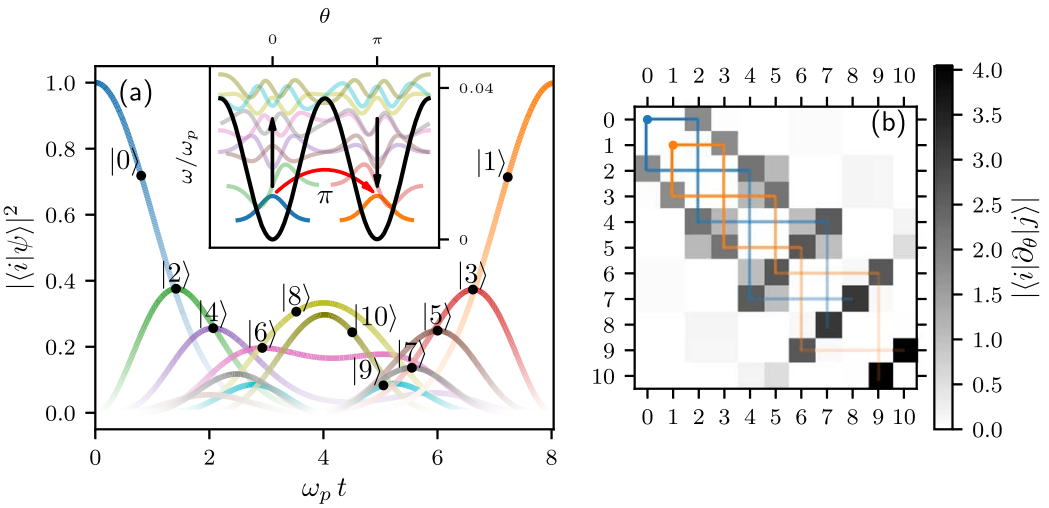

Figure 8. Multilevel excursion during the gate time. (a) State population as a function of $\omega_p t$, with initial condition $|0\rangle$. Level transparency weighted by the state population has been introduced to facilitate viewing. The insets shows the corresponding wave functions within the effective 1D model. There, black arrows illustrate how the qubit population (initially in the ground state) is transferred to higher energy doublets bridging the two potential wells, and finally transferred back to the excited state. (b) Matrix elements proportional to the charge operator q_θ. There exist two disjoint paths connecting the ground and excited states to the higher energy doublets. We observe that the state population closely follows such paths for the few first excited levels, both at the beginning and at the end of the gate. Doublets with a higher degree of hybridization, such as (4, 5) and (6, 7), make it possible to transition between these two paths and from one potential well to the other. Qubit parameters $(E_L/\hbar\omega_p,\ E_{C_\phi}/\hbar\omega_p,\ E_{C_\theta}/\hbar\omega_p,\ E_J/\hbar\omega_p) = (10^{-3},\ 0.378,\ 1.75\times 10^{-4},\ 0.165.)$.

Considering the initial state $|0\rangle$, figure 8(a) shows the eigenstates population as a function of time as obtained by numerical integration under the Hamiltonian equation (15). There, we observe how the initial $|0\rangle$ population is transferred by means of the voltage drive to higher energy doublets that bridge the two 0–π potential wells. We note that the qubit population is almost completely restored to the qubit subspace at time $t = t_g$, leaving the qubit in the state $|1\rangle$.

The multilevel excursion in figure 8(a) can be partially anticipated by considering the matrix elements of the 0–π charge operator q_θ, as shown in figure 8(b). There, we observe a clear path leaving the ground state through levels 2 and 4, and arriving to the excited state through levels 3 and 5 after going through higher excited states. During the gate time, levels which are part of doublets with higher wave function hybridization make it possible to transfer the population between the two potential wells. Numerical experiments have shown that the number of doublets involved in the transition from $|0\rangle$ to $|1\rangle$ gives a qualitative estimate of the gate fidelity: because it leads to reduced leakage, qubit design parameters leading to excursions involving fewer levels exhibit larger fidelities. Since the number of occupied doublets grows with the height of the double-well energy barrier ($\propto E_J$), longer multilevel excursions also explain the decrease in gate fidelity observed in figure 7(b).

5.5. Tuning the gate from X to Z for greater qubit control

The continuity of the gate rotation angle as a function of the system parameters could be used to obtain a larger set of single-qubit gates. In principle, this could be achieved by adiabatically sweeping E_J (e.g., replacing single junctions by tunable SQUID loops) or varying φ_{ext} from 0 to π. However, the adiabatic condition is difficult to satisfy in the qubit subspace, requiring sweep times as large as a few milliseconds for a device in the deep 0–π regime. Pulse shaping and optimal control techniques [45, 46] might offer an alternative to adiabatic sweeps and need to be explored further.

6. Fighting photon shot noise by cooling the ζ-mode

For realistic circuit parameters in near-term experiments, a limiting factor for the qubit coherence times, and thus also gate and readout fidelities, is spurious coupling to the low-frequency ζ-mode [22]. We now discuss a method to enhance the coherence times of the 0–π qubit by cooling this mode.

In [22], we have shown that thermal-photon population in the low-frequency ζ-mode limits the coherence time of 0–π qubits with realistic circuit parameters. To reduce the impact of this type of noise, it is essential to minimize the circuit-element disorder leading to parasitic coupling of the qubit degrees of freedom to the ζ-mode. Moreover, if a device can be built in the deep 0–π regime, we have shown that there exists a threshold

value $Z_\phi > Z_{\text{threshold}}$, such that the qubit will be protected from photon shot noise, even with circuit disorder [22]. Here, however, we consider an active approach to mitigate this problem. We engineer a protocol to boost the coherence time by cooling the ζ-mode using an additional frequency-tunable resonator. Importantly, this scheme should be applicable to near-term, more realistic parameter regimes.

6.1. 0–π qubit dephasing time with a cooled ζ-mode

Cooling of an oscillator by periodically modulating its linear coupling to a second heavily damped mode has been studied in the context of nanomechanical resonators [47]. There, the periodical modulation of the coupling leads to sideband transitions between the two modes, allowing for excitation of the first mode to be damped by the second. This approach is not directly applicable to our system since, as discussed in section 3.2, we restrict ourselves to the use of capacitors as coupling elements. We therefore propose a modification of the protocol of [47] which relies, instead, on frequency modulation of the heavily damped mode. In practice, modulating this mode frequency also leads to a modulation of the coupling strength. Below, we develop a theory accounting for both modulated quantities, and we find that efficient cooling of the ζ-mode is possible with realistic circuit parameters.

We consider an additional frequency-tunable resonator capacitively coupled to the 0–π circuit and addressing the ζ-mode as specified in table 1. The Hamiltonian for the coupled oscillators is

$$H_{\text{cooling}} = \hbar\omega_\zeta a^\dagger a + \hbar\omega_b(t) b^\dagger b - \hbar g(t)(a^\dagger - a)(b^\dagger - b), \tag{17}$$

where a and b are, respectively, the ζ- and external-mode annihilation operators. The omission of the qubit degrees of freedom $\{\phi, \theta\}$ in equation (17) is justified below. The time-varying coupling constant,

$$g(t) = \frac{C_g}{C_\zeta C_b} \frac{1}{2\sqrt{Z_\zeta Z_b(t)}}, \tag{18}$$

takes into account the coupling capacitance C_g between the two modes as well as the capacitances C_ζ, C_b, and the impedances Z_ζ, Z_b, of the ζ- and b-modes. The time dependence of the resonator frequency and the coupling strength in equations (17), (18) is assumed to arise from the flux modulation of a tunable inductance $L_b[\Phi(t)]$ forming the b-mode. In particular, we assume $\omega_b(t) = \bar{\omega}_b + \varepsilon \cos(\omega_m t)$, where $\bar{\omega}_b$, ε and ω_m are, respectively, the mean value, modulation amplitude and modulation frequency of the b-mode frequency. Accordingly, the time dependence of the coupling strength takes the form $g(t) = \bar{g}[1 + \frac{\varepsilon}{2\bar{\omega}_b}\cos(\omega_m t)]$, up to first order in deviations of L_b from its mean value.

We derive an effective master equation for the ζ-mode by imposing the constraint $\bar{g} \ll \omega_\zeta,\ \omega_b$, which allows to treat the two modes as independently coupled to their respective baths. The mean frequency of the b-mode is chosen such that thermal excitation can safely be ignored ($\hbar\bar{\omega}_b \gg k_B T$). Moreover, the strength of the coupling between the b-mode and its reservoir is assumed to be frequency-independent in the range covered by the frequency modulation. Under these assumptions, the master equation of the system reads

$$\dot{\rho} = -\frac{\mathrm{i}}{\hbar}[H_{\text{cooling}}, \rho] + \kappa_\zeta[n_{\text{th}}(\omega_\zeta) + 1]\mathcal{D}[a]\rho + \kappa_\zeta n_{\text{th}}(\omega_\zeta)\mathcal{D}[a^\dagger]\rho + \kappa_b\mathcal{D}[b]\rho, \tag{19}$$

where κ_ζ and κ_b are the respective photon-loss rates of the ζ- and the b-mode, while $n_{\text{th}}(\omega_\zeta) = 1/(\mathrm{e}^{\hbar\omega_\zeta/k_B T} - 1)$ is the number of thermal photons in the ζ-mode. To activate sideband transitions between the two systems, we choose the modulation frequency to be $\omega_m = \bar{\omega}_b - \omega_\zeta$. This choice allows for the up-conversion mechanism where photons, initially populating the ζ-mode, are transferred to the external resonator and then lost to the environment at a rate κ_b. Because the external-mode remains approximately in the vacuum state at all times, the inverse process is highly suppressed [47].

Assuming the b-mode to be low-Q, we employ the technique of adiabatic elimination to remove this mode from the above master equation. As discussed in more details in appendix E, this leads to the reduced master equation

$$\dot{\rho}_I^\zeta(t) = [\kappa_\zeta(n_{\text{th}}(\omega_\zeta) + 1) + \Gamma_\downarrow]\mathcal{D}[a]\rho_I^\zeta(t) + [\kappa_\zeta n_{\text{th}}(\omega_\zeta) + \Gamma_\uparrow]\mathcal{D}[a^\dagger]\rho_I^\zeta(t), \tag{20}$$

in the interaction frame defined from equation (17). In this expression, we have defined the effective rates $\Gamma_\downarrow = \frac{4g'^2}{\kappa_b}$ and $\Gamma_\uparrow = \frac{4g'^2}{\kappa_b}\Big/\left[\left(\frac{2\omega_\zeta}{\kappa_b/2}\right)^2 + 1\right]$, expressed in terms of the effective coupling strength

$$g' = \bar{g}J_1\left(\frac{\varepsilon}{\omega_m}\right) - \frac{\varepsilon}{4\bar{\omega}_b}\left[J_0\left(\frac{\varepsilon}{\omega_m}\right) + J_2\left(\frac{\varepsilon}{\omega_m}\right)\right], \tag{21}$$

where $J_k(x)$ is a Bessel function of the first kind. In accordance with our assumptions, the validity of equation (20) is subject to the condition $\kappa_b \gg g'$. Assuming the ζ-mode to be in a thermal state, the steady-state photon population under equation (20) is given by

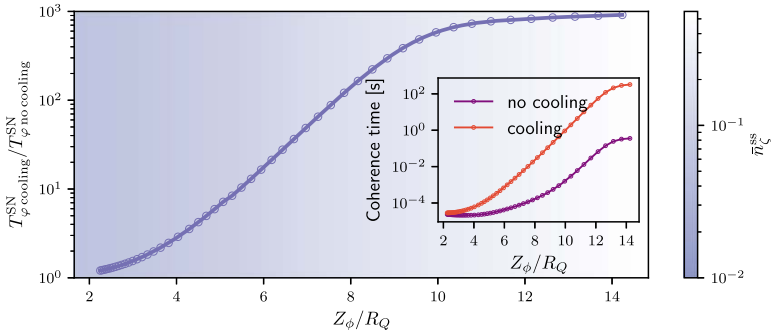

Figure 9. Photon-shot noise coherence time ($T^{SN}_\varphi = 1/\Gamma^{SN}_\varphi$) with and without cooling of the ζ-mode. The inset displays the respective absolute values. Devices that can be fabricated with today's superconducting technology would be situated at the left side of this plot. Next-generation devices are expected to range between the left and the middle of the plot, where improvements on the coherence time vary between one and two orders of magnitude. In the deep 0–π regime (to the right), major improvements will result in other noise mechanism (potentially flux noise) to be dominant. The inset displays the coherence time with and without cooling. The background density plot shows the steady-state population of the ζ-mode, $\bar{n}^s_\zeta$. We note that the increase in this quantity as one moves to the deep 0–π regime is due to the decrease of the ζ-mode frequency and effective coupling to the b-mode, thus compromising ground state cooling. The cooling power, however, is enough to considerably reduce the dephasing rate. Circuit parameters: $E_L/\hbar\omega_p \in [1.25 \times 10^{-4}, 5 \times 10^{-3}]$ and $(E_{C_\phi}/\hbar\omega_p, E_{C_\theta}/\hbar\omega_p, E_J/\hbar\omega_p) = (0.25, 0.5 \times 10^{-3}, 0.25)$, $\varepsilon/2\pi = 200$ MHz (compatible with a SQUID-array frequency-tunable resonator [49, 50]), $\omega_b/2\pi = 5$ GHz, $Q_\zeta = 30\,000$, and $T = 15$ mK.

$$\bar{n}^s_\zeta = \frac{\kappa_\zeta}{\gamma_{\mathrm{cooling}}} n_{\mathrm{th}}(\omega_\zeta) + \frac{\Gamma_\uparrow}{\gamma_{\mathrm{cooling}}}, \tag{22}$$

where

$$\gamma_{\mathrm{cooling}} = \kappa_\zeta + \Gamma_\downarrow - \Gamma_\uparrow \tag{23}$$

is the cooling rate of our scheme [48]. Thermal equilibrium is therefore reached in a time $t_{\mathrm{cooling}} = 1/\gamma_{\mathrm{cooling}}$.

In order to show the impact of this protocol on the coherence time of the 0–π qubit, we follow [15] to obtain the photon-shot noise dephasing rate for the master equation of equation (20). In the limit $\chi^\zeta_{01} \ll \gamma_{\mathrm{cooling}}$, this rate takes the form

$$\Gamma^{\mathrm{SN}}_\varphi \simeq \frac{4(\chi^\zeta_{01})^2}{\gamma_{\mathrm{cooling}}} \bar{n}^{ss}_\zeta (\bar{n}^{ss}_\zeta + 1), \tag{24}$$

where we note that $\Gamma^{\mathrm{SN}}_\varphi \propto \gamma^{-2}_{\mathrm{cooling}}$ for $\bar{n}^{ss}_\zeta \ll 1$. We do not find improvements on $\Gamma^{\mathrm{SN}}_\varphi$ in the inverse limit $\chi^\zeta_{01} \gg \gamma_{\mathrm{cooling}}$. Consequently, we observe that our cooling scheme significantly enhances the device's coherence times as long as the dispersive coupling to the ζ-mode is not too large.

The cooling protocol is therefore applicable in a moderate-to-deep 0–π regime, where we find improvements on the dephasing rate of the qubit by up to three orders of magnitude. The coherence time improvement due to cooling is shown in figure 9 as function of Z_ϕ/R_Q. We note that the circuit parameters are the same as those in figure 2(b), and correspond to the set defined as PS2 (moderate 0–π regime) in [22], varying the superinductance value between those in the sets PS1 (deep 0–π regime) and PS3 (near-term regime) of the same paper. As anticipated, the relative gain becomes significant as one moves towards the deep 0–π regime (large Z_ϕ/R_Q), before reaching saturation. The saturation value can be understood from equation (24) in the limit of $n_{\mathrm{th}}(\omega_\zeta) \to \infty$, where it is only a function of $\bar{g}$ and $\varepsilon/\bar{\omega}_b$.

The interaction with the b-mode further broadens the ζ-mode, resulting in larger 0–π-qubit Purcell relaxation and excitation rates. Given that such rates have been found not to limit the qubit coherence, we do not expect this effect to be a limiting factor in practice [22]. In fact, we predict the increase of the Purcell rates to be one order of magnitude, which is still far from compromising the device.

6.2. Effect of parasitic coupling and implementation details

Circuit-element disorder responsible for the coupling between the qubit degrees of freedom and the ζ-mode also introduces a parasitic coupling between $\{\phi, \theta\}$ and the b-mode. As a result, the fact that ω_m is specially chosen to activate a resonant interaction between the ζ-mode and the frequency-tunable device, implies that any qubit transition matching ω_ζ will also be resonant. Given that, by design, the 0–π qubit transition should not be resonant with the ζ-mode, accidental resonances might arise within the multilevel structure of the device. This possibility, however, can be minimized by circuit design. Additionally, resonances between the 0–π circuit transitions and the mean frequency of the b-mode should be avoided by properly choosing $\bar{\omega}_b$.

Finally, we discuss some of the implementation details leading to a correction of the modulation frequency. We first address the effect the dispersive interaction between the qubit degrees of freedom and the ζ-mode [22, 23]. In the limit $\chi_{01}^{\zeta} \ll \gamma_{\text{cooling}}$, the frequency of the ζ-mode is approximately independent of the qubit state. Therefore, we account for the mean ζ-mode frequency shift due to the dispersive interaction by redefining the b-mode modulation frequency as

$$\omega_m \rightarrow \omega_m - (\chi_0^{\zeta} + \chi_1^{\zeta})/2, \tag{25}$$

where χ_0^{ζ} (χ_1^{ζ}) is the dispersive shift for the qubit being in the ground (excited) state [22] [see also equation (14)]. A similar effect is expected to arise from nonlinear terms in the b-mode Hamiltonian. In fact, it is worthwhile to note that current implementations of frequency-tunable resonators rely on Josephson junctions which introduce a small Kerr nonlinearity, K, and comparable shift to ω_b [49–53]. Given that, by design, the b-mode is kept in a nearly vacuum state at all times during the cooling protocol, the effect of the nonlinearity is limited to a frequency shift. The latter can again be compensated by changing the modulation frequency according to $\omega_m \rightarrow \omega_m - K/2$. We note that the results of this section, including the reduced master equation equation (20) and the effect of nonlinearities, were validated against the integration of the full time-dependent master equation of equation (19).

7. Conclusion

The 0–π circuit is a promising candidate for the realization of a protected superconducting qubit. However, both fabrication and control challenges need to be overcome. In this paper, we considered control strategies exploiting the multilevel structure of this device, within a realistic circuit model.

We explored the possibility of dispersively coupling the 0–π qubit to a resonator, which can be used for standard dispersive readout and resonator-mediated gates. In general, dispersive coupling is extremely small in the moderate-to-deep 0–π regime due to the highly symmetric double-well structure of the qubit potential. Nevertheless, we found a remarkably large dispersive shift by coupling to the ϕ mode of the 0–π qubit, and operating in a regime reminiscent of the straddling regime of a transmon qubit. Dispersive shifts around a hundred kHz could be achievable, even rather deep in the 0–π regime. This is promising for qubit characterization through spectroscopy, and might also be promising for readout and gates due to the extremely long qubit lifetimes that are possible in this regime.

We moreover proposed a new, fast and high-fidelity single-qubit gate that can smoothly interpolate between logical X and Z by varying the qubit operation point. We studied the gate fidelity as a function of the 0–π circuit and control parameters, and the amount of circuit-element disorder. We found that the gate fidelity is not significantly affected for small deviations from optimal parameters and moderate disorder. Future work will concentrate on extending the gate operation to a universal set of single-qubit gates. Finally, we note that qubits with a similar level structure to that of the 0–π qubit might leverage related ideas [36, 54–59].

In addition, we have designed a protocol to enhance the qubit coherence time due to photon shot noise from the ζ-mode. Our scheme couples this mode to a frequency-modulated and highly damped resonator, which is used as a zero temperature-bath for the ζ-mode. We characterized the improvement in the qubit photon-shot-noise dephasing time as a function of the circuit design parameters. While the coherence time enhancement for near-term devices is expected to provide a 2–10 times gain on coherence, we predict improvements of one and two orders of magnitude for the future generations. We also envision that this active cooling protocol could be useful in a more general context of superconducting devices with low-frequency modes or with residual thermal population.

Several open questions remain about how to best use the ingredients presented in this paper for a *universal* set of logical operations. A quantitative analysis is needed to determine the potential use of dispersive coupling for readout and gates, taking into account any possible degradation of qubit coherence due to coupling to the resonator, and whether gate times can be sufficiently fast compared to the coherence times to achieve high-fidelity gates. It would also be interesting to exploit the tunability of the gate introduced in section 5 to achieve a larger set of single qubit gates. Finally, the original proposal for protected phase gates from [20] should be investigated in a more realistic setting, to determine the potential use of this approach for near-to-medium term experiments.

Acknowledgments

We acknowledge valuable discussions with András Gyenis, Samuel Boutin and Christian K Andersen. ADP acknowledges support from the Fundación Williams en Argentina and the Bourse d'excellence de 3e cycle, Faculté des Sciences, Université de Sherbrooke. This work was supported by the Army Research Office under

Grant no. W911NF-15-1-0421 and NSERC. This research was undertaken thanks in part to funding from the Canada First Research Excellence Fund. This work is supported by the Australian Research Council (ARC) via Centre of Excellence in Engineered Quantum Systems (EQUS) Project No. CE170100009.

Appendix A. Circuit Hamiltonian in presence of gate- and ground-capacitance disorder

The effective capacitances C_μ of the 0–π circuit modes ($\phi, \theta, \zeta, \Sigma$) introduced in equation (10) are given by

$$\begin{aligned} C_\phi &= C_0 + C_g + 2C_\mathrm{J}, \\ C_\theta &= C_0 + C_g + 2(C + C_\mathrm{J}), \\ C_\zeta &= C_0 + C_g + 2C, \\ C_\Sigma &= C_0 + C_g. \end{aligned} \tag{A.1}$$

Using definitions found in section 3.3, the full expression of the term $H_{\mathrm{d}C_g,\mathrm{d}C_0}$ in equation (11) is

$$\begin{aligned} H_{\mathrm{d}C_g,\mathrm{d}C_0} = &-\sum_\mu \frac{1}{2C_\mu^2}[(C_g/2)\mathrm{d}C_{g_\Sigma} + (C_0/2)\mathrm{d}C_{0_\Sigma}]q_\mu^2 \\ &- \frac{1}{2}\sum_{\mu\neq\nu\neq\sigma \text{ all } \neq\Sigma} \frac{1}{C_\mu C_\nu}[(C_g/2)\mathrm{d}C_{g_\sigma} + (C_0/2)\mathrm{d}C_{0_\sigma}]q_\mu q_\nu \\ &- \sum_{\mu\neq\Sigma} \frac{1}{C_\Sigma C_\mu}[(C_g/2)\mathrm{d}C_{g_\mu} + (C_0/2)\mathrm{d}C_{0_\mu}]q_\mu q_\Sigma. \end{aligned} \tag{A.2}$$

Disorder of the from $\mathrm{d}C_{g_\mu}$, $\mathrm{d}C_{0_\mu} \neq 0$, is assumed to be small compared to all other capacitances in the circuit, and $H_{\mathrm{d}C_g,\mathrm{d}C_0}$ is therefore neglected in this work. The expression for $H_\mathrm{drive}^\mathrm{asymm}$ in equation (9) is

$$\begin{aligned} H_\mathrm{drive}^\mathrm{asymm} = &-\frac{C_g\, C_\mathrm{J}\, \mathrm{d}C_\mathrm{J}}{C_\phi C_\theta}(V_\theta q_\phi + V_\phi q_\theta) - \frac{C_g\, C\, \mathrm{d}C}{C_\zeta C_\theta}(V_\theta q_\zeta + V_\zeta q_\theta) \\ &+ \sum_{\mu\neq\Sigma} \frac{C_g}{C_\mu^2}[(C_\mu - C_g/2)\mathrm{d}C_{g_\Sigma} - (C_0/2)\mathrm{d}C_{0_\Sigma}]V_\mu q_\mu \\ &+ \sum_{\mu\neq\Sigma} \frac{C_g}{C_\mu C_\Sigma}[(C_\Sigma - C_g/2)\mathrm{d}C_{g_\mu} - (C_0/2)\mathrm{d}C_{0_\mu}]V_\Sigma q_\mu \\ &+ \sum_{\mu\neq\nu\neq\sigma \text{ all } \neq\Sigma} \frac{C_g}{C_\mu C_\nu}[(C_\nu - C_g/2)\mathrm{d}C_{g_\sigma} - (C_0/2)\mathrm{d}C_{0_\sigma}]V_\nu q_\mu \\ &+ \sum_\mu \frac{C_g}{C_\mu C_\Sigma}[(C_\mu - C_g/2)\mathrm{d}C_{g_\mu} - (C_0/2)\mathrm{d}C_{0_\mu}]V_\mu q_\Sigma. \end{aligned} \tag{A.3}$$

In these two expressions, V_μ, $\mathrm{d}C_{g_\mu}$ and $\mathrm{d}C_{0_\mu}$ are given in terms of V_i, $\mathrm{d}C_{g_i}$ and $\mathrm{d}C_{0_i}$, respectively, according to the transformation rule specified in equation (1) (where Greek indices denote the normal-mode variables and Latin indices indicate node variables).

Appendix B. One-dimensional effective model

The reduction from the 0–π Hamiltonian to a 1D effective model was first motivated in [20] and analytically studied in [60] in the context of the Born–Oppenheimer approximation. In section 2.2, moreover, we have provided an intuitive justification for such a model. Here, we perform a numerical calculation which, in contrast to analytical approaches, does not require additional approximations.

Starting with the 0–π circuit Hamiltonian in absence of disorder, i.e. equation (2), we define

$$H_\phi = \frac{q_\phi^2}{2C_\phi} - 2E_\mathrm{J}\cos\tilde{\theta}\cos(\phi - \varphi_\mathrm{ext}/2) + E_L\phi^2, \tag{B.1}$$

where $\tilde{\theta} \in [-\pi/2,\, 3\pi/2)$ acts here as a parameter. This corresponds to the first step of the Born–Oppenheimer approximation, where only the less massive degrees of freedom (ϕ in our case) are considered. We then find the ground state energy $E_0(\tilde{\theta})$ of H_ϕ, as a function of θ. As a next step, we define a second 1D problem by the Hamiltonian

$$H_\theta = \frac{q_\theta^2}{2C_\theta} + E_0(\theta), \tag{B.2}$$

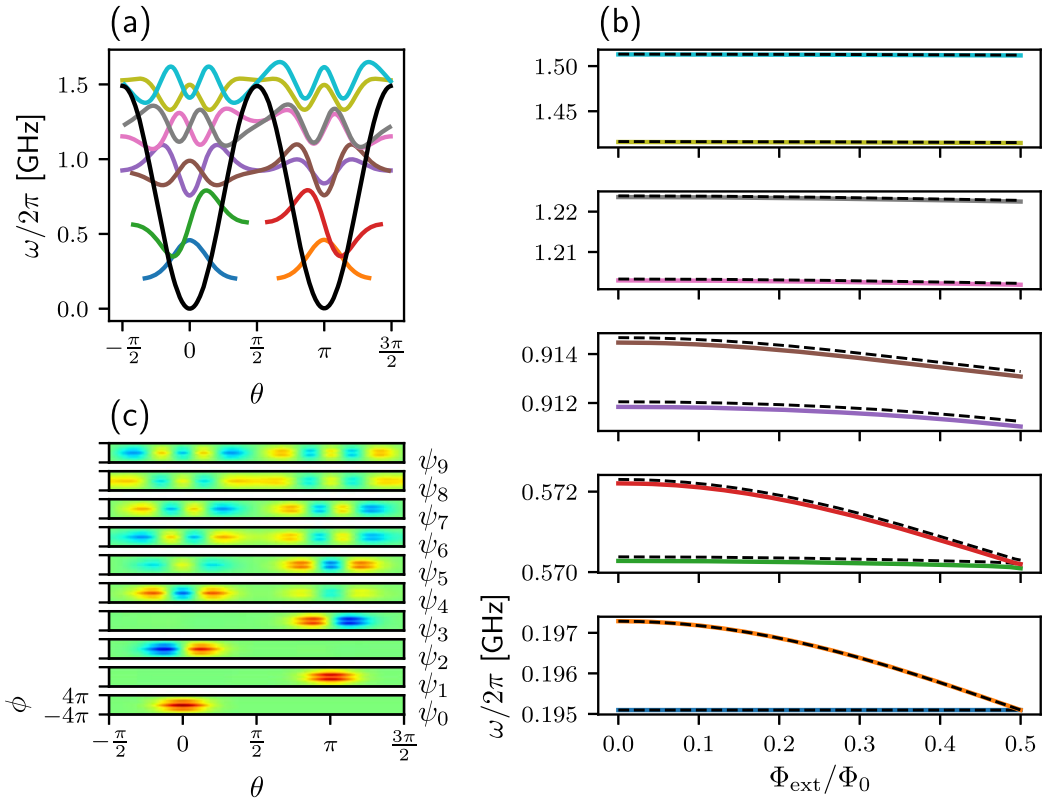

Figure B1. 1D effective model for the 0–π qubit. (a) 1D effective potential (black) and 1D wave functions (color) offset by their respective energy. The wave functions corresponding to the H_θ eigenstates are displayed in panel (a) for $\varphi_{\rm ext} = 0$, along with the resulting 1D effective potential. Panel (b) shows the respective eigenvalues (solid colored lines), along with the spectrum of the full 0–π Hamiltonian equation (2) (black dashed lines). In (c), we show the two-dimensional eigenfunctions corresponding to equation (2) (for $\varphi_{\rm ext} = 0$), which should be contrasted with those of the 1D model in (a). The effective 1D potential has an exact 2π- and approximately π-periodic structure. Qubit parameters $(E_L/\hbar\omega_p, E_{C_\phi}/\hbar\omega_p, E_{C_\theta}/\hbar\omega_p, E_J/\hbar\omega_p) = (10^{-3}, 0.378, 1.75 \times 10^{-4}, 0.165)$ and $\omega_p/2\pi = 40$ GHz.

where $E_0(\tilde{\theta} \to \theta)$ is used as an effective potential and θ is now the qubit phase operator. Note that, in contrast to equation (B.1), H_θ governs the motion of the massive degrees of freedom (θ in our case).

Equation (B.2) represents the one-dimensional effective Hamiltonian for the 0–π qubit. The corresponding eigenvalues and eigenstates are shown in figure B1 as a function of the external flux. Remarkably, we find excellent agreement with the complete two-dimensional circuit Hamiltonian equation (2) for several excited doublets. By fitting the effective potential, we find that equation (B.2) can very accurately be written as

$$H^{\rm eff} = 4E_{C_\theta}(n_\theta - n_g^\theta)^2 - E_2(\varphi_{\rm ext})\cos 2\theta - E_1(\varphi_{\rm ext})\cos\theta, \tag{B.3}$$

where we incorporate the offset charge n_g^θ. In the above expression, the potential energy coefficients read $E_2(\varphi_{\rm ext}) = E_\alpha - E_\beta\cos(\varphi_{\rm ext})$ and $E_1(\varphi_{\rm ext}) = E_\gamma\cos(\varphi_{\rm ext}/2)$ regardless of the qubit design parameters. The relations $E_\alpha \gg E_\gamma$ and $E_\alpha \gg E_{C_\theta}$, satisfied in the deep 0–π limit, ensure exponential suppression of relaxation and dephasing rates [30]. For the set of parameters in figure B1, we find $E_\alpha/\hbar\omega_p = 1.8608 \times 10^{-2}$, $E_\beta/\hbar\omega_p = 1.0073 \times 10^{-8}$, $E_\gamma/\hbar\omega_p = 2.6625 \times 10^{-5}$. Finally, we note that an expression similar to equation (B.3) has been theoretically proposed in [60]. We have found, however, necessary to incorporate additional flux-dependence to the potential energy coefficients.

Appendix C. Raman processes for qubit control

We now consider enabling a Raman-type gate operation by virtually populating the excited states of the qubit. In particular, we study the effective dynamics in the ground state manifold $\{|0\rangle, |1\rangle\}$ by performing adiabatic elimination of the first few qubit excited level. As only virtual transitions to high-energy levels are involved, Raman-type gates could, in principle, preserve the device's noise protection to some degree. However, as shown below, the transition amplitude $|0\rangle \leftrightarrow |1\rangle$ vanishes in a large parameter range because of an approximate

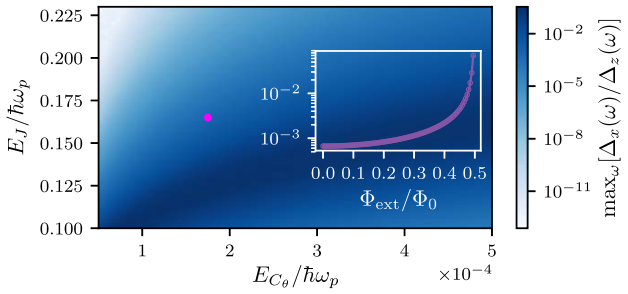

Figure C1. Ratio $\Delta_x(\omega)/\Delta_z(\omega)$ optimized over the drive frequency ω under the off-resonant drive condition, as a function of the 0–π circuit design parameters. Inset: optimal $\max_\omega[\Delta_x(\omega)/\Delta_z(\omega)]$ as a function of the external flux for the parameters $(E_L/\hbar\omega_p, E_{C_\phi}/\hbar\omega_p, E_{C_\theta}/\hbar\omega_p, E_J/\hbar\omega_p) = (10^{-3}, 0.378, 1.75 \times 10^{-4}, 0.165)$. The simulations included 30 qubit levels.

selection rule. To arrive at this result, we make use of the adiabatic elimination procedure developed in [61], which applies to weakly and off-resonantly driven multilevel systems.

C.1. Single-tone driving

We consider the 0–π circuit capacitively coupled to microwave voltage sources addressing θ, as described in the second row of table 1. Including a total of M qubit levels, the driven 0–π qubit Hamiltonian can be written as

$$H/\hbar = \sum_{i=0}^{M}\omega_i\sigma_{ii} + \sum_{i=0,1}\sum_{j=2}^{M}(\Omega_{ij}e^{-i\omega t}\sigma_{ji} + \text{h.c.}). \tag{C.1}$$

Here, ω_i is the frequency of the ith eigenstate, ω the frequency of the drive and $\Omega_{ij} = \frac{C_g}{C_\theta}(eV)e^{-i\beta}\langle j|n_\theta|i\rangle$ is the coupling strength between levels (i, j) for a voltage pulse of the from $V_\theta(t) = V\cos(\omega t + \beta)$. We note that rapidly rotating terms have been dropped in equation (C.1) under the assumption of a weak drive ($\Omega_{ij}/\omega \ll 1$). Moreover, we neglect the effect of Ω_{01}, which is exponentially small for typical qubit design parameters.

By numerically solving the Schrödinger equation, we find that equation (C.1) hardly generates qubit population inversion. In fact, we observe that states from the few excited doublets destructively interfere with each other, thus leading to a negligible transition amplitude. This cancellation is preserved in a broad range of qubit design parameters, including flux excursions from the standard operating point $\varphi_{\rm ext} = 0$.

To understand this effect, we reduce the multilevel dynamics to the qubit subspace. Following [61] and modeling dissipation by the set of collapse operators $\{L_{j0} = \sqrt{\gamma_{j0}}\sigma_{0j}, L_{j1} = \sqrt{\gamma_{j1}}\sigma_{1j}; j = 2, \ldots, M\}$, we find

$$H^{\rm eff}/\hbar = \sum_{i,i'=0,1}\left(\omega_i\delta_{ii'} - \frac{1}{2}\sum_{j=2}^{M}\frac{(\Omega_{ij})^*\Omega_{i'j}[\Delta_{ji}(\omega) + \Delta_{ji'}(\omega)]}{\left[i\frac{\gamma_j}{2} + \Delta_{ji}(\omega)\right]\left[-i\frac{\gamma_j}{2} + \Delta_{ji'}(\omega)\right]}\right)\sigma_{ii'}, \tag{C.2}$$

where $\gamma_j = \gamma_{j0} + \gamma_{j1}$ is the total decay rate from the jth level to the ground state manifold and $\Delta_{ji}(\omega) = (\omega_j - \omega_i) - \omega$ is the detuning of the drive with respect to the transition frequency $\omega_j - \omega_i$. The validity of this effective model is subject to the off-resonant driving condition $|\Omega_{ij}/\Delta_{ji}(\omega)| \ll 1$. By taking into account the phase of the drive, the effective Hamiltonian can be written as

$$H^{\rm eff}/\hbar = \frac{\Delta_z(\omega)}{2}\sigma_z + \frac{\Delta_x(\omega)}{2}\sigma_x, \tag{C.3}$$

from which we expect to see Rabi oscillations for $\Delta_x(\omega)/\Delta_z(\omega) \gg 1$ (Raman gate). Figure C1 shows this ratio as a function of the 0–π-circuit design parameters and optimized with respect to the drive frequency ω under the off-resonant-drive condition. We observe that $\Delta_x(\omega)/\Delta_z(\omega)$ remains small throughout the analyzed range of parameters. Furthermore, this ratio is smaller than 10^{-4} when considering the 0–π parameters of figure C1 with vanishing overlap between logical wave functions. Additionally, we show the result of the optimization for a full flux excursion (figure inset). Despite an appreciable increase of $\Delta_x(\omega)/\Delta_z(\omega)$ with $\Phi_{\rm ext}/\Phi_0$, we find this improvement not enough to allow for qubit control.

Considering instead a drive addressing ϕ, we perform the optimization of $\Delta_x(\omega)/\Delta_z(\omega)$ to again find, in the majority of cases, only a negligible σ_x component in the effective Hamiltonian equation (C.3). Interestingly, we have also identified some qubit design parameters for which $H^{\rm eff} \propto \sigma_x$. However, such configurations are sparsely distributed over the range numerically explored, and the results are sensitive to small parameter deviations. Therefore, driving ϕ does not appear to be a practical solution.

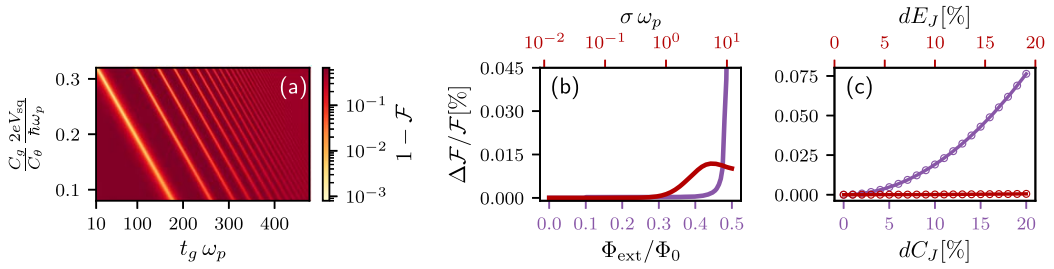

Figure D1. Variation in the gate fidelity for the 0–π qubit design parameters $(E_L/\hbar\omega_p,\ E_{C_\phi}/\hbar\omega_p,\ E_{C_\theta}/\hbar\omega_p,\ E_J/\hbar\omega_p) = (10^{-3},\ 0.378,\ 1.75\times10^{-4},\ 0.165)$. (a) Gate infidelity in the (V_θ, t_g) plane. Brighter regions correspond to high-fidelity qubit operations from where the optimal drive amplitude and duration is determined (see appendix D.1). (b) Relative change in gate fidelity as a function of the voltage-drive turn-on and -off time σ (in red), and the phase associated to the external magnetic flux $\Phi_{\rm ext}$ (in violet). (c) Effect of disorder in E_J (in red) and C_J (in violet) on the gate fidelity.

C.2. Two-tone driving

We now investigate if the presence of multiple drives could help to overcome the off-diagonal component cancellation found above, in particular by optimizing on the relative phase of these drives. In the presence of two microwave voltage pulses (labeled as d_1 and d_2), the qubit Hamiltonian reads

$$H/\hbar = \sum_{i=0}^{M}\omega_i\sigma_{ii} + \sum_{i=0,1}\sum_{j=2}^{M}\sum_{k=1,2}(\Omega_{ij}^{k}e^{-i\omega^{d_k}t}\sigma_{ji} + \text{h.c.}). \tag{C.4}$$

Following again the procedure in [61], we find

$$H^{\rm eff}/\hbar = \sum_{i,i'=0,1}\left(\omega_i\delta_{ii'} - \frac{1}{2}\sum_{k,l=1,2}\sum_{j=2}^{M}e^{i\omega^{d_{kl}}t}\frac{(\Omega_{ij}^{d_k})^{*}\Omega_{i'j}^{l}[\Delta_{ji}(\omega^{d_k}) + \Delta_{ji'}(\omega^{d_l})]}{\left[i\frac{\gamma_j}{2} + \Delta_{ji}(\omega^{d_k})\right]\left[-i\frac{\gamma_j}{2} + \Delta_{ji'}(\omega^{d_l})\right]}\right)\sigma_{ii'}, \tag{C.5}$$

where $\omega^{d_{kl}} = \omega^{d_k} - \omega^{d_l}$ is the difference between two drive frequencies. We note that, if the two drives have the same frequency, their relative phase is factored out of the transition amplitude, thus reducing equation (C.5) to equation (C.2). The most general situation, however, was investigated by numerical simulation of equation (C.4) and equation (C.5). None of the explored qubit design parameters and drive frequencies have shown a significant change with respect to what was found in the single-drive case.

Appendix D. Gate fidelity as a function of control parameters and circuit-element disorder in E_J and C_J

In this section, we study the gate fidelity accounting for the effect of pulse shaping and moderate deviations in the external flux that sets the qubit operating point. Moreover, we investigate the gate fidelity in the presence of circuit-element disorder introducing additional $\phi \leftrightarrow \theta$ coupling and a spurious drive on ϕ, without involving the ζ-mode.

D.1. Gate fidelity as a function of drive strength and duration

To understand how pulse shaping affects the gate performance, we first analyze the effect of the drive strength and duration. In figure D1(a), we show the gate infidelity considering a square voltage pulse of amplitude $V_{\rm sq}$ and duration t_g. There, the diagonal features are high-fidelity regions. While the first of these (starting from the left) corresponds to a σ_x gate operation, the second corresponds to an identity operation or σ_x^2. This pattern repeats itself for the subsequent pairs of features as t_g increases, but with decreasing gate fidelity due to leakage errors. The nonregular spacing of the high-fidelity regions indicates that, in contrast to more standard gate schemes, the proposed single-qubit gate has a nonlinear dependence on the drive strength and the evolution time. In fact, the first high-fidelity feature has a hyperbolic shape (visible on a larger scale) defined by the relation $(C_g/C_\theta)2eV_{\rm sq}/\hbar \times t_g \simeq \pi$, which is derived from a short-time approximation of the gate propagator. The fidelity along such hyperbola is not constant, and there exist an optimal drive strength and gate time about which the gate fidelity is maximal and, to first order, insensitive to deviations. Such an optimal point, computed as a function of the qubit design parameters, has been used to produce the results in figure 7. Away from the optimal point, however, the slow decrease of the gate fidelity along the mentioned hyperbola could be leveraged to extend the gate time if necessary for control purposes.

D.2. Variations in gate fidelity for a shaped pulse

We now consider the effect of a hyperbolic-tangent pulse shape with a finite turn on and shutdown time σ. In this section, the pulse area and maximum drive strength are kept constant and equal to those of the optimal square pulse. The latter is also used as a standard to obtain the relative change of the gate fidelity shown in red in figure D1(b). As can be seen, the gate fidelity remains almost unchanged in a wide range of σ, including turn-on and -off times that are comparable to the total optimal square-pulse length. The same conclusion applies to all the qubit design parameters considered in this work.

D.3. Gate fidelity as a function of flux

We have so far discussed the gate fidelity for a qubit operating at $\Phi_{\rm ext}/\Phi_0 = 0$ ($\varphi_{\rm ext} = 0$). In this section, however, we investigate the effect of external flux variations. Figure D1(b) shows the relative change of the gate fidelity as a function of $\Phi_{\rm ext}/\Phi_0$ (in violet). Here, the fidelity is computed with respect to a fixed gate unitary determined at $\Phi_{\rm ext}/\Phi_0 = 0$, while the voltage-drive parameters are kept to the optimal values determined for such a configuration. These conditions ensure that we only observe the effect of varying the external flux. We note that gate fidelity remains essentially unchanged for small-to-moderate flux excursions from the qubit operating point. This behavior, which is in part a consequence of the small flux dispersion of the 0–π qubit, shows that the proposed gate will tolerate the small flux fluctuations that could arise in practice.

Since the external flux affects the hybridization of the 0–π logical wave functions, the former could be used to tune the gate operation similarly to what was shown in figure 7(b). Choosing the qubit design parameters such that the gate implements a σ_x operation at $\Phi_{\rm ext}/\Phi_0 = 0$, a slowly varying external flux would smoothly rotate the gate operation implementing a σ_z gate for $\Phi_{\rm ext}/\Phi_0 = 0.5$ ($\varphi_{\rm ext} = \pi$). However and as discussed above, because of the near degeneracy of the qubit states a device in the deep 0–π regime implies adiabatic sweep times in the millisecond range, thus limiting the applicability of the gate flux tunability.

D.4. Gate fidelity in presence of $E_{\rm J}$ and $C_{\rm J}$ disorder

Having previously considered the effect of circuit-element disorder that leads to coupling of the qubit degrees of freedom to the ζ-mode, we now consider disorder leading to additional parasitic coupling between ϕ and θ. Figure D1(c) shows the relative change of the gate fidelity due to disorder in $E_{\rm J}$ (in red) and $C_{\rm J}$ (in violet). We observe that the gate performance is only slightly affected in a realistic range of asymmetries, expected to be between 1% and 10%. A non-zero $\mathrm{d}C_{\rm J}$ results in a parasitic drive on the ϕ coordinate which has also been included in the simulations. For this same reason, we expect the gate fidelity to be robust to similar spurious-drive terms that could arise from slight differences in the response functions of the control circuitry. Because $E_{\rm J}$ disorder does not lead to such an unwanted drive, its effect on the gate fidelity is negligible in comparison.

Appendix E. Master equation for a cooled ζ-mode

In this section, we derive the effective ζ-mode master equation of equation (20). This is done using an adiabatic elimination of the external resonator under the assumption $g' \ll \kappa_b$. Recall that g' is the effective interaction strength between the b and the ζ modes in the interaction frame. Following [48], we treat the heavily damped external resonator as a bath for the ζ-mode. To this end, we specify the system and bath Hamiltonians, as $\hbar\omega_\zeta a^\dagger a$ and $\hbar\omega_b(t) b^\dagger b$, respectively. Going to a frame rotating at ω_ζ for the ζ-mode and at the modulated frequency $\omega_b(t)$ for the b-mode, the interaction Hamiltonian reads

$$H_I^{\rm int}(t) = -\bar{g}\,(a^\dagger f^*(t) - a f(t))(b_I^\dagger(t) - b_I(t)), \tag{E.1}$$

where $f(t) = \mathrm{e}^{-\mathrm{i}\omega_a t} + \frac{\varepsilon}{4\bar{\omega}_b}[\mathrm{e}^{-\mathrm{i}(\omega_a-\omega_m)t} + \mathrm{e}^{\mathrm{i}(\omega_a+\omega_m)t}]$, $b_I(t) = b\mathrm{e}^{-\mathrm{i}[\bar{\omega}_b t + \frac{\varepsilon}{\omega_m}\sin(\omega_m t)]}$. Here, the subindex I denotes the change of frame. Treating the bath in the Markov approximation, we compute the evolution of the ζ-mode density matrix as

$$\dot{\rho}_I^\zeta = -\mathrm{tr}_{\rm bath}[H_I^{\rm int}(t), \int_0^\infty \mathrm{d}t'[H_I^{\rm int}(t'),\, \rho_I(t)]]. \tag{E.2}$$

Factorizing $\rho_I(t) \simeq \rho_I^\zeta(t) \otimes \rho_I^{\rm bath}$, we expand the double commutator in equation (E.2) as a function of the b-mode correlation functions, which are computed neglecting backaction from the ζ-mode. More precisely, we employ the quantum regression formula [62] to obtain

$$\langle b_I(t+\tau) b_I^\dagger(t)\rangle = \langle b_I(t) b_I^\dagger(t)\rangle \exp\left[-\int_t^{t+\tau} \mathrm{d}t'(\mathrm{i}\omega_b(t') + \frac{\kappa_b}{2})\right]. \tag{E.3}$$

Assuming that the external resonator is in a state very close to vacuum at all times, we approximate $\langle b_I(t) b_I^\dagger(t)\rangle \simeq 1$, while the other three possible correlation functions being taken equal to zero. The validity of these various assumptions was verified with numerical simulations by plotting the corresponding expectation

values obtained from the full time-dependent master equations. Next, we use the Jacobi–Anger expansion to expand equation (E.3) as

$$\langle b_I(t)b_I^\dagger(t')\rangle \simeq \mathrm{e}^{-\frac{\kappa_b}{2}(t-t')}\mathrm{e}^{-\mathrm{i}\bar{\omega}_b(t-t')}\sum_{n,n'=-\infty}^{\infty} J_n\left(\frac{\varepsilon}{\omega_m}\right)J_{n'}\left(\frac{\varepsilon}{\omega_m}\right)\mathrm{e}^{-\mathrm{i}\omega_m(nt-n't')}. \tag{E.4}$$

Inserting equation (E.4) in (E.2), and retaining only the non-rotating terms, we obtain the following dissipative rates

$$\begin{aligned}\Gamma_\downarrow = \sum_{n=-\infty}^{\infty}\Bigg\{&\frac{\kappa_b\bar{g}^2J_n^2\left(\frac{\varepsilon}{\omega_m}\right)}{(\omega_\zeta-\bar{\omega}_b+n\omega_m)^2+\left(\frac{\kappa_b}{2}\right)^2}+\frac{\kappa_b\bar{g}^2\left(\frac{\varepsilon}{4\bar{\omega}_b}\right)^2J_n^2\left(\frac{\varepsilon}{\omega_m}\right)}{(\omega_\zeta-\bar{\omega}_b+(n-1)\omega_m)^2+\left(\frac{\kappa_b}{2}\right)^2}\\&+\frac{\kappa_b\bar{g}^2\left(\frac{\varepsilon}{4\bar{\omega}_b}\right)^2J_n^2\left(\frac{\varepsilon}{\omega_m}\right)}{(\omega_\zeta-\bar{\omega}_b+(n+1)\omega_m)^2+\left(\frac{\kappa_b}{2}\right)^2}+\frac{2\kappa_b\bar{g}^2\left(\frac{\varepsilon}{4\bar{\omega}_b}\right)J_n\left(\frac{\varepsilon}{\omega_m}\right)J_{n+1}\left(\frac{\varepsilon}{\omega_m}\right)}{(\omega_\zeta-\bar{\omega}_b-n\omega_m)^2+\left(\frac{\kappa_b}{2}\right)^2}\\&+\frac{2\kappa_b\bar{g}^2\left(\frac{\varepsilon}{4\bar{\omega}_b}\right)J_n\left(\frac{\varepsilon}{\omega_m}\right)J_{n+1}\left(\frac{\varepsilon}{\omega_m}\right)}{(\omega_\zeta-\bar{\omega}_b-(n+1)\omega_m)^2+\left(\frac{\kappa_b}{2}\right)^2}+\frac{2\kappa_b\bar{g}^2\left(\frac{\varepsilon}{4\bar{\omega}_b}\right)^2J_n\left(\frac{\varepsilon}{\omega_m}\right)J_{n+2}\left(\frac{\varepsilon}{\omega_m}\right)}{(\omega_\zeta-\bar{\omega}_b-(n+1)\omega_m)^2+\left(\frac{\kappa_b}{2}\right)^2}\Bigg\},\end{aligned} \tag{E.5}$$

and

$$\begin{aligned}\Gamma_\uparrow = \sum_{n=-\infty}^{\infty}\Bigg\{&\frac{\kappa_b\bar{g}^2J_n^2\left(\frac{\varepsilon}{\omega_m}\right)}{(\omega_\zeta+\bar{\omega}_b-n\omega_m)^2+\left(\frac{\kappa_b}{2}\right)^2}+\frac{\kappa_b\bar{g}^2\left(\frac{\varepsilon}{4\bar{\omega}_b}\right)^2J_n^2\left(\frac{\varepsilon}{\omega_m}\right)}{(\omega_\zeta+\bar{\omega}_b-(n+1)\omega_m)^2+\left(\frac{\kappa_b}{2}\right)^2}\\&+\frac{\kappa_b\bar{g}^2\left(\frac{\varepsilon}{4\bar{\omega}_b}\right)^2J_n^2\left(\frac{\varepsilon}{\omega_m}\right)}{(\omega_\zeta+\bar{\omega}_b-(n-1)\omega_m)^2+\left(\frac{\kappa_b}{2}\right)^2}+\frac{2\kappa_b\bar{g}^2\left(\frac{\varepsilon}{4\bar{\omega}_b}\right)J_n\left(\frac{\varepsilon}{\omega_m}\right)J_{n+1}\left(\frac{\varepsilon}{\omega_m}\right)}{(\omega_\zeta+\bar{\omega}_b+n\omega_m)^2+\left(\frac{\kappa_b}{2}\right)^2}\\&+\frac{2\kappa_b\bar{g}^2\left(\frac{\varepsilon}{4\bar{\omega}_b}\right)J_n\left(\frac{\varepsilon}{\omega_m}\right)J_{n+1}\left(\frac{\varepsilon}{\omega_m}\right)}{(\omega_\zeta+\bar{\omega}_b+(n+1)\omega_m)^2+\left(\frac{\kappa_b}{2}\right)^2}+\frac{2\kappa_b\bar{g}^2\left(\frac{\varepsilon}{4\bar{\omega}_b}\right)^2J_n\left(\frac{\varepsilon}{\omega_m}\right)J_{n+2}\left(\frac{\varepsilon}{\omega_m}\right)}{(\omega_\zeta+\bar{\omega}_b+(n+1)\omega_m)^2+\left(\frac{\kappa_b}{2}\right)^2}\Bigg\}.\end{aligned} \tag{E.6}$$

Maximizing each of the summands in equations (E.5) and (E.6), and discarding all but most significant terms, these expressions reduce to the forms $\Gamma_\downarrow = \frac{4g'^2}{\kappa_b}$ and $\Gamma_\uparrow = \frac{4g'^2}{\kappa_b}\Big/\left[\left(\frac{2\omega_\zeta}{\kappa_b/2}\right)^2+1\right]$ quoted in the main text of the article. We note that the interaction of the ζ-mode with the b-mode also leads to a frequency shift which can be taken into account by a slight renormalization of the modulation frequency ω_m. This effect is negligible for the parameter regime considered here.

References

[1] Fowler A G, Mariantoni M, Martinis J M and Cleland A N 2012 *Phys. Rev.* A **86** 032324
[2] Reiher M, Wiebe N, Svore K M, Wecker D and Troyer M 2017 Elucidating reaction mechanisms on quantum computers *Proc. Natl Acad. Sci.* **114** 7555–60
[3] Bacon D, Flammia S T, Harrow A W and Shi J 2017 *IEEE Trans. Inf. Theory* **63** 2464–79
[4] Pastawski F and Yoshida B 2015 *Phys. Rev.* A **91** 012305
[5] Jones C, Brooks P and Harrington J 2016 *Phys. Rev.* A **93** 052332
[6] Tuckett D K, Bartlett S D and Flammia S T 2018 Ultrahigh error threshold for surface codes with biased noise *Phys. Rev. Lett.* **120** 050505
[7] Delfosse N and Nickerson N H 2017 arXiv:1709.06218
[8] Martinis J M 2015 Qubit metrology for building a fault-tolerant quantum computer *npj Quantum Inf.* **1** 15005
[9] Devoret M H and Schoelkopf R J 2013 *Science* **339** 1169–74
[10] Gu X, Kockum A F, Miranowicz A, Liu Y X and Nori F 2017 *Phys. Rep.* **718** 1–102
[11] Martinis J M *et al* 2005 *Phys. Rev. Lett.* **95** 210503
[12] Geerlings K, Shankar S, Edwards E, Frunzio L, Schoelkopf R and Devoret M 2012 *Appl. Phys. Lett.* **100** 192601
[13] Barends R *et al* 2011 *Appl. Phys. Lett.* **99** 113507
[14] Córcoles A D, Chow J M, Gambetta J M, Rigetti C, Rozen J R, Keefe G A, Beth Rothwell M, Ketchen M B and Steffen M 2011 *Appl. Phys. Lett.* **99** 181906
[15] Rigetti C *et al* 2012 *Phys. Rev.* B **86** 100506
[16] Paik H *et al* 2011 *Phys. Rev. Lett.* **107** 240501
[17] Reagor M *et al* 2013 *Appl. Phys. Lett.* **102** 192604
[18] Koch J, Yu T M, Gambetta J M, Houck A A, Schuster D I, Majer J, Blais A, Devoret M H, Girvin S M and Schoelkopf R J 2007 *Phys. Rev.* A **76** 42319
[19] Manucharyan V E, Koch J, Glazman L I and Devoret M H 2009 *Science* **326** 113–6

[20] Brooks P, Kitaev A and Preskill J 2013 *Phys. Rev.* A **87** 52306
[21] Kitaev A 2006 arXiv:cond-mat/0609441
[22] Groszkowski P, Di Paolo A, Grimsmo A, Blais A, Schuster D, Houck A and Koch J 2018 *New J. Phys.* **20** 043053
[23] Dempster J M, Fu B, Ferguson D G, Schuster D I and Koch J 2014 *Phys. Rev.* B **90** 94518
[24] Masluk N A, Pop I M, Kamal A, Minev Z K and Devoret M H 2012 *Phys. Rev. Lett.* **109** 137002
[25] Bell M, Sadovskyy I, Ioffe L, Kitaev A Y and Gershenson M 2012 *Phys. Rev. Lett.* **109** 137003
[26] Hazard T, Gyenis A, Di Paolo A, Asfaw A, Lyon S, Blais A and Houck A 2019 *Phys. Rev. Lett.* **122** 010504
[27] Manucharyan V E 2012 Superinductance *Ph.D. Thesis* Yale University
[28] Masluk N A, Pop I M, Kamal A, Minev Z K and Devoret M H 2012 *Phys. Rev. Lett.* **109** 137002
[29] Bell M, Sadovskyy I, Ioffe L, Kitaev A Y and Gershenson M 2012 *Phys. Rev. Lett.* **109** 137003
[30] Bell M T, Paramanandam J, Ioffe L B and Gershenson M E 2014 *Phys. Rev. Lett.* **112** 167001
[31] Devoret M H *et al* 1995 Quantum fluctuations in electrical circuits *Les Houches, Session LXIII* **7** 8
[32] Burkard G, Koch R H and DiVincenzo D P 2004 *Phys. Rev.* B **69** 064503
[33] Zhu G, Ferguson D G, Manucharyan V E and Koch J 2013 *Phys. Rev.* B **87** 024510
[34] Cross A W and Gambetta J M 2015 *Phys. Rev.* A **91** 032325
[35] Puri S and Blais A 2016 *Phys. Rev. Lett.* **116** 180501
[36] Douçot B and Ioffe L 2012 *Rep. Prog. Phys.* **75** 072001
[37] Goerz M H, Gualdi G, Reich D M, Koch C P, Motzoi F, Whaley K B, Vala J, Müller M M, Montangero S and Calarco T 2015 *Phys. Rev.* A **91** 062307
[38] Reich D and Goerz M 2018 private communication
[39] Johansson J, Nation P and Nori F 2012 *Comput. Phys. Commun.* **183** 1760–72
[40] Raftery J, Vrajitoarea A, Zhang G, Leng Z, Srinivasan S and Houck A 2017 arXiv:1703.00942
[41] Czylwik A, Bieder S and Sichma M 2017 Extreme wideband arbitrary waveform generator based on frequency multiplexing *32nd URSI GASS* (https://doi.org/10.23919/URSIGASS.2017.8105129)
[42] Khaneja N, Reiss T, Kehlet C, Schulte-Herbrüggen T and Glaser S J 2005 *J. Magn. Reson.* **172** 296–305
[43] Schulte-Herbrüggen T, Spörl A, Khaneja N and Glaser S 2011 *J. Phys. B: At. Mol. Opt. Phys.* **44** 154013
[44] Boutin S, Andersen C K, Venkatraman J, Ferris A J and Blais A 2017 *Phys. Rev.* A **96** 042315
[45] Berry M 2009 *J. Phys. A: Math. Theor.* **42** 365303
[46] Motzoi F and Wilhelm F K 2013 *Phys. Rev.* A **88** 062318
[47] Tian L 2009 *Phys. Rev.* B **79** 193407
[48] Marquardt F, Clerk A and Girvin S 2008 *J. Mod. Opt.* **55** 3329–38
[49] Castellanos-Beltran M and Lehnert K 2007 *Appl. Phys. Lett.* **91** 083509
[50] Stockklauser A, Scarlino P, Koski J V, Gasparinetti S, Andersen C K, Reichl C, Wegscheider W, Ihn T, Ensslin K and Wallraff A 2017 *Phys. Rev.* X **7** 011030
[51] Sandberg M, Wilson C, Persson F, Bauch T, Johansson G, Shumeiko V, Duty T and Delsing P 2008 *Appl. Phys. Lett.* **92** 203501
[52] Hatridge M, Vijay R, Slichter D, Clarke J and Siddiqi I 2011 *Phys. Rev.* B **83** 134501
[53] Eichler C, Salathe Y, Mlynek J, Schmidt S and Wallraff A 2014 *Phys. Rev. Lett.* **113** 110502
[54] Kitaev A Y 2001 *Phys.—Usp.* **44** 131
[55] Lutchyn R M, Sau J D and Sarma S D 2010 *Phys. Rev. Lett.* **105** 077001
[56] Oreg Y, Refael G and von Oppen F 2010 *Phys. Rev. Lett.* **105** 177002
[57] Huang W C, Liang Q F, Yao D X and Wang Z 2015 *Phys. Rev.* A **92** 012308
[58] Aasen D *et al* 2016 *Phys. Rev.* X **6** 031016
[59] Petrescu A, Türeci H E, Ustinov A V and Pop I M 2018 *Phys. Rev.* B **98** 174505
[60] Shen F 2015 Theoretical analysis of a protected superconducting qubit *Master's Thesis* University of Waterloo
[61] Reiter F and Sørensen A S 2012 *Phys. Rev.* A **85** 032111
[62] Gardiner C and Zoller P 2000 *Quantum Noise: A Handbook of Markovian and Non-Markovian Quantum Stochastic Methods with Applications to Quantum Optics* vol 56 (Berlin: Springer)

Chapter 5

Experimental realization of an intrinsically error-protected superconducting qubit

5.1 Motivation

In this section, we present the paper titled "Experimental realization of an intrinsically error-protected superconducting qubit". This work, done in collaboration with the group of Andrew Houck at Princeton, is the first experimental demonstration of a $0-\pi$ qubit.

As argued in previous sections, realizing the $0-\pi$ qubit requires to overcome several challenges. Firstly, one needs to be able to build large superinductors with greatly reduced stray capacitances. Secondly, the device layout needs to be optimized such that the large cross-capacitances of the circuit dress the capacitance of the ϕ mode (C_ϕ) as little as possible. Achieving these conditions is part of an engineering and fabrication problem.

In this experiment, the large cross-capacitances are realized by two tightly interdigitated (niobium) capacitors placed at a large distance from each other. Interdigitated capacitors are known to cause dielectric losses due to the small gap between the capacitor fingers and the large electric fields at the edges of such features. For this reason, while the first implementations of the transmon qubit employed this type of design [96, 97] , the field has moved away from it in more recent years. However, the small gap between the capacitor fingers condenses a large portion of the electric field within the capacitor fingers, resulting in a large capacitance between the electrodes. Furthermore, since the electric field

is heavily localized to this part of the circuit, the formation of spurious stray capacitances with other parts of the circuit is reduced. Due to the extremely small overlap of the logical wavefunctions of the $0-\pi$ qubit, dielectric losses are not as detrimental as in the case of the transmon qubit. Thus, the $0-\pi$ qubit can afford relatively lossy capacitors in order to realize a sufficiently light ϕ mode. In some sense, the realization of this qubit has been made possible by unlearning the lessons learned working for many years on the transmon qubit.

This work introduces the soft $0-\pi$ regime. In this regime, the sensitivity to charge noise is exponentially reduced and flux-noise insensitivity is realized at first order. Moreover, relaxation due to charge, flux and other sources of noise is exponentially reduced by engineering two logical states with exponentially small overlap. We find that a detailed theoretical model based on the circuit Hamiltonian introduced in chapter 2 captures very accurately the device transitions as a function of both the offset charge and the external flux. This confirmation is of great value for the design of the next generation of devices towards the noise-protected regime.

5.2 Main results of the paper

The main results of this paper is the realization of the $0-\pi$ qubit in a 'soft' parameter regime [see Fig. 5.1 (a)]. In particular, the energy parameters for the device are $E_L/h \simeq 0.38\,\mathrm{GHz}$, $E_{C_\theta}/h \simeq 0.092\,\mathrm{GHz}$, $E_J/h \simeq 6.0\,\mathrm{GHz}$ and $E_{C_\phi}/h \simeq 1.14\,\mathrm{GHz}$. In order to achieve the soft $0-\pi$ regime, the experimental setup includes two superinductors realized by 200 junctions each [Fig. 5.1 (b)], and two large interdigitated capacitances [Fig. 5.1 (c)]. The qubit is also capacitively coupled to a coplanar-waveguide resonator operated in transmission mode, with a coupling geometry that minimizes stray capacitances. As discussed in chapter 4, coupling to the ϕ degree of freedom is in general more advantageous than coupling to the θ mode. For this reason, while the resonator couples to both ϕ and θ in the experiment, the coupling capacitance matrix is engineered such that $\beta_\phi \simeq 0.27 \gg \beta_\theta \simeq 6.6\times10^{-3}$.

In the soft $0-\pi$ regime, the ground state is localized within the $\theta = 0$ valley, due to the exponentially suppressed tunneling amplitude in the θ direction. However, due to the relatively large (low) value of E_L (E_J) compared to what is needed to reach the deep $0-\pi$ regime, the first excited state is also localized in the $\theta = 0$ valley. The ground state of the $\theta = \pi$ valley appears at a higher energy and corresponds to the second excited state of the circuit for zero flux bias. Since the potential energy of the π valley has two

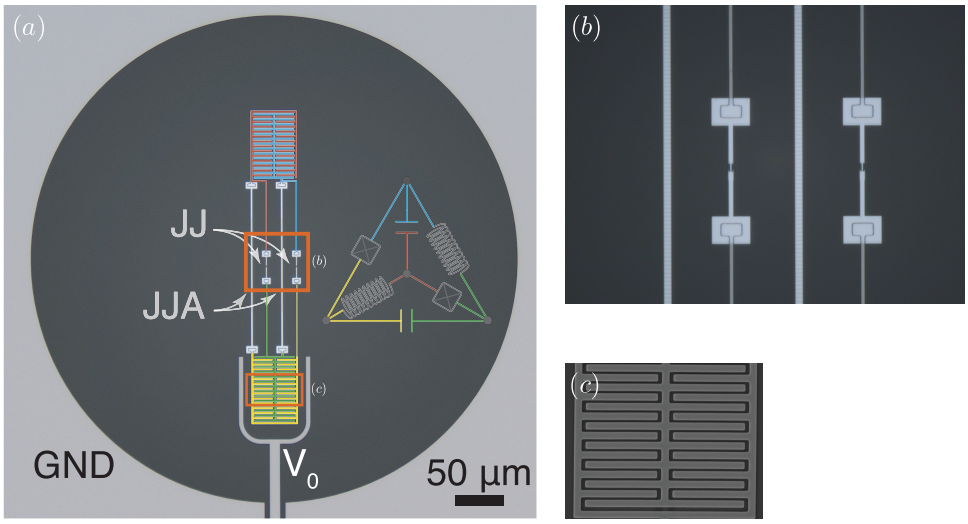

Figure 5.1 Experimental realization of the $0-\pi$ qubit. The color code for capacitors, junctions and inductors is provided by the accompanying schematic. The label JJ indicates the two 'black-sheep' Josephson junctions of the circuit, while 'JJA' indicates the array junctions. (a) Full $0-\pi$ circuit. (b) Zoom in on the 'black-sheep' junctions and superinductors. (c) Zoom in on the cross-capacitances. Adapted from [105].

degenerate wells corresponding to $\phi \simeq \pm\pi$, the second excited state of the circuit is given by the symmetric (bonding) combination of two fluxon-like states, one of which being located at $(\theta, \phi) = (\pi, \pi)$ and the other at $(\theta, \phi) = (\pi, -\pi)$. The third excited state corresponds to the antisymmetric (antibonding) combination of the same fluxon-like states and, therefore, the third excitation is also located in the $\theta = \pi$ valley. The energy splitting between these bonding and antibonding states is given by the tunneling energy along the ϕ direction, leading to a gap $\Delta/h \simeq 20\,\text{MHz}$ between these states. This gap is large enough to selectively address the second excited level and use it as a logical $|1\rangle$. As a result, that state and the groundstate of the $\theta = 0$ valley realize two qubit states with disjoint support.

Since the logical states have exponentially small overlap, the only option to control the qubit is to exploit the multilevel structure of the device. This is done by using an intermediary level that has support in both $\theta = 0$ and $\theta = \pi$ potential wells. This way, the intermediary level can connect the two logical states by a virtual transition. Importantly, the intermediary state needs to be carefully selected to avoid the effect of charge dispersion. Indeed, since states with support in both potential wells appear at high energies, the charge dispersion for such levels is expected to be generally large. Quite interestingly, however, the existence of symmetry rules leads to some of the high-frequency levels to displaying a very weak charge dispersion, and thus to become ideal ancillary states. This is one of the important findings of this work.

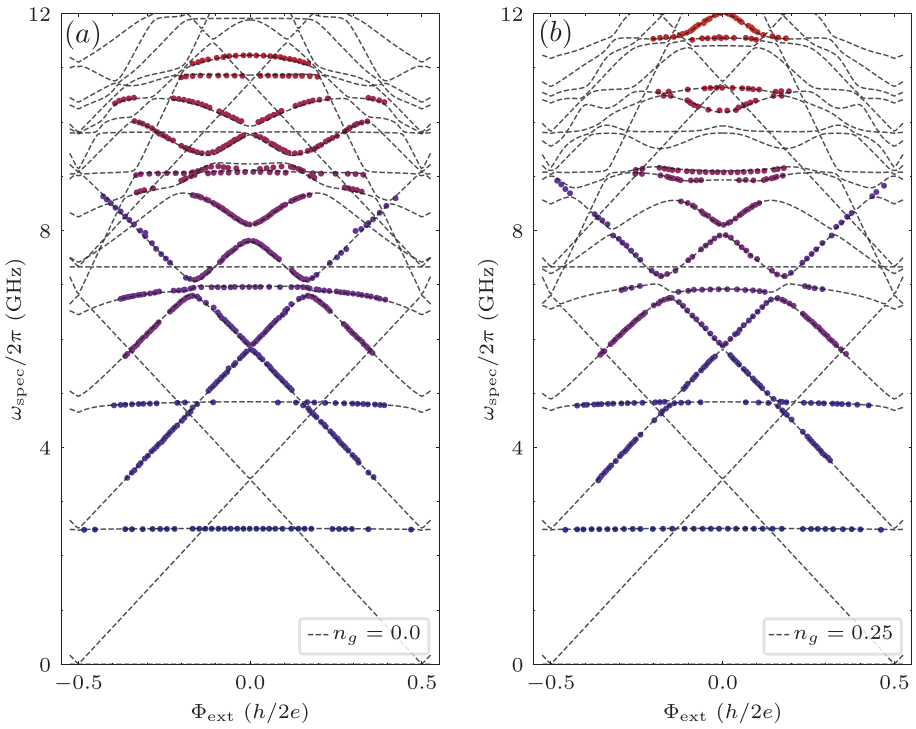

Figure 5.2 Two-tone spectroscopy results for the soft $0-\pi$ device and spectrum fit as a function of flux for the offset-charge biases $n_g = 0$ (a) and $n_g = 0.25$ (b). Colored circles correspond to the experimental data while the theory fit is shown as black dashed lines. The agreement on a large frequency range is remarkable. Note that some of the qubit transitions are invisible in the experiment due to exponentially small matrix elements or vanishing dispersive shifts. The transition around 7.35 GHz corresponds to the readout resonator. Adapted from [105].

In the experiment, the ancillary level corresponds to the 9th excited state of the circuit. In order to characterize the energy spectrum, we use two-tone spectroscopy and Autler-Townes spectroscopy [106] (see also Sect. 6.2.2). Autler-Townes spectroscopy is key to the experiment, as it allows us to determine an optimal offset-charge bias point for the qubit which we find to be $n_g = 0.25$. Operating at this bias point renders the transition matrix element between the logical and ancillary states insensitive to quasiparticle poisoning. This allows us to tune Raman-type gates to achieve universal single-qubit control of the qubit manifold. This is used to determine $T_1 \simeq 1.6\,\text{ms}$ and $T_{2,\text{echo}} \simeq 25\,\mu\text{s}$ at the flux sweet spot. The remarkably large value of T_1 demonstrates the metastable character of the logical states, while a measurement of $T_{2,\text{echo}}$ as a function of the external flux demonstrates first order insensitivity for $\Phi_{\text{ext}} = 0$ (not shown).

From a theoretical point of view, the main result of this paper is the confirmation of the $0-\pi$ qubit Hamiltonian in Eq. (2.13). Fig. 5.2 shows a theory fit of the experimental

data using this Hamiltonian and incorporating the readout resonator into the model. The fit explains very well the experimental data in a very large frequency range ($\sim 12\,\mathrm{GHz}$), both as a function of the external flux and the offset-charge bias. Moreover, the theoretical model also describes some of the transition matrix elements that can be measured [105]. We provide more details on this in the paper attached below.

5.3 Conclusion and outlook

This work demonstrates the first experimental realization of the $0-\pi$ qubit. It moreover demonstrates exponential noise protection against relaxation and first-order protection against dephasing due to flux noise.

This experimental realization also confirms the theoretical model used for many years to study the $0-\pi$ qubit. This is a remarkable finding, where a two-mode Hamiltonian is able to capture at least 17 transitions of a complex artificial atom that involves more than 400 Josephson junctions. This is an excellent example of the agreement between experiments and theory that is possible in the field of superconducting circuits. The modeling, however, includes many details that are necessary to describe the experimental setup accurately. These theoretical details were addressed for the first time in this work.

Finally, we hope that the quality of the experimental results, and the simplicity of the theoretical model, will motivate future work on the $0-\pi$ qubit and suggest that this device can be the building block of a scalable quantum-information processing architecture.

Experimental realization of an intrinsically error-protected superconducting qubit

András Gyenis,[1*] Pranav S. Mundada,[1*] Agustin Di Paolo,[2*] Thomas M. Hazard,[1] Xinyuan You,[3] David I. Schuster,[4] Jens Koch,[5] Alexandre Blais,[2,6] Andrew A. Houck,[1†]

[1]Department of Electrical Engineering, Princeton University, Princeton, New Jersey 08544, USA

[2]Institut quantique & Département de Physique, Université de Sherbrooke, Sherbrooke J1K2R1 Quebec, Canada

[3] Graduate Program in Applied Physics, Northwestern University, Evanston, Illinois 60208, USA

[4] The James Franck Institute and Department of Physics, University of Chicago, Chicago, Illinois 60637, USA

[5] Department of Physics and Astronomy, Northwestern University, Evanston, Illinois 60208, USA

[6]Canadian Institute for Advanced Research, Toronto, M5G1M1 Ontario, Canada

[*]These authors contributed equally to this work.

[†]To whom correspondence should be addressed; E-mail: aahouck@princeton.edu.

Encoding a qubit in logical quantum states with wavefunctions characterized by disjoint support and robust energies can offer simultaneous protection against relaxation and pure dephasing. Using a circuit-quantum-electrodynamics architecture, we experimentally realize a superconducting $0-\pi$ qubit, which hosts protected states suitable for quantum-information processing. Multi-tone spectroscopy measurements reveal the energy level structure of the system, which can be precisely described by a simple two-mode Hamiltonian. We find that the parity symmetry of the qubit results in charge-insensitive levels connecting the protected states, allowing for logical operations. The measured relaxation (1.6 ms) and dephasing times (25 μs) demonstrate that our implementation of the $0-\pi$ circuit not only broadens the family of superconducting qubits, but also represents a promising candidate for the building block of a fault-tolerant quantum processor.

Preserving the coherence of a quantum superposition over prolonged times is key for large-scale quantum-information processing (*1–3*). For example, quantum error correction protects states by using a large number of physical qubits to encode a single logical qubit (*4–7*). A complementary approach to maintain coherence over long timescales is to develop qubits which are intrinsically protected against decoherence (*8–19*). Such protection arises because quantum information in these circuits is encoded in delocalized collective states capable of withstanding errors originating from local noise. One of the most promising candidates for a fully-protected qubit is the $0-\pi$ circuit (Fig. 1A) proposed by Kitaev, Brooks and Preskill (*11, 12*). However, protected circuits generally impose taxing requirements on the parameters of the physical device that are beyond the feasibility of current technologies. In this work, we realize a slightly modified version of the $0-\pi$ qubit by reducing the energy scales of its parameters to an experimentally obtainable regime. We demonstrate exponential protection against relaxation for the offset-charge-insensitive logical states, and show that dephasing due to flux noise is first-order suppressed. This manifests in significantly enhanced relaxation and coherence times and makes the $0-\pi$ circuit a leading contender for a superconducting quantum computer.

Because the coherence of a qubit is affected by energy relaxation and pure-dephasing processes, protected qubits must be robust against both of these mechanisms. According to Fermi's golden rule, the decay rate of an excited state is proportional to the square of the matrix element that connects it to other states via a noise operator. Thus, a circuit with a Hamiltonian that has eigenstates with disjoint support can prevent rapid loss of information (*20, 21*). Such protection against relaxation, however, is insufficient to stabilize the phase of a superposition of logical states. The key idea of our work is to engineer a superconducting circuit where the energies of disjoint states are also robust against environmental noises. As we show here, this can be achieved in certain parameter regimes of the $0-\pi$ circuit.

The $0-\pi$ qubit consists of identical pairs of small Josephson junctions, large shunting capacitors and superinductors, which are all organized in a single closed loop geometry with four nodes (Fig. 1A). The circuit has four degrees of freedom (*13*), which we refer to as the ϕ, θ, ζ and Σ modes,

and correspond to the linear combinations of the phase difference of the superconducting order parameter across the various elements in the circuit (Fig. 1C). Among them, the Σ mode is cyclic, while the ζ mode represents a harmonic mode that decouples from the other modes in the absence of circuit-element disorder. The remaining ϕ and θ modes describe the qubit degrees of freedom of the circuit with the following two-mode Hamiltonian

$$H_{0-\pi} = 4E_C^{\theta}(n_\theta - n_g^{\theta})^2 + 4E_C^{\phi}n_\phi^2 - 2E_J\cos\theta\cos(\phi - \pi\Phi_{\rm ext}/\Phi_0) + E_L\phi^2. \quad (1)$$

Here, $E_C^{\theta(\phi)} = e^2/2C_{\theta(\phi)}$ denotes the charging energy corresponding to the θ (ϕ) mode with total capacitance of $C_{\theta(\phi)}$, E_J is the Josephson energy, $E_L = \Phi_0^2/4\pi^2 L$ is the inductive energy of the superinductor with inductance L, $\Phi_0 = h/2e$ is the magnetic flux quantum (with e the electron charge and h the Planck's constant), $\Phi_{\rm ext}$ is the external magnetic flux threaded through the loop of the device, n_g^{θ} is the offset-charge bias due to the electrostatic environment, whereas n_θ and n_ϕ are the canonical charge operators corresponding to the phase operators (in units of $2e$). In the phase representation of quantum electromagnetic circuits (*22*), the capacitive energies of the device determine the kinetic energies of the modes, while the staggered double well potential of the $0-\pi$ qubit is realized by the inductors and Josephson junctions (Fig. 1B).

Remarkably, the three physical modes of the $0-\pi$ circuit are analogous to the three fundamental representatives of superconducting qubits: the transmon (*23*), the fluxonium (*24*) and the cavity (*25*). Indeed, as Fig. 1C shows, the θ mode describes the superconducting phase difference across the large shunting capacitors and the Josephson junctions, leading to a transmon-like behavior (*23*). On the other hand, the ϕ mode corresponds to the phase drop across the Josephson junctions and the superinductors, which features a fluxonium-type response (*24*). Finally, the ζ mode arises from the phase difference across the superinductances and the shunting capacitors, resulting in a low-energy harmonic mode.

As the intrinsic protection of the $0-\pi$ qubit emerges from the interplay of its effective double-well potential and the anisotropic kinetic energy of the modes (*11–15*), engineering the proper energy scales in the $0-\pi$ qubit is crucial. We first consider the case of protection against energy relaxation, which is provided by localizing the qubit wavefunctions in either the $\theta = 0$ or in the $\theta = \pi$ valley

(Fig. 1B). The circuit realizes a double-well potential with two fluxonium-like potentials, $V(\phi, \theta = 0, \pi) = \mp 2E_J \cos(\phi) + E_L\phi^2$, along the 0 and π valleys. The two potentials are displaced with respect to each other such that the $\theta = 0$ valley has a single minimum at $\phi = 0$, whereas the $\theta = \pi$ valley features two minima around $\phi \simeq \pm\pi$. Importantly, the potential energy difference between the valleys ($E_L\pi^2$) due to the quadratic inductive term corresponds approximately to the transition frequency between the ground states of the two valleys, i.e., the logical qubit energy. To ensure that the logical excited state is localized along the θ direction, first, the effective barrier height separating the valleys ($\sim 4E_J$) is required to be much larger than the qubit transition energy, which we realize with $E_J/E_L \approx 16$. Second, as the tunneling amplitude between the valleys is exponentially reduced with the ratio of barrier height and kinetic energy (*23*), we choose $E_J/E_C^\theta \approx 65$.

As the $0 - \pi$ qubit couples to charge and flux degrees of freedom through the θ and ϕ modes, we achieve protection from dephasing by taking advantage of the two-dimensional nature of the potential to combine the beneficial parameter regimes of the transmon and fluxonium qubits. First, to exponentially suppress the charge sensitivity of the qubit, we simply operate the compact θ mode in the transmon regime with $E_J/E_C^\theta \approx 65$ (*23*). Second, to overcome the flux sensitivity, we exploit the avoided crossing of the two lowest-lying levels of $\theta = \pi$ valley to engineer a first-order-insensitive magnetic sweet spot (Fig. 1D). Indeed, the presence of the $\phi \to -\phi$ symmetry at $\Phi_{\rm ext} = 0$ accompanied by two local minima in the potential of the π valley leads to degenerate doublets, which are hybridized due to the finite kinetic energy along the ϕ direction. Such hybridized (symmetric and antisymmetric) states show a hyperbolic dispersion as a function of external flux and a first-order-insensitive sweet spot at zero field (Fig. 1D). The gap size of the avoided crossing and consequently the protection against flux noise, is proportional to the tunneling rate between the two local minima of the π valley, therefore requiring a sufficiently large E_C^ϕ. Ultimately, the θ and ϕ modes are rendered heavy and light, respectively, by an anisotropic kinetic-energy ratio of $E_C^\phi/E_C^\theta \approx 12$.

Figure 1E shows the energy spectrum and wavefunctions of our $0 - \pi$ circuit in the absence of external magnetic fields. In the 0 valley, the excitations are plasmon-like with wavefunctions similar to those of an anisotropic, two-dimensional harmonic oscillator. The nodes of the wavefunctions

appear first along the θ direction as the kinetic energy of the θ mode is much lower than that of the ϕ mode. In the π valley, the states appear in symmetric-antisymmetric pairs, with nodes again developing first along the θ direction. Inspired by the quantum numbers of natural atoms, we denote low-lying energy levels as $|n^j_{lm}\rangle$, where the first quantum number $n = 0, \pi$ refers to the valley index, $l = s, p, d, f \ldots$ specifies the number of the nodes of the wavefunction, and $m = \theta, \phi$ determines the orientation of the nodes. Finally, for the states in the π valley, the superscript $j = +, -$, refers to the ϕ-parity of the state. In this work, we use the ground states of the two valleys, $|0_s\rangle$ and $|\pi^+_s\rangle$, as the logical qubit states.

We fabricated the $0 - \pi$ device using conventional lithographic techniques in a two-dimensional circuit-QED architecture (Fig. 2A and B). To probe the qubit using dispersive readout (*26, 27*), we capacitively coupled it to a coplanar-waveguide cavity with resonant frequency $\omega_c/2\pi = 7.328$ GHz and photon decay rate $\kappa/2\pi = 1.6$ MHz. As Fig. 2B shows, our primary goal for the circuit layout is to implement the highly anisotropic nature of the kinetic energies of the θ and ϕ modes with two tightly interdigitated niobium capacitors placed at a large distance from each other. Although this design increases the susceptibility of the device to dielectric losses due to the extremely small gap between the capacitor fingers (600 nm), it reduces the cross capacitances contributing to the light ϕ mode while maintaining a large enough capacitance ($C = 101$ fF) for the heavy θ mode, yielding $E^\theta_C/h = 92$ MHz and $E^\phi_C/h = 1.14$ GHz. The two small Josephson junctions are double-angle evaporated Al-AlO_x-Al Dolan-type junctions with $E_J/h = 6.0$ GHz, and each superinductor is realized by an array of 200 large Josephson junctions resulting in $E_L/h = 0.38$ GHz. We choose a hybrid resonator-coupling scheme where all four nodes of the qubit have considerable coupling capacitance to both the centerpin of the resonator and the ground plane, which allows us to address both the ϕ and θ modes in our measurements (*28*). The value of these coupling capacitances are carefully chosen to realize sufficiently large coupling rates for the qubit operation while minimizing stray capacitances associated with the light ϕ mode. Additionally, DC voltage-biasing the centerpin of the resonator allows us to tune the offset charges on the islands of the device.

To map out the energy spectrum of the $0 - \pi$ qubit, we perform standard two-tone spectroscopy

as a function of external magnetic flux and offset-charge bias. In the dispersive limit of circuit QED (*26, 27*), we can probe the excitation of various transitions by monitoring the transmission at the cavity frequency while sweeping the frequency of a second spectroscopic tone. At low frequencies (Fig. 2C), we detect the response of the harmonic ζ mode (*29*), while at higher frequencies the excitations of the anharmonic qubit modes are probed (Fig. 2D to F). As expected, the spectroscopic data obtained as a function of flux (Fig. 2D and E) reveal two types of transitions: intra-valley plasmon transitions in the 0 valley, which are characterized by flat almost flux-independent dispersions, and inter-valley fluxon excitations between the 0 and π wells, which have strong flux dependence. At offset charge $n_g^\theta = 0$ (Fig. 2D), we observe two distinct sets of transitions corresponding to the odd and even charge parity of the islands, which is the signature of the intermittent tunneling of unpaired quasiparticles across the junctions (*30–34*). By contrast, at $n_g^\theta = 0.25$ (Fig. 2E), we observe only one set of transitions, which indicates the insensitivity of the qubit to individual quasiparticle tunneling events. The dependence of the transition frequency on the charge parity is more apparent when we measure the qubit spectrum as a function of n_g^θ (Fig. 2F). At low energies, the transmon-like excitations have exponentially suppressed charge dispersions (*23, 31*), where we are unable to resolve the different charge-parity states. At higher frequencies, however, eye-like patterns appear with dispersions up to ~ 1 GHz due to the strong charge-sensitivity of the higher-lying levels. The spectral weight of the transitions with opposite parity is equal, which implies that both parities occur during the integration time of the spectroscopic measurements.

It is worth emphasizing that we find remarkable agreement between the simple two-mode Hamiltonian in Eq. (1) of the $0 - \pi$ qubit and the experimental data over the entire range of both offset charge and external flux (solid dashed lines in Fig. 2D to F). The relatively simple theoretical model not only captures accurately the energy level structure with at least 17 transitions and over a 12 GHz frequency range, but also predicts the cavity-assisted sideband transitions and qubit transitions due to thermal occupation of low-lying levels (*28*). This excellent agreement highlights that although the $0 - \pi$ artificial atom is constructed from the combination of 400 Josephson junctions and large capacitors, its effective dynamics is fairly simple, which is an inevitable requirement for a qubit to be

implemented in a large scale quantum processor.

Owing to the exponentially small dipole matrix element between the ground states of the valleys ($|0_s\rangle$ and $|\pi_s^+\rangle$), direct transitions between these protected states are strongly suppressed. To control the qubit, we therefore take advantage of higher energy states with support in both valleys. These levels, however, are more sensitive to offset charge: both the excitation energies and the transition dipole elements are dependent on n_g^θ.

We stress that higher-lying levels must have small charge dispersion and non-vanishing coupling to both logical states to serve as ancillary states for qubit operation. To shed light on how to simultaneously satisfy these two requirements, we adopt a simple band-structure picture based on the analogy between the periodic Coulomb potential of a solid crystal and the periodic potential of the compact θ mode of the $0-\pi$ circuit (Fig. 3). By extending the $0-\pi$ potential beyond the $\theta \in [0, 2\pi)$ region, the θ phase can be understood as describing the position along a fictitious one-dimensional crystal in phase space (Fig. 3A), and the eigenfunctions are quasi-periodic Bloch states $\Psi_{n_g}(\theta, \phi)$ (Fig. 3B and C). In a tight-binding approximation, the charge dispersion takes the usual form $\Delta\epsilon(n_g^\theta) \approx 2t\cos(2\pi n_g^\theta)$ where t is the hopping matrix element between localized atomic (Wannier) states. Similarly, drive-assisted transitions between qubit states can be expressed by transitions between neighboring Wannier states (*28*).

We first focus on the charge dispersion of the higher-lying levels and establish that states located mostly in the $\theta = \pi$ valley that are antisymmetric in ϕ are suitable intermediate levels for population transfer between the logical states. To show this symmetry-protected charge insensitivity, we carry out spectroscopic measurements as a function of n_g^θ on the members of the $|\pi_{d\theta}^\pm\rangle$ symmetric-antisymmetric states (Fig. 3D). We find that while the symmetric state $|\pi_{d\theta}^+\rangle$ exhibits a strong charge dispersion, its antisymmetric partner $|\pi_{d\theta}^-\rangle$ is almost offset-charge insensitive. This behavior is in complete agreement with the tight-binding picture where the strongly localized $|\pi_{d\theta}^-\rangle$ state (Fig. 3E) results in a small hopping integral t^- and a heavy flat band, in contrast to the light band associated with the more delocalzied $|\pi_{d\theta}^+\rangle$ state (Fig. 3F). We note that the different degrees of localization of the atomic states with opposite ϕ parity can be attributed to the anisotropic kinetic energies of the

modes. This important observation is the foundation of our protocol for coherent control of the $0-\pi$ qubit where we use the charge-insensitive state $|\pi^-_{d\theta}\rangle$ as the ancillary level.

Unitary control relying on higher energy states imposes a second demand on the ancillary level: the transition matrix elements connecting the intermediate state to both logical states must be finite. Intriguingly, in the $0-\pi$ circuit these matrix elements have an anomalous offset-charge dependence with $4e$ periodicity, which is a manifestation of the Aharonov-Casher interference effect (*28, 35–38*). To understand this feature of the inter-valley transitions, we again harness the tight-binding approximation. In this picture (Fig. 3G and H), there are two paths for the coherent drive to excite a fluxon transition: an initial Wannier state located in the 0 valley can be excited to a final Wannier state in the π valley or in the $-\pi$ valley (*28*), while transitions to more distant valleys are strongly suppressed. The geometric phase (*39*) difference between the states in the $\pm\pi$ valleys leads to the offset-charge dependent interference pattern of the matrix element related to the double-Cooper-pair tunneling events.

We experimentally measure the drive-assisted interference effect on the charge matrix element to find the optimal charge bias point of the $0-\pi$ qubit. In our scheme (Fig. 3I inset), we monitor a plasmon transition ($|0_s\rangle \rightarrow |0_{p\theta}\rangle$) with a weak probe tone, while irradiating the qubit with a strong coupler drive that addresses a fluxon transition ($|0_{p\theta}\rangle \rightarrow |\pi^-_{p\theta}\rangle$). The purpose of the probe tone is to map out the dressed states formed by driving the fluxon transition with the coupler tone. As Fig. 3I shows, when the coupler drive is on resonance with the fluxon frequency, the transition is split into two levels, known as the Autler-Townes doublet (*40–42*). The doublet is separated by the Rabi splitting Ω_c, which is proportional to the voltage amplitude of the drive and the dipole matrix element of the transition. In fact, we observe a pair of Autler-Townes doublets for each offset-charge bias point (*28*), corresponding to the even or odd charge states due to the aforementioned quasiparticle poisoning. By keeping the drive strength constant and changing the induced bias n^θ_g, we monitor the Rabi splitting of the fluxon state to determine the behavior of the charge matrix element. This reveals an interference pattern in excellent agreement with the theoretical calculations (Fig. 3J) and shows that the optimal point for qubit operations is $n^\theta_g = 1/4$ where the Rabi frequency associated to both even and charge

charge states coincide.

Having established the charge-dependent nature of the excited levels of the circuit and the optimal charge operation point of the qubit, we now turn to the population transfer between the protected ground states using the charge-insensitive $|\pi_{d\theta}^{-}\rangle$ ancillary state. First, to unambiguously demonstrate the existence of protected states, we again perform multi-tone spectroscopy between the lowest-lying states of the valleys ($|0_s\rangle$, $|\pi_s^{+}\rangle$, $|\pi_s^{-}\rangle$) and the ancillary level, which form a double Λ-configuration (Fig. 4A inset). By strongly driving the system near the $|\pi_{d\theta}^{-}\rangle \leftrightarrow |\pi_s^{\pm}\rangle$ transitions and probing $|0_s\rangle \leftrightarrow |\pi_{d\theta}^{-}\rangle$, we resolve two Autler-Townes doublets (Fig. 4A). These correspond to the dressed states associated with the fluxon transitions of the lowest-lying symmetric $|\pi_s^{+}\rangle$ and antisymmetric $|\pi_s^{-}\rangle$ states. This scheme enables us to map the excitations of the protected states without excessive drive amplitudes. At finite detunings from the ancillary level, we observe the signature of stimulated Raman transitions as a pair of lines with the slope of +1 when the frequency difference of the probe and coupler tones is on resonance with the transitions of $|0_s\rangle \leftrightarrow |\pi_s^{-}\rangle$ or $|0_s\rangle \leftrightarrow |\pi_s^{+}\rangle$. In the vicinity of $\Phi_{\text{ext}} = 0$ (Fig. 4B), the Raman transitions allow us to map out the hybridization gap formed between the lowest-lying states $|\pi_s^{\pm}\rangle$ of the $\theta = \pi$ valley . The spectroscopy data showcase a magnetic-flux sweet spot and a hybridization gap of $\Delta_H/2\pi \approx 20$ MHz for the disjoint levels. This demonstrates that the $0-\pi$ circuit harbors protected qubit states, which can easily be coupled to each other by an ancillary higher energy level.

We achieve coherent control of the qubit states using Raman gates via $|\pi_{d\theta}^{-}\rangle$. To coherently transfer the population between the $|0_s\rangle$ and $|\pi_s^{+}\rangle$ ground states, we use two simultaneous Gaussian-shaped pulses with amplitudes Ω_α and Ω_β. The frequencies of the pulses are chosen to link the two protected ground states via the ancillary level, and have a detuning of $\Delta/2\pi$ from $|\pi_{d\theta}^{-}\rangle$ (Fig. 4C inset). In this Raman scheme, the two pulses and the truncated three-level system effectively exhibit two-level dynamics with only negligible occupation of the intermediate state (*28, 43*). In this way, we demonstrate Rabi oscillations between the protected ground states by first fixing the detuning of the pulses and independently varying the amplitudes of the two drives (Fig. 4C). In this protocol (*44*), the largest population transfer can be realized when the two amplitudes are equal ($\Omega_\alpha = \Omega_\beta$). In Fig. 4D, we

show coherent manipulation by keeping equal drive amplitudes ($\Omega_\alpha = \Omega_\beta = \Omega$) and varying the detuning Δ from the intermediate level, which results in oscillations in good agreement with an effective Rabi amplitude of $\Omega_R \propto \Omega^2/\Delta$ (*28, 43*).

These time-domain measurements allow us to find the amplitudes for π and π/2 pulses between the protected states to characterize the lifetime and coherence of the protected states. Energy relaxation measurements yield $T_1 = 1.56 \pm 0.1$ ms, which is an order of magnitude improvement over current state-of-the-art transmons (*45*) and comparable to the results reported on highly flux-sensitive heavy fluxonium (*20, 21*). Moreover, Ramsey interferometry yields $T_{2R} = 8.5 \pm 0.6$ μs and Hahn echo measurement results in $T_{2E} = 25.8 \pm 1.4$ μs at $\Phi_{\text{ext}} = 0$, which demonstrates first-order protection against flux noise and an order of magnitude improvement for the coherence times of qubits with disjoint suppport (*20, 21*). We anticipate that the coherence times and gate operations can be further improved with future designs by increasing the kinetic energy anisotropy (for instance by moving to a layered three-dimensional capacitor structure), reducing the susceptibility of the junctions to quasiparticle poisoning, and taking advantage of optimal control techniques (*46*).

Our work demonstrates the experimental realization of an intrinsically error-protected $0 - \pi$ superconducting qubit, opening new avenues for robust encoding of quantum information in artificial atoms. The ability to engineer eigenstates of a qubit Hamiltonian with disjoint support yields prospects not only for the exploration of protected devices with superior coherence times, but also for simulation of solid state systems and the exploration of fundamental physical phenomena.

References

1. M. A. Nielsen, I. L. Chuang, *Quantum Computation and Quantum Information* (Cambridge University Press, NY, 2011).
2. M. H. Devoret, R. J. Schoelkopf, *Science* **339**, 1169 (2013).
3. E. Knill, *Nature* **434**, 3944 (2005).
4. P. W. Shor, *Phys. Rev. A* **52**, R2493 (1995).
5. M. D. Reed, *et al.*, *Nature* **482**, 382 (2012).
6. J. Kelly, *et al.*, *Nature* **519**, 66 (2015).

7. N. Ofek, *et al.*, *Nature* **536**, 441 (2016).
8. L. B. Ioffe, *et al.*, *Nature* **415**, 503 (2002).
9. B. Douçot, M. V. Feigel'man, L. B. Ioffe, *Phys. Rev. Lett.* **90**, 107003 (2003).
10. A. Kitaev, *Ann. Phys.* **303**, 2 (2003).
11. A. Kitaev, *arXiv:cond-mat/0609441v2* (2006).
12. P. Brooks, A. Kitaev, J. Preskill, *Phys. Rev. A* **87**, 052306 (2013).
13. J. M. Dempster, B. Fu, D. G. Ferguson, D. I. Schuster, J. Koch, *Phys. Rev. B* **90**, 094518 (2014).
14. P. Groszkowski, *et al.*, *New J. Phys.* **20**, 043053 (2018).
15. A. D. Paolo, A. L. Grimsmo, P. Groszkowski, J. Koch, A. Blais, *New J. Phys.* **21**, 043002 (2019).
16. B. Douçot, L. B. Ioffe, *Rep. Prog. Phys.* **75**, 072001 (2012).
17. S. Gladchenko, *et al.*, *Nat. Physics* **5**, 48 (2008).
18. M. T. Bell, J. Paramanandam, L. B. Ioffe, M. E. Gershenson, *Phys. Rev. Lett.* **112**, 167001 (2014).
19. W. C. Smith, A. Kou, X. Xiao, U. Vool, M. H. Devoret, *arXiv:1905.01206v1* (2019).
20. N. Earnest, *et al.*, *Phys. Rev. Lett.* **120**, 150504 (2018).
21. Y.-H. Lin, *et al.*, *Phys. Rev. Lett.* **120**, 150503 (2018).
22. U. Vool, M. Devoret, *Int. J. Circ. Theor. App.* **45**, 897 (2017).
23. J. Koch, *et al.*, *Phys. Rev. A* **76**, 042319 (2007).
24. V. E. Manucharyan, J. Koch, L. I. Glazman, M. H. Devoret, *Science* **326**, 113 (2009).
25. S. Krastanov, *et al.*, *Phys. Rev. A* **92**, 040303 (2015).
26. A. Wallraff, *et al.*, *Nature* **431**, 162 (2004).
27. A. Blais, R.-S. Huang, A. Wallraff, S. M. Girvin, R. J. Schoelkopf, *Phys. Rev. A* **69**, 062320 (2004).
28. Materials, methods are available as supplementary materials.
29. N. A. Masluk, I. M. Pop, A. Kamal, Z. K. Minev, M. H. Devoret, *Phys. Rev. Lett.* **109**, 137002 (2012).
30. J. Aumentado, M. W. Keller, J. M. Martinis, M. H. Devoret, *Phys. Rev. Lett.* **92**, 066802 (2004).
31. J. A. Schreier, *et al.*, *Phys. Rev. B* **77**, 180502 (2008).
32. L. Sun, *et al.*, *Phys. Rev. Lett.* **108**, 230509 (2012).
33. D. Ristè, *et al.*, *Nat. Commun.* **4**, 1913 EP (2013).

34. K. Serniak, *et al.*, *Phys. Rev. Lett.* **121**, 157701 (2018).
35. J. R. Friedman, D. V. Averin, *Phys. Rev. Lett.* **88**, 050403 (2002).
36. V. E. Manucharyan, *et al.*, *Phys. Rev. B* **85**, 024521 (2012).
37. I. M. Pop, *et al.*, *Phys. Rev. B* **85**, 094503 (2012).
38. M. T. Bell, W. Zhang, L. B. Ioffe, M. E. Gershenson, *Phys. Rev. Lett.* **116**, 107002 (2016).
39. F. Wilczek, A. Shapere, *Geometric Phases in Physics* (World Scientific, 1989).
40. M. Baur, *et al.*, *Phys. Rev. Lett.* **102**, 243602 (2009).
41. M. A. Sillanpää, *et al.*, *Phys. Rev. Lett.* **103**, 193601 (2009).
42. S. Novikov, *et al.*, *Phys. Rev. B* **88**, 060503 (2013).
43. D. A. Steck, *Quantum and Atom Optics* (available online at http://steck.us/teaching, 2017).
44. G. Chimczak, R. Tanaś, *Phys. Rev. A* **77**, 032312 (2008).
45. O. Dial, *et al.*, *Supercond. Sci. Technol.* **29**, 044001 (2016).
46. M. Abdelhafez, *et al.*, *arXiv:1908.07637* (2019).
47. J. Johansson, P. Nation, F. Nori, *Comp. Phys. Comm.* **183**, 1760 (2012).
48. W. Kohn, *Phys. Rev.* **115**, 809 (1959).

Acknowledgments

We thank A. Vrajitoarea, P. Groszkowski, N. Earnest and A. Shearrow for helpful discussions. Work at Princeton, Northwestern and Chicago was supported by Army Research Office Grant No. W911NF-1910016. Devices were fabricated in the Princeton University Quantum Device Nanofabrication Laboratory and in the Princeton Institute for the Science and Technology of Materials (PRISM) cleanroom. The authors acknowledge the use of Princeton's Imaging and Analysis Center, which is partially supported by the Princeton Center for Complex Materials, a National Science Foundation (NSF)-MRSEC program (DMR-1420541). This work was undertaken in part thanks to funding from NSERC and the Canada First Research Excellence Fund.

Supplementary materials

Materials and Methods

Supplementary Text

Figs. S1 to S7

Tables S1 to S4

References (*47, 48*)

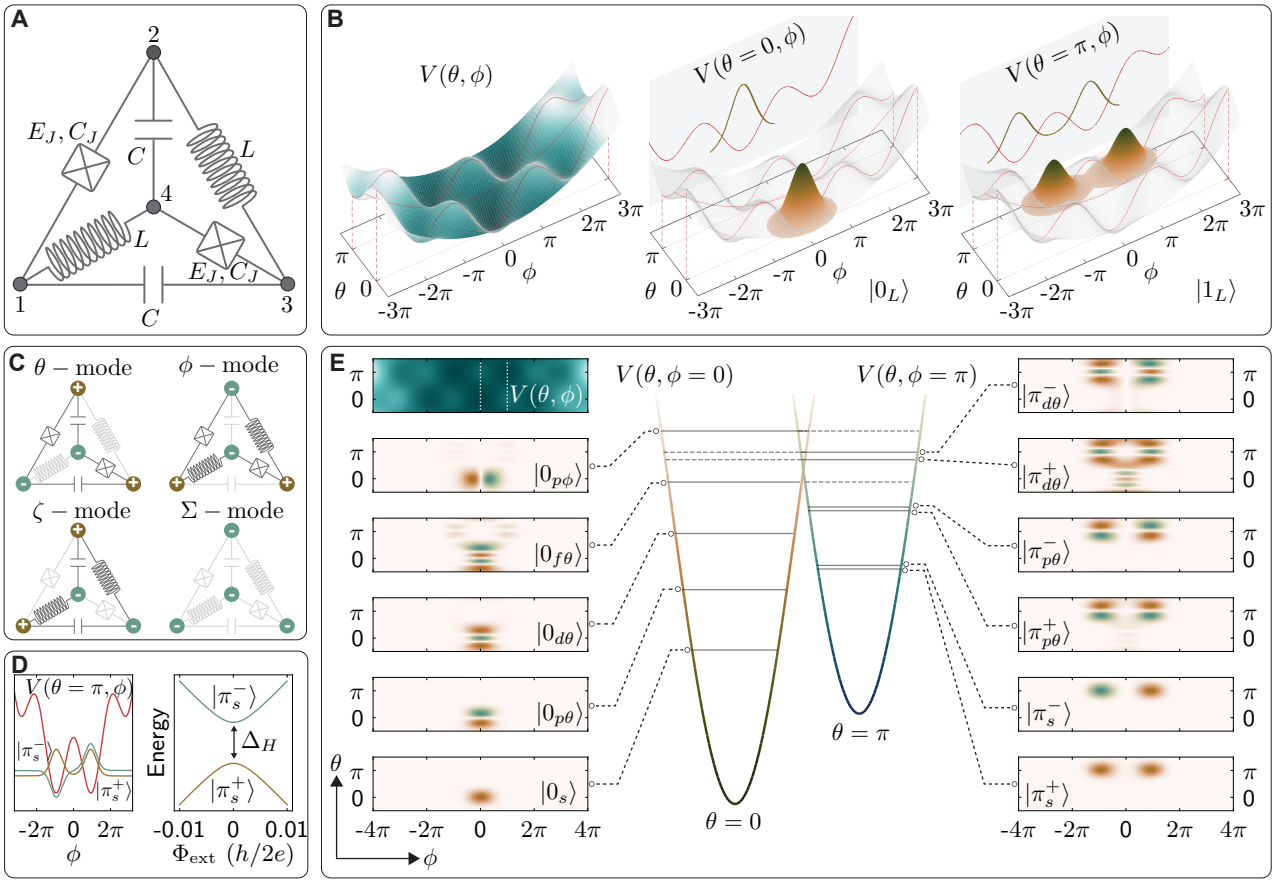

Fig. 1. The $0-\pi$ superconducting qubit and its energy level structure. (**A**) The circuit diagram of the $0-\pi$ qubit (*11, 12*). The circuit has one closed loop with four nodes connected by a pair of Josephson junctions (E_J, C_J), large capacitors (C) and superinductors (L). (**B**) Left panel: the $V(\theta,\phi)$ double-well potential landscape of the circuit in the absence of magnetic fields. The ground state of the 0 valley is localized along $\theta = 0$ (middle panel), while the lowest-lying state of the π valley along $\theta = \pi$ (right panel). The line cuts along the two valleys in the ϕ direction show that the potential resembles a fluxonium potential. (**C**) The four modes of the $0-\pi$ circuit with colors of the nodes indicating the sign of normal-mode amplitudes. (**D**) Left panel: schematic of the symmetric and antisymmetric ground states of the π valley. The hybridization of these states leads to a magnetic sweet spot (right panel). (**E**) The two-dimensional wavefunctions of the eigenstates, which are located mostly in the 0 (left) or in the π (right) valleys. Middle panel: linecuts of the potential along $\phi = 0$ and $\phi = \pi$ as indicated with white dotted lines on the image of the potential.

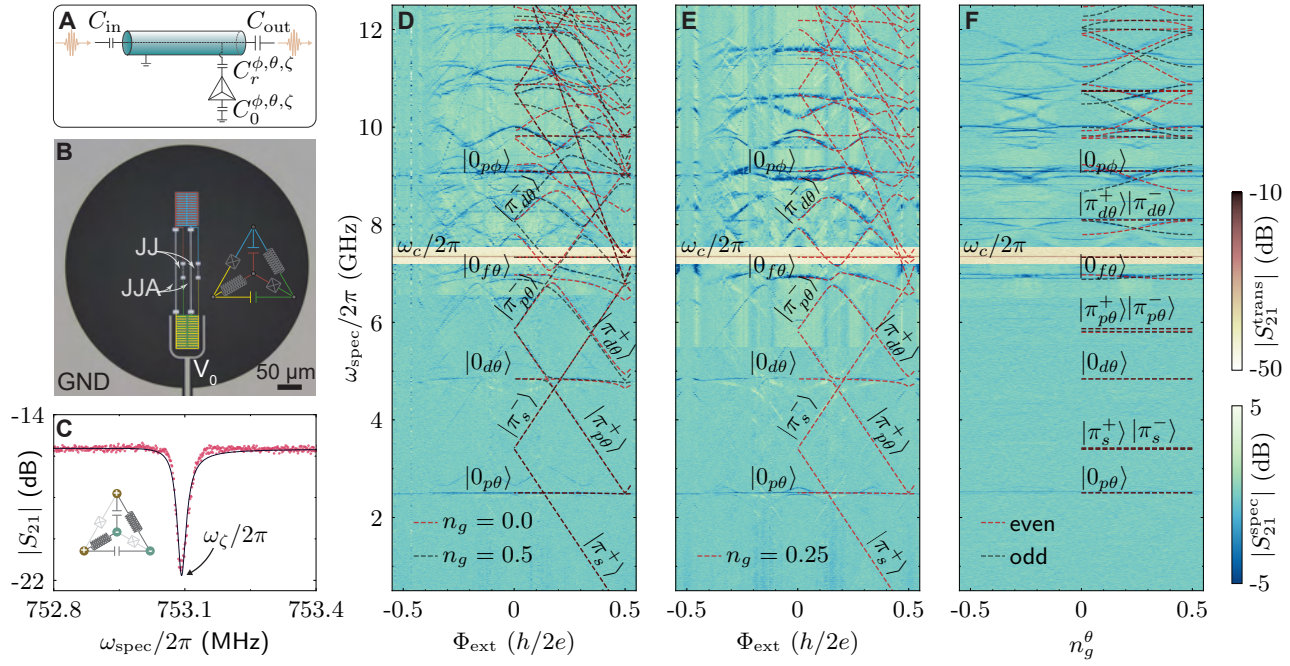

Fig. 2. Circuit QED with the $0-\pi$ qubit. (**A**) Schematic of the capacitive coupling scheme between the qubit and the transmission-line resonator. The capacitances between the four nodes of the circuit and the resonator determine the effective coupling capacitances for the modes. (**B**) False-color optical image of the $0-\pi$ device with colors referring to the four nodes of the circuit. GND: ground plane of the resonator; V_0: centerpin of the resonator; JJ: Josephson junction; JJA: Josephson junction array. (**C**) The spectroscopic response of the harmonic ζ mode. Solid line shows the fit (*29*) with quality factors of $Q^{\zeta}_{\mathrm{ext}} = 41,600$ and $Q^{\zeta}_{\mathrm{int}} = 42,500$. (**D** to **F**) Transmission and spectroscopy measurements (background subtracted) of the $0-\pi$ qubit as a function of external magnetic field (**D**) at $n^{\theta}_g = 0.0/0.5$ and (**E**) at $n^{\theta}_g = 0.25$, and as a function of offset-charge bias (**F**) at $\Phi_{\mathrm{ext}} = 0$. The transmission measurements around 7.3 GHz (yellow-pink) show negligible dependence of the cavity resonance on external parameters. The spectroscopic data (green-blue) demonstrate the energy level structure of the $0-\pi$ qubit, which is in excellent agreement with a coupled resonator-qubit theoretical fit (dashed lines). The result of the fit is plotted over only the positive side of the data for clarity. The low-energy fluxon transitions are not visible in the spectroscopy data due to the small dipole elements.

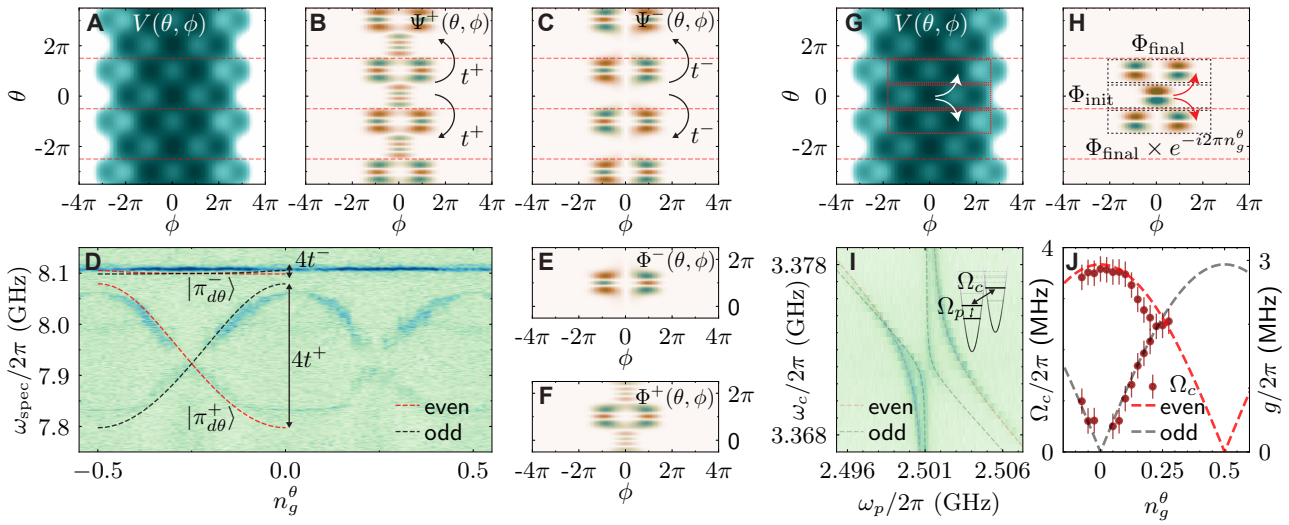

Fig. 3. Symmetry-induced offset-charge insensitivity and drive-assisted Aharonov-Casher effect. (**A**) The extended potential of the $0-\pi$ circuit with red dashed lines indicating the border of the phase unit cells. (**B** and **C**) The eigenstates are Bloch-waves $\Psi(\theta,\phi)$, which are shown for the $|\pi^{\pm}_{d\theta}\rangle$ pair at $n_g^\theta = 0.5$. (**E** and **F**) The antisymmetric Wannier wavefunction $\Phi^-(\theta,\phi)$ is significantly more localized than the symmetric state $\Phi^+(\theta,\phi)$, leading to a decreased hopping rate between adjacent unit cells: $t^- \ll t^+$. (**D**) Spectroscopic measurement of the charge dispersion of the $|\pi^{\pm}_{d\theta}\rangle$ pair (dashed lines show the same theoretical fit as in Fig. 2D to F). The antisymmetric state has suppressed charge sensitivity compared to the symmetric state in agreement with the different hopping rates. (**G**) Fluxon transition in the extended picture showing that a state located in the 0 valley can be excited to the valleys at $\pm\pi$. (**H**) Wannier function of the initial state $|0_{p\theta}\rangle$ located in the 0 valley and the final state $|\pi^-_{p\theta}\rangle$ located in the π valley or in the $-\pi$ valley. The state in the $-\pi$ valley has a non-zero geometric phase due to the quasiperiodic boundary conditions (*28*). (**I**) Autler-Townes spectroscopy between $|0_s\rangle$, $|0_{p\theta}\rangle$ and $|\pi^-_{p\theta}\rangle$ at $n_g = 0.1$ [dashed lines show the fit based on Rabi splitting of levels (*28*)]. (**J**) The extracted Rabi splitting as a function of charge bias and the theoretically expected coupling rate $g/2\pi$ between the levels, which demonstrates the interference pattern with $|\cos\pi n_g^\theta|$ dependence. Error bars are estimates based on the linewidth of the transitions.

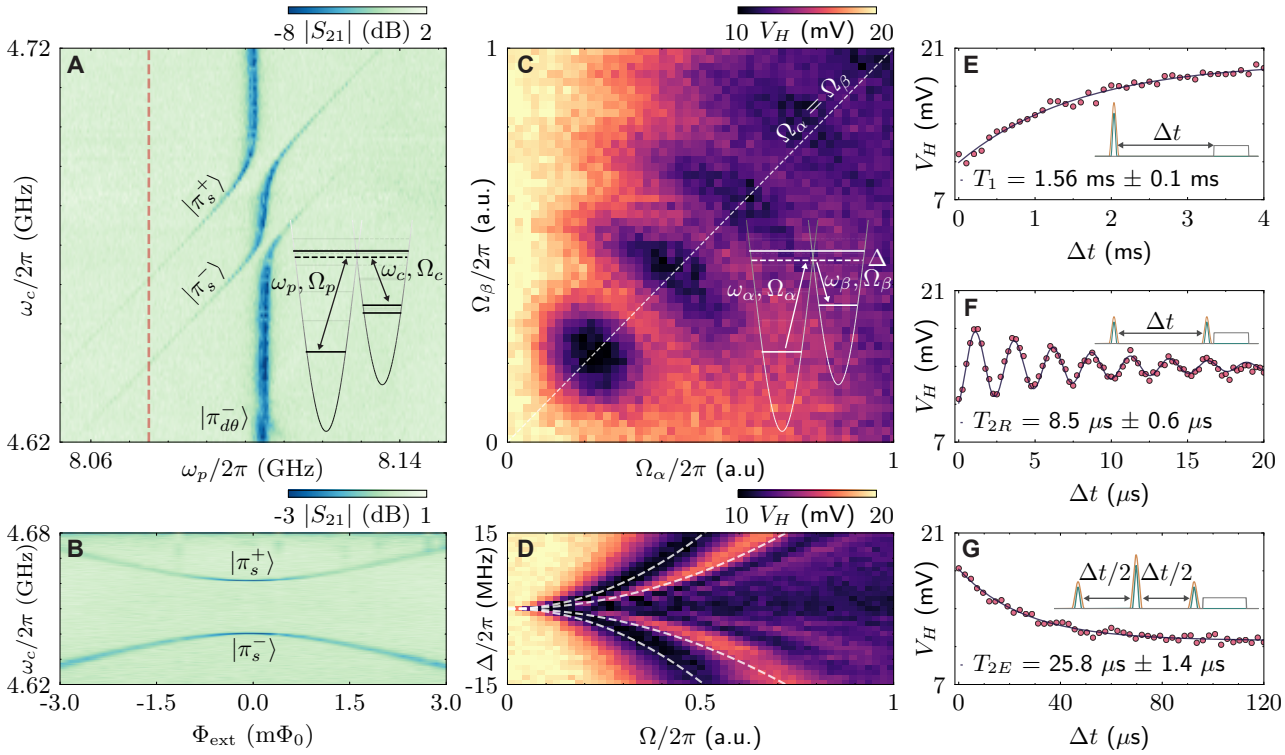

Fig. 4. Mapping and coherent control of protected quantum states. (**A**) Autler-Townes spectroscopy (background subtracted) between the ground states of the $0-\pi$ qubit using the ancillary $|\pi^-_{d\theta}\rangle$ level. Inset shows the continuous drive scheme. (**B**) Raman spectroscopy at the detuning of $\Delta/2\pi$ = -30 MHz from the ancillary level [red dashed line in (A)] as a function of external magnetic field, which demonstrates a magnetic sweet spot for the disjoint ground states. (**C** and **D**) Coherent Rabi oscillations between the protected ground states $|0_s\rangle$ and $|\pi^+_s\rangle$ obtained by using two, overlapping Gaussian pulses with width of 4σ. (**C**) The measured homodyne voltage V_H as a function of drive amplitudes at a fixed detuning ($\Delta/2\pi$ = -3 MHz, $\sigma = 1$ μs), and (**D**) V_H as a function of detuning at equal drive amplitudes ($\Omega_1 = \Omega_2$, $\sigma = 0.8$ μs). The maximum population transfer occurs when the two drive amplitudes are equal. The dashed lines in (D) show a fit according to the effective Rabi rate of the Raman pulses. (**E** to **G**) Relaxation, Ramsey and spin-echo measurements of the protected $|\pi^+_s\rangle$ state, with insets showing the pulse scheme ($\Delta/2\pi$ = -4 MHz and σ = 200 ns). All data were taken at $n^\theta_g = 0.25$ charge bias point.

Supplementary Materials for

Experimental realization of an intrinsically error-protected superconducting qubit

András Gyenis, Pranav S. Mundada, Agustin Di Paolo, Thomas M. Hazard, Xinyuan You, David I. Schuster, Jens Koch, Alexandre Blais, Andrew A. Houck*

*Corresponding author. Email: aahouck@princeton.edu

1 Materials and Methods

1.1 Sample fabrication

The device was fabricated on a 530 μm thick, polished c-plane sapphire substrate, on which 200 nm thick niobium was sputtered using an AJA superconducting deposition system. We used optical lithography to define the resonators and shunting capacitances. AZ1505 positive photoresist was spun on the chip, baked at 95°C for 1 min and patterned using the 2 mm write-head of a Heidelberg DWL66+ tool. After developing the chip in AZ300MIF for 1 min and rinsed in running DI water for $\sim$1 min, the sample was dry-etched in PlasmaTherm APEX SLR using the mixture of CHF_3, O_2, SF_6, Ar gases (with 40:1:15:10 ratios). The photoresist was stripped by Microposit Remover 1165 and solvent-cleaned by toluene, acetone, methanol, isopropanol involving sonication and a nitrogen blow-dry. For electron-beam lithography, we span MMA/PMMA bilayer on the chip (baked for 2 + 30 min at 175°C), evaporated 40 nm thick anticharging aluminum layer, and diced the sample into single chips. We exposed the Josephson junctions in a 125 keV Elionix e-beam system (at beam current of 1 nA and aperture of 60 μm). The anticharging layer was removed by soaking the chip in MF319 for 3 min and the e-beam resists were developed in the 1:3 mixture of methyl isobutyl ketone (MIBK) to isopropanol for 50 sec and pure isopropanol for 10 sec. The Josephson junctions were double-angle-evaporated in a Plassys e-beam-evaporator system with base pressure less than 10^{-7} mbar. Before the evaporation, an *in-situ* argon ion beam etch was used to clean the surface of the sample. We evaporated 20 nm + 50 nm thick Al layers at a rate of 0.4 nm/s and oxidized the first layer for 10 min at 200 mbar in a 15% oxygen-in-argon environment to realize the tunnel junction. The Al layer was lift-off in PG Remover at $\sim$70°C and cleaned with isopropanol.

The device was placed in a copper PCB and wirebonded (Fig. S1). An off-chip copper coil was attached to the PCB. The sample holder had an aluminum shield (covered with Eccosorb CR-124 and wrapped with thin Mylar layers) and an outer mu-metal shield. The sample holder was attached to the mixing chamber plate of a dilution refrigerator with base temperature of 10 mK (Fig. S2).

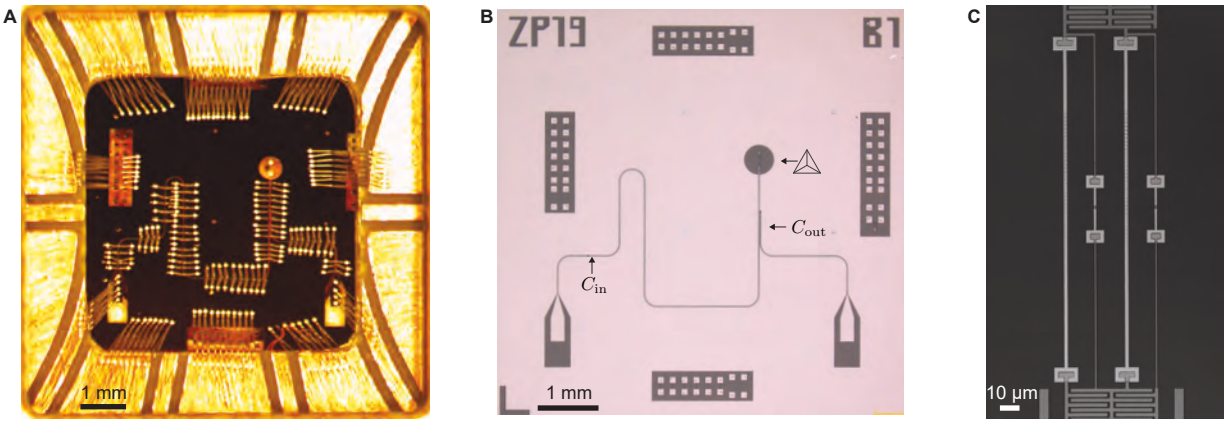

Fig. S1: (**A**) Optical image of a wire-bonded $0-\pi$ device mounted into the sample holder. (**B**) Image of the 7 mm x 7 mm chip showing the resonator with its coupling capacitors and the qubit. (**C**) Enlarged image of the middle region of the $0-\pi$ device, which displays the pairs of superinductors and Josephson junctions.

1.2 Finite-element simulation of the capacitances

As mentioned in the main text, realizing the proper capacitance values in the $0-\pi$ circuit is a key requirement to achieve the protected regime. The large shunting capacitance in the circuit is denoted by C, while the cross capacitance between the nodes enclosing the superinductances (Josephson junctions) is C_L^x (C_J^x). In our design, all four nodes are coupled to both the centerpin (C_r^i) and the ground plane (C_0^i) of the resonator (Fig. S3). We used ANSYS Maxwell electromagnetic field simulation software to determine the capacitance values in the circuit, which are summarized in Table S1. These parameters (with the assumptions of dielectric constant $\epsilon_r = 10.7$ for sapphire, C_J = 2 fF and $E_L =$ 0.38 GHz) results in energy scales of $E_C^\theta/h = 88$ MHz, $E_C^\phi/h = 1.02$ GHz and $\omega_\zeta/2\pi = 742$ MHz, which are in excellent agreement with our experimental findings.

C	C_L^x	C_J^x	C_r^1	C_r^2	C_r^3	C_r^4	C_0^1	C_0^2	C_0^3	C_0^4
100.5	0.7	1.0	9.1	0.3	3.8	0.3	8.2	7.9	6.2	11.6

Table S1: Finite-element simulation of the device capacitances. All values are given in fF units.

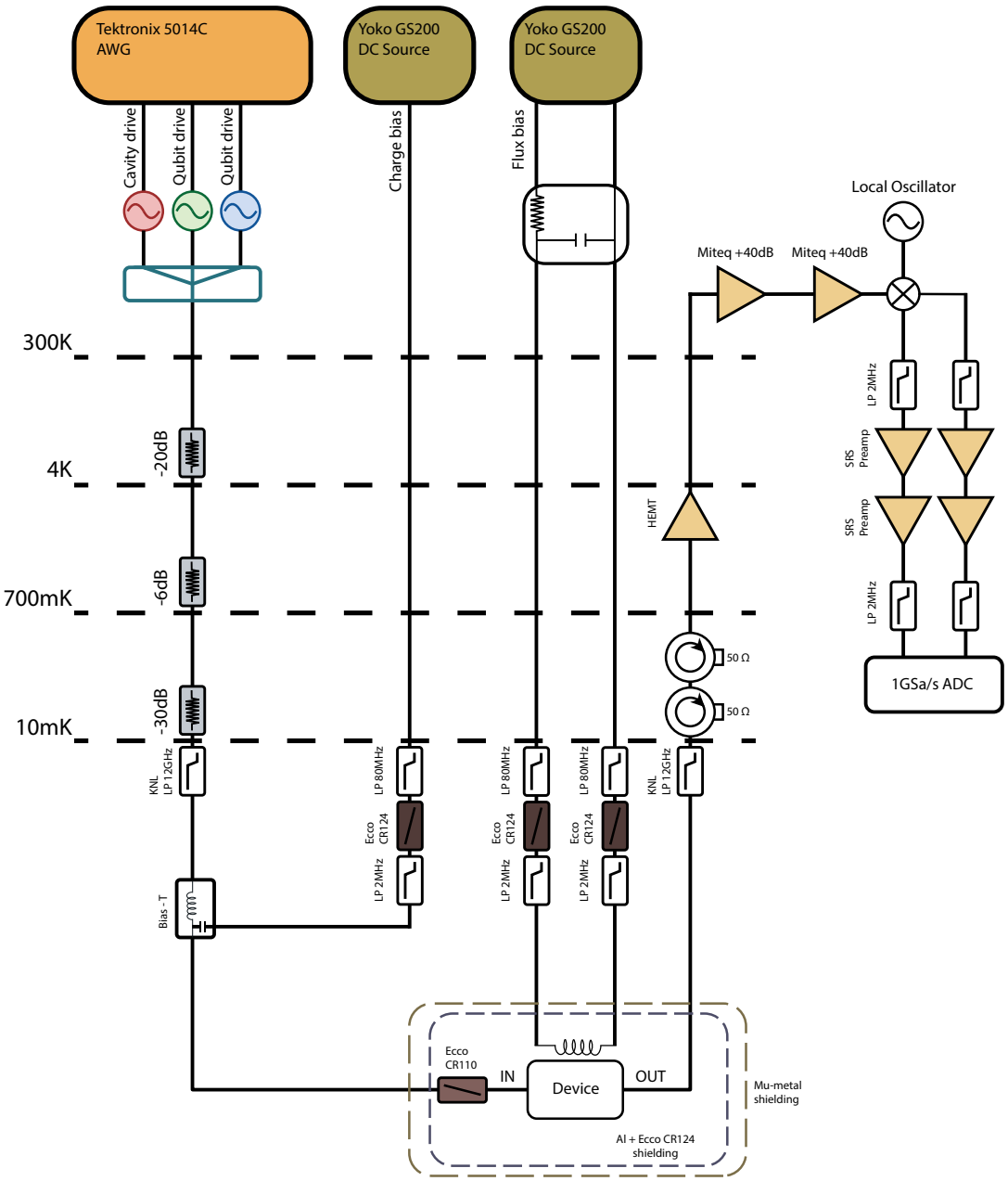

Fig. S2: Wiring diagram of the cryogenic- and room-temperature measurement setup.

1.3 Spectrum fit

Here we describe the multivariate fit to the experimental data based on a detailed theoretical model for the $0-\pi$ device. We consider the circuit scheme of Fig. S3, where we have introduced additional

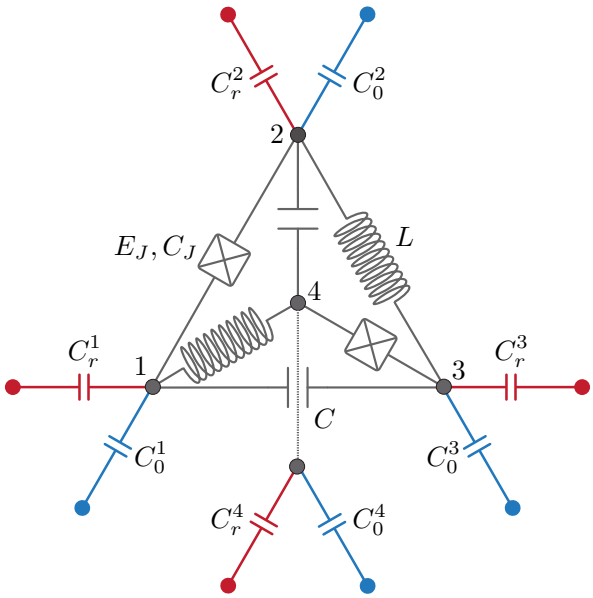

Fig. S3: Full capacitance network of the $0-\pi$ device. Red (blue) colors indicate coupling to the centerpin (ground plane) of the resonator.

gate (C_r^i) and ground (C_0^i) capacitances for nodes $i \in [1,4]$. In the flux node basis $\{\Phi_i\}$, the circuit Lagrangian takes the form

$$\mathcal{L}_\Phi = \dot{\mathbf{\Phi}}^T \cdot \frac{\mathbf{C}_\Phi}{2} \cdot \dot{\mathbf{\Phi}} - \dot{\mathbf{\Phi}}^T \cdot \mathbf{C}_r \cdot \mathbf{V}_\Phi - U(\mathbf{\Phi}, \Phi_{\text{ext}}), \tag{1}$$

where $\mathbf{\Phi} = (\Phi_1, \ldots, \Phi_4)^T$, $\mathbf{C}_\Phi$ is the capacitance matrix of the circuit (including gate and ground capacitances), $\mathbf{V}_\Phi = V_r(1,1,1,1)^T$ is a voltage-drive vector defined in terms of the resonator voltage, V_r, $\mathbf{C}_r = \text{diag}(C_r^1, \ldots, C_r^4)$ is the gate capacitance matrix, and $U(\mathbf{\Phi}, \Phi_{\text{ext}})$ is the potential energy corresponding to the Josephson junctions and inductances of the circuit. More precisely, the circuit capacitance matrix is given by

$$\mathbf{C}_\Phi = \begin{pmatrix} C_1 & -C_J & -C & 0 \\ -C_J & C_2 & 0 & -C \\ -C & 0 & C_3 & -C_J \\ 0 & -C & -C_J & C_4 \end{pmatrix}, \tag{2}$$

where $C_i = C_J + C + C_r^i + C_0^i$ for $i \in [1,4]$. We now move to the $0-\pi$ mode basis defined by $\mathbf{\Theta} = (\phi, \theta, \zeta, \Sigma)^T$, by the rotation $\mathbf{\Theta} = \mathbf{R} \cdot \mathbf{\Phi}$, where

$$\mathbf{R} = \frac{1}{2}\begin{pmatrix} -1 & 1 & -1 & 1 \\ -1 & 1 & 1 & -1 \\ 1 & 1 & -1 & -1 \\ 1 & 1 & 1 & 1 \end{pmatrix}. \tag{3}$$

Under such a transformation, Eq. (1) becomes

$$\mathcal{L}_\Theta = \dot{\mathbf{\Theta}}^T \cdot \frac{\mathbf{C}_\Theta}{2} \cdot \dot{\mathbf{\Theta}} - \dot{\mathbf{\Theta}}^T \cdot \tilde{\mathbf{C}}_r \cdot \mathbf{V}_\Theta - U(\mathbf{\Theta}, \Phi_{\text{ext}}), \tag{4}$$

where $\mathbf{C}_\Theta = (\mathbf{R}^{-1})^T \cdot \mathbf{C}_\Phi \cdot \mathbf{R}^{-1}$ and $\tilde{\mathbf{C}}_r = (\mathbf{R}^{-1})^T \cdot \mathbf{C}_r \cdot \mathbf{R}^{-1}$ are the transformed capacitance matrices, and $\mathbf{V}_\Theta = \mathbf{R} \cdot \mathbf{V}_\Phi$ is the voltage-drive vector expressed in the $0-\pi$ mode basis. By performing a Legendre transformation, we arrive at the circuit Hamiltonian

$$H = (\mathbf{q}_\Theta + \tilde{\mathbf{C}}_r \cdot \mathbf{V}_\Theta)^T \cdot \frac{\mathbf{C}_\Theta^{-1}}{2} \cdot (\mathbf{q}_\Theta + \tilde{\mathbf{C}}_r \cdot \mathbf{V}_\Theta) + U(\mathbf{\Theta}, \Phi_{\text{ext}}), \tag{5}$$

where $\mathbf{q}_\Theta = \partial \mathcal{L}_\Theta / \partial \dot{\mathbf{\Theta}}$ is the conjugate charge vector operator. Note that Eq. (5) can be split as

$$H = H_{0-\pi} + H_{\text{drive}}, \tag{6}$$

where

$$H_{0-\pi} = \mathbf{q}_\Theta^T \cdot \frac{\mathbf{C}_\Theta^{-1}}{2} \cdot \mathbf{q}_\Theta + U(\mathbf{\Theta}, \Phi_{\text{ext}}), \tag{7}$$

is the undriven $0-\pi$ qubit Hamiltonian and

$$H_{\text{drive}} = \mathbf{q}_\Theta^T \cdot (\mathbf{C}_\Theta^{-1} \cdot \tilde{\mathbf{C}}_r) \cdot \mathbf{V}_\Theta, \tag{8}$$

is the drive term.

While all circuit details are taken into account in Eq. (6), the spectrum fit that is presented in the main text aims to provide the simplest possible accurate description of the device Hamiltonian. Thus, in order to simplify our treatment, we implement a few approximations. In particular, we omit any coupling to the ζ and Σ modes, neglecting a potential capacitive interaction between these and the qubit modes and reducing the qubit Hamiltonian to

$$H_{0-\pi} \simeq 4E_C^\phi n_\phi^2 + 4E_C^\theta (n_\theta - n_g)^2 + \hbar g_{\phi\theta} n_\phi n_\theta + U(\mathbf{\Theta}, \Phi_{\text{ext}}). \tag{9}$$

Here, $E_C^\phi = e^2/2C_\phi$ and $E_C^\theta = e^2/2C_\theta$ are the charging energies of the ϕ and θ modes and $\hbar g_{\phi\theta}$ is the strength of a capacitive interaction between these modes due to the asymmetry of the circuit capacitance matrix. Accordingly, we also approximate Eq. (8) by

$$H_{\text{drive}} \simeq (\beta_\phi n_\phi + \beta_\theta n_\theta) \times 2eV_r, \tag{10}$$

where β_ϕ and β_θ are capacitive coupling ratios for the ϕ and θ modes. We moreover set $g_{\phi\theta} \to 0$ in Eq. (10), eliminating one fit parameter. We observed, however, that deviations from $g_{\phi\theta} \simeq 0$ within bounds given by finite-element estimations of the coupling capacitance do not significantly modify the quality of the fit.

For the multivariate fit, we treat all energy and coupling variables as fit parameters, including E_{C_ϕ}, E_{C_θ}, β_ϕ, β_θ and those in the potential energy

$$U(\mathbf{\Theta}, \Phi_{\text{ext}}) = -2E_J \cos\theta \cos(\phi - \pi\Phi_{\text{ext}}/\Phi_0) + E_L\phi^2 + E_J dE_J \sin\theta \sin(\phi - \pi\Phi_{\text{ext}}/\Phi_0), \quad (11)$$

defined in terms of the junction energy E_J, the superinductance energy E_L and the relative junction-energy asymmetry dE_J. The fit also incorporates the resonator mode with nominal impedance $Z_r = 50\,\Omega$ and frequency $f_r \simeq 7.35\,\text{GHz}$ parameters, for which the voltage operator reads

$$V_r = V_{\text{rms}}(a + a^\dagger), \quad (12)$$

where $V_{\text{rms}} = \sqrt{2hf_r^2 Z_r}$ for a $\lambda/2$ resonator, and a and $a^\dagger$ are the respective harmonic-oscillator ladder operators. The fit takes into account two sets of data corresponding to a sweep of the magnetic flux for the offset charges $n_g = 0.0$ and $n_g = 0.25$. A single error metric measures the distance between the result of the exact diagonalization of the qubit-resonator Hamiltonian and both data sets. The result of the fit is shown in Fig. S4A and B (in addition to the figures in the main manuscript) and the fit parameters are provided in Table S2. These parameters are in excellent agreement with those expected from a finite-element simulation of the device.

E_C^ϕ/h	E_C^θ/h	E_J/h	E_L/h	dE_J	β_ϕ	β_θ
1.142	0.092	6.013	0.377	0.1	0.27	6.6×10^{-3}

Table S2: Result of the multivariate fit to the experimental data. All energy parameters are given in GHz units.

We find an excellent agreement between the theoretical model and the experimental data, both for $n_g = 0$ and $n_g = 0.25$. As Fig. 2 of the main text shows, the obtained parameters also describe the transitions at $n_g = 0.5$, and generally, the entire charge dependence of the levels. In Fig. S4C, we also show that additional features in the spectroscopy data can be explained by transitions between the thermally occupied fluxon states to higher levels. Furthermore, the theoretical model not only captures accurately the qubit transitions, but also the cavity-assited sideband transitions. Since the latter transitions were not originally taken into account for the fit, this fact provides further confirmation of the validity of the theoretical model.

2 Supplementary text

2.1 Tight-binding approximation

In the main text, we introduced a tight-binding model to explain the charge dependence of the fluxon transitions and dipole matrix elements. Here, we provide additional information regarding this model.

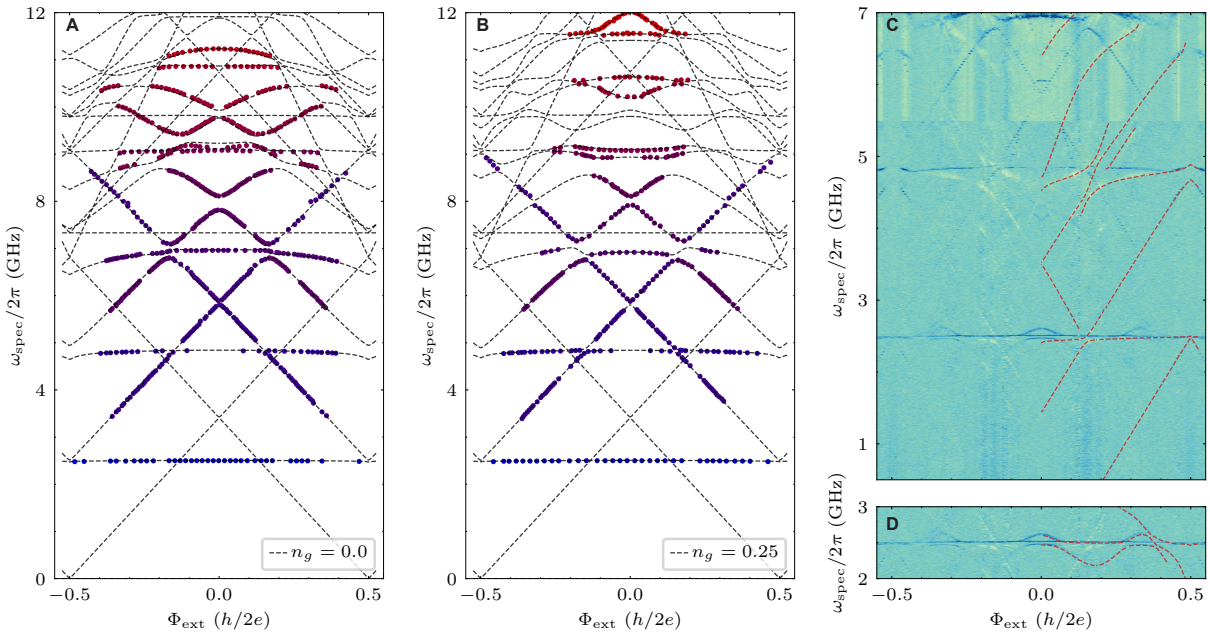

Fig. S4: Spectrum fit of the $0-\pi$ device. (**A**) and (**B**) correspond to the cases of $n_g = 0$ and $n_g = 0.25$, respectively. The experimental data used for the fit are displayed by colored circles while the theory results are given by the black dashed lines. Note that some of the qubit transitions are invisible in the experiment due to exponentially small matrix elements or vanishing dispersive shifts. The transition around $7.35\,\mathrm{GHz}$ corresponds to the readout resonator. (**C**) Overlay of the transitions predicted by our model on the experimental data by assuming thermal population of the lowest two levels in the π valley, which explains the origin of the *bright* transitions in the spectrum ($n_g = 0.25$). (**D**) A set of cavity-assited sideband transtions that are also captured by the theory model ($n_g = 0.25$).

We present a bottom-up approach considering first the case of a charge-sensitive transmon, after which we focus on the case of the $0-\pi$ qubit.

To make the connection between a charge-sensitive qubit and a periodic lattice, we briefly review the definitions of Bloch states and Wannier states in solid-state physics. The single-particle Hamiltonian describing electrons moving in a one-dimensional crystal with a periodic potential is

$$H_{\rm crystal} = -\frac{\hbar^2}{2m}\partial_x^2 + V(x), \tag{13}$$

where m is the mass of the electron and $\hbar$ is the reduced Planck constant. The eigenstates belonging to a single band are quasi-periodic Bloch states $\Psi_k(x) = e^{ikx}u_k(x)$, where $u_k(x)$ is a lattice periodic function and k is the crystal-momentum.

We define the Wannier function corresponding to a molecular orbital at a lattice site x_0 by

$$\Phi(x - x_0) = \frac{1}{\sqrt{N}}\sum_k e^{-ikx_0}\Psi_k(x), \tag{14}$$

where N is the number of sites in the lattice. An advantage of using Wannier functions is that they provide a natural choice for localized, orthonormal atomic states. The Wannier functions are non-unique due to the unconstrained phase degree of freedom of the Bloch electrons. However, there exists only one maximally localized Wannier wavefunction that is real, exponentially localized and symmetric or antisymmetric (*48*).

We can express the Bloch states as a function of the Wannier states corresponding to different lattice sites by an inverse Fourier transform

$$\Psi_k(x) = \frac{1}{\sqrt{N}} \sum_{x_0} e^{ikx_0} \Phi(x - x_0). \tag{15}$$

The energy of the eigenstates as a function of momentum can be approximated by the well-known tight-binding dispersion relation of $\epsilon_k = \epsilon_0 + 2t \cos ka$, where the energy scales are related to the localized Wannier functions as $\epsilon_0 = \int dx \Phi^*(x) H \Phi(x)$ and $t = \int dx \Phi^*(x - a) H \Phi(x)$.

Charge-sensitive transmon We now consider the case of the offset-charge sensitive transmon qubit

$$H = 4E_C(i\partial_\theta - n_g)^2 - E_J \cos\theta, \tag{16}$$

where E_C is the charging energy and E_J is the Josephson energy. The pth eigenstate of this Hamiltonian for a given n_g obeys

$$H u^p_{n_g}(\theta) = \epsilon^p_{n_g} u^p_{n_g}(\theta), \tag{17}$$

where $u^p_{n_g}(\theta)$ is a 2π-periodic function of the superconducting phase across the Josephson junction, i.e.,

$$u^p_{n_g}(\theta) = u^p_{n_g}(\theta + 2\pi). \tag{18}$$

Next, we perform a gauge transformation defined by the unitary $U = e^{in_g\theta}$, in order to eliminate the offset-charge dependence of the transmon Hamiltonian which becomes

$$\bar{H} = -4E_C \partial^2_\theta - E_J \cos\theta, \tag{19}$$

and thus

$$\Psi^p_{n_g}(\theta) = e^{in_g\theta} u^p_{n_g}(\theta). \tag{20}$$

We note that, in this gauge, the transmon Hamiltonian [Eq. (19)] is identical to the Hamiltonian of a one-dimensional crystal [Eq. (13)]. Therefore, the eigenstates of Eq. (19) are also quasi-periodic Bloch waves.

In analogy to the solid state case, we introduce the Wannier functions for the transmon qubit by Fourier transforming the Bloch states in n_g

$$\Phi_p(\theta - 2\pi l) = \frac{1}{\sqrt{N}} \sum_{n_g} e^{-i2\pi l \cdot n_g} \Psi^p_{n_g}(\theta), \tag{21}$$

where l is an integer that corresponds to the number of the unit cell where the Wannier function is localized. The inverse Fourier transform thus reads

$$\Psi^p_{n_g}(\theta) = \frac{1}{\sqrt{N}} \sum_{\theta_0} e^{i2\pi l \cdot n_g} \Phi_p(\theta - 2\pi l). \tag{22}$$

The n_g dispersion of the low-lying transmon energy levels is determined by the hopping matrix element: $\epsilon^p_{n_g} = \epsilon^p_0 + 2t^p \cos 2\pi n_g$, where $\epsilon^p_0 = \int d\theta \Phi^{p*}(\theta) H \Phi^p(\theta)$ and $t^p = \int d\theta \Phi^{p*}(\theta - 2\pi) H \Phi^p(\theta)$.

Next, we consider the charge matrix element $n_{pq} = \langle u^p | i\partial_\theta | u^q \rangle$ in the tight-binding approximation. Since the states are assumed to be localized, we only consider the contribution of two states which are in the same well or nearest neighbours, thus

$$\begin{aligned}\langle u^p | i\partial_\theta | u^q \rangle = & i \int d\theta \Phi^*_p(\theta) \partial_\theta \big(\Phi_q(\theta) + \Phi_q(\theta + 2\pi) e^{-i2\pi n_{\rm g}} + \Phi_q(\theta - 2\pi) e^{i2\pi n_{\rm g}} \big) \\ & + n_{\rm g} \int d\theta \Phi^*_p(\theta) \big(\Phi_q(\theta) + \Phi_q(\theta + 2\pi) e^{-i2\pi n_{\rm g}} + \Phi_q(\theta - 2\pi) e^{i2\pi n_{\rm g}} \big),\end{aligned} \tag{23}$$

and for further reference, we define the following variables

$$\begin{aligned} \eta^{\rm C}_0 &= \int d\theta \Phi^*_p(\theta) \Phi_q(\theta), \qquad \eta^{\rm L}_0 = \int d\theta \Phi^*_p(\theta) \Phi_q(\theta + 2\pi), \\ \eta^{\rm R}_0 &= \int d\theta \Phi^*_p(\theta) \Phi_q(\theta - 2\pi), \qquad \eta^{\rm C}_1 = i \int d\theta \Phi^*_p(\theta) \partial_\theta \Phi_q(\theta), \\ \eta^{\rm L}_1 &= i \int d\theta \Phi^*_p(\theta) \partial_\theta \Phi_q(\theta + 2\pi), \qquad \eta^{\rm R}_1 = i \int d\theta \Phi^*_p(\theta) \partial_\theta \Phi_q(\theta - 2\pi). \end{aligned}$$

The matrix element can be written as

$$\langle u^p | i\partial_\theta | u^q \rangle = (\eta^{\rm C}_1 + \eta^{\rm L}_1 e^{-i2\pi n_{\rm g}} + \eta^{\rm R}_1 e^{i2\pi n_{\rm g}}) + n_{\rm g} (\eta^{\rm C}_0 + \eta^{\rm L}_0 e^{-i2\pi n_{\rm g}} + \eta^{\rm R}_0 e^{i2\pi n_{\rm g}}). \tag{24}$$

We now consider the case where Φ_p and Φ_q have the same parity. It follows then, that $\eta^{\rm C}_0 = \eta^{\rm C}_1 = 0$, $\eta^{\rm L}_1 = -\eta^{\rm R}_1$, and $\eta^{\rm L}_0 = \eta^{\rm R}_0$. The matrix element thus simplifies to

$$|\langle u^p | i\partial_\theta | u^q \rangle| = | -2i\eta^{\rm L}_1 \sin 2\pi n_{\rm g} + 2n_{\rm g} \eta^{\rm L}_0 \cos 2\pi n_{\rm g}|. \tag{25}$$

Since the states are all localized in the corresponding wells, the part that contributes to the integral is the tail of the wavefunction. Assuming the tail is of Gaussian type $\exp(-\theta^2)$, we have $|\eta^{\rm L}_1| \gg |\eta^{\rm L}_0|$, and the matrix element is further simplified

$$|\langle u^p | i\partial_\theta | u^q \rangle| = |2\eta^{\rm L}_1 \sin 2\pi n_{\rm g}|. \tag{26}$$

The case in which Φ_p and Φ_q have opposite parities leads to $\eta^{\rm C}_0 = 0$, $\eta^{\rm L}_1 = \eta^{\rm R}_1$, and $\eta^{\rm L}_0 = -\eta^{\rm R}_0$. The matrix element is then

$$|\langle u^p | i\partial_\theta | u^q \rangle| = |\eta^{\rm C}_1 + 2\eta^{\rm L}_1 \cos 2\pi n_{\rm g} - 2in_{\rm g} \eta^{\rm L}_0 \sin 2\pi n_{\rm g}|. \tag{27}$$

Taking into account $|\eta^{\rm C}_1| \gg |\eta^{\rm L}_1| \gg |\eta^{\rm L}_0|$, we have

$$|\langle u^p | i\partial_\theta | u^q \rangle| = |\eta^{\rm C}_1 + 2\eta^{\rm L}_1 \cos 2\pi n_{\rm g}|. \tag{28}$$

Charge-sensitivity in the $0-\pi$ qubit The charge sensitivity in the $0-\pi$ qubit enters through the θ mode as

$$H_{0-\pi} = 4E_C^{\theta}(n_\theta - n_g^{\theta})^2 + 4E_C^{\phi} n_\phi^2 + V(\theta,\phi). \tag{29}$$

The $u_p(\theta,\phi)$ eigenstates of the $0-\pi$ Hamiltonian are 2π-periodic in θ as $u_p(\theta,\phi) = u_p(\theta+2\pi,\phi)$. We define the Bloch states again as $\Psi^p_{n_g}(\theta,\phi) = e^{in_g\theta}u_p(\theta,\phi)$ and the Wannier states as $\Phi_p(\theta-2\pi l,\phi) = \frac{1}{\sqrt{N}}\sum_{n_g} e^{-i2\pi l\cdot n_g}\Psi^p_{n_g}(\theta,\phi)$, where l is an integer.

The low-energy levels are either localized in the 0 or in the π-valley, which we here explicitly note by a superscript: $u_p^0(\theta,\phi)$ and $u_p^\pi(\theta,\phi)$. We also distinguish between Wannier wavefunctions localized in the two different valleys by introducing

$$\Phi_p^0(\theta,\phi) = \Phi_p(\theta,\phi), \tag{30}$$

$$\Phi_p^\pi(\theta,\phi) = \Phi_p(\theta+\pi,\phi), \tag{31}$$

which are centered around the center of the 0 and π valley, respectively.

Next we consider the charge matrix elements $\langle u_p^0|i\partial_\theta|u_q^\pi\rangle$ and $\langle u_p^0|i\partial_\phi|u_q^\pi\rangle$. Since the states are assumed to be localized either in the $\theta=0$ or $\theta=\pi$ well, we only consider the contribution of two states being the nearest neighbours, i.e. for l component of u_p^0, we only keep l, $l+1$ components of u_q^π. The matrix elements are then

$$\begin{aligned}\langle u_p^0|i\partial_\theta|u_q^\pi\rangle =& i\int d\theta d\phi\, \Phi_p^0(\theta,\phi)\partial_\theta\big(\Phi_q^\pi(\theta-\pi,\phi) + \Phi_q^\pi(\theta+\pi,\phi)e^{-i2\pi n_{\rm g}}\big) \\ &+ n_{\rm g}\int d\theta d\phi\, \Phi_p^0(\theta,\phi)\big(\Phi_q^\pi(\theta-\pi,\phi) + \Phi_q^\pi(\theta+\pi,\phi)e^{-i2\pi n_{\rm g}}\big),\end{aligned} \tag{32}$$

$$\langle u_p^0|i\partial_\phi|u_q^\pi\rangle = i\int d\theta d\phi\, \Phi_p^0(\theta,\phi)\partial_\phi\big(\Phi_q^\pi(\theta-\pi,\phi) + \Phi_q^\pi(\theta+\pi,\phi)e^{-i2\pi n_{\rm g}}\big). \tag{33}$$

For simplicity, we define the following variables

$$\eta_0^{\rm L} = \int d\theta d\phi \Phi_p^0(\theta,\phi)\Phi_q^\pi(\theta+\pi,\phi), \qquad \eta_0^{\rm R} = \int d\theta d\phi \Phi_p^0(\theta,\phi)\Phi_q^\pi(\theta-\pi,\phi),$$

$$\eta_1^{\rm L} = i\int d\theta d\phi \Phi_p^0(\theta,\phi)\partial_\theta\Phi_q^\pi(\theta+\pi,\phi), \qquad \eta_1^{\rm R} = i\int d\theta d\phi \Phi_p^0(\theta,\phi)\partial_\theta\Phi_q^\pi(\theta-\pi,\phi),$$

$$\eta^{\rm L} = i\int d\theta d\phi \Phi_p^0(\theta,\phi)\partial_\phi\Phi_q^\pi(\theta+\pi,\phi), \qquad \eta^{\rm R} = i\int d\theta d\phi \Phi_p^0(\theta,\phi)\partial_\phi\Phi_q^\pi(\theta-\pi,\phi).$$

The matrix element thus can be written as

$$\langle u_p^0|i\partial_\theta|u_q^\pi\rangle = (\eta_1^{\rm L}e^{-i2\pi n_{\rm g}} + \eta_1^{\rm R}) + n_{\rm g}(\eta_0^{\rm L}e^{-i2\pi n_{\rm g}} + \eta_0^{\rm R}), \tag{34}$$

$$\langle u_p^0|i\partial_\phi|u_q^\pi\rangle = \eta^{\rm L}e^{-i2\pi n_{\rm g}} + \eta^{\rm R}. \tag{35}$$

The dipole matrix elements can be further simplified depending on the parities along the θ and ϕ directions, which eventually leads to the charge dependence of the fluxon dipole matrix elements summarized in Table S3. The plasmon transition in the $0-\pi$ qubit is similar to the case of the transmon qubit, and the result is summarized in the Table S4.

	$\Pi_i^\theta = \Pi_j^\theta$, $\Pi_i^\phi = \Pi_j^\phi$	$\Pi_i^\theta = -\Pi_j^\theta$, $\Pi_i^\phi = \Pi_j^\phi$	$\Pi_i^\theta = \Pi_j^\theta$, $\Pi_i^\phi = -\Pi_j^\phi$	$\Pi_i^\theta = -\Pi_j^\theta$, $\Pi_i^\phi = -\Pi_j^\phi$
$\lvert\langle i\rvert i\partial_\theta\lvert j\rangle\rvert$	$\lvert\sin \pi n_{\rm g}\rvert$	$\lvert\cos \pi n_{\rm g}\rvert$	0	0
$\lvert\langle i\rvert i\partial_\phi\lvert j\rangle\rvert$	0	0	$\lvert\cos \pi n_{\rm g}\rvert$	$\lvert\sin \pi n_{\rm g}\rvert$

Table S3: Matrix elements for fluxon transition.

	$\Pi_i^\theta = \Pi_j^\theta$, $\Pi_i^\phi = \Pi_j^\phi$	$\Pi_i^\theta = -\Pi_j^\theta$, $\Pi_i^\phi = \Pi_j^\phi$	$\Pi_i^\theta = \Pi_j^\theta$, $\Pi_i^\phi = -\Pi_j^\phi$	$\Pi_i^\theta = -\Pi_j^\theta$, $\Pi_i^\phi = -\Pi_j^\phi$
$\lvert\langle i\rvert i\partial_\theta\lvert j\rangle\rvert$	$\lvert\sin 2\pi n_{\rm g}\rvert$	$\lvert 1+\epsilon\cos 2\pi n_{\rm g}\rvert$	0	0
$\lvert\langle i\rvert i\partial_\phi\lvert j\rangle\rvert$	0	0	$\lvert 1+\epsilon\cos 2\pi n_{\rm g}\rvert$	$\lvert\sin 2\pi n_{\rm g}\rvert$

Table S4: Matrix elements for plasmon transition.

2.2 Population transfer in the two-tone Raman pulse scheme

We model the Raman pulse scheme in the $0-\pi$ qubit by truncating the energy level structure to the ground states of the valleys $|0_s\rangle$, $|\pi_s^+\rangle$ and the intermediate level $|\pi_{d\theta}^-\rangle$. For simplicity, we relabel these levels by $|0_s\rangle \to |0\rangle$, $|\pi_s^+\rangle \to |2\rangle$ and $|\pi_{d\theta}^-\rangle \to |1\rangle$ (see Fig. S5A). We first consider the unitary evolution of this Λ-system driven by two classical fields (*44*)

$$H/\hbar = \omega_1\sigma_{11} + \omega_2\sigma_{22} + \left[\Omega_\alpha \cos(\omega_\alpha t)\sigma_{01} + \Omega_\beta \cos(\omega_\beta t)\sigma_{12} + h.c.\right], \tag{36}$$

where $\omega_0 = 0 < \omega_2 < \omega_1$ are the eigenfrequencies of $|0\rangle$, $|2\rangle$ and $|1\rangle$, respectively, ω_α and ω_β are the frequencies of the drive tones with amplitudes Ω_α and Ω_β, respectively, while $\sigma_{ij} = |i\rangle\langle j|$ for $i,j \in [1,2,3]$. We moreover assume that the α (β) drive addresses only the $|0\rangle \leftrightarrow |1\rangle$ ($|1\rangle \leftrightarrow |2\rangle$) transition.

Moving to a rotating frame where the drives are equally detuned from the ancillary level $|1\rangle$, i.e. $\omega_\alpha = \omega_1 - \Delta$, $\omega_\beta = \omega_1 - \omega_2 - \Delta$, and performing the RWA approximation, Eq. (36) takes the time-independent form of

$$\tilde{H}/\hbar = \Delta\sigma_{11} + \left[\frac{1}{2}\Omega_\alpha\sigma_{01} + \frac{1}{2}\Omega_\beta\sigma_{12} + h.c.\right]. \tag{37}$$

Defining $\tilde{\Omega} = \sqrt{\Delta^2 + \Omega_\alpha^2 + \Omega_\beta^2}$, the eigenfrequencies of Eq. (37) are given by

$$\begin{aligned} \epsilon_0 &= 0, \\ \epsilon_\pm &= \frac{1}{2}\left(\Delta \pm \tilde{\Omega}\right), \end{aligned} \tag{38}$$

and correspond to the dressed states

$$\begin{aligned} |\Psi_0\rangle &= -\Omega_\beta|0\rangle + \Omega_\alpha|2\rangle, \\ |\Psi_\pm\rangle &= \Omega_\alpha|0\rangle + (\Delta \pm \tilde{\Omega})|1\rangle + \Omega_\beta|2\rangle, \end{aligned} \tag{39}$$

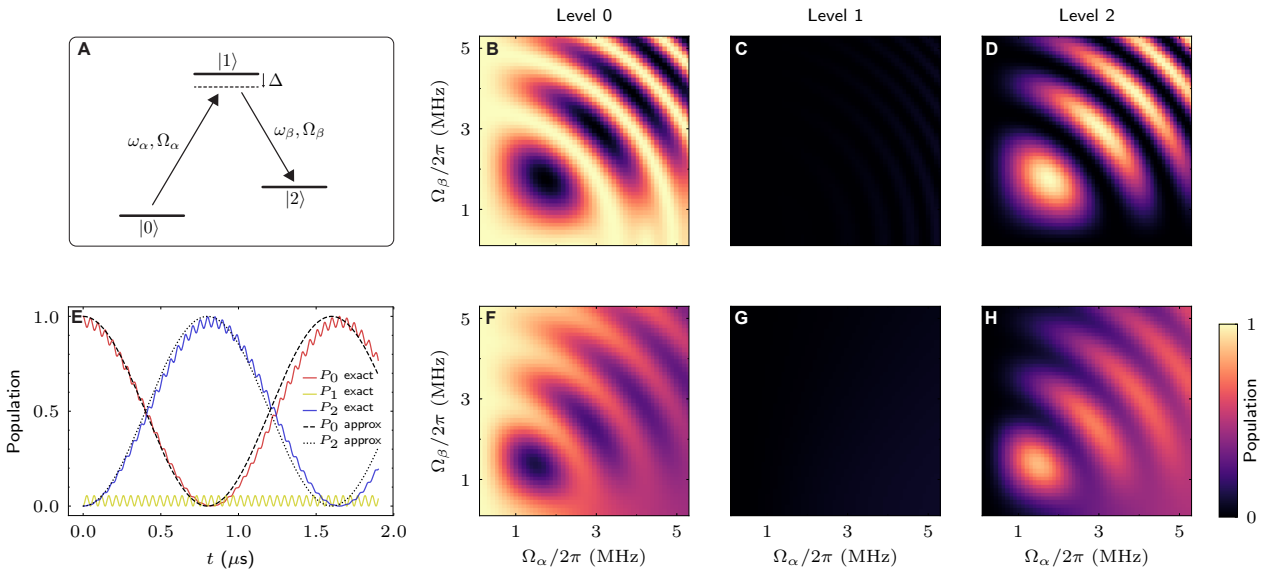

Fig. S5: (**A**) Schematic representation of three $0-\pi$ qubit levels coupled to two microwave drives forming a Λ-system. (**B** to **D**) Level population as a function of the drive amplitudes based on the analytical results of the time-evolution of the system ($t = 6.7$ μs, $\Delta/2\pi$ = 20 MHz). (**E**) Level population as a function of time based on the exact results for the effective two level system ($\Omega_\alpha/2\pi = \Omega_\beta/2\pi = 5$ MHz, $\Delta/2\pi$ = 20 MHz). (**F** to **H**) Results of the numerical simulation for two Gaussian pulses with $\sigma = 1$ μs, $\Delta/2\pi$ = 3 MHz, relaxation rates of $\Gamma_{10}/2\pi = \Gamma_{12}/2\pi = 100$ kHz and dephasing rate of $\Gamma_1^\phi/2\pi = 500$ kHz.

respectively.

We assume that the system at $t = 0$ is initialized in the $|0\rangle$ state when the drives are instantaneously turned on (square pulse). The time-evolution of the system can be obtained by using a basis transformation into the dressed basis. The system evolves to the state $|\Psi(t)\rangle = \alpha(t)|0\rangle + \beta(t)|1\rangle + \gamma(t)|2\rangle$ at time t, where

$$\begin{aligned}
\alpha(t) &= \frac{\Omega_\alpha^2}{\Omega_\alpha^2+\Omega_\beta^2} \times \left[\frac{\Omega_\beta^2}{\Omega_\alpha^2} + e^{-i\Delta t/2}\left(\cos\frac{\tilde{\Omega}t}{2} + i\frac{\Delta}{\tilde{\Omega}}\sin\frac{\tilde{\Omega}t}{2}\right)\right], \\
\beta(t) &= \frac{\Omega_\alpha}{\tilde{\Omega}} \times \left[-ie^{-i\Delta t/2}\sin\frac{\tilde{\Omega}t}{2}\right], \\
\gamma(t) &= \frac{\Omega_\alpha\Omega_\beta}{\Omega_\alpha^2+\Omega_\beta^2} \times \left[-1 + e^{-i\Delta t/2}\left(\cos\frac{\tilde{\Omega}t}{2} + i\frac{\Delta}{\tilde{\Omega}}\sin\frac{\tilde{\Omega}t}{2}\right)\right].
\end{aligned} \tag{40}$$

Fig. S5E shows the level populations as a function of time for $\Omega_1 = \Omega_2$. We observe Rabi oscillations between the two ground states $|0\rangle$ and $|2\rangle$ with only a negligible population in the intermediate level $|1\rangle$. Interestingly, the Rabi oscillation features a superimposed low amplitude, high frequency

modulation (*44*). We note that adiabatic elimination of the intermediate level in the vicinity of equal drives $\Omega_1 \approx \Omega_2$ leads to an effective two-level system (*43*) with Rabi rate of $\Omega_R = \Omega_1\Omega_2/2\Delta$. This effective model is in good agreement with the exact analytical solution (dashed and dotted lines in Fig. S5E).

Fig. S5B to D show the level population at a given time as function of the drive amplitude and detuning, similar to the pulsed measurements carried out in our experiment. The results show that maximal population transfer between $|0\rangle$ and $|2\rangle$ is possible when the drives are equal.

Additionally to the exact solutions, we carried out numerical simulations using the QuTiP software package (*47*) to solve the time evolution of the system involving Gaussian-shaped pulses and decay mechanisms using a Lindblad Master-equation solver. The result of the numerical simulation is in very good agreement with our experimental findings, see Fig. 4C and Fig. S5F to H.

2.3 Coherence times as a function of external flux

We mapped out the flux-dependence of the coherence times of the logical qubit states in the close vicinity of $\Phi_{\text{ext}} = 0$ (Fig. S6). The data demonstrate that the Ramsey coherence times have strong dependence on the magnetic flux with a significant enhancement around the sweet spot.

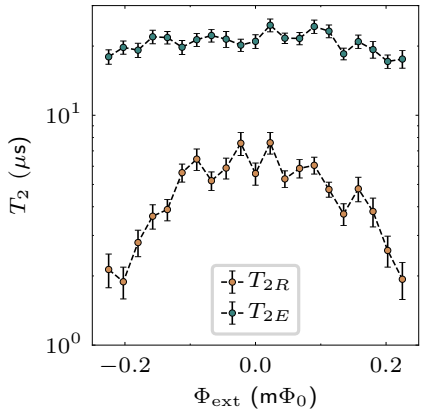

Fig. S6: Measured T_{2R} and T_{2E} values around the magnetic sweet spot. Dashed lines are a guide to the eye.

2.4 Autler-Townes spectroscopy as a function of the offset charge

For completeness, we report all measured Autler-Townes spectroscopy maps obtained at different offset-charge bias, in addition to the one presented in Fig. 3I. As discussed in the main text, we use a strong drive to dress the $|0_{p\theta}\rangle \leftrightarrow |\pi^-_{p\theta}\rangle$ transition. Denoting the qubit transition by ω_q, the coupling rate by Ω_c and the coupler drive frequency by ω_c, the dispersion of the dressed states takes the form of $\epsilon_\pm = (\omega_q - \omega_c) \pm \sqrt{(\omega_q - \omega_c)^2 + \Omega_c^2}$, which can be measured by an additional weak probe tone.

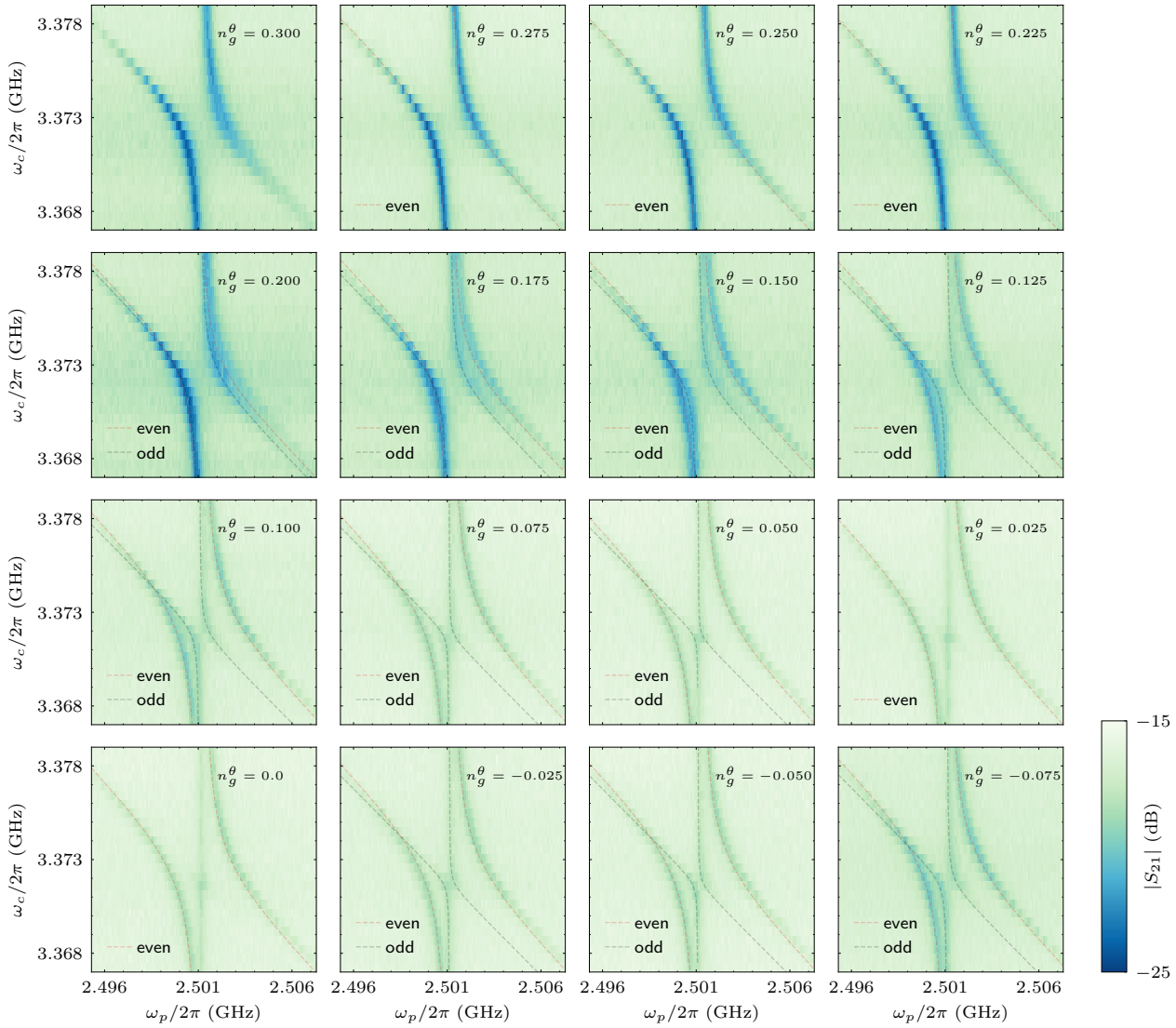

Fig. S7: Raw data of the Autler-Townes spectroscopy as a function of the offset-charge. Black and red dashed lines show the least-squares fit to the data in case of odd and even charge parity.

Chapter 6

Probing superinductances via the fluxonium qubit architecture

6.1 Multimode theories for nonlinear high-impedance modes

Strictly speaking, superconducting quantum circuits are described by an infinite number of electromagnetic modes. However, physical reasons often allow us to reduce the number of modes that need to be taken into account to model such devices, for instance by introducing frequency cutoffs [6]. A general method for deriving multimode circuit Hamiltonians is to split the energy contribution of the circuit elements into a linear and a nonlinear part [43, 107]. The linear part defines the normal modes of the circuit that can be determined without the need of a quantum theory. In most cases, the normal modes are a good starting point to quantize the problem. By promoting the normal-mode variables to quantum operators, the nonlinear part of the circuit Hamiltonian can be expanded in this basis. This general procedure can be used to treat weakly anharmonic devices embedded in 3D cavities [43, 108] or arbitrary microwave environments [109, 110], in addition to strongly nonlinear multimode circuits [73, 107, 111, 112, 113, 114]. As shown below, the resulting multimode theory can be truncated to a finite number of modes that describe efficiently the effect of the nonlinearities in the circuit.

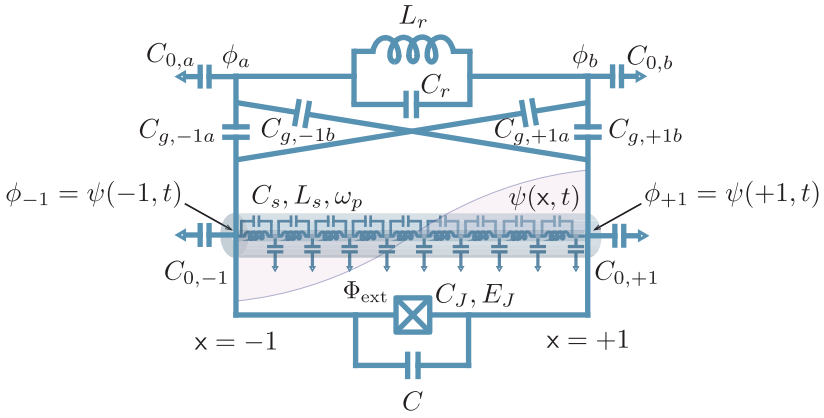

Figure 6.1 Nanowire-superinductance fluxonium qubit coupled to a lumped-element resonator. We include the complete capacitance network that is relevant for the experimental setup in Ref. [73]. The nanowire is illustrated as a transmission line where $\psi(x,t)$ is a field operator corresponding to the flux.

6.1.1 Hamiltonian of the nanowire-superinductance fluxonium qubit

We now illustrate the application of the normal-mode framework to the case of a fluxonium qubit composed of a nanowire superinductance. The essential ingredients in the derivation that follows have been key to explain the experiment of Ref. [73], that we present in Sect. 6.2. Let us consider the circuit in Fig. 6.1, which shows a fluxonium qubit (bottom) capacitively coupled to a lumped-element LC resonator (top). The circuit also includes spurious ground and stray capacitances that are important to describe the experimental setup accurately. The black-sheep junction of the fluxonium qubit has energy (inductance) E_J (L_J) and capacitance C_J, and it is shunted by a capacitance C. The nanowire superinductance is treated as a high-impedance transmission-line of length $2l$ (light blue), which extends from $x = -1$ to $x = +1$, where $x = x/l \in [-1,1]$ is a dimensionless coordinate along the nanowire. Moreover, the nanowire is assumed to be homogeneous, with plasma frequency ω_p and distributed capacitance $C_s/2l$ and inductance $L_s/2l$, where C_s and L_s are the total ground capacitance and inductance of this device. As pointed out below, this theory can also describe nanowires with disorder if a simple modification is made. The intrinsic nonlinearity of the nanowire is however neglected, as it can be made small by design [78].

Let us first analyze the subsystem defined by the fluxonium circuit. Under the above assumptions, the Lagrangian of the nanowire takes the form [115]

$$\mathcal{L}_s = \int_{-1}^{1} dx \frac{(C_s/2)}{2} [\dot{\psi}(x,t)]^2 - \frac{1}{2(L_s/2)} [\partial_x \psi(x,t)]^2 + \frac{1}{2\omega_p^2 (L_s/2)} [\partial_x \dot{\psi}(x,t)]^2, \tag{6.1}$$

where $\psi(x,t)$ is a (continuous) flux degree of freedom (see Fig. 6.1). Introducing the differential operator

$$\mathcal{C}[f(x,t)] = (C_s/2)f(x,t) - \frac{1}{\omega_p^2(L_s/2)}\partial_x^2 f(x,t), \tag{6.2}$$

the Euler-Lagrange equation for Eq. (6.1) is the generalized wave equation

$$\mathcal{C}\ddot{\psi}(x,t) = \frac{1}{(L_s/2)}\partial_x^2\psi(x,t), \tag{6.3}$$

Introducing the Ansatz $\psi(x,t) \sim e^{-ik_\omega x}e^{-i\omega t}$ in Eq. (6.3), we arrive at the dispersion relation of this medium

$$k_\omega^2 = \frac{\omega^2/\omega_s^2}{1-\omega^2/\omega_p^2}, \tag{6.4}$$

where k_ω is a dimensionless wave vector, $\omega_s = 1/\sqrt{(C_s/2)(L_s/2)}$ is a characteristic frequency, and $\omega < \omega_p$. We note that disorder in the nanowire simply leads to a different dispersion relation.

While Eq. (6.3) holds in the bulk of the nanowire, the field operator is subject to the boundary conditions that are imposed by the rest of the circuit. To determine these boundary conditions, it is useful to write a lattice (or lumped-element) model for the nanowire, which consists of an array of small LC circuits and ground capacitances as illustrated in Fig. 6.1. By writing the equations of motion for the node operators of the lattice that correspond to the boundaries of the nanowire and taking the continuous limit, one finds the effective boundary conditions for the field

$$(\boldsymbol{C} + \boldsymbol{\partial C})\cdot\ddot{\boldsymbol{\phi}} + (\boldsymbol{L}^{-1} + \boldsymbol{\partial L}^{-1})\cdot\boldsymbol{\phi} = \boldsymbol{0}, \tag{6.5}$$

where $\boldsymbol{\phi} = (\phi_{-1},\phi_{+1}) \equiv (\psi(-1,t),\psi(+1,t))^T$ is the field amplitude at the boundaries. Here, $\boldsymbol{C} = \mathrm{diag}_{x=\mp1}\left(\sum_{\alpha=a,b} C_{g,x\alpha} + C_{0,x} + C_J + C\right) - (C_J + C)\sigma_x$ and $\boldsymbol{L}^{-1} = (\mathbb{1} - \sigma_x)/L_J$ are, respectively, the capacitance and (inverse) inductance matrices of the fluxonium circuit, and $\boldsymbol{\partial C} = \mathrm{diag}(x\,\partial_x)|_{x=\mp1}/[\omega_p^2(L_s/2)]$ and $\boldsymbol{\partial L}^{-1} = \mathrm{diag}(x\,\partial_x)|_{x=\mp1}/(L_s/2)$ are diagonal matrices that enforce the boundary conditions.

We now consider a normal-mode solution to Eq. (6.5) of the form $\psi_m(x,t) = \xi_m(t)u_m(x)$, where $\xi_m(t) \sim e^{-i\omega_m t}$ is a time-dependent amplitude and

$$u_m(x) = A_m\cos(k_m x) + B_m\sin(k_m x_m), \tag{6.6}$$

is the spatial profile of the normal-mode function along the nanowire. Note that Eq. (6.6)

incorporates both right- and left-propagating waves for $k_m > 0$. Inserting this Ansatz in Eq. (6.5) leads to the condition

$$[-\omega_m^2(\boldsymbol{C}+\partial\boldsymbol{C})+(\boldsymbol{L}^{-1}+\partial\boldsymbol{L}^{-1})]\cdot\boldsymbol{u}_m(x)=\boldsymbol{0}, \tag{6.7}$$

where $\boldsymbol{u}_m(x)=(u_m(x=-1),u_m(x=+1))^T$ is a vector composed by the normal mode function Eq. (6.6) evaluated at the boundaries $x=\pm 1$. Equation (6.7) determines the normal modes of the circuit. Indeed, by expressing k_m in terms of ω_m using the dispersion relation Eq. (6.4), Eq. (6.7) can be put in the form $\boldsymbol{M}(\omega_m)\cdot(A_m,B_m)^T=\boldsymbol{0}$, where $\boldsymbol{M}(\omega_m)$ is a 2×2 matrix. The normal-mode frequencies are determined by the condition $\det[\boldsymbol{M}(\omega_m)]=0$ ensuring nontrivial solutions to the this system of equations, while $(A_m,B_m)^T$ follows from the null space of $\boldsymbol{M}(\omega_m)$. Finally, it can be shown that the mode functions $\{u_m(x)\}$ obey the orthogonality conditions [112]

$$\langle\boldsymbol{u}_m,\boldsymbol{u}_n\rangle_C=\boldsymbol{u}_m^T\cdot\boldsymbol{C}\cdot\boldsymbol{u}_n+\int_{-1}^{1}dx(C_s/2)u_m(x)u_n(x)+\int_{-1}^{1}dx\frac{u_m'(x)u_n'(x)}{\omega_p^2(L_s/2)}\equiv C_m\delta_{mn}, \tag{6.8}$$

and

$$\langle\boldsymbol{u}_m,\boldsymbol{u}_n\rangle_L=\boldsymbol{u}_m^T\cdot\boldsymbol{L}^{-1}\cdot\boldsymbol{u}_n+\int_{-1}^{1}dxu_m'(x)u_n'(x)/(L_s/2)\equiv L_m^{-1}\delta_{mn}, \tag{6.9}$$

where $(C_mL_m)^{-1}=\omega_m^2$. Equations (6.8) and (6.9) can be used to normalize the coefficients $\{A_m,B_m\}$.

We have now completed the first part of the derivation, which requires to find the circuit normal modes. Next, we aim to write the circuit Hamiltonian in this useful basis. To this end, we first consider the Lagrangian of the circuit. Expanding the nanowire field operator in the normal mode basis as

$$\psi(x,t)=\sum_m\xi_m(t)u_m(x), \tag{6.10}$$

inserting this definition in Eq. (6.1) and incorporating the readout resonator to the model, we arrive at the circuit Lagrangian

$$\begin{aligned}L=&\sum_m\frac{C_m}{2}\dot{\xi}_m^2-\frac{\xi_m^2}{2L_m}+E_J[\cos(\delta_\psi/\varphi_0)+(\Delta\psi/\varphi_0)/2]\\&+\frac{C_a}{2}\dot{\phi}_a^2+\frac{C_b}{2}\dot{\phi}_b^2+\frac{C_r}{2}(\dot{\phi}_a-\dot{\phi}_b)^2-\frac{1}{2L_r}(\phi_a-\phi_b)^2\\&-\sum_m\sum_{x=\mp1}u_m(x)\sum_{\alpha=a,b}C_{g,x\alpha}\dot{\xi}_m\dot{\phi}_\alpha,\end{aligned} \tag{6.11}$$

where $\Delta\psi=\psi(-1,t)-\psi(1,t)$, $\delta_\psi=\Delta\psi+\Phi_{\text{ext}}$, and $C_\alpha=\sum_{x=\mp1}C_{g,x\alpha}+C_{0,\alpha}$ are effective capacitances for $\alpha=\{a,b\}$. Here, C_r and L_r are the inductance and capacitance of the

lumped-element resonator. Assuming that there exists some circuit-element disorder, all nanowire modes have a nonzero phase drop $\Delta u_m = u_m(-1) - u_m(1)$ across the black-sheep Josephson junction. We can thus rewrite Eq. (6.11) in terms of the new flux operators $\phi_m = \Delta u_m \xi_m$, resulting in

$$\begin{aligned} L = &\sum_m \frac{\tilde{C}_m}{2}\dot{\phi}_m^2 - \frac{\phi_m^2}{2\tilde{L}_m} + E_J \cos\Big(\sum_m \phi_m/\varphi_0 + \varphi_{\text{ext}}\Big) + \sum_{n>m}\frac{1}{L_J}\phi_m\phi_n \\ &+ \frac{\tilde{C}_r}{2}\dot{\phi}_-^2 - \frac{1}{2L_r}\phi_-^2 - \sum_m \sum_{\mathrm{x}=\mp 1} \frac{u_m(\mathrm{x})}{\Delta u_m}\Delta C_{g,\mathrm{x}}\dot{\phi}_m\dot{\phi}_-, \end{aligned} \tag{6.12}$$

where we have introduced the resonator modes $\phi_\pm = \phi_a \pm \phi_b$, eliminated the cyclic variable ϕ_+, and defined the effective circuit parameters

$$\begin{aligned} \tilde{C}_m &= \frac{C_m}{|\Delta u_m|^2}, \\ \tilde{L}_m^{-1} &= \frac{1}{|\Delta u_m|^2}\int_{-1}^{1} d\mathrm{x}\frac{[u_m'(\mathrm{x})]^2}{L_s/2}, \end{aligned} \tag{6.13}$$

for the normal modes, $\tilde{C}_r = (C_a + C_b)/4 + C_r$ for the resonator, and $\Delta C_{g,\mathrm{x}} = (C_{g,\mathrm{x}a} - C_{g,\mathrm{x}b})/2$ for the coupling capacitances.

Having obtained Eq. (6.12), it is now straightforward to derive the circuit Hamiltonian. The conjugate charges follow as

$$\begin{aligned} q_m = &\frac{\partial L}{\partial \dot{\phi}_m} = \tilde{C}_m\dot{\phi}_m - \sum_{\mathrm{x}=\mp 1}\frac{u_m(\mathrm{x})}{\Delta u_m}\Delta C_{g,\mathrm{x}}\dot{\phi}_- \\ q_- = &\frac{\partial L}{\partial \dot{\phi}_-} = \tilde{C}_r\dot{\phi}_- - \sum_m\sum_{\mathrm{x}=\mp 1}\frac{u_m(\mathrm{x})}{\Delta u_m}\Delta C_{g,\mathrm{x}}\dot{\phi}_m, \end{aligned} \tag{6.14}$$

and need to be inverted to find $\dot{\phi}_m = \dot{\phi}_m(\{q_m\}, q_-)$ and $\dot{\phi}_- = \dot{\phi}_-(\{q_m\}, q_-)$. Doing this, the circuit Hamiltonian $H = \sum_m q_m\dot{\phi}_m + q_-\dot{\phi}_- - L$ takes the form

$$\begin{aligned} H = &\sum_m \frac{q_m^2}{2\tilde{C}_m} + \frac{\phi_m^2}{2\tilde{L}_m} - E_J\cos\Big(\sum_m \phi_m/\varphi_0 + \varphi_{\text{ext}}\Big) - \sum_{n>m}\frac{1}{L_J}\phi_m\phi_n + \frac{q_-^2}{2\tilde{C}_r'} + \frac{\phi_-^2}{2L_r} \\ &+ \sum_m\sum_{\mathrm{x}=\mp 1}\frac{u_m(\mathrm{x})}{\Delta u_m}\frac{\Delta C_{g,\mathrm{x}}}{\tilde{C}_r'\tilde{C}_m}q_-q_m \\ &+ \frac{1}{2}\sum_{m,m'}\sum_{\mathrm{x},\mathrm{x}'=\mp 1}\frac{u_m(\mathrm{x})u_{m'}(\mathrm{x}')}{\Delta u_m \Delta u_{m'}}\frac{\Delta C_{g,\mathrm{x}}\Delta C_{g,\mathrm{x}'}}{\tilde{C}_r'\tilde{C}_m\tilde{C}_{m'}}q_mq_{m'}, \end{aligned} \tag{6.15}$$

where we have defined the effective capacitance

$$\tilde{C}_r' = \tilde{C}_r - \sum_m \sum_{\mathrm{x},\mathrm{x}'=\mp 1} \frac{u_m(\mathrm{x})u_m(\mathrm{x}')}{(\Delta u_m)^2} \frac{\Delta C_{g,\mathrm{x}} \Delta C_{g,\mathrm{x}'}}{\tilde{C}_m}. \tag{6.16}$$

Equation (6.15) is a complete multimode model for the device in Fig. 6.1. The first line of this full circuit Hamiltonian includes the multimode fluxonium Hamiltonian and the readout resonator. The second line contains a multimode qubit-resonator capacitive interaction. The third line represents a capacitive coupling between the fluxonium modes, which is due to the resonator and only second order in the coupling capacitances. We observe that we have been able to extend this formalism to a general superconducting circuit including distributed circuit elements, such as the nanowire in Fig. 6.1, and any number of Josephson junctions with arbitrary connectivity. For reasons of brevity, however, these results will be reported elsewhere. The next section suggests a proper truncation of the multimode Hamiltonian.

6.1.2 Truncating the multimode Hamiltonian to a finite number of modes

So far, the model in Eq. (6.15) considers an infinite number of degrees of freedom. To obtain a tractable description, we now truncate the number of modes that are kept in this theory. The reasons for the existence of a proper truncation can be made clear with the help of Fig. 6.2. There, we consider the mode structure of a granular Aluminum device fabricated in the group of Andrew Houck at Princeton University. This fluxonium device is coupled to a lumped-element readout resonator as in Fig. 6.1. Figure 6.2 (a) shows the normal-mode frequency as a function of the mode number. As a result of the large plasma frequency of granular Aluminum nanowires [78], the frequency scale is also large. Note that there are only about three modes below the experimentally relevant frequency range $\omega/2\pi \lesssim 12\,\mathrm{GHz}$. Physical intuition suggests that higher frequency modes would not significantly affect the low-frequency spectrum. More importantly, Fig. 6.2 (b) shows the effective mode impedance $\tilde{z}_m = \sqrt{\tilde{L}_m/\tilde{C}_m}/R_Q$ as a function of the mode number. Since the mode operator scale as $\phi_m \sim \sqrt{\tilde{z}_m}$, the rapid decay of $\tilde{z}_m$ indicates that the multimode coupling in Eq. (6.15), due to the black-sheep junction, becomes negligible as the mode number increases. Thus, high-frequency modes are more linear and effectively decouple from the low-frequency (and high-impedance) modes.

To see this more clearly, Fig. 6.2 (c) shows the low-frequency energy spectrum of the device, which is computed considering the first three normal modes. The highly anhar-

monic fluxonium transitions are due to the first (highest impedance) mode, which is greatly affected by the nonlinearity of the black-sheep junction. The transitions due to this first mode hybridize with the almost flux-insensitive transitions corresponding to the next two nanowire modes (at frequencies $\sim 6\,\mathrm{GHz}$ and $\sim 10.3\,\mathrm{GHz}$). We also indicate the resonator transition with frequency $\omega_r/2\pi$. We verify that taking the fourth mode into consideration does not significantly affect the spectrum. Thus, for the purpose of an experiment, retaining only the first three nanowire modes is enough to describe the device very accurately in the frequency range of interest. This is a consequence of the rapid decay of the mode impedances.

Additionally, Fig. 6.2 (d) illustrates the mode functions corresponding to the four lowest frequency circuit modes. Note that the first mode [with mode function $u_0(x)$] cannot be recognized in the spectrum due to the strong renormalization effect of the black-sheep junction potential on this mode. The next two modes, with mode functions $u_1(x)$ and $u_2(x)$, can be clearly identified. Finally, the frequency of the fourth mode, with mode function $u_3(x)$, lies beyond the frequency range of Fig. 6.2 (b). Note that the modes are not perfectly symmetric or antisymmetric due to the presence of (large) circuit-element disorder.

The ingredients presented in this section lay the basis for the content of the research papers included in this chapter. The mode structure of devices with high-impedance modes is crucial to model these systems accurately. This is particularly true in cases where multilevel transitions are exploited to perform gate operations. Moreover, being able to derive effective circuit Hamiltonians from a multimode theory has the potential to improve circuit design and enhance our predictive power. We address other interesting aspects of the multimode structure of the fluxonium qubit below.

6.2 Nanowire-superinductance fluxonium qubit

This section is dedicated to an introductory discussion of the paper entitled "Nanowire-superinductance fluxonium qubit".

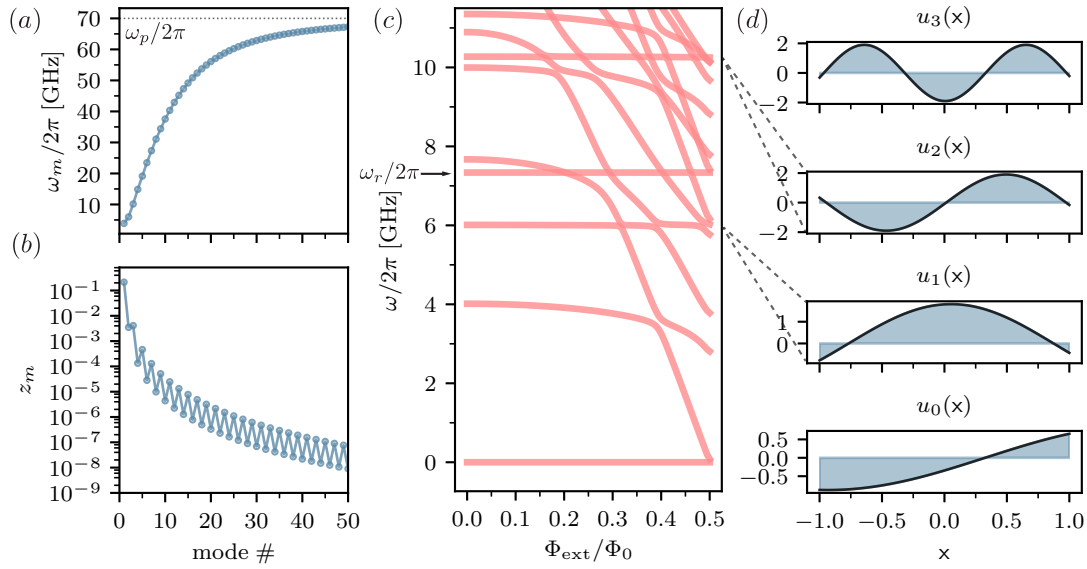

Figure 6.2 Properties of a nanowire-superinductance fluxonium qubit capacitively coupled to a readout resonator. (a) Mode frequency as a function of the mode number (light blue). The dotted black line indicates the plasma frequency of the nanowire [see Eq. (6.4)]. (b) Reduced mode impedance as a function of the mode number. (c) Device spectrum as a function of the external flux, including the readout resonator and nanowire modes. (d) First four nanowire mode functions as a function of the reduced coordinate x. The vertical axes display the (dimensionless) mode function $u_m(x)$, where m is the mode number. Parameters: $C_J = 3.5\,\text{fF}$, $L_J = 35.16\,\text{nH}$, $C = 20.5\,\text{fF}$, $L_s = 139.84\,\text{nH}$, $C_s = 73.62\,\text{fF}$, $\omega_p/2\pi = 70.0\,\text{GHz}$, $\omega_r/2\pi = 7.34\,\text{GHz}$, $Z_r = 78\,\Omega$ (resonator impedance), $C_{g,-1a} = 36.7\,\text{fF}$, $C_{g,-1b} = 1.82\,\text{fF}$, $C_{g,+1a} = 41.83\,\text{fF}$, $C_{g,+1b} = 37.8\,\text{fF}$, $C_{0,-1} = 0.0\,\text{fF}$ and $C_{0,+1} = 1.56\,\text{fF}$, corresponding to a granular Aluminum device at HouckLab (Princeton University).

6.2.1 Motivation

Fluxonium qubit devices have mostly been built using Josephson-junction-array superinductances. Junction-array superinductances are attractive because of design flexibility and very low losses [74, 90]. Moreover, these devices leverage the fabrication techniques developed for high-quality Josephson junctions.

A thin-film nanowire built from a disordered superconductor is an alternative approach to obtain large inductances. Although it is difficult to provide a quantitative comparison between junction arrays and nanowires, the latter are particularly attractive because of their very little stray capacitances, large plasma frequencies and reduced Kerr nonlinearities [78]. Moreover, high-kinetic inductance superconducting materials, such as NbTiN, TiN and grAl have already been used in the context of microwave detectors [116, 72, 117], para-

metric amplifiers [118, 119, 120], and rf-SQUID qubits [121].

In this paper in collaboration with the group of Andrew Houck at Princeton, we report the first realization of a fluxonium qubit with a nanowire superinductance based on NbTiN. Moreover, we develop a new theory to study the multimode structure of these devices, modeling the nanowire as a high-impedance transmission line.

6.2.2 Main results of the paper

The main result of this paper is the demonstration of coherent control of a nanowire-based fluxonium qubit in the heavy-fluxonium regime. We report the fabrication of 3 devices with nanowire thickness, widths and lengths that are in the range $10-15\,\mathrm{nm}$, $40-100\,\mathrm{nm}$ and $630-730\,\mu\mathrm{m}$, respectively. The reported nanowire-superinductance values range from $\sim 120\,\mathrm{nH}$ to $\sim 310\,\mathrm{nH}$, with impedances in the range of $\sim 2-12\,\mathrm{k}\Omega$ (determined from a theory fit).

Since, in the heavy-fluxonium regime, tunneling between the two logical states (fluxons) is exponentially small, direct driving of the qubit transition as a way of realizing logical operations is not possible with high fidelity. Thus, in order to achieve coherent control of this device, one has to rely on the multilevel structure of the qubit [88, 89]. However, characterizing completely the low-frequency spectrum of the device is challenging. Indeed, as the matrix element corresponding to fluxon transitions is exponentially small, these transitions cannot be probed by two-tone spectroscopy.

To overcome this issue, in our work, the low-frequency spectrum is determined experimentally by a technique known as Autler-Townes spectroscopy [106]. With knowledge of the level structure, three intermediate levels are used to transfer population between the two logical qubit levels by means of fast ($\sim 15\,\mathrm{ns}$) sequential π-pulses between the intermediary states. This allow us to perform the measurement of T_1 for two heavy fluxonium devices. The largest T_1 is found to be in the order of $20\,\mu\mathrm{s}$ and is limited by inductive losses in the nanowire.

This T_1 measurement protocol is however not useful for demonstrating the coherent control of a nanowire fluxonium. In order to do so, a third device was built in a still lighter fluxonium regime, which is thus amenable to control by direct driving of the qubit transition. With this device, it is possible to measure both T_1 and T_2 as a function of the qubit frequency (external flux), and characterize capacitive and inductive losses in the nanowire.

The main theoretical result of this work is the derivation of a multimode theory for the

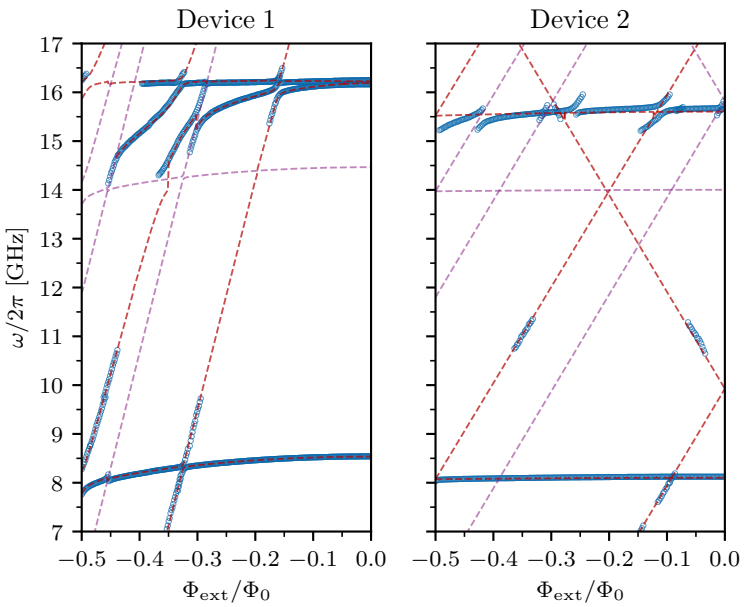

Figure 6.3 Two-tone spectroscopy results for nanowire-superinductance fluxonium devices as a function of the external flux. Light-blue markers correspond to the experimental data. Red dashed lines represent the result of the fit using the two-mode Hamiltonian. Dashed purple lines indicate sideband transitions. Adapted from [73].

device, similar to the treatment presented in Sect. 6.1.1. This multimode theory retains two modes that couple strongly to the black-sheep Josephson junction of the fluxonium, and an additional mode corresponding to the readout resonator to fit the experimentally measured spectra. As illustrated in Fig. 6.3, we find a remarkable agreement between tour theory and the experimental data for two devices and in a very large frequency range. We can moreover describe the anticrossings between the second nanowire mode for Device 1 in Fig. 6.3 (flux-insensitive transition around 16.3 GHz) and fluxon transitions that originate from the first mode. This theory goes significantly beyond previous works on the fluxonium qubit where the effect of additional circuit modes was described phenomenologically [65]. Our multimode theory was also verified using a newly developed DMRG algorithm that we describe in Sect. 6.3.

6.2.3 Conclusion and outlook

Our work demonstrates the first realization and coherent control of a fluxonium qubit with a nanowire superinductance. This shows that this architecture can indeed compete with junction-array realizations of the fluxonium qubit.

We also provide, for the first time, a complete multimode theory for the device that does significantly beyond previous work in the fluxonium architecture and fits the experimental data with very good accuracy in a large frequency range. Our theory represents an important step towards understanding the multimode structure of other superconducting circuits based on high-impedance modes, with applications to the $0 - \pi$ qubit.

Nanowire Superinductance Fluxonium Qubit

T. M. Hazard,[1,†] A. Gyenis,[1,†] A. Di Paolo,[2,†] A. T. Asfaw,[1] S. A. Lyon,[1] A. Blais,[2,3] and A. A. Houck[1,*]
[1]Department of Electrical Engineering, Princeton University, Princeton, New Jersey 08544, USA
[2]Institut quantique and Département de Physique, Université de Sherbrooke, Sherbrooke J1K 2R1 Quebec, Canada
[3]Canadian Institute for Advanced Research, Toronto, M5G 1M1 Ontario, Canada

(Received 30 May 2018; revised manuscript received 5 October 2018; published 10 January 2019)

We characterize a fluxonium qubit consisting of a Josephson junction inductively shunted with a NbTiN nanowire superinductance. We explain the measured energy spectrum by means of a multimode theory accounting for the distributed nature of the superinductance and the effect of the circuit nonlinearity to all orders in the Josephson potential. Using multiphoton Raman spectroscopy, we address multiple fluxonium transitions, observe multilevel Autler-Townes splitting and measure an excited state lifetime of $T_1 = 20\ \mu$s. By measuring T_1 at different magnetic flux values, we find a crossover in the lifetime limiting mechanism from capacitive to inductive losses.

DOI: 10.1103/PhysRevLett.122.010504

The development of superinductors [1–5] has received significant interest due to their potential to provide noise protection in superconducting qubits [6–8]. Moreover, inductively shunted Josephson junction based superconducting circuits are known to be immune to charge noise [1], and to flux noise in the limit of large inductances [9–12]. Despite remarkable progress, the superinductances that have been so far reported in the literature are still small compared to those needed for qubit protection [7,8,11,12].

A thin-film nanowire built from a disordered superconductor constitutes an alternative approach to reach the required superinductance regime. High-kinetic inductance superconducting materials, such as NbTiN and TiN, have been studied in the context of microwave detectors [13–15], parametric amplifiers [16–18], and rfSQUID qubits [19,20]. In a nanowire, the inertia of the Cooper pair condensate is manifested as the kinetic inductance of the superconducting wire, and can be expressed as

$$L_k = \left(\frac{m}{2e^2 n_s}\right)\left(\frac{l}{wd}\right), \tag{1}$$

where m is the free electron mass, e is the electron charge, and n_s is the density of Cooper pairs [14,21]. The second bracketed term in Eq. (1) is a geometric factor dependent on the length l, width w, and thickness d of the nanowire. By choosing a disordered superconductor with a low n_s and fabricating a sufficiently long and thin wire, the kinetic inductance can be made large enough to reach the superinductance regime. In this regime, the presence of stray ground capacitance and the large kinetic inductance lower the frequencies of the self-resonant modes of the device. As is the case of long junction arrays [2], the multimode structure of the device needs to be taken into account to produce an accurate theoretical description [22,23].

In this Letter, we demonstrate a fluxonium circuit integrating a NbTiN nanowire superinductance. We characterize the effect of the nanowire modes on the qubit spectrum with a multimode circuit theory accounting for the distributed nature of the superinductance. Importantly, and in contrast to previous approaches tailored to weakly anharmonic qubits [24,25], our theory incorporates the circuit nonlinearity to all orders in the Josephson potential. Such difference allows us to treat the strong anharmonicity of the fluxonium qubit efficiently, and to retain the effect of charge dispersion in the multimode Hamiltonian.

A simplified circuit schematic of the nanowire superinductance fluxonium is shown in Fig. 1(a). In contrast to standard fluxonium devices, where a lumped element inductor shunts the Josephson junction [1,3,4,26–28], our circuit model takes into account the fact that the nanowire superinductor is a high-impedance transmission line. We present data from measurements of three devices fabricated on two different films. The nanowires in devices 1 and 2 have widths of 110 and 40 nm, respectively, equal lengths of 730 μm, and a film thickness of 15 nm. The nanowire in device 3 is fabricated on a 10 nm thick film, has a width of 100 nm, and length of 630 μm. All the nanowires are fabricated by etching a wire pattern into the NbTiN film, with a single $\mathrm{Al/AlO_x/Al}$ junction connecting the two ends of the superinductor together. The qubit on devices 1 and 2 is capacitively coupled to a lumped element Nb resonator, with resonance frequency $\omega_r/2\pi = 6.08$ GHz and a loaded quality factor of $Q = 8,400$. The qubit on device 3 is coupled to a half-wavelength coplanar waveguide resonator with $Q = 14\,800$ and $\omega_r/2\pi = 7.50$ GHz. An optical image of device 1 is shown in Fig. 1(c).

The fluxonium energy spectrum is obtained by performing two-tone spectroscopy measurements as a function of the external magnetic flux, Φ_{ext}. The amplitude of the

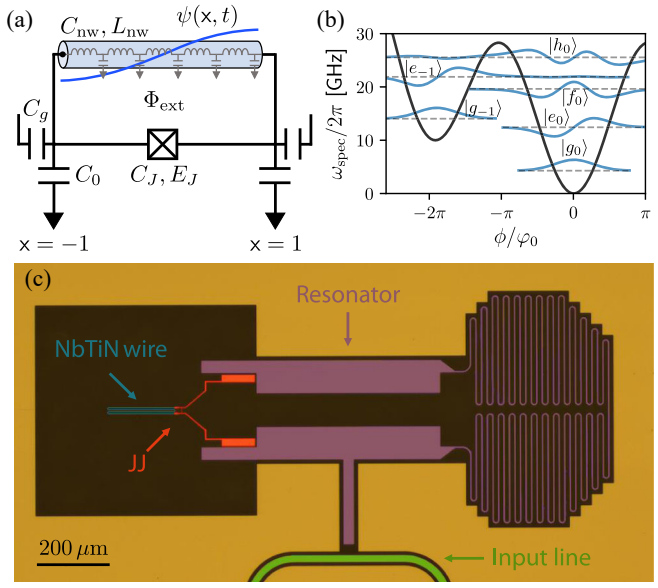

FIG. 1. (a) The circuit diagram for the qubit, with the first antisymmetric standing wave nanowire mode in blue. $\psi(\mathsf{x},t)$ denotes the flux operator as a function of the dimensionless coordinate $\mathsf{x} = x/l$. An off-chip coil generates the magnetic flux (Φ_{ext}) that is threaded through the loop formed by the nanowire and the junction. C_g and C_0 are the coupling capacitances to the readout resonator and to ground, respectively. (b) The first few fluxonium eigenstates plotted for $\Phi_{\text{ext}}/\varphi_0 = -0.38\pi$, and the respective qubit potential with wells around $\phi/\varphi_0 = -2\pi$ and $\phi/\varphi_0 = 0$, where $\varphi_0 = \hbar/2e$. (c) False colored image of the device with the NbTiN nanowire shown in blue, the single Josephson junction and gate capacitors in red, the readout resonator in purple, and the input transmission line in green.

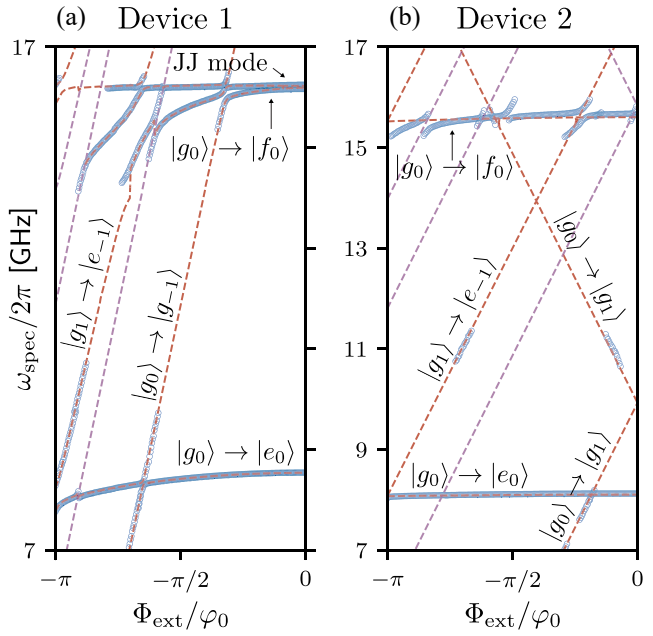

FIG. 2. Two-tone spectroscopy of device 1 (a) and device 2 (b) as a function of Φ_{ext}. The experimentally measured transition frequencies are indicated with blue markers. The result of a fit to the two-mode Hamiltonian in Eq. (5) and detailed in Ref. [30] is shown with red dashed lines corresponding to the fluxonium spectrum and with purple dashed lines indicating sideband transitions [31]. In (a), the inscription "JJ mode" (Josephson junction mode) identifies the second antisymmetric nanowire mode.

transmitted power is monitored at the dressed cavity frequency while sweeping a second spectroscopic tone of frequency $\omega_{\text{spec}}/2\pi$. The measurement results are shown in Fig. 2. Labeling the energy eigenstates within a single potential well as $|g_i\rangle, |e_i\rangle, |f_i\rangle, \ldots$, where the index i indicates the potential well to which these belong [see Fig. 1(b)], the fluxonium transitions are classified in two types: intrawell plasmons, such as $|g_0\rangle \to |e_0\rangle$, and interwell fluxons, such as $|g_0\rangle \to |g_{-1}\rangle$. Parity selection rules of the fluxonium circuit allow for transitions between adjacent plasmon states by absorption of a single photon. However, the direct transition $|g_0\rangle \to |f_0\rangle$ can only be completed via a two-photon process in which $|e_0\rangle$ serves as an intermediate virtual state. We note that devices 1 and 2 operate in a similar parameter regime to "heavy fluxonium" [9,29], where the ratio between the Josephson (E_J) and charging (E_C) energies is large. As a consequence, transitions between the fluxonium potential wells are exponentially attenuated. Therefore, such excitations are most clearly visible in the regions where they hybridize with the plasmon energy levels.

Figure 2(a) shows the presence of a second fluxonium mode for device 1 at 16.3 GHz. While similar characteristics have been observed in previous fluxonium devices, high-frequency modes have been so far phenomenologically modeled as harmonic oscillators linearly coupled to the qubit degree of freedom [1]. Here we go beyond such an approximation and derive a multimode Hamiltonian considering the complete device Lagrangian, which accounts for the distributed nature of the superinductance. Importantly, we find that the qubit spectrum is determined by the nonlinear interaction of the circuit modes which are antisymmetric at the Josephson junction ports [see Fig. 1(a)]. The agreement with the measured data is excellent over a very large frequency range.

The nanowire is described as a homogeneous transmission line with distributed capacitance $c = C_{\text{nw}}/2l$ and inductance $\ell = L_{\text{nw}}/2l$, where C_{nw}, L_{nw}, and $2l$ are, respectively, the total ground capacitance, inductance, and length of the nanowire. Defining the flux operator $\psi(\mathsf{x},t)$ in terms of the dimensionless coordinate $\mathsf{x} = x/l$, the nanowire Lagrangian can be written as

$$\mathcal{L}_{\text{nw}} = \int_{-1}^{1} d\mathsf{x} \frac{(C_{\text{nw}}/2)}{2} \dot{\psi}(\mathsf{x},t)^2 - \frac{1}{2(L_{\text{nw}}/2)} \psi(\mathsf{x},t)^2. \quad (2)$$

Additionally, we consider gate capacitances (C_g) placed at the two ports of the device ($\mathsf{x}_p = \pm 1$) with respective driving voltages $\{V_{\mathsf{x}_p}\}$, as well as ground capacitances (C_0).

The Lagrangian of the inductively shunted Josephson junction then reads

$$\mathcal{L} = \sum_{\mathsf{x}_p} \frac{C_g}{2}(\dot{\psi}(\mathsf{x}_p,t) - V_{\mathsf{x}_p})^2 + \frac{C_0}{2}\dot{\psi}(\mathsf{x}_p,t)^2 + \mathcal{L}_{\mathrm{nw}} + \frac{C_J}{2}\dot{\delta}_\psi(t)^2 + E_J\cos(\delta_\psi(t)/\varphi_0), \quad (3)$$

where

$$\delta_\psi(t)/\varphi_0 = (\Delta\psi(t) + \Phi_{\mathrm{ext}})/\varphi_0 \quad (4)$$

is the gauge-invariant superconducting phase difference across the junction, $\Delta\psi(t) = \psi(1,t) - \psi(-1,t)$ is the flux operator difference at the boundaries of the superinductor, and E_J is the Josephson energy [32,33].

To obtain a tractable theoretical description of our device, we map Eq. (3) into the Lagrangian of an infinite number of nonlinearly interacting normal modes [30]. We observe that modes which are symmetric at the junction ports are not coupled to the Josephson nonlinearity, and thus do not contribute to the qubit Hamiltonian. We therefore derive a multimode Hamiltonian for the antisymmetric normal modes, which is later truncated to a finite number of modes. The truncation is possible due to the fact that only few antisymmetric modes lie in the frequency range of interest. Furthermore, the effective normal mode impedance decreases quickly with the mode number such that high-frequency modes are only weakly anharmonic.

We find that the spectra of our devices can be accurately described by a two-mode Hamiltonian of the form

$$H_{\text{two-mode}} = \frac{(q_0 - q_{g0})^2}{2\tilde{C}_0} + \frac{\phi_0^2}{2\tilde{L}_0} + \frac{(q_1 - q_{g1})^2}{2\tilde{C}_1} + \frac{\phi_1^2}{2\tilde{L}_1} - \frac{\phi_0\phi_1}{L_J} - E_J\cos\left(\frac{\phi_0 + \phi_1}{\varphi_0} + \frac{\Phi_{\mathrm{ext}}}{\varphi_0}\right), \quad (5)$$

where $\tilde{C}_i$, $\tilde{L}_i$, and q_{gi} are, respectively, the effective capacitance, inductance, and offset charge corresponding to the first two antisymmetric modes labeled by $i = \{0,1\}$ and $L_J = E_J/\varphi_0^2$. The definitions of the various parameters in Eq. (5) is provided in Ref. [30]. The results in Fig. 2 are obtained by numerical diagonalization of the complete Hamiltonian of the device, including Eq. (5), the resonator Hamiltonian, and the interaction between such systems [30].

From our two-mode fit to the qubit spectrum, we find nanowire inductances of 121, 314, and 309 nH for devices 1, 2, and 3, respectively, and corresponding characteristic impedances ($Z_{\mathrm{nw}} = \sqrt{L_{\mathrm{nw}}/C_{\mathrm{nw}}}$) of about 1.85, 7.38, and 12.43 kΩ. The inductance values from the fit are within 7% of the theoretical prediction given by Eq. (1) [30]. Table I provides the Hamiltonian parameters extracted from a single-mode fit allowing direct comparison to previous implementations of JJ array based fluxonium devices [1,3,9,10,29].

TABLE I. Device parameter table obtained from a single-mode fit to the fluxonium qubit spectrum, for devices 1, 2, and 3.

Device	E_C [GHz]	E_L [GHz]	E_J [GHz]
1	0.89	1.37	10.95
2	0.56	0.52	16.16
3	1.90	0.53	5.90

In devices 1 and 2, the small dipole element between the fluxon states makes it experimentally challenging to directly drive the $|g_{-1}\rangle \rightarrow |g_0\rangle$ transition. By using multiple drives, we are able to transfer the ground state population between the neighboring wells using the intermediate $|h_0\rangle$ state, which is located close to the top of the barrier and has spectral weight in both wells. We apply three coherent and simultaneous drives of frequencies $\omega_\alpha/2\pi$, $\omega_\beta/2\pi$, and $\omega_\gamma/2\pi$, respectively, targeting the $|g_0\rangle \rightarrow |f_0\rangle$ (two-photon), the $|f_0\rangle \rightarrow |h_0\rangle$ (one-photon), and the $|h_0\rangle \rightarrow |e_{-1}\rangle$ (one-photon) transitions [see Fig. 3(a)].

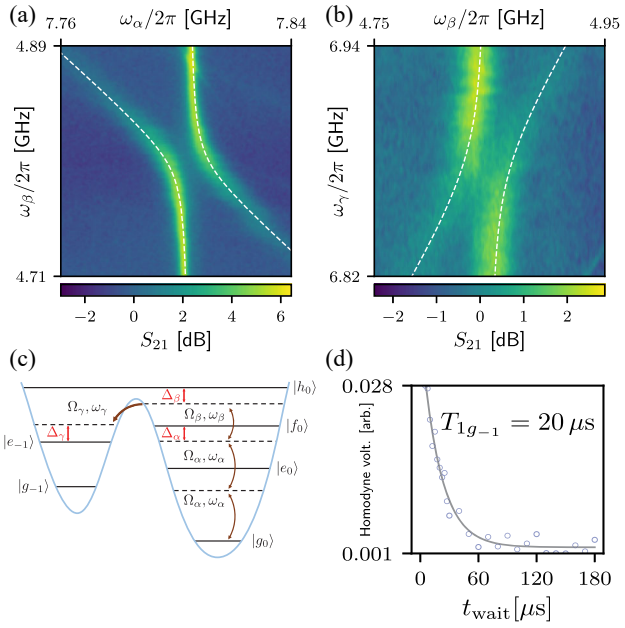

FIG. 3. The multitone spectroscopy data, taken at $\Phi_{\mathrm{ext}}/\varphi_0 = -0.46\pi$, demonstrating population transfer between $|g_0\rangle$ and $|h_0\rangle$ (a) with $\Omega_\gamma = 0$, and $|h_0\rangle$ to $|e_{-1}\rangle$ (b) with fixed $\omega_\alpha/2\pi =$ 7.78 GHz. The white dashed lines indicate the maximum population from a multilevel master equation simulation [30]. (c) A schematic diagram of the device 2 level structure in the presence of coherent external drives. The drives, with frequencies $\omega_i/2\pi$ and amplitudes Ω_i are detuned from the levels by $\Delta_i/2\pi$. (d) Three sequential π pulses ($\sigma = 15$ ns) are applied at the transition frequencies to perform T_1 measurements of the $|g_{-1}\rangle$ state. The demodulated homodyne voltage from the readout resonator is measured as a function of t_{wait}.

At $\Phi_{\text{ext}}/\varphi_0 = -0.46\pi$, we set $\Omega_\gamma = 0$ and simultaneously vary $\omega_\alpha/2\pi$ and $\omega_\beta/2\pi$ around the $|g_0\rangle \rightarrow |f_0\rangle$ and $|f_0\rangle \rightarrow |h_0\rangle$ transitions. We observe a vertical band corresponding to the $|g_0\rangle \rightarrow |f_0\rangle$ transition at 7.8 GHz, and a diagonal band with a slope of $\omega_\alpha/\omega_\beta = -1/2$, corresponding to the Raman transition between the $|g_0\rangle$ and $|h_0\rangle$ states [Fig. 3(a)]. Around the resonance condition ($2\hbar\omega_\alpha \approx E_{f_0} - E_{g_0}$ and $\hbar\omega_\beta \approx E_{h_0} - E_{f_0}$), the two bands exhibit an avoided crossing, which is the hallmark of the Autler-Townes doublet previously observed in other superconducting qubits [34–37]. Next, we fix the frequency of the α tone at $\Delta_\alpha/2\pi = 20$ MHz, turn on the γ drive, and simultaneously scan the frequencies $\omega_\beta/2\pi$ and $\omega_\gamma/2\pi$. Figure 3(b) displays the resulting Autler-Townes splitting, where the Raman transition manifests itself here with a slope of $\omega_\gamma/\omega_\beta = +1$, corresponding to the three-drive Raman condition. This method allows us to experimentally determine the energy levels of the fluxonium qubit using population transfer.

With complete information regarding the energy of the fluxonium excited states, we determine the relaxation rate of the $|g_{-1}\rangle$ state by performing time-resolved measurements [38]. We use the frequency values obtained from the Raman spectroscopy and perform a pulse sequence which consists of three sequential π pulses at the transition frequencies $(E_{f_0} - E_{g_0})/h$, $(E_{h_0} - E_{f_0})/h$ and $(E_{h_0} - E_{e_{-1}})/h$ to prepare the system in the $|e_{-1}\rangle$ state. At the end of this procedure, the system relaxes into the $|g_{-1}\rangle$ state, on the timescale of the plasmon T_1 (~600 ns). On a longer timescale, the system relaxes back to $|g_0\rangle$. For $t_{\text{wait}} \gg T_{1e_0}$, the reduction in $|g_{-1}\rangle$ population follows an exponential decay with $T_{1g_{-1}} = 20$ μs.

Because of the high E_J/E_C ratio, devices 1 and 2 lack flux insensitive sweet spots at zero and half flux. In order to fully characterize the coherence properties of the qubit and demonstrate coherent control between the fluxon states, we reduced the E_J/E_C ratio in device 3. The overlap between the fluxon wave functions is made sufficiently large to directly observe the transition with a one-photon drive, which comes at the cost of increased sensitivity to different relaxation mechanisms. The low frequency, two-tone spectroscopy data for device 3 are shown in Fig. 4. At $\Phi_{\text{ext}}/\varphi_0 = -\pi$, the spectrum shows a flux-insensitive fluxon transition, where we perform coherence measurements and find $T_1 = 220$ ns, $T_{2\text{Ramsey}} = 380$ ns, and $T_{2\text{Echo}} \approx 2T_1$ indicating that the qubit dephasing is dominated by qubit relaxation.

By changing Φ_{ext}, we measure T_1 of the fluxon transition as a function of qubit frequency. The data show an increase in T_1 as the qubit frequency is increased to a maximal value of 7 μs for frequencies between 2–3 GHz. Upon further increasing the qubit frequency, T_1 decreases by an order of magnitude [Fig. 4(c)].

To understand the T_1 frequency dependence, we take into account inductive and capacitive loss mechanisms, which can be described with the following expressions:

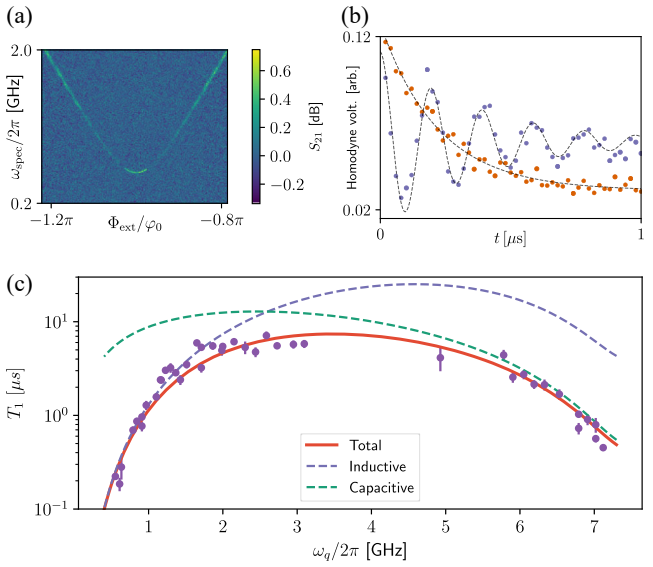

FIG. 4. (a) Low frequency spectroscopy data from device 3. (b) T_1 (red) and $T_{2\text{Ramsey}}$ (blue) data taken at $\Phi_{\text{ext}}/\varphi_0 = -\pi$. (c) T_1 as a function of qubit frequency. The lines represent the theory fits for total (red), inductive (blue), and capacitive (green) T_1. The T_1 values were obtained with both pulsed and mixed state driving. Measurements using both types of excited state preparation at the same flux gave the same value of T_1.

$$\Gamma_{\text{ind}} = \frac{E_L}{\hbar Q_L}\left(\coth\left(\frac{\hbar\omega_q}{2k_BT}\right) + 1\right)|\langle g_{-1}|\hat{\varphi}|g_0\rangle|^2, \tag{6}$$

$$\Gamma_{\text{cap}} = \frac{\hbar\omega_q^2}{8E_CQ_C}\left(\coth\left(\frac{\hbar\omega_q}{2k_BT}\right) + 1\right)|\langle g_{-1}|\hat{\varphi}|g_0\rangle|^2, \tag{7}$$

where $|\langle g_{-1}|\hat{\varphi}|g_0\rangle|^2$ is the transition matrix element between the fluxon states, Q_L and Q_C are the inductive and capacitive quality factors, respectively, k_B is the Boltzmann constant, T is the temperature, and ω_q is the fluxon transition frequency [39]. Based on previously reported measurements [3], the lifetime limitation from nonequilibrium quasiparticles is at least an order of magnitude larger than the observed relaxation times at all frequencies and is therefore not considered. Radiative loss due to the Purcell effect [40] is only significant when the qubit frequency is within ~50 MHz of $\omega_r/2\pi = 7.5$ GHz [30]. Figure 4(c) shows the measured T_1 (blue markers) values along with the fitted $T_1 = (\Gamma_{\text{cap}}^{-1} + \Gamma_{\text{ind}}^{-1})^{-1}$ (red line). The fit of T_1 vs ω_q in Fig. 4, gives $Q_L = 39,000$ and $Q_C = 15,100$, where the lifetime at low ω_q is dominated by inductive loss and at high ω_q by capacitive loss. The inductor can be modeled as a lossless inductor in series with a frequency dependent resistor, where $R = \omega L/Q_{\text{ind}}$ corresponds to $R = 27$ mΩ at $\omega/2\pi = 550$ MHz. The possible sources of the inductive loss can arise from a finite contact resistance between the NbTiN wire and the Al Josephson junction leads, loss from charge impurities on

the surface of the wire, or some intrinsic loss from the bulk NbTiN material. In future devices, the geometry of the Al/NbTiN contact and nanowire dimensions could be modified to better determine what limits the inductive quality factor. Improvements to Q_C could be made by moving to a 3D architecture, where the electric field participation at lossy interfaces is reduced [41].

In conclusion, we have fabricated and measured a nanowire superinductance fluxonium qubit. We find that the transition energy levels are modified due to the distributed nature of the nanowire, which is well explained in the framework of a multimode theory. As the modes of the nanowire strongly depend on the parasitic and stray capacitances of the wire, using a shorter wire with higher sheet inductance (for example high quality granular aluminum films with one hundred times larger $L_k = 2$ nH/□ [42–44]), or integrating the fluxonium into a 3D cavity or waveguide [45], could reduce unwanted capacitances and help to push the nanowire self-resonant modes to higher frequencies. The multimode theory developed here is an important step towards understanding large circuits beyond the lumped element approximation, such as the $0-\pi$ qubit [7,8], where the distributed nature of the circuit elements is critical to device design.

We thank Andrei Vrajitoarea, Zhaoqi Leng, and Jérôme Bourassa for useful discussions. Research was supported by the Army Research Office Grant No. W911NF-15-1-0421 and the Princeton Center for Complex Materials through the NSF, DMR-1420541. This work was undertaken thanks in part to funding from NSERC and the Canada First Research Excellence Fund.

*corresponding author.
aahouck@princeton.edu
†These authors contributed equally to this work.

[1] V. E. Manucharyan, J. Koch, L. I. Glazman, and M. H. Devoret, Science **326**, 113 (2009).
[2] N. A. Masluk, I. M. Pop, A. Kamal, Z. K. Minev, and M. H. Devoret, Phys. Rev. Lett. **109**, 137002 (2012).
[3] I. M. Pop, K. Geerlings, G. Catelani, R. J. Schoelkopf, L. I. Glazman, and M. H. Devoret, Nature (London) **508**, 369 (2014).
[4] U. Vool, I. M. Pop, K. Sliwa, B. Abdo, C. Wang, T. Brecht, Y. Y. Gao, S. Shankar, M. Hatridge, G. Catelani, M. Mirrahimi, L. Frunzio, R. J. Schoelkopf, L. I. Glazman, and M. H. Devoret, Phys. Rev. Lett. **113**, 247001 (2014).
[5] M. T. Bell, I. A. Sadovskyy, L. B. Ioffe, A. Y. Kitaev, and M. E. Gershenson, Phys. Rev. Lett. **109**, 137003 (2012).
[6] L. B. Ioffe, M. V. Feigel'man, A. Ioselevich, D. Ivanov, M. Troyer, and G. Blatter, Nature (London) **415**, 503 (2002).
[7] P. Brooks, A. Kitaev, and J. Preskill, Phys. Rev. A **87**, 052306 (2013).
[8] A. Kitaev, arXiv:cond-mat/0609441.
[9] N. Earnest, S. Chakram, Y. Lu, N. Irons, R. K. Naik, N. Leung, L. Ocola, D. A. Czaplewski, B. Baker, J. Lawrence, J. Koch, and D. I. Schuster, Phys. Rev. Lett. **120**, 150504 (2018).
[10] U. Vool, A. Kou, W. C. Smith, N. E. Frattini, K. Serniak, P. Reinhold, I. M. Pop, S. Shankar, L. Frunzio, S. M. Girvin, and M. H. Devoret, Phys. Rev. Applied **9**, 054046 (2018).
[11] J. M. Dempster, B. Fu, D. G. Ferguson, D. I. Schuster, and J. Koch, Phys. Rev. B **90**, 094518 (2014).
[12] P. Groszkowski, A. D. Paolo, A. L. Grimsmo, A. Blais, D. I. Schuster, A. A. Houck, and J. Koch, New J. Phys. **20**, 043053 (2018).
[13] A. J. Kerman, E. A. Dauler, J. K. W. Yang, K. M. Rosfjord, V. Anant, K. K. Berggren, G. N. Goltsman, and B. M. Voronov, Appl. Phys. Lett. **90**, 101110 (2007).
[14] A. J. Annunziata, D. F. Santavicca, L. Frunzio, G. Catelani, M. J. Rooks, A. Frydman, and D. E. Prober, Nanotechnology **21**, 445202 (2010).
[15] D. F. Santavicca, J. K. Adams, L. E. Grant, A. N. McCaughan, and K. K. Berggren, J. Appl. Phys. **119**, 234302 (2016).
[16] B. Ho Eom, P. K. Day, H. G. LeDuc, and J. Zmuidzinas, Nat. Phys. **8**, 623 (2012).
[17] M. R. Vissers, R. P. Erickson, H.-S. Ku, L. Vale, X. Wu, G. C. Hilton, and D. P. Pappas, Appl. Phys. Lett. **108**, 012601 (2016).
[18] S. Chaudhuri, D. Li, K. D. Irwin, C. Bockstiegel, J. Hubmayr, J. N. Ullom, M. R. Vissers, and J. Gao, Appl. Phys. Lett. **110**, 152601 (2017).
[19] A. J. Kerman, Phys. Rev. Lett. **104**, 027002 (2010).
[20] J. T. Peltonen, P. C. J. J. Coumou, Z. H. Peng, T. M. Klapwijk, J. S. Tsai, and O. V. Astafiev, Sci. Rep. **8**, 10033 (2018).
[21] M. Tinkham, *Introduction to Superconductivity*, 2nd ed. (Dover Publications, Mineola, 2004).
[22] G. Viola and G. Catelani, Phys. Rev. B **92**, 224511 (2015).
[23] D. G. Ferguson, A. A. Houck, and J. Koch, Phys. Rev. X **3**, 011003 (2013).
[24] S. E. Nigg, H. Paik, B. Vlastakis, G. Kirchmair, S. Shankar, L. Frunzio, M. H. Devoret, R. J. Schoelkopf, and S. M. Girvin, Phys. Rev. Lett. **108**, 240502 (2012).
[25] F. Solgun, D. W. Abraham, and D. P. DiVincenzo, Phys. Rev. B **90**, 134504 (2014).
[26] J. Koch, V. Manucharyan, M. H. Devoret, and L. I. Glazman, Phys. Rev. Lett. **103**, 217004 (2009).
[27] V. E. Manucharyan, N. A. Masluk, A. Kamal, J. Koch, L. I. Glazman, and M. H. Devoret, Phys. Rev. B **85**, 024521 (2012).
[28] G. Zhu, D. G. Ferguson, V. E. Manucharyan, and J. Koch, Phys. Rev. B **87**, 024510 (2013).
[29] Y.-H. Lin, L. B. Nguyen, N. Grabon, J. San Miguel, N. Pankratova, and V. E. Manucharyan, Phys. Rev. Lett. **120**, 150503 (2018).
[30] See Supplemental Material at http://link.aps.org/supplemental/10.1103/PhysRevLett.122.010504 for detailed information on the multimode Hamiltonian fitting, the multilevel master equation simulation, and sample fabrication.
[31] A. Wallraff, D. I. Schuster, A. Blais, J. M. Gambetta, J. Schreier, L. Frunzio, M. H. Devoret, S. M. Girvin, and R. J. Schoelkopf, Phys. Rev. Lett. **99**, 050501 (2007).
[32] J. Bourassa, F. Beaudoin, J. M. Gambetta, and A. Blais, Phys. Rev. A **86**, 013814 (2012).

[33] H. L. Mortensen, K. Mølmer, and C. K. Andersen, Phys. Rev. A **94**, 053817 (2016).
[34] M. Baur, S. Filipp, R. Bianchetti, J. M. Fink, M. Göppl, L. Steffen, P. J. Leek, A. Blais, and A. Wallraff, Phys. Rev. Lett. **102**, 243602 (2009).
[35] M. A. Sillanpää, J. Li, K. Cicak, F. Altomare, J. I. Park, R. W. Simmonds, G. S. Paraoanu, and P. J. Hakonen, Phys. Rev. Lett. **103**, 193601 (2009).
[36] S. Novikov, J. E. Robinson, Z. K. Keane, B. Suri, F. C. Wellstood, and B. S. Palmer, Phys. Rev. B **88**, 060503 (2013).
[37] B. Suri, Z. K. Keane, R. Ruskov, L. S. Bishop, C. Tahan, S. Novikov, J. E. Robinson, F. C. Wellstood, and B. S. Palmer, New J. Phys. **15**, 125007 (2013).
[38] M. J. Peterer, S. J. Bader, X. Jin, F. Yan, A. Kamal, T. J. Gudmundsen, P. J. Leek, T. P. Orlando, W. D. Oliver, and S. Gustavsson, Phys. Rev. Lett. **114**, 010501 (2015).
[39] R. J. Schoelkopf, A. A. Clerk, S. M. Girvin, K. W. Lehnert, and M. H. Devoret, arXiv:cond-mat/0210247.
[40] A. A. Houck, J. A. Schreier, B. R. Johnson, J. M. Chow, J. Koch, J. M. Gambetta, D. I. Schuster, L. Frunzio, M. H. Devoret, S. M. Girvin, and R. J. Schoelkopf, Phys. Rev. Lett. **101**, 080502 (2008).
[41] H. Paik, D. I. Schuster, L. S. Bishop, G. Kirchmair, G. Catelani, A. P. Sears, B. R. Johnson, M. J. Reagor, L. Frunzio, L. I. Glazman, S. M. Girvin, M. H. Devoret, and R. J. Schoelkopf, Phys. Rev. Lett. **107**, 240501 (2011).
[42] L. Grünhaupt, N. Maleeva, S. T. Skacel, M. Calvo, F. Levy-Bertrand, A. V. Ustinov, H. Rotzinger, A. Monfardini, G. Catelani, and I. M. Pop, Phys. Rev. Lett. **121**, 117001 (2018).
[43] N. Maleeva, L. Grnhaupt, T. Klein, F. Levy-Bertrand, O. Dupre, M. Calvo, F. Valenti, P. Winkel, F. Friedrich, W. Wernsdorfer, A. V. Ustinov, H. Rotzinger, A. Monfardini, M. V. Fistul, and I. M. Pop, Nat. Commun. **9**, 3889 (2018).
[44] L. Grnhaupt, M. Spiecker, D. Gusenkova, N. Maleeva, S. T. Skacel, I. Takmakov, F. Valenti, P. Winkel, H. Rotzinger, A. V. Ustinov, and I. M. Pop, arXiv:1809.10646.
[45] A. Kou, W. C. Smith, U. Vool, R. T. Brierley, H. Meier, L. Frunzio, S. M. Girvin, L. I. Glazman, and M. H. Devoret, Phys. Rev. X **7**, 031037 (2017).

I. SUPPLEMENTARY INFORMATION

A. Fabrication details

Device fabrication begins with sputtering 15 nm of NbTiN onto a 500 μm thick C-plane sapphire substrate. A small patch of NbTiN, where the nanowire will be fabricated later in the process, is protected with Microposit$^{\text{TM}}$ S1811 photoresist and the remaining NbTiN is removed with an SF_6/Ar dry etch. For the lumped element readout resonator and transmission line, 200 nm of Nb is sputtered over the areas of the chip which had no NbTiN and subsequently patterned and etched with another SF_6/Ar dry etch. Next, a layer of ZEP520A (1:1 dilution in anisole) e-beam resist is spun on the chip and the nanowire pattern is exposed and developed with standard e-beam lithography techniques. Finally, an MMA/PMMA bilayer e-beam resist is placed on the chip and the Josephson junction layer is patterned with e-beam lithography. To ensure metallic contact between the junction and the NbTiN nanowire, a high-voltage Ar ion beam milling process is used to remove the native oxid layer formed on the surface of the NbTiN film. The JJ layer is fabricated with a double angle evaporation of 30 nm and 60 nm of Al, with a 15 minute oxidation step in between the first and second evaporation angles to form the oxide layer of the junction. For measurement, the samples are attached to the base plate of a dilution refrigerator with a mixing chamber temperature of 12 mK.

B. Properties of NbTiN film

Room temperature resistance measurements are performed on 7 different nanowires with $l = 100$ μm and varying widths, ranging from 50 to 900 nm. From these measurements, we extract a sheet resistivity of $R = 97 \pm 5$ $\Omega/\square$. Temperature dependent resistivity measurements on the film used in devices 1 and 2 show a superconducting critical temperature of $T_c = 9.5$ K. The resistance increases by $\sim$20 % as the film is cooled from room temperature to right above T_c. From scanning electron microscope images and the resistance measurements of the test structures, we infer nanowire widths of 110 $\pm$ 5 nm and 40 $\pm$ 5 nm for the two devices. Based on the resistivity, T_c, and the geometry of the nanowires, we estimate an $n_s = 7.0 \times 10^{25}$ m^{-3}. The predicted inductances based on Eq. (1) are $L_k = 112$ and $L_k = 309$ nH for devices 1 and 2, respectively. This is within 7% and 2% of the two-mode fit values in Eq. 5 of the main text. Similar resistance and T_c measurements on the 10 nm thick NbTiN film used for device 3 predict an $L_k = 307$ nH, which is $< 1\%$ from the measured value of 308 nH.

C. Modeling of the Autler-Townes splitting

We model the system with a four-level Hamiltonian which, in the $(|g_0\rangle, |f_0\rangle, |h_0\rangle, |e_{-1}\rangle)$ energy eigenbasis and in the absence of external drives, reads

$$\begin{aligned} H_0 =& E_{g_0} |g_0\rangle \langle g_0| + E_{f_0} |f_0\rangle \langle f_0| + \\ & E_{h_0} |h_0\rangle \langle h_0| + E_{e_{-1}} |e_{-1}\rangle \langle e_{-1}|, \end{aligned} \tag{1}$$

where the groundstate energy is chosen to be $E_{g_0} = 0$, and the energies of excited levels satisfy the relations $E_{g_0} < E_{f_0}$, $E_{e_{-1}} < E_{h_0}$ (see figure 3 (a) of the main text). We work in a semiclassical picture where the external drives $\omega_\alpha/2\pi$, $\omega_\beta/2\pi$, $\omega_\gamma/2\pi$ with respective Rabi frequencies Ω_α, Ω_β, Ω_γ introduce coupling exclusively between neighboring energy levels. In the rotating-wave approximation, this situation is described by the interaction Hamiltonian

$$\begin{aligned} H_{\text{int}} =& \frac{1}{2}\hbar\Omega_\alpha \left(|f_0\rangle \langle g_0| e^{-i2\omega_\alpha t} + |g_0\rangle \langle f_0| e^{i2\omega_\alpha t} \right) + \\ & \frac{1}{2}\hbar\Omega_\beta \left(|h_0\rangle \langle f_0| e^{-i\omega_\beta t} + |f_0\rangle \langle h_0| e^{i\omega_\beta t} \right) + \\ & \frac{1}{2}\hbar\Omega_\gamma \left(|e_{-1}\rangle \langle h_0| e^{i\omega_\gamma t} + |h_0\rangle \langle e_{-1}| e^{-i\omega_\gamma t} \right). \end{aligned} \tag{2}$$

Since $E_{h_0} > E_{e_{-1}}$, the time-dependent phase corresponding to the third term in Eq. (2) has the opposite sign. Combining the above expressions, the total Hamiltonian of the system is defined as $H = H_0 + H_{\text{int}}$

$$H = \begin{bmatrix} 0 & \frac{\hbar\Omega_\alpha}{2}e^{i2\omega_\alpha t} & 0 & 0 \\ \frac{\hbar\Omega_\alpha}{2}e^{-i2\omega_\alpha t} & E_{f_0} & \frac{\hbar\Omega_\beta}{2}e^{i\omega_\beta t} & 0 \\ 0 & \frac{\hbar\Omega_\beta}{2}e^{-i\omega_\beta t} & E_{h_0} & \frac{\hbar\Omega_\gamma}{2}e^{-i\omega_\gamma t} \\ 0 & 0 & \frac{\hbar\Omega_\gamma}{2}e^{i\omega_\gamma t} & E_{e_{-1}} \end{bmatrix}. \tag{3}$$

We now move to the rotating frame of the drives by applying the unitary $U = |g_0\rangle\langle g_0| + e^{i2\omega_\alpha t}|f_0\rangle\langle f_0| + e^{i(2\omega_\alpha+\omega_\beta)t}|h_0\rangle\langle h_0| + e^{i(2\omega_\alpha+\omega_\beta-\omega_\gamma)t}|e_{-1}\rangle\langle e_{-1}|$, which results in

$$\tilde{H} = \begin{bmatrix} 0 & \frac{1}{2}\hbar\Omega_\alpha & 0 & 0 \\ \frac{1}{2}\hbar\Omega_\alpha & \hbar\Delta_\alpha & \frac{1}{2}\hbar\Omega_\beta & 0 \\ 0 & \frac{1}{2}\hbar\Omega_\beta & \hbar(\Delta_\alpha+\Delta_\beta) & \frac{1}{2}\hbar\Omega_\gamma \\ 0 & 0 & \frac{1}{2}\hbar\Omega_\gamma & \hbar(\Delta_\alpha+\Delta_\beta-\Delta_\gamma) \end{bmatrix}. \tag{4}$$

Here, the detunings are $\hbar\Delta_\alpha = E_{f_0} - 2\hbar\omega_\alpha$, $\hbar\Delta_\beta = E_{h_0} - E_{f_0} - \hbar\omega_\beta$ and $\hbar\Delta_\gamma = E_{h_0} - E_{e_{-1}} - \hbar\omega_\gamma$. We account for dissipation in the system with a Lindblad master equation of the form

$$\dot{\rho} = -\frac{i}{\hbar}[H,\rho] + \sum_j \left[c_j\rho c_j^\dagger - \frac{1}{2}\{c_j^\dagger c_j,\rho\}\right], \tag{5}$$

where the collapse operators c_j are defined as $c_j = \sum_i \sqrt{\Gamma_{ij}}\sigma_{ij}$, for given energy states $|i\rangle$ and $|j\rangle$, where Γ_{ij} is the decay rate between them and $\sigma_{ij} = |i\rangle\langle j|$. The steady-state solution of Eq. (5) is numerically obtained and the maximal excited state population, $\max\left(\rho_{f_0f_0} + \rho_{h_0h_0} + \rho_{e_{-1}e_{-1}}\right)$, is shown with dashed lines in figure 3 (b) and (c) of the main text.

D. Pulse calibration for population transfer

The amplitude of the π pulses is found by measuring Rabi-oscillations between consecutive levels in device 2 at $\Phi_{\text{ext}}/\phi_0 = -0.46\pi$. The amplitude of each pulse is chosen based on the value for which the oscillation between adjacent levels reaches its first extrema. First, we determine the amplitude of the $g_0 \to f_0$ pulse. Second, after applying a π pulse between states g_0 and f_0, we apply a second pulse of varying amplitude corresponding to the $h_0 \to f_0$ transition frequency to observe Rabi oscillations between h_0 and f_0. Finally, we apply these two π pulses ($g_0 \to f_0$, $f_0 \to h_0$), and then a third pulse of varying amplitude to perform Rabi oscillation between h_0 and e_{-1}. The measured T_1 of e_{-1} state is ~ 600 ns.

E. Raw Two-tone spectroscopy data

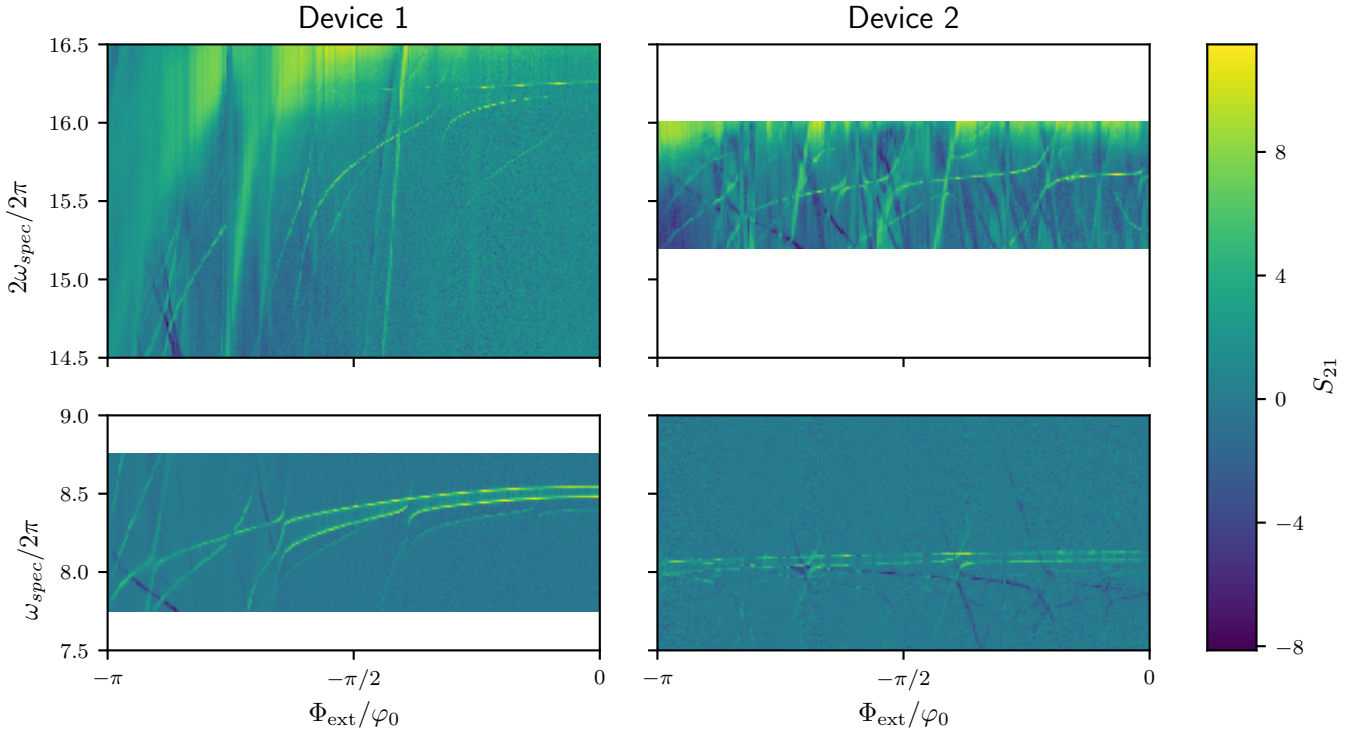

FIG. 1. The amplitude response of the cavity transmission when applying a second spectroscopic tone ($\omega_{\rm spec}/2\pi$) taken at different $\Phi_{\rm ext}$ for devices 1 and 2. The data points in Fig. 2 of the main text were obtained by finding the peak positions of the spectroscopic data. The upper panels correspond to the two-photon peaks and the lower panels correspond to the single photon data. The satellite peaks on the raw data is a result of the presence of thermal cavity photons.

F. Spectrum Characterization

1. *Multimode Hamiltonian*

In this section, we outline the theory developed to treat the multimode structure of the device in figure 1 (a) of the main text. Our derivation is inspired by ideas introduced in Refs. [1–3]. For simplicity, we assume the absence of disorder in gate and ground capacitances, although the effect of a small amount of disorder is discussed below.

Considering the fluxonium Lagrangian of main text Eq. 3, we first introduce approximations to reduce the problem to that of two nonlinearly interacting bosonic modes, which is then numerically diagonalized to fit the experimentally measured spectrum of Fig. 2 in the main text.

The circuit normal modes are a convenient basis where the fluxonium Hamiltonian is diagonal to second order in the Josephson nonlinearity. In addition, the symmetry of such modes unequivocally identifies the degrees of freedom that are effectively coupled to the JJ. For these modes only does the Josephson non-linearity needs to be taken into account. Writing the wave equation which holds in the bulk of the nanowire $\partial_t^2\psi(\mathsf{x},t) = \omega_{\rm nw}^2\partial_{\mathsf{x}}^2\psi(\mathsf{x},t)$, with $\omega_{\rm nw} = 1/\sqrt{(C_{\rm nw}/2)(L_{\rm nw}/2)}$, we look for normal modes of the form

$$\psi_m(\mathsf{x},t) = u_m(\mathsf{x})\xi_m(t), \tag{6}$$

satisfying $u_m''(\mathsf{x}) = -\mathsf{k}_m^2 u_m(\mathsf{x})$ and $\ddot{\xi}_m(t) = -\omega_m^2\xi_m(t)$. Here, k_m is a dimensionless wave vector and $\omega_m = \omega_{\rm nw}\mathsf{k}_m$ (linear dispersion). The mode frequencies are determined by the boundary conditions that we derive taking the continuous limit of the equations of motion for the discretized field $\psi(\mathsf{x},t) \to \{\phi(\mathsf{x}_n)\}$, where $\phi(\mathsf{x}_n)$ is defined in a

lattice with $2N+1$ points in the range $[-1,1]$. To this end, we consider the lattice Lagrangian linearized in absence of the external voltage drives and flux ($V_{\pm 1}, \varphi_{\rm ext} \to 0$), for which the equations of motion simply read

$$\boldsymbol{C}\ddot{\boldsymbol{\phi}} + \boldsymbol{L}^{-1}\boldsymbol{\phi} = \boldsymbol{0}. \tag{7}$$

Here, $\boldsymbol{C}$ and $\boldsymbol{L}^{-1}$ are, respectively, the capacitance and (inverse) inductance matrices for the lattice model, while $\boldsymbol{\phi}$ is the corresponding $2N+1$-dimensional node-flux vector. As illustrated in Fig. 2, the transmission line is modeled as a chain of $2N$ LC resonators, with single nodes connected to ground by a capacitance $\Delta \mathsf{x} C_{\rm nw}/2$ and neighboring nodes coupled by an inductance $\Delta \mathsf{x} L_{\rm nw}/2$. Taking the continuous limit of Eq. (7) by letting $\Delta \mathsf{x} \to 0$ and $N \to \infty$ with $N\Delta \mathsf{x} = 1$, we find the field boundary conditions

$$\boldsymbol{C}_{\rm bc}\ddot{\boldsymbol{\psi}}_{\rm bc} + \boldsymbol{L}_{\rm bc}^{-1}\boldsymbol{\psi}_{\rm bc} = \boldsymbol{0}, \tag{8}$$

where $\boldsymbol{\psi}_{\rm bc} = (\psi(1,t), \psi(-1,t))^T$, $\boldsymbol{C}_{\rm bc} = C_\Sigma \mathbb{1} - C_J \sigma_x$ and $\boldsymbol{L}_{\rm bc} = \left[\frac{\mathsf{x}}{(L_{\rm nw}/2)}\partial_{\mathsf{x}} + \frac{1}{L_J}\right]\mathbb{1} - \frac{1}{L_J}\sigma_x$. Here, we have defined the identity ($\mathbb{1}$) and Pauli-X (σ_x) matrices, the capacitances $C_\Sigma = C_p + C_J$ and $C_p = C_g + C_0$, and the operators $(\mathsf{x}, \partial_{\mathsf{x}})$, which are evaluated at the boundaries $\mathsf{x}_p = \pm 1$. We note that our formalism can be also applied to more general superconducting circuits including distributed elements.

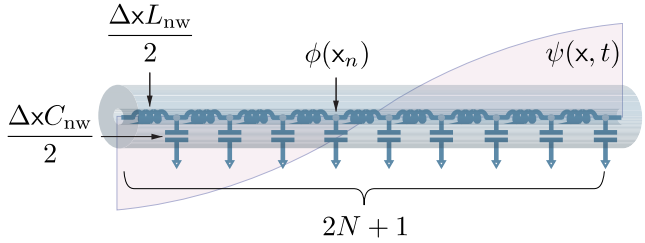

FIG. 2. Discretized model for the nanowire including $2N+1$ nodes with ground capacitance $\Delta \mathsf{x} C_{\rm nw}/2$ and couping inductance $\Delta \mathsf{x} L_{\rm nw}/2$. The field operator $\psi(\mathsf{x},t)$ is replaced by the node flux operators $\{\phi(\mathsf{x}_n)\}$ defined in the lattice.

We now consider $\psi(\mathsf{x},t)$ to be the normal mode solution in Eq. (6), and parametrize the mode function as

$$u_m(\mathsf{x}) = A_m \cos(\mathsf{k}_m \mathsf{x}) + B_m \sin(\mathsf{k}_m \mathsf{x}), \tag{9}$$

where A_m, B_m are constants to be determined. With this choice, Eq. (8) can be rewritten in the form $\boldsymbol{M}(A_m, B_m)^T = \boldsymbol{0}$, where $\boldsymbol{M}$ is a coefficient matrix (omitted for brevity). Nontrivial solutions to this homogeneous system of equations follow from the condition $\det(\boldsymbol{M}) = 0$, implying

$$\frac{C_p}{2} L_{\rm nw} \omega_m^2 + \mathsf{k}_m \tan \mathsf{k}_m = 0, \tag{10}$$

or

$$\frac{L_J}{L_{\rm nw}} \mathsf{k}_m + \left[1 - \left(C_J + \frac{C_p}{2}\right) L_J \omega_m^2\right] \tan \mathsf{k}_m = 0. \tag{11}$$

Eq. (10) and Eq. (11) allow us to find the modes frequencies $\{\omega_m\}$, which are then plugged back into Eq. (8) to determine the mode function Eq. (9). We stress that Eq. (10) does not includes any of the Josephson junction parameters. In fact, this equation determines the frequency of symmetric nanowire modes, which have zero voltage difference across the Josephson junction: $\Delta u_m = u_m(1) - u_m(-1) = 0$. In contrast, Eq. (11) depends on C_J and L_J, and determines the frequency of antisymmetric modes which do couple to the junction ($\Delta u_m \neq 0$). This fundamental difference is discussed in more detail below.

We are now in position to expand the field in the normal mode basis, as

$$\psi(\mathsf{x},t) = \sum_m u_m(\mathsf{x}) \xi_m(t), \tag{12}$$

where, in principle, the sum over m is extended to all circuit modes. Making use of the orthogonality relations [1, 4]

$$\begin{aligned}\int_{-1}^{1} d\mathsf{x}(C_{\rm nw}/2)u_m(\mathsf{x})u_n(\mathsf{x}) + C_J\Delta u_m\Delta u_n \\ + \sum_{\mathsf{x}_p} C_p u_m(\mathsf{x}_p)u_n(\mathsf{x}_p) = C_m\delta_{mn},\end{aligned} \tag{13}$$

and

$$\int_{-1}^{1} d\mathsf{x}\frac{1}{(L_{\rm nw}/2)}u_m'(\mathsf{x})u_n'(\mathsf{x}) + \frac{\Delta u_m\Delta u_n}{L_J} = \frac{\delta_{mn}}{L_m}, \tag{14}$$

where $L_m^{-1} = C_m\omega_m^2$, and substituting Eq. (12) into Eq. 3 of the main text, we arrive to the circuit Lagrangian in the normal mode basis

$$\begin{aligned}\mathscr{L} = &\sum_m \frac{C_m}{2}\dot{\xi}_m^2 + \sum_{\mathsf{x}_p} C_g u_m(\mathsf{x}_p)V_{\mathsf{x}_p}\dot{\xi}_m - \frac{\xi_m^2}{2L_m} \\ &+ E_J\big[\cos(\delta_\psi/\varphi_0) + (\Delta\psi/\varphi_0)^2/2\big],\end{aligned} \tag{15}$$

where explicit time dependence has been omitted and δ_ψ/φ_0 is defined in Eq. 4 of the main text. We note that Eq. (15) is diagonal to second order in the Josephson potential for $\Phi_{\rm ext} = 0$, as a consequence of our normal mode basis choice. Writing

$$\Delta\psi = \sum_m \Delta u_m\xi_m, \tag{16}$$

we verify that symmetric modes do not couple to the Josephson nonlinearity, thus behaving as a collection of non-interacting harmonic oscillators. Accordingly, we disregard symmetric modes in our treatment and consider the set $\{\mathring{m}\}$, consisting of antisymmetric modes for which $\Delta u_{\mathring{m}} \neq 0$. With the change of variables $\phi_{\mathring{m}} = \Delta u_{\mathring{m}}\xi_{\mathring{m}}$, we rewrite Eq. (15) as

$$\begin{aligned}\mathscr{L} = &\sum_{\mathring{m}} \frac{\tilde{C}_{\mathring{m}}}{2}\dot{\phi}_{\mathring{m}}^2 + \sum_{\mathsf{x}_p} C_g\frac{u_{\mathring{m}}(\mathsf{x}_p)}{\Delta u_{\mathring{m}}}V_{\mathsf{x}_p}\dot{\phi}_{\mathring{m}} - \frac{\phi_{\mathring{m}}^2}{2\tilde{L}_{\mathring{m}}} \\ &+ \sum_{\mathring{m}<\mathring{n}} \frac{1}{L_J}\phi_{\mathring{m}}\phi_{\mathring{n}} + E_J\cos(\delta_\psi/\varphi_0),\end{aligned} \tag{17}$$

where δ_ψ/φ_0 conserves the definition in main text Eq. 4 with the replacement $\Delta\psi/\varphi_0 = \sum_{\mathring{m}}\phi_{\mathring{m}}/\varphi_0$. Here,

$$\begin{aligned}\tilde{C}_{\mathring{m}} &= C_{\mathring{m}}/\Delta u_{\mathring{m}}^2, \\ \tilde{L}_{\mathring{m}}^{-1} &= \frac{1}{\Delta u_{\mathring{m}}^2}\int_{-1}^{1} d\mathsf{x}\frac{u_{\mathring{m}}'(\mathsf{x})^2}{(L_{\rm nw}/2)},\end{aligned} \tag{18}$$

denote the mode $\mathring{m}$ effective capacitance and inductance, respectively. The multimode Hamiltonian

$$H = \sum_{\mathring{m}} H_{\mathring{m}}^{(0)} + H_{\rm int}, \tag{19}$$

follows immediately from Eq. (17), and includes the set of noninteracting terms $\{H_{\mathring{m}}^{(0)}\}$, with

$$H_{\mathring{m}}^{(0)} = \frac{(q_{\mathring{m}} - q_{g\mathring{m}})^2}{2\tilde{C}_{\mathring{m}}} + \frac{\phi_{\mathring{m}}^2}{2\tilde{L}_{\mathring{m}}}, \tag{20}$$

where $q_{g\mathring{m}} = \sum_{\mathsf{x}_p} C_g u_{\mathring{m}}(\mathsf{x}_p) V_{\mathsf{x}_p}/\Delta u_{\mathring{m}}$, and the interaction potential

$$H_{\rm int} = -\sum_{\mathring{m}<\mathring{n}} \frac{\phi_{\mathring{m}}\phi_{\mathring{n}}}{L_J} - E_J \cos\left(\sum_{\mathring{m}} \frac{\phi_{\mathring{m}}}{\varphi_0} + \frac{\Phi_{\rm ext}}{\varphi_0}\right). \tag{21}$$

Eq. (19) is approximated into a tractable Hamiltonian making use of a frequency and effective impedance hierarchy of the normal modes. Indeed, if these are sorted in frequency as $\omega_0 < \omega_1 < ... < \omega_n$, it is possible to see that $Z_0 \gg Z_1 \gg ... \gg Z_n$. Therefore, as the frequency range of interest is bounded, a good approximation for Eq. (19) can be obtained taking into account a finite number of modes covering such a spectral range, and considering the rest of the modes in a vacuum state. We note that vacuum fluctuations are strongly suppressed for high-frequency modes, thanks to their vanishing effective impedance. In our particular case, the experiment probes frequencies in $[0, \omega_{\rm max}]$, with $\omega_0 < \omega_{\rm max} < \omega_1$, $\omega_{\rm max} \ll \omega_2$. Therefore, we approximate the device's Hamiltonian by the two-mode Hamiltonian in main text Eq. 5, which includes the two first antisymmetric modes. As shown in Fig. 2 of the main text, we find excellent agreement between the main text Eq. 5 diagonalization and the measured fluxonium spectrum. Moreover, we verify that the inclusion of the third antisymmetric normal mode in the fluxonium Hamiltonian does not modify appreciably the qubit spectrum. Regarding device 1, an estimation of a dispersive-like coupling strength for the first order mode-mode interaction gives $g^2/\Delta < 100\,$kHz between the first and third JJ modes, and $g^2/\Delta < 1\,$kHz between the second and third JJ modes, while the same quantities are negligible for device 2.

We note that the symmetry of the self-resonant nanowire modes is lost in the presence of circuit disorder. However, if disorder is small ($< 10\%$), one can still work in the symmetric-antisymmetric normal mode basis, deriving a capacitive coupling between the two sets of modes proportional to the amount of disorder. Therefore, the effect of symmetric modes could be taken into account within a dispersive (thus perturbative) theory, as it was previously done in the literature [5, 6]. However, due to the generality of our fit routine (see Sect. I F 2), we do not find necessary to consider such a dispersive shift (which adds a fit parameter) to obtain a high-accuracy agreement between theory and experiment.

Finally, we highlight some important differences of our formalism to previous approaches. We note that the full cosine potential of the Josephson junction has been exactly resummed in Eq. (17), before proceeding to the quantization in Eq. (19). Importantly, this step allows us to treat the strong nonlinearity of the fluxonium qubit efficiently by exact diagonalization of Eq. (19) in the phase basis, and to recover the effect of charge dispersion. Other approaches including Black-Box quantization [7, 8], rely on a series expansion of the cosine potential in terms of bosonic creation and annihilation operators for the normal modes. While this method has been proved to be convenient for the study of weakly anharmonic devices, it is not straightforward to capture the physics of strongly nonlinear devices for which a potentially infinite number of terms in the series expansion of the cosine potential needs to be considered.

The problem of characterizing the multimode structure of the fluxonium qubit has also been addressed for the case of Josephson junction array based devices by considering the normal modes of the superinductor [2, 3]. While this approach was successfully used to understand the overall complexity of these devices and study the effect of the multimode structure on the coherence times of the qubit, it is not of direct applicability to our experimental setup and to our experimental results.

To conclude, we note that our theory admits a purely discrete formulation where the nanowire is modeled as chain of LC oscillators (see Fig. 2) and the normal modes of the fluxonium device are computed by means of Eq. (7). For $N > 100$, the normal mode structure of such a system converges quickly to the result in the continuous limit and reproduces the results in Fig. 2 of the main text.

2. Fluxonium Spectrum

As the two-tone spectroscopy experiment probes the qubit spectrum in presence of the resonator, our data includes the Lamb shift contribution arising as a consequence of the dispersive coupling between the fluxonium and the resonator.

Lamb and dispersive shifts can be computed by means of the bare qubit level structure using the framework developed in [6], for any qubit-resonator system in the dispersive regime. Equivalently, such quantities can be obtained from full diagonalization of the transversally coupled qubit-resonator Hamiltonian. In this work, we use the second approach to compute the qubit spectrum.

We assume a readout resonator of nominal frequency (ω_r) and impedance (Z_r), according to the measured resonator mode frequency and specifications. Considering first, a single mode $\mathring{m}$ in Eq. (20), and making use of the antisymmetry of the mode function, the corresponding voltage coupling operator, as derived from the offset charge term, takes the

form $-q_{\mathring{m}}(C_g/\tilde{C}_{\mathring{m}})(V_1 - V_{-1})/2$. In the present case, the weak fluxonium-resonator coupling Hamiltonian is obtained by replacing the voltage difference $(V_1 - V_{-1})$ by the resonator voltage operator $V_r = \sqrt{\hbar Z_r/2}(a + a^\dagger)$, where a ($a^\dagger$) is the photon annihilation (creation) operator. Therefore, in a two-mode approximation for the fluxonium qubit, we consider the complete Hamiltonian

$$H = H_r + H_{\text{two-mode}} + H_{r0} + H_{r1}, \tag{22}$$

where $H_r = \omega_r a^\dagger a$ denotes the resonator Hamiltonian, $H_{\text{two-mode}}$ is given in Eq. 5 of the main text, and $H_{r\mathring{m}}$

$$H_{r\mathring{m}} = -q_{\mathring{m}}(C_g/\tilde{C}_{\mathring{m}})\sqrt{\hbar Z_r/2}(a + a^\dagger)/2 \tag{23}$$

is the coupling Hamiltonian between the resonator and the $\mathring{m}^{\text{th}}$ fluxonium mode.

The Lamb-shifted i^{th} qubit energy-level is identified by the energy eigenstate of Eq. (22) exhibiting maximum overlap with $|0, i\rangle$ (0 resonator excitations, i fluxonium excitations). The fluxonium parameters $C_p, C_J, L_J, C_{\text{nw}}, L_{\text{nw}}$, and the fluxonium-resonator coupling capacitance C_c, are considered input variables for the qubit spectrum fit in Fig. 2 of the main text. The results of the fit are listed in Table I.

Device	C_g [fF]	C_p [fF]	C_J [fF]	L_J [nH]	C_{nw} [fF]	L_{nw} [nH]
1	14.33	30.20	3.52	14.33	35.49	121.38
2	15.89	60.89	4.67	9.82	5.79	314.75

TABLE I. Circuit element parameters as obtained from the two-mode fit to the fluxonium qubit spectra presented in Fig. 2 of the main text.

[1] J. Bourassa, F. Beaudoin, J. M. Gambetta, and A. Blais, Phys. Rev. A **86**, 013814 (2012).
[2] G. Viola and G. Catelani, Phys. Rev. B **92**, 224511 (2015).
[3] D. G. Ferguson, A. A. Houck, and J. Koch, Phys. Rev. X **3**, 011003 (2013).
[4] H. L. Mortensen, K. Mølmer, and C. K. Andersen, Phys. Rev. A **94**, 053817 (2016).
[5] V. E. Manucharyan, J. Koch, L. I. Glazman, and M. H. Devoret, Science **326**, 113 (2009).
[6] G. Zhu, D. G. Ferguson, V. E. Manucharyan, and J. Koch, Phys. Rev. B **87**, 024510 (2013).
[7] S. E. Nigg, H. Paik, B. Vlastakis, G. Kirchmair, S. Shankar, L. Frunzio, M. H. Devoret, R. J. Schoelkopf, and S. M. Girvin, Phys. Rev. Lett. **108**, 240502 (2012).
[8] F. Solgun, D. W. Abraham, and D. P. DiVincenzo, Phys. Rev. B **90**, 134504 (2014).

6.3 Efficient modeling of superconducting quantum circuits with tensor networks

In this section, we introduce the paper "Efficient modeling of superconducting quantum circuits with tensor networks". This work demonstrates a new numerical method for finding the low-lying eigenvalues and eigenstates of large-scale superconducting quantum circuits. We first provide a brief motivation for this new method before highlighting the main results of the paper.

6.3.1 Going beyond exact diagonalization

The current generation of superconducting quantum circuits can incorporate from 10s [65] to 100s [89], 1,000s [122] and even 10,000s [123] Josephson junctions in a single device. For these systems, the circuit Hamiltonian describes a complex theory with nonlinear interactions between many bosonic modes. Treating the problem by exact diagonalization is not possible as soon as the number of modes in a circuit becomes large. This situation adds to the urgent need to develop tools capable of handling circuits of growing size and complexity [31].

In many cases, these devices operate in regimes where effective models with a reduced number of degrees of freedom, such as the multimode theories presented above, are accurate enough to describe the physics of interest. However, such effective models are inevitably based on approximations that allow extracting only limited information about the system. Furthermore, there are cases in which effective models with only a few degrees of freedom do not exist or are simply too difficult to derive [124].

The reason for the breakdown of exact-diagonalization techniques is the exponential increase of the Hilbert-space dimension of a many-body superconducting circuit with the size of the system. An strategy to avoid the manipulation of an exponentially large wavefunction is to work with a compressed representation of this object. From a physical point of view, we can certainly motivate the existence of compressed representations of the state of a system in a physically relevant regime. Part of the motivation comes from the fact that in most cases, low-energy eigenstates of models with local interactions involve strong correlations between subsystems on a local scale. Thus, the portion of the Hilbert space that is in practice accessible can be very small compared to the full Hilbert space [125].

Quite notably, the compression of a quantum state can be done by means of linear-algebra techniques that are also used for compressing other types of data, including images.

To illustrate this, we follow part of the discussion of Ref. [126]. Let us consider a bipartite quantum system, that we call the supersystem. One of the two parts of the supersystem is referred to as the system, while the other part is referred to as the environment. A pure state of the supersystem can be written as

$$|\psi\rangle = \sum_{ij} c_{ij} |i\rangle \otimes |j\rangle, \tag{6.17}$$

where $\{|i\rangle\}$ and $\{|j\rangle\}$ are complete bases for the system and the environment, respectively. From Eq. (6.17), the reduced density matrix of the system is $\rho_S = \text{Tr}_E[|\psi\rangle\langle\psi|]$, with components $[\rho_S]_{ii'} = \sum_j c_{ij} c^*_{i'j}$, where Tr_E indicates the trace operator over the environment.

Let us imagine now that we wish to compute the expectation value of an observable O that belongs to the system. If $\{\nu_\alpha, |v_\alpha\rangle\}$ is a basis of eigenvalues $\nu_\alpha > 0$ and eigenvectors $|v_\alpha\rangle$ for the density matrix ρ_S, then we have $\langle O\rangle = \sum_\alpha \nu_\alpha \langle v_\alpha|O|v_\alpha\rangle$. Naively, this indicates that the eigenvectors that contribute the most to $\langle O\rangle$ are those that have the largest eigenvalues. Note that the number of elements in $\{\nu_\alpha, |v_\alpha\rangle\}$ grows exponentially with the size of the system. Thus, if we want to approximate the expectation value of an observable using only a small number of states, the eigenvalues $\{\nu_\alpha\}$ are useful to decide which states in $\{|v_\alpha\rangle\}$ should be kept.

Indeed, it is possible to rigorously show that the eigenvectors of ρ_S with the largest eigenvalues provide an efficient representation of the state in Eq. (6.17), which can be made more accurate by increasing the number of states that are kept [126]. To see this, let us consider a change of basis of the form $|v_\alpha\rangle = \sum_i v^i_\alpha |i\rangle$, where v^i_α are complex coefficients, and construct the representation $|\tilde{\psi}\rangle$ of $|\psi\rangle$, using a relatively small number of states $m_s < l_s$ in $\{|v_\alpha\rangle\}$ where l_s is dimension of the basis set $\{|i\rangle\}$. $|\tilde{\psi}\rangle$ is an accurate representation of the original state if the functional $S = ||\psi\rangle - |\tilde{\psi}\rangle|^2$ is minimized. Let us now explore the conditions for this to happen by expressing $|\tilde{\psi}\rangle$ as

$$|\tilde{\psi}\rangle = \sum_{\alpha j} a_{\alpha j} |v_\alpha\rangle \otimes |j\rangle \equiv \sum_\alpha a_\alpha |v_\alpha\rangle \otimes |w_\alpha\rangle, \tag{6.18}$$

where α ranges from 1 to m_s, and we have defined the new environment states $\{|w_\alpha\rangle\}$ satisfying $\langle j|w_\alpha\rangle = N_\alpha a_{\alpha j} \equiv w^j_\alpha$, with N_α a normalization constant. The functional S can then be put in the form

$$S = \sum_{ij} \left(c_{ij} - \sum_{\alpha=1}^{m_s} a_\alpha v^i_\alpha w^j_\alpha \right)^2. \tag{6.19}$$

In this way, S becomes a function of the variables a_α, v^i_α, w^j_α, for a given value of m_s. The

functional optimization problem has been mapped to a linear algebra problem with a known solution [127]. If the coefficients of $|\psi\rangle$ are arranged into a matrix form $\psi = [c_{ij}]$, the optimal solution is found from a singular value decomposition (SVD) of the form $\psi = VDW^{\dagger}$[1], where V and D have dimensions $l_s \times l_s$ and $W^{\dagger}$ is a $l_s \times l_e$ matrix with l_e the dimension of the environment assumed to be greater than l_s. The first m_s elements of the diagonal matrix D, sorted in decreasing order, correspond to the coefficients a_α in Eq. (6.18). Moreover, the eigenvectors $|v_\alpha\rangle$ and $|w_\alpha\rangle$ are defined by the columns of V and W. By recalling that $[\rho_S]_{ii'} = \sum_j c_{ij}c^*_{i'j}$, we have $\rho_S = VD^2V^{\dagger}$, demonstrating that $|v_\alpha\rangle$ are also eigenvectors of ρ_S with eigenvalues $\nu_\alpha = a_\alpha^2$. These eigenvectors are the most efficient basis to represent the state of the system $|\psi\rangle$, with an accuracy that increases with m_s.

For a lattice of multiple sites, the modern formulation of these ideas decompose the quantum state $|\psi\rangle$ into a series of tensors, each representing a single site. The form of the localized wavefunction is known as a matrix product state (MPS). The exact many-body wavefunction of the lattice can be written as

$$|\psi\rangle = \sum_{\{\sigma_i\}} c_{\sigma_1\sigma_2\ldots\sigma_{N_J}} |\sigma_1\sigma_2\ldots\sigma_{N_J}\rangle, \tag{6.20}$$

where σ_i indexes orbitals of the ith site. The amplitude $c_{\sigma_1\sigma_2\ldots\sigma_{N_J}}$ is interpreted as a tensor with N_J indices, N_J being the number of sites. The MPS representation of $|\psi\rangle$, is obtained by performing successive SVDs on the full original tensor, leading to a representation of the wavefunction of the form [128]

$$|\psi\rangle = \sum_{\{\sigma_i\},\{a_i\}} A^{\sigma_1}_{a_1} A^{\sigma_2}_{a_1 a_2} \ldots A^{\sigma_{N_J-1}}_{a_{N_J-2}a_{N_J-1}} A^{\sigma_{N_J}}_{a_{N_J-1}} |\sigma_1\sigma_2\ldots\sigma_{N_J}\rangle, \tag{6.21}$$

where $A^{\sigma_i}_{a_{i-1}a_i}$ is the tensor of the MPS corresponding to the ith site. Here, an extra index a_i appears corresponding to a link index that connects to an adjacent site. The dimension of this additional index is known as the bond dimension and is controlled by truncating the number of nonzero singular values that are kept in the diagonal matrix D. Physical systems that have short-range interactions in one dimension can be modeled efficiently by an MPS with much smaller bond dimension than the full wavefunction [129]. Other cases can also work, but at the price of using a larger bond dimension.

In practice, the MPS is obtained by first constructing the Hamiltonian as a tensor network or matrix product operator (MPO). Once the MPO is known, an algorithm can be designed to converge a starting initial state to the correct ground state. One of the most

[1]Note that the standard convention in the literature is to write this equation as $\psi = UDV^{\dagger}$. In this thesis, we avoid this notation in order to prevent labeling different variables by the same name.

well-known tensor network methods for this task is the density matrix renormalization group (DMRG) algorithm [130, 131]. This approach is known to be very efficient for solving systems that are well captured by an MPS and can converge to the ground state in only a few variational iterations [132, 129, 133]. More importantly, the complexity of this algorithm scales linearly with the number of sites allowing us to treat systems that are far beyond what is possible with exact diagonalization.

In the context of superconducting qubits, we require the ground state but also some of low-energy excited states. The conventional approach to compute excitations with DMRG is to add to the system Hamiltonian an energy penalty of the form $\sum_{i\in \text{ex.}} \Lambda |i\rangle\langle i|$, with $\Lambda > 0$. This forces previously determined low-energy excitations above the next excited state, which becomes the ground state of the modified Hamiltonian and for which standard DMRG can be ran [128]. However, we notice that this technique can miss excited states and suffers from convergence issues.

To remedy this problem, we employ an extension of the DMRG algorithm that can compute a number of desired excitations simultaneously and will be published elsewhere, see Ref. [134]. We have used this method to obtain tens or hundreds of excitations simultaneously in a single run of the algorithm. We have been able to address several types of circuit Hamiltonians using this method, and we describe some of the results below.

6.3.2 Motivation

Part of the motivation behind our work on novel numerical techniques for superconducting circuits is the observation that certain aspects of the physics of large-scale devices cannot be captured with multimode series expansions. One of these aspects is the charge dispersion, something that is particularly interesting in the case of the fluxonium qubit. Moreover, while truncating the multimode theories to a few modes is often justified, one can imagine cases in which the number of modes that needs to be retained is simply too large. An example of this is provided by the current-mirror qubit [82, 124]. However, powerful numerical techniques can be useful to investigate multi-qubit devices, something that is very much needed for the development of the field [31]

In this work, we apply DMRG techniques to the case of the fluxonium qubit. From a numerical point of view, the fluxonium qubit is interesting because it displays short- and long-range linear and nonlinear interactions that are subject to periodic boundary conditions. As discussed above, this sets a challenging scenario for the DMRG algorithm. On the other hand, the fluxonium device is to some extent a simple device, and we can derive

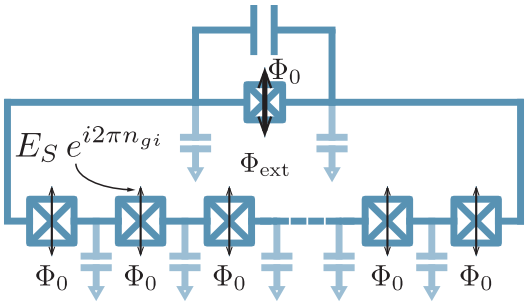

Figure 6.4 Coherent quantum phase slips in a fluxonium qubit. The arrows are proportional to the flux-tunneling amplitude for each junction. $E_S e^{i2\pi n_{gi}}$ is the total flux-tunneling amplitude through the ith junction of the superinductance.

effective models that are used to assert the validity of the DMRG approximation. Moreover, we use the DMRG technique to investigate quantities that are not possible to extract from the effective model, such as the charge dispersion. This allow us to compute the coherence time of a realistic fluxonium device.

6.3.3 Main results of the paper

In this paper, we demonstrate the successful DMRG implementation of the fluxonium circuit Hamiltonian for devices that integrate up to 180 array Josephson junctions. Since each of these junctions is represented as a site with 15 states, which are properly chosen from a convenient basis, the many-body wavefunction is defined in a Hilbert space of dimension 15^{180}. We moreover argue that the ingredients needed for the implementation of the fluxonium circuit Hamiltonian are applicable to many other superconducting circuits beyond the fluxonium qubit.

A complementary result to the DMRG implementation is the development of a single-mode theory for the fluxonium qubit that captures all circuit details. This new model is crucial to our paper, as it provides us with an independent model to validate the results from DMRG in certain limits. We show that the single-mode theory and DMRG agree with each other in a broad regime of parameters and for system sizes that go from a few to 100s of Josephson junctions. Moreover, we can benchmark the results of both of these models against exact diagonalization for circuit with less than 6 array Josephson junctions, also finding a perfect agreement.

The DMRG method gives us access to new insights about the physics of the fluxonium qubit. In particular, this technique allows us to evaluate the charge dispersion of this qubit, which arises from interference of flux-tunneling processes in the array junctions. As ex-

plained in Sect. 1.5.5, the role of the black-sheep Josephson junction of the fluxonium qubit is to couple flux states of the loop that have a different number of flux quanta. The effective strength of the coupling is proportional to the impedance of the black-sheep junction. In this picture, however, we omit the fact that the superinductance is made itself from Josephson junctions. Thus, if the impedance of an array junction is large enough, the flux-tunneling amplitude through that junction can be non-negligible. Since each junction of the superinductance defines an opening where a quantum of flux can tunnel in and out of the loop, the added flux-tunneling amplitude across the superinductance scales as the number of junctions. Thus, for large arrays made of high-impedance junctions, the tunneling amplitude can be significant, and even larger than that of the black-sheep junction.

The absolute magnitude of the flux-tunneling amplitude is by itself not specially relevant. The problem is, however, that the phase of the tunneling amplitude across one of the array junctions depends on the offset-charge distribution associated with this particular junction. Figure 6.4 illustrates this effect, where the tunneling amplitude through the ith circuit junction is $E_S e^{i2\pi n_{gi}}$, with E_S an energy constant and n_{g_i} the offset-charge parameter associated with this junction. The tunneling amplitude adds coherently across the array, leading to interference between flux-tunneling events on different junctions. We stress that E_S grows exponentially with the impedance of the array junctions, and thus this effect is more importantly relevant for high-impedance junctions.

As we have described in Sect. 1.5.5, the flux-tunneling amplitude determines the frequency of the fluxonium qubit at the sweet spot $\Phi_{\text{ext}} = \Phi_0/2$. Thus, if the total flux-tunneling amplitude through the superinductance is comparable to that of the black-sheep junction, the qubit frequency around $\Phi_{\text{ext}} = \Phi_0/2$ features an offset-charge dependence (charge dispersion). This is illustrated in Fig. 6.5, where the top panel shows the fluxon transition for different values of the offset charge n_{gi}, which is assumed to be the same for all junctions. Each panel corresponds to a different value of the array junction impedance z. As expected, we observe that the charge dispersion grows rapidly with z. The bottom panel of the figure shows the total charge dispersion as a function of the impedance of the array junction. Light-blue circles correspond to the estimation from DRMG, while black dashed lines are obtained from a phenomenological theory introduced in Ref. [37]. This theory is valid only in the limit of small impedance. We find a very good agreement between these two models, providing strong supporting evidence for the validity of the theoretical model. The confirmation of this theory is our main result with respect to the physics of the fluxonium qubit.

Finally, it is important to note that charge dispersion, combined with charge noise, lead to decoherence. In our paper, we quantify the coherence time expected for a realistic device.

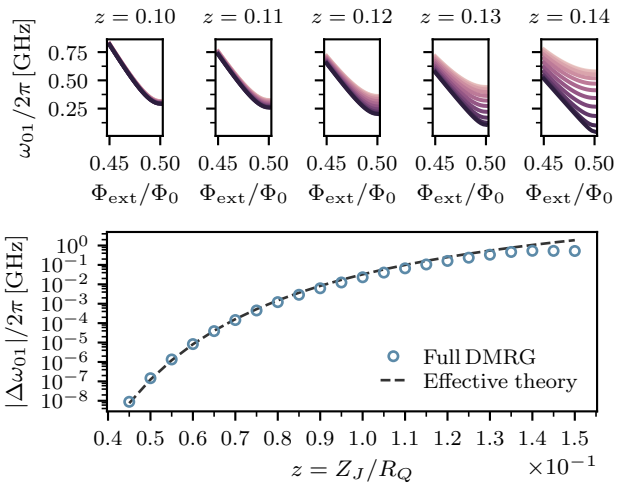

Figure 6.5 Charge dispersion of a 40-junction superinductance fluxonium qubit as a function of the reduced impedance of the array junctions. Top panel: Broadening of the fluxon transition around $\Phi_{\rm ext} = \Phi_0/2$ for $n_g \in [0, 0.5]$. Bottom panel: Total charge dispersion of the fluxon transition at $\Phi_{\rm ext} = \Phi_0/2$ according to the DMRG calculation (circles) against the prediction of the theory in Ref. [37] (black dashed lines).

Our estimation agrees with the experimental observation of Ref. [37].

6.3.4 Conclusion and outlook

We have developed a novel DMRG algorithm allowing us to simulate large-scale superconducting quantum devices. We applied this technique to the fluxonium qubit, and we asserted the validity of the DMRG implementation by developing a new single-mode theory for the device. Moreover, we used the DMRG technique to estimate the effects of charge dispersion in the fluxonium-qubit architecture.

We believe that these numerical techniques represent an important advancement. In particular, we envision applying these methods to explore new approaches to encode quantum information nonlocaly motivated by the distribution of many-body entanglement in a circuit. We also believe that these techniques can be useful to advance our understanding of dissipation and decoherence mechanisms and for the design of scalable superconducting-qubit architectures.

Efficient modeling of superconducting quantum circuits with tensor networks

Agustin Di Paolo,[1] Thomas E. Baker,[1] Alexandre Foley,[1] David Sénéchal,[1] and Alexandre Blais[1,2]

[1] *Institut quantique & Département de physique, Université de Sherbrooke, Sherbrooke, Québec J1K 2R1, Canada*
[2] *Canadian Institute for Advanced Research, Toronto, ON, Canada*

(Dated: November 18, 2019)

We introduce an efficient tensor network toolbox to compute the low-energy excitations of large-scale superconducting quantum circuits up to a desired accuracy. We benchmark this algorithm on the fluxonium qubit, a superconducting quantum circuit based on a Josephson junction array with over a hundred junctions. As an example of the possibilities offered by this tool, we compute the pure-dephasing coherence time of the fluxonium qubit due to charge noise and coherent quantum phase slips taking into account the array degrees of freedom corresponding to a Hilbert space as large as 15^{120}. Our algorithm is applicable to the wide variety of circuit-QED systems and may be auseful tool in scaling-up superconducting-qubit technologies.

I. INTRODUCTION

Superconducting qubits are a leading platform for quantum information processing [1, 2]. These qubits are built from superconducting quantum circuits integrating linear elements, such as capacitors and inductors, together with the only known nonlinear and nondissipative circuit component: the Josephson junction. These circuits operate at milliKelvin temperatures where macroscopic electromagnetic degrees of freedom associated to currents and voltages in the circuit are described quantum mechanically [3, 4]. In this regime, nodes (or branches) of the circuit are represented by bosonic fields with, in principle, infinite Hilbert-space dimension. The circuit topology defines the linear and nonlinear interactions between these bosonic modes, and finding the circuit excitations requires the diagonalization of the full circuit Hamiltonian. However, for circuits with more than a few nodes, this task rapidly becomes intractable by exact diagonalization. With current devices integrating 10s [5] to 100s [6], 1,000s [7] and even 10,000s [8] Josephson junctions, this is a real challenge that the field is facing.

Fortunately, in many cases these devices operate in regimes where effective models with a reduced number of degrees of freedom are accurate enough to describe the physics of interest. These effective models, however, are based on approximations that allow extracting only limited information about the system. Moreover, it is often not possible to trace back the original circuit parameters from the effective model and, when it is possible, these parameters often have to be inferred indirectly from complex multivariate fits to the experimental data. This loss of information can be detrimental to circuit design.

In this work, we adapt to many-body superconducting quantum circuits a numerical tensor network method that we have introduced in Ref. [9]. We use this numerical toolbox to compute the relevant low-energy excitations of a large-scale superconducting circuit taking into consideration all of its degrees of freedom of a lumped-element model of the device. We show how this gives access to information about the system that can be used, for instance, to make predictions about the system such as estimating its coherence time from first principles.

As an example of application of this method, we consider the fluxonium qubit [5]. This superconducting quantum circuit is made of a small Josephson junction fabricated in parallel with an array of ~ 100 Josephson junctions. Because of the large number of elements it contains, it is an ideal test bed for our numerical approach. To help in benchmarking our tensor network implementation, we develop an effective model for the fluxonium qubit that captures the essential circuit details and which can easily be solved by exact diagonalization. To assert the validity of the tensor network method, we first compare results obtained with the tensor network method to the those obtained with the approximate effective model in regimes where the latter approach is expected to faithfully describe the device. We then push the tensor network method to regimes where deriving an accurate effective theory is challenging. The effective model and the tensor network toolbox are used to investigate the charge dispersion of the fluxonium qubit in a broad range of parameters, confirming an existing theory [10] and clarifying its regime of validity. Finally, we use the tensor network method to estimate the pure-dephasing time of a realistic fluxonium device. We provide direct numerical evidence of the potentially harmful effects of charge noise in this system for certain circuit parameters.

This paper is organized as follows. In Sect. II, we first summarize the tensor network method introduced in Ref. [9]. In Sect. III, we provide a tensor network implementation of the complete fluxonium-qubit Hamiltonian, describe an effective model for this qubit and compare results obtained with both approaches. Sect. IV discusses the interplay between charge noise and coherent quantum phase slips in this system. The main result of this section is the direct numerical evidence of the charge dispersion in fluxonium devices supporting a previously developed theory [10]. Sect. V is dedicated to the conclusions and to an outlook of the results of this work.

II. THE MULTI-TARGETED DMRG ALGORITHM

To obtain the low-energy excitations of a quantum system, a strategy that scales better than exact diagonalization is to decompose the quantum problem into a network of tensors. This approach can scale far better than exact diagonalization by treating the problem locally. Indeed, for a lattice of multiple sites, instead of handling the complete wavefunction of the many-body system at once, the quantum state is decomposed into a series of tensors, each representing a single site. The form of the localized wavefunction is known as a matrix product state (MPS) and has been known for some time [11].

The exact many-body wavefunction of the lattice can be written as

$$|\psi\rangle = \sum_{\{\sigma_i\}} c_{\sigma_1\sigma_2\ldots\sigma_{N_J}} |\sigma_1\sigma_2\ldots\sigma_{N_J}\rangle, \tag{1}$$

where σ_i indexes orbitals (or levels) of the ith site. The amplitude $c_{\sigma_1\sigma_2\ldots\sigma_{N_J}}$ is interpreted as a tensor with N_J indices, N_J being the number of sites. In order to obtain a MPS representation of $|\psi\rangle$, a series of tensor decompositions can be performed using the singular value decomposition (SVD). The SVD decomposes a tensor into two unitary tensors, U and V, and a diagonal matrix D such that the original tensor may be reconstructed as $UDV^\dagger$. By performing successive SVDs on the full original tensor, one obtains a site-by-site representation of the wavefunction of the form [12]

$$\begin{aligned}|\psi\rangle = \sum_{\{\sigma_i\},\{a_i\}} & A^{\sigma_1}_{a_1} A^{\sigma_2}_{a_1 a_2} \ldots A^{\sigma_{N_J-1}}_{a_{N_J-2} a_{N_J-1}} A^{\sigma_{N_J}}_{a_{N_J-1}} \\ & \times |\sigma_1\sigma_2\ldots\sigma_{N_J}\rangle,\end{aligned} \tag{2}$$

where $A^{\sigma_i}_{a_{i-1}a_i}$ is the tensor of the MPS corresponding to the ith site. Here, an extra index a_i appears corresponding to a link index that connects to an adjacent site. The dimension of this additional index is known as the bond dimension and is controlled by truncating the number of nonzero singular values that are kept in the diagonal matrix D, effectively leaving out small entries of this density matrix. For short-range interactions and low dimensions, the physical system can be modeled efficiently by an MPS with much smaller bond dimension than the full wavefunction [13]. Other cases can also be captured by the MPS at the price of using a larger bond dimension [12, 14].

Eq. (2) is represented in the left-normalized basis where the tensor A is determined from the U tensor of the SVD. The MPS can also be written with right-normalized tensors (creating tensors from $V^\dagger$). The most common gauge to choose is the mixed-canonical representation. In the mixed gauge, left- and right-normalized tensors are separated by one site where the D matrix has been contracted on to the site. This site is known as the orthogonality center, and represents the information passed between left and right parts of the system.

In practice, the MPS is obtained by first constructing the Hamiltonian written as a tensor network, known as matrix product operator (MPO). Once the MPO is known, an algorithm can be designed to converge a starting initial state to the correct ground state. One of the most well-known tensor network methods for this task is the density matrix renormalization group (DMRG) algorithm [15, 16]. This approach is known to be very efficient for solving systems that are well captured by the MPS and can converge to the ground state in only a few iterations of the algorithm [13, 17, 18]. More importantly, the complexity of this algorithm scales linearly with the number of sites, making it possible to treat systems of sizes beyond what is possible with exact diagonalization.

While DMRG is most commonly used to study groundstates, the analysis of superconducting quantum circuits requires to correctly capture several excitations. For example, for the case of a single superconducting qubit built out of a large superconducting circuit, the ground state and the two first lowest-energy excitations are needed to estimate the qubit frequency ω_{01} and anharmonicity $\omega_{12} - \omega_{01}$, where $\hbar\omega_i$ is the energy of the ith eigenstate of the circuit and $\omega_{ij} = \omega_j - \omega_i$. If n_q such qubits are integrated on a chip, the number of excitations required to characterize the device typically scales as n_q^2.

The conventional approach to compute excitations with DMRG is to add to the system Hamiltonian an energy penalty of the form $\sum_{i\in\mathrm{ex.}} \lambda|i\rangle\langle i|$, with $\lambda > 0$. This forces previously determined low-energy excitations above the next excited state, which becomes the ground state of the modified Hamiltonian and for which standard DMRG can be run [12]. However, we noticed that this technique can miss excited states and suffers from convergence issues.

To remedy this problem, we have derived an extension of the DMRG algorithm that includes the excitations computed directly in the Lanczos step of the algorithm [9]. We extended the original MPS to a bundled MPS, where the orthogonality center has been given an additional index that identifies excitations in the system. By attaching the additional index to the state, we can derive an efficient tensor network update at each step of the DMRG algorithm that modifies the wavefunction until each excitation is variationally minimized to the correct eigenvalue. This procedure is numerically stable and agrees with exact diagonalization in all tested situations. This multi-targeted DMRG technique does not miss excitations or introduce numerical degeneracies. We have used this method to obtain tens or hundreds of excitations simultaneously in a single run of the multi-targeted DMRG algorithm. This is where our multi-targeted DMRG algorithm differs significantly from the traditional DMRG approach for computing excitations, which needs to be run sequentially, once per required excitation. Furthermore, an important benefit of our multi-targeted DMRG algorithm is that the orthogonality of the computed excited states is guaranteed up to numerical precision. In contrast, in the traditional DMRG ap-

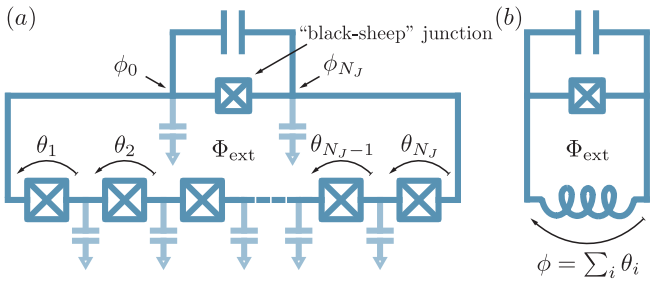

FIG. 1. Lumped-element model of the fluxonium qubit. (a) Detailed circuit scheme including a "black-sheep" junction (center) shunted by a capacitance (top) and a junction-array superinductance with N_J junctions (bottom). Stray capacitances to ground are depicted in a lighter shade of blue. (b) Effective circuit in which the junction-array is modeled as a linear inductance. ϕ_i for $i \in [0, N_J]$ denotes the superconducting phase at every circuit node, while θ_i for $i \in [1, N_J]$ is the phase difference at every junction of the array. The superinductance (or fluxonium) mode is defined as the phase difference across the black-sheep junction: $\phi = \phi_0 - \phi_{N_J} = \sum_{i=1}^{N_J} \theta_i$.

proach, the orthogonality of an excitation with respect to previously determined eigenstates is controlled by the accuracy of the associated eigenvalues. More information on the multi-targeted DMRG algorithm can be found in Ref. [9].

III. DMRG IMPLEMENTATION OF THE FLUXONIUM-QUBIT HAMILTONIAN

We choose the fluxonium qubit [5] as a testbed for the multi-targeted DMRG approach. Because of its relatively complex structure, with an Hamiltonian that includes periodic boundary conditions as well as short- and long-range linear and nonlinear interactions (see appendix A), this is an ideal test circuit for this numerical method.

The fluxonium qubit is a variation on the transmon qubit [19] in which a large shunt inductor is added to protect the device against low frequency charge noise [20]. Recent experiments have demonstrated long coherence times with this qubit [6, 21, 22]. The fluxonium circuit (see Fig. 1) consists of a small Josephson junction, referred to as the "black-sheep" junction, shunted by a superinductance, i.e. a circuit element with effective impedance greater than the quantum of resistance $R_Q = h/(2e)^2 \simeq 6.5\,\text{k}\Omega$ and self-resonance frequencies above 10 GHz [23–27]. Superinductances have been made using Josephson junction arrays [26], high-kinetic-inductance superconductors [28, 29] and granular aluminium [30]. Superinductances are also crucial to other qubit designs such as the noise-protected $0-\pi$ qubit [24, 31]. While a superinductance is in principle a multimode device, it can behave as a single-mode linear inductance under appropriate conditions [26, 32, 33]. The multimode structure of such a device has, however, important consequences [26, 29], some of which are investigated below.

A. Setting-up the DMRG algorithm

With the objective of determining the low-energy excitations of the full fluxonium device shown in Fig. 1 (a) using our DMRG algorithm, we first describe the associated circuit Hamiltonian. In this circuit, the black-sheep junction is described by its Josephson energy E_{J_b} and its capacitance C_{J_b} which may include a shunt capacitance. We take the superinductance to be realized by an array of Josephson junctions, with L_{J_i} and C_{J_i} the ith junction inductance and capacitance. Moreover, a capacitance to ground C_{0_i} is associated to the ith circuit node. In absence of circuit element disorder, these parameters take the constant values L_J, C_J and C_0, respectively. We also define the junction plasma frequency $\omega_p = 1/\sqrt{L_J C_J}$ and reduced impedance $z = \sqrt{L_J/C_J}/R_Q$. Following the standard circuit-quantization procedure [3], the Hamiltonian of the circuit of Fig. 1 takes the form (see appendix A)

$$H = \sum_{i=1}^{N_J} H_{0_i} + \sum_{j>i}^{N_J} \hbar g_{ij}\, n_i n_j - E_{J_\text{b}} \cos\left(\sum_{i=1}^{N_J} \theta_i + \frac{\Phi_\text{ext}}{\varphi_0}\right). \tag{3}$$

In this expression, $H_{0_i} = 4E_{C_i}(n_i - n_{g_i})^2 - E_{J_i}\cos\theta_i$ is a noninteracting (or site) Hamiltonian for the ith array junction with θ_i is the phase difference across thatjunction and n_i the conjugate charge. Moreover, n_{g_i} is an offset-charge parameter, E_{C_i} the effective charging energy and $E_{J_i} = \varphi_0^2/L_{J_i}$ the effective Josephson energy with $\varphi_0 = \Phi_0/2\pi$ where $\Phi_0 = h/2e$ is the flux quantum. In addition to the on-site energies, Eq. (3) includes a bilinear interaction $\propto n_i n_j$ arising from the ground, black-sheep and array-junction capacitances and which couples the sites with comparable strength and all-to-all connectivity (see appendix A). Furthermore, the last term of Eq. (3) is a nonlocal interaction that depends on the external flux Φ_ext and which results from the strongly nonlinear Josephson potential of the black-sheep junction. Because Eq. (3) includes a very large numbers of degrees of freedom and is therefore difficult to work with, this Hamiltonian is typically not directly employed in the literature to describe the fluxonium qubit. Instead, fluxonium devices are usually modeled by a phenomenological Hamiltonian that incorporates a single bosonic degree of freedom, $\phi = \sum_{i=1}^{N_J} \theta_i$, known as superinductance or fluxonium mode.

To obtain the low-energy excitations of Eq. (3) by means of a tensor network and in this way go beyond the effective model, the Hamiltonian must first be converted to its matrix product operator form. Crucially, the long-range cosine interaction is ideally suited to matrix product states and operators, preventing an increase of the bond dimension with the number of sites. This remarkable observation is one of the key findings of our work and extends to all circuit-QED Hamiltonians, from lumped-element models to black-box-quantization [34, 35] and energy-participation-ratio [36] formalisms. Indeed, we

have successfully implemented a wide variety of such models and circuit Hamiltonians, results that will be reported elsewhere. On the other hand, the all-to-all capacitive interaction in Eq. (3) does not have an efficient matrix-product-operator representation. However, this unfavorable interaction does not prevent a efficient implementation of the multi-targeted DMRG algorithm and the results presented below have a relatively small bond dimension thanks to matrix-product-operator compression techniques [37]. The efficient matrix-product-operator representation of the black-sheep Josephson potential in Eq. (3), and the possibility of handling an arbitrary capacitive coupling Hamiltonian by compression techniques, makes our DMRG implementation readily applicable to many other circuit-QED setups.

B. Effective single-mode theory

To assert the validity of our DMRG method, we derive in Appendix B an effective single-mode theory from Eq. (3) that can be solved by exact diagonalization and which goes beyond the standard treatment found in the litterature. Under approximations controlled by the parameter regime of the device, we arrive at the Hamiltonian

$$H' = 4E_C n'^2 - N_J^2 E_L \cos(\phi'/N_J) - E_J \cos\left(\phi' + \frac{\Phi_{\rm ext}}{\varphi_0}\right), \tag{4}$$

where the mode described by ϕ' is closely related to the superinductance (or fluxonium) mode ϕ, and n' the conjugate charge. Here, E_C, E_L and E_J are effective capacitive, inductive and Josephson energies, respectively, obtained from the classical normal-mode structure of the circuit. If the capacitances to ground C_{0_i} for $i \in [1, N_J]$ can be neglected, then $\phi' = \phi$ and $n' = n = N_J^{-1}\sum_{i=1}^{N_J} n_i$, where n is the conjugate charge operator to ϕ. Otherwise, the ϕ' mode includes corrections to ϕ that are linear in C_0.

Although in the limit of large N_J Eq. (4) reduces to the original fluxonium-qubit Hamiltonian [see Fig. 1 (b)] [5], the parameters of Eq. (4) capture all details of the circuit's capacitance network and contain important corrections which are due to the nonlinearity of the array junctions. To the best of our knowledge, these corrections have not been discussed before and can lead to significant frequency shifts of the qubit transitions (see appendix B 3). Crucially, because of its single-mode nature, Eq. (4) can easily be diagonalized numerically by truncating the Hilbert space of the ϕ' mode to finite dimension.

C. Comparison

Having derived the effective model of Eq. (4) which will be use as a benchmark, we are now in a position to demonstrate the results of our DMRG approach and to explore the capabilities of this method. To this end, we consider a device in the "heavy fluxonium" regime [6, 21, 29] with a large shunt capacitance and a superinductance made of $N_J = 120$ identical junctions where $\omega_p/2\pi = 25\,\text{GHz}$ and $z = 0.03$ [26]. See appendix B 2 for a qualitative description of the different regimes of the fluxonium qubit Hamiltonian. Each junction is modeled as a multilevel system using the 15 lowest energy eigenstates of the site Hamiltonian H_{0_i}. We find that for low-impedance junctions, the site eigenbasis requires a smaller number of states to avoid truncation errors as compared to other local basis such as charge basis. The DMRG implementation is thus defined in a product basis of local wavefunctions spanning a many-body Hilbert space as large as 15^{120} and that has, a priori, no built-in information about collective modes of the system. Importantly, this choice of basis also makes our treatment readily extensible to other superconducting quantum circuits.

Figure 2 (a) shows the energy spectrum of the fluxonium device of Fig. 1 for both DMRG (Eq. (3), light-blue circles) and exact diagonalization of the effective single-mode theory (Eq. (4), black dashed lines) as a function of the external flux $\Phi_{\rm ext}$. We find excellent agreement between these two independent models. Importantly, this observation extends to all systems sizes and parameter sets that we have tested, from a few-sites fluxonium-like device to circuits with more than 200 junctions. These results provide supporting evidence that the DMRG method can be applied in regimes where deriving an effective model is not possible. Further numerical evidences are presented in appendix B.

In addition to computing global properties of the circuit, such as its energy spectrum, the multi-targeted DMRG algorithm also gives access to local site properties which we now explore. These operators can give insights into the many-body structure of the fluxonium eigenstates. Fig. 2 (b) shows the mean photon-number population $\langle p_i\rangle = \langle\psi_k|H_{0_i}|\psi_k\rangle/\hbar\omega_p$ of the ith site, for all sites ($i \in [1, N_J]$, vertical axis of each of the 6 density plots) as a function of $\Phi_{\rm ext}$. These expectation values are computed for a given eigenstate $|\psi_k\rangle$ of the full fluxonium circuit, from the groundstate ($k = 0$, bottom density plot) to the 5th excited state ($k = 5$, top density plot). Because of the absence of circuit-element disorder in these simulations, the result do not show any variations with site number. We observe that flux-sensitive (fluxon) transitions have the lowest values of photon population, while the flux-insensitive (plasmon) transitions involve nonzero population of the sites' excited states.

We interpret Fig. 2 (b) with the help of Fig. 2 (c), which illustrates a portion of the local Josephson potential of an array junction and its single-site wavefunctions. From the point of view of this site (left panel), a fluxon state $|\psi_k\rangle$ at $\Phi_{\rm ext} \neq 0, \Phi_0/2$ involves a small displacement by α_k/N_J of the site's wavefunction (red) away from its noninteracting ground state position (pink).With the

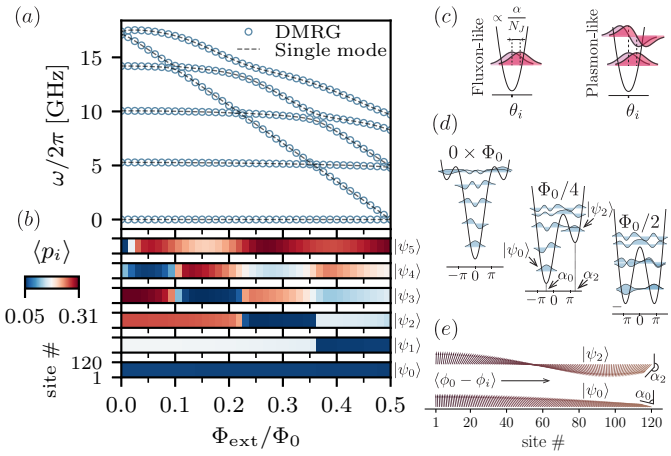

FIG. 2. A 120-junction superinductance heavy fluxonium as a function of $\Phi_{\rm ext}$. (a) Energy spectrum of the Hamiltonians in Eq. (3) (DMRG) and Eq. (4) (single mode). (b) Mean photon-number population of the array Josephson junctions (sites) for every eigenstate $|\psi_k\rangle$ of the fluxonium circuit. (c) Single-junction picture of fluxon- and plasmon-like excitations. (d) Effective potential energy and wavefuctions of the single-mode Hamiltonian for $\Phi_{\rm ext} \in \{0, \Phi_0/4, \Phi_0/2\}$. (e) Expectation value of the phase operator at every circuit node of the superinductance for the fluxonium eigenstates labeled by $|\psi_0\rangle$ and $|\psi_2\rangle$. Circuit parameters: $C_{J_{\rm b}} = 40\,{\rm fF}$, $E_{J_{\rm b}}/h = 7.5\,{\rm GHz}$, $C_J \simeq 32.9\,{\rm fF}$ and $L_J \simeq 1.23\,{\rm nH}$ (from $\omega_p/2\pi = 25\,{\rm GHz}$ and $z = 0.03$ [26]) and $C_0 = 0$. Single-mode model parameters: $E_C/h \simeq 0.48\,{\rm GHz}$, $E_L/h \simeq 1.27\,{\rm GHz}$ (i.e., $L \simeq 129.1\,{\rm nH}$) and $E_J = E_{J_{\rm b}}$.

current operator associated to the ith junction given by $I_i = I_c \sin\theta_i$ where I_c is critical current, this displacement results in a circulating current. Collectively, since $\phi = \sum_{i=1}^{N_J} \theta_i$, these displacements add to a mean value $\langle\psi_k|\phi|\psi_k\rangle \equiv \alpha_k$ which coincide with a local minimum of the effective fluxonium potential [see also Fig. 2 (d)]. A similar mean-field displacement is found for the plasmon states (right panel), although these involve important contributions from the site's excited states.

The above interpretation becomes clearer by considering the effective potential and wavefunctions obtained from the single-mode Hamiltonian Eq. (4) shown in Fig. 2 (d) for $\Phi_{\rm ext} \in \{0, \Phi_0/4, \Phi_0/2\}$. The shape of the effective potential is determined by the cosine potential of the black-sheep junction and the inductive energy $-N_J^2 E_L \cos(\phi'/N_J) \simeq E_L \phi'^2/2$ of the array. While fluxon states are the lowest energy eigenstates associated to the local minima of this effective potential, the plasmon states correspond to intra-well excitations. Since the positions of the potential wells shift significantly with $\Phi_{\rm ext}$, the energy of fluxon-like excitations is highly sensitive to the external flux [see also Fig. 2 (a)]. In contrast, plasmon excitations have a very weak flux sensitivity in comparison, corresponding to the flux-insensitive transitions in Fig. 2 (a). For some flux biases, these two types of excitations hybridize, leading to anticrossings in the spectrum of Fig. 2 (a). A more in-depth description of fluxon and plasmon excitations of the fluxonium can be found in appendix B 2.

Fig. 2 (e) combines insights from both panels (c) and (d), It shows the expectation value of the phase drop $\phi_0 - \phi_i \equiv \sum_{j=1}^{i} \theta_j$ obtained from DMRG and plotted as a function of the site number for the fluxon states $|\psi_0\rangle$ and $|\psi_2\rangle$ at $\Phi_{\rm ext} = \Phi_0/4$. These expectations values are illustrated by the direction of a vector with respect to the vertical direction. The angle of this vector between the first and last sites is in perfect agreement with the positions of the local minima α_0 and α_2 of the effective potential of Eq. (4) [see (d), middle panel].

Overall, Fig. 2 shows that the multi-targeted DMRG algorithm correctly reproduces the results of the effective single-mode theory. It can also provide information that is not accessible from this theory. This comparison provides solid evidence of a correct DMRG implementation of the full circuit Hamiltonian of the fluxonium qubit. It also suggests that other circuit Hamiltonians can benefit from this numerical method. Moreover, the local physical quantities such as those illustrated in Fig. 2 (b), contain information about the energy-participation ratio of all circuit components for a given collective excitation. This information could be used to identify dissipation channels and to understand the effect of circuit-element disorder. We return to these aspects in Sect. V.

IV. CHARGE DISPERSION AND COHERENCE TIME

We now proceed with a concrete application that shows how our DMRG implementation can be leveraged to produce coherence-time estimates from first principles. In particular, we are interested in quantifying the coherence time of the fluxonium due to the combined effect of charge noise and coherent quantum phase slips [10, 27].

A. Charge dispersion

In the fluxonium qubit, the black-sheep junction acts as a weak link that couples flux states of the superconducting loop. This makes quantum control of the flux degree of freedom possible but can also be a source of errors. In a semiclassical picture, the rate at which a quantum of flux can tunnel in and out of the loop through the black-sheep junction is proportional to the junction impedance, while the energy cost associated to the addition of a quantum of flux to the loop scales as $1/L$. Since the tunneling of a flux quantum corresponds to a change of 2π in the phase of the superconducting order parameter, this phenomenon is known as coherent quantum phase slip (CQPS) [10, 38–43]. In experiments, fluxonium devices exploit a wide range of black-sheep junction impedances, ranging from relatively small in the heavy-fluxonium [6, 21, 29], to moderate in the fluxonium

[5, 10] and to large values for the light-fluxonium [44]. See appendix B 2 for a qualitative discussion of these parameter regimes. Ideally, the total amplitude for CQPS events is largely dominated by the contribution from the black-sheep junction. However, if the impedance of the array junctions is large enough, the added CQPS amplitude due to the superinductance can be non-negligible. In this limit, the junction array may be regarded as a "slippery" superinductance [27].

Ref. [10] introduced an effective model describing the effect of CQPS occurring in the superinductance of a fluxonium qubit. In this model, CQPS due to the black-sheep junction are captured by a phenomenological single-mode fluxonium qubit Hamiltonian similar in spirit to Eq. (4). On the other hand, CQPS due to the superinductance enter in the effective Hamiltonian via the external flux. More precisely, the parameter Φ_{ext} in Eq. (4) is replaced by $\Phi_{\text{ext}} + m\,\Phi_0$, where m is an integer-valued number operator that counts the number of CQPS in the superinductance. Since a CQPS event at any junction of the superinductance leads to a jump $m \to m \pm 1$, it can be interpreted as a 2π phase bias on ϕ.

To quantify the total CQPS amplitude resulting from the superinductance, we consider a realistic model of this composite circuit element with its N_J islands and their independent offset charges [see Fig. 1 (a)]. As a consequence of the Aharonov-Casher effect, the flux-tunneling amplitude at a given array junction has a well-defined phase given by the offset-charge n_{g_i} associated to that junction [10, 38, 43, 45–47]. By adding coherently the contributions from the N_J array junctions, the total CQPS amplitude (excluding the black-sheep junction) takes the form $E_S = \sum_{i=1}^{N_J} \epsilon_{0_i} e^{i2\pi n_{g_i}}$, where

$$\epsilon_{0_i} = 8\sqrt{2}\,\hbar\omega_{p_i} \exp(-4/\pi z_i)/\sqrt{\pi z_i}, \tag{5}$$

determines the charge dispersion of the groundstate energy of the transmon Hamiltonian H_{0_i} in terms of the reduced impedance z_i and plasma frequency ω_{p_i} of the ith array junction [19, 27, 38, 48]. Importantly, this result only holds in the low-impedance limit ($z_i \ll 1$).

CQPS events in the superinductance can then be described by a phenomenological flux-tunneling Hamiltonian of the form $H_{\text{CQPS}} = (E_S\, m^- + E_S^*\, m^+)/2$, where the operator m^- [$m^+ = (m^-)^\dagger$] removes (adds) a single flux quantum from the loop through any of the array junctions. In the limit of rare CQPS, $|E_S| \ll E_L$, H_{CQPS} can be regarded as a small perturbation to the fluxonium Hamiltonian. In this situation, first-order perturbation theory predicts a shift $\delta\omega_{ij} = \text{Re}[E_S](\langle T\rangle_j - \langle T\rangle_i)/\hbar$ of the qubit's $i \to j$ transition frequency, where $T = \exp(-i2\pi n)$ is a 2π-displacement operator whose expectation values are computed using the unperturbed eigenstates $\{|\psi_i\rangle\}$ with $m = 0$ [10]. For a homogeneous array ($\epsilon_{0_i} \equiv \epsilon_0$ for $i \in [1, N_J]$), one has $-N_J\epsilon_0 \le \text{Re}[E_S] \le N_J\epsilon_0$, and the total charge dispersion of the qubit transition frequency is

$$|\Delta\omega_{01}| = 2N_J\epsilon_0 |\langle T\rangle_1 - \langle T\rangle_0|/\hbar. \tag{6}$$

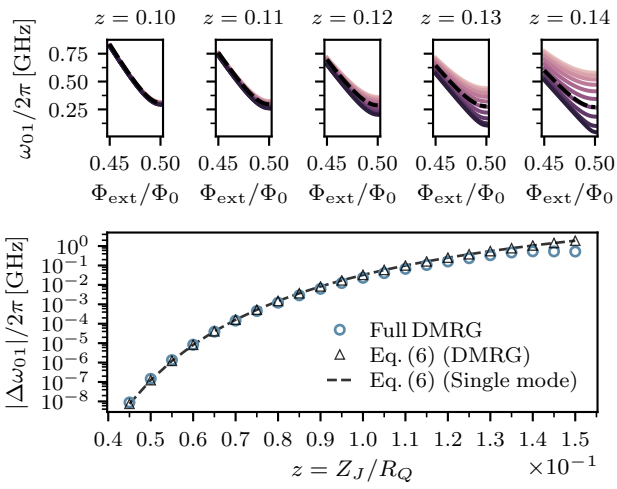

FIG. 3. Charge dispersion of a 40-junction superinductance fluxonium qubit as a function of the reduced impedance of the array junctions. Top panel: Broadening of the fluxon transition around $\Phi_{\text{ext}} = \Phi_0/2$ for $n_g \in [0, 0.5]$. Color lines are obtained from DMRG while dashed black lines correspond to estimations using Eq. (4). Bottom panel: Total charge dispersion of the fluxon transition at $\Phi_{\text{ext}} = \Phi_0/2$ according to the DMRG calculation (circles) contrasted to the prediction of Eq. (6) with matrix elements evaluated by means of DMRG (triangles) or the single-mode model (dashed lines). Parameters: $C_{J_b} = 7.5\,\text{fF}$, $E_{J_b}/h = 8.9\,\text{GHz}$, $\omega_p/2\pi = 12.5$ and $C_0 = 0$, according to Ref. [10].

As the classical flux states of the loop are degenerate at $\Phi_{\text{ext}} = \Phi_0/2$, the effect of a nonzero E_S is stronger close this flux.

Fig. 3 shows the charge dispersion of the fluxon transition of a fluxonium device with parameter values chosen to be as close as possible to those of the experiment of Ref. [10]. The top panel shows the qubit transition frequency as a function of the external flux close to $\Phi_{\text{ext}} = \Phi_0/2$ for different values of the offset charge $n_{g_i} \equiv n_g$, assumed to be the same on every junction of the array. Each sub-panel shows the DMRG results for a given value of the array-junction impedance. The lightest (darkest) transition in purple corresponds to $n_g = 0$ ($n_g = 0.5$). Dashed black lines show the qubit transition according to Eq. (4) which does not have an offset-charge parameter. Note that the offset-charge dependence of the CQPS tunneling energy leads to constructive ($|E_S| > 0$) and destructive ($E_S \to 0$) interference of CQPS events.

Qualitatively, charge dispersion increases rapidly with z due to the exponential scaling of Eq. (5). This is best illustrated by the bottom panel of Fig. 3, which shows the charge dispersion for $\Phi_{\text{ext}} = \Phi_0/2$ as a function of z. Light-blue circles (Full DMRG) correspond to a fully numerical estimation using DMRG for which the charge dispersion is computed by taking the difference between the energy of the fluxon transition for $n_g = 0$ and $n_g = 0.5$. Black triangle markers [Eq. (6) (DMRG)] are the result

of Eq. (6) for which the matrix elements are evaluated using the eigenstates obtained from DMRG for $n_g = 0$. The black dashed line [Eq. (6) (Single mode)], in contrast, is obtained by evaluating the matrix elements using the single-mode Hamiltonian Eq. (4). We find no significant difference between the DMRG [Eq. (6) (DMRG)] and the single-mode [Eq. (6) (Single mode)] implementations of Eq. (6), with both approaches showing a small but clearly visible deviations from the results obtain from fully numerical DMRG estimation (Full DMRG) at large z.

Indeed, up to array-junction impedances as high as $z \simeq 0.1$ we observe a remarkable agreement between the estimation of the total charge dispersion from fully numerical DMRG and that predicted by Eq. (6). This provides evidence in support of the theoretical model introduced in Ref. [27]. Although not visible in Fig. 3, small deviations between the fully numerical DMRG estimation and those based on Eq. (6) are present for $z \lesssim 0.06$. The largest truncation error for all simulations in Fig. 3 is of order 10^{-11}, and the error tolerance on the eigenvalues is set to 10^{-12}, guaranteeing the convergence of the fully numerical DMRG results to the same accuracy. DMRG being a variational method, we have verified that the convergence to the reported accuracy is also well behaved. We also note that we have observed deviations with the same order between the fully numerical DMRG estimation and the prediction of Eq. (6) for devices with different sets of circuit parameters. However, in all of these cases, the deviations are too small to be relevant when computing coherence times (see below).

On the other hand the larger relative difference between the full numerical DMRG estimation and those based on Eq. (6) in the range of $z \gtrsim 0.1$ is expected. Indeed, in this regime Eq. (5) which neglects the contribution of all but the one array junction that undergoes the CQPS and the assumption that $|E_S| \ll E_L$ are both no longer valid [27]. Therefore, $z \gtrsim 0.1$ is a regime in which the DMRG method is at a clear advantage over effective theories.

B. Coherence-time estimations

Because of unavoidable charge noise, the value of $\delta\omega_{ij}$ fluctuates in time leading to broadening of the qubit transition. For large charge dispersion, this effect can severely compromise qubit coherence. This observation is the basis of the experimental study of Ref. [10], where the degradation of the qubit coherence time around the flux sweet spot is taken as indirect evidence of CQPS events in the "slippery" superinductance. In support of the experimental observation and as a further example of the power multi-targeted DMRG, we show here that full DMRG simulations of a device with similar circuit parameters to those reported in Ref. [10] predicts the pure-dephasing coherence times around $\Phi_{\rm ext} = \Phi_0/2$ to be dominated by the combined effect of charge noise and CQPS.

To estimate the coherence time, we follow closely Ref. [10] which assumes that the variables n_{g_i} are independent and randomly distributed. The probability density function of $\mathrm{Re}[E_S]$ can then be approximated by a Gaussian distribution with zero mean and standard deviation $\sqrt{N_J/2}\,\epsilon_0$ [10]. Following this expression, the effective broadening of the qubit transition scales as $\sqrt{N_J}$, something which translates to the pure-dephasing coherence time $1/T_{\varphi,\mathrm{CQPS}} = |\Delta\omega_{01}|/4\sqrt{N_J}$ [10, 27]. To identify the domimant dephasing mechanism, we compare this timescale to that expected for $1/f$ flux noise by deriving in appendix C a multilevel pure-dephasing master equation of the form

$$\begin{aligned}\partial_t\rho = &\sum_k \Gamma_\varphi^{kk}\,\mathscr{D}[\sigma_{kk},\sigma_{kk}]\,\rho \\ &+ \sum_{k>l}\Gamma_\varphi^{kl}\left(\mathscr{D}[\sigma_{kk},\sigma_{ll}]\,\rho + \mathscr{D}[\sigma_{ll},\sigma_{kk}]\,\rho\right),\end{aligned} \tag{7}$$

where Γ_φ^{kl} are time-dependent pure-dephasing rates proportional to the $1/f$ flux noise amplitude, $\sigma_{kl} = |\psi_k\rangle\langle\psi_l|$, and $\mathscr{D}[x,y]\,\rho = x\rho y^\dagger - \{y^\dagger x,\rho\}/2$ is a generalized dissipator operator. By integrating Eq. (7) in the qubit subspace, we define the flux-noise coherence time $T_{\varphi,\mathrm{Flux}}$ by the implicit equation $\rho_{01}(T_{\varphi,\mathrm{Flux}})/\rho_{01}(0) = 1/e$ that we solve numerically (see appendix C).

First, Fig. 4 (a) shows the energy spectrum versus the external flux, results that should be compared to those of Ref. [10]. In contrast to the results in Fig. 2 (a), the DMRG and single-mode simulations for the parameters of Ref. [10] differ more noticeably due to the low plasma frequency of the array junctions ($\omega_p/2\pi = 12.5\,\mathrm{GHz}$) around which ~ 40 other additional circuit modes lie [29] (see also appendix B 3). This makes any single-mode approximation invalid, except at low frequencies. Fig. 4 (b) shows the estimation of the device's coherence times using only the results from DMRG as a function of the external flux and close to the bias point $\Phi_{\rm ext} = \Phi_0/2$. We find values similar to the experimental observation (see Fig. 4 in Ref. [10]), thus providing further numerical evidence of the combined effects of charge noise and CQPS. In the flux range that is presented, this mechanism dominates over flux noise and result in sub-μs coherence times for the device parameters of Ref. [10].

Combined, the results in Fig. 3 and Fig. 4 illustrate the rich interplay between charge noise and CQPS in the fluxonium architecture. Added to the improved simulation capabilities provided by DMRG, these findings motivate a systematic experimental study to understand these effects to a greater extent.

V. CONCLUSIONS AND OUTLOOK

We have developed a multi-targeted DMRG algorithm allowing us to simulate large-scale superconducting quantum devices. As an example, we have applied this numerical technique to the fluxonium qubit. To assert the

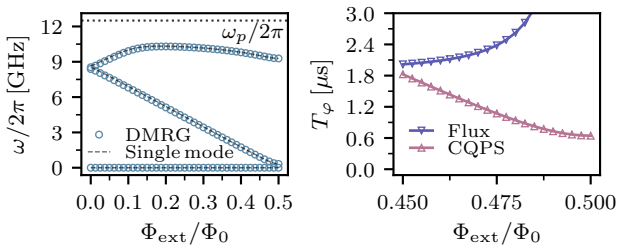

FIG. 4. Coherence time of a 40-junction superinductance fluxonium qubit. (a) Energy spectrum according to DMRG and single-mode estimations as a function of $\Phi_{\rm ext}$. The black dotted line is the plasma frequency. (b) Pure-dephasing coherence times for flux and charge (CQPS) noise as obtained from DMRG. Parameters: $C_{J_{\rm b}} = 7.5\,{\rm fF}$, $E_{J_{\rm b}}/h = 8.9\,{\rm GHz}$, $z = 0.09$, $\omega_p/2\pi = 12.5$ and $C_0 = 0$, extracted from Ref. [10].

validity of the DMRG simulations and to help in the interpretation of the numerical results, we have developed a detailed single-mode theory for this qubit. Finally, we employed DMRG to investigate the combined effect of charge noise and coherent quantum phase slips in the fluxonium qubit, confirming the theoretical model introduced in Ref. [10] and reproducing some of the experimental findings of that work.

Having access to the expectation values of local and of n-body operators makes it possible to investigate the many-body properties of superconducting quantum circuits. This could help, for instance, in finding new approaches to encode quantum information nonlocaly in protected subspaces by exploiting entanglement in these systems. Moreover, local information of large-scale superconducting quantum circuits may be used to evaluate the impact of dissipation channels and circuit-element disorder. This might also lead to a more detailed understanding of dissipation and decoherence mechanisms. Our numerical approach also has the potential to enable advancements in several areas of superconducting-qubit research. In particular, we envision future applications to the analysis of multi-qubit devices and the design of scalable superconducting-qubit architectures.

ACKNOWLEDGMENTS

We thank J. Cohen, A. Gyenis, C. Leroux, Z. Minev and A. Petrescu for stimulating discussions. T.E.B. thanks the support of the Postdoctoral Fellowship from Institut quantique and support from Institut Transdisciplinaire d'Information Quantique (INTRIQ). This work was undertaken in part thanks to funding from NSERC, the Canada First Research Excellence Fund and the ARO grant No. W911NF-17-S-0008.

Appendix A: Fluxonium Circuit Hamiltonian

1. Hamiltonian without gate voltages

We derive the circuit Hamiltonian used in the DMRG calculations presented in the main text. We consider a fluxonium device where a black-sheep Josephson junction with capacitance $C_{J_{\rm b}}$ (including both shunt and junction capacitances) and Josephson energy $E_{J_{\rm b}}$ is shunted by a superinductance made of N_J junctions, each of capacitance C_{J_i} and energy E_{J_i} with $i \in [1, N_J]$. We moreover assume that each circuit node of the superinductance is connected to ground by a stray capacitance C_{0_i}. The $N_J + 1$ node flux (phase) variables of the circuit are denoted by Φ_i ($\phi_i = \Phi_i/\varphi_0$), where $\varphi_0 = \hbar/2e$ is the reduced quantum of magnetic flux and $i \in [0, N_J]$. The circuit Lagrangian can then be written as [3]

$$\begin{aligned} L(\mathbf{\Phi}, \dot{\mathbf{\Phi}}) = &\frac{C_{J_{\rm b}}}{2}(\dot\Phi_{N_J} - \dot\Phi_0)^2 + \sum_{i=1}^{N_J} \frac{C_{Ji}}{2}(\dot\Phi_i - \dot\Phi_{i-1})^2 \\ &+ \sum_{i=0}^{N_J} \frac{C_{0_i}}{2}\dot\Phi_i^2 + \sum_{i=1}^{N_J} E_{J_i}\cos(\phi_i - \phi_{i-1}) \\ &+ E_{J_{\rm b}}\cos\Big(\phi_{N_J} - \phi_0 + \frac{\Phi_{\rm ext}}{\varphi_0}\Big), \end{aligned} \tag{A1}$$

where $\Phi_{\rm ext}$ is the flux through the circuit loop. A more convenient basis is defined by the phase variables $\theta_i = \phi_{i-1} - \phi_i$ for $i \in [1, N_J]$ and the cyclic mode $\sigma = \sum_{i=0}^{N_J} \phi_i$. The relation between the new modes and the original node variables can be expressed concisely by $\boldsymbol{\theta} = \mathbf{R}\cdot\boldsymbol{\phi}$, where $\boldsymbol{\theta} = (\theta_1, \ldots, \theta_{N_J}, \sigma)^T$, $\boldsymbol{\phi} = (\phi_0, \ldots, \phi_{N_J})^T$ and $\mathbf{R}$ is the $N_J + 1 \times N_J + 1$ rotation matrix

$$\mathbf{R} = \begin{pmatrix} 1 & -1 & 0 & \cdots & \cdots & \cdots & 0 \\ 0 & 1 & -1 & 0 & \cdots & \cdots & 0 \\ 0 & 0 & 1 & -1 & 0 & \cdots & 0 \\ \vdots & \vdots & \ddots & \ddots & \ddots & \ddots & \vdots \\ 0 & \cdots & \cdots & 0 & 1 & -1 & 0 \\ 0 & \cdots & \cdots & \cdots & 0 & 1 & -1 \\ 1 & 1 & 1 & \cdots & \cdots & 1 & 1 \end{pmatrix}. \tag{A2}$$

Under this change of coordinates, Eq. (A1) becomes

$$\begin{aligned} L(\mathbf{\Theta}, \dot{\mathbf{\Theta}}) = &\dot\Theta^T \cdot \frac{\boldsymbol{C}_\Theta}{2} \cdot \dot\Theta + \sum_{i=1}^{N_J} E_{J_i}\cos\theta_i \\ &+ E_{J_{\rm b}}\cos\left(\sum_{i=1}^{N_J}\theta_i + \frac{\Phi_{\rm ext}}{\varphi_0}\right), \end{aligned} \tag{A3}$$

where $\boldsymbol{C}_\Theta = (\mathbf{R}^{-1})^T \cdot \boldsymbol{C}_\Phi \cdot \mathbf{R}^{-1}$ is defined in terms of the capacitance matrix $[\boldsymbol{C}_\Phi]_{ij} = \partial^2 L(\mathbf{\Phi}, \dot{\mathbf{\Phi}})/\partial\dot\Phi_i\partial\dot\Phi_j$, for $i, j \in [0, N_J + 1]$. Note that the σ mode does not enter in the potential energy.

After a Legendre transformation, we arrive at the Hamiltonian

$$H = \boldsymbol{q}_\Theta^T \cdot \frac{\boldsymbol{C}_\Theta^{-1}}{2} \cdot \boldsymbol{q}_\Theta - \sum_{i=1}^{N_J} E_{J_i} \cos\theta_i - E_{J_\mathrm{b}} \cos\left(\sum_{i=1}^{N_J} \theta_i + \frac{\Phi_\mathrm{ext}}{\varphi_0}\right), \tag{A4}$$

where $\boldsymbol{q}_\Theta \equiv \partial L(\boldsymbol{\Theta}, \dot{\boldsymbol{\Theta}})/\partial\dot{\boldsymbol{\Theta}} = \boldsymbol{C}_\Theta \cdot \dot{\boldsymbol{\Theta}}$ is a vector of conjugate charge operators. In the absence of circuit-element disorder, the σ mode decouples from the θ_i modes. In the presence of disorder, these modes are coupled by capacitive terms which, for small disorder, can in principle be treated as a perturbation. Here, since for small disorder the frequency of the mode associated to σ is very large, we simply neglect this contribution. The inverse capacitance matrix can thus be truncated to include only the θ_i modes, i.e. $\boldsymbol{C}_\Theta^{-1} \to \boldsymbol{C}_\Theta^{-1}[0 : N_J - 1, 0 : N_J - 1]$, reducing Eq. (A4) to an Hamiltonian of N_J interacting degrees of freedom. Note that the resulting pairwise θ_i-θ_j capacitive coupling has all-to-all connectivity and exhibits no particular structure in the θ_i basis.

2. Accounting for charge dispersion

To model charge dispersion, we assume that each of the $N_J + 1$ circuit islands is coupled to a local fictitious voltage source V_i for $i \in [0, N_J]$. The associated terms in the Lagrangian can generically be written asb $\sum_{i=0}^{N_J}(C_{g_i}/2)(\dot{\Phi}_i - V_i)^2$, where C_{g_i} is a gate capacitance for the ith circuit node. Equivalently, this can be expressed as

$$L_g(\boldsymbol{\Phi}, \dot{\boldsymbol{\Phi}}) = -\dot{\boldsymbol{\Phi}}^T \cdot \boldsymbol{C}_g \cdot \boldsymbol{V}, \tag{A5}$$

where $\boldsymbol{C}_g = \mathrm{diag}(C_{g_0}, C_{g_1}, \ldots, C_{g_{N_J+1}})$ and $\boldsymbol{V} = (V_0, V_1, \ldots, V_{N_J+1})^T$. In addition to Eq. (A5), the capacitance matrix of the circuit is modified to account for the gate capacitances as $\boldsymbol{C}_\Phi \to \widetilde{\boldsymbol{C}}_\Phi = \boldsymbol{C}_\Phi + \boldsymbol{C}_g$.

Defining $\boldsymbol{d}_\Phi = \boldsymbol{C}_g \cdot \boldsymbol{V}$, the conjugate charge operators are given by

$$\boldsymbol{q}_\Theta = \widetilde{\boldsymbol{C}}_\Theta \cdot \dot{\boldsymbol{\Theta}} - \boldsymbol{d}_\Theta, \tag{A6}$$

where $\widetilde{\boldsymbol{C}}_\Theta = (\mathbf{R}^{-1})^T \cdot \widetilde{\boldsymbol{C}}_\Phi \cdot \mathbf{R}^{-1}$ and $\boldsymbol{d}_\Theta = (\mathbf{R}^{-1})^T \cdot \boldsymbol{d}_\Phi$. Note that due to charge conservation $[\boldsymbol{d}_\Theta]_{N_J+1} = \sum_{i=0}^{N_J}[\boldsymbol{d}_\Phi]_i/(N_J + 1)$ is a constant of motion, and only N_J of the $N_J + 1$ offset charges are strictly independent.

Using these expressions, the Hamiltonian finally takes the form

$$H = (\boldsymbol{q}_\Theta + \boldsymbol{d}_\Theta)^T \cdot \frac{\widetilde{\boldsymbol{C}}_\Theta^{-1}}{2} \cdot (\boldsymbol{q}_\Theta + \boldsymbol{d}_\Theta) - \sum_{i=1}^{N_J} E_{J_i} \cos\theta_i - E_{J_\mathrm{b}} \cos\left(\sum_{i=1}^{N_J} \theta_i + \frac{\Phi_\mathrm{ext}}{\varphi_0}\right). \tag{A7}$$

Omitting irrelevant constants ands the cyclic mode σ from the kinetic energy the above expression simplifies to

$$H = \sum_{i=1}^{N_J}\left[\frac{[\widetilde{\boldsymbol{C}}_\Theta^{-1}]_{ii}}{2}(q_i - q_{g_i})^2 - E_{J_i}\cos\theta_i\right] + \sum_{j>i}^{N_J}[\widetilde{\boldsymbol{C}}_\Theta^{-1}]_{ij} q_i q_j - E_{J_\mathrm{b}} \cos\left(\sum_{i=1}^{N_J}\theta_i + \frac{\Phi_\mathrm{ext}}{\varphi_0}\right), \tag{A8}$$

where $q_{g_i} = [\widetilde{\boldsymbol{C}}_\Theta^{-1} \cdot \boldsymbol{d}_\Theta]_i/2[\widetilde{\boldsymbol{C}}_\Theta^{-1}]_{ii}$ for $i \in [1, N_J]$ are effective offset charges in the θ_i basis and $q_i = [q_\Theta]_i$. This Hamiltonian is equivalent to Eq. (3). Each of the bracketed terms in Eq. (A8) define a site Hamiltonian, while the remaining terms correspond to both linear and nonlinear all-to-all interactions between the sites. Since the sites' noninteracting eigenstates form a complete basis and are $2e$-periodic in the offset charge and invariant under $q_{g_i} \to -q_{g_i}$, it is enough to restrict the offset charges to the range $q_{g_i} \in [0, e]$.

Appendix B: Effective models for the fluxonium qubit

1. Effective single-mode Hamiltonian

We derive an effective single-mode Hamiltonian for the fluxonium qubit that captures all circuit details. Because it is simple yet accurate, this model is used in the main text to assert the validity of the DMRG simulations in appropriate parameter ranges.

To obtain this effective model, we first consider a change of coordinates in which adiabatically eliminating the circuit modes other than the superinductance mode $\phi = \sum_{i=1}^{N_J}\theta_i$ is simple. To find this appropriate change of coordinates, we reverse engineer the following Ansatz defining the new change of basis

$$\mathbf{R}^{(1)} = \begin{pmatrix} 1 - \sum_{k=1}^{N_J-1} a_k^{(1)} & 1 + a_1^{(1)} & \cdots & 1 + a_{N_J-1}^{(1)} & 0 \\ -1 & 1 & 0 & \cdots & 0 \\ \vdots & 0 & \ddots & \ddots & \vdots \\ -1 & \vdots & \ddots & 1 & 0 \\ 0 & 0 & 0 & 0 & 1 \end{pmatrix}, \tag{B1}$$

where the constants $\{a_k^{(1)}\}$ are defined by

$$a_k^{(1)} = \frac{\sum_{i,j=0}^{N_J-1}(N_J[\boldsymbol{C}_\Theta]_{ik}\delta_{jk} - [\boldsymbol{C}_\Theta]_{ij})}{\sum_{i,j=0}^{N_J-1}[\boldsymbol{C}_\Theta]_{ij}}, \tag{B2}$$

for $k \in [1, N_J - 1]$. Note that Eq. (B1) acts as identity in the subspace of the σ mode and none of the σ-mode components of the capacitance matrix $\boldsymbol{C}_\Theta$ are included in Eq. (B2). The role of $\mathbf{R}^{(1)}$ is to capacitively decouple

a superinductance-like mode of the form

$$\phi^{(1)} = \phi + \sum_{k=1}^{N_J-1} a_k^{(1)}(\theta_k - \theta_1), \tag{B3}$$

from all other circuit modes while leaving the σ mode invariant. Indeed, the new capacitance matrix

$$\boldsymbol{C}_X^{(1)} = [(\mathbf{R}^{(1)})^{-1}]^T \cdot \boldsymbol{C}_X^{(0)} \cdot (\mathbf{R}^{(1)})^{-1}, \tag{B4}$$

with $\boldsymbol{C}_X^{(0)} = \boldsymbol{C}_\Theta$ is block-diagonal in the absence of disorder. The first block has dimension 1×1 and corresponds to the $\phi^{(1)}$ mode; the second block has dimension $(N_J-1)\times(N_J-1)$ and involves all circuit modes except $\phi^{(1)}$ and σ; the last 1×1 block corresponds to the σ mode. By design, the first and second blocks of Eq. (B4) are exactly decoupled from each other, even in the presence of circuit-element disorder. In this case the first two blocks can be weakly coupled to the third block. Because the σ as a very high frequency for standard fluxonium circuit parameters, we neglect this coupling.

While the transformation Eq. (B1) isolates the most relevant circuit mode, we iterate recursively this transformation to decouple all remaining circuit modes in the capacitive interaction. Doing this will allow us to trace out such degrees of freedom. We proceed by defining an additional set of rotation matrices $\{\mathbf{R}^{(n)}\}$, for $n \in [2, N_J-1]$, with the general form

$$\mathbf{R}^{(n)} = \begin{pmatrix} 1 & 0 & 0 & \cdots & \cdots & \cdots & \cdots & \cdots & \cdots & 0 \\ 0 & 1 & 0 & \cdots & \cdots & \cdots & \cdots & \cdots & \cdots & 0 \\ \vdots & \ddots & \ddots & \ddots & \cdots & \cdots & \cdots & \cdots & \cdots & 0 \\ \vdots & \vdots & 0 & 1 & 0 & \cdots & \cdots & \cdots & \cdots & 0 \\ \vdots & \vdots & \vdots & 0 & 1-\sum_{k=n}^{N_J-1} a_k^{(n)} & 1+a_n^{(n)} & 1+a_{n+1}^{(n)} & \cdots & 1+a_{N_J-1}^{(n)} & 0 \\ \vdots & \vdots & \vdots & \vdots & -1 & 1 & 0 & \cdots & 0 & \vdots \\ \vdots & \vdots & \vdots & \vdots & -1 & 0 & 1 & 0 & 0 & \vdots \\ \vdots & \vdots & \vdots & \vdots & \vdots & \vdots & \ddots & \ddots & \ddots & \vdots \\ \vdots & \vdots & \vdots & \vdots & -1 & 0 & \cdots & 0 & 1 & 0 \\ 0 & 0 & 0 & 0 & 0 & \cdots & \cdots & \cdots & 0 & 1 \end{pmatrix}. \tag{B5}$$

Similarly to $\mathbf{R}^{(1)}$, the matrix $\mathbf{R}^{(n)}$ is composed by a $n\times n$ identity block for the modes labeled by $k < n$; a $(N_J-n+1)\times(N_J-n+1)$ block for modes labeled by $k \in [n, N_J-1]$; and a 1×1 block for the σ mode. The coefficients $\{a_k^{(n)}\}$ are defined as

$$a_k^{(n)} = \frac{\sum_{i,j=n}^{N_J-1}\{(N_J-1+n)[\boldsymbol{C}_X^{(n-1)}]_{ik}\delta_{jk} - [\boldsymbol{C}_X^{(n-1)}]_{ij}\}}{\sum_{i,j=n}^{N_J-1}[\boldsymbol{C}_X^{(n-1)}]_{ij}}, \tag{B6}$$

which is a direct generalization of Eq. (B2).

The transformations $\mathbf{R}^{(n<N_J-1)}$ are designed to each decouple a single mode, while $\mathbf{R}^{(N_J-1)}$ decouples the last two modes, $n = N_J-1$ and $n = N_J$. Therefore, these N_J-1 successive transformations exactly diagonalize the upper $N_J \times N_J$ block of the capacitance matrix $\boldsymbol{C}_\Theta$ that does not include the σ mode. We can then invert these transformations arriving at the expression

$$\theta_i = \frac{\phi^{(1)}}{N_J} + \sum_{n=2}^{N_J} v_{ni}\phi^{(n)}, \tag{B7}$$

where the coefficient v_{ni} quantifies how much the $\phi^{(n)}$ mode couples to the ith Josephson junction of the array. Using Eq. (B7) and the definition $\phi = \sum_{i=1}^{N_J}\theta_i$ we moreover have

$$\phi = \phi^{(1)} + \sum_{n=2}^{N_J} \mathscr{V}_n\phi^{(n)}, \tag{B8}$$

where $\mathscr{V}_n = \sum_{i=1}^{N_J} v_{ni}$. If $C_0 = 0$, it follows that $\mathscr{V}_n = 0$ for $n \in [2, N_J]$, and $\phi^{(1)} \equiv \phi$ is the only mode that couples to the black-sheep junction. In other case, all modes are weakly coupled to the black-sheep junction, but this undesired coupling can be easily taken into account as we show in the following.

The relations Eq. (B7) and Eq. (B8) are now incorporated back to the potential energy of Eq. (A4). In order to trace out the unwanted degrees of freedom, we write the operator $\phi^{(n)}$ for $n > 1$ in terms of the harmonic-oscillator ladder operators as $\phi^{(n)} = \sqrt{\pi z_n}(a_n + a_n^\dagger)$. Here, $z_n = \sqrt{L_n/C_n}/R_Q$ is the effective reduced impedance of the nth mode, given in terms of the effective inductance L_n and capacitance C_n. While C_n can be readout directly from the block-diagonal capacitance matrix, the reduced inductance is determined by the product $L_n^{-1} = \boldsymbol{X}_n^T \cdot (\boldsymbol{M}^{-1})^T \cdot \boldsymbol{L}^{-1} \cdot \boldsymbol{M}^{-1} \cdot \boldsymbol{X}_n$, where $\boldsymbol{X}^n$ is the mode vector associated to $\phi^{(n)}$ and

$\boldsymbol{M} = (\prod_{n=1}^{N_J-1} \boldsymbol{R}^{(n)})^T \cdot \boldsymbol{R}$ is a matrix that reverses the multiple changes of basis. The trace can then be performed straightforwardly, noticing that

$$e^{ix\phi^{(n)}} = e^{-\pi x^2 z_n/2} e^{ix\sqrt{\pi z_n} a_n^\dagger} e^{ix\sqrt{\pi z_n} a_n}, \tag{B9}$$

and thus $\mathrm{tr}_n[e^{ix\phi^{(n)}}\rho] = e^{-\pi x^2 z_n/2}$ where we assume that the nth mode remains in its noninteracting vacuum state. Following to Eq. (B7) and Eq. (B8), we approximate

$$\cos\theta_i \simeq x_i \cos[\phi^{(1)}/N_J], \tag{B10}$$

where $x_i = \prod_{n=2}^{N_J} e^{-\pi v_{ni}^2 z_n/2}$, and

$$\cos(\phi + \varphi_{\mathrm{ext}}) \simeq x_{\mathrm{b}} \cos[\phi^{(1)} + \varphi_{\mathrm{ext}}], \tag{B11}$$

with $x_{\mathrm{b}} = \prod_{n=2}^{N_J} e^{-\pi \mathscr{V}_n^2 z_n/2}$. Thus, by renaming $\phi^{(1)} \to \phi'$, we arrive at the effective single-mode Hamiltonian

$$\begin{aligned} H = {} & 4E_C n'^2 - \sum_{i=1}^{N_J} x_i E_{J_i} \cos(\phi'/N_J) \\ & - x_{\mathrm{b}} E_{J_{\mathrm{b}}} \cos\Big(\phi' + \frac{\Phi_{\mathrm{ext}}}{\varphi_0}\Big), \end{aligned} \tag{B12}$$

where E_C is taken to be the charging energy $E_C = e^2/2[\boldsymbol{C}_X^{(1)}]_{00}$ of the ϕ' mode and $[\phi', n'] = i$. Note that Eq. (B12) is equivalent to Eq. (4) of the main text. Up to corrections of order N_J^{-3}, Eq. (B12) reduces to

$$H = 4E_C n'^2 + \frac{E_L}{2}\phi'^2 - E_J \cos\Big(\phi' + \frac{\Phi_{\mathrm{ext}}}{\varphi_0}\Big), \tag{B13}$$

where $E_L = \sum_{i=1}^{N_J} x_i E_{J_i}/N_J^2$ and $E_J = x_{\mathrm{b}} E_{J_{\mathrm{b}}}$ are the effective inductive and Josephson-junction energies. Eq. (B13) corresponds to the original fluxonium-qubit model in Ref. [5]. Here, however, all energies entering Eq. (B13) are specified by a function of the circuit-element parameters.

2. Qualitative regimes of the fluxonium qubit

Despite the apparent simplicity of the effective fluxonium Hamiltonian Eq. (B13), its eigenstates can display a rich structure that depends on the parameter regime. For a systematic analysis, it is useful to redefine the parameters in Eq. (B13) in terms of the effective black-sheep junction plasma frequency $\omega_p^{\mathrm{b}} = \sqrt{8E_J E_C}/\hbar$ and the effective (reduced) impedance $z_{\mathrm{b}} = \pi^{-1}\sqrt{2E_C/E_J}$. The potential energy of Eq. (B13) has a quadratic component given by the inductive term $E_L\phi^{2\prime}/2$ modulated by the cosine potential of the black-sheep junction and the external flux. Qualitatively, $\hbar\omega_p^{\mathrm{b}}$ defines the characteristic energy of intra-well excitations within a given well defined by the Josephson potential, while z_{b} is a measure of the tunneling energy between such wells.

Figure 5 (a-c) shows the wavefunctions of the fluxonium qubit for different values of z_{b}, taking $\omega_p^{\mathrm{b}}/2\pi = 10\,\mathrm{GHz}$ and $E_L/h = 0.2\,\mathrm{GHz}$ constants and for $\Phi_{\mathrm{ext}}/\Phi_0 = 0.35$. Panel (a) corresponds to the case of a small effective impedance with $z_{\mathrm{b}} = 0.1$, in which tunneling between states localized in different wells is exponentially suppressed in $1/z_{\mathrm{b}}$ (see below). In this regime, the eigenstates of the fluxonium Hamiltonian are therefore localized within the deep potential wells of the potential-energy landscape. Excitations localized in a given potential well are approximately separated by the energy difference $\hbar\omega_p^{\mathrm{b}}$. For this reason, a transition between two of such states is called plasmon (or intra-well) transition. Indistinctly, the excited states belonging to a given potential well are simply called plasmon states. On the other hand, a transition between two states that belong to different potential wells is called fluxon (or inter-well) transition, while the lowest energy state of a given potential well is called fluxon state. Since the relative position between potential wells shifts significantly with Φ_{ext}, fluxon transitions are highly sensitive to the external flux. In contrast, plasmon transitions are flux-insensitive. Since the low-impedance limit requires the fluxonium mode ϕ' to have a large effective capacitance (or "mass"), this regime is referred to as "heavy-fluxonium" regime [6, 21, 29].

Figure 5 (b) shows an intermediate value of $z_{\mathrm{b}} = 0.3$, where the energy barrier ($\propto E_J$) between the potential wells due to the black-sheep junction has been reduced with respect to panel (a). Moreover, the effective capacitive energy E_C has been increased, such that quantum tunneling between states localized in two neighboring potential wells is now non-negligible. This favors states that are delocalized across multiple potential wells and are the result of significant hybridization between plasmon and fluxon excitations. This intermediate regime for z_{b} corresponds to the original fluxonium-qubit regime [5, 27].

If the impedance of the black-sheep junction z_{b} is increased further, the fluxonium wavefunctions can spread over many potential wells thanks to a lower E_J and a larger E_C. This situation is illustrated in Fig. 5 (c) where the distinction between plasmon and fluxon transitions is no longer useful and the spectrum is mostly determined by the harmonic part of Eq. (B13). The Josephson potential acts as a perturbation leading to a weak flux sensitivity of the qubit transitions. Since the effective capacitance of the fluxonium mode needs to be lowered in order to make z_{b} larger, this is known as the "light-fluxonium" regime [44].

With the purpose of making the comparison above more precise, we now analyze the energy spectrum of fluxonium devices from the heavy- to the light-fluxonium regimes. The present discussion is straightforward if the intuition developed in the previous paragraphs is leveraged. Fig. 5 (d) shows the result of the diagonalization of Eq. (B13) (light-blue lines) for the configuration of Fig. 5 (a). In this case, the low-frequency spectrum is highly sensitive to the external flux, corresponding to a set of fluxon transitions. For a small z_{b}, the low-frequency spectrum around $\Phi_{\mathrm{ext}}/\Phi_0 = 0.5$ can be modeled by the

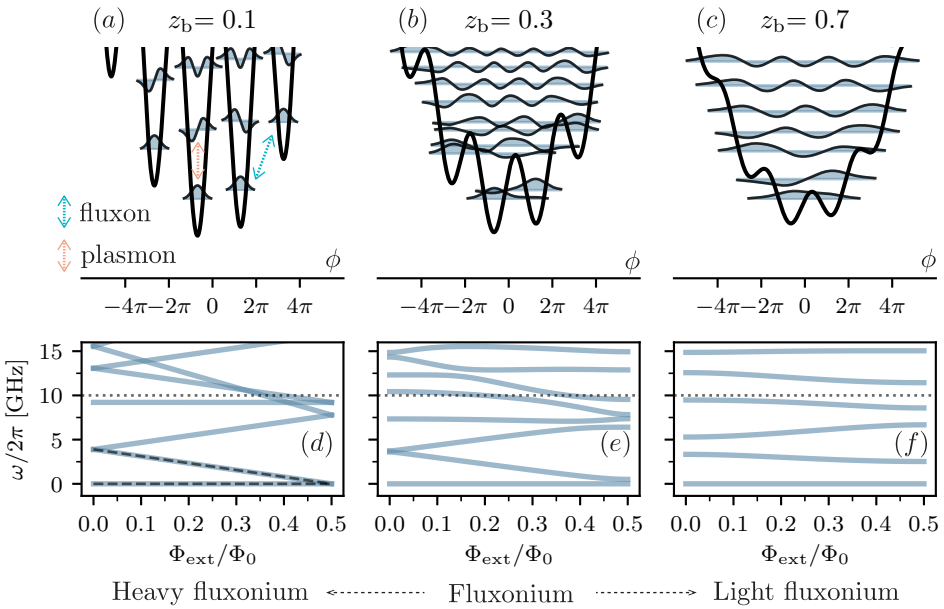

FIG. 5. Qualitative behavior of the eigenstates of the fluxonium qubit Hamiltonian Eq. (B13). $(a-c)$ display the qubit wavefunctions (light-blue lines) within the effective potential (thick black line) for $z_b \in [0.1, 0.3, 0.7]$, respectively. $(d-f)$ show the low-frequency spectrum as a function of Φ_{ext} (light-blue lines) for $z_b \in [0.1, 0.3, 0.7]$, respectively. Black dotted lines correspond to the bare black-sheep junction plasma frequency ω_p^b. Additional parameters: $\omega_p^b/2\pi = 10\,\text{GHz}$ and $E_L/h = 0.2\,\text{GHz}$.

weak coupling of two fluxon-like states $\{|m\rangle, |m+1\rangle\}$ of the form $\langle\phi'|m\rangle \propto z_b^{-1/4} \exp[-(\phi'-\phi_m)^2/4\pi z_b]$, localized around the flux-dependent positions $\{\phi_m\}$ of two nearly degenerate potential wells [48]. Indeed, assuming that $E_L \ll E_J$, the fluxonium Hamiltonian restricted to the subspace $\{|m\rangle, |m+1\rangle\}$ can be approximated by the spin Hamiltonian

$$H = \sum_{m'=\{m,m+1\}} \frac{\bar{E}_L}{2}\left(2\pi m' - 2\pi\frac{\Phi_{ext}}{\Phi_0}\right)^2 |m'\rangle\langle m'| - \frac{\bar{\epsilon}}{2}\Big(|m\rangle\langle m+1| + |m+1\rangle\langle m|\Big). \tag{B14}$$

Here, the effective inductive energy $\bar{E}_L = E_L(1-d^{-1})$ incorporates a first-order correction in $d^{-1} = E_L/E_J \ll 1$, while $\bar{\epsilon} = 8\sqrt{2}\,\hbar\bar{\omega}_p^b \exp(-4/\pi\bar{z}_b)/\pi\sqrt{\bar{z}_b}$ is a tunneling matrix element between the two fluxon states where the effective parameters $\bar{\omega}_p^b = (8\bar{E}_J\bar{E}_C)^{1/2}$ and $\bar{z}_b = \pi^{-1}(2\bar{E}_C/\bar{E}_J)^{1/2}$ are defined in terms of $\bar{E}_J = E_J[1 - \pi^2(1-d^{-1})/4d]$ and $\bar{E}_C = E_C/(1-d^{-1})^2$ [48].

The two-level model in Eq. (B14) predicts a linear dispersion $\propto 1/L$ of the first fluxon transition with the external flux and an gap opening at $\Phi_{ext}/\Phi_0 = 0.5$ due to fluxon tunneling, that is exponentially small in $\bar{z}_b$. The result of the diagonalization of Eq. (B14) for the device in Fig. 5 (a) is show as black dashed lines in Fig. 5 (d). We note that Eq. (B14) can be extended to a multilevel Hamiltonian valid beyond the low-impedance regime [49, 50].

In addition to the fluxon transitions, Fig. 5 (d) reveals the first plasmon transition of the device in Fig. 5 (a). The plasmon transition corresponds to the flux-insensitive eigenvalue around $\omega_p^b/2\pi = 10\,\text{GHz}$. For small z_b, the plasmon transitions result slightly shifted with respect to the bare plasma frequency ω_p^b due to the nonlinearity of the black-sheep junction. For particular values of Φ_{ext}, the frequency of a plasmon excitation coincides with that of a fluxon transitions. In that case, plasmon and fluxon states hybridize leading an exponentially small anticrossing for the current parameters.

As z_b increases, hybridization between plasmon and fluxon states becomes more noticeable. Fig. 5 (e) shows the result for moderate values of z_b corresponding to the case of Fig. 5 (b). Coupling between plasmon a fluxon states is now stronger, as it can be seen from the size of the plasmon-fluxon anticrossing. However, for these parameters, the character of the plasmon and fluxon excitations are preserved, except at accidental degeneracy points. This is no longer true if z_b is made too large, as shown in Fig. 5 (f) for the case in Fig. 5 (c). In this case, plasmon and fluxon state undergo strong hybridization and the distinction between such excitations becomes meaningless. In contrast, the circuit eigenstate are closer to excitations of the harmonic part of Eq. (B13), bounded by the quadratic potential $E_L\phi^{2\prime}/2$. In this limit, the fluxonium eigenstates become insensitive to the external magnetic flux, leading to a very small flux dispersion of the qubit transition. The low-energy spectrum of the device resembles that of a transmon qubit, where the now external flux plays the role of the offset-charge parameter for the transmon [44].

Finally, we note that the qualitative behavior described

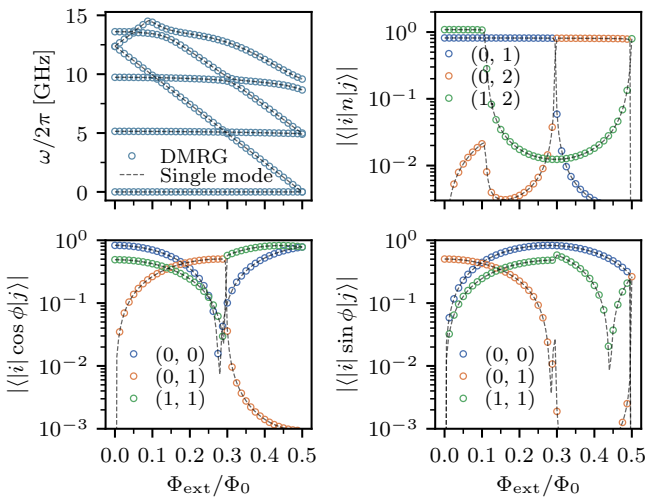

FIG. 6. Comparison of results from Eq. (A4) (DMRG, circles) and Eq. (B12) (Single-mode, black dashed lines) circuit Hamiltonians as a function of $\Phi_{\rm ext}$. Top left panel: Energy spectrum. Top right panel: Matrix elements of the charge n operator for the superinductance mode. Bottom panels: Matrix elements of periodic functions of the phase ϕ operators for the superinductance mode. DMRG parameters: $N_J = 180$, $C_{J_{\rm b}} = 40\,{\rm fF}$, $E_{J_{\rm b}}/h = 7.5\,{\rm GHz}$, $C_J \simeq 32.9\,{\rm fF}$, $L_J \simeq 1.23\,{\rm nH}$ (from $\omega_p/2\pi = 25\,{\rm GHz}$, and $z = 0.03$) and $C_0 = 0$. Single-mode model parameters: $E_C/h \simeq 0.48\,{\rm GHz}$, $E_L/h \simeq 1.27\,{\rm GHz}$ ($L \simeq 129.1\,{\rm nH}$) and $E_J = E_{J_{\rm b}}$.

in this section generalizes to other parameter regimes for $\omega_p^{\rm b}$ and E_L if the flux-tunneling energy is measured relative to the inductive energy. In practice, the value of these parameters may be found typically in the range $\omega_p^{\rm b}/2\pi \in [5, 40]\,{\rm GHz}$ and $E_L/h \in [0.05, 1.0]\,{\rm GHz}$. This completes the qualitative description of possible solutions of the fluxonium-qubit Hamiltonian.

3. Exploration of various parameter regimes

In this section, we provide further numerical evidence of the exceptional agreement between the DMRG simulations and the single-mode theory of appendix B 1. For this purpose, Fig. 6 shows an extension of the results in the main text, including the spectrum of a fluxonium device with $N_J = 180$ array junctions and matrix elements of the phase and charge operators corresponding to the superinductance mode. As in the main body of the paper, the array junctions are modeled as multilevel systems including the first 15 eigenstates of the site Hamiltonian. The remarkable agreement between the DMRG simulation of the full model Eq. (A4) [symbols] and the effective single-mode Hamiltonian Eq. (B12) [dashed lines] serves as a further validation of the DMRG results.

To demonstrate that the agreement between these two approaches extends to all parameter sets for which the array junctions behave as weakly anharmonic oscillators, we compare Eq. (A4) and Eq. (B12) for various circuit design parameters. We stress the accuracy of our single-mode theory by contrasting the result to a purely linear approximation for the junction array. The linear theory is adapted from Ref. [29] where a nanowire superinductance takes the place of the junction array. More precisely, we employ a single-mode approximation of the multimode Hamiltonian of Ref. [29]. The objective of this additional comparison is to highlight the effect of the array-junction nonlinearity which, as shown below, renormalizes the effective superinductance.

In particular, we test circuit Hamiltonians for various black-sheep junction capacitances (Fig. 7) and array-junction impedances (Fig. 8). In both cases, we observe very good agreement between the DMRG calculations and the single-mode theory of appendix B 1. By comparing the results to a single-mode approximation for a purely linear superinductance [29], it becomes clear that the nonlinearilty of the array junctions provides a significant renormalization to the frequency of the fluxon transitions. In fact, since the renormalization of the effective superinductance scales exponentially with the array-junction impedance [see Eq. (B10)], the frequency correction from the junction nonlinearity is more noticeable for larger z.

While, in most cases the single-mode theory of appendix B 1 provides an excellent estimation of the frequency of all fluxonium transitions, its predictive power weakens as z becomes larger (see Fig. 8 for $z \gtrsim 0.08$). We attribute this discrepancy to the unfavorable scaling of the multimode coupling in Eq. (A4) with z. This makes the approximation used to take the trace in Eq. (B10) and Eq. (B11) not completely justified. Although further refinement of the theory of appendix B 1 might be possible, the breakdown of the noninteracting approximation defines a parameter regime where the DMRG estimations are in principle out of reach of a simple theory.

Finally, we point out that our effective single-mode theory works well for systems with any number of junctions. Since all numerical evidence has been so far provided for devices with 10s to 100s of Josephson junctions, Fig. 9 shows an extension of the results, now for fluxonium-like circuits with $N_J < 10$. Some of these systems ($N_J \in [2, 5]$) are small enough to be handled by exact diagonalization of the full model Eq. (A4) that is otherwise diagonalized by the multi-targeted DMRG algorithm for larger systems sizes.

We show that the single-mode approximation Eq. (B12) describes the frequency transitions of these small-scale systems with high accuracy in all cases. We moreover find perfect agreement between the DMRG and exact-diagonalization implementations of Eq. (A4), strengthening the validity of our DMRG algorithm. Note that for these smaller devices the first few excitations already include those from high-frequency modes (around $\omega_p/2\pi = 25\,{\rm GHz}$) which are not described by the single-mode approximation.

These numerical tests provide solid evidence of a suc-

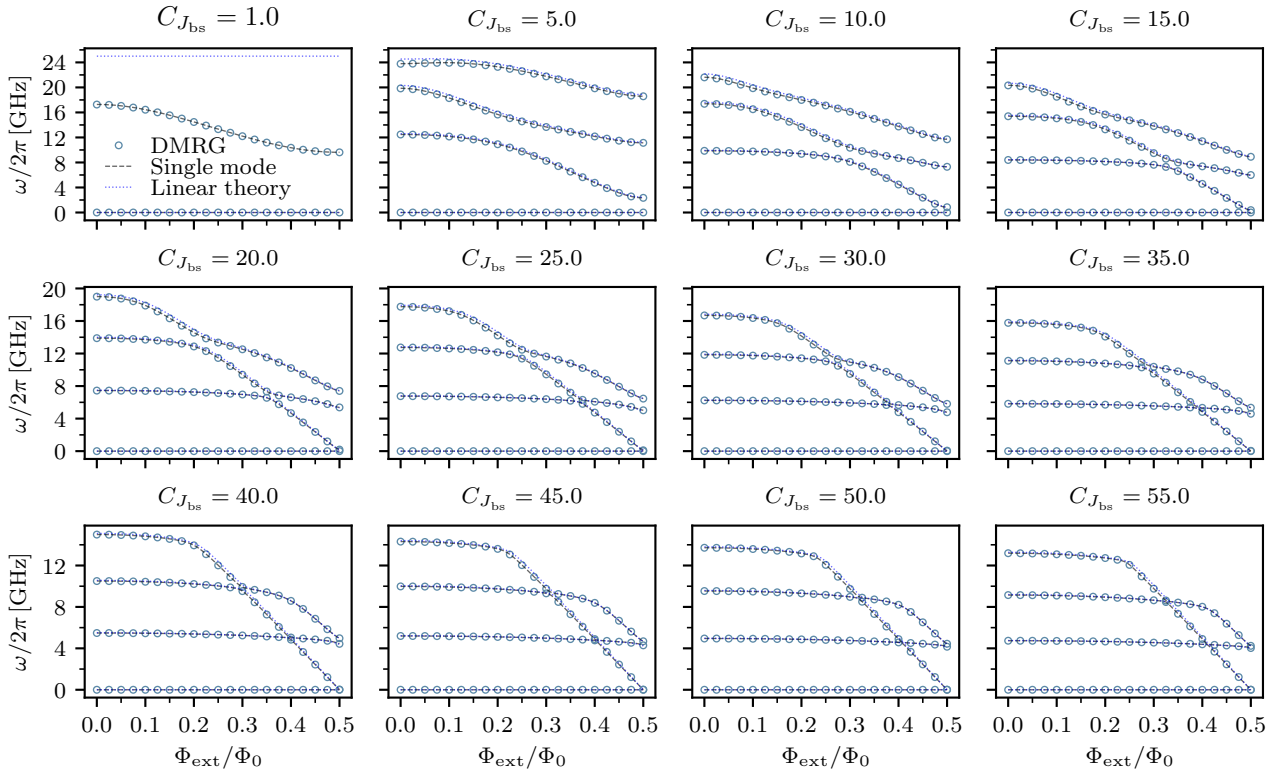

FIG. 7. Comparison of results from Eq. (A4) (DMRG, circles), Eq. (B12) (Single-mode, black dashed lines) and single-mode approximation based on Ref. [29] (Linear theory) Hamiltonians for an 80-junction superinductance fluxonium device with a varying black-sheep capacitance in the range of $C_{J_b} \in [1, 55]$ fF, as a function of Φ_{ext}. Additional parameters: $E_{J_b}/h = 7.5$ GHz, $C_J \simeq 32.9$ fF and $L_J \simeq 1.23$ nH (from $\omega_p/2\pi = 25$ GHz and $z = 0.03$) and $C_0 = 0$.

cessful DMRG implementation of the full fluxonium Hamiltonian, thus complementing the results provided in the main text.

Appendix C: Multilevel pure-dephasing master equation for flux noise

In this section, we derive a master equation describing pure dephasing due to $1/f$ flux noise in the fluxonium qubit. Assuming weak system-bath coupling, the master equation is obtained from the standard integro-differential equation

$$\partial_t \rho(t) = -\frac{1}{\hbar^2}\int_0^t d\tau \, \mathrm{tr}_B[H_{\mathrm{int}}(t), [H_{\mathrm{int}}(t-\tau), \rho(t-\tau)\otimes\rho_B]], \tag{C1}$$

where $\rho(t)\otimes\rho_B$ is the system-bath density matrix, assumed to be separable at all times [51]. Assuming that the bath correlation functions are sharp around $\tau = 0$, $\rho(t-\tau)$ in Eq. (C1) can be approximated by $\rho(t)$ with negligible error. This standard approximation conveniently leads to a Markovian master equation and allows us to extend the integral in Eq. (C1) to infinitely negative times. To capture the Gaussian decay of the density matrix coherences in the presence of $1/f$ noise, this last step is not done here in order.

The system-bath interaction Hamiltonian can be obtained from the fluxonium circuit Hamiltonian assuming that $\Phi_{ext} = \Phi^0_{ext} + \delta\Phi$, where Φ^0_{ext} is the applied flux bias and $\delta\Phi$ represents fluctuations. To first order in $\delta\Phi$, the interaction Hamiltonian can be written as [52]

$$H_{\mathrm{int}} = \frac{\partial H}{\partial \Phi_{ext}} \times \delta\Phi, \tag{C2}$$

where H is the Hamiltonian of the fluxonium qubit and the derivative is evaluated at $\Phi_{ext} = \Phi^0_{ext}$. Expanding Eq. (C1) in the eigenbasis $\{|\psi_k\rangle\}$ of the full circuit, we then arrive at

$$\partial_t \rho = -\frac{E^2_{J_b}}{\hbar^2\varphi_0^2}\int_0^t d\tau \sum_{\substack{k,k'\\ l,l'}} s(k,k')s(l,l')e^{-i(\omega_{ll'}+\omega_{kk'})t + i\omega_{kk'}\tau} \times \mathrm{tr}_B[|\psi_l\rangle\langle\psi_{l'}|\delta\Phi(t), [|\psi_k\rangle\langle\psi_{k'}|\delta\Phi(t-\tau), \rho\otimes\rho_B]], \tag{C3}$$

where we have introduced the matrix elements $s(k,k') = \langle k|\sin(\phi + \Phi_{ext}/\varphi_0)|k'\rangle$, and omitted the explicit time dependence of $\rho(t) \to \rho$. Note that we have rearranged terms in Eq. (C3) such that $\omega_{kk'} > 0$.

Tracing out the bath degrees of freedom leads to the so-called Bloch-Redfield equation [51]. This equation has,

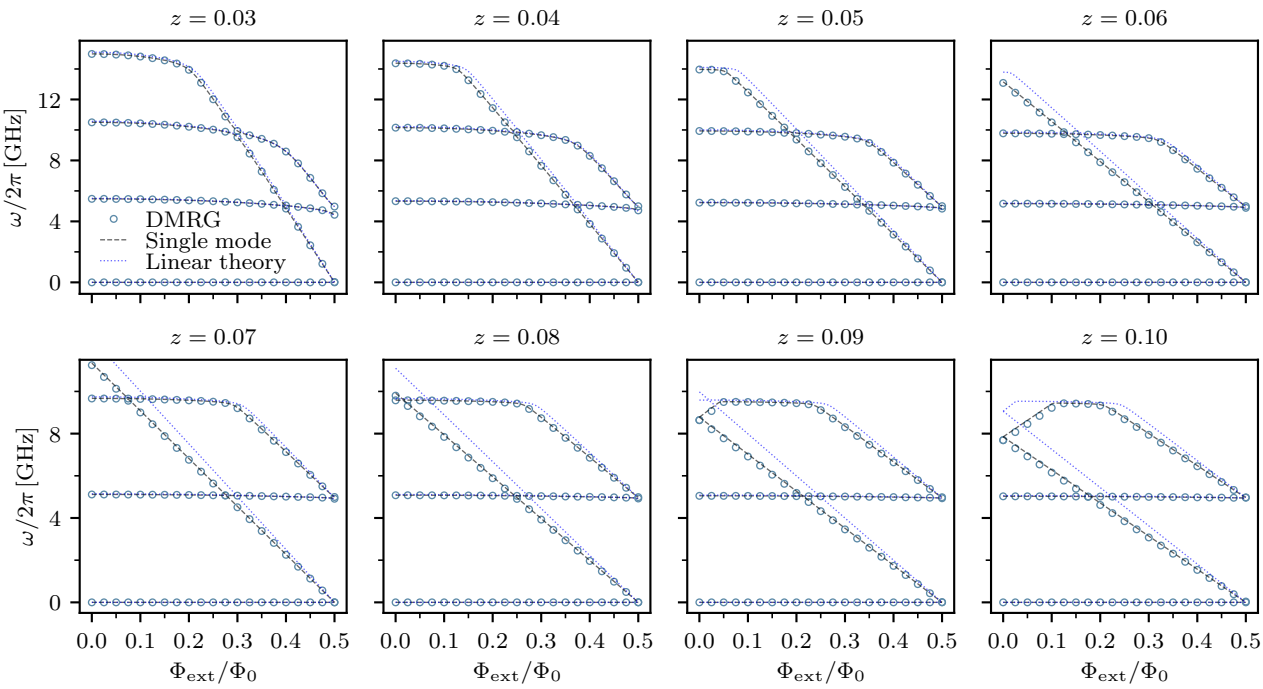

FIG. 8. Comparison of results from Eq. (A4) (DMRG, circles), Eq. (B12) (Single-mode, black dashed lines) and single-mode approximation based on Ref. [29] (Linear theory) Hamiltonians for an 80-junction superinductance fluxonium device with a varying array-junction reduced impedance in the range of $z \in [0.03, 0.10]$, as a function of $\Phi_{\rm ext}$. Additional parameters: $C_{J_b} = 40\,\mathrm{fF}$, $E_{J_b}/h = 7.5\,\mathrm{GHz}$, $\omega_p/2\pi = 25\,\mathrm{GHz}$ and $C_0 = 0$.

however, a number of disadvantages that can potentially lead to unphysical dissipation results. Thus, for practical purposes we use the rotating-wave approximation, discarding terms for which $\omega_{ll'} + \omega_{kk'} \neq 0$. As shown below, this approximation reduces Eq. (C3) to a Lindblad-form master equation. Assuming that the qubit has a set of nondegenerate energy transitions, this approximation is equivalent to the conditions $l = k'$ and $l' = k$ for $\omega_{kk'} \neq 0$, and $l = l'$ for $\omega_{kk'} = 0$. In this way, Eq. (C3) simplifies to

$$\begin{aligned}\partial_t\rho = &-\frac{E_{J_b}^2}{\hbar^2\varphi_0^2}\sum_{k'>k}\int_0^\infty d\tau s_{\uparrow\downarrow}(k,k')e^{i\omega_{kk'}\tau}\mathrm{tr}_B[|\psi_{k'}\rangle\langle\psi_k|\delta\Phi(t),[|\psi_k\rangle\langle\psi_{k'}|\delta\Phi(t-\tau),\rho\otimes\rho_B]]\\ &-\frac{E_{J_b}^2}{\hbar^2\varphi_0^2}\sum_{k'>k}\int_0^\infty d\tau s_{\uparrow\downarrow}(k,k')e^{-i\omega_{kk'}\tau}\mathrm{tr}_B[|\psi_k\rangle\langle\psi_{k'}|\delta\Phi(t),[|\psi_{k'}\rangle\langle\psi_k|\delta\Phi(t-\tau),\rho\otimes\rho_B]]\\ &-\frac{E_{J_b}^2}{\hbar^2\varphi_0^2}\sum_{k,l}\int_0^\infty d\tau s_{\varphi}(k,l)\mathrm{tr}_B[|\psi_l\rangle\langle\psi_l|\delta\Phi(t),[|\psi_k\rangle\langle\psi_k|\delta\Phi(t-\tau),\rho\otimes\rho_B]],\end{aligned} \tag{C4}$$

where $s_{\uparrow\downarrow}(k,k') = |\langle k|\sin(\phi + \Phi_{\rm ext}/\varphi_0)|k'\rangle|^2$ and $s_\varphi(k,l) = \langle k|\sin(\phi+\Phi_{\rm ext}/\varphi_0)|k\rangle\langle l|\sin(\phi+\Phi_{\rm ext}/\varphi_0)|l\rangle$.

We now assume that $\delta\Phi(t)$ can be modeled as a (real) stationary random process. This assumption is motivated by physical models of bistable two-level-system defects that are known to produce noise of type $1/f$. Furthermore, we make the usual assumption that the weight of the $1/f$ noise spectral density is negligible at the qubit transition frequencies such that it does not significantly contribute to the device's T_1 time. The pure-dephasing master equation is therefore derived from the third line of Eq. (C4), i.e.,

$$\begin{aligned}\partial_t\rho = &-\frac{E_{J_b}^2}{\hbar^2\varphi_0^2}\sum_{k,l}\int_0^\infty d\tau s_\varphi(k,l)\\ &\times\mathrm{tr}_B[|\psi_l\rangle\langle\psi_l|\delta\Phi(t),[|\psi_k\rangle\langle\psi_k|\delta\Phi(t-\tau),\rho\otimes\rho_B]].\end{aligned} \tag{C5}$$

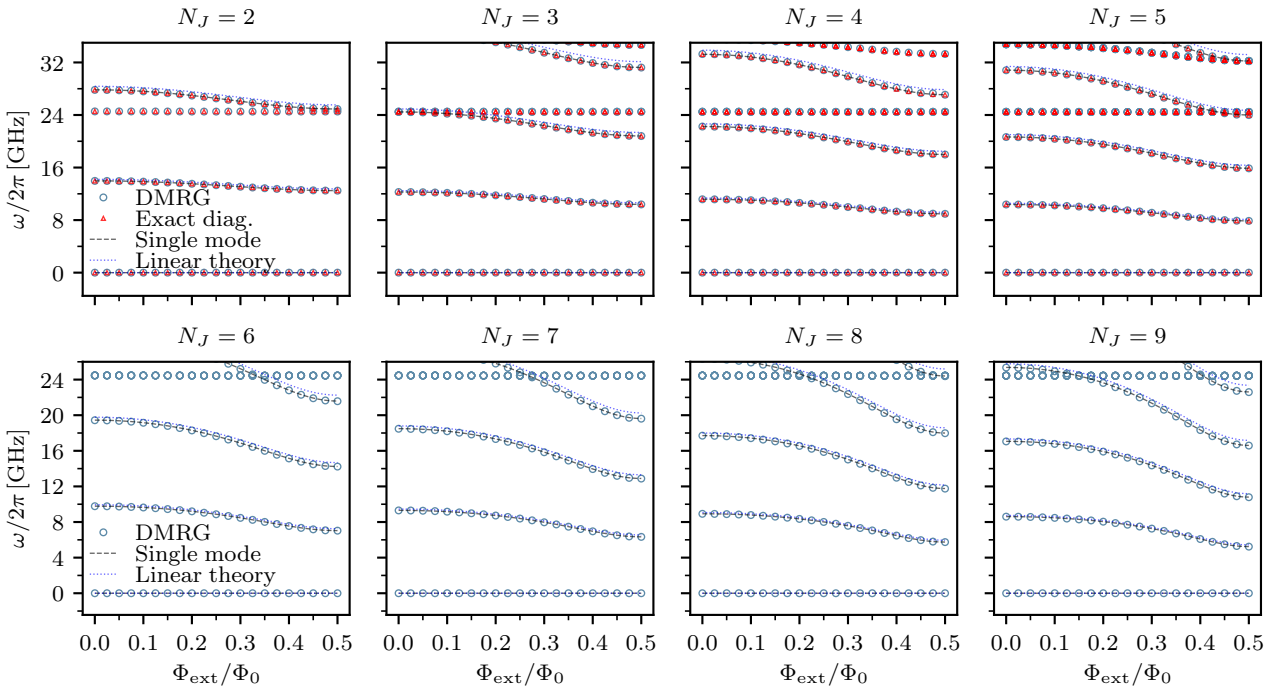

FIG. 9. Test small size on systems ($N_J < 10$). Comparison of results from Eq. (A4): DMRG and exact diagonalization (when possible), Eq. (B12) (Single-mode, black dashed lines) and single-mode approximation based on Ref. [29] (Linear theory). Parameters: $C_{J_b} = 40\,\mathrm{fF}$, $E_{J_b}/h = 7.5\,\mathrm{GHz}$, $C_J \simeq 32.9\,\mathrm{fF}$, $L_J \simeq 1.23\,\mathrm{nH}$ (from $\omega_p/2\pi = 25\,\mathrm{GHz}$, and $z = 0.03$) and $C_0 = 0$.

Since we are dealing with a classical random process, we expand Eq. (C5) noticing that

$$\left.\begin{aligned}&\int_0^t d\tau\,\mathrm{tr}_B[\rho_B\delta\Phi(t)\delta\Phi(t-\tau)]\\&\int_0^t d\tau\,\mathrm{tr}_B[\rho_B\delta\Phi(t-\tau)\delta\Phi(t)]\end{aligned}\right\} \tag{C6}$$

$$= \frac{1}{2\pi}\int_0^t d\tau\int_{-\infty}^{\infty} d\omega e^{-i\omega\tau}S_\Phi^{1/f}(\omega), \tag{C7}$$

where $S_\Phi^{1/f}(\omega) = \int_{-\infty}^{\infty} d\tau e^{i\omega\tau}\langle\delta\Phi(\tau)\delta\Phi(0)\rangle$ is the noise spectral density defined in terms of the noise correlation function $\langle\delta\Phi(\tau)\delta\Phi(0)\rangle$. We moreover assume that

$$S_\Phi^{1/f}(\omega) = \frac{A_\Phi^2}{|\omega|/2\pi}, \tag{C8}$$

where A_Φ is the $1/f$ flux-noise amplitude, typically reported to be in the range $1 - 10\,\mu\Phi_0$ [19].

With this form of spectral density, the integral in the r.h.s of Eq. (C7) can be expressed in a closed form

$$\int_0^t d\tau\int_{-\infty}^{\infty}\frac{d\omega}{2\pi}e^{-i\omega\tau}S_\Phi(\omega) = \lim_{\omega_{\rm ir}\to 0} -2A_\Phi^2\int_0^t d\tau\,\mathrm{Ci}(\omega_{\rm ir}\tau), \tag{C9}$$

where $\mathrm{Ci}(w) = -\int_w^\infty dx\,x^{-1}\cos x$ is the cosine integral. Here, an infrared frequency cutoff $\omega_{\rm ir}/2\pi \sim 1\,\mathrm{Hz}$ is introduced to regularize the integral in Eq. (C9) and is physically motivated [53].

Since the time t over which we are interested in calculating the time evolution of the density matrix is small compared to the time scale set by $\omega_{\rm ir}^{-1}$, we make use of the series expansion

$$\mathrm{Ci}(w) = \gamma + \log(w) + \sum_{k=1}^{\infty}\frac{(-w^2)^k}{2k(2k)!}, \tag{C10}$$

where $\gamma \simeq 0.58$ is the Euler's constant, approximating

$$\int_0^t d\tau\int_{-\infty}^{\infty}\frac{d\omega}{2\pi}e^{-i\omega\tau}S_\Phi(\omega) \simeq 2A_\Phi^2\times t\times[(1-\gamma)-\log(\omega_{\rm ir}t)]. \tag{C11}$$

Replacing Eq. (C11) in Eq. (C5) and expanding the double commutators, we arrive at a pure-dephasing master equation of the form $\partial_t\rho = \mathscr{L}_\varphi\rho$, where

$$\begin{aligned}\mathscr{L}_\varphi\rho = &\sum_k \Gamma_\varphi^{kk}(t)\,\mathscr{D}[\sigma_{kk},\sigma_{kk}]\,\rho\\&+\sum_{k>l}\Gamma_\varphi^{kl}(t)\Big(\mathscr{D}[\sigma_{kk},\sigma_{ll}]\,\rho+\mathscr{D}[\sigma_{ll},\sigma_{kk}]\,\rho\Big).\end{aligned} \tag{C12}$$

In this expression, we have defined the time-dependent pure-dephasing rates

$$\Gamma_\varphi^{kl}(t) = \frac{4E_{J_b}^2A_\Phi^2}{\hbar^2\varphi_0^2}\,s_\varphi(k,l)\,\times t[(1-\gamma)-\log(\omega_{\rm ir}t)], \tag{C13}$$

$\sigma_{kl} = |\psi_k\rangle\langle\psi_l|$, and $\mathscr{D}[x,y]\,\rho = x\rho y^\dagger - \{y^\dagger x,\rho\}/2$ is a generalized dissipator superoperator. Equivalently,

Eq. (C12) can be recast in the more familiar form

$$\mathscr{L}_\varphi \rho = \sum_k \Gamma_\varphi^{kk}(t)\, \mathscr{D}[\sigma_{kk}]\, \rho + \sum_{k>l} \Gamma_\varphi^{kl}(t) \Big(\mathscr{D}[\sigma_{kk}+\sigma_{ll}] - \mathscr{D}[\sigma_{kk}] - \mathscr{D}[\sigma_{ll}] \Big) \rho, \tag{C14}$$

where $\mathscr{D}[x]\,\rho = x\rho x^\dagger - \{x^\dagger x, \rho\}/2$ is the standard dissipator superoperator. By projecting Eq. (C14) in the fluxonium eigenbasis

$$\langle \psi_k | \mathscr{L}_\varphi \rho | \psi_l \rangle = -\frac{1}{2} \Big[\Gamma_\varphi^{kk} + \Gamma_\varphi^{ll} - 2\Gamma_\varphi^{kl} \Big] \langle \psi_k | \rho | \psi_l \rangle, \tag{C15}$$

we verify that, since $[\Gamma_\varphi^{kk} + \Gamma_\varphi^{ll} - 2\Gamma_\varphi^{kl}] \propto (\partial \omega_{kl}/\partial \Phi_{\rm ext})^2$, the decay of the coherences of the density matrix is proportional to the flux dispersion of the $k \leftrightarrow l$ qubit transition, as expected for first-order dephasing processes. Since second-order corrections to the pure-dephasing rate at sweet spots are of order A_Φ^4 and thus vanishing small, most devices are T_1-limited at such operating points.

In order to produce an estimate of the pure-dephasing coherence time due to $1/f$ flux noise, we simply integrate Eq. (C15) for $(k,l) = (0,1)$, arriving at the expression

$$\rho_{01}(t) = \rho_{01}(0) \exp\Big\{ -\frac{D_{01} t^2}{2} \Big[\Big(\frac{3}{2} - \gamma \Big) - \log(\omega_{\rm ir} t) \Big] \Big\}, \tag{C16}$$

where

$$D_{01} = \frac{4 E_{J_{\rm b}}^2 A_\Phi^2}{\hbar^2 \varphi_0^2} [s_\varphi(0,0) + s_\varphi(1,1) - 2 s_\varphi(0,1)]. \tag{C17}$$

We then define the coherence time T_φ as the solution of the implicit equation $\rho_{01}(T_\varphi)/\rho_{01}(0) = 1/e$.

[1] M. H. Devoret and R. J. Schoelkopf, Science **339**, 1169 (2013).
[2] F. Arute, K. Arya, R. Babbush, D. Bacon, J. C. Bardin, R. Barends, R. Biswas, S. Boixo, F. G. Brandao, D. A. Buell, et al., Nature **574**, 505 (2019).
[3] M. H. Devoret et al., Les Houches, Session LXIII **7** (1995).
[4] G. Burkard, R. H. Koch, and D. P. DiVincenzo, Physical Review B **69**, 064503 (2004).
[5] V. E. Manucharyan, J. Koch, L. I. Glazman, and M. H. Devoret, Science **326**, 113 (2009).
[6] N. Earnest, S. Chakram, Y. Lu, N. Irons, R. K. Naik, N. Leung, L. Ocola, D. A. Czaplewski, B. Baker, J. Lawrence, et al., Physical Review Letters **120**, 150504 (2018).
[7] C. Macklin, K. O'Brien, D. Hover, M. Schwartz, V. Bolkhovsky, X. Zhang, W. Oliver, and I. Siddiqi, Science **350**, 307 (2015).
[8] R. Kuzmin, R. Mencia, N. Grabon, N. Mehta, Y.-H. Lin, and V. E. Manucharyan, Nature Physics , 1 (2019).
[9] T. E. Baker et al., manuscript in preparation (2019).
[10] V. E. Manucharyan, N. A. Masluk, A. Kamal, J. Koch, L. I. Glazman, and M. H. Devoret, Physical Review B **85**, 024521 (2012).
[11] I. Affleck, T. Kennedy, E. H. Lieb, and H. Tasaki, in Condensed matter physics and exactly soluble models (Springer, 1988) pp. 253–304.
[12] U. Schollwöck, Annals of Physics **326**, 96 (2011).
[13] F. Verstraete and J. I. Cirac, Physical Review B **73**, 094423 (2006).
[14] U. Schollwöck, Reviews of Modern Physics **77**, 259 (2005).
[15] S. R. White, Physical Review Letters **69**, 2863 (1992).
[16] S. R. White, Physical Review B **48**, 10345 (1993).
[17] F. Verstraete and J. I. Cirac, arXiv preprint cond-mat/0407066 (2004).
[18] G. Vidal, Physical Review Letters **99**, 220405 (2007).
[19] J. Koch, M. Y. Terri, J. Gambetta, A. A. Houck, D. Schuster, J. Majer, A. Blais, M. H. Devoret, S. M. Girvin, and R. J. Schoelkopf, Physical Review A **76**, 042319 (2007).
[20] J. Koch, V. Manucharyan, M. H. Devoret, and L. I. Glazman, Phys. Rev. Lett. **103**, 217004 (2009).
[21] Y.-H. Lin, L. B. Nguyen, N. Grabon, J. San Miguel, N. Pankratova, and V. E. Manucharyan, Physical Review Letters **120**, 150503 (2018).
[22] L. B. Nguyen, Y.-H. Lin, A. Somoroff, R. Mencia, N. Grabon, and V. E. Manucharyan, arXiv preprint arXiv:1810.11006 (2018).
[23] A. Kitaev, arXiv preprint cond-mat/0609441 (2006).
[24] P. Brooks, A. Kitaev, and J. Preskill, Physical Review A **87**, 052306 (2013).
[25] M. Bell, I. Sadovskyy, L. Ioffe, A. Y. Kitaev, and M. Gershenson, Physical review letters **109**, 137003 (2012).
[26] N. A. Masluk, I. M. Pop, A. Kamal, Z. K. Minev, and M. H. Devoret, Physical review letters **109**, 137002 (2012).
[27] V. E. Manucharyan, Superinductance, Ph.D. thesis, Yale University (2012).
[28] N. Maleeva, L. Grünhaupt, T. Klein, F. Levy-Bertrand, O. Dupre, M. Calvo, F. Valenti, P. Winkel, F. Friedrich, W. Wernsdorfer, et al., Nature communications **9**, 3889 (2018).
[29] T. Hazard, A. Gyenis, A. Di Paolo, A. Asfaw, S. A. Lyon, A. Blais, and A. A. Houck, Physical review letters **122**, 010504 (2019).
[30] L. Grünhaupt, M. Spiecker, D. Gusenkova, N. Maleeva, S. T. Skacel, I. Takmakov, F. Valenti, P. Winkel, H. Rotzinger, W. Wernsdorfer, A. V. Ustinov, and I. M. Pop, Nature Materials **18**, 816 (2019).
[31] A. Gyenis, P. S. Mundada, A. Di Paolo, T. M. Hazard, X. You, D. I. Schuster, J. Koch, A. Blais, and A. A. Houck, arXiv preprint arXiv:1910.07542 (2019).
[32] D. G. Ferguson, A. A. Houck, and J. Koch, Physical Review X **3**, 011003 (2013).
[33] G. Viola and G. Catelani, Physical Review B **92**, 224511 (2015).
[34] S. E. Nigg, H. Paik, B. Vlastakis, G. Kirchmair,

S. Shankar, L. Frunzio, M. Devoret, R. Schoelkopf, and S. Girvin, Physical Review Letters **108**, 240502 (2012).
[35] J. Bourassa, F. Beaudoin, J. M. Gambetta, and A. Blais, Physical Review A **86**, 013814 (2012).
[36] Z. K. Minev, arXiv preprint arXiv:1902.10355 (2019).
[37] C. Hubig, I. McCulloch, and U. Schollwöck, Physical Review B **95**, 035129 (2017).
[38] K. Matveev, A. Larkin, and L. Glazman, Physical review letters **89**, 096802 (2002).
[39] J. Mooij and C. Harmans, New Journal of Physics **7**, 219 (2005).
[40] J. Mooij and Y. V. Nazarov, Nature Physics **2**, 169 (2006).
[41] A. Hriscu and Y. V. Nazarov, Physical Review B **83**, 174511 (2011).
[42] G. Rastelli, I. M. Pop, and F. W. Hekking, Physical Review B **87**, 174513 (2013).
[43] R. Süsstrunk, I. Garate, and L. I. Glazman, Physical Review B **88**, 060506 (2013).
[44] I. V. Pechenezhskiy, R. A. Mencia, L. B. Nguyen, Y.-H. Lin, and V. E. Manucharyan, arXiv preprint arXiv:1907.02937 (2019).
[45] J. R. Friedman and D. V. Averin, Physical review letters **88**, 050403 (2002).
[46] I.-M. Pop, B. Douçot, L. Ioffe, I. Protopopov, F. Lecocq, I. Matei, O. Buisson, and W. Guichard, Physical Review B **85**, 094503 (2012).
[47] M. Bell, W. Zhang, L. Ioffe, and M. Gershenson, Physical review letters **116**, 107002 (2016).
[48] G. Catelani, R. J. Schoelkopf, M. H. Devoret, and L. I. Glazman, Physical Review B **84**, 064517 (2011).
[49] J. Koch, V. Manucharyan, M. Devoret, and L. Glazman, Physical review letters **103**, 217004 (2009).
[50] J. Ulrich and F. Hassler, Physical Review B **94**, 094505 (2016).
[51] H.-P. Breuer, F. Petruccione, et al., The theory of open quantum systems (Oxford University Press on Demand, 2002).
[52] G. Ithier, E. Collin, P. Joyez, P. J. Meeson, D. Vion, D. Esteve, F. Chiarello, A. Shnirman, Y. Makhlin, J. Schriefl, and G. Schon, Phys. Rev. B **72**, 134519 (2005).
[53] P. Groszkowski, A. Di Paolo, A. Grimsmo, A. Blais, D. Schuster, A. A. Houck, and J. Koch, New Journal of Physics **20**, 043053 (2018).

Conclusion

This document summarizes my work on the development of novel qubits such as the fluxonium and the $0-\pi$ qubits. In chapter 3, we studied the coherence properties of the $0-\pi$ qubit using a detailed theoretical model of this device. We theoretically demonstrated the noise protection of the $0-\pi$ qubit in useful regimes of parameters, and investigated the sources of noise that can compromise the qubit coherence in realistic scenarios. The main result of this chapter is the estimation of the coherence times of the $0-\pi$ device in presence of circuit-element disorder leading to coupling to the ζ mode. In chapter 4, we addressed control and readout strategies for the $0-\pi$ qubit. Importantly, we first made clear that the original proposal for gates and measurement in Ref. [66] cannot work in practice. We moreover developed new intuition for the $0-\pi$ that was formalized by a semi-analytical effective model for the device. We suggested regimes of parameters and coupling schemes that can make dispersive readout of the $0-\pi$ possible. We moreover introduced a novel high-fidelity single-qubit gate that can interpolate between logical X and logical Z depending on the circuit parameters and flux bias. We also proposed a method to fight the main decoherence channel of a realistic device by active cooling of the ζ mode.

Chapter 5 described the first experimental realization of the $0-\pi$ qubit. This work was made possible by careful engineering and theoretical modeling of the device. In addition to the large relaxation and coherence times that were measured, and the demonstration of coherent control of a $0-\pi$ qubit, this work provides physical insights on the $0-\pi$ device that will be certainly useful to other groups pursuing this path. This work also shows that the detailed theoretical model introduced in chapter 2 provides a very accurate description of the experimental data. This is a crucial finding that enables us to reliably engineer the next generation of $0-\pi$ devices with better noise protection.

Having presented a number of results regarding the $0-\pi$ qubit, we turned to the fluxonium qubit in chapter 6. There, we explored the intrinsic multimode structure of such a device, that is inherited from the superinductance. Following a general discussion about

our newly developed theories for describing the multimode structure of superinductance-based devices, we presented two research articles. The first of these articles, presented in Sect. 6.2, described the first experimental realization of a nanowire-superinductance fluxonium qubit. The main theoretical result there is a very accurate description of the multimode spectrum up to frequencies at high as $\sim 17\,\mathrm{GHz}$ for three devices. This is an important step towards accurate modeling of strongly nonlinear high-impedance modes, which is of fundamental relevance to many other devices and also applies to junction-array realizations of superinductances. Following this work, we presented in Sect. 6.3 a new tensor network method (DMRG) to numerically solve for the low-lying excitations of many-body superconducting circuits. We demonstrated the applicability of this tool in the context of superconducting quantum circuits treating the fluxonium qubit Hamiltonian. Given that the fluxonium includes all the basic elements of superconducting quantum circuits, this suggests that our method is generally applicable to other circuit QED setups. For the case of the fluxonium qubit, we demonstrated the validity of the DMRG results by developing a new single-mode theory that takes into account all circuit details, including the nonlinearity of the array junctions. We have also verified a long-standing theory describing the combined effect of coherent quantum phase slips and charge noise in the fluxonium-qubit architecture. This is the first time that these effects can be computed from first principles without the need of additional approximations. Moreover, we used DMRG to estimate the coherence times of a realistic device, finding values that are in good agreement with those experimentally reported. Finally, in appendices A and B we presented other research works related to noise-protected devices and quantum simulation, respectively.

Several research avenues follow from the results reported in this thesis. With respect to the $0-\pi$ qubit, new strategies to realize a universal gate set are still required. As shown by recent work [41], optimal control techniques can be very useful for this task. The applicability of these methods to two-qubit gates remains an open question. In this context, exploiting optimal control and enhanced dispersive shifts resulting from straddling-like regimes of operation (see chapter 4) could enable high-fidelity dispersive two-qubit gates. As devices are built with a lighter ϕ mode but still far from the deep $0-\pi$ regime, AC flux-driving and mutual-inductance coupling should also be considered as a way of performing single- and two-qubit control. Studying these strategies in parameter regimes of current experimental reach is now crucial, as the first realization of the $0-\pi$ qubit is out. Moreover, methods for cooling of the ζ mode with less complexity that the one suggested in chapter 4 could also be useful in the near-future as experimental efforts advance. In terms of the experimental realization, there exist an urgent need for scalable design with a lighter ϕ mode. Lifting off superinductances from the ground plane [76] is unlikely to help in the long run and significant effort is required to overcome stray capacitances using a strictly

two-dimensional architecture.

With respect to the multimode theories of chapter 6, further work is needed to take advantage of these new methods which are now confirmed by several independent techniques. As devices exploiting strongly nonlinear high-impedance modes grow in complexity, theoretical work should ideally account for the multimode structure and derive more accurate effective Hamiltonians. This would result in more reliable circuit designs and greater predictive power. From a theoretical point of view, a very promising avenue is to extend the use of tensor network techniques. We have now demonstrated the use of these techniques to the case of a many-body superconducting qubit (the fluxonium qubit). Beyond the fluxonium circuit, we have already applied these techniques to many other systems (not reported here), including weakly nonlinear multimode cavities [43, 108] and concept designs for multi-qubit chips. From these preliminary studies, we believe that we can compute up to 100s of excitations of (in principle) any superconducting circuit. With the demonstration of quantum computational supremacy [31], it is now the right time for theorists to start modeling these large devices in greater detail. In particular, studying crosstalk and spurious interactions is an important avenue, as this has been crucial for the supremacy and many other experiments. Our tensor network technique is a powerful new resource to tackle this problem. In addition, exploring the many-body structure of superconducting devices by means of tensor networks is also an interesting avenue. In particular, a starting point could be to evaluate the effects of dissipation and circuit-element disorder by examining the expectation values of local operators in a circuit. Finally, as the structure of many-body entanglement in these systems can also be examined using this numerical method, new ways to encode quantum information nonlocally exploiting noise-protected subspaces might arise from these studies.

Appendix A

Bifluxon: fluxon-parity-protected superconducting qubit

Bifluxon: Fluxon-Parity-Protected Superconducting Qubit

Konstantin Kalashnikov,[1,*] Wen Ting Hsieh,[2] Wenyuan Zhang,[1] Wen-Sen Lu,[1]
Plamen Kamenov,[1] Agustin Di Paolo,[3] Alexandre Blais,[3,4] Michael E. Gershenson,[1] and Matthew Bell[2,†]

[1] *Department of Physics and Astronomy, Rutgers University, Piscataway, NJ*
[2] *Engineering Department, University of Massachusetts Boston, Boston, MA*
[3] *Institut Quantique and Département de Physique, Université de Sherbrooke, Sherbrooke J1K 2R1 QC, Canada*
[4] *Canadian Institute for Advanced Research, Toronto, ON, Canada*

(Dated: October 10, 2019)

We have developed and characterized a symmetry-protected superconducting qubit that offers simultaneous exponential suppression of energy decay from charge and flux noise, and dephasing from flux noise. The qubit consists of a Cooper-pair box (CPB) shunted by a superinductor, thus forming a superconducting loop. Provided the offset charge on the CPB island is an odd number of electrons, the qubit potential corresponds to that of a $\cos(\phi/2)$ Josephson element, preserving the parity of fluxons in the loop via Aharonov-Casher interference. In this regime, the logical-state wavefunctions reside in disjoint regions of phase space, thereby ensuring the protection against energy decay. By switching the protection on, we observed a ten-fold increase of the decay time, reaching up to 100 μs. Though the qubit is sensitive to charge noise, the sensitivity is much reduced in comparison with the charge qubit, and the charge-noise-induced dephasing time of the current device exceeds 1 μs. Implementation of the full dephasing protection can be achieved in the next-generation devices by combining several $\cos(\phi/2)$ Josephson elements in a small array.

I. INTRODUCTION

Superconducting qubits have emerged as one of the most promising platforms for quantum computing [1]. Over the past two decades, the coherence of these qubits has been improved by five orders of magnitude [2]. Even with this spectacular progress, implementation of error correction codes remains very challenging [3]. Further improvement in coherence will require the development of new approaches for mitigating harmful effects due to uncontrollable microscopic degrees of freedom, such as two-level systems (TLS) in the qubit environment [4]. This route is provided by the improvement of materials involved in fabrication of superconducting qubits, which can lead to the reduction of the TLS density. A complementary approach, which we consider below, is based on the reduction of the qubit-TLS coupling by qubit design.

Qubit coherence is characterized by the energy relaxation (decay) time T_1 and the dephasing time T_φ. The decay rate $\Gamma_1 \equiv 1/T_1$ due to coupling to a fluctuating quantity λ is proportional to the transition amplitude $|\langle g|H_\lambda|e\rangle|^2$, where H_λ is the coupling Hamiltonian and $\{|g\rangle, |e\rangle\}$ are the qubit's logical states. Since the external noise couples to local operators, decreasing of the overlap of $|g\rangle$ and $|e\rangle$ wavefunctions can significantly reduce Γ_1. This strategy is exploited by several qubit designs in which localization of the logical-state wavefunctions occurs within distinct and well-separated minima of the qubit potential, such as the "heavy fluxonium" qubit [5, 6].

On the other hand, a small dephasing rate $\Gamma_\varphi \equiv 1/T_\varphi$ requires the qubit transition frequency ω_{ge} to be insensitive to fluctuations of λ. The first-order decoupling of a qubit from noise has been achieved at the so-called "sweet spot" λ_0, where $\partial\omega_{ge}/\partial\lambda|_{\lambda_0} = 0$ [7]. However, the coherence times achieved with this approach are insufficient for the implementation of the error correction codes, even if the drifts of the qubit operating point are eliminated over the timescale of operations. To remedy

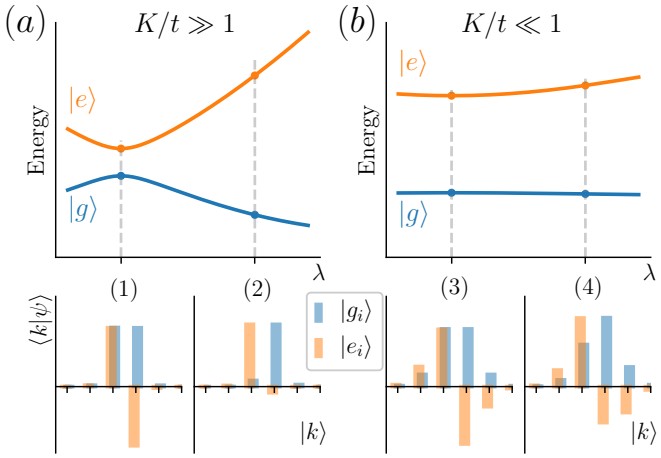

FIG. 1. The trade-off between the decay and dephasing protection in superconducting qubits with a single charge or flux degree of freedom. The band structure (top panels) and wavefunctions (bottom panels) of a particle in quasiperiodic potentials: (a) the free-particle regime and (b) the tight-binding regime. The wavefunction overlap and the energy sensitivity $\partial E_{eg}^{(i)}/\partial\lambda$ do not simultaneously vanish for any point (i). Flux (charge) qubits correspond to the case of the control parameter $\lambda = \Phi_{\rm ext}$ (q_g), kinetic energy $K = E_L$ (E_C), tunneling energy $t = E_{sps}$ (E_J), and $|k\rangle$ as a fluxon (charge) basis.

* kostya.kalashnikov@rutgers.edu
† Matthew.Bell@umb.edu

this, a "sweet-spot-everywhere" approach has been realized in the transmon qubit [8, 9]: an exponentially strong suppression of the qubit sensitivity to noise has been achieved by delocalization of the qubit wavefunctions in charge space.

It is, however, worth noticing that the two approaches of T_1 and T_φ protection by qubit design come into conflict in the case of devices with a single degree of freedom in the qubit Hamiltonian (which we will refer to as 1D qubits). For instance, at the dephasing sweep spot of the "heavy fluxonium" [5, 6] wavefunctions become delocalized due to its hybridization, which limits decay time [Fig. 1(a), $i = 1$], whereas T_1 protection can be realized only at the slope of dispersion curve where T_φ is small. [Fig. 1(a), $i = 2$]. In turn, the charge insensitivity of the transmon qubit is accompanied with strong dipole matrix elements that limit T_1 [Fig. 1(b), $i = 3, 4$]. Additionally, the flatness of the transmon-qubit bands results in a strong reduction of the spectrum anharmonicity, potentially leading to a leakage of information outside of the computational subspace [10].

These examples suggest that a qubit Hamiltonian with full noise protection against relaxation and dephasing, i.e. exponentially large T_1 and T_φ, cannot be implemented in a single-mode superconducting quantum device. This conflict, however, can be reconciled by the so-called "few-body" qubits [11], that incorporate more than one degree of freedom in the qubit Hamiltonian (the dimentionality $D > 1$) [12–15].

An example of simultaneous decay and dephasing protection in circuits with $D > 1$ is given by the 0-π qubit [16]. Its $D = 2$ Hamiltonian combines one "light" ϕ and one "heavy" θ variable. The logical wavefunctions are delocalized along the ϕ direction, while being localized in two disconnected potential wells labeled by $\theta = [0, \pi]$. These properties lead to exponentially reduced sensitivity to flux-noise fluctuations, i.e. negligible dephasing, and exponentially small matrix elements, i.e. long decay time [17]. Noise protection in this device is hard-wired by circuit design, making the qubit robust against external perturbations. Fabricating such a circuit, however, entails several serious challenges, among which are very strict requirements on the parameters of all circuit elements and symmetry constraints. Moreover, since the built-in protection permanently decouples the qubit from the environment, new approaches to state preparation, qubit manipulation, and readout are required [18].

Another concept of qubit protection exploits symmetries of Hamiltonians with $D > 1$ [19], an example being the qubit based on Josephson rhombi arrays [20], experimentally realized in Ref. [13]. In a single rhombus threaded by half of the magnetic flux quantum, the transport of individual Cooper pairs (CP) is suppressed due to destructive Aharonov-Bohm interference, such that the rhombi chain supports correlated transport of CP pairs [i.e., acts as a $\cos(2\phi)$ Josephson element]. The dephasing time of the qubit can be enhanced by delocalization of wavefunctions over the states with the same CP parity, which does not compromise T_1. Importantly, this qubit design enables on-demand tuning the qubit coupling to the environment (including the read-out) on and offs, which facilitates qubit manipulations. This also provides a route to fault-tolerant gates immune to noises in the control lines [21]. An improved version of the rhombus qubit can be built by parallel connection of several rhombi chains [22].

Here we focus on the implementation of a complementary circuit preserving the parity of fluxons in a superconducting loop, which consists of a split Cooper-pair box (CPB) and a superinductor (SI), and is depicted in Fig. 2(a). The probability of single fluxon tunneling in and out of the loop can be tuned by the CPB charge q_g of the CPB island (hereafter we refer to CPB charge modulo 2 due to periodicity). At $q_g = 1e$ (where e is the electron charge) Aharonov-Casher interference results in a 4π-periodic potential [i.e. $\cos(\phi/2)$ Josephson element], which preserves the fluxon parity in the loop [23–25]. In the case of perfectly symmetric CPB junctions, the two degenerate logical states with different fluxon-number parity reside in disjoint regions of the Hilbert space, forbidding qubit decay. It is moreover possible to delocalize the wavefunction within each parity state via double fluxon tunneling in order to provide protection against pure dephasing by flux noise. Below we refer to such an element as a "Bifluxon" qubit.

In this paper, we have designed and characterized a prototype of the bifluxon qubit and demonstrated the decay protection by setting the CPB charge to the value of $1e$. By turning protection on, we observe a ten-fold increase of the decay time, up to 100 μs. We also report the measurement of the qubit phase-coherence time T_φ, exceeding 1 μs.

The paper is organized as follows. In Sect. II we elaborate on the coherence properties of the bifluxon qubit by analyzing the symmetries of the logical wavefunctions and the resulting selection rules, as well as possible ways to realize dephasing protection. In Sect. III we present experimental implementation of the bifluxon qubit and discuss coherence-time measurement protocols. In Sect. IV we analyse the coherence limitations of the bifluxon qubit, and discuss a number of possibilities for further coherence-time improvements.

II. THEORY

This section outlines the theory of the bifluxon qubit and the origin of its noise protection. We assume for simplicity that the Josephson junctions (JJs) forming the CPB are identical with Josephson energy E_J and charging energy E_C. The charging and inductive energies of the superinductance L are denoted by E_{CL} and $E_L = (\Phi_0/2\pi)^2/L$, respectively, where $\Phi_0 = h/2e$ is the quantum of magnetic flux.

The behavior of the system is determined by two controllable parameters: the offset charge q_g of the CPB island and the external flux $\Phi_{\rm ext}$ through the device's loop. In this section we will use the dimensionless quan-

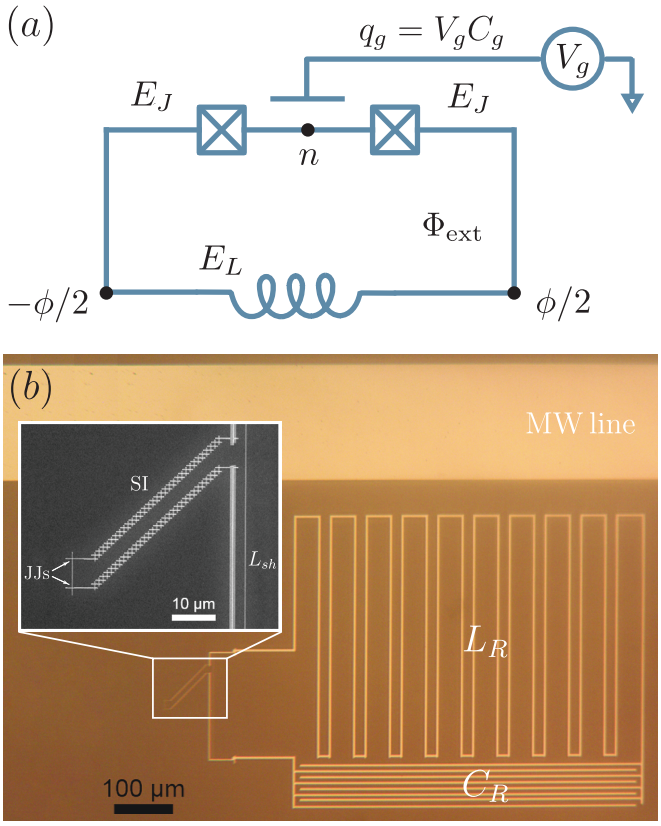

FIG. 2. (a) Simplified circuit scheme of the bifluxon qubit, described by Eq. (1). Charging energies of the superinductor and CPB are E_{CL} and E_C, respectively. The qubit is controlled by the CPB charge q_g and the magnetic flux $\Phi_{\rm ext}$. (b) Optical image of the bifluxon qubit, readout resonator, and the microwave (MW) transmission line. The inset shows the SEM image of its central part: two JJs form CPB island, the long array of larger JJs acts as a superinductor.

tities $\varphi_{\rm ext} = 2\pi\Phi_{\rm ext}/\Phi_0$ and $n_g = q_g/2e$, and restore the dimensionful values in the experimental section. The circuit Hamiltonian has three degrees of freedom (see appendix A): the superconducting phase of the CPB island, φ, and the sum and difference of the phases at the ends of the superinductor, respectively denoted by ϕ_+ and ϕ. For simplicity, we assume that the high-frequency circuit mode ϕ_+ is not excited. Under this approximation, the qubit Hamiltonian is two-dimensional. In the charge basis for the CPB degree of freedom, the circuit Hamiltonian can be written as

$$H = \sum_n \left[4E_C(n-n_g)^2|n\rangle\langle n| - E_J\cos(\phi/2)(\sigma_n^+ + \sigma_n^-)\right] - 4E_{CL}\partial_\phi^2 + \frac{E_L}{2}(\phi-\varphi_{\rm ext})^2, \tag{1}$$

where n represents the number of Cooper pairs in the CPB island, and we have defined $\sigma_n^+ = |n+1\rangle\langle n|$ and $\sigma_n^- = (\sigma_n^+)^\dagger$.

To illustrate the working principles of the bifluxon qubit, here we examine the limiting case $E_C \gg E_J$, although full numerical diagonalization is used to analyze the data from devices with $E_J \gtrsim E_C$ below. Let us consider two cases for the offset charge n_g. If n_g is set near an integer number N, the CPB degree of freedom can be thought as "frozen" close to the charge state that minimizes the kinetic-energy term in Eq. (1). In this case, the circuit Hamiltonian is reduced to a 1D fluxonium-like Hamiltonian with a renormalized Josephson energy $E_J^2/4E_C$ (see appendix B). To operate the bifluxon qubit in the protected regime, the offset charge instead should be set close to half-integer, i.e. $n_g \approx 1/2$. With $E_C \gg E_J$, it is sufficient to consider only two nearly degenerate CPB states $|0\rangle$ and $|1\rangle$. Projecting the circuit Hamiltonian in this two-dimensional subspace, we find

$$H_r = 4E_C\left(\frac{1}{2}-n_g\right)\sigma^z - E_J\cos(\phi/2)\sigma^x - 4E_{CL}\partial_\phi^2 + \frac{E_L}{2}(\phi-\varphi_{\rm ext})^2, \tag{2}$$

where $\sigma^z = |1\rangle\langle 1| - |0\rangle\langle 0|$ and $\sigma^x = \sigma^+ + \sigma^-$. Eq. (2) is diagonal in the σ^x basis for $n_g = 1/2$. Therefore, the lowest-energy eigenstates can be factorized as $|\psi^n\rangle\otimes|\psi^\phi\rangle$, where the superscripts n and ϕ denote the charge- and flux-like components of the wavefunctions, respectively. In particular, the charge-like component results in either the symmetric or anti-symmetric combinations $|\pm^n\rangle = (|0\rangle \pm |1\rangle)/\sqrt{2}$. The flux-like component is an eigenstate of the one-dimensional Hamiltonian $H_\pm = -4E_{CL}\partial_\phi^2 + V_\pm$, with a potential energy that depends on the charge state

$$V_\pm = \mp E_J\cos(\phi/2) + \frac{E_L}{2}(\phi-\varphi_{\rm ext})^2. \tag{3}$$

The local minima of the fluxonium-like potential V_+ (V_-) are positioned near $\phi_m = 2\pi m$, where m is an even (odd) integer. An harmonic-oscillator wavefunction of the form $\psi_m(\phi) \sim \exp(-\sqrt{E_J/E_{CL}}\,(\phi-\phi_m)^2/4)$, localized at m-th minimum, can be associated with a fluxon excitation $|m\rangle$. Using the fluxon representation, the eigenstates of Eq. (2) can be expressed as $|m\rangle = \{|2k\rangle\}\cup\{|2k+1\rangle\}$, where $|2k\rangle = |+^n, \psi_{2k}^\phi\rangle$ and $|2k+1\rangle = |-^n, \psi_{2k+1}^\phi\rangle$ have an even and odd number of fluxons in the loop, respectively [see Fig. 3(a)].

Figure 3(b) presents the spectrum of the qubit for $n_g = 1/2$ as a function of $\varphi_{\rm ext}$. Since the single phase-slip (SPS) processes connecting $|m\rangle \leftrightarrow |m+1\rangle$ are forbidden due to the symmetry of the wavefunctions

$$E_{\rm sps} = \langle m|H_r|m+1\rangle \propto \langle +^n|-^n\rangle = 0, \tag{4}$$

the two neighboring parabolas cross at half-integer $\varphi_{\rm ext}/2\pi$. This can be interpreted as a fluxon-parity conservation rule due to the Aharonov-Casher effect [23], which has been experimentally observed in Refs. [24–26]. Therefore, at a half-integer n_g, the considered system resembles a fluxonium qubit made up of a 4π-periodic Josephson element, justifying the name "bifluxon".

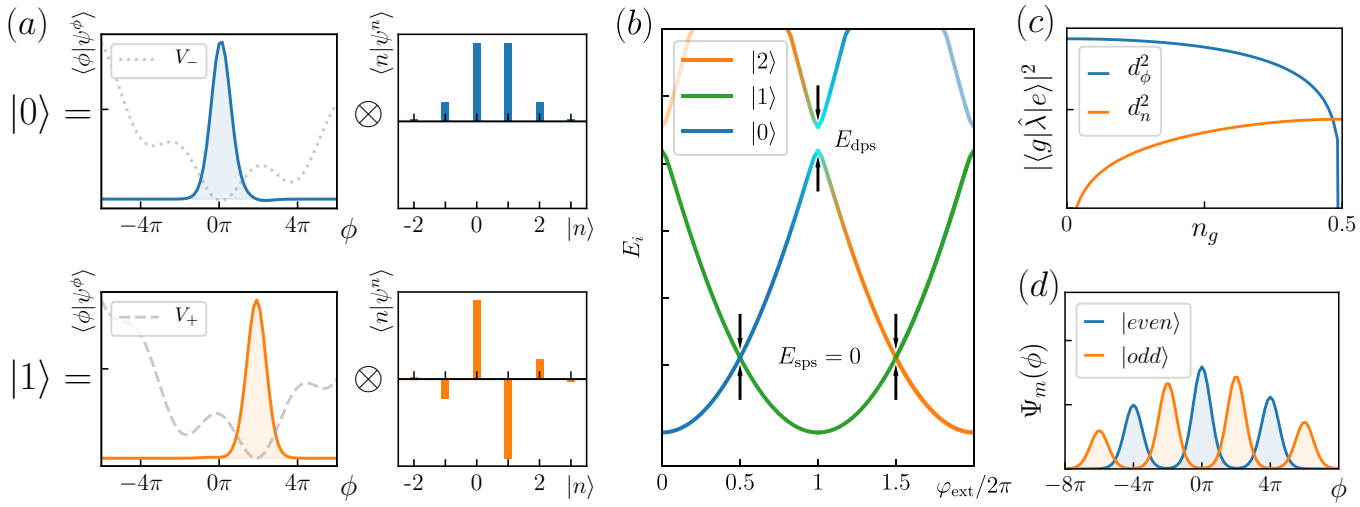

FIG. 3. (a) The ground and first excited states of the bifluxon qubit shown as products of the fluxon wavefunctions in the $V_\pm$ potentials and CPB state, for $\varphi_{\rm ext} = \pi$, $n_g = 0.5$. The parity of the $\cos(\phi/2)$ term is controlled by the CPB state $|\pm^n\rangle$. (b) Bifluxon energy bands as a function of $\varphi_{\rm ext}$ at $n_g = 0.5$. Color gradient represents the hybridization of the states with different fluxon numbers. Note the crossing of the parabolas at half-integer $\varphi_{\rm ext}/2\pi$ due to $E_{\rm sps} = 0$ and the avoided crossing between the next-to-neighbor parabolas $E_{\rm dps} > 0$. (c) Dependence of the flux and charge matrix elements on the CPB charge. The decay protection is realized at $n_g = 0.5$, where d_ϕ is zero and d_n is significantly suppressed. (d) Delocalization of the even (odd) fluxon states in the regime $E_{\rm dps} \gg 2\pi^2 E_L$ leads to suppression of dephasing due to the flux noise.

Double phase-slip (DPS) processes mix fluxon states with the same parity (m and $m+2$), opening energy gaps in the spectrum. The DPS amplitude is given by

$$E_{\rm dps} = \langle m|H_r|m+2\rangle = \hbar\omega_p \langle \psi^\phi_m|\psi^\phi_{m+2}\rangle \approx \hbar\omega_p \exp(-\pi^2\beta), \tag{5}$$

where $\omega_p = \sqrt{8E_J E_{CL}}$ is a plasma frequency for the $V_\pm$ potentials and $\beta = \sqrt{2E_J/E_{CL}}$.

The symmetry of states with distinct fluxon parity makes the qubit immune to energy decay due to both flux and charge noises. Indeed, the phase dipole-moment matrix element is identically zero

$$d_\phi \sim \langle m|\hat{\phi}|m+1\rangle \propto \langle +^n|-^n\rangle = 0, \tag{6}$$

while, provided $E_J \gg E_{CL}$, the matrix element of the charge-noise operator is exponentially suppressed in comparison with the charge qubit [27]

$$d_n \sim \langle m|\sigma^z|m+1\rangle = \langle \psi^\phi_m|\psi^\phi_{m+1}\rangle = \exp(-\pi^2\beta/4). \tag{7}$$

Figure 3(c) shows the charge and phase dipole-moment matrix elements obtained by numerical diagonalization of the full Hamiltonian Eq. (1). The weak sensitivity to charge noise is comparable to the flux sensitivity of a heavy fluxonium [5, 6], and can be suppressed by stronger localization of the single-well excitations within the $V_\pm$ potential minima by increasing the E_J/E_{CL} ratio.

The decay protection due to symmetries of the bifluxon-circuit wavefunctions can also be understood in the following way. Consider a logical qubit made of two faulty qubits labelled σ and τ, with the two lowest-energy states $|g\rangle = |\uparrow^\sigma\downarrow^\tau\rangle$ and $|e\rangle = |\downarrow^\sigma\uparrow^\tau\rangle$ separated from the others by a sizeable energy gap ΔE. Since uncorrelated fluctuations of σ and τ cannot induce $g \leftrightarrow e$ transition and the leakage out of computation space is penalized by ΔE, the qubit is protected against local noise in the σ and τ subsystems. Accordingly, the bifluxon qubit is protected against decay due to uncorrelated charge and flux noises.

In addition to the decay protection, the bifluxon qubit can also be robust to flux-noise dephasing. Indeed, similarly to the case of the fluxonium qubit, the flux dispersion of the qubit can be reduced by increasing the superinductance value. This enables wider delocalization of the qubit wavefunctions in disjoint subspaces with different fluxon parities, as shown in Fig. 3(d). Quantitatively, the wavefunctions spread out over $G \approx \sqrt{E_{\rm dps}/E_L}$ potential wells. The flux dispersion is then suppressed by a factor of $\exp(-G)$ for $G \gg 1$. Therefore, the bifluxon qubit becomes exponentially insensitive to flux-noise dephasing under the condition $E_{\rm dps} \gg 2\pi^2 E_L$. Although this requirement is a challenge for the current fabrication capabilities, the implementation of ultrahigh-impedance superinductors has already been demonstrated [28, 29].

Finally, it should be noted that, since the bifluxon is inherently a charge-sensitive device, a single qubit does not offer a protection against the charge-noise-induced dephasing. As we will discuss in Sect. IV, small array of such elements can in principle provide a polynomial increase of the dephasing time and help to overcome this limitation.

III. EXPERIMENT

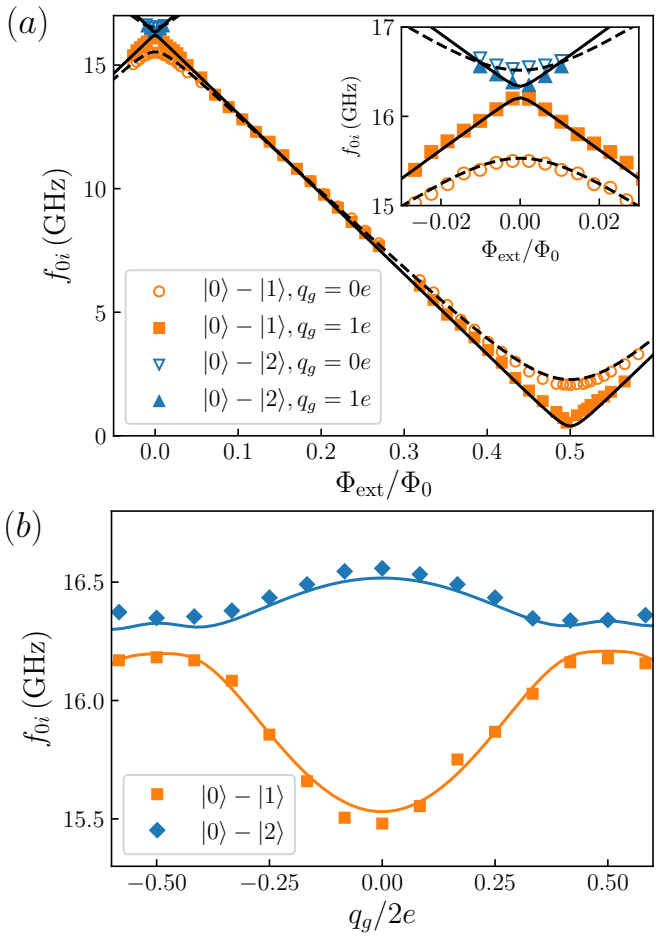

FIG. 4. Spectra of the bifluxon qubit: experimental data for the $|0\rangle - |1\rangle$ and $|0\rangle - |2\rangle$ transitions (symbols) and the result of exact diagonalization of the circuit Hamiltonian in Eq. (1) (solid lines). (a) Flux dispersion of the transition frequencies f_{0i} for two values of the CPB charge $q_g = 0, 1\,e$. The inset is a zoom in of the qubit spectrum near $\Phi_{\rm ext} = 0$, displaying the avoided crossing that characterizes the rate of double phase slips E_{dps}. (b) Charge dispersion of the f_{0i} transition frequency for $\Phi_{\rm ext} = 0$.

In this work, the bifluxon qubit is realized as a split-junction CPB [a superconducting island flanked by two small nominally identical JJs with Josephson and charging energies E_J and E_{CJ}, respectively; see Fig. 2(b)] shunted by a superinductor (SI), which is implemented as an array of $N_A = 122$ larger JJs with corresponding energies E_{JA} and E_{CA}. The sizes of small ($0.11\,\mu\text{m} \times 0.16\,\mu\text{m}$) and large ($0.21\,\mu\text{m} \times 0.30\,\mu\text{m}$) junctions are chosen in order to allow phase-slip events across the CPB junctions ($E_J/E_{CJ} \sim 1$), but suppress the phase slips in the array ($E_{JA}/E_{CA} \gg 1$). As long as the inductive energy of the SI chain $E_L = E_{JA}/N_A$ is much smaller than E_J, the phase across the SI is close to integer number of 2π. The stray capacitance of the superconducting islands to the ground in combination with the junction capacitances results in charging energies E_C and E_{CL} of the CPB and the SI, respectively (see appendix A for details). The self-resonant mode of the SI with the frequency $\sim \sqrt{E_L E_{CL}}/h$ should remain well above the qubit transition frequency (usually $\sim$ few GHz) in order to avoid qubit coupling to this mode.

The bifluxon qubit is controlled by the magnetic flux in the loop $\Phi_{\rm ext}$ and the offset charge q_g, induced by applying the dc bias voltage to the coupling capacitor C_g between the microstrip line and the CPB island. In order to perform the dispersive measurements of the bifluxon qubit, the device is inductively coupled to a lumped-element readout resonator with capacitance $C_R = 120\,\text{fF}$ and inductance $L_R = 4\,\text{nH}$. For the coupling, a portion of the bifluxon superconducting loop with kinetic inductance $L_{sh} = 0.4\,\text{nH}$ is shared with the readout resonator. The qubit-resonator coupling constant for the device described in this paper is found to be $g/2\pi = 52\,\text{MHz}$.

In the transmission measurements, the microwave signals travel along the microstrip line which is coupled to the readout resonators of up to 5 different bifluxon qubits measured in the same cooldown. The qubits could be individually addressed due to different resonant frequencies of the read-out resonators. The bifluxon qubit, read-out resonator, and microstrip transmission lines are fabricated in a single multi-angle electron-beam deposition of aluminum through a lift-off mask (for fabrication and measurement details, see Refs. [13, 24]).

The pump tone f_p induces the $|0\rangle - |i\rangle$ transitions at the resonance frequencies $f_{0i} = (E_i - E_0)/h$. The measurement tone f_m probes the dispersive shift of the coupled read-out resonator. Although the dispersive measurements in the protected regime are complicated by significantly reduced qubit-readout coupling, the signal-to-noise ratio in the spectroscopic measurements was sufficiently high to identify the resonances even in the protected regime. The flux dependences of the resonance frequences f_{01} and f_{02} at $q_g = 0, 1e$ are shown in Fig. 4(a). The obtained spectra are in a good agreement with the results of diagonalization of the circuit Hamiltonian [Eq. (1), solid lines in Fig. 4(a)], with the fitting parameters $E_J/h = 27.2\,\text{GHz}$, $E_C/h = 7.7\,\text{GHz}$, $E_L/h = 0.94\,\text{GHz}$, $E_{CL}/h = 10\,\text{GHz}$, and asymmetry between the CPB junctions $\Delta E_J/h = 6\,\text{GHz}$.

The extracted values are consistent with the expected JJ parameters. The normal-state resistance of the CPB junctions extracted from E_J using the Ambegaokar-Baratoff relation agrees within 20% with the resistance of test junctions fabricated on the same chip. Both CPB and SI charging energies agree well with the typical aluminum-based junction capacitance $50\,\text{fF}/\mu\text{m}^2$ and specific capacitance of micron-size islands on silicon substrates $0.04\,\text{fF}/\mu\text{m}$ [30].

We also observed an additional resonance at 13.9 GHz, whose position did not depend on $\Phi_{\rm ext}$ and q_g. We attribute this resonance to the lowest-frequency mode of the superinductor, which corresponds to characteristic impedance of the SI $Z = 14\,\text{k}\Omega$.

In the time-domain experiments the signal-to-noise ra-

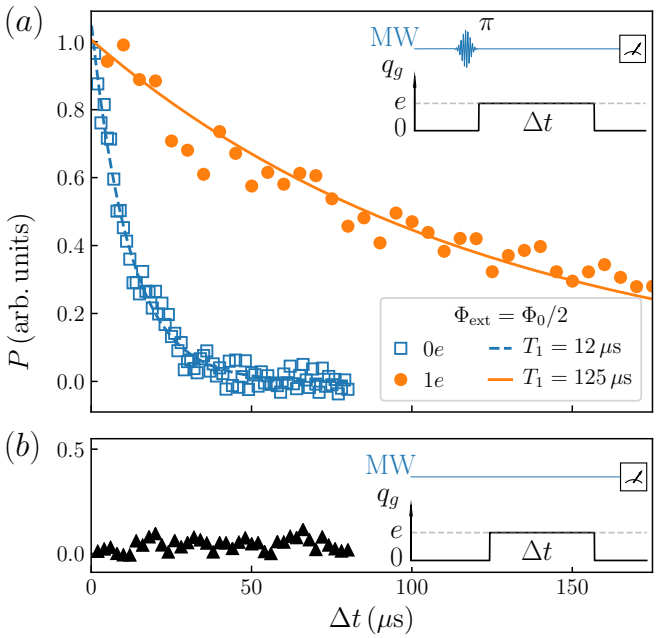

FIG. 5. (a) Measurements of the bifluxon energy relaxation in the protected state (red circles) and unprotected state (blue squares). The sequence of pulses is shown in the inset. The exponential fits are shown by solid and dashed lines, respectively. (b) Demonstration of an absence of qubit excitation by the gate voltage pulses.

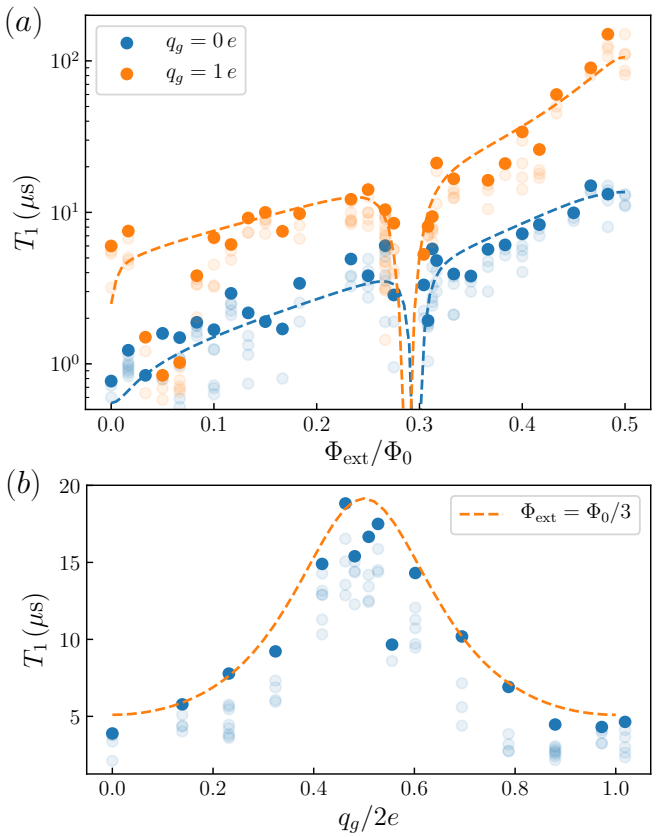

FIG. 6. Energy relaxation time T_1 as a function of the flux frustration Φ_{ext}/Φ_0 (a) and the CPB charge q_g (b). The pale dots represent all the measured data, the bright dots show the longest T_1 measured for a given operation point. The dashed lines correspond to fitting to the resistive noise theory (appendix C).

tio, reduced by weak qubit-readout coupling, is too low to employ conventional pulse protocols (decay, Rabi oscillations and Ramsey fringes). For this reason we designed special pulse sequences for T_1 and T_2 measurements in the protected regime. The pulse sequence used for probing the decay is show in Fig. 5(a). Initially the qubit is prepared in the ground unprotected state ($q_g = 0e$). A microwave π-pulse at the resonant frequency $f_{01}^{(0e)}$ excited the qubit, and then the protection is turned on by applying a pulse of the gate voltage V_g corresponding to the offset charge $q_g = 1e$. We have used V_g pulses with the rise/drop time ~ 30 ns, which is sufficiently long to ensure adiabatic evolution of the qubit between protected and unprotected states. After time Δt, the protection is removed by setting $q_g = 0$ and the qubit state is measured. As a control experiment, we apply the gate voltage pulses alone, without a π-pulse; the absence of qubit excitation proved the adiabaticity of gate manipulations, see Fig. 5(b).

The main result of this paper - the dependence of T_1 on the qubit control parameters Φ_{ext} and q_g - is presented in Fig. 6. Dashed lines represent fits to the model that takes into account resistive losses in the capacitively coupled environment and readout resonator (Purcell effect). The details of the T_1 calculations are provided in appendix C. An increase of T_1 in the protected regime by an order of magnitude provides evidence for the qubit's dipole moment suppression. The longest decay time $> 100\,\mu$s is measured at full flux frustration $\Phi_{ext} = \Phi_0/2$, which corresponds to a minimum qubit energy $f_{01}^{(1e)} = 0.4$ GHz. The routs to further increase of T_1 are discussed in Sect. IV.

Direct measurements of the decoherence time T_ϕ in the protected regime, by either Rabi or Ramsey techniques, are not feasible because of vanishing coupling of the qubit to microwave pulses. For this reason we have modified the measurements of Ramsey fringes by analogy with the aforementioned T_1 measurements. The pulse sequence is shown in Fig. 7(a). Both 30 ns long $\pi/2$ microwave pulses detuned from the qubit transition frequency by 4 MHz are applied in the unprotected state ($q_g = 0$), and the qubit is measured after the end of the second pulse. Between the $\pi/2$ pulses, while the qubit underwent free precession, the qubit's protected state is restored by applying a gate voltage pulse ($q_g = 1e$). After averaging over 1000 cycles, the Ramsey fringes are recorded by varying the delay between the end of the gate pulse and the second $\pi/2$ pulse.

Ramsey fringes measured according to this procedure for one of the flux "sweet spots" at $\Phi_{ext} = 0$ are shown in Fig. 7(b); the V_g pulse for these measurements is 0.27 μs long. The difference between the amplitudes of Ramsey

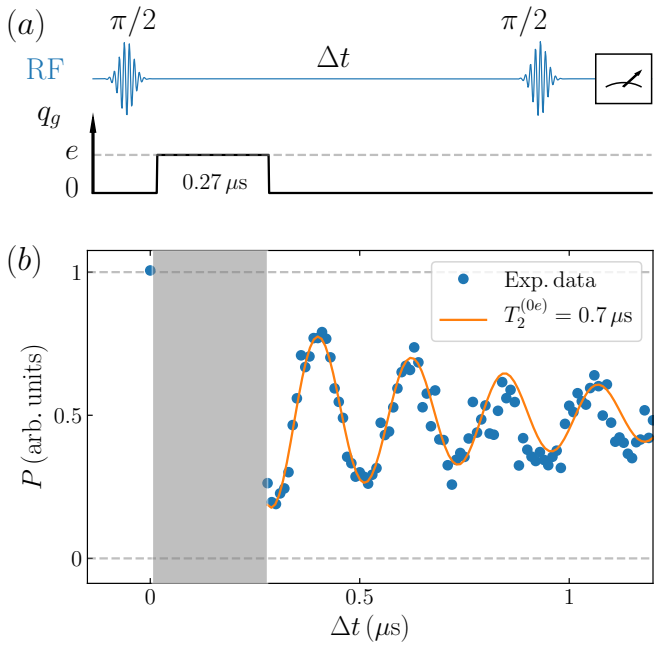

FIG. 7. The Ramsey fringes measurement. (a) The pulse protocol for T_2 evaluation in the protected state. The protection is turned on for a fixed time of 270 ns; the time delay between two $\pi/2$ pulses is varied in order to record Ramsey fringes. (b) The experimental data (dots) and the damped-oscillation fitting (the solid line). Note that the value of $T_2 = 0.7\mu s$ describes the fringe damping in the unprotected state. Damping of Ramsey fringes in the protected state ($0 < \Delta t < 270$ ns) is caused by the V_g pulse jitter rather than dephasing (see the text).

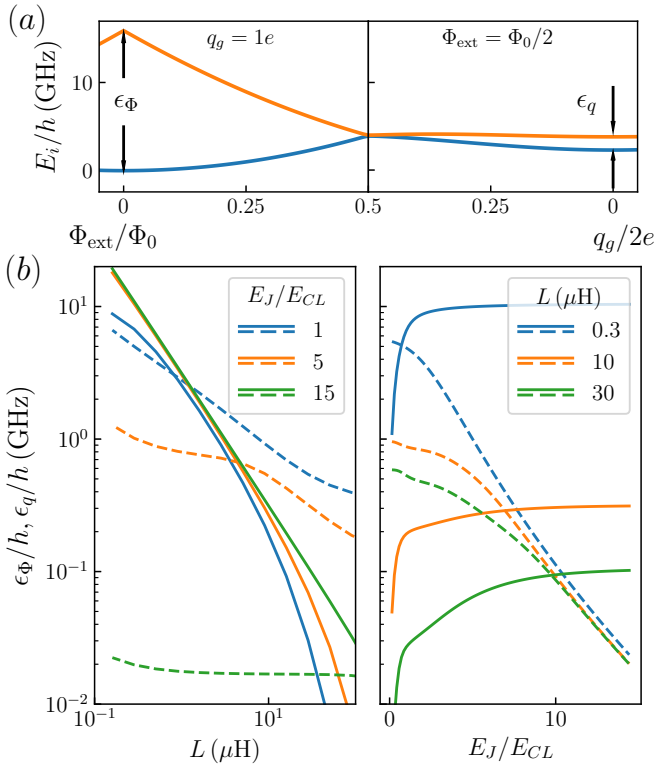

FIG. 8. (a) Two first energy levels of the bifluxon qubit as a function of detuning from degeneracy point. Energy dispersion, which leads to decoherence, can be characterized by amplitudes ϵ_Φ and ϵ_q [see Eq. (8), note that $E_{01}(\Phi_0/2, 1e) = 0$ for a symmetric device]. (b) Calculated amplitudes of the flux (solid lines) and charge (dashed lines) energy dispersion as a function of qubit parameters.

fringes at moments $\Delta t = 0, 0.27\,\mu s$ may provide information on dephasing in the protected state if this is the only source of dephasing. However, the accuracy of this technique is limited by the V_g pulse jitter. Indeed, in the rotating frame of the unprotected state, the qubit's state vector rotates in the equatorial plane of the Bloch sphere as soon as the protection is turned on. The angular velocity of these rotations, $\omega = \left(E_{01}^{(0e)} - E_{01}^{(1e)}\right)/\hbar$, is large ($\omega > 2\pi \cdot 1$GHz) at both flux sweet spots $\Phi_{ext} = 0,\ \Phi_0/2$, and even a small jitter can result in a significant error in the position of the qubit's state vector at the end of the V_g pulse. According to the specification, the jitter time of the pulse generator used in our experiments could be as large as 0.3 ns. This jitter-induced phase uncertainty alone, without invoking any dephasing in the protected state, is sufficient to explain the reduced amplitude of Ramsey fringes at $\Delta t = 0.28\,\mu s$. Thus, these measurements can impose only the lower limit on T_ϕ, which is close to $1\,\mu s$ for the data in Fig. 7(b). Future experiments with better-controlled V_g pulses of different lengths may provide a more detailed information on T_ϕ at both sweet spots.

It should be noticed that, since the state of the bifluxon qubit is governed by the CPB charge q_g, the device is sensitive to the offset charge drifts and quasiparticle poisoning of the CPB island. In order to eliminate the effect of these fluctuations, q_g is measured and, if necessary, re-adjusted to the desired value before each T_1 and T_2 measurement. For calibration, we tracked one period of the readout dispersive shift oscillations $\delta f_r(V_g)$, with minima and maxima corresponding to integer values of the CPB charge. This measurement allows us to estimate the q_g drift rate to be less than $10^{-2}e$/min, the quasiparticle tunneling is as rare as 1 event per 30 min due to the engineered difference between the superconducting gaps in the CPB island and its surroundings (see appendix D).

IV. DISCUSSION

In this section we discuss possible modifications to the bifluxon design that could enable further improvement of the qubit coherence beyond the readily available energy decay protection.

First, let us consider the fully symmetric bifluxon qubit with CPB junctions of identical Josephson energy, where charge noise can still potentially flip the fluxon parity and induce energy relaxation. As we have pointed out earlier, the absolute value of the charge dipole moment

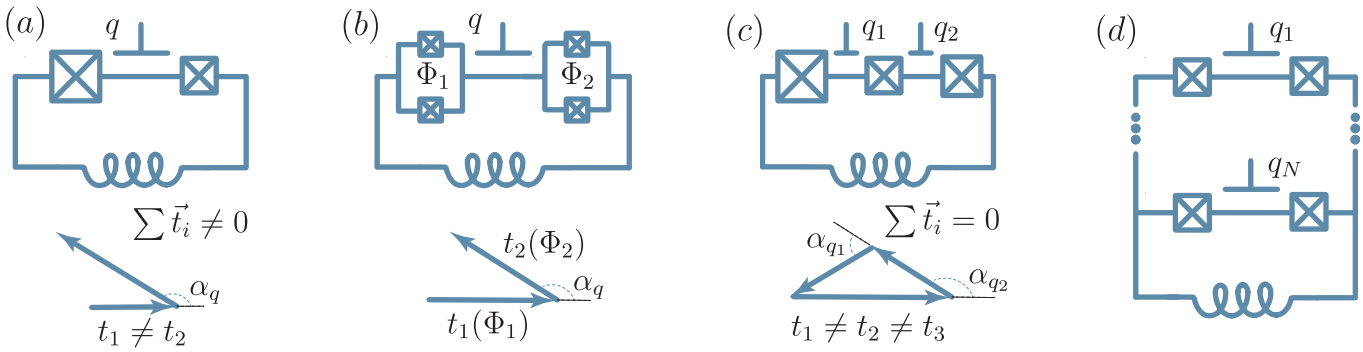

FIG. 9. Possible ways towards further coherence improvements for the bifluxon qubit. (a) Present design: The asymmetry in the JJs of the circuit leads to distinct complex tunneling amplitudes t_i, represented by the vectors at the bottom. As a result, the single phase-slip rate cannot be completely suppressed for any AC phase $\alpha_q = \pi q_g/e$. (b) Device with controllable tunneling probability: disorder of the effective Josephson energies can now be mitigated by the local SQUID frustrations Φ_1 and Φ_2. (c) Adding a second circuit island. The SPS rate can be completely suppressed even for asymmetric junctions as a zero sum of three vectors with comparable lengths. (d) Stacking of the islands into an array: gate charge $q_i = 1e$ on any CPB protects the fluxon parity in the loop, which can be used for expanding the charge sweet spot, similar to Ref. [22].

[Eq. (7)] is strongly suppressed in comparison to that of a conventional charge qubit. Thus, we find that the condition $E_J/E_{CL} > 10$, similar to the parameter regime of a heavy fluxonium qubit [5, 6], is in principle enough to achieve T_1 times in excess of 10 ms.

Although the lowest-energy states of the fully symmetric device are exactly degenerate at $\Phi_{\rm ext}/\Phi_0 = q_g/2e = 0.5$, deviations from this point open a gap in the spectrum, which leads to decoherence Fig. 8(a). A good measure of the qubit sensitivity to pure-dephasing processes is the amplitude of the charge and flux dispersion of the $0-1$ transition energy $E_{01}(\Phi_{\rm ext}, q_g)$, defined as

$$\begin{aligned} \epsilon_\Phi &= E_{01}(0, 1e) - E_{01}(\Phi_0/2, 1e), \\ \epsilon_q &= E_{01}(\Phi_0/2, 0) - E_{01}(\Phi_0/2, 1e). \end{aligned} \tag{8}$$

As it follows from Fig. 8(b), in order to mitigate dephasing due to both charge and flux noises, the optimal strategy is to combine an increase of E_J/E_{CL} with strong reduction of the inductive energy E_L. As it was mentioned above, an exponentially small flux dispersion can be achieved in the regime $E_{\rm dps} \gg 2\pi^2 E_L$. Fulfilling this condition requires the implementation of a ultrahigh-impedance superinductor with $L > 30$ μH and self-resonance frequencies > 1 GHz. Such an element with a characteristic impedance $Z > 200\,\mathrm{k}\Omega$ could be realized by using strongly disordered superconductor nanowires [31–35] or suspended chains of JJs [29].

If asymmetry between the CPB junctions is present, the SPS amplitude remains non-zero for any charge on the CPB island [Fig. 9(a)]. This leads to mixing of the bifluxon states with different parity and increased susceptibility to flux noise. One of the ways to recover the symmetry is to replace the junctions with SQUIDs of a size much smaller than the bifluxon loop area [see Fig. 9(b)]. This would allow for changing the SQUID's Josephson energy without affecting the optimal flux in the device loop. Alternatively, the SPS can be completely suppressed by introducing a third Josephson junction and an additional gate control line. Indeed, by independently controlling charges on two CPB islands, the SPS amplitude can be tuned to zero [Fig. 9(c)].

The sensitivity of a tunable qubit to fluctuations of a control parameter – the offset charge in our particular case – is the price to pay for the ability to turn on and off the qubit protection and thus facilitate the gate operations. This sensitivity could be suppressed by combining several qubits in a small array [19], as it has been demonstrated for the rhombi qubit in Ref. [22]. In a chain of symmetric Josephson rhombi qubits, the transport of single Cooper pairs is forbidden when $\Phi_{\rm ext} = \Phi_0/2$ for any rhombus in the chain. Accordingly, the range of values of $\Phi_{\rm ext}$ where the qubit is protected (i.e. the size of the sweet spot) increases polynomially with the number of rhombi elements in the chain. Similarly, a bifluxon qubit made of a small parallel array of CPBs, as shown in Fig. 9(d), is expected to demonstrate a wider range of q_g tunability for which the $|g\rangle$ and $|e\rangle$ states remain generate. Realization of such an array would lead to further increase of both the decay and dephasing times beyond the coherence times measured for our proof-of-principle bifluxon-qubit design.

V. CONCLUSION

In this work we have developed and characterized a quantum superconducting circuit which serves as a platform for the realization of protected qubits with simultaneous exponential suppression of energy decay from charge and flux noise, and dephasing from flux noise. The circuit is realized as a superconducting loop containing a charge-sensitive Josephson element (a.k.a. Cooper-pair box) and a superinductor. This circuit with two control parameters - the charge on the CPB island and the magnetic flux in the loop - is described by a "two-

dimensional" Hamiltonian. Its dimensionality $D > 1$ is critical to simultaneous suppression of decay and dephasing via localization of the qubit's wavefunctions in disparate regions of the phase space. The ability to turn the protection on and off by controlling the charge on the CPB island facilitates gate operations with protected qubits. By switching the protection on, we observed a ten-fold increase of the decay time, up to $100\,\mu$s. The studied circuit was not expected to demonstrate a long dephasing time because of its sensitivity to fluctuations of charge on the CPB island. However, the bifluxon sensitivity to charge noise is much reduced in comparison with the charge qubit, and the charge-noise-induced dephasing time in the protected state exceeded $1\,\mu$s. Further improvement of the coherence times can be achieved in the next-generation devices by the optimization of their parameters and combining several $\cos(\phi/2)$ elements in a small array.

ACKNOWLEDGMENTS

We would like to thank Elio König, Yashar Komijani, Lev Ioffe and Vladimir Manucharyan for helpful discussions. The work at Rutgers University was supported in part by the NSF awards DMR-1708954, DMR-1838979, and the ARO award W911NF-17-C-0024. The work at the University of Massachusetts Boston was supported in part by a 2019 Google Faculty Research Award and NSF Awards ECCS-1608448, DUE-1723511 and DMR-1838979. The work at the Université of Sherbrooke was supported in part by the NSERC and the Canada First Research Excellence Fund.

Appendix A: Derivation of the circuit Hamiltonian

In this section, we derive a Hamiltonian for the circuit that includes both the bifluxon qubit and the readout resonator of capacitance C_R and inductance L_R (Fig. 10). Assuming that the phase difference across the inductor shared by the readout resonator and the bifluxon $L_{\rm sh} \ll L$ is negligible with respect to the total phase drop across the superinductor (see below), we can write an effective circuit Lagrangian of the form

$$\begin{aligned}\mathscr{L} = {}& \frac{C_0}{2}(\dot\Phi_a^2+\dot\Phi_b^2) + \frac{C_{0_g}}{2}\dot\Phi^2 + \frac{C_g}{2}(\dot\Phi - V_g)^2 \\ & + \frac{C_J}{2}[(\dot\Phi-\dot\Phi_a)^2 + (\dot\Phi-\dot\Phi_b)^2] - \frac{1}{2L}(\Phi_a - \Phi_b + \Phi_{\rm ext})^2 \\ & + E_J\Big\{\cos\Big[\frac{2\pi}{\Phi_0}(\Phi-\Phi_a)\Big] + \cos\Big[\frac{2\pi}{\Phi_0}(\Phi-\Phi_b)\Big]\Big\} \\ & + \frac{C_R}{2}\dot\Phi_r^2 - \frac{1}{2L_R}(\Phi_r - \Delta\Phi)^2 + \frac{C_{\Delta\Phi}}{2}\Delta\dot\Phi^2 - \frac{1}{2L_{\rm sh}}\Delta\Phi^2,\end{aligned} \tag{A1}$$

where Φ, Φ_a and Φ_b are the circuit flux node variables, Φ_r and $\Delta\Phi$ are flux branch variables, $\Phi_{\rm ext}$ is the external flux through the bifluxon-qubit loop, V_g is the gate voltage,

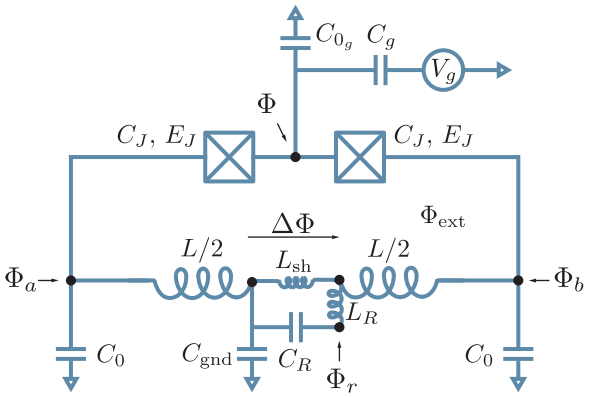

FIG. 10. Schematic diagram of the bifluxon device including the readout resonator, and the gate and stray ground capacitances $(C_0, C_{0_g}, C_{\rm gnd})$. V_g denotes the gate voltage that controls the offset charge n_g^φ. $\Delta\Phi/\varphi_0$ is the phase drop across the inductance $L_{\rm sh}$, which is shared between the qubit and the resonator.

and $C_{\Delta\Phi}$ is an effective capacitance for the $\Delta\Phi$ mode. A more convenient basis to treat the qubit Hamiltonian is given by the modes $\Phi_- = \Phi_b - \Phi_a$ and $\Phi_+ = \Phi_b + \Phi_a$, in terms of which Eq. (A1) reads

$$\begin{aligned}\mathscr{L} = {}& \frac{C_{0_c}+C_g+2C_J}{2}\dot\Phi^2 + \frac{C_0+C_J}{4}(\dot\Phi_-^2+\dot\Phi_+^2) \\ & - C_J\dot\Phi\dot\Phi_+ - C_g\dot\Phi V_g - \frac{1}{2L}(\Phi_- - \Phi_{\rm ext})^2 \\ & + 2E_J\cos\Big[\frac{2\pi}{\Phi_0}\frac{\Phi_-}{2}\Big]\cos\Big[\frac{2\pi}{\Phi_0}\Big(\Phi - \frac{\Phi_+}{2}\Big)\Big] \\ & + \frac{C_R}{2}\dot\Phi_r^2 - \frac{1}{2L_R}(\Phi_r-\Delta\Phi)^2 + \frac{C_{\Delta\Phi}}{2}\Delta\dot\Phi^2 - \frac{1}{2L_{\rm sh}}\Delta\Phi^2.\end{aligned} \tag{A2}$$

Since $\Delta\Phi$ is a high-frequency and low-impedance mode, it is assumed to be locked to the semiclassical value $\Delta\Phi \to L_{\rm sh}\Phi_-/(L+L_{\rm sh}) \simeq L_{\rm sh}\Phi_-/L$. Substituting this in Eq. (A2), and performing a Legendre transformation, we arrive at the effective circuit Hamiltonian

$$\begin{aligned}H = {}& 4E_{C_\varphi}(n_\varphi - n_g^\varphi)^2 + 4E_{C_\phi}n_\phi^2 + 4E_{C_{\phi_+}}n_{\phi_+}^2 \\ & - 2E_J\cos(\phi/2)\cos(\varphi-\phi_+/2) + \frac{E_L}{2}(\phi-\varphi_{\rm ext})^2 \\ & + \hbar g_{\varphi\phi_+}n_\varphi n_{\phi_+} + \hbar\omega_R a^\dagger a + \eta_{\rm sh}E_L\phi_r\phi\end{aligned} \tag{A3}$$

where we have defined the phase variables $\varphi = \Phi/\varphi_0$, $\phi = \Phi_-/\varphi_0$ and $\phi_+ = \Phi_+/\varphi_0$, the respective conjugate charge operators n_φ, n_ϕ and n_{ϕ_+}, and the charging energies $E_{C_\mu} = e^2/2C_\mu$ for $\mu \in [\varphi, \phi, \phi_+]$ in terms of the mode capacitances

$$\begin{aligned}C_\varphi &= C^2/(C_0+C_J) \\ C_\phi &= (C_0+C_J)/2 \\ C_{\phi_+} &= C^2/2(C_{0_g}+C_g+2C_J),\end{aligned} \tag{A4}$$

with $C^2 = (C_{0_g}+C_g)C_J + C_0(C_{0_g}+C_g+2C_J)$. Note that we neglect a small renormalization of the capacitance of

the ϕ mode due to $C_{\Delta\Phi}$. We also introduce an effective coupling constant $\hbar g_{\varphi\phi_+} = e^2/2C_{\varphi\phi_+}$ where $C_{\varphi\phi_+} = C^2/(16C_J)$, and the offset charge $n_g^\varphi = -\beta_\varphi \frac{2eV_g}{8E_{C_\varphi}}$ with $\beta_\varphi = C_g/C_\varphi$. The resonator Hamiltonian is written in terms of its resonance frequency ω_R and the ladder operators $(a, a^\dagger)$, and we define the inductive participation ratio $\eta_{\rm sh} = L_{\rm sh}/L_R$ that quantifies the coupling between the bifluxon qubit and the resonator.

We assume that ϕ_+ is a high-frequency mode detuned away from the qubit transitions of interest [36]. Under this approximation, the coupling $g_{\varphi\phi_+}$ leads to a small dispersive shift which, however, is not needed to describe the experimental data of the device studied in this work. Under these assumptions, Eq. (A3) reduces to a model of a two-dimensional (φ, ϕ) qubit Hamiltonian coupled to the resonator mode ϕ_r, which we use in the main text.

Finally, in order to account for the effect of circuit-element disorder on the circuit junctions, we derive a perturbative correction to Eq. (A3) of the form

$$\delta H = \Delta E_J \sin(\phi/2)\sin(\varphi - \phi_+/2) \tag{A5}$$

where $\Delta E_J = E_{Ja} - E_{Jb}$ is the junction asymmetry, defined in terms of the junction energies E_{Ja} and E_{Jb}, and $\bar{E}_J = (E_{Ja} + E_{Jb})/2$. Note that the replacement $E_J \to \bar{E}_J$ in Eq. (A3) should also be made.

Appendix B: Integer charge on the island $n_g = N$

Let us consider the reduced Hamiltonian Eq. (2) for the case of an integer charge n_g on the CPB island. In the limit $E_C \gg E_J$, we can restrict the analysis to two charge states. The matrix representation of the Hamiltonian then reads

$$H = \begin{pmatrix} \mathbb{A} + \mathbb{C} & -\mathbb{B} \\ -\mathbb{B} & \mathbb{A} - \mathbb{C} \end{pmatrix}, \tag{B1}$$

where

$$\begin{aligned} \mathbb{A} &= -4E_{CL}\partial_\phi^2 + \frac{E_L}{2}(\phi - \varphi_{\rm ext})^2, \\ \mathbb{B} &= E_J \cos(\phi/2), \\ \mathbb{C} &= 2E_C. \end{aligned} \tag{B2}$$

If $\mathbb{C}$ is the dominant term in Eq. (B1), the charge component of the lowest energy eigenvector is close to a pure $|N\rangle$ state

$$|\psi^n\rangle = \begin{pmatrix} \alpha \\ 1 \end{pmatrix}, \tag{B3}$$

for $\alpha \ll 1$. The eigenvalue

$$\mathbb{E} = \mathbb{A} - \sqrt{\mathbb{C}^2 + \mathbb{B}^2} \approx \mathbb{A} - \mathbb{C} - \frac{\mathbb{B}^2}{2\mathbb{C}}, \tag{B4}$$

corresponds to a fluxonium-like Hamiltonian of the form

$$H = -4E_{CL}\partial_\phi^2 + \frac{1}{2}E_L(\phi - \varphi_{\rm ext})^2 - E_J^* \cos\phi, \tag{B5}$$

where $E_J^* = E_J^2/4E_C$ is a renormalized Josephson energy.

Appendix C: Coupling to the environment and decoherence

In this section, we consider the coupling of the qubit modes to environmental sources of noise, and derive the relaxation rates that are used in the main text to fit T_1. Figure 11 illustrates the coupling of the bifluxon qubit to external (noisy) degrees of freedom.

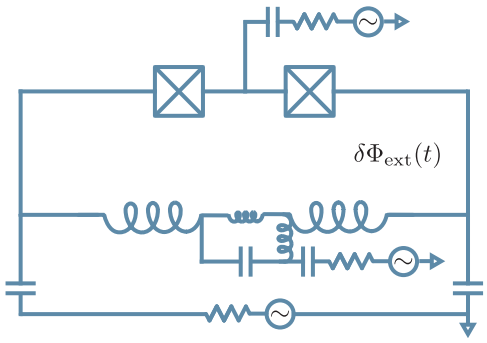

FIG. 11. Bifluxon device coupled to environmental degrees of freedom leading to decoherence. The resistors model dissipative circuit elements coupled capacitively to the qubit. $\delta\Phi_{\rm ext}(t)$ represents the magnetic flux fluctuations.

Charge-induced decay occurs due to coupling of the Cooper-pair-box variable (φ) to the environment, mainly via the voltage line that is used to control n_g^φ. The coupling Hamiltonian is of the form $\delta H = 2en_\varphi\beta_\varphi\Delta V$, where ΔV is a voltage-noise operator leading to fluctuations of the offset charge. Using the Fermi's golden rule, we derive the transition rate $\Gamma = |\langle 0|2en_\varphi\beta_\varphi|1\rangle|^2 S_V(\omega_{01})/\hbar^2 \equiv 1/T_1$, where $S_V(\omega_{01})$ is the noise spectral density evaluated at the qubit transition frequency. Denoting the impedance of the environment coupled to the qubit port as $Z(\omega)$ and assuming an Ohmic spectral density of the form $S_V(\omega) = \hbar\omega {\rm Re}[Z(\omega)]\left[1 + \coth\left(\frac{\hbar\omega}{2k_BT}\right)\right]$ [37], we arrive at the expression

$$\frac{1}{T_1} = \beta_\varphi^2 |\langle 0|n_\varphi|1\rangle|^2 r_{\rm env}\,\omega_{01}\left[1 + \coth\left(\frac{\hbar\omega_{01}}{2k_BT}\right)\right], \tag{C1}$$

where $r_{\rm env} = {\rm Re}[Z(\omega_{01})]/R_K$ is the effective resistance of the electromagnetic environment in units of the reduced superconducting quantum of resistance, $R_K = \hbar/(2e)^2 \simeq 1\,{\rm k}\Omega$.

Coupling of noise to the fluxonium-like degree of freedom (ϕ) can be treated similarly. Instead of rewriting Eq. (C1) for n_ϕ, however, we derive an expression that involves the transition matrix elements of the phase operator. This is useful for the discussion of results in the main text. As a consequence of the commutation relation $[\phi, n_\phi] = i$, $[\phi, H] = i8E_{C_\phi}n_\phi$ and thus $\hbar\omega_{01}\langle 0|\phi|1\rangle = i8E_{C_\phi}\langle 0|n_\phi|1\rangle$ [38]. This relation allows us to rewrite Eq. (C1) as

$$\frac{1}{T_1} = \beta_\phi^2 |\langle 0|\phi|1\rangle|^2 r_{\rm env}\left(\frac{\hbar\omega_{01}}{8E_{C_\phi}}\right)^2 \omega_{01}\left[1 + \coth\left(\frac{\hbar\omega_{01}}{2k_BT}\right)\right]. \tag{C2}$$

In order to fit T_1, we require the two parameters $\beta_{\varphi,\phi}$ and $r_{\rm env}$ to be small compared to unity. Moreover, the parameter $r_{\rm env}$ could in principle have different values in Eq. (C1) and Eq. (C2), because the environment impedance can be different as measured from the multiple qubit ports.

Finally, we discuss Purcell decay due to coupling of the qubit to the readout resonator. We account for this effect by using a simple model that takes Eq. (A3) into consideration. Rewriting the qubit-resonator coupling as $\delta H = \eta_{\rm sh} E_L \phi \sqrt{z_r/2}(a + a^\dagger)$, where $z_r = Z_r/R_K$ is the reduced impedance of the resonator, we follow Ref. [17] to arrive at

$$\frac{1}{T_{1\rm P}} = \eta_{\rm sh}^2 \frac{z_r}{2} \frac{\omega_r}{Q_r} \frac{(E_L/\hbar)^2}{|\omega_{01} - \omega_r|^2}, \qquad \text{(C3)}$$

where Q_r is the quality factor of the readout resonator. As expected, the Purcell rate has a significant contribution to T_1 only close to the readout resonance frequency (see Fig. 6). Away from this very narrow frequency range, we find that the qubit relaxation time is very well described by the sum of the two contributions in Eq. (C1) and Eq. (C2).

Appendix D: Gap engineering for mitigation of quasiparticle poisoning

Quasiparticle poisoning (QP) presents a problem for charge-sensitive quantum superconducting devices [39, 40]. In particular, for a bifluxon qubit in a protected state, tunneling of a non-equilibrium quasiparticle into/out of the CPB island would remove protection. To minimize QP, we used the so-called gap engineering [41, 42]. Figure 12(a) shows the superconducting gap in the CPB island and the outer electrodes that form the CPB Josephson junctions. Because of the dependence of the critical temperature of Al films on their thickness, the gap in the thin (20 nm) CPB island is greater than that in thicker (60 nm) outer electrodes. This difference $\delta\Delta$, which we estimate to be $\sim (0.3 - 0.4)K$, is sufficiently large to block tunneling of non-equilibrium quasiparticles with energies greater than $\delta\Delta$ onto the CPB island at sufficiently low temperatures.

The efficiency of this technique is demonstrated in Figs. 12(b)-(d). If both the CPB island and outer electrodes are thick ($\delta\Delta \simeq 0$), we observe a characteristic "eye" pattern [41] in the spectroscopic measurements, which reflects rapid $\pm e$ jumps of the CPB charge on the timescale of a single scan of the resonance of the readout resonator, see Fig. 12(b). This pattern vanishes if the gap engineering is employed and re-appears only at higher temperatures, where the quasiparticles are thermally excited in the CPB island [compare panels (c) and (d) of Fig. 12]. Gap engineering and careful infrared and magnetic shielding of the device allowed us to increase the time intervals between the QP events up to 30 mins. Figure 12(e) shows that, in addition to rare QP events,

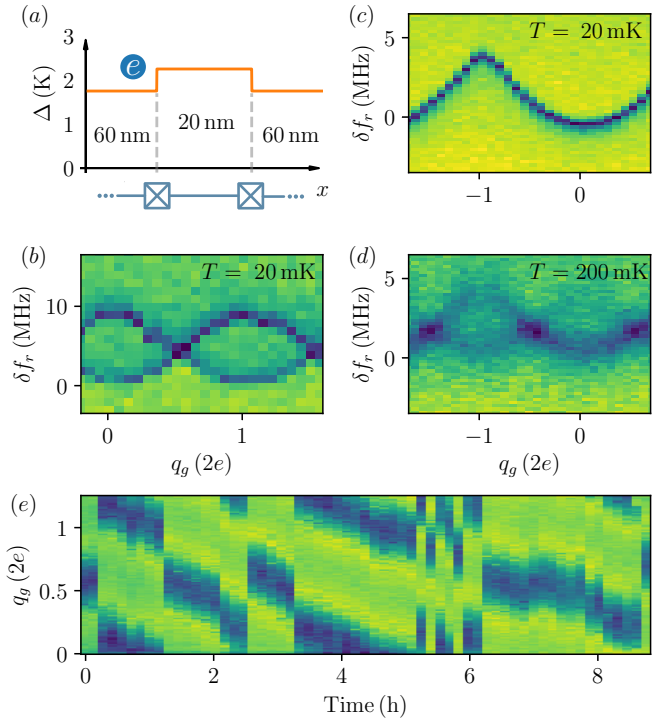

FIG. 12. Suppression of quasiparticle poisoning by gap engineering. (a) Profile of the superconducting gap across the CPB island. The critical temperature of the thin CPB island is by $0.2 - 0.3\,$K higher than that in the thicker electrodes. (b)-(d) Spectroscopy of the read-out resonator as a function of q_g for bifluxon qubits: without gap modulation at 20 mK (b), and with gap modulation at (c) 20 mK and 200 mK (d). (e) The dispersive shift δf_r of the readout resonator (color-coded), measured at a fixed gate voltage V_g over 9 hours. The shift δf_r is converted into δq_g using the data of panel (c). Abrupt jumps reflect the QP events ($\delta q_g = \pm e$), gradual shift corresponds to a monotonic drift of q_g with the rate $< 10^{-2} e$/min.

we observed slow monotonic drift of q_g whose origin remains unclear. Because of this drift, we had to measure (and, if necessary, re-adjust) q_g before each time-domain measurement.

[1] M. Kjaergaard, M. E. Schwartz, J. Braumüller, P. Krantz, J. I.-J. Wang, S. Gustavsson, and W. D. Oliver, "Superconducting qubits: Current state of play," arXiv:1905.13641 (2019).

[2] M. H. Devoret and R. J. Schoelkopf, "Superconducting circuits for quantum information: an outlook," Science

339, 1169–1174 (2013).
[3] J. Preskill, "Quantum computing in the NISQ era and beyond," Quantum **2**, 79 (2018).
[4] C. Müller, J. H. Cole, and J. Lisenfeld, "Towards understanding two-level-systems in amorphous solids - insights from quantum devices," arXiv:1705.01108 (2017).
[5] N. Earnest, S. Chakram, Y. Lu, N. Irons, R. K. Naik, N. Leung, L. Ocola, D. A. Czaplewski, B. Baker, J. Lawrence, J. Koch, and D.I. Schuster, "Realization of a λ system with metastable states of a capacitively shunted fluxonium," Phys. Rev. Lett **120**, 150504 (2018).
[6] Y.-H. Lin, L. B. Nguyen, N. Grabon, J. San Miguel, N. Pankratova, and V. E. Manucharyan, "Demonstration of protection of a superconducting qubit from energy decay," Phys. Rev. Lett **120**, 150503 (2018).
[7] D. Vion, A. Aassime, A. Cottet, P. Joyez, H. Pothier, C. Urbina, D. Esteve, and M. H. Devoret, "Manipulating the quantum state of an electrical circuit," Science **296**, 886–889 (2002).
[8] A. A. Houck, J. Koch, M. H. Devoret, S. M. Girvin, and R. J. Schoelkopf, "Life after charge noise: recent results with transmon qubits," Quantum Inf. Process. **8**, 105–115 (2009).
[9] J. Koch, T. M. Yu, J. Gambetta, A. A. Houck, D. I. Schuster, J. Majer, A. Blais, M. H. Devoret, S. M. Girvin, and R. J. Schoelkopf, "Charge-insensitive qubit design derived from the Cooper pair box," Phys. Rev. A **76**, 042319 (2007).
[10] M. Brink, J. M. Chow, J. Hertzberg, E. Magesan, and S. Rosenblatt, "Device challenges for near term superconducting quantum processors: frequency collisions," (IEEE, 2018) pp. 6–1.
[11] W. C. Smith, A. Kou, X. Xiao, U. Vool, and M. H. Devoret, "Superconducting circuit protected by two-Cooper-pair tunneling," arXiv:1905.01206 (2019).
[12] A. Kitaev, "Protected qubit based on a superconducting current mirror," arXiv:cond-mat/0609441 (2006).
[13] M. T. Bell, J. Paramanandam, L. B. Ioffe, and M. E. Gershenson, "Protected Josephson rhombus chains," Phys. Rev. Lett **112**, 167001 (2014).
[14] J. M. Dempster, B. Fu, D. G. Ferguson, D. I. Schuster, and J. Koch, "Understanding degenerate ground states of a protected quantum circuit in the presence of disorder," Phys. Rev. B **90**, 094518 (2014).
[15] A. Kou, W. C. Smith, U. Vool, R. T. Brierley, H. Meier, L. Frunzio, S. M. Girvin, L. I. Glazman, and M. H. Devoret, "Fluxonium-based artificial molecule with a tunable magnetic moment," Phys. Rev. X **7**, 031037 (2017).
[16] P. Brooks, A. Kitaev, and J. Preskill, "Protected gates for superconducting qubits," Phys. Rev. A **87**, 052306 (2013).
[17] P. Groszkowski, A. Di Paolo, A. L. Grimsmo, A. Blais, D. I. Schuster, A. A. Houck, and J. Koch, "Coherence properties of the 0-π qubit," New J. Phys. **20**, 043053 (2018).
[18] A. Di Paolo, A. L. Grimsmo, P. Groszkowski, J. Koch, and A. Blais, "Control and coherence time enhancement of the 0–π qubit," New J. Phys. **21**, 043002 (2019).
[19] B. Douçot and L. B. Ioffe, "Physical implementation of protected qubits," Rep. Prog. Phys. **75**, 072001 (2012).
[20] B. Douçot and J. Vidal, "Pairing of Cooper pairs in a fully frustrated Josephson-junction chain," Phys. Rev. Lett **88**, 227005 (2002).
[21] A. R. Klots and L. B. Ioffe, "Set of holonomic and protected gates on topological qubits for realistic quantum computer," arXiv:1907.04379 (2019).
[22] S. Gladchenko, D. Olaya, E. Dupont-Ferrier, B. Douçot, L. B. Ioffe, and M. E. Gershenson, "Superconducting nanocircuits for topologically protected qubits," Nat. Phys. **5**, 48 (2009).
[23] J. R. Friedman and D. V. Averin, "Aharonov-Casher-effect suppression of macroscopic tunneling of magnetic flux," Phys. Rev. Lett **88**, 050403 (2002).
[24] M. T. Bell, W. Zhang, L. B. Ioffe, and M. E. Gershenson, "Spectroscopic evidence of the Aharonov-Casher effect in a Cooper pair box," Phys. Rev. Lett **116**, 107002 (2016).
[25] S. E. De Graaf, S. T. Skacel, T. Hönigl-Decrinis, R. Shaikhaidarov, H. Rotzinger, S. Linzen, M. Ziegler, U. Hübner, H.-G. Meyer, V. Antonov, and O. V. Astafiev, "Charge quantum interference device," Nat. Phys. **14**, 590 (2018).
[26] I. M. Pop, I. Protopopov, F. Lecocq, Z. Peng, B. Pannetier, O. Buisson, and W. Guichard, "Measurement of the effect of quantum phase slips in a Josephson junction chain," Nat. Phys. **6**, 589 (2010).
[27] O. Astafiev, Yu. A. Pashkin, Y. Nakamura, T. Yamamoto, and J.-S. Tsai, "Quantum noise in the Josephson charge qubit," Phys. Rev. Lett **93**, 267007 (2004).
[28] M. T. Bell, I. A. Sadovskyy, L. B. Ioffe, A. Yu. Kitaev, and M. E. Gershenson, "Quantum superinductor with tunable nonlinearity," Phys. Rev. Lett **109**, 137003 (2012).
[29] I. V. Pechenezhskiy, R. A. Mencia, L. B. Nguyen, Y.-H. Lin, and V. E. Manucharyan, "Quantum dynamics of quasicharge in an ultrahigh-impedance superconducting circuit," arXiv:1907.02937 (2019).
[30] D. M. Pozar, Microwave engineering (John Wiley & Sons, 2009).
[31] W. Zhang, K. Kalashnikov, W.-S. Lu, P. Kamenov, T. DiNapoli, and M. E. Gershenson, "Microresonators fabricated from high-kinetic-inductance aluminum films," Phys. Rev. Applied **11**, 011003 (2019).
[32] H. Rotzinger, S. T. Skacel, M. Pfirrmann, J. N. Voss, J. Münzberg, S. Probst, P. Bushev, M. P. Weides, A. V. Ustinov, and J. E. Mooij, "Aluminium-oxide wires for superconducting high kinetic inductance circuits," Supercond. Sci. Tech. **30**, 025002 (2016).
[33] P. C. J. J. Coumou, E. F. C. Driessen, J. Bueno, C. Chapelier, and T. M. Klapwijk, "Electrodynamic response and local tunneling spectroscopy of strongly disordered superconducting tin films," Phys. Rev. B **88**, 180505(R) (2013).
[34] D. Niepce, J. Burnett, and J. Bylander, "High kinetic inductance NbN nanowire superinductors," Phys. Rev. Applied **11**, 044014 (2019).
[35] P. Kamenov, W.-S. Lu, K. Kalashnikov, T. DiNapoli, M. T. Bell, and M. E. Gershenson, "Granular aluminum meandered superinductors for quantum circuits," arXiv:1910.00996 (2019).
[36] T. M. Hazard, A. Gyenis, A. Di Paolo, A. T. Asfaw, S. A. Lyon, A. A. H. A. Blais, and A. A. Houck, "Nanowire superinductance fluxonium qubit," Phys. Rev. Lett **122**, 010504 (2019).
[37] M. H. Devoret, "Quantum fluctuations in electrical circuits," Les Houches, Session LXIII **7** (1995).
[38] V. E. Manucharyan, Superinductance, Ph.D. thesis, Yale University (2012).
[39] J. Aumentado, M. W. Keller, J. M. Martinis, and M. H.

Devoret, "Nonequilibrium quasiparticles and 2e periodicity in single-Cooper-pair transistors," Phys. Rev. Lett **92**, 066802 (2004).

[40] D. Rainis and D. Loss, "Majorana qubit decoherence by quasiparticle poisoning," Phys. Rev. B **85**, 174533 (2012).

[41] L. Sun, L. DiCarlo, M. D. Reed, G. Catelani, L. S. Bishop, D. I. Schuster, B. R. Johnson, G. A. Yang, L. Frunzio, L. Glazman, M. H. Devoret, and R. J. Schoelkopf, "Measurements of quasiparticle tunneling dynamics in a band-gap-engineered transmon qubit," Phys. Rev. Lett **108**, 230509 (2012).

[42] N. A. Court, A. J. Ferguson, R. Lutchyn, and R. G. Clark, "Quantitative study of quasiparticle traps using the single-Cooper-pair transistor," Phys. Rev. B **77**, 100501(R) (2008).

Appendix B

Variational quantum simulation of ultrastrong light-matter coupling

Variational Quantum Simulation of Ultrastrong Light-Matter Coupling

Agustin Di Paolo,[1] Panagiotis Kl. Barkoutsos,[2] Ivano Tavernelli,[2] and Alexandre Blais[1,3]

[1] *Institut quantique and Département de Physique, Université de Sherbrooke, Sherbrooke J1K 2R1 QC, Canada*

[2] *IBM Research GmbH, Zurich Research Laboratory, Säumerstrasse 4, 8803 Rüschlikon, Switzerland.*

[3] *Canadian Institute for Advanced Research, Toronto, ON, Canada*

(Dated: September 20, 2019)

We propose the simulation of quantum-optical systems in the ultrastrong-coupling regime using a variational quantum algorithm. More precisely, we introduce a short-depth variational form to prepare the groundstate of the multimode Dicke model on a quantum processor and present proof-of-principle results obtained via cloud access to an IBM device. We moreover provide an algorithm for characterizing the groundstate by Wigner state tomography. Our work is a first step towards digital quantum simulation of quantum-optical systems with potential applications to the spin-boson, Kondo and Jahn-Teller models.

Quantum simulation is one of the most prominent applications of quantum processors for solving problems in quantum physics and chemistry. Importantly, quantum simulation aims to circumvent the limited capabilities of classical computers to represent quantum states in exponentially large Hilbert spaces. Recently, a hybrid, quantum-classical simulation paradigm exploiting quantum variational principles has been introduced [1]. Following this pioneering work, many other realizations of what is known as Variational Quantum Algorithm (VQA) have appeared in the literature [2–5].

VQAs have been shown to have some robustness against noise and thus appear appropriate for the current generation of Noise-Intermediate-Scale-Quantum (NISQ) processors [4, 6, 7]. Although considerable effort has been devoted to solving proof-of-principle instances of problems in quantum chemistry [2–5] and optimization [8], the general applicability of this approach to other domains in physics is still a subject of debate and interest [9, 10]. Here, we use a VQA to simulate strongly interacting light-matter models. In particular, we focus on obtaining the groundstate of a set of two-level atoms coupled to electromagnetic modes, which is of fundamental interest and has practical applications for example for quantum-information processing and sensing [11–15].

The simplest case corresponds to that of a two-level atom coupled to a cavity mode and is described by the quantum Rabi Hamiltonian

$$H/\hbar = \frac{\omega_q}{2}\sigma^z + \omega_c a^\dagger a + g\sigma^x(a + a^\dagger). \tag{1}$$

Here, ω_q and ω_c are the atomic and the electromagnetic-mode frequencies, σ^μ ($\mu = x, y, z$) the Pauli matrices and a ($a^\dagger$) the annihilation (creation) operator for the oscillator, respectively. If the light-matter coupling constant, g, is small compared to the systems' frequencies, Eq. (1) reduces to the Jaynes-Cummings Hamiltonian [16]. Under these conditions, the terms $\sigma^+ a$ and $\sigma^- a^\dagger$, where $\sigma^\pm = (\sigma^x \pm i\sigma^y)/2$, lead to an exchange of a single excitation between the atom and the oscillator mode. Provided that g is greater than the decoherence rates of the atom and the cavity, this regime of light-matter interaction is referred to as strong coupling, and it is widely exploited for quantum-information processing purposes [17].

As g approaches a significant fraction of the bare atom and cavity frequencies, or becomes the largest energy scale in Eq. (1), the atom-cavity system enters the ultrastrong- (USC) and deep-strong-coupling (DSC) regimes, respectively [11, 14, 15, 18, 19]. In these cases, the presence of the counter-rotating terms ($\sigma^+ a^\dagger$ and $\sigma^- a$) in Eq. (1) needs to be taken into account. Perturbation theory provides an accurate description for coupling strengths in the range of $10\% - 30\%$ of the system's frequencies, but has limited applicability beyond that regime [14]. While an exact analytical solution in principle exists for Eq. (1) [20], larger systems involving multiple atoms and/or electromagnetic modes can only be handled numerically.

In the large-g limit, however, the mean cavity-mode occupation number and its quantum fluctuations are large and a sizable Fock space is required for numerical simulations. The total Hilbert-space dimension can thus quickly become unpractical for many-particle systems. This fact motivates the search for powerful analytical and numerical methods [11–13, 21–24] and quantum-simulation algorithms [14, 15, 19, 25–27] for this problem.

We consider the generalization of Eq. (1) to N atoms and M electromagnetic modes, given by

$$H/\hbar = \sum_{i=1}^{N} \frac{\omega_{qi}}{2}\sigma_i^z + \sum_{k=1}^{M} \omega_k a_k^\dagger a_k + \sum_{i=1}^{N}\sum_{k=1}^{M} g_{ik}\sigma_i^x(a_k + a_k^\dagger), \tag{2}$$

where the constants $\{g_{ik}\}$ quantify the coupling strength between the i^{th} atom (of frequency ω_{q_i}) and the k^{th} cavity mode (of frequency ω_k) referred below to as k-mode. For $M = 1$, Eq. (2) reduces to the Dicke model, while the special case $N = 1$ corresponds to the multimode quantum Rabi model. Digital quantum simulation of such models requires the encoding of the bosonic modes into qubit registers. We choose to use a Single-

Excitation-Subspace (SES) encoding, in which the Fock space of a given k-mode is truncated to a maximum photon number $n_k^{\max}$, and represented by a qubit register of size $n_k^{\max}+1$ [28–31]. A mapping from the k-mode Fock space to the single-excitation subspace of the qubit register is then defined as $|n_k\rangle \to |\tilde{n}_k\rangle = |0_0 \dots 0_{n_k-1} 1_{n_k} 0_{n_k+1} \dots 0_{n_k^{\max}}\rangle$ for $n_k \in [0, n_k^{\max}]$, where the tilde is used hereafter to indicate encoded states and operators. Importantly, under SES encoding, quadratic bosonic Hamiltonians lead to next-neighbor interactions at most [28]. Indeed, the k-mode annihilation operator maps to $a_k \to \tilde{a}_k = \sum_{n_k=0}^{n_k^{\max}-1} \sqrt{n_k+1}\sigma_{n_k}^+ \sigma_{n_k+1}^-$, where $\sigma_{n_k}^{\pm}$ acts on the n_kth qubit of the k-mode register. The 2-local form of $\tilde{a}_k$ relaxes connectivity requirements on the k-mode qubit register and thus leads to a reduced gate count. Other encodings can be found in Refs. [27, 32, 33].

Finding the groundstate $|G\rangle$ of Eq. (2) by means of a VQA requires first to construct a proper variational form [1, 6]. That is, a unitary $U(\boldsymbol{\theta})$ parametrized by a real-valued vector $\boldsymbol{\theta}$, such that

$$|\widetilde{G}\rangle \simeq U(\boldsymbol{\theta}^*)|\widetilde{\text{vac}}\rangle, \tag{3}$$

where $|\widetilde{\text{vac}}\rangle = |0_q\rangle \otimes_{k=1}^M |\widetilde{0}_k\rangle$ is the (encoded) noninteracting vacuum state, and $\boldsymbol{\theta}^*$ is obtained by classical minimization of the energy $E(\boldsymbol{\theta}) = \langle\widetilde{\text{vac}}|U^\dagger(\boldsymbol{\theta})\widetilde{H}U(\boldsymbol{\theta})|\widetilde{\text{vac}}\rangle$. Some intuition about a convenient choice of $U(\boldsymbol{\theta})$ can be gained from approximate disentangling transformations for Eq. (2) [22, 23]. We refer to such transformations indistinctly as polaron Ansätze. The simplest transformation is obtained for the case of $N=1$, where it is useful to rotate $H \to H' = P^\dagger H P$ by means of a qubit-state-dependent displacement of the k-modes

$$P = \prod_{k=1}^M \exp[g_k \sigma^x (a_k + a_k^\dagger)/(\omega_k + \omega_q')], \tag{4}$$

where ω_q' is a renormalized frequency for the atom. As illustrated in Sect. IA of the Supplemental Material, the groundstate of H' approaches the noninteracting groundstate of the atom-cavities system, $|\text{vac}\rangle$, in most coupling regimes. Therefore, the state $P|\text{vac}\rangle$ approximates the groundstate $|G\rangle$ in the laboratory frame.

Exploiting this fact to prepare $|\widetilde{G}\rangle$ on a quantum computer requires compiling $\widetilde{P}$ from single- and two-qubit gates, for instance, using a Trotter decomposition. The need for reducing the Trotter error, however, can lead to quantum circuits of large depth. Moreover, this approach is sensitive to errors arising from imperfect qubit control and noise. As a way around this problem, we propose to leverage the structure of the polaron transformation to obtain a short-depth variational from. We do this by parameterizing the Trotter decomposition of $\widetilde{P}$ and letting the variational algorithm adjust the unitary such that the groundstate-Ansatz energy is minimized. The variational form has not only the purpose of discovering short-depth quantum circuits for synthesizing the USC groundstate, but also to potentially improving on the disentangling capabilities of Eq. (4).

We construct the variational form by choosing a convenient Trotter decomposition of $\widetilde{P}$, first for the case of $N=1$. We introduce two k-mode operators, $\widetilde{X}_k^e$ and $\widetilde{X}_k^o$, which are defined such that $\widetilde{P} = \prod_{k=1}^M \exp[f_k \sigma^x (\widetilde{X}_k^e + \widetilde{X}_k^o)]$, where $\{f_k = g_k/(\omega_k + \omega_q')\}$ is a set of constants that will latter play the role of variational parameters. Although $[\widetilde{X}_k^e, \widetilde{X}_k^o] \neq 0$, $\widetilde{X}_k^e$ and $\widetilde{X}_k^o$ are respectively composed of commuting terms that act on even and odd sites of the k-mode qubit register (see the Supplemental Material, Sect. IB). The 2-local form of the encoded bosonic operators leads to an efficient implementation of the Trotter-expanded unitary

$$\widetilde{P}_{\boldsymbol{d}} \simeq \prod_{k=1}^M \prod_{s=1}^{d_k} \exp\Big(\frac{f_k}{d_k}\sigma^x \widetilde{X}_k^e\Big) \exp\Big(\frac{f_k}{d_k}\sigma^x \widetilde{X}_k^o\Big), \tag{5}$$

where d_k is the number of Trotter steps, that may vary with the k-mode index. As shown in Sect. IB of the Supplemental Material, the exponentials in this equation factorize exactly into a product of $n_k^{\max}$ controlled-exchange gates acting on next-neighbor qubits of the k-mode register with the atom register being the control qubit. The implementation of Eq. (5) requires thus $n_k^{\max} \times d_k$ such gates per k-mode, adding to a total gate count of $\sum_{k=1}^M n_k^{\max} d_k$ before quantum-circuit compilation. This number grows linearly with the number of k-modes, their Fock-space dimension and the order of the Trotter expansion (Trotter depth). Interestingly, since Eq. (5) parallelizes over the k-modes, its quantum-circuit depth does not scale with M.

For $N>1$, the resulting variational form incorporates blocks of the form of Eq. (5) where the two-level-atom operator $\sigma^x \to \sigma_i^x$ is now labeled by $i \in [1, N]$ and alternated among the respective qubit registers (see the Supplemental Material, Sect. IC). This observation leads to the more general expression

$$\text{Varform} = \prod_{i=1}^N \prod_{k=1}^M \prod_{s=1}^{d_{ik}} \exp\Big(\frac{f_{ik}^s}{d_{ik}}\sigma_i^x \widetilde{X}_k^e\Big) \exp\Big(\frac{f_{ik}^s}{d_{ik}}\sigma_i^x \widetilde{X}_{ik}^o\Big), \tag{6}$$

where the coefficients $f_k \to f_{ik}^s$ are variational parameters that depend on the Trotter step $s \in [1, \dots, d_{ik}]$. Additionally, f_{ik}^s can also be made a function of the k-mode photon number, such that $f_{ik}^s \to f_{ik}^s(n_k)$. As argued below, this trades shorter circuit depths for longer optimization runtime.

Important additional details apply, however, between the cases of $N=1$ and $N>1$. In particular, the case $N>1$ requires Eq. (6) to be complemented by single-layer short-depth variational form that acts on the atoms' registers. This extra step initializes the polaron variational circuit to the state $|\widetilde{\text{vac}}'\rangle = \prod_{k=1}^M |\psi_a\rangle|\tilde{0}_k\rangle$, where $|\psi_a\rangle$ is an entangled state of the atoms. The state $|\psi_a\rangle$

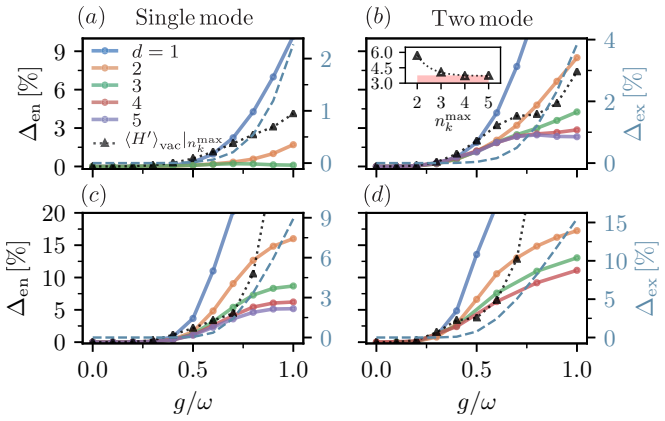

FIG. 1. Groundstate-energy estimation for the single- and two-mode version of the Rabi and Dicke models in resonance conditions. Fock-space truncation in panels (a)-(d) is set to $n_k^{\max} = 3, 3, 5$ and 4 corresponding to 5, 9, 8 and 12 qubits, respectively. The legend is shared between all panels, although (a) and (d) display results only for $d_i < 4$ and $d_{ik} < 5$, respectively. We show the error metrics $\Delta_{\rm en}$ (left scale) and $\Delta_{\rm ex}$ (light-blue dashed line and right scale) defined in the main text, along with $\langle H' \rangle_{\rm vac}|_{n_k^{\max}}$ (triangular markers). The inset in panel (b) shows $\langle H' \rangle_{\rm vac}|_{n_k^{\max}}$ converging to a 4% in the limit of large $n_k^{\max}$ (pink baseline) for $g/\omega = 0.8$. This indicates that the minimum value of $\Delta_{\rm en}$ is reduced exponentially with $n_k^{\max}$, reaching an absolute lower bound determined by the entanglement capabilities of the polaron Ansatz. Simulations do not include noise and are done using Qiskit [34].

is determined by an auxiliary optimization loop specified in Sect. IC of the Supplemental Material.

Fig. 1 shows the results for the (a) single- and (b) two-mode Rabi Hamiltonian, and (c) single- and (d) two-mode Dicke model for $N = 2$. The simulations assume the resonant case where atom and k-mode frequencies are set to $\omega_{q_i} = \omega_k \equiv \omega$ and $g_{ik} \equiv g$ is swept in $[0, \omega]$. The resonance condition leads to strong entanglement between the atoms and cavity modes due to the energetically favorable exchange of excitations. To quantify the performance of the variational form, we define the error metric $\Delta_{\rm en} = |(E_{\rm vqe} - E_{\rm en})/E_{\rm en}|$, accounting for the relative difference between the groundstate energy found by the VQA, $E_{\rm vqe}$, and the energy of the encoded groundstate, $E_{\rm en}$. An additional metric $\Delta_{\rm ex} = |(E_{\rm en} - E_{\rm ex})/E_{\rm ex}|$ quantifies the difference between $E_{\rm en}$ and the numerically exact groundstate energy. We evaluate $\Delta_{\rm en}$ and $\Delta_{\rm ex}$ as a function of g/ω for circuits with Trotter depth $d_{ik} = d$. The chosen Fock space truncation (see figure caption) leads to a small number of qubits while ensuring a relatively small $\Delta_{\rm ex}$. This choice seeks to reduce the quantum-hardware resources needed for simulation.

Results in panel (a) show that relative errors $\Delta_{\rm en}$ below 1% are achieved by state-preparation circuits containing only 3 variational parameters ($d = 3$). A similar accuracy is obtained for circuits with $d = 2$ if additional parameters dependent on the k-mode photon-number are incorporated (not shown). Remarkably, for $d > 1$, the energy of the variational Ansatz is significantly lower than $\langle H' \rangle_{\rm vac}|_{n_k^{\max}}$. The latter is the expectation value of Eq. (2) on the state $P|{\rm vac}\rangle|_{n_k^{\max}}$ within a truncated Fock space. This indicates that the variational algorithm can leverage the Trotter error to outperform the full polaron Ansatz under the same Fock-space restrictions and with very low circuit depth. Interestingly, we also find that the energy of the variational state falls below $\langle H' \rangle_{\rm vac}|_{n_k^{\max} \to \infty}$ in the full range of $g/\omega \in [0, 1]$ (not shown). The error metric $\Delta_{\rm ex}$ remains below $\sim 2\%$ in all the cases.

We observe a similar qualitative behavior for the two-mode simulations in panel (b), although $\Delta_{\rm en}$ increases to $\sim 2.5\%$ for $d = 4$. The same accuracy is reached for circuits with $d = 2$ when variational parameters for each k-mode photon number are introduced (not shown). We find that the accuracy limit is both due to finite Fock-space truncation errors and the disentangling capabilities of the polaron Ansatz. Increasing the number of two-level atoms in the model, while keeping the number of qubits of the order of 10, leads to the results in panels (c)-(d) for which we find a maximum error of $\Delta_{\rm en} \simeq 5\%$ for $d = 5$ in the first case, and of $\Delta_{\rm en} \simeq 8\%$ for $d = 4$ in the second case. These results, however, are limited by Fock space truncation errors and can be improved by increasing the number of qubits in the simulations. It is worth noticing that, similarly to the case of $N = 1$, these variational circuits outperform the polaron Ansatz significantly for the same conditions.

The performance of the variational form may be improved further by means of simple modifications. For instance, a layer of a hardware-efficient (HE) gates [3] could be appended after each Trotter step, providing greater entangling capabilities for state preparation. Ideally, gates on such HE layers should conserve the number of excitations in the k-mode registers [30]. Generalizations of Eq. (4) incorporating additional parameters are also a possibility [35].

As the number of qubits scales with $\sim (n^{\max} + 1)^M$, simulating the performance of the proposed VQA on a classical computer becomes quickly expensive. Moreover, circuits of larger depth and number of qubits could likely benefit from quantum devices tailored to compile the polaron Ansatz in fewer gates. An option is to engineer the required controlled-two-qubit gates directly on the quantum hardware. Sect. V of the Supplemental Material illustrates such special-purpose devices in the context of circuit QED.

The results of Fig. 1 suggest that the polaron variational form is a promising tool for investigating the USC groundstate in near-term quantum devices. For this reason, we implement the aforementioned strategy in currently available quantum hardware. Here, we use the IBM Q Poughkeepsie chip via the open-source framework Qiskit, taking advantage of the built-in SPSA opti-

mizer [3, 36] and the readout error mitigation techniques of Qiskit-Ignis [34]. We use three qubits for the quantum simulation, two of them encoding the bosonic mode. The groundstate energies found this way, shown in Fig. 2 (star-shaped data points), are in good qualitative agreement with the theoretical estimations.

We find that the main limitations on the accuracy of the VQA are due to the level of noise in the quantum processor and to the capabilities of the SPSA optimizer given a finite number of optimization steps. To investigate the effect of the latter against the former, we perform the VQA with a desktop computer, assuming a larger number of optimization steps and the calibrated noise model of the quantum hardware. This produces a set of variational states with optimal parametrization according to the classical simulation. We then evaluate the energy expectation value of such states on the quantum processor, performing mitigation of readout errors. The result of this experiment (triangular-shaped data points) reach better accuracies than those obtained by means of the hybrid quantum-classical VQA. This suggests that noise processes on the quantum hardware prevent high-accuracy solutions to be reached in a reasonable number of optimization steps via cloud access, in the order of 150 SPSA trials. By controlling the level of noise in classical simulation, we also find that hybrid quantum-classical VQA solutions with $\Delta_{\rm en} \sim 1-2\%$ for 150 SPSA trials are expected for noise levels one order of magnitude smaller than the present value. Note that in absence of noise, the number of optimizer steps required to reach numerical accuracy with respect to the reference value is very small in comparison, below 30 in the entire $g/\omega \in [0, 1]$ range. This allow us to conclude that the discrepancies encountered in the quantum-hardware runs are due the effect of noise and the limited optimizer calls rather than limitations of the proposed Ansatz.

Following this proof-of-principle demonstration, we present an alternative method for characterizing the prepared groundstate. This technique could be useful to probe entanglement metrics and to distinguish between nearly degenerate states. The latter situation occurs, for instance, within the groundstate manifold of the quantum Rabi model approaching the DSC regime. To this end, we introduce the joint Wigner function for a set of N qubits and M bosonic modes as

$$W_{\boldsymbol{l}}(\boldsymbol{\alpha}) = \mathrm{Tr}[\rho \sigma_1^{l_1} \dots \sigma_N^{l_N} \, 2^M \Pi(\boldsymbol{\alpha})/\pi^M], \tag{7}$$

generalizing the definition given in Ref. [37] for the case of $N = M = 1$. Here, $\{\sigma_i^{l_i}, l_i \in [0, x, y, z]\}$ are the Pauli matrices for the $i^{\rm th}$ atom with $\sigma_i^0 = \mathbb{1}$. $\Pi(\boldsymbol{\alpha}) = D(\boldsymbol{\alpha}) \Pi D^\dagger(\boldsymbol{\alpha})$, where $\boldsymbol{\alpha} = (\alpha_1, \dots, \alpha_M)$, is a displaced joint-parity operator with $\Pi = \prod_{k=1}^M \exp(i\pi a_k^\dagger a_k)$ and $D(\boldsymbol{\alpha}) = \prod_{k=1}^M \exp(\alpha_k a_k^\dagger - \alpha_k^* a_k)$ for $\alpha_k \in \mathbb{C}$. Inversion of Eq. (7) gives the system's density matrix as $\rho = 2^{M-N} \sum_{\boldsymbol{l}} \int W_{\boldsymbol{l}}(\boldsymbol{\alpha}) \sigma_1^{l_1} \dots \sigma_N^{l_N} \Pi(\boldsymbol{\alpha}) d^2\boldsymbol{\alpha}$, where the integral is performed over $d^2\boldsymbol{\alpha} = \prod_{k=1}^M d^2\alpha_k$ and the sum is extended to the 4^N possible values of $\boldsymbol{l} = (l_1, \dots, l_N)$. This relation can be used for state reconstruction [37].

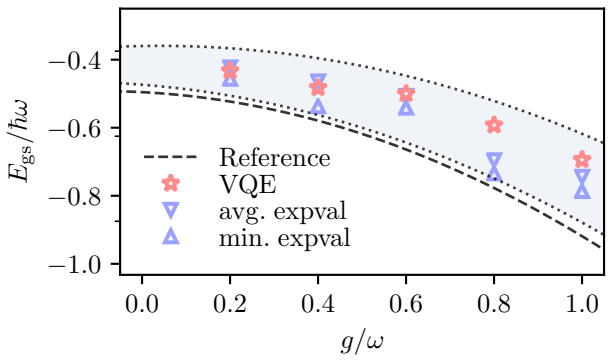

FIG. 2. Variational quantum-optics simulation of the Rabi model in resonance conditions on a quantum processor. Shown is the groundstate energy as a function of the coupling strength, both in units of ω. The cavity mode is encoded in a two-qubit register ($n_k^{\rm max} = 1$). The light-blue bands enclose the range of results that are expected for 150 SPSA trials with levels of noise in the order of 0.1 and 1.0, relative to calibrated values (dotted lines). The black-dashed line is the encoded-groundstate energy. The star-shaped markers are the result of VQA runs for up to 150 SPSA trials on the quantum device. The pointing-up (pointing-down) triangular markers are the minimum (average) expectation value on quantum hardware of states that have been entirely optimized in the classical processor. The dispersion of such values is due to fluctuations in the level of noise of the quantum device between runs. Further details are provided in Sect. II of the Supplemental Material.

Expanding Eq. (7) in the Fock-state basis within the SES encoding we arrive to

$$\widetilde{W}_{\boldsymbol{l}}(\boldsymbol{\alpha}) = \sum_{\tilde{\boldsymbol{n}}=0}^{\tilde{\boldsymbol{n}}^{\rm max}} (-1)^{\sum_{k=1}^M \tilde{n}_k} \, \mathrm{Tr}_q[2^M \Omega_{\tilde{\boldsymbol{n}}}(\boldsymbol{\alpha}) \sigma_1^{l_1} \dots \sigma_N^{l_N} / \pi^M], \tag{8}$$

where Tr_q is the trace operator over the atom registers and $\Omega_{\tilde{\boldsymbol{n}}} = \langle \tilde{n}_1 \dots \tilde{n}_M | \widetilde{D}^\dagger(\boldsymbol{\alpha}) \tilde{\rho} \widetilde{D}(\boldsymbol{\alpha}) | \tilde{n}_1 \dots \tilde{n}_M \rangle$. $\widetilde{W}_{\boldsymbol{l}}(\boldsymbol{\alpha})$ can be sampled by executing a quantum circuit that performs the necessary state-tomography gates. While these gates are simply single-qubit rotations for the atom registers, tomography gates correspond to the application of $\widetilde{D}(\boldsymbol{\alpha})$ for the k-mode registers. Fortunately, the displacement operators can be easily implemented by a sequence of one- and two-qubit gates derived from a Trotter decomposition similar to that of the polaron transformation. Sect. III of the Supplemental Material includes further details.

We demonstrate this approach numerically for the case of a single atom and a cavity mode in resonance with $g/\omega = 1$. Fig. 3 shows the reconstructed joint Wigner function $\widetilde{W}_{\sigma^z}(\alpha)$ for an 8-qubit k-mode register. The result is compared to the numerically exact distribution, which is not affected by Trotter or Fock space truncation

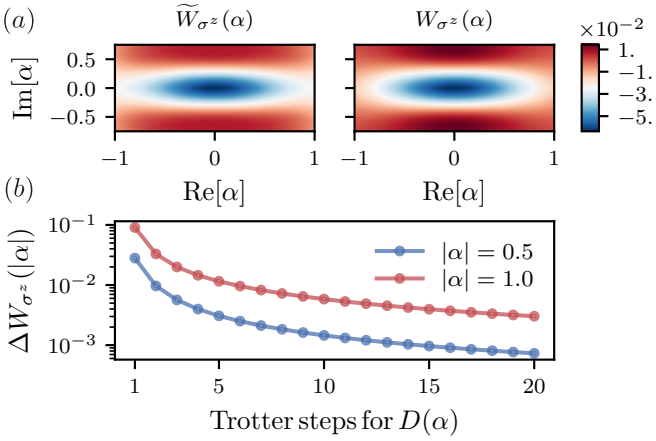

FIG. 3. Reconstruction of the joint Wigner function of the Rabi model in resonance conditions and with $g/\omega = 1$. (a) (Left) Sampled distribution, $\widetilde{W}_{\sigma^z}(\alpha)$, for an 8-qubit k-mode register and 2 Trotter steps per imaginary and real components of $\widetilde{D}(\boldsymbol{\alpha})$. (Right) Numerically exact result $W_{\sigma^z}(\alpha)$. (b) Effect of the Trotter order of $D(\boldsymbol{\alpha})$ on the reconstructed distribution. The error metric is defined as $\Delta W_{\sigma^z}(|\alpha|) = \sqrt{\int_{|\alpha'|=0}^{|\alpha'|=|\alpha|}[\widetilde{W}_{\sigma^z}(\alpha') - W_{\sigma^z}(\alpha')]^2 d^2\alpha'/\mathcal{N}_{|\alpha|}}$, where $1/\mathcal{N}_{|\alpha|}$ is a normalization factor. The scaling of this metric with $|\alpha|$ follows the Trotter error, which scales as $|\alpha|^2/d$ with d being the Trotter depth. For $|\alpha|$ fixed, the discrepancy between the two distributions saturates to a nonzero lower bound due to Fock-space truncation errors. The effect of noise has not been taken into account.

errors. We observe a good qualitative agreement between the two distributions even for a few as 2 Trotter steps. This agreement improves as the number of Trotter steps used to implement $D(\boldsymbol{\alpha})$ is increased, although the discrepancy between the two distributions remains bounded from below due to finite-dimensional encoding errors.

Finally, we discuss briefly the effect of common quantum error channels on the performance of the proposed VQA. It is worth highlighting that a SES encoding allows for damping errors of the form $|\tilde{n}_k\rangle \to |\widetilde{0}_k\rangle$ to be detectable by joint-parity measurements of the k-mode register. This enables postselection of uncorrupted states, which can significantly reduce the impact of noise on the proposed variational algorithm. However, the downsides of using a SES encoding reside in two main points. First, this encoding trades shorter quantum-circuit depths for a relatively large qubit overhead compared to other possible encodings [32, 33]. On the flip side, this compromise might be leveraged by current quantum processors, which are mostly limited by decoherence rather than by the number of qubits [38]. Second, noise channels that do not conserve the number of excitations in the k-mode qubit registers can become dominant for large qubit arrays (see Supplemental Material). This is a direct consequence of an exponential growth of the size of the complement of SES with the number of qubits in the simulation. We also note that the observations above are generic to other proposals using SES encodings [28–31].

In conclusion, we introduced a short-depth and few-parameter variational form to study the interacting light-matter groundstate of N atoms and M electromagnetic modes. We found that such a variational circuit can approximate the ultrastrong-coupling groundstate with very good accuracy. We implemented a proof-of-principle example on an IBM quantum processor, performing the mitigation of readout errors. Finally, we demonstrated the use of Wigner state-tomography to characterize the groundstate, and discussed the impact of noise on the variational algorithm. As the light-matter interaction Hamiltonian considered in this work is formally identical to the few-impurity spin-boson model, we envision applications to problems in condensed-matter physics for which the polaron transformation was originally introduced. The demonstration of quantum advantage by the variational approach introduced here is likely to require quantum-hardware of size and noise-resilience significantly beyond what is currently available. Our work is, however, a first step towards digital simulation of strongly interacting light-matter models with a quantum processor.

ACKNOWLEDGMENTS

We thank Catherine Leroux, Andy C. Y. Li and David Poulin for insightful discussions and the members of the Qiskit-Aqua team, Richard Chen and Marco Pistoia, for support. PKB and IT acknowledge financial support from the Swiss National Science Foundation (SNF) through the grant No. 200021-179312. This work was undertaken thanks in part to funding from NSERC and the Canada First Research Excellence Fund.

[1] A. Peruzzo, J. McClean, P. Shadbolt, M.-H. Yung, X.-Q. Zhou, P. J. Love, A. Aspuru-Guzik, and J. L. O'brien, Nature communications **5**, 4213 (2014).
[2] P. J. O'Malley, R. Babbush, I. D. Kivlichan, J. Romero, J. R. McClean, R. Barends, J. Kelly, P. Roushan, A. Tranter, N. Ding, et al., Physical Review X **6**, 031007 (2016).
[3] A. Kandala, A. Mezzacapo, K. Temme, M. Takita, M. Brink, J. M. Chow, and J. M. Gambetta, Nature **549**, 242 (2017).
[4] J. I. Colless, V. V. Ramasesh, D. Dahlen, M. S. Blok, M. Kimchi-Schwartz, J. McClean, J. Carter, W. De Jong, and I. Siddiqi, Physical Review X **8**, 011021 (2018).

[5] C. Hempel, C. Maier, J. Romero, J. McClean, T. Monz, H. Shen, P. Jurcevic, B. P. Lanyon, P. Love, R. Babbush, et al., Physical Review X **8**, 031022 (2018).

[6] J. R. McClean, J. Romero, R. Babbush, and A. Aspuru-Guzik, New Journal of Physics **18**, 023023 (2016).

[7] A. Kandala, K. Temme, A. D. Córcoles, A. Mezzacapo, J. M. Chow, and J. M. Gambetta, Nature **567**, 491 (2019).

[8] N. Moll, P. Barkoutsos, L. S. Bishop, J. M. Chow, A. Cross, D. J. Egger, S. Filipp, A. Fuhrer, J. M. Gambetta, M. Ganzhorn, et al., Quantum Science and Technology **3**, 030503 (2018).

[9] J.-M. Reiner, M. Marthaler, J. Braumüller, M. Weides, and G. Schön, Phys. Rev. A **94**, 032338 (2016).

[10] E. F. Dumitrescu, A. J. McCaskey, G. Hagen, G. R. Jansen, T. D. Morris, T. Papenbrock, R. C. Pooser, D. J. Dean, and P. Lougovski, Physical Review Letters **120**, 210501 (2018).

[11] C. Ciuti and I. Carusotto, Physical Review A **74**, 033811 (2006).

[12] S. Ashhab and F. Nori, Physical Review A **81**, 042311 (2010).

[13] F. Beaudoin, J. M. Gambetta, and A. Blais, Physical Review A **84**, 043832 (2011).

[14] A. F. Kockum, A. Miranowicz, S. De Liberato, S. Savasta, and F. Nori, Nature Reviews Physics **1**, 19 (2019).

[15] P. Forn-Díaz, L. Lamata, E. Rico, J. Kono, and E. Solano, Rev. Mod. Phys. **91**, 025005 (2019).

[16] S. Haroche and J.-M. Raimond, Exploring the quantum: atoms, cavities, and photons (Oxford university press, 2006).

[17] A. Blais, R.-S. Huang, A. Wallraff, S. M. Girvin, and R. J. Schoelkopf, Physical Review A **69**, 062320 (2004).

[18] J. Bourassa, J. M. Gambetta, A. A. Abdumalikov Jr, O. Astafiev, Y. Nakamura, and A. Blais, Physical Review A **80**, 032109 (2009).

[19] D. Ballester, G. Romero, J. J. García-Ripoll, F. Deppe, and E. Solano, Physical Review X **2**, 021007 (2012).

[20] D. Braak, Physical Review Letters **107**, 100401 (2011).

[21] J. Hausinger and M. Grifoni, Physical Review A **82**, 062320 (2010).

[22] G. Dìaz-Camacho, A. Bermudez, and J. J. García-Ripoll, Physical Review A **93**, 043843 (2016).

[23] T. Shi, Y. Chang, and J. J. García-Ripoll, Physical Review Letters **120**, 153602 (2018).

[24] N. Rivera, J. Flick, and P. Narang, Physical Review Letters **122**, 193603 (2019).

[25] J. Braumüller, M. Marthaler, A. Schneider, A. Stehli, H. Rotzinger, M. Weides, and A. V. Ustinov, Nature communications **8**, 779 (2017).

[26] A. L. Grimsmo and S. Parkins, Physical Review A **87**, 033814 (2013).

[27] A. C. Y. Li, A. Macridin, and P. Spentzouris, manuscript in preparation (2019).

[28] R. Somma, G. Ortiz, E. Knill, and J. Gubernatis, International Journal of Quantum Information **1**, 189 (2003).

[29] M. R. Geller, J. M. Martinis, A. T. Sornborger, P. C. Stancil, E. J. Pritchett, H. You, and A. Galiautdinov, Physical Review A **91**, 062309 (2015).

[30] P. K. Barkoutsos, J. F. Gonthier, I. Sokolov, N. Moll, G. Salis, A. Fuhrer, M. Ganzhorn, D. J. Egger, M. Troyer, A. Mezzacapo, et al., Physical Review A **98**, 022322 (2018).

[31] M. Avalle and A. Serafini, Physical Review Letters **112**, 170403 (2014).

[32] A. Macridin, P. Spentzouris, J. Amundson, and R. Harnik, Physical Review A **98**, 042312 (2018).

[33] A. Macridin, P. Spentzouris, J. Amundson, and R. Harnik, Physical Review Letters **121**, 110504 (2018).

[34] G. Aleksandrowicz, T. Alexander, P. Barkoutsos, L. Bello, Y. Ben-Haim, D. Bucher, F. J. Cabrera-Hernádez, J. Carballo-Franquis, A. Chen, C.-F. Chen, J. M. Chow, A. D. Córcoles-Gonzales, A. J. Cross, A. Cross, J. Cruz-Benito, C. Culver, S. D. L. P. González, E. D. L. Torre, D. Ding, E. Dumitrescu, I. Duran, P. Eendebak, M. Everitt, I. F. Sertage, A. Frisch, A. Fuhrer, J. Gambetta, B. G. Gago, J. Gomez-Mosquera, D. Greenberg, I. Hamamura, V. Havlicek, J. Hellmers, Ł. Herok, H. Horii, S. Hu, T. Imamichi, T. Itoko, A. Javadi-Abhari, N. Kanazawa, A. Karazeev, K. Krsulich, P. Liu, Y. Luh, Y. Maeng, M. Marques, F. J. Martín-Fernández, D. T. McClure, D. McKay, S. Meesala, A. Mezzacapo, N. Moll, D. M. Rodríguez, G. Nannicini, P. Nation, P. Ollitrault, L. J. O'Riordan, H. Paik, J. Pérez, A. Phan, M. Pistoia, V. Prutyanov, M. Reuter, J. Rice, A. R. Davila, R. H. P. Rudy, M. Ryu, N. Sathaye, C. Schnabel, E. Schoute, K. Setia, Y. Shi, A. Silva, Y. Siraichi, S. Sivarajah, J. A. Smolin, M. Soeken, H. Takahashi, I. Tavernelli, C. Taylor, P. Taylour, K. Trabing, M. Treinish, W. Turner, D. Vogt-Lee, C. Vuillot, J. A. Wildstrom, J. Wilson, E. Winston, C. Wood, S. Wood, S. Wörner, I. Y. Akhalwaya, and C. Zoufal, "Qiskit: An open-source framework for quantum computing," (2019).

[35] A. W. Chin, J. Prior, S. F. Huelga, and M. B. Plenio, Physical Review Letters **107**, 160601 (2011).

[36] J. C. Spall et al., IEEE transactions on automatic control **37**, 332 (1992).

[37] B. Vlastakis, A. Petrenko, N. Ofek, L. Sun, Z. Leghtas, K. Sliwa, Y. Liu, M. Hatridge, J. Blumoff, L. Frunzio, et al., Nature communications **6**, 8970 (2015).

[38] A. W. Cross, L. S. Bishop, S. Sheldon, P. D. Nation, and J. M. Gambetta, arXiv preprint arXiv:1811.12926 (2018).

Supplemental Material for "Variational Quantum Simulation of Ultrastrong Light-Matter Coupling"

Agustin Di Paolo,[1] Panagiotis Kl. Barkoutsos,[2] Ivano Tavernelli,[2] and Alexandre Blais[1,3]

[1]*Institut quantique and Département de Physique, Université de Sherbrooke, Sherbrooke J1K 2R1 QC, Canada*
[2]*IBM Research GmbH, Zurich Research Laboratory, Säumerstrasse 4, 8803 Rüschlikon, Switzerland.*
[3]*Canadian Institute for Advanced Research, Toronto, ON, Canada*

(Dated: September 18, 2019)

I. POLARON TRANSFORMATION AND QUANTUM-CIRCUIT COMPILATION OF THE POLARON VARIATIONAL FORM

A. Polaron transformation for the multimode quantum Rabi Hamiltonian

In this section, we study the effect of the polaron transformation [Eq. (4) of the main text] on the multimode Rabi Hamiltonian [$N = 1$ in Eq. (2) of the main text]. We first consider a slightly more general unitary of the form

$$P_{\boldsymbol{f}} = \exp\Big[\sigma^x \sum_{k=1}^{M} f_k (a_k - a_k^\dagger)\Big], \tag{1}$$

where $\{f_k\}$ are real parameters to be determined below. By transforming $H \to H'_{\boldsymbol{f}} = P_{\boldsymbol{f}}^\dagger H P_{\boldsymbol{f}}$, where $\boldsymbol{f} = (f_1, \ldots, f_M)$, we arrive at

$$\begin{aligned} H'_{\boldsymbol{f}}/\hbar =& \frac{\omega'_q}{2}\sigma^z q_{-\boldsymbol{f}}^\dagger q_{\boldsymbol{f}} + \sum_{k=1}^{M} \omega_k a_k^\dagger a_k + g'_k \sigma^x (a_k + a_k^\dagger) \\ &+ E_{\boldsymbol{f}}. \end{aligned} \tag{2}$$

Here, $\omega'_q = \omega_q e^{-2\boldsymbol{f}\cdot\boldsymbol{f}}$ is a renormalized frequency for the two-level atom, $g'_k = g_k - \omega_k f_k$ are new light-matter coupling parameters and $E_{\boldsymbol{f}} = \sum_{k=1}^{M} \omega_k f_k^2 - 2 g_k f_k$ is an energy constant. We have moreover defined the operator $q_{\boldsymbol{f}} = \exp(2\sigma^x \sum_{k=1}^{M} f_k a_k)$.

The parameters f_k in Eq. (2) can reduce the effective light-matter coupling strength g'_k and thus make the groundstate of such a Hamiltonian closer to that of the noninteracting case. This, however, holds if the higher-order corrections to σ^z from the operator $q_{-\boldsymbol{f}}^\dagger q_{\boldsymbol{f}}$, which mixes the k-modes, can be made small at the same time. This leads to a compromise for the best value of $\boldsymbol{f}$ that can be resolved by optimization of such a parameter [1, 2]. More precisely, assuming that the groundstate of Eq. (2) results close to vacuum, minimizing the groundstate energy $E_{\boldsymbol{f}} - \omega'_q/2$ leads to the optimal condition $f_k = g_k/(\omega_k + \omega'_q)$ and to the implicit equation

$$\omega'_q = \omega_q e^{-2\sum_{k=1}^{M} [g_k/(\omega_k + \omega'_q)]^2}, \tag{3}$$

for the renormalized frequency of the atom. We note that the difficulty of solving the scalar equation Eq. (3) does not scale with the number of bosonic modes under consideration. This fact deserves to be highlighted as the optimal value of $\boldsymbol{f}$ is used to initialize the optimizer before executing the variational quantum algorithm presented in the main text and in more details in Sect. I B. As discussed in Sect. I C, this is no longer true in the general case of $N > 1$, where the complexity of initialization scales exponentially with N.

We can gain an understanding of how the polaron transformation works by analyzing the behavior of approximate solutions to Eq. (3) at the boundaries of the range $1 \geq \omega'_q/\omega_q \geq 0$. Indeed, for small coupling strengths g_k, we expect ω'_q to differ only slightly from ω_q and thus to be able to approximate $\omega'_q/\omega_q \simeq 1 - \epsilon$, where $\epsilon \ll 1$. In contrast, for large coupling strengths compared to the system frequencies, we expect ω'_q to vanish exponentially and thus $\omega'_q/\omega_q \simeq \epsilon$ to hold. In the latter situation, the parameters of the polaron transformation approach the asymptotic scaling $f_k \simeq g_k/\omega_k$ leading to $g'_k \to 0$ (along with $\omega'_q \to 0$). This analysis indicates that the light-matter system effectively decouples in the polaron frame [see Eq. (2)], both in the strong and deep-strong coupling regimes. As demonstrated below, the disentangling capabilities of this transformation and the solution of Eq. (3) interpolate smoothly in the intermediate ultrastrong coupling regime, making this tool suitable for investigating the light-matter groundstate in a very broad range of parameters.

We confirm the intuition developed in the above paragraph by analyzing both the single- and two-mode quantum Rabi Hamiltonians in resonance conditions $\omega_q = \omega_k \equiv \omega$, for $g_k \equiv g \in [0, \omega]$. This is also the regime of parameters considered in the main text. Here, however, we are also interested in quantifying how well the state $P|\text{vac}\rangle$ approximates the groundstate of the multimode Rabi Hamiltonian in all coupling regimes. Fig. 1 (a) compares the expectation value $\langle H' \rangle_{\text{vac}}$ to the exact groundstate energy of the single-mode (left) and two-mode configurations (right). We observe that $\langle H' \rangle_{\text{vac}}$ follows closely the exact solution in the range $g/\omega \in [0, 2]$. This agreement is even improved for larger coupling strengths. Panels (b)-(d) show the effective atom frequency ω'_q and coupling strengths g'_k along with the f_k parameters of the polaron transformation. Solid lines correspond to the numerical optimization of ω'_q, while dashed lines are obtained analytically from a series expansion of the right-hand side of Eq. (3) to second order

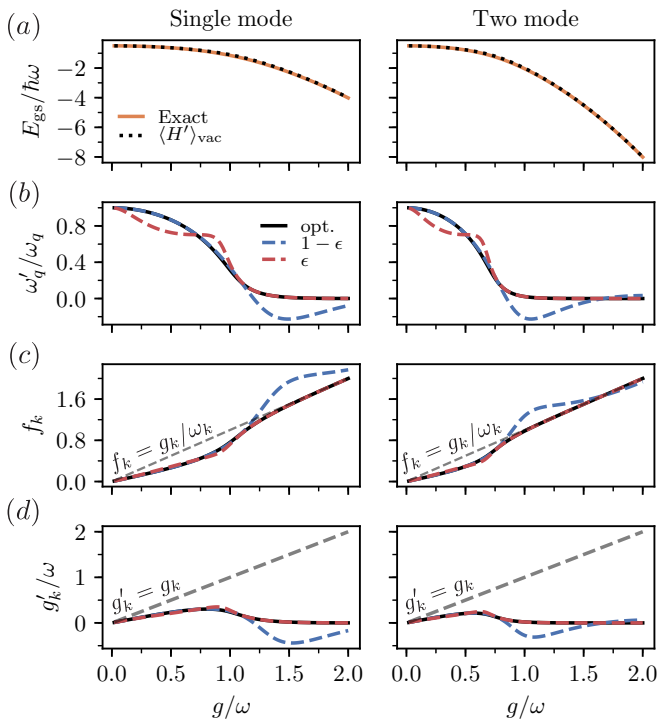

FIG. 1. Performance of polaron transformation in the strong-, ultrastrong- and deep-strong-coupling regimes for the single- and two-mode quantum Rabi models in resonance conditions. (a) Comparison between $\langle H'\rangle_{\rm vac}$ and the exact groundstate energy. The present scale emphasizes the qualitative agreement between these two quantities, although it does not capture relatively small deviations which can be appreciated in the main text. Panels (b)-(d) show the polaron transformation parameters (black solid lines) obtained by numerical optimization. Dashed lines are analytical approximations of Eq. (3) at the boundaries of $1 \geq \omega'_q/\omega_q \geq 0$. The asymptotic regime of $f_k \simeq g_k/\omega_k$ is indicated in panel (c) (gray dashed lines). A similar line style in (d) indicates the coupling in the bare frame, g_k. We observe that g'_k becomes exponentially small compared to g_k as the bare coupling strength increases. This fact highlights the advantages of working in the polaron frame.

in the small parameter ϵ for both $\omega'_q/\omega_q \simeq 1-\epsilon$ and $\omega'_q/\omega_q \simeq \epsilon$ regimes. As anticipated, we observe an exponential reduction of the ratio ω'_q/ω_q along with the asymptotic tendency $f_k \simeq g_k/\omega_k$ and $g'_k \to 0$ as g increases. Although the energy of the state $P|\text{vac}\rangle$ follows closely that of the groundstate in the laboratory frame in the DSC regime, we note that f_k grows linearly with g_k in such conditions. This unfavorable scaling would make the Trotter-decomposition-based approach employed in the main text rather inefficient, requiring quantum-circuits of larger depth to reach convergence.

The advantages of investigating the groundstate properties in the polaron frame are also emphasized by noticing that Eq. (2) can be recast into

$$H'_{\boldsymbol{f}}/\hbar \simeq \frac{\omega'_q}{2}\sigma^z + \sum_{k=1}^{M}\omega_k a_k^\dagger a_k + 2\omega'_q f_k(\sigma^+ a_k + \sigma^- a_k^\dagger) - 2\omega'_q\sigma^z \sum_{k,k'=1}^{M} f_k f_{k'} a_k^\dagger a_{k'} - \sum_{k=1}^{M}\frac{g_k^2}{\omega_k+\omega'_q} + \ldots, \tag{4}$$

assuming $g'_k/(\omega_k+\omega'_q) \ll 1$ and expanding $q_{\boldsymbol{f}}$ to first order. Eq. (4) is reminiscent of the multimode Jaynes-Cummings model, with an additional term $\propto \sigma^z a_k^\dagger a_{k'}$, that can either shift the frequency of the atom as a function of the number of photons in the k-modes ($k = k'$) or allow for the exchange of an excitation between two k-modes through the atom ($k \neq k'$). Provided that the effect of the latter interaction is only perturbative, the groundstate of Eq. (4) is the vacuum state. As shown in the main text, these conditions also lead to relatively small f_k parameters, making it possible to construct a short-depth variational form by Trotter decomposition of the polaron transformation.

B. Quantum-circuit compilation of the polaron variational form

We now provide further details on the quantum circuit compilation of the polaron variational form designed for the multimode quantum Rabi model. Specifically, we seek to rewrite the unitary

$$\text{Varform} = \prod_{k=1}^{M}\prod_{s=1}^{d_k}\exp\left(\frac{f_k^s}{d_k}\sigma^x\widetilde{X}_k^e\right)\exp\left(\frac{f_k^s}{d_k}\sigma^x\widetilde{X}_k^o\right), \tag{5}$$

as a sequence of single- and two-qubit gates available on IBM's on-line quantum platform. The operator $\widetilde{X}_k^e$ in Eq. (5), which was introduced in the main text, is defined as

$$\widetilde{X}_k^e = -i\sum_{n_k\ \text{even}}^{n_k^{\max}-1}\sqrt{n_k+1}(\sigma_{n_k}^x\sigma_{n_k+1}^y - \sigma_{n_k}^y\sigma_{n_k+1}^x)/2. \tag{6}$$

$\widetilde{X}_k^o$ is defined analogously, with n_k running over odds numbers in $[0, n_k^{\max}-1]$. Since the Pauli products in Eq. (6) commute with each other, unitaries of the form $\exp(f_k^s\sigma^x\widetilde{X}_k^{e,o}/d_k)$ factorize into a sequence of controlled two-qubit gates that can be parallelized over the k-mode qubit registers. As shown in Fig. 2 (a), these two-qubit gates operate on pairs of next-neighbor qubits of the k-mode registers and are controlled by the atom qubit. Panel (b) provides the compilation of the controlled two-qubit gates in elementary single- and two-qubit gates [3].

The atom and the k-mode registers are initialized to the states $|0\rangle$ and $|\widetilde{0}_k\rangle = |10\ldots0\rangle$, respectively, which correspond to the noninteracting groundstates. This step

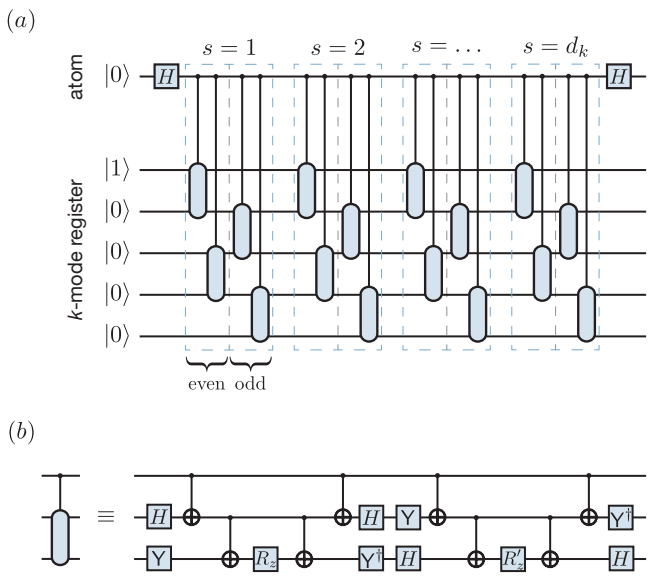

FIG. 2. Quantum-circuit compilation of the polaron variational form [Eq. (5)] for one of the k-mode registers. (a) Schematic representation of the variational form as a sequence of controlled two-qubit gates. Such gates correspond to the unitaries $\exp(f_k^s \sigma^x \widetilde{X}_k^e/d_k)$ and $\exp(f_k^s \sigma^x \widetilde{X}_k^o/d_k)$, performed at each Trotter step labeled by s. (b) Compilation of the controlled two-qubit gate in one- and two-qubit gates available on the IBM quantum hardware [3]. Here, H denotes the Hadamard gate, $Y = R_x(\pi/2)$, and R_z, R_z' are rotations around the Z axis using the conventional notation in which $R_\mu(\theta) = \exp(-i\theta\sigma^\mu/2)$ for $\mu = x, y, z$. If the parameters f_k^s are taken to be independent of the k-mode photon number, then $R_z = R_z(f_k^s\sqrt{n_k+1}/d_k)$ and $R_z' = R_z^\dagger$, where n_k labels the sites within the k-mode register. If, in contrast, $f_k^s \to f_k^s(n_k)$ is allowed to vary from site to site, then $R_z = R_z[f_k^s(n_k)\sqrt{n_k+1}/d_k]$ and $R_z' = R_z^\dagger$–or $R_z' = R_z[f_k^{s\prime}(n_k)\sqrt{n_k+1}/d_k]$ if one wishes to introduce an extra degree of freedom, $f_k^{s\prime}(n_k)$, per controlled two-qubit gate. Importantly, the parameters of the variational form are initialized to the value specified by the polaron transformation in Eq. (4) of the main text.

is followed by d_k sets of gates, where d_k is the Trotter depth used to decompose the polaron unitary for mode k. In its simplest form, the polaron variational form has a single parameter per Trotter step. For a given s, the two-qubit-gate rotation angle is determined by such a parameter and the site index n_k which introduces an additional scaling factor $\propto \sqrt{n_k}$ to this angle. The latter factor arises from the $\sqrt{n_k}$ scaling of the matrix elements of the harmonic-oscillator ladder operators (a_k and $a_k^\dagger$) in the photon-number basis. A version of the variational form with a larger number of parameters can easily be crafted by letting the two-qubit-gate rotation angle vary and potentially depart from the $\sqrt{n_k}$ scaling. Moreover, an additional parameter can be introduced if the controlled two-qubit gates are implemented as in Fig. 2 (b), as this gate compilation uses two R_z rotations that could be made independent from each other. In all cases, the initial value of the variational-form parameters must be set to that of the polaron transformation in Eq. (4) of the main text.

An alternative option to the gate in Fig. 2 (b) is the implementation a three-qubit gate at a hardware level without the need of gate compilation. This possibility, investigated in depth in Sect. V, has a number of advantages with respect to the compiled version of such gate. In fact, a hardware-level implementation of the controlled two-qubit gates would lead to a reduction of the gate count, potentially enabling the simulation of systems of larger size. Moreover, the gate generator can be engineered to conserve the number of excitations in the k-mode registers and thus the SES encoding. Since this criteria is not guaranteed by the complied version of the gate in Fig. 2 (b), an error occurring half-way in such a sequence could severely impact the state fidelity.

C. Polaron transformation and variational form for the multimode Dicke Hamiltonian

In this section, we extend our approach to treat the multimode Dicke Hamiltonian [Eq. (2) of the main text]. To this end, the polaron transformation needs to be modified to include the N atoms as

$$P_{\{\boldsymbol{f}_i\}} = \exp\Big[\sum_{i=1}^{N}\sum_{k=1}^{M} \sigma_i^x f_{ik}(a_k - a_k^\dagger)\Big], \tag{7}$$

where the real parameters f_{ik}, organized in the vectors $\boldsymbol{f}_i = (f_{i1}, \ldots, f_{iM})$, for $i = 1, \ldots, N$, now depend on both the atom and the k-mode indices [4]. By transforming the Hamiltonian in Eq. (2) of the main text as $H \to H'_{\{\boldsymbol{f}_i\}} = P^\dagger_{\{\boldsymbol{f}_i\}} H P_{\{\boldsymbol{f}_i\}}$, we find

$$\begin{aligned} H'_{\{\boldsymbol{f}_i\}}/\hbar = &\sum_{i=1}^{N} \frac{\omega'_{qi}}{2}\sigma_i^z q^\dagger_{-\boldsymbol{f}_i} q_{\boldsymbol{f}_i} + \sum_{k=1}^{M}\omega_k a_k^\dagger a_k \\ &+ \sum_{i=1}^{N}\sum_{k=1}^{M} g'_{ik}\sigma_i^x(a_k + a_k^\dagger) \\ &+ \sum_{i,i'=1}^{N} J_{ii'}\sigma_i^x\sigma_{i'}^x, \end{aligned} \tag{8}$$

which generalizes Eq. (2). Here, we derive parameters analogous to those introduced for the quantum Rabi model, including renormalized atom frequencies $\omega'_{qi} = \omega_{qi} e^{-2\boldsymbol{f}_i\cdot\boldsymbol{f}_i}$ and light-matter coupling constants $g'_{ik} = (g_{ik} - \omega_k f_{ik})$, along with the set of operators $q_{\boldsymbol{f}_i} = \exp(2\sigma_i^x \sum_{k=1}^{M} f_{ik} a_k)$ for $i = 1, \ldots, N$. Unlike the $N = 1$ case, Eq. (8) also includes an effective two-body coupling $J_{ii'} = \sum_{k=1}^{M}(\omega_k f_{ik} f_{i'k} - 2 g_{ik} f_{i'k})$ between two atoms i and i', which is mediated by the k-modes.

Due to the latter interaction, the groundstate of Eq. (8) is not necessarily close to that of the noninteracting case. Instead, we assume a groundstate Ansatz of the form

$\prod_{k=1}^{M}|\psi_a\rangle|\widetilde{0}_k\rangle$, where $|\psi_a\rangle$ is the groundstate of the effective spin Hamiltonian

$$H_a/\hbar = \sum_{i=1}^{N}\frac{\omega'_{qi}}{2}\sigma_i^z + \sum_{i,i'=1}^{N} J_{ii'}\sigma_i^x\sigma_{i'}^x. \tag{9}$$

By minimizing the energy of H_a, one finds a parameterization $\{\boldsymbol{f}_i\}$ of the polaron transformation, that approximately decouples the atoms from the k-modes in Eq. (8) [4]. In contrast to the case of the quantum Rabi model, the cost of finding a proper disentangling transformation now scales exponentially with system size.

Focusing on the limit of small N, Eq. (9) can still be handled on a classical processor which is used for diagonalizing H_a and optimizing its groundstate energy as a function of $\{\boldsymbol{f}_i\}$. It is worth mentioning that quantum routines, such as variational eigensolvers and quantum annealing, might also be useful for this task. In particular, the latter method is attractive for large N due to the possibility of embedding Ising-type Hamiltonians with long-range interactions into physical models with bounded connectivity.

Regardless of how the above optimization is performed, a quantum circuit is needed to prepare the state $|\psi_a\rangle$ on the atom registers. This initialization step is followed by the application of the polaron variational form

$$\text{Varform} = \prod_{i=1}^{N}\prod_{k=1}^{M}\prod_{s=1}^{d_{ik}} \exp\left(\frac{f_{ik}^s}{d_{ik}}\sigma_i^x\widetilde{X}_k^e\right)\exp\left(\frac{f_{ik}^s}{d_{ik}}\sigma_i^x\widetilde{X}_k^o\right), \tag{10}$$

where σ_i^x is the Pauli-X operator for the i^{th} atom, and d_{ik} is the Trotter order of the polaron unitary involving this qubit and the k-mode labeled by k. Furthermore, f_{ik}^s are the parameters of the polaron variational form, adding to a total of $\sum_{i=1}^{N}\sum_{k=1}^{M} d_{ik}$ parameters, which scales linearly with the number of atoms. Additional parameters can be introduced by allowing $f_{ik}^s \to f_{ik}^s(n_k)$ to depend on the k-mode photon-number index.

Fig. 3 shows a schematic of the variational form including the initialization step. We assume that $|\psi_a\rangle$ can be synthesized by a set of d_a hardware-efficient layers acting on the atom registers [5]. Although this is not scalable to large N, the choice of a hardware-efficient approach is motivated by the lack of structure in Eq. (9). As previously shown in Fig. 2, the polaron variational form contains sets of controlled two-qubit gates acting on the k-mode registers. In the present case, the control qubit is swept across the atom registers, while the number of Trotter steps d_{ik} may vary form one set to the other. Finally, we note that the compilation of the controlled two-qubit gates in one- and two-qubit gates is the same as in Fig. 2 (b).

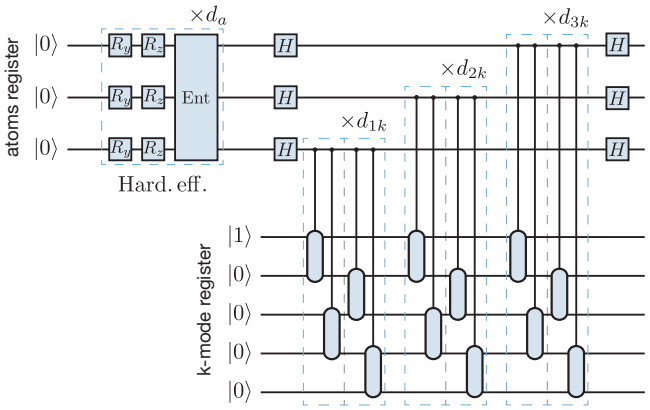

FIG. 3. Quantum circuit compilation of the variational form for the multimode Dicke problem for 3 atoms and a single k-mode register. The variational form is initialized on the state $\prod_{k=1}^{M}|\psi_a\rangle|\widetilde{0}_k\rangle$ by means of hardware-efficient layers acting on the atom registers. The hardware-efficient variational form is followed by layer of controlled two-qubit gates identical to those in Fig. 2 (b). Here, the control qubit is swept over the atom registers, and the number of Trotter steps may vary with the atom and k-mode indices.

II. PERFORMANCE OF THE VQA ON A QUANTUM PROCESSOR

A. VQA simulations with different hardware-noise levels

Mitigating the effect of noise is one of the greatest challenges for near term quantum computers. In order to first quantify this effect, it is useful to investigate the performance of the VQA for a variable noise strength. One way to modify the effective level of noise that a quantum algorithm is subject to, is to perform the quantum gates necessary for the computation having made these artificially slower. This enhances the effect of any decoherence channel and thus leads to an increased noise strength. Although we do not have low-level access to the pulses applied on the quantum hardware, like in Ref. [6], we can simulate the effect of a variable noise strength on the VQA by modifying the error model accordingly. This strategy also allow us to simulate a noise level below the calibrated values for the quantum device in use, which are provided by Qiskit [7].

We modify the noise level in simulation defining a noise factor, η_{noise}, such that

$$\begin{aligned} T_1 &= T_1^{\text{device}}/\eta_{\text{noise}} \\ T_2 &= T_2^{\text{device}}/\eta_{\text{noise}} \\ r_{1\text{q}-\text{g}} &= \eta_{\text{noise}}\; r_{1\text{q}-\text{g}}^{\text{device}} \\ r_{2\text{q}-\text{g}} &= \eta_{\text{noise}}\; r_{2\text{q}-\text{g}}^{\text{device}} \\ r_{\text{readout}} &= \eta_{\text{noise}}\; r_{\text{readout}}^{\text{device}}, \end{aligned} \tag{11}$$

where T_1 and T_2 are single-qubit relaxation and dephasing times, $r_{1\text{q}-\text{g}}$ and $r_{2\text{q}-\text{g}}$ are single- and two-qubit gate

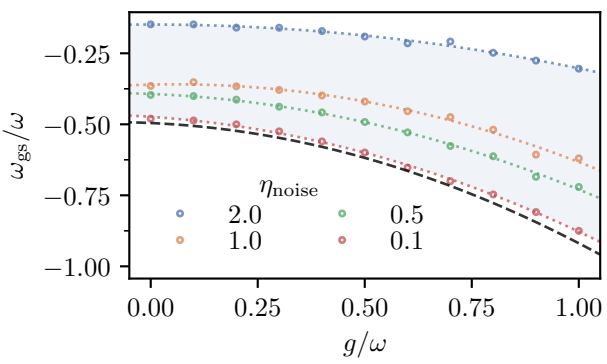

FIG. 4. Simulation of the VQA performance under variable noise strength. $\eta_{\rm noise} = 1$ corresponds to the realistic noise model provided by Qiskit for the IBM Q Poughkeepsie device. The shared area indicates the range of results which are possible with levels of noise $\eta_{\rm noise} = 0.1 - 2$. Extrapolation to zero-noise indicates that results with acceptable accuracy are only attainable with levels of noise one order of magnitude smaller than those in the current generation of devices.

error probabilities and $r_{\rm readout}$ is the readout error probability, respectively. The quantities in Eq. (11) which are labeled as "device" correspond to calibrated values for the day that the runs were executed.

Fig. 4 shows the result of the simulations with variable noise strength. We use the Simultaneous-Perturbation-Stochastic-Approximation (SPSA) method as classical optimizer, with parameters $\alpha = 0.602$ and $\gamma = 0.101$ defined in Ref. [5]. We perform 25 calibration steps to compute the parameters a and c and another 100 SPSA trials for the actual optimization procedure. From the simulations, we conclude that VQA results with acceptable accuracy with respect to the exact groundstate energy would be attainable with noise levels that are one order of magnitude smaller than the actual ones. We note that extrapolation schemes to the zero-noise regime, like the ones discussed in Refs. [6, 8], can potentially help to further mitigate the effects of noise.

B. Simulations on the quantum processor

For the quantum-hardware runs we use three qubits out of the twenty available on the IBM Q Poughkeepsie chip. The connectivity map of the device is shown in Fig. 5. The average error rates recorded throughout our experiments were $(5.25 \pm 0.212) \times 10^{-3}$ and $(3.75 \pm 0.364) \times 10^{-2}$ for single-quit gates and CNOT gates, respectively. These error rates are highly depended on the actual date on which the experiment took place. Mitigation of readout errors is done with the standardized methods provided by Qiskit-Ignis. There, a measurement calibration matrix is used to identify readout errors by preparing 2^N basis states and estimating the probability distribution of such state, with N the number of qubits in simulation. The probability distribution of an unknown state can then be corrected based on these estimates. The calibration matrix was updated after every run or every 120 minutes of wall-clock time for the VQA runs.

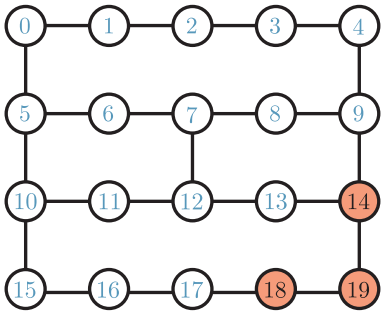

FIG. 5. Connectivity map of IBM Q Poughkeepsie quantum processor. Qubits 14, 18 and 19 (highlighted) were used for our experiment. The choice of qubits was depended on the respective single and two quit gate errors.

Beyond coherent and incoherent errors on quantum hardware, the main limitation to greater accuracy has been found to be the classical optimizer. Indeed, the SPSA method fails to acquire the expected solution in several cases, potentially getting stuck into local minima. We confirm this hypothesis indirectly by performing the optimization of the variational Ansatz in simulation assuming the calibrated noise model for the device. We then compute the expectation value of such variational states on quantum hardware. This additional experiment can reach significantly better accuracy than those obtained by running the optimization over quantum-hardware energy estimations, as shown in Fig. 2 of the main text. We therefore expect new and more powerful optimization algorithms to enable higher accuracy VQA results.

III. SAMPLING THE JOINT WIGNER FUNCTION

We now provide details about the sampling of the joint Wigner distribution in Eq. (8) of the main text. We begin by noticing that measurements of the Pauli products $\sigma_1^{l_1} \dots \sigma_N^{l_N}$ can be done in the computational basis, provided that a set of single-qubit gates $\{R_{l_i}\}$ are executed on the atom register prior to qubit readout. Taking this into consideration, we now focus on the case where the Pauli string $\sigma_1^{l_1} \dots \sigma_N^{l_N}$ contains only σ^z and/or identity operators and no prior rotation of ρ is needed.

Eq. (8) of the main text makes use of the probability distribution of the displaced density matrix $\widetilde{D}^\dagger(\boldsymbol{\alpha})\tilde{\rho}\widetilde{D}(\boldsymbol{\alpha})$. In order to sample such a distribution, $\widetilde{D}^\dagger(\boldsymbol{\alpha})$ needs first to be compiled into single- and two-qubit gates. Since this joint-displacement operator is a product of single-mode displacements of the form

$\widetilde{D}^\dagger(\alpha_k)$, we only provide the quantum-circuit compilation for the latter unitary. To this end, it is convenient to introduce the real (α_k^R) and imaginary (α_k^I) parts of the displacement parameter $\alpha_k = \alpha_k^R + i\alpha_k^I$, and to expand the displacement operator as $\widetilde{D}^\dagger(\alpha_k) \simeq \exp[\alpha_k^R(\tilde{a}_k - \tilde{a}_k^\dagger)]\exp[-i\alpha_k^I(\tilde{a}_k + \tilde{a}_k^\dagger)]$, where "$\simeq$" indicates an equivalence up to a global phase. Making use of the site operators of the k-mode registers, we find

$$\tilde{a}_k - \tilde{a}_k^\dagger = -i \sum_{n_k=0}^{n_k^{\max}-1} \sqrt{n_k+1}(\sigma_{n_k}^x \sigma_{n_k+1}^y - \sigma_{n_k}^y \sigma_{n_k+1}^x)/2$$
$$\tilde{a}_k + \tilde{a}_k^\dagger = \sum_{n_k=0}^{n_k^{\max}-1} \sqrt{n_k+1}(\sigma_{n_k}^x \sigma_{n_k+1}^x - \sigma_{n_k}^y \sigma_{n_k+1}^y)/2. \tag{12}$$

Splitting the k-mode registers into even- and odd-index qubit subsets, the exponentiation of the operators in Eq. (12) can be implemented by a Trotter expansion, as it was done for the polaron variational form.

Fig. 6 summarizes the procedure for sampling the joint Wigner function with a set of tomography gates applied on the ultrastrong-coupling groundstate synthesized by the polaron variational form in panel (a). A first set of two-qubit gates, compiled in panel (b), implements a displacement operator along the imaginary-α_k axis with a Trotter order d^I. This is followed by a similar set of gates, compiled in panel (c), implementing a displacement along the real-α_k axis with Trotter depth d^R. Additionally, single-qubit tomography gates are applied on the atom registers. The circuit is terminated by readout of both the atom and k-mode registers. An histogram of counts (d) is constructed by repeating this procedure for a fixed $(\boldsymbol{l}, \boldsymbol{\alpha})$ pair. The joint Wigner function can then be computed from this histogram approximating the trace operator in Eq. (8) of the main text by

$$\mathrm{Tr}_q[\dots] \simeq \frac{2^M}{\pi^M} \sum_{\boldsymbol{q}} (-1)^{\sum_{i=1}^N \beta_{q_i}} c(q_1, \dots, q_N; \tilde{n}_1, \dots, \tilde{n}_M), \tag{13}$$

where $c(q_1, \dots, q_N; \tilde{n}_1, \dots, \tilde{n}_M)$ are the normalized counts for the basis vector $|q_1, \dots, q_N; \tilde{n}_1, \dots, \tilde{n}_M\rangle$ in which $q_i \in [0,1]$ is the state of the i^{th} atom, and $\beta_{q_i} \in [0,1]$ accounts for the presence of a σ_i^z operator before qubit readout. More precisely, such a parameter is set according to the rules $\beta_{q_i} = 1 - q_i$ if $l_i = z$, and $\beta_{q_i} = 0$ if $l_i = 0$. We note that the approximate relation in Eq. (13) can be replaced by an exact equivalence in the limit of large counts.

The reconstruction error scales with the amplitude of the displacement parameters $|\alpha_k|^2$, although it can be reduced by increasing the Trotter order in the implementation of the unitaries $\widetilde{D}^\dagger(\alpha_k)$. The finite Fock-state truncation of the encoded bosonic modes sets an upper bound to the accuracy of the reconstructed joint Wigner distribution, as demonstrated in Fig. 3 of the main text. Given that the quantum circuit corresponding to such operators is appended to that of the polaron variational form, this procedure would ultimately be limited by the strength of the noise in the quantum processor. However, we find that Trotter depths as small as 2 are enough to demonstrate the qualitative features of the joint Wigner distribution.

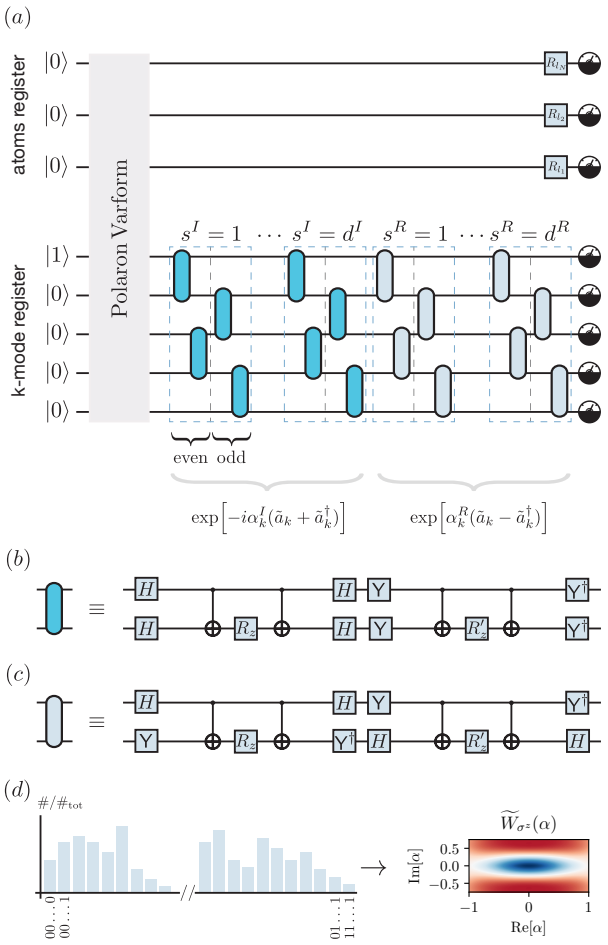

FIG. 6. Sampling the joint Wigner distribution corresponding to the atom and k-mode registers. (a) Quantum-circuit compilation of the displacement operators applied on the k-mode registers (here shown for a single mode), along with the single-qubit gates needed for tomography of the atom registers. These gates are executed on the ultrastrong-coupling groundstate synthesized by the polaron variational form. The k-mode displacement unitary is split in real and imaginary components, implemented by gate sequences with Trotter depth d^R and d^I, respectively, which may in general be different. The imaginary component is depicted first, and makes use of the two-qubit gates in (b) where $R_z = R_z(\alpha_k^I\sqrt{\tilde{n}_k+1}/d^I)$ and $R_z' = R_z^\dagger$. What follows is the implementation of the real component of the displacement operator, which executes the two-qubit gates in (c) where $R_z = R_z(\alpha_k^R\sqrt{\tilde{n}_k+1}/d^R)$ and $R_z' = R_z^\dagger$. Qubit readout is performed at the end of the quantum circuit in (a), leading to the histogram of counts in (d) after several repetitions of the experiment. This allows for reconstruction of the joint Wigner function as described in the main text.

IV. EFFECT OF PHASE- AND BIT-FLIP NOISE CHANNELS UNDER A SES ENCODING

This section discuses the so-called memory error of a small qubit register encoding a bosonic mode. We consider both phase- and bit-flip error channels acting on a copy of the maximally entangled state $|\psi\rangle \sim \sum_{n_k=0}^{n_k^{\max}} |n_k\rangle$, in absence of logical gates. Specifically, we compute the state fidelity $F(\rho,\rho') = \mathrm{Tr}[\sqrt{\rho}\rho'\sqrt{\rho}]$ [9], where $\rho = |\psi\rangle\langle\psi| \otimes |\psi\rangle\langle\psi|$ and $\rho' \sim \sum_{n_k,n_k'=0}^{n_k^{\max}} |n_k\rangle\langle n_k'| \otimes \mathscr{E}_{\mathrm{C}}(|n_k\rangle\langle n_k'|)$. Here, $\mathscr{E}_{\mathrm{C}}$ are multiqubit error channels obtained by composition of single-qubit ones, $\mathscr{E}_{q,\mathrm{C}}$. The latter have the general form $\mathscr{E}_{q,\mathrm{C}}(\bullet) = \sum_{i=0}^{1} E_i \bullet E_i^\dagger$, where $\{E_i\}$ are the Kraus operator for the channel C. Denoting the error probability with r, we define the phase-flip channel by $E_0 = \sqrt{1-r}\mathbb{1}$, $E_1 = \sqrt{r}\sigma^z$, while $E_0 = \sqrt{1-r}\mathbb{1}$, $E_1 = \sqrt{r}\sigma^x$ correspond to the bit-flip channel.

Fig. 7 shows the result for the state fidelity assuming a k-mode register containing up to a maximum of 7 qubits. As anticipated in the main text, we find that bit-flip errors are the most relevant as the size of the k-mode register is increased. This can be understood intuitively by looking at the complement $\overline{\mathrm{SES}}$ of the SES subspace used for the encoding. Since the number of basis vectors in $\overline{\mathrm{SES}}$, and thus the dimension of this subspace, grows exponentially with $n_k^{\max}$, a noise operator breaking the SES symmetry could significantly affect the state fidelity in the limit of large $n_k^{\max}$. On the other hand, it is worth noticing that this might not necessarily limit the performance of near-term algorithms requiring only a small number of qubits. Alternatives for scaling-up to larger devices include the use of qubits with naturally long T_1 times, or a different encoding for the bosonic modes [10, 11]. Future work will investigate the performance crossover of the various possible encodings as the variational circuit is scaled up. Finally, we note that state fidelity, although standard, is a strong metric to evaluate the performance of our variational algorithm, and provides only a qualitative estimation of the impact on the energy of the variational ansatz.

V. CIRCUIT-QED IMPLEMENTATION OF THE CONTROLLED-EXCHANGE GATES

With the purpose of reducing the gate count of the polaron variational form, we now present a superconducting-qubit implementation of a controlled-exchange gate. We stress, however, that the proposed approach could be leveraged by any other quantum-hardware platform with native interactions similar to those found in a standard circuit-QED setup. Below, we provide an ideal implementation of the gate interaction and then suggest a superconducting circuit that approaches the ideal scheme.

We first consider the case of a single atom and k-mode

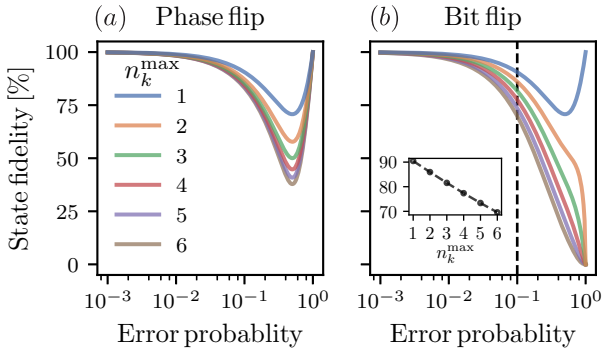

FIG. 7. Effect of phase-flip (a) and bit-flip (b) error channels on the fidelity of a maximally entangled state as a function of the total error probability. We consider a k-mode qubit register of size $n_k^{\max}+1 \leq 7$. The legend applies for both left and right plots. We observe a significant decrease of the state fidelity as the size of the qubit register is increased. As discussed in the main text, bit-flip errors are expected to be dominant as the register size is scaled up to simulate a larger number of modes with also greater Fock-state truncation. The inset shows the state fidelity as a function of $n_k^{\max}$ for an error probability of 10^{-1}.

registers. The frequency of the *physical* qubit corresponding to the atom is denoted by ω_ν, while the frequencies of the qubits belonging to the k-mode register are denoted by ω_{n_k}, with $n_k \in [0,1,\ldots,n_k^{\max}]$. Note that these frequencies are not related to the parameters of the problem that one wishes to simulate. With the purpose of engineering a controlled two-qubit gate, we assume the two qubits of the k-mode register–labeled by $\mu \in [n_k, n_k+1]$–to be independently coupled to the atom qubit with a time-dependent interaction strength. This situation is described by a 3-qubit Hamiltonian of the form

$$H_{\mathrm{ideal}}/\hbar = \frac{\omega_\nu}{2}\sigma_\nu^z + \sum_\mu \left[\frac{\omega_\mu}{2}\sigma_\mu^z + \Omega_\mu(t)(\sigma_\mu^+\sigma_\nu^- + \sigma_\mu^-\sigma_\nu^+)\right] \tag{14}$$

where we take, in particular, $\Omega_\mu = \Omega_\mu^0 + 2\varepsilon_\mu \sin[(\omega_\mu - \omega_\nu + \delta_\mu)t + \phi_\mu]$. Here, Ω_μ^0 is an always-on interaction strength, $2\varepsilon_\mu$ is the modulation amplitude, δ_μ is a frequency detuning with respect to the μ-ν transition and ϕ_μ is a relative phase. Counter-rotating terms of the form $\sigma_\mu^+\sigma_\nu^+$ and its Hermitian conjugate have been omitted after a RWA.

To make the three-qubit-gate interaction explicit, we now perform a standard time-dependent Schrieffer-Wolff transformation with generator

$$S = \sum_\mu \left[\frac{\Omega_\mu^0}{\omega_\mu - \omega_\nu} + \frac{i\varepsilon_\mu e^{-i[(\omega_\mu-\omega_\nu+\delta_\mu)t+\phi_\mu]}}{2(\omega_\mu-\omega_\nu)+\delta_\mu}\right]\sigma_\mu^+\sigma_\nu^- - \mathrm{H.c.}, \tag{15}$$

conceived to remove first-order interaction terms by the condition $H_0 + [H_0, S] + H_{\mathrm{int}} - i\dot{S} = 0$, where $H_0 = \frac{\omega_\nu}{2}\sigma_\nu^z + \sum_\mu \frac{\omega_\mu}{2}\sigma_\mu^z$ and $H_{\mathrm{int}} = \sum_\mu \Omega_\mu(t)(\sigma_\mu^+\sigma_\nu^- + \sigma_\mu^-\sigma_\nu^+)$. Assuming $\Omega_\mu^0/(\omega_\mu - \omega_\nu) \ll 1$ (dispersive regime)

and $\varepsilon_\mu/[2(\omega_\mu-\omega_\nu)+\delta_\mu] \ll 1$, we expand the transformed Hamiltonian up to second order in the interaction strength, and move to a frame rotating at frequencies ω_ν for the atom qubit and $\omega_\mu+\delta_\mu$ for the k-mode qubits, where the modulated interaction is resonant. Setting the phase of the drives as $\phi_{n_k}=0$ and $\phi_{n_k+1}=-\pi/2$, and performing a second RWA, we find the effective Hamiltonian

$$H'_{\rm ideal}/\hbar = \frac{\xi_{n_k}}{2}\sigma^z_\mu(\sigma^x_{n_k}\sigma^y_{n_k+1}-\sigma^y_{n_k}\sigma^x_{n_k+1})+\frac{\delta\omega_\nu}{2}\sigma^z_\nu, \quad (16)$$

where drive parameters have been chosen to satisfy $-\delta_\mu+(\Omega^0_\mu)^2/(\omega_\mu-\omega_\nu)+\varepsilon^2_\mu/\delta'_\mu=0$, with $\delta'_\mu=2(\omega_\mu-\omega_\nu)+\delta_\mu$. The drive condition removes terms $\propto\sigma^z_\mu$ from Eq. (16) and makes the three-qubit interaction resonant in the current frame. Moreover, ξ_{n_k} has been defined as an effective exchange-interaction rate between the two neighboring qubits of the k-mode register, that is mediated by the atom qubit and given by

$$\xi_{n_k} = \frac{1}{2}\frac{\varepsilon_{n_k}\varepsilon_{n_k+1}}{\delta'_{n_k}\delta'_{n_k+1}}(\delta'_{n_k}+\delta'_{n_k+1}). \quad (17)$$

Additionally, we derive a shift to the frequency of the atom qubit given by $\delta\omega_\nu=-(\Omega^0_\mu)^2/(\omega_\mu-\omega_\nu)-\varepsilon^2_\mu/\delta'_\mu$, due to the interaction with the two other qubits and the presence of the drive.

Evolution under the Hamiltonian in Eq. (16) generates the desired controlled-exchange gate operation $\exp[-i(\xi_{n_k}t/2)\sigma^z_\mu(\sigma^x_{n_k}\sigma^y_{n_k+1}-\sigma^y_{n_k}\sigma^x_{n_k+1})]$ which is key to the polaron variational form. Due to the presence of the term $\propto\delta\omega_\nu$ in Eq. (16), an unintentional R_z rotation on the atom qubit needs to be corrected for by applying an additional single-qubit gate. Modulation amplitudes $\varepsilon_\mu/2\pi$ of the order of 10 MHz and typical values of $\delta'_\mu/2\pi$ of the order of the GHz lead to controlled-exchange rates $\xi_{n_k}/2\pi$ in the range $0.1-0.5$ MHz. Despite this number being small compared to standard rates of one- and two-qubit gates in superconducting-qubit architectures, counting with a direct implementation of the three-qubit gate still provides a significant advantage with respect to its compiled counterpart in Fig. 2. In fact, the proposed gate is designed to conserve the excitation number of the k-mode registers and thus the SES encoding. Furthermore, while the gate time of the direct implementation is proportional to the desired rotation angle, the compiled version of the gate has an approximately fixed gate time determined by the number of CNOT gates in the circuit. This important difference would be leveraged further as the Trotter order of the polaron variational form is increased, making the controlled rotations closer to the identity.

Having presented an ideal model for the controlled-exchange gate, we now elaborate on a possible superconducting-circuit implementation of the Hamiltonian in Eq. (14). In particular, we consider an architecture made of transmon qubits and tunable couplers (see Fig. 8), similar to that studied in Ref. [12]. Using couplers to mediate parametric interactions allows us

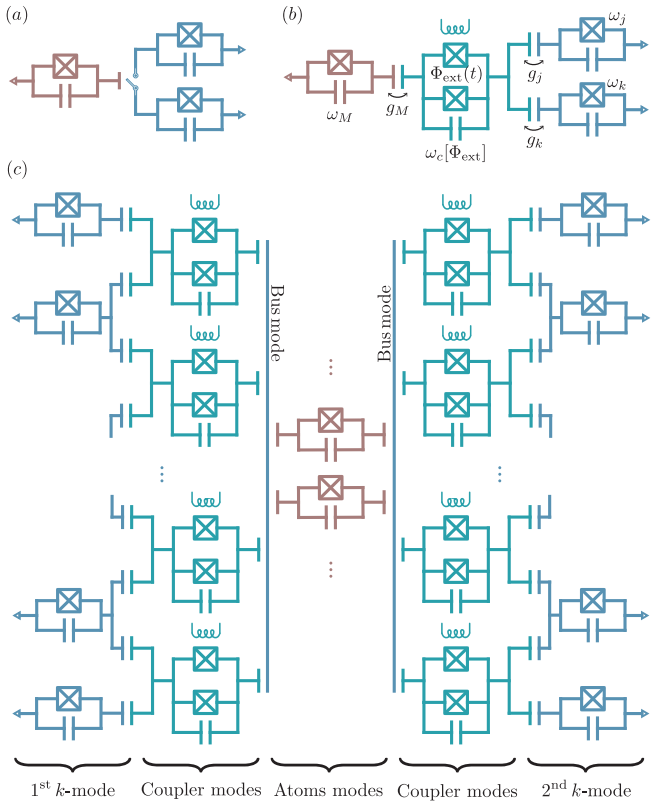

FIG. 8. Variational quantum-optics (VQO) superconducting processor. (a) Schematic of a controlled-exchange gate between three transmon qubits. The qubit in red plays the role of the atom register, controlling the switch on and off of an exchange interaction between two neighboring transmons belonging to the k-mode register. (b) Superconducting-qubit implementation of the concept in (a). A tunable-coupler (light green) is introduced to mediate the interaction between the atom and k-mode registers. (c) Device for the VQO simulation of the ultrastrong interaction between N atoms (in red) and two bosonic modes (light blue, left and right). A superconducting resonator acting as a quantum bus is require to enable long-range interactions between the atoms and the coupler modes. Moreover, the bus mode enables dispersive two-qubit gates between the atom qubits if made frequency-tunable [13], which are required for state preparation in the case of $N>1$.

to remove the need for frequency tunability of the qubit modes resulting in greater coherence times. Standard circuit quantization of the unit-cell device in Fig. 8 (b), followed by a two-level and rotating-wave approximations leads to the Hamiltonian

$$\begin{aligned} H = &\frac{\omega^{\rm b}_c[\Phi_{\rm ext}]}{2}\sigma^z_c+\frac{\omega^{\rm b}_\nu}{2}\sigma^z_\nu+\sum_\mu\frac{\omega^{\rm b}_\mu}{2}\sigma^z_\mu \\ &+g_\nu(\sigma^+_\mu\sigma^-_c+\sigma^-_\mu\sigma^+_c)+\sum_\mu g_\mu(\sigma^+_\mu\sigma^-_c+\sigma^-_\mu\sigma^+_c), \end{aligned} \quad (18)$$

where $\omega^{\rm b}_c[\Phi_{\rm ext}]$ denotes the bare frequency of the tunable coupler, $\omega^{\rm b}_\nu$ is the bare frequency of the atom qubit, $\{\omega^{\rm b}_\mu\}$ are the bare frequencies of two neighboring qubits

in the k-mode register and $\{g_\nu, g_\mu\}$ are the respective coupling strengths between such qubits and the coupler. We assume that the coupler frequency can be tuned and modulated by a external magnetic flux $\Phi_{\rm ext}$ through the coupler's SQUID loop.

Following [12], we perform the adiabatic elimination of the coupler mode by means of a Schrieffer-Wolff transformation in the dispersive regime $g_\nu \ll \Delta^{\rm b}_\nu[\Phi_{\rm ext}]$, $g_\mu \ll \Delta^{\rm b}_\mu[\Phi_{\rm ext}]$, where $\Delta^{\rm b}_\beta[\Phi_{\rm ext}] = \omega^{\rm b}_\beta - \omega^{\rm b}_c[\Phi_{\rm ext}]$. Assuming that the coupler mode remains in its groundstate at all times, we derive an effective Hamiltonian of the form $H_{\rm eff} = H_{\rm ideal} + H_{\rm err}$, where $H_{\rm ideal}$ is the ideal interaction model given in Eq. (14) with frequency parameters $\omega_\nu = \omega^{\rm b}_\nu + g^2_\nu/\Delta^{\rm b}_\nu[\Phi_{\rm ext}]$, $\omega_\mu = \omega^{\rm b}_\mu + g^2_\mu/\Delta^{\rm b}_\mu[\Phi_{\rm ext}]$ and flux-tunable coupling strengths

$$\Omega_\mu[\Phi_{\rm ext}(t)] = \frac{g_\mu g_\nu}{2}\frac{(\Delta^{\rm b}_\mu[\Phi_{\rm ext}] + \Delta^{\rm b}_\nu[\Phi_{\rm ext}])}{\Delta^{\rm b}_\mu[\Phi_{\rm ext}]\Delta^{\rm b}_\nu[\Phi_{\rm ext}]}. \qquad (19)$$

$H_{\rm err}$ is a spurious off-resonant term coupling directly the two qubits of the k-mode register. Implementation of the interaction model in Eq. (16) from $H_{\rm eff}$ requires a two-tone modulation of $\Phi_{\rm ext}(t)$ at frequencies $\omega_\mu - \omega_\nu + \delta_\mu$ for $\mu \in [n_k, n_k+1]$. We observe that the effect of $H_{\rm err}$ can be exactly canceled by tuning the qubits to the destructive-interference condition $\Delta^{\rm b}_{n_k}[\Phi_{\rm ext}] = -\Delta^{\rm b}_{n_k+1}[\Phi_{\rm ext}]$. However, this also leads to a small interaction strength for the controlled-exchange operation. A better alternative is to consider the two k-mode qubits being coupled to an additional ancillary mode whose frequency is chosen to counteract the effect of $H_{\rm err}$. Moreover, if the k-mode qubits are properly detuned the residual interaction only leads to a frequency renormalization of the drive condition above and to an off-resonant controlled-exchange interaction between ν and n_k (n_k+1) via n_k+1 (n_k) which can be dropped by means of a RWA. As anticipated, we find that for typical circuit parameters and without optimization, the gate-interaction rate ξ_{n_k} can reach values in the range of $0.1 - 0.5$ MHz, assuming a modulation amplitude between $25 - 50\%$ of Ω^0_μ [12]. Further improvements on the speed of the gate might be enabled by optimization of the proposed circuit, the use of other possible coupling schemes implementing Eq. (16), or optimal control techniques [14].

The proposed implementation may be scaled-up to a larger number qubits, as shown schematically in Fig. 8 (c) for the case of N atoms and two k-modes. A cavity bus mode is used to enable long-range interactions between the tunable couplers and the qubits playing the role of atoms registers. Moreover, the bus mode allows for the implementation of two-qubit gates between the atom qubits, which are necessary to initialize the polaron variational form for $N > 1$. We note that the controlled-exchange gates can be parallelized over even and odd qubits of the k-mode registers. Finally, we stress that scaling-up to a larger number of qubits entails issues that are beyond the scope of the present work and require to be examined in greater detail. The analysis of this section, however, provides a path forward towards the implementation of variational-quantum optics algorithms on special-purpose hardware.

[1] R. Silbey and R. A. Harris, The Journal of Chemical Physics **80**, 2615 (1984).

[2] T. Shi, Y. Chang, and J. J. García-Ripoll, Physical Review Letters **120**, 153602 (2018).

[3] J. D. Whitfield, J. Biamonte, and A. Aspuru-Guzik, Molecular Physics **109**, 735 (2011).

[4] G. Dìaz-Camacho, A. Bermudez, and J. J. García-Ripoll, Physical Review A **93**, 043843 (2016).

[5] A. Kandala, A. Mezzacapo, K. Temme, M. Takita, M. Brink, J. M. Chow, and J. M. Gambetta, Nature **549**, 242 (2017).

[6] A. Kandala, K. Temme, A. D. Córcoles, A. Mezzacapo, J. M. Chow, and J. M. Gambetta, Nature **567**, 491 (2019).

[7] G. Aleksandrowicz, T. Alexander, P. Barkoutsos, L. Bello, Y. Ben-Haim, D. Bucher, F. J. Cabrera-Hernádez, J. Carballo-Franquis, A. Chen, C.-F. Chen, J. M. Chow, A. D. Córcoles-Gonzales, A. J. Cross, A. Cross, J. Cruz-Benito, C. Culver, S. D. L. P. González, E. D. L. Torre, D. Ding, E. Dumitrescu, I. Duran, P. Eendebak, M. Everitt, I. F. Sertage, A. Frisch, A. Fuhrer, J. Gambetta, B. G. Gago, J. Gomez-Mosquera, D. Greenberg, I. Hamamura, V. Havlicek, J. Hellmers, Ł. Herok, H. Horii, S. Hu, T. Imamichi, T. Itoko, A. Javadi-Abhari, N. Kanazawa, A. Karazeev, K. Krsulich, P. Liu, Y. Luh, Y. Maeng, M. Marques, F. J. Martín-Fernández, D. T. McClure, D. McKay, S. Meesala, A. Mezzacapo, N. Moll, D. M. Rodríguez, G. Nannicini, P. Nation, P. Ollitrault, L. J. O'Riordan, H. Paik, J. Pérez, A. Phan, M. Pistoia, V. Prutyanov, M. Reuter, J. Rice, A. R. Davila, R. H. P. Rudy, M. Ryu, N. Sathaye, C. Schnabel, E. Schoute, K. Setia, Y. Shi, A. Silva, Y. Siraichi, S. Sivarajah, J. A. Smolin, M. Soeken, H. Takahashi, I. Tavernelli, C. Taylor, P. Taylour, K. Trabing, M. Treinish, W. Turner, D. Vogt-Lee, C. Vuillot, J. A. Wildstrom, J. Wilson, E. Winston, C. Wood, S. Wood, S. Wörner, I. Y. Akhalwaya, and C. Zoufal, "Qiskit: An open-source framework for quantum computing," (2019).

[8] K. Temme, S. Bravyi, and J. M. Gambetta, Physical Review Letters **119**, 180509 (2017).

[9] J. R. Johansson, P. D. Nation, and F. Nori, Computer Physics Communications **184**, 1234 (2013).

[10] A. Macridin, P. Spentzouris, J. Amundson, and R. Harnik, Physical Review Letters **121**, 110504 (2018).

[11] A. Macridin, P. Spentzouris, J. Amundson, and R. Harnik, Physical Review A **98**, 042312 (2018).

[12] D. C. McKay, S. Filipp, A. Mezzacapo, E. Magesan, J. M. Chow, and J. M. Gambetta, Physical Review Applied **6**, 064007 (2016).

[13] A. Blais, J. Gambetta, A. Wallraff, D. I. Schuster, S. M. Girvin, M. H. Devoret, and R. J. Schoelkopf, Physical Review A **75**, 032329 (2007).

[14] P. J. Liebermann, P.-L. Dallaire-Demers, and F. K. Wilhelm, arXiv preprint arXiv:1701.07870 (2017).

Bibliography

[1] Caldeira, A. and Leggett, A. J. *Annals of physics* **149**(2), 374–456 (1983).

[2] Leggett, A. J. *Journal of Physics: Condensed Matter* **14**(15), R415 (2002).

[3] Martinis, J. M. and Osborne, K. *arXiv preprint cond-mat/0402415* (2004).

[4] Girvin, S. M. *Quantum Machines: Measurement and Control of Engineered Quantum Systems* , 113 (2011).

[5] Devoret, M. H. et al. *Les Houches, Session LXIII* **7**(8) (1995).

[6] Blais, A., Huang, R.-S., Wallraff, A., Girvin, S. M., and Schoelkopf, R. J. *Physical Review A* **69**(6), 062320 (2004).

[7] Wallraff, A., Schuster, D. I., Blais, A., Frunzio, L., Huang, R.-S., Majer, J., Kumar, S., Girvin, S. M., and Schoelkopf, R. J. *Nature* **431**(7005), 162 (2004).

[8] Martinis, J. M., Devoret, M. H., and Clarke, J. *Physical Review Letters* **55**(15), 1543 (1985).

[9] Shnirman, A., Schön, G., and Hermon, Z. *Physical Review Letters* **79**(12), 2371 (1997).

[10] Bouchiat, V., Vion, D., Joyez, P., Esteve, D., and Devoret, M. *Physica Scripta* **1998**(T76), 165 (1998).

[11] Bocko, M. F., Herr, A. M., and Feldman, M. J. *IEEE Transactions on Applied Superconductivity* **7**(2), 3638–3641 (1997).

[12] Nakamura, Y., Pashkin, Y. A., and Tsai, J. S. *Nature* **398**(6730), 786 (1999).

[13] Mooij, J., Orlando, T., Levitov, L., Tian, L., Van der Wal, C. H., and Lloyd, S. *Science* **285**(5430), 1036–1039 (1999).

[14] Martinis, J. M., Nam, S., Aumentado, J., and Urbina, C. *Physical Review Letters* **89**(11), 117901 (2002).

[15] Vion, D., Aassime, A., Cottet, A., Joyez, P., Pothier, H., Urbina, C., Esteve, D., and Devoret, M. H. *Science* **296**(5569), 886–889 (2002).

[16] Blais, A., Gambetta, J., Wallraff, A., Schuster, D. I., Girvin, S. M., Devoret, M. H., and Schoelkopf, R. J. *Physical Review A* **75**(3), 032329 (2007).

[17] Raimond, J.-M., Brune, M., and Haroche, S. *Reviews of Modern Physics* **73**(3), 565 (2001).

[18] Haroche, S. and Raimond, J.-M. *Exploring the quantum: atoms, cavities, and photons*. Oxford university press, (2006).

[19] Day, P. K., LeDuc, H. G., Mazin, B. A., Vayonakis, A., and Zmuidzinas, J. *Nature* **425**(6960), 817 (2003).

[20] Buisson, O. and Hekking, F. In *Macroscopic Quantum Coherence and Quantum Computing*, 137–145. Springer (2001).

[21] You, J., Tsai, J. S., and Nori, F. *Physical Review Letters* **89**(19), 197902 (2002).

[22] Yang, C.-P., Chu, S.-I., and Han, S. *Physical Review A* **67**(4), 042311 (2003).

[23] Blais, A., van den Brink, A. M., and Zagoskin, A. M. *Physical review letters* **90**(12), 127901 (2003).

[24] Plastina, F. and Falci, G. *Physical Review B* **67**(22), 224514 (2003).

[25] Sornborger, A. T., Cleland, A. N., and Geller, M. R. *Physical Review A* **70**(5), 052315 (2004).

[26] Childress, L., Sørensen, A., and Lukin, M. D. *Physical Review A* **69**(4), 042302 (2004).

[27] Kjaergaard, M., Schwartz, M. E., Braumüller, J., Krantz, P., Wang, J. I.-J., Gustavsson, S., and Oliver, W. D. *arXiv preprint arXiv:1905.13641* (2019).

[28] Walter, T., Kurpiers, P., Gasparinetti, S., Magnard, P., Potočnik, A., Salathé, Y., Pechal, M., Mondal, M., Oppliger, M., Eichler, C., et al. *Physical Review Applied* **7**(5), 054020 (2017).

[29] Petersson, K. D., McFaul, L. W., Schroer, M. D., Jung, M., Taylor, J. M., Houck, A. A., and Petta, J. R. *Nature* **490**(7420), 380 (2012).

[30] Aasen, D., Hell, M., Mishmash, R. V., Higginbotham, A., Danon, J., Leijnse, M., Jespersen, T. S., Folk, J. A., Marcus, C. M., Flensberg, K., et al. *Physical Review X* **6**(3), 031016 (2016).

[31] Arute, F., Arya, K., Babbush, R., Bacon, D., Bardin, J. C., Barends, R., Biswas, R., Boixo, S., Brandao, F. G., Buell, D. A., et al. *Nature* **574**(7779), 505–510 (2019).

[32] Rigetti, C., Gambetta, J. M., Poletto, S., Plourde, B., Chow, J. M., Córcoles, A., Smolin, J. A., Merkel, S. T., Rozen, J., Keefe, G. A., et al. *Physical Review B* **86**(10), 100506 (2012).

[33] Paik, H., Schuster, D., Bishop, L. S., Kirchmair, G., Catelani, G., Sears, A., Johnson, B., Reagor, M., Frunzio, L., Glazman, L., et al. *Physical Review Letters* **107**(24), 240501 (2011).

[34] Boissonneault, M., Gambetta, J. M., and Blais, A. *Physical Review A* **79**(1), 013819 (2009).

[35] Zhu, G., Ferguson, D. G., Manucharyan, V. E., and Koch, J. *Physical Review B* **87**(2), 024510 (2013).

[36] Theis, L. and Wilhelm, F. *Physical Review A* **95**(2), 022314 (2017).

[37] Manucharyan, V. E., Masluk, N. A., Kamal, A., Koch, J., Glazman, L. I., and Devoret, M. H. *Physical Review B* **85**(2), 024521 (2012).

[38] Gambetta, J., Blais, A., Boissonneault, M., Houck, A. A., Schuster, D., and Girvin, S. M. *Physical Review A* **77**(1), 012112 (2008).

[39] Schuster, D., Wallraff, A., Blais, A., Frunzio, L., Huang, R.-S., Majer, J., Girvin, S., Schoelkopf, and RJ. *Physical Review Letters* **94**(12), 123602 (2005).

[40] Wallraff, A., Schuster, D., Blais, A., Frunzio, L., Majer, J., Devoret, M., Girvin, S., and Schoelkopf, R. *Physical Review Letters* **95**(6), 060501 (2005).

[41] Abdelhafez, M., Baker, B., Gyenis, A., Mundada, P., Houck, A. A., Schuster, D., and Koch, J. *arXiv preprint arXiv:1908.07637* (2019).

[42] Burkard, G., Koch, R. H., and DiVincenzo, D. P. *Physical Review B* **69**(6), 064503 (2004).

[43] Nigg, S. E., Paik, H., Vlastakis, B., Kirchmair, G., Shankar, S., Frunzio, L., Devoret, M., Schoelkopf, R., and Girvin, S. *Physical Review Letters* **108**(24), 240502 (2012).

[44] Ulrich, J. and Hassler, F. *Physical Review B* **94**(9), 094505 (2016).

[45] Pop, I. M., Geerlings, K., Catelani, G., Schoelkopf, R. J., Glazman, L. I., and Devoret, M. H. *Nature* **508**(7496), 369 (2014).

[46] Ithier, G., Collin, E., Joyez, P., Meeson, P., Vion, D., Esteve, D., Chiarello, F., Shnirman, A., Makhlin, Y., Schriefl, J., et al. *Physical Review B* **72**(13), 134519 (2005).

[47] Gardiner, C., Zoller, P., and Zoller, P. *Quantum noise: a handbook of Markovian and non-Markovian quantum stochastic methods with applications to quantum optics*, volume 56. Springer Science & Business Media, (2004).

[48] Lescanne, R., Verney, L., Ficheux, Q., Devoret, M. H., Huard, B., Mirrahimi, M., and Leghtas, Z. *Physical Review Applied* **11**(1), 014030 (2019).

[49] Verney, L., Lescanne, R., Devoret, M. H., Leghtas, Z., and Mirrahimi, M. *Physical Review Applied* **11**(2), 024003 (2019).

[50] Amin, M. H., Averin, D. V., and Nesteroff, J. A. *Physical Review A* **79**(2), 022107 (2009).

[51] Breuer, H.-P., Petruccione, F., et al. *The theory of open quantum systems*. Oxford University Press on Demand, (2002).

[52] Bialczak, R. C., McDermott, R., Ansmann, M., Hofheinz, M., Katz, N., Lucero, E., Neeley, M., O'Connell, A., Wang, H., Cleland, A., et al. *Physical Review Letters* **99**(18), 187006 (2007).

[53] Koch, R. H., DiVincenzo, D. P., and Clarke, J. *Physical Review Letters* **98**(26), 267003 (2007).

[54] Schreier, J., Houck, A. A., Koch, J., Schuster, D. I., Johnson, B., Chow, J., Gambetta, J. M., Majer, J., Frunzio, L., Devoret, M. H., et al. *Physical Review B* **77**(18), 180502 (2008).

[55] Yan, F., Gustavsson, S., Kamal, A., Birenbaum, J., Sears, A. P., Hover, D., Gudmundsen, T. J., Rosenberg, D., Samach, G., Weber, S., et al. *Nature communications* **7**, 12964 (2016).

[56] Koch, J., Terri, M. Y., Gambetta, J., Houck, A. A., Schuster, D., Majer, J., Blais, A., Devoret, M. H., Girvin, S. M., and Schoelkopf, R. J. *Physical Review A* **76**(4), 042319 (2007).

[57] Slichter, D., Vijay, R., Weber, S., Boutin, S., Boissonneault, M., Gambetta, J. M., Blais, A., and Siddiqi, I. *Physical Review Letters* **109**(15), 153601 (2012).

[58] Devoret, M. H. and Schoelkopf, R. J. *Science* **339**(6124), 1169–1174 (2013).

[59] Gu, X., Kockum, A. F., Miranowicz, A., Liu, Y.-x., and Nori, F. *Physics Reports* **718**, 1–102 (2017).

[60] Martinis, J. M., Cooper, K. B., McDermott, R., Steffen, M., Ansmann, M., Osborn, K., Cicak, K., Oh, S., Pappas, D. P., Simmonds, R. W., et al. *Physical Review Letters* **95**(21), 210503 (2005).

[61] Geerlings, K., Shankar, S., Edwards, E., Frunzio, L., Schoelkopf, R., and Devoret, M. *Applied Physics Letters* **100**(19), 192601 (2012).

[62] Barends, R., Wenner, J., Lenander, M., Chen, Y., Bialczak, R. C., Kelly, J., Lucero, E., O'Malley, P., Mariantoni, M., Sank, D., et al. *Applied Physics Letters* **99**(11), 113507 (2011).

[63] Córcoles, A. D., Chow, J. M., Gambetta, J. M., Rigetti, C., Rozen, J. R., Keefe, G. A., Beth Rothwell, M., Ketchen, M. B., and Steffen, M. *Applied Physics Letters* **99**(18), 181906 (2011).

[64] Reagor, M., Paik, H., Catelani, G., Sun, L., Axline, C., Holland, E., Pop, I. M., Masluk, N. A., Brecht, T., Frunzio, L., et al. *Applied Physics Letters* **102**(19), 192604 (2013).

[65] Manucharyan, V. E., Koch, J., Glazman, L. I., and Devoret, M. H. *Science* **326**(5949), 113–116 (2009).

[66] Brooks, P., Kitaev, A., and Preskill, J. *Physical Review A* **87**(5), 052306 (2013).

[67] Gross, R., Marx, A., and Einzel, D. *Journal of superconductivity and novel magnetism* **19**(3-5), 331–340 (2006).

[68] Koch, J., Manucharyan, V., Devoret, M., and Glazman, L. *Physical Review Letters* **103**(21), 217004 (2009).

[69] Manucharyan, V. E. *Superinductance*. PhD thesis, Yale University, (2012).

[70] Houck, A. A., Koch, J., Devoret, M. H., Girvin, S. M., and Schoelkopf, R. J. *Quantum Information Processing* **8**(2-3), 105–115 (2009).

[71] Christensen, B., Wilen, C., Opremcak, A., Nelson, J., Schlenker, F., Zimonick, C., Faoro, L., Ioffe, L., Rosen, Y., DuBois, J., et al. *arXiv preprint arXiv:1905.13712* (2019).

[72] Annunziata, A. J., Santavicca, D. F., Frunzio, L., Catelani, G., Rooks, M. J., Frydman, A., and Prober, D. E. *Nanotechnology* **21**(44), 445202 (2010).

[73] Hazard, T., Gyenis, A., Di Paolo, A., Asfaw, A., Lyon, S. A., Blais, A., and Houck, A. A. *Physical Review Letters* **122**(1), 010504 (2019).

[74] Masluk, N. A., Pop, I. M., Kamal, A., Minev, Z. K., and Devoret, M. H. *Physical review letters* **109**(13), 137002 (2012).

[75] Greiner, W. and Reinhardt, J. *Field quantization*. Springer Science & Business Media, (2013).

[76] Pechenezhskiy, I. V., Mencia, R. A., Nguyen, L. B., Lin, Y.-H., and Manucharyan, V. E. *arXiv preprint arXiv:1907.02937* (2019).

[77] Bell, M., Sadovskyy, I., Ioffe, L., Kitaev, A. Y., and Gershenson, M. *Physical Review Letters* **109**(13), 137003 (2012).

[78] Maleeva, N., Grünhaupt, L., Klein, T., Levy-Bertrand, F., Dupre, O., Calvo, M., Valenti, F., Winkel, P., Friedrich, F., Wernsdorfer, W., et al. *Nature communications* **9**(1), 3889 (2018).

[79] Niepce, D., Burnett, J., and Bylander, J. *Physical Review Applied* **11**(4), 044014 (2019).

[80] Grünhaupt, L., Spiecker, M., Gusenkova, D., Maleeva, N., Skacel, S. T., Takmakov, I., Valenti, F., Winkel, P., Rotzinger, H., Wernsdorfer, W., et al. *Nature materials* , 1 (2019).

[81] Kamenov, P., Lu, W.-S., Kalashnikov, K., DiNapoli, T., Bell, M. T., and Gershenson, M. E. *arXiv preprint arXiv:1910.00996* (2019).

[82] Kitaev, A. *arXiv preprint cond-mat/0609441* (2006).

[83] Cottet, A. PhD thesis, Universite Paris VI, (2002).

[84] Motzoi, F., Gambetta, J. M., Rebentrost, P., and Wilhelm, F. K. *Physical Review Letters* **103**(11), 110501 (2009).

[85] Chow, J. M., DiCarlo, L., Gambetta, J. M., Motzoi, F., Frunzio, L., Girvin, S. M., and Schoelkopf, R. J. *Physical Review A* **82**(4), 040305 (2010).

[86] Motzoi, F., Gambetta, J. M., Merkel, S., and Wilhelm, F. *Physical Review A* **84**(2), 022307 (2011).

[87] Khaneja, N., Reiss, T., Kehlet, C., Schulte-Herbrüggen, T., and Glaser, S. J. *Journal of magnetic resonance* **172**(2), 296–305 (2005).

[88] Lin, Y.-H., Nguyen, L. B., Grabon, N., San Miguel, J., Pankratova, N., and Manucharyan, V. E. *Physical Review Letters* **120**(15), 150503 (2018).

[89] Earnest, N., Chakram, S., Lu, Y., Irons, N., Naik, R. K., Leung, N., Ocola, L., Czaplewski, D. A., Baker, B., Lawrence, J., et al. *Physical Review Letters* **120**(15), 150504 (2018).

[90] Nguyen, L. B., Lin, Y.-H., Somoroff, A., Mencia, R., Grabon, N., and Manucharyan, V. E. *arXiv preprint arXiv:1810.11006* (2018).

[91] Nesterov, K. N., Pechenezhskiy, I. V., Wang, C., Manucharyan, V. E., and Vavilov, M. G. *Physical Review A* **98**(3), 030301 (2018).

[92] Ferguson, D. G., Houck, A. A., and Koch, J. *Physical Review X* **3**(1), 011003 (2013).

[93] Viola, G. and Catelani, G. *Physical Review B* **92**(22), 224511 (2015).

[94] Catelani, G., Schoelkopf, R. J., Devoret, M. H., and Glazman, L. I. *Physical Review B* **84**(6), 064517 (2011).

[95] Kerman, A. J. *Physical Review Letters* **104**(2), 027002 (2010).

[96] Schuster, D., Houck, A. A., Schreier, J., Wallraff, A., Gambetta, J., Blais, A., Frunzio, L., Majer, J., Johnson, B., Devoret, M., et al. *Nature* **445**(7127), 515 (2007).

[97] Majer, J., Chow, J., Gambetta, J., Koch, J., Johnson, B., Schreier, J., Frunzio, L., Schuster, D., Houck, A. A., Wallraff, A., et al. *Nature* **449**(7161), 443 (2007).

[98] Di Paolo, A., Grimsmo, A. L., Groszkowski, P., Koch, J., and Blais, A. *New Journal of Physics* **21**(4), 043002 (2019).

[99] Dempster, J. M., Fu, B., Ferguson, D. G., Schuster, D., and Koch, J. *Physical Review B* **90**(9), 094518 (2014).

[100] Devoret, M. H. Personal communication, (2017).

[101] Groszkowski, P., Di Paolo, A., Grimsmo, A., Blais, A., Schuster, D., Houck, A. A., and Koch, J. *New Journal of Physics* **20**(4), 043053 (2018).

[102] Bertet, P., Chiorescu, I., Burkard, G., Semba, K., Harmans, C., DiVincenzo, D. P., and Mooij, J. *Physical Review Letters* **95**(25), 257002 (2005).

[103] Clerk, A. and Utami, D. W. *Physical Review A* **75**(4), 042302 (2007).

[104] Tian, L. *Physical Review B* **79**(19), 193407 (2009).

[105] Gyenis, A., Mundada, P. S., Di Paolo, A., Hazard, T. M., You, X., Schuster, D. I., Koch, J., Blais, A., and Houck, A. A. *arXiv preprint arXiv:1910.07542* (2019).

[106] Baur, M., Filipp, S., Bianchetti, R., Fink, J., Göppl, M., Steffen, L., Leek, P., Blais, A., and Wallraff, A. *Physical Review Letters* **102**(24), 243602 (2009).

[107] Bourassa, J., Beaudoin, F., Gambetta, J. M., and Blais, A. *Physical Review A* **86**(1), 013814 (2012).

[108] Minev, Z. K. *arXiv preprint arXiv:1902.10355* (2019).

[109] Solgun, F., Abraham, D. W., and DiVincenzo, D. P. *Physical Review B* **90**(13), 134504 (2014).

[110] Solgun, F., DiVincenzo, D. P., and Gambetta, J. M. *IEEE Transactions on Microwave Theory and Techniques* **67**(3), 928–948 (2019).

[111] Smith, W., Kou, A., Vool, U., Pop, I., Frunzio, L., Schoelkopf, R., and Devoret, M. *Physical Review B* **94**(14), 144507 (2016).

[112] Mortensen, H. L., Mølmer, K., and Andersen, C. K. *Physical Review A* **94**(5), 053817 (2016).

[113] Gely, M. F., Parra-Rodriguez, A., Bothner, D., Blanter, Y. M., Bosman, S. J., Solano, E., and Steele, G. A. *Physical Review B* **95**(24), 245115 (2017).

[114] Parra-Rodriguez, A., Rico, E., Solano, E., and Egusquiza, I. *Quantum Science and Technology* **3**(2), 024012 (2018).

[115] Grimsmo, A. L. and Blais, A. *npj Quantum Information* **3**(1), 20 (2017).

[116] Kerman, A. J., Dauler, E. A., Yang, J. K., Rosfjord, K. M., Anant, V., Berggren, K. K., Gol'tsman, G. N., and Voronov, B. M. *Applied Physics Letters* **90**(10), 101110 (2007).

[117] Santavicca, D. F., Adams, J. K., Grant, L. E., McCaughan, A. N., and Berggren, K. K. *Journal of Applied Physics* **119**(23), 234302 (2016).

[118] Eom, B. H., Day, P. K., LeDuc, H. G., and Zmuidzinas, J. *Nature Physics* **8**(8), 623 (2012).

[119] Vissers, M. R., Erickson, R. P., Ku, H.-S., Vale, L., Wu, X., Hilton, G., and Pappas, D. P. *Applied Physics Letters* **108**(1), 012601 (2016).

[120] Chaudhuri, S., Li, D., Irwin, K., Bockstiegel, C., Hubmayr, J., Ullom, J., Vissers, M., and Gao, J. *Applied Physics Letters* **110**(15), 152601 (2017).

[121] Peltonen, J., Coumou, P., Peng, Z., Klapwijk, T., Tsai, J. S., and Astafiev, O. *Scientific reports* **8**(1), 1–8 (2018).

[122] Macklin, C., O'Brien, K., Hover, D., Schwartz, M., Bolkhovsky, V., Zhang, X., Oliver, W., and Siddiqi, I. *Science* **350**(6258), 307–310 (2015).

[123] Kuzmin, R., Mencia, R., Grabon, N., Mehta, N., Lin, Y.-H., and Manucharyan, V. E. *Nature Physics* , 1 (2019).

[124] Weiss, D., Li, A. C., Ferguson, D., and Koch, J. *arXiv preprint arXiv:1908.04615* (2019).

[125] Poulin, D., Qarry, A., Somma, R., and Verstraete, F. *Physical Review Letters* **106**(17), 170501 (2011).

[126] Peschel, I., Wang, X., and Kaulke, M. *Density-Matrix Renormalization: A New Numerical Method in Physics Lectures of a Seminar and Workshop Held at the Max-Planck-Institut Für Physik Komplexer Systeme Dresden, Germany, August 24th to September 18th, 1998*. Springer, (1999).

[127] Press, W. H., Teukolsky, S. A., Vetterling, W. T., and Flannery, B. P. *Numerical recipes in Fortran 77: The art of scientific computing*, volume 2. Cambridge university press Cambridge, (1992).

[128] Schollwöck, U. *Annals of Physics* **326**(1), 96–192 (2011).

[129] Verstraete, F. and Cirac, J. I. *Physical Review B* **73**(9), 094423 (2006).

[130] White, S. R. *Physical Review Letters* **69**(19), 2863 (1992).

[131] White, S. R. *Physical Review B* **48**(14), 10345 (1993).

[132] Verstraete, F. and Cirac, J. I. *arXiv preprint cond-mat/0407066* (2004).

[133] Vidal, G. *Physical Review Letters* **99**(22), 220405 (2007).

[134] Baker, T. E. et al. *manuscript in preparation* (2019).